

ornl

ORNL/Sub/89-SC674/1/V1

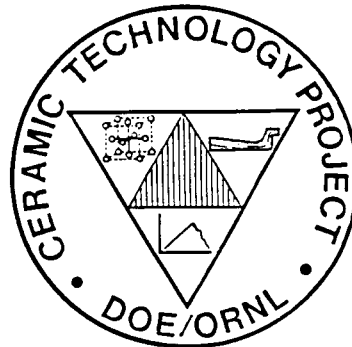
**OAK RIDGE
NATIONAL
LABORATORY**

MARTIN MARIETTA

Life Prediction Methodology
for Ceramic Components of
Advanced Heat Engines
Phase 1

J. C. Cuccio, P. Brehm, H. T. Fang, J. Hartman,
W. Meade, M. N. Menon, A. Peralta, J. Z. Song,
T. Strangman, J. Wade, J. Wimmer, and D. C. Wu

CERAMIC TECHNOLOGY PROJECT



Prepared by AlliedSignal Engines
2739 E. Washington Street
Phoenix, Arizona

MANAGED BY
MARTIN MARIETTA ENERGY SYSTEMS, INC.
FOR THE UNITED STATES
DEPARTMENT OF ENERGY

DISCLAIMER

This report was prepared as an account of work sponsored by an agency of the United States Government. Neither the United States Government nor any agency Thereof, nor any of their employees, makes any warranty, express or implied, or assumes any legal liability or responsibility for the accuracy, completeness, or usefulness of any information, apparatus, product, or process disclosed, or represents that its use would not infringe privately owned rights. Reference herein to any specific commercial product, process, or service by trade name, trademark, manufacturer, or otherwise does not necessarily constitute or imply its endorsement, recommendation, or favoring by the United States Government or any agency thereof. The views and opinions of authors expressed herein do not necessarily state or reflect those of the United States Government or any agency thereof.

DISCLAIMER

Portions of this document may be illegible in electronic image products. Images are produced from the best available original document.

This report has been reproduced directly from the best available copy.

Available to DOE and DOE contractors from the Office of Scientific and Technical Information, P.O. Box 62, Oak Ridge, TN 37831; prices available from (615) 576-8401, FTS 626-8401.

Available to the public from the National Technical Information Service, U.S. Department of Commerce, 5285 Port Royal Rd., Springfield, VA 22161.

This report was prepared as an account of work sponsored by an agency of the United States Government. Neither the United States Government nor any agency thereof, nor any of their employees, makes any warranty, express or implied, or assumes any legal liability or responsibility for the accuracy, completeness, or usefulness of any information, apparatus, product, or process disclosed, or represents that its use would not infringe privately owned rights. Reference herein to any specific commercial product, process, or service by trade name, trademark, manufacturer, or otherwise, does not necessarily constitute or imply its endorsement, recommendation, or favoring by the United States Government or any agency thereof. The views and opinions of authors expressed herein do not necessarily state or reflect those of the United States Government or any agency thereof.

LIFE PREDICTION METHODOLOGY
FOR CERAMIC COMPONENTS OF
ADVANCED HEAT ENGINES

Phase 1

J. C. Cuccio, P. Brehm, H. T. Fang, J. Hartman,
W. Meade, M. N. Menon, A. Peralta, J. Z. Song,
T. Strangman, J. Wade, J. Wimmer, and D. C. Wu

Date Published: March 1995

VOLUME ONE - FINAL REPORT

Prepared by
AlliedSignal Engines
2739 E. Washington Street
Phoenix, Arizona
Subcontract No. 62X-SC674C

Funded by
Propulsion System Materials Program
Office of Transportation Technologies
the Assistant Secretary for
Energy Efficiency and Renewable Energy
U.S. Department of Energy
EE 51 05 00 0

for
OAK RIDGE NATIONAL LABORATORY
Oak Ridge, Tennessee 37831-6285
managed by
MARTIN MARIETTA ENERGY SYSTEMS, INC.
for the
U.S. DEPARTMENT OF ENERGY
under Contract DE-AC05-84OR21400



MASTER

DISTRIBUTION OF THIS DOCUMENT IS UNLIMITED

DKS

ACKNOWLEDGEMENTS

The work presented in this report was performed by AlliedSignal Engines, Phoenix, Arizona as part of the Life Prediction Methodology for Ceramic Components of Advanced Heat Engines Program funded by the U.S. Department of Energy (DOE) and administered by Oak Ridge National Laboratory (ORNL) under Contract No. 86X-SC674C, WBS Element 3.2.2.3. The ORNL Program Monitor was Dr. C. Brinkman. The AlliedSignal team included: J.C. Cuccio (Principal Investigator), P. Brehm, H.T. Fang, J. Hartman, W. Meade, M.N. Menon, A. Peralta, J.Z. Song, T. Strangman, J. Wade, J. Wimmer, and D.C. Wu. We would like to acknowledge the efforts of C. Domme, R. Schultze, and J. Smyth for administrative support, and V.E. Largesse, T. Eull, and G.A. Lucas for editorial and reporting support.

We would also like to acknowledge the test support and fruitful discussions with M. Ferber, M. Jenkins (now at the University of Washington), and A. Wereszczak at the ORNL High Temperature Materials Laboratory (HTML); and S. Wiederhorn of the National Institute of Standards and Technology (NIST). The support of Dr. V.J. Tennery, Director of ORNL-HTML, is also appreciated. Finally, we acknowledge the outstanding support of the subcontractor teams: C.A. Johnson and W. Tucker at the General Electric Corporate Research and Development Center (GE-CRDC); B. Ellingson and G. Foster at Argonne National Laboratory; D.K. Shetty and L.-Y. Chao at the University of Utah; A.S. Kim and S. Suresh at Brown University; R. Gilmore of GE-CRDC; M. Keller and J. Portaz at General Electric Aircraft Engines; S. Bradley, F. Friedrich, K. Karasek, D.J. Lee, C.W. Li, and J. Palley at AlliedSignal Research and Technology (ASR&T); and A. Nagy at the Southwest Research Institute (SWRI).

Research sponsored by the U.S. Department of Energy, Assistant Secretary for Energy Efficiency and Renewable Energy, Office of Transportation Technologies, as part of the Ceramic Technology Project of the Propulsion System Materials Program, under contract DE-AC05-84OR21400 with Martin Marietta Energy Systems, Inc.

TABLE OF CONTENTS

	Page
<u>Volume One</u>	
1.0 ABSTRACT AND CONCLUSIONS	1-1
1.1 Data Base	1-1
1.2 Behavior Models	1-1
1.3 Probabilistic Methods	1-3
1.4 Methods Confirmation	1-3
1.5 Nondestructive Evaluation (NDE)	1-5
1.6 Conclusions	1-6
References	1-7
2.0 INTRODUCTION	2-1
2.1 The Need For Life Prediction Methodology Development	2-1
2.2 Approach	2-1
2.3 Material Selection And Processing	2-1
2.4 Material Characterization	2-1
2.5 Life Prediction Methods And Verification	2-2
2.6 NDE Methods Development And Application	2-3
2.7 Appendices	2-4
3.0 MATERIAL SELECTION AND PROCESSING	3-1
3.1 Material Selection	3-1
3.2 Processing Procedures And Sequence	3-2
3.2.1 Inspection Process	3-4
3.2.2 Certification Process	3-5
3.3 Machining Study And Vendor Evaluation	3-5
3.4 Specimen Quality	3-10
3.5 Heat Treatment	3-10
4.0 MATERIAL CHARACTERIZATION	4-1
4.1 Test Matrices And Specimen Geometries	4-1
4.1.1 Test Matrix - Data Base Specimens	4-4
4.1.2 Test Matrix - Confirmatory Specimens	4-4
4.1.3 Specimen Geometries	4-5
4.1.4 Specimen Allocation	4-11
4.2 Test Procedures	4-11
4.2.1 Data Base Specimen Testing	4-12
4.2.2 Confirmatory Specimen Testing	4-18
4.2.3 Fractography	4-19
4.2.4 Microstructural Characterization	4-23

TABLE OF CONTENTS (Contd)

	<u>Page</u>
<u>Volume One (Contd)</u>	
4.3 Test Results	4-24
4.3.1 Testing	4-25
4.3.2 Fractography	4-45
4.4 Microstructural Characterization *	4-70
4.4.1 Microstructure Of The As-Received Material	4-70
4.4.2 Phase Changes In Creep	4-76
4.4.3 Creep Cavitation	4-76
4.4.4 Correlation Of Cavitation With Creep	4-81
4.4.5 Microstructure Analysis Of Oxidized Specimens	4-84
References	4-84
5.0 LIFE PREDICTION METHODS AND VERIFICATION	5-1
5.1 Material Behavior Models	5-1
5.1.1 Aging	5-1
5.1.2 Mixed-Mode Fracture/Flaw Shear-Sensitivity	5-1
5.1.3 Oxidation	5-5
5.1.4 Creep Behavior	5-6
5.1.5 Stress Rupture	5-31
5.2 Life Prediction Methods And Verification	5-57
5.2.1 Weibull Strength Model Applied To Structural Ceramics	5-57
5.2.2 Multiaxial Fracture And Anisotropic Flaw Distribution	5-58
5.2.3 Maximum Likelihood Parameter Estimation Methods	5-64
5.2.4 Confidence Bounds On Predictions And Parameter Estimates	5-82
5.2.5 Component Predictions And Size Integration	5-89
5.3 Estimation Of Strength And Life Parameters From Specimen Data	5-93
5.3.1 Material Consistency	5-93
5.3.2 Weibull Strength Parameters Estimated From Pooled Data	5-103
5.3.3 Anisotropy And Shear Sensitivity	5-117
5.3.4 Evaluation Of SCG Parameters	5-130
5.4 Confirmatory Specimen Predictions	5-142
5.4.1 Notched Tensile Specimens	5-143
5.4.2 Plate Bending and Tension-Torsion Confirmatory Specimen Testing	5-153
5.4.3 Spin Disk Test Results And Predictions	5-161
5.4.4 Prediction Summary	5-181
References	5-184

TABLE OF CONTENTS (Contd)

	<u>Page</u>
<u>Volume One (Contd)</u>	
6.0 NDE DATA METHODS DEVELOPMENT AND APPLICATION	6-1
6.1 NDE Program Objectives	6-1
6.2 NDE Reference Standards Development And Fabrication	6-3
6.2.1 Laser Drilled Standards	6-3
6.2.2 Photolithographically Etched And Bonded Standards	6-6
6.2.3 Surface Crack And Volumetrically Seeded Standards	6-7
6.3 NDE Technique Development And Calibration	6-10
6.3.1 Acoustic Microscopy Development And Calibration	6-10
6.3.2 Computed Tomography (CT) Development	6-16
6.3.3 Radiographic Inspection And Film Enhancement Development	6-19
6.4 Specimen Inspection	6-30
6.5 Data Review And Correlation	6-34
6.6 Conclusions	6-40
References	6-43
<u>Volume Two</u>	
APPENDIX I - CERAMIC TEST SPECIMEN DRAWINGS AND SCHEMATICS (8 pages)	
APPENDIX II - STUDIES OF MIXED-MODE AND BIAXIAL STRESS FRACTURE OF STRUCTURAL CERAMICS FOR ADVANCED VEHICULAR HEAT ENGINES (UNIVERSITY OF UTAH REPORT) (42 pages)	
APPENDIX III - MODE I/MODE II FRACTURE TOUGHNESS AND TENSION/TORSION FRACTURE STRENGTH OF NT154 SILICON NITRIDE (BROWN UNIVERSITY REPORT) (19 pages)	
APPENDIX IV - SUMMARY OF STRENGTH TEST RESULTS AND FRACTOGRAPHY (43 pages)	
APPENDIX V - FRACTOGRAPHY PHOTOGRAPHS (42 pages)	
APPENDIX VI - DERIVATIONS OF STATISTICAL MODELS (70 pages)	
APPENDIX VII - WEIBULL STRENGTH PLOTS FOR FAST FRACTURE TEST SPECIMENS (33 pages)	
APPENDIX VIII - SIZE FUNCTIONS (41 pages)	

LIST OF FIGURES

Figure	Title	Page
2-1	AlliedSignal Approach For Ceramic Life Prediction Methodology Development	2-2
3-1	Strength Comparison Of Candidate Ceramic Materials	3-1
3-2	Comparison Of Candidate Materials Stress Rupture Properties	3-2
3-3	Material Uniformity Was Assured By Selected Processing Methods	3-3
3-4	Test Specimens Were Processed From One Of Three Billet Geometries	3-4
3-5	Less Than 10 Percent Of The Surface Failures Were Expected In The Chamfer Areas	3-5
3-6	Failure Probabilities Were Calculated For The Five Regions Indicated	3-6
3-7	Stresses In Chamfer Region Were Modified As Shown When A Stress Concentration Of Five Percent Was Used For Corner Flaws	3-7
3-8	Predicted Percent Chamfer Failures For A Corner Stress Concentration of 1.00 (W And H Are Flexure Bar Dimensions In mm)	3-8
3-9	Predicted Percent Chamfer Failures For A Corner Stress Concentration of 1.05 (W And H Are Flexure Bar Dimensions In mm)	3-8
4-1	Test Matrix For Data Base Included 1069 Specimen Tests	4-2
4-2	Test Matrix For Confirmatory Test Specimens	4-3
4-3	Static Air Furnace Exposure Test Conditions	4-5
4-4	Notch Test Specimens Were Redesigned To Eliminate Notch Radius Surface Finish Differences	4-7
4-5	Prototype Of Early Design Notch Test Specimens Showed Unacceptable Differences In Surface Finish In The Notch Radius	4-8
4-6	Spin Disk Geometry Was Modified To Increase Maximum Volume Stress Relative To Maximum Surface Stress. Stresses Shown Are For 100,000 rpm Cold Rotation	4-9
4-7	Spin Disk Risk Analyses Show The New Geometry Has Higher Volume Failure Risk Than Area Risk And Required Test Speeds Up To 120,000 rpm	4-10
4-8	Processing Sequence Was Defined To Monitor Material Consistency	4-11
4-9	More Detailed Specimen Allocation Plan Was Devised For Cylindrical Tensile Test Specimens	4-12
4-10	Pull Rods Were Equipped With Strain Gages To Monitor Bending	4-14
4-11	Loading Configuration For Creep Measurements	4-16
4-12	Successful Precracking Was Achieved By Preloading Followed By Surface Grinding	4-17

LIST OF FIGURES (Contd)

Figure	Title	Page
4-13	AlliedSignal Room-Temperature Whirlpit Used For Ceramic Spin Disk Tests	4-20
4-14	Spin Pit Was Lined With Absorbing Material To Collect Fragments	4-21
4-15	Following A Test Burst, The Fragments Were Collected For Determination Of The Failure Origin	4-21
4-16	High-Speed Photography Verified Successful Disk Burst And Showed Possible Impacts Of Fragments Following Burst	4-22
4-17	Hot Spin Pit Layout For 2200F and 2500F Tests	4-23
4-18	Four-Point Flexural Strength Of NT154	4-26
4-19	Dependence Of Flexure Strength On Surface Machining Direction	4-26
4-20	Air Furnace Oxidation Exposures Initially Improved Strength Of Transverse Machined NT154 Specimens	4-27
4-21	Tensile Strength Of NT154 ORNL Buttonhead Specimens	4-29
4-22	Effect Of Test Machine On Failure Time	4-34
4-23	Residual Strength Of Creep-Tested Specimens	4-35
4-24	Strain Versus Time For NT154 Replicate Creep Tests At 1371C/145 MPa	4-36
4-25	Strain Versus Time For NT154 Replicate Creep Tests At 1371C/180 MPa	4-36
4-26	Strain Versus Time For NT154 Replicate Creep Tests At 1204C/375 MPa	4-37
4-27	Secondary (Minimum) Creep Rate Versus Stress At Various Replicate Test Temperatures. Note Scatter in Replicate Tests At 1371C And 1204C	4-37
4-28	Monkman-Grant Plot Of Rupture Life Data	4-38
4-29	Effects Of Aging On NT154 Tensile Creep Rate. Log-Log Plot Of Stress Versus Strain. (NIST Data By S. Wiederhorn.)	4-39
4-30	Effects Of Aging On NT154 Tensile Creep Rate. Log Strain Versus Temperature. (NIST Data By S. Wiederhorn.)	4-40
4-31	Fracture Toughness (K_{IC}) Test Results	4-41
4-32	Notch Stress Rupture Lives Versus Average Net Section Stress	4-44
4-33	Flexure Bar Failure Originating At Machining Chip On Chamfer Corner. Chips Could Be Removed By Polishing. MOR = 66.0 ksi	4-46

LIST OF FIGURES (Contd)

Figure	Title	Page
4-34	Flexure Bar Failure Originating At Machining Chip On Chamfer Corner. Chips Too Severe To Be Removed By Polishing. MOR = 134.5 ksi	4-47
4-35	Failure Origins Of Oxidized Specimens	4-48
4-36	Internal Failure Originating At Inclusion In MIL-B Flexure Bar Tested At 2100F. MOR = 105.6 ksi	4-49
4-37	(a) Closeup View Of Internal Failure Site in Figure 4-36; (b) Through (d) Fe, Ni, And Cr WDX Maps	4-50
4-38	Failure Originating From A Surface Crack Or Fold In MIL-B Flexure Bar Tested At 2300F. MOR = 72.7 ksi	4-51
4-39	Oxidation Increased Flexure Strength Of Transverse-Machined Specimens And Reduced Incidence Of Chamfer-Initiated Failures	4-53
4-40	NT154 Exhibited Logarithmic Oxidized Layer Growth Below 1371C (2500F)	4-54
4-41	Oxygen Gradient Exists At The Surface Of Oxidized Specimens	4-54
4-42	Internal Failure Of Room-Temperature Tensile Specimen Showed No Elemental Indications	4-56
4-43	Lowest Strength (336 MPa) Tensile Specimen Failed From Aluminum (Al) Surface Inclusion	4-57
4-44	Void At Failure Origin Of Tensile Specimen Tested At 2200F. WDX Fe Map (d) Shows Cluster Of Iron Particles In Void	4-58
4-45	Histogram Of Failure Locations About the Midpoint Of The Gage Section Of Tensile Creep Rupture Specimens	4-59
4-46	Optical Photomicrographs Of Fracture Surface From (a) Internal Initiation, And (b) Surface Initiation	4-60
4-47	SEM Photomicrographs Showing Subcritical Crack Growth Zones Increased With Decreasing Applied Stress. (a) 1204C/325 MPa/68 hr; (b) 1260C/295 MPa/560 hr; (c) 1371C/180 MPa/19 hr; (d) 1400C/150 MPa/80 hr	4-63
4-48	Plot Of $\sigma a^{1/2}$ Versus Temperature Shows Relatively Constant Value	4-64
4-49	SEM Photomicrograph Of Fracture Surface In Surface-Initiated Failure At 1371C (Also Shown In Figure 4-46(b))	4-64
4-50	Plot Of Stress Intensity (On Fracture) Versus Time At Edge Of SCG Region	4-65
4-51	SCG Zone In Specimen Tested At 1371C. $K_t = 1.6$	4-67
4-52	SCG Zone In Specimen Tests At 1371C. $K_t = 2.1$	4-68

LIST OF FIGURES (Contd)

<u>Figure</u>	<u>Title</u>	<u>Page</u>
4-53	Spin Disk Stress Rupture Failure From Internal Volume Flaw At 2200F	4-71
4-54	Possible Crack Generated During 50 Hours Spin Disk Stress Rupture Testing At 75,000 rpm/2200F; Fracture Initiated On Speed Increase To 84,500 rpm. (a), (b) Surface Views; (c), (d) Edge On Views	4-72
4-55	Fracture Origin And Possible Crack Generated During Initial Spin Disk Stress Rupture Testing At 71,000 rpm/100 hrs Plus 75,000 rpm/10 hours. Disk Burst Occurred At 82,000 rpm	4-73
4-56	(a) SEM Photomicrograph Of Polished And Etched Surface Shows Acicular Grains Enveloping Pockets Of Smaller Equiaxed Grains; (b) SEM Of Room-Temperature Fracture Surface Showing Acicular Grains	4-74
4-57	TEM Photomicrograph Of NT154 Microstructure, Showing Yttrium-Rich Triple-Junction Crystalline Phases (Arrows)	4-75
4-58	TEM Photomicrograph Of Amorphous Phase (Between Arrows) Separating Two Si ₃ N ₄ Grains	4-75
4-59	SEM Photomicrograph Of Two-Grain Junction Cavities In Specimens Tested At (a) 1422K/425 MPa/509 hrs; (b) 1477K/337 MPa/593 hrs; (c) 1589K/233 MPa/297 hrs; (d) 1673K/100 MPa/462 hrs	4-77
4-60	TEM Photomicrograph Of Two-Grain Junction Cavitation In A Specimen Tested At 1477K And 315 MPa. Note Lenticular Shape(s) And High Density	4-79
4-61	TEM Photomicrograph Showing An Enlarged View Of A Facet Of A Two-Grain Junction Cavity In A Specimen Tested At 1533K and 285 MPa	4-79
4-62	TEM Photomicrograph Of Triple-Junction Cavitation(s) In Specimens Tested At (a) 1477K; (b) 1589K; and (c) 1673K. Note Size Of Triple-Junction Cavities (C ₃) Relative To The Size Of Two-Grain Junction Cavities (C ₂)	4-80
4-63	Representative SEM Photomicrographs Of Polished Surfaces Of Longitudinal Sections Showing Triple-Junction Cavitation: (a) Extensive At 1673K; (b) Less Extensive At 1589K; and (c) Least Extensive At 1477K	4-81
4-64	Two-Grain Junction Cavity Size Increases With Increase In Creep Strain	4-82
4-65	Two-Grain Junction Cavity Size Increases With Increase In Secondary Creep Rate	4-83
5-1	Modes I And II Stress Intensity Factors For Mixed-Mode Fracture Of Silicon Nitride Disks In Diametral Compression Tests. C = 2.0739. (Data From D. Shetty, U. of Utah)	5-3
5-2	Modes I And III Stress Intensity Factors/Fracture Envelopes For Mixed-Mode Fracture Of Notched Bars Tested Under Tension-Torsion Loading. C=2.10	5-4
5-3	Temperature-Modified Secondary Creep Rate Plotted Against Modulus Normalized Stress	5-8

LIST OF FIGURES (Contd)

<u>Figure</u>	<u>Title</u>	<u>Page</u>
5-4	Secondary Creep Rate As A Function Of Modulus Normalized Stress	5-9
5-5	Scatter And Predictability Of Secondary Creep Rates	5-10
5-6	Schematic Of A Typical Creep Curve For A Material Showing Only Primary And Secondary Regimes	5-14
5-7	Creep Data For A NT154 Specimen Tested At 1533K And 285 MPa, With The Predicted Line From Equations [5-9] Through [5-12]	5-17
5-8	Dependence Of Temperature-Modified Initial Primary Creep Rate On Normalized Stress	5-20
5-9	Dependence Of Temperature-Modified Rate Parameter, α , On Normalized Stress	5-21
5-10	Dependence Of Temperature-Modified Primary Creep Rate At $t = 0.5t_{ps}$ On Normalized Stress	5-22
5-11	Scatter And Predictability Of Creep Rates In The Primary Regime	5-23
5-12	Two-Grain Junction Cavitation On An Acicular Grain (A) At 1477K	5-28
5-13	Schematic Of Model Explaining Change In Stress Dependence Of Creep Rate In Low- And High-Temperature Regimes	5-30
5-14	Temperature Dependence Of The Monkman-Grant Lines Correlated With An Additional Temperature Term	5-35
5-15	Comparison Of The Average Lines Predicted Versus The Unmodified Data	5-35
5-16	Stratification Of The Monkman-Grant Lines Can Be Correlated With An Additional Stress Term	5-36
5-17	Dependence Of Creep Failure Strain On Applied Stress	5-37
5-18	Monkman-Grant Plot For GN-10 Silicon Nitride	5-39
5-19	Rupture Data Plotted Versus Predictions From The Modified Monkman-Grant Relation	5-45
5-20	Model Based On OSD Parameter For Rupture Strength	5-47
5-21	Comparison Of Stress Rupture Data With Model Based On OSD Parameter	5-48
5-22	Comparison Of Rupture Strength Predictions From Modified Monkman-Grant Relation Versus Model Based On OSD Parameter	5-49
5-23	Stress Rupture Model Based On OSD Parameter For PY6 Silicon Nitride	5-50

LIST OF FIGURES (Contd)

Figure	Title	Page
5-24	Stress Rupture Data At 1149C (2100F) Showing A Wide Scatter. (Replicate Tests Conducted At 450 MPa)	5-51
5-25	Stress Rupture Data At 1204C (2200F) Showing A Wide Scatter. (Replicate Tests Conducted At 375 MPa)	5-52
5-26	Stress Rupture Data At 1371C (2500F). (Replicate Tests Conducted At 180 And 145 MPa)	5-53
5-27	Failure Strain Versus Stress Rupture Life From The Replicate Tests Conducted At 1371C (2500F)	5-55
5-28	Failure Strain Versus Stress Rupture Life Over Temperature Range 1204C To 1371C (2200F To 2500F)	5-56
5-29	Coordinate Axes For Spatial Integration. (a) Volume Failure Mode; (b) Surface Failure Mode	5-62
5-30	Weibull Moduli For Several Failure Modes Show No Apparent Temperature Dependence. (ATTAP NT154 Data)	5-69
5-31	Weibull Moduli For Different NT154 Specimens And Test Temperatures	5-70
5-32	Floating-Point Temperature Scaling Scheme	5-72
5-33	Characteristic Strength Versus Temperature For Floating Point And Curve-Fitting Schemes	5-74
5-34	Example Of CERAMIC Code Graphic Capabilities To Plot Maximum Likelihood, Likelihood Ratio, Bootstrap, And Median Ranks	5-81
5-35	Confidence Interval Calculation Using The Likelihood Ratio Technique	5-84
5-36	Bootstrap Algorithm To Predict Confidence Interval For Components With Thermal Gradient Temperature Distribution	5-88
5-37	Similarity Of Internal Volume And Inclusion Failure Data Leads To Combining The Two Failure Modes	5-94
5-38	Material Consistency Comparison For E-Size Flexure Specimens	5-95
5-39	Material Consistency Comparison For Tensile Specimens	5-97
5-40	Scatter In Fast Fracture Data For E-Size Flexure Specimens	5-101
5-41	Scatter In Fast Fracture Data For Tensile Specimens	5-102
5-42	Weibull Plot Of Surface Strength From Room-Temperature E-Size Flexure Test Data. All Non-Surface Failures Are Censored	5-106

LIST OF FIGURES (Contd)

Figure	Title	Page
5-43	Weibull Plot Of Volume Strength From Room-Temperature E-Size Flexure Test Data. All Non-Volume Failures Are Censored	5-107
5-44	Weibull Plot Of Chamfer Strength From Room-Temperature E-Size Flexure Test Data. All Non-Chamfer Failures Are Censored	5-108
5-45	Weibull Plot Of Combined Surface, Internal, And Chamfer Failures From Room-Temperature E-Size Flexure Test Data	5-109
5-46	Surface Strength Parameter Estimates From Several Sets Of Specimen Data	5-110
5-47	Volume Strength Parameter Estimates From Several Sets Of Specimen Data. Arrows Indicate Insufficient Data To Calculate Confidence Bounds	5-111
5-48	Chamfer Strength Parameter Estimates From Several Sets Of Specimen Data	5-112
5-49	Weibull Plot Of Pooled Surface Strength From Tensile And MIL-B Specimens Tested At Multiple Temperatures	5-114
5-50	Weibull Plot Of Pooled Volume Strength From All Specimens/Types And Multiple Temperatures	5-115
5-51	Temperature Dependence Of The Second Weibull Parameter, Estimated For NT154 Surface And Volume Strength	5-116
5-52	Angle Between Fracture Plane And Machining Direction On Plate Bending Specimens	5-119
5-53	Location And Orientation Of Fracture Origins Relative To The Machining Direction In The Plate Bending Specimens	5-120
5-54	Weibull Plot Of Room-Temperature Surface Strength From MIL-B Specimens Sectioned From Flat Spin Disks With Longitudinal Machining. Non-Surface Failures Were Censored	5-123
5-55	Weibull Plot Of Room-Temperature Surface Strength From MIL-B Specimens Sectioned From Flat Spin Disks Machined 45 Degrees To The Stress Direction. Non-Surface Failures Were Censored	5-124
5-56	Weibull Plot Of Room-Temperature Surface Strength From MIL-B Specimens Sectioned From Flat Spin Disks Transversely Machined. Non-Surface Failures Were Censored	5-125
5-57	Weibull Surface Strength Data Estimated From Pooled Longitudinal, 45-Degree, And Transverse-Machined MIL-B Specimens Sectioned From Flat Spin Disks	5-127
5-58	Stress Rupture (2200F/54.4 ksi) Test Data Compared To 2200F Fast Fracture Data	5-134

LIST OF FIGURES (Contd)

Figure	Title	Page
5-59	V-K Curve (Linear Fit) Plot Of 2200F/54.4 ksi Stress Rupture And 2200F Fast Fracture Test Data	5-135
5-60	Weibull Plot Of Censored Surface-Initiated Stress Rupture Failures Tested At 2200F/54.4 ksi. Characteristic Life = 348.9 Hours; Slope = 0.58	5-136
5-61	Weibull Plot Of Censored Internal-Initiated Stress Rupture Failures Tested At 2200F/54.4 ksi. Characteristic Life = 380.6 Hours; Slope = 0.52	5-137
5-62	Comparison Of Predicted 2200F Volume Stress Rupture Failures, Utilizing Three Sets Of SCG Parameters	5-141
5-63	Comparison Of Predicted 2200F Surface Stress Rupture Failures, Using SCG Parameters From Pooled And 2200F-Only Fast Fracture Data	5-141
5-64	Two Notched-Tensile Specimen Designs (Differing In Notch Depth) Were Used For Confirmatory Tests	5-143
5-65	Finite Element Stress Analysis Stress Contours For The Shallow-Notch Tensile Test Specimens	5-145
5-66	Finite Element Stress Analysis Stress Contours For The Deep-Notch Tensile Test Specimens	5-146
5-67	Comparison Of Predicted Fast Fracture And Confirmatory Test Results For Notched-Tensile Test Specimens	5-147
5-68	Differences In Surface Finish Of Notched Specimens Could Account For Discrepancies In Observed Strength Values	5-149
5-69	Comparison Of Slow Crack Growth Predicted Life And Actual Life For Notched-Tensile Test Specimens	5-151
5-70	Comparison Of 2500F Stress Rupture Test Data For $K_t = 1.6$ Notched-Tensile Test Specimen Geometry	5-152
5-71	Comparison Of 2500F Stress Rupture Test Data For $K_t = 2.1$ Notched-Tensile Test Specimen Geometry	5-152
5-72	Maximum Principal Stress Distribution In Tension-Torsion Specimen No. 9 At Failure. Specimen Loaded In Pure Torsion	5-154
5-73	Maximum Principal Stress Distribution In Tension-Torsion Specimen No. 15 At Failure. Specimen Loaded In Axial Tension And Torsion. Nominal Tensile To Shear Stress Ratio = 0.5 At Gage Section Surface	5-155
5-74	Comparison Of Group 1 Tension-Torsion Test Data. (A) Surface Failures; (B) Internal Failures; (C) Combined Surface and Internal Failures With Maximum Likelihood (Solid Lines) and 95-Percent Confidence Bounds (Dashed Lines) Predictions	5-157

LIST OF FIGURES (Contd)

<u>Figure</u>	<u>Title</u>	<u>Page</u>
5-75	Comparison Of Group 2 Tension-Torsion Test Data. (A) Surface Failures; (B) Internal Failures; (C) Combined Surface and Internal Failures With Maximum Likelihood (Solid Lines) and 95-Percent Confidence Bounds (Dashed Lines) Predictions	5-158
5-76	Comparison Of Group 3 Tension-Torsion Test Data. (A) Surface Failures; (B) Internal Failures; (C) Combined Surface and Internal Failures With Maximum Likelihood (Solid Lines) and 95-Percent Confidence Bounds (Dashed Lines) Predictions	5-159
5-77	Comparison Of Group 4 (Pure Tension) Test Data. (A) Surface Failures; (B) Internal Failures; (C) Combined Surface and Internal Failures With Maximum Likelihood (Solid Lines) and 95-Percent Confidence Bounds (Dashed Lines) Predictions	5-160
5-78	Spin Disk Maximum Principal Stress Distribution Under Centrifugal Loading Only, 50,000 rpm	5-162
5-79	Spin Disk Temperature Distribution At 2200F Test Condition, Thermal Loading And 50,000 rpm	5-163
5-80	Spin Disk Maximum Principal Stress Distribution Under Thermal Loading Only, At 2200F Test Condition (Units = psi)	5-164
5-81	Spin Disk Maximum Principal Stress Distribution At 2200F Test Condition, Thermal Loading And 50,000 rpm (Units = psi)	5-165
5-82	Spin Disk Maximum Temperature Distrubition At 2500F Test Condition	5-166
5-83	Spin Disk Maximum Principal Stress Distribution Under Thermal Loading Only, At 2500F Test Condition. These Stress Values Are Added To The Centrifugal Stresses To Obtain The Overall Stress Field At These Test Conditions (Units = psi)	5-167
5-84	Spin Disk Maximum Principal Stress Distribution At 2500F Test Condition, Thermal Loading and 50,000 rpm (Units = psi)	5-168
5-85	Spin Disk Room-Temperature Fast Fracture Volume Failure Predictions From Pooled Data Set	5-170
5-86	Spin Disk Room-Temperature Fast Fracture Surface Failure Predictions From Pooled Data Set	5-171
5-87	Spin Disk 2200F Fast Fracture Volume Failure Predictions From Pooled Data Set	5-172
5-88	Failure Originated From Deep Surface Machining Line And Associated Damage On 2200F, Fast Fracture Tested Spin Disk (Burst Speed = 60,800 rpm). Machining Damage Was Typical Of Spin Disks Tested	5-173
5-89	Predicted (Lines) And Observed (Points) Surface Failures In Spin Disks Tested At 2200F	5-175
5-90	Predicted (Lines) And Observed (Point) Volume Failure(s) In Spin Disks Tested At 2200F	5-175

LIST OF FIGURES (Contd)

Figure	Title	Page
5-91	Raw Data Analysis Of Spin Disk Room-Temperature Volume Failure Mode	5-176
5-92	Raw Data Analysis Of Spin Disk Room-Temperature Surface Failure Mode	5-177
5-93	Raw Data Analysis Of Spin Disk 2200F Volume Failure Mode. (Data Used In SCG Life Prediction.)	5-178
5-94	Raw Data Analysis Of Spin Disk 2200F Surface Failure Mode. (Data Used In SCG Life Prediction.)	5-179
6-1	NDE Can Be Used As An Effective Screening Tool To Assess The Upper Limit Of The Inherent Flaw Population In Ceramics	6-1
6-2	Laser Drilling Was Used To Fabricate NDE Standards (Size Table Applies To Both (A) And (B))	6-4
6-3	ASTM Penetrameter Design Was Modified For Small Flaw Detection	6-5
6-4	Computed Tomography Standards Were Designed To Evaluate Both Detection And Resolution	6-5
6-5	Photolithographic Process For Sapphire AM Resolution Standard Developed At UC Berkeley	6-6
6-6	Commercial Transducers Provided Full Inspection Coverage For Flat Specimens	6-11
6-7	Acoustic Microscopy Calibration Verified 50 Micron Detection Capability	6-12
6-8	Resolution Standard Used To Verify Theoretical Resolution Limits In Acoustic Microscopy	6-14
6-9	Surface Wave Propagation Is Achieved At The Outer Diameter When The Ultrasonic Beam Is At The Critical Angle For Surface Wave Mode Conversion. Figure After Gilmore, et. al. (Ref. 6-3)	6-16
6-10	Filtering The CT Images Improved Quality	6-18
6-11	Grey Scale Line Scans Show Reduced Noise (Less Variation) For 60 kV Voltage Setting	6-21
6-12	Magnification Attained Through Projection Radiography Is Limited By Exposure Time	6-22
6-13	Projection Radiographic Image At 1X Enlargement Of Seeded Iron Defects	6-23
6-14	Projection Radiographic Image At 2X Enlargement Improves Visual Detection Of Some Iron Defects	6-24
6-15	LaPlacian Filtering Improves Visual Detectability Of Holes In Penetrameters	6-26
6-16	Sobel Filtering Improves Visual Detectability Of Holes In Penetrameters	6-27
6-17	LaPlacian Filtered Image Of Seeded Iron Inclusions	6-28

LIST OF FIGURES (Contd)

Figure	Title	Page
6-18	Sobel Filtered Image Of Seeded Iron Inclusions Improves Visual Detection Slightly Over The LaPlacian Filtering	6-29
6-19	Acoustic Microscopy Indications Confirmed By Visual Inspection As Atypical Of The Machining Process Were Removed Prior To Testing	6-31
6-20	Acoustic Microscopy Inspections Revealed Vibrations In Tensile Rods That Were Tested As-Received	6-32
6-21	E-Size Flexure Specimens Received Partial Volumetric Inspection With Acoustic Microscopy	6-33
6-22	Spin Disk Inspection Coverage During Acoustic Microscopy Included Most Of Disk	6-34
6-23	CT Tensile Rod Inspections Showed Density Variation In Cross Sections	6-35

LIST OF TABLES

<u>Table</u>	<u>Title</u>	<u>Page</u>
1-1	SUMMARY OF STRENGTH AND LIFE PREDICTION CAPABILITIES FROM COMPARISONS OF PREDICTED AND MEASURED CONFIRMATORY SPECIMEN STRENGTHS AND LIVES	14
4-1	SMOOTH TENSILE RUPTURE TEST MATRIX	4-3
4-2	NOTCHED TENSILE RUPTURE TEST MATRIX	44
4-3	SUMMARY OF SMOOTH TENSILE CREEP/RUPTURE TEST RESULTS	4-30
4-4	SUMMARY OF FAILURE TYPES AT EACH TEMPERATURE	4-34
4-5	SUMMARY OF NOTCHED TENSILE RUPTURE TEST DATA	4-43
4-6	SUMMARY OF PERCENT INTERNAL FAILURE INITIATION SITES IN REPLICATE TESTS	4-61
4-7	RESULTS OF X-RAY ANALYSIS ON THE RATIO OF α/β NT154 PHASES	4-76
5-1	DIAMETRAL COMPRESSION DISK TEST CONDITIONS	5-2
5-2	LONG-BEAM K_{Ic} TEST DATA	5-3
5-3	REGRESSION ESTIMATES FOR $\dot{\epsilon}_s$	5-7
5-4	REGRESSION ESTIMATES FOR RATE PARAMETERS $\dot{\epsilon}_s$, $\dot{\epsilon}_{pi}$, AND α	5-19
5-5	VALUES FOR ACTIVATION ENERGY AND STRESS EXPONENTS	5-24
5-6	COEFFICIENTS FOR THE OSD MODEL	5-49
5-7	NONPARAMETRIC TEST FOR THREE GROUPS OF E-SIZE FLEXURE SPECIMENS	5-99
5-8	NONPARAMETRIC TEST FOR THREE GROUPS OF TENSILE SPECIMENS	5-100
5-9	WEIBULL STRENGTH PARAMETER ESTIMATES AND 95 PERCENT CONFIDENCE BOUNDS FOR INDIVIDUAL AND POOLED DATA SETS	5-105
5-10	FLAW/STRENGTH TYPES DEFINED FOR EACH SET OF SPECIMENS IN THE POOLED DATA SET	5-113
5-11	SHEAR SENSITIVITY ESTIMATED FROM DIAMETRAL COMPRESSION TEST RESULTS	5-118
5-12	WEIBULL PARAMETER ESTIMATES FROM ROOM-TEMPERATURE FLEXURE DATA USED TO EVALUATE SURFACE STRENGTH ANISOTROPY	5-121
5-13	COMPARISON OF σ_o ESTIMATES FROM TENSILE AND TORSION STRENGTH DATA	5-126

LIST OF TABLES (Contd)

Table	Title	Page
5-14	ASSESSMENT OF CANDIDATE SURFACE STRENGTH MODELS BASED ON SUPPORTING SPECIMEN DATA	5-129
5-15	REGRESSED 'n' AS A FUNCTION OF TEMPERATURE	5-132
5-16	2200F FAST FRACTURE STRENGTH AND STRESS RUPTURE LIFE PAIRS STRESS RUPTURE TESTS CONDUCTED AT 54.4 ksi	5-133
5-17	2200F LIFE AND STRENGTH PARAMETERS USED TO CALCULATE SCG PARAMETERS	5-138
5-18	SCG PARAMETERS FROM 2200F LIFE AND STRENGTH DATA	5-138
5-19	2100F LIFE, STRENGTH, AND SCG PARAMETERS	5-139
5-20	TENSION-TORSION CONFIRMATORY TEST SPECIMEN STRESS RATIOS	5-153
5-21	SPIN DISK LIFE PREDICTIONS VERSUS OBSERVED DATA	5-174
5-22	SUMMARY OF STRENGTH AND LIFE PREDICTION CAPABILITIES FROM COMPARISON OF PREDICTED AND MEASURED CONFIRMATORY SPECIMEN STRENGTHS AND LIVES	5-181
6-1	SEEDED DEFECT SPECIMEN DIAMETERS	6-8
6-2	TRANSDUCER BEAM DIAMETERS AND VOID DETECTION CAPABILITY	6-13
6-3	RESOLUTION VARIATION IS A FUNCTION OF FREQUENCY, F: NUMBER, AND SCANNING PARAMETERS. (MATERIAL PATH = 2 mm)	6-15
6-4	CT PARAMETER OPTIMIZATION EVALUATED KEY VARIABLES	6-17
6-5	COMPARISON OF CT EXPOSURES USING PENETRAMETER EDGE VERSUS GRAIN NOISE VALUES IN GRAY SCALE LEVELS	6-20
6-6	INSPECTION MATRIX CONCENTRATED NDE COVERAGE IN THE AREAS WHERE SPECIMENS WERE EXPECTED TO FAIL	6-30
6-7	SUMMARY OF TENSILE SPECIMENS WITH SUSPECT NDE INDICATIONS	6-37
6-8	SUMMARY OF E-SIZE FLEXURE SPECIMEN CORRELATION DATA	6-38
6-9	POSSIBLE DEFECTS DETECTED IN ENHANCED IMAGES	6-39
6-10	COMPARISON OF CALIBRATION RESPONSE AMPLITUDES WITH SEEDED DEFECT AMPLITUDES AT 6 mm FOCAL LENGTH	6-40

LIST OF ABBREVIATIONS AND ACRONYMS

A	Area
ACC	AlliedSignal Ceramic Components
AGFA	General Aniline and Film Corp.
Al	Aluminum
AM	Acoustic Microscopy
ANSYS	General Purpose Finite Element Modelling Code
ASEA	Swedish Corporation associated with Norton Advanced Ceramics
ASTM	American Society for Testing and Materials
ATTAP	Advanced Turbine Technology Applications Project
a	Crack Size
a ₀	Initial Crack Size
BOMAS	Ceramics grinding vendor, Somerville, MA
C	Carbon, Centigrade, Ratio of K_{IIIC}/K_{IC} , K_{IIIIC}/K_{IC}
C _i	Temperature Factor for Characteristic Strengths at Different Temperatures
CCD	Charge Coupled Device
cm ³	Cubic Centimeter
CMSX-3	Single Crystal Nickel-Based Superalloy
CNC	Computer Numeric Controlled
CIP	Cold Isostatically Pressed
Co	Cobalt
Cr	Chromium
CT	Computed Tomography
d	Transducer Element Diameter
dB	DeciBel
DOE	Department of Energy
DOS	Disk Operating System
EDX	Energy Dispersive X-ray

LIST OF ABBREVIATIONS AND ACRONYMS (Contd)

E	Elastic Modulus
E-size	Size E Ceramic Test Specimen (18.3 x 8.89 x 152.4 mm)
exp	Exponent, Exponential
F	Fahrenheit, Focal Length
Fe	Iron
F:	Focal Number (ratio F/d)
FF	Fast Fracture
FOL	Failed On Loading
FPI	Fluorescent Penetrant Inspection
GE-CRDC	General Electric Corporate Research and Development Center
g.mol	Gram-Mole
GN-10	AlliedSignal Ceramic Components Silicon Nitride
GSL	Gray Scale Level
H	Height
HIP	Hot Isostatically Pressed
hrs	Hours
HTML	High Temperature Materials Laboratory (ORNL)
I	Stress Gradient and Multiaxiality Factor
I _v	Volume Stress Gradient and Multiaxiality Factor
I _A	Area Stress Gradient And Multiaxiality Factor
IV, I _v V	Effective Volume Relative to Unit Volume and Triaxial Tension
IA, I _A A	Effective Area Relative to Unit Area and Biaxial Tension
IBM	International Business Machines Corp.
IEA	International Energy Agency
IMAGE	Image Processing Program
IN718	Nickel-Based Superalloy
IN738	Nickel-Based Superalloy

LIST OF ABBREVIATIONS AND ACRONYMS (Contd)

IR	Infrared
K	Kelvin (Absolute Temperature)
K_c	Critical Stress Intensity
KHROS	University of New Mexico Image Processing Program
K_i	Initial Stress Intensity
K_I	Mode I Stress Intensity Factor
K_{IC}	Mode I Fracture Toughness
K_{II}	Mode II Stress Intensity Factor
K_{IIC}	Mode II Fracture Toughness
K_{III}	Mode III Stress Intensity Factor
K_{IIIC}	Mode III Fracture Toughness
kJ	KiloJoules
KOH	Potassium Hydroxide
ksi	Thousands of Pounds Per Square Inch
K_t	Stress Concentration Value
kV	KiloVolt
L	Likelihood Function
l	Log of Likelihood Function
lb	Pound
ln	Natural Logarithm
m	Weibull Modulus
\hat{m}	Estimate of Weibull Modulus
\tilde{m}	Estimate of Weibull Modulus from Simulated Data
MarM-247	High-Temperature Nickel-Based Superalloy
MgO	Magnesium Oxide
MGP	Monkman-Grant Parameter
MHz	MegaHertz
MIL-A	Specification for ceramic test specimen, 1.5 x 2 x 20mm
MIL-B	Specification for ceramic test specimen, 3 x 4 x 40mm

LIST OF ABBREVIATIONS AND ACRONYMS (Contd)

MIL-HDBK	Military Handbook
MIL-STD	Military Standard
min	Minute, Minimum
mm	Millimeter
MOR	Modulus of Rupture (Strength)
MPa	MegaPascals
n	Stress Exponent in Creep Rate, Stress Rupture Expressions; Stress Intensity Exponent in Subcritical Crack Growth Rate Expressions
N	Nitrogen
NAC	Norton Advanced Ceramics, Worcester, MA
NASA	National Aeronautics and Space Administration
NC132	Hot-Pressed Silicon Nitride with MgO Sintering Aid
NDE	Nondestructive Evaluation
Ni	Nickel
NIH	National Institutes of Health
NIST	National Institute of Standards and Technology
nm	Nanometer (One-Millionth of a Millimeter)
NRC	Nuclear Regulatory Commission
NT154	Norton Advanced Ceramics HIPped Silicon Nitride
O	Oxygen
ORNL	Oak Ridge National Laboratory
OSD	Orr-Sherby-Dorn Parameter
PC	Personal Computer
psi	Pounds Per Square Inch
P/S	Primary-to-Secondary
PY6	Ytria-Sintered Silicon Nitride
Q	Activation Energy, Measure of Shear Sensitivity

LIST OF ABBREVIATIONS AND ACRONYMS (Contd)

R	Universal Gas Constant
RT	Radiographic Inspection
s	Number of Simulations in Bootstrap Method
S	Fast Fracture Strength in Inert Environment
SCG	Subcritical Crack Growth, Slow Crack Growth
SC-180	Single-Crystal Nickel-Based Superalloy
SEE	Standard Error of Estimate
SEM	Scanning Electron Microscopy
Si ₃ N ₄	Silicon Nitride
SiC	Silicon Carbide
SPC	Statistical Process Control
SR	Stress Rupture
STEM	Scanning Transmission Electron Microscopy
S/N	Serial Number, Signal-To-Noise Ratio
t	Time
T	Temperature
t _f	Time to Failure, Life
T _p	Time Spent in Crack Propagation
T _{ps}	Primary-to-Secondary Creep Strain Transition Time
TBD	To Be Determined
TEM	Transmission Electron Microscopy
Ti	Titanium
UDRI	University of Dayton Research Institute
UNIX	Computer Operating System
U.S.	United States
UV	Ultraviolet
V	Volume

LIST OF ABBREVIATIONS AND ACRONYMS (Contd)

W	Width
WDX	Wavelength Dispersive X-ray
X	Times Magnification, X-ray
XRD	X-Ray Diffraction
Y	Yttrium
YAG	Yttrium Aluminum Garnet
Y_2O_3	Yttrium Oxide
2-D	Two-Dimensional
3-D	Three-Dimensional
α	Alpha, Rate Parameter for Primary Creep
β	Beta, Scaling Parameter for Primary Creep
ϵ	Epsilon, Strain
ϵ_{ps}	Primary-to-Secondary Transition Strain
$\dot{\epsilon}$	Epsilon Dot, Strain Rate
$\dot{\epsilon}_p$	Primary Creep Strain Rate
$\dot{\epsilon}_{pi}$	Initial Primary Strain Rate
$\dot{\epsilon}_s$	Secondary Creep Strain Rate
λ	Lambda, Wavelength
μm	Micron (One-Thousandth of a Millimeter)
μsec	Microsecond
ϕ	Psi, Logarithm of Orr-Sherby-Dom (OSD) Parameter
ρ	Rho, Radius of Curvature of Crack Tip
σ	Sigma, Stress
σ_{loc}	Crack Tip Local Stress
σ_o	Second Weibull Parameter
$\hat{\sigma}_o$	Estimate of Second Weibull Parameter
$\check{\sigma}_o$	Estimate of Second Weibull Parameter From Simulated Data

LIST OF ABBREVIATIONS AND ACRONYMS (Contd)

σ_E	Effective Stress
σ_τ	Shear Stress
σ_{50}	Calculated 50-Percent Strength
σ_x	Cartesian Stress in X-Direction
τ	Tau, Mathematical Constant

1. ABSTRACT AND CONCLUSIONS

This final report summarizes the accomplishments and work performed during the period April, 1989 through September, 1993 in Phase I of the ongoing program being conducted by AlliedSignal Engines, Phoenix, Arizona for the U.S. Dept. of Energy/Oak Ridge National Laboratory (DOE/ORNL) to develop and demonstrate life prediction methods for ceramic components of advanced vehicular engines. The program was conducted under Contract No. 86X-SC674C, WBS element 3.2.2.3. The emphasis of this program is to develop and demonstrate ceramics life prediction technologies including methods for fast fracture, stress rupture, creep, oxidation, and nondestructive evaluation (NDE). Significant advancements were made in these methods and their predictive capabilities were successfully demonstrated.

1.1 Data Base

A large data base from ceramic specimen tests for developing and confirming life prediction technologies was successfully developed. This data base includes results from 1400 strength, stress rupture, and creep tests conducted using 14 different specimen geometries. The success of these tests was demonstrated through specimen strain gage testing and detailed analysis of the test results. All tests were performed with specimens manufactured from one selected advanced structural ceramic, NT154 silicon nitride (Si_3N_4) from Norton Advanced Ceramics, Worcester, Massachusetts. To ensure consistency, all the specimens were fabricated from one raw powder lot. Specimen manufacturing consisted of forming by cold isostatic pressing, densification by glass encapsulated hot isostatic pressing (HIPping), and machining of all surfaces.

Included in the data base are results from extensive fractography and microscopy examinations. This is likely the largest data base successfully amassed to date on a single advanced structural ceramic material. This data base was used to identify failure mechanisms and guide the development of behavior models to predict failures from fast fracture, oxidation, creep, and stress rupture modes.

1.2 Behavior Models

Fast fracture prediction requires a multiaxial fracture model and determination of the material sensitivity to shear stresses ($C_{II}=K_{IIc}/K_{Ic}$, and $C_{III}=K_{IIIc}/K_{Ic}$). Several tests were performed to calculate this material property. Results from precracked specimens, diametral compression disks, and notched tension-torsion bars showed low sensitivity to shear; $C_{II}=2.1$ and $C_{III}=2.1$. A low shear sensitivity also seems to apply to machining surface flaws. Strengths of tension-torsion and flexure specimens (with zero, 45-degree, and 90-degree tensile surface machining angles) could be predicted with $C_{II}=2.1$ or higher. These tests were not conclusive for

estimating C_{II} for inherent flaws (pits, inclusions, voids, and machining damage) because it was difficult to separate the anisotropy from the shear sensitivity effects in these specimens. For consistency, it was assumed that the material is shear-insensitive ($C_{II}=\infty$) for all confirmatory test specimen predictions.

Future efforts to define shear sensitivity should include tests that separate the effects of anisotropy and shear sensitivity, or strength testing should be performed at sufficient stress orientations relative to the machining direction, to allow anisotropy and shear sensitivity for inherent flaws to be evaluated concurrently.

Stress rupture and creep models were developed from tensile creep/stress rupture test results. Detailed fractography and microscopy was performed to identify deformation and failure mechanisms. The mechanistic information helped guide the material behavior and design model development.

A large data base of tensile creep rupture test results was compiled. Primary and secondary creep modes dominated, with little indication of tertiary creep behavior. A creep rate model was developed to correlate the measured creep strains. The creep rate model encompassed primary and secondary creep regimes and is applicable for prediction of elevated-temperature stress relaxation and deformation.

When stress rupture life was correlated with steady-state creep rates from the Monkman-Grant perspective, temperature stratification was observed. This temperature stratification could be explained based on crack growth considerations. Stress rupture life was also successfully modelled, following the Orr-Sherby-Dorn (OSD) parameter approach.

The stress rupture and fast fracture data were used in combination to derive subcritical crack growth (SCG) parameters that could be used in probabilistic component design. The creep rate and stress rupture models described earlier provided means for temperature interpolation of the SCG parameters.

An oxidation study was performed to measure and model the influence of oxidation on residual strength. Residual strength tests on flexure specimens with transversely-machined tensile surfaces demonstrated an increase in strength with short exposures (~10 hours), and a slow decrease in strength for longer exposures (~1000 hours). These tests found NT154 to be very resistant to oxidation up to 2550F. Future efforts should focus on the degradation of mechanical properties from hot corrosion.

The effects of aging were also found to be negligible. The creep characteristics of earlier vintages of NT154 were affected by long-term static exposure to elevated temperatures. Tests with the later NT154

specimens manufactured for this program showed no significant change in creep behavior after aging. This material had an additional heat treatment that apparently stabilized the grain boundary phases.

1.3 Probabilistic Methods

The application of behavior models to ceramic component life prediction requires use of probabilistic methods. These methods account for the large scatter in strength and life, size effects, and multiple flaw distributions. Considerable progress was made in applying advanced statistical techniques to probabilistic methods for ceramic component design.

The resulting probabilistic methods were developed by combining maximum likelihood estimation, censored data analyses, pooled data techniques, and likelihood ratio and bootstrap techniques for calculating confidence intervals into a single analysis computer code. The result is a code that allows strength data with multiple specimen sizes, multiple/competing strength distributions, and multiple-temperature data to be pooled for estimating Weibull strength parameters and component reliability with confidence intervals. Previously, ceramic components could not be designed to levels of confidence; without confidence intervals, component designers/analysts were left to design to the best estimate of median strength and life properties without accounting for the uncertainty in estimates due to limited sample sizes.

These improved probabilistic methods allowed 405 specimens with 4 different geometries to be combined into one data set (i.e., pooled) for estimating strength parameters and predicting confirmatory specimen failures. Pooling data results in more confidence in predictions (narrow confidence bounds) which allows components to be designed closer to the true capability of the material. As a final test of these prediction methods, reliability estimates were made with confidence intervals and these were compared with measured confirmatory specimen strengths and lives.

1.4 Methods Confirmation

Confirmatory test specimens were designed and tested to evaluate the predictive capabilities of these life prediction methods under stress, size and loading conditions that represent actual engine components. The three specimen types used to confirm life prediction methods were: notched-tensile, tension-torsion, and spin disks. The capabilities of the life prediction methods developed in this program were evaluated by comparing predicted and measured strengths and lives of the confirmatory specimens. These comparisons are summarized in Table 1-1.

TABLE 1-1. SUMMARY OF STRENGTH AND LIFE PREDICTION CAPABILITIES FROM COMPARISONS OF PREDICTED AND MEASURED CONFIRMATORY SPECIMEN STRENGTHS AND LIVES

	Fast Fracture		Elevated Temperature Fast Fracture		Slow Crack Growth (2200F)		Creep Rupture (2500F)
	Volume	Surface	Volume	Surface	Volume	Surface	Combined
Notched Tensile	N/A	Inc	N/A	N/A	Mod	Mod	Mod
Tension-Torsion	N/A	Good	N/A	N/A	N/A	N/A	N/A
Spin Disk	Good	Inc	Mod	Inc	Mod	Mod	Inc
Notes: Mod = Moderate success N/A = Not applicable, tests were not performed for these conditions. Inc = Inconclusive							

Volume fast fracture predictions were generally very successful. Volume strength properties (Weibull parameters) were found to be very consistent between all baseline flexure and tensile specimens. This allowed 405 strength data points to be combined for predictions. The quality of these predictions, as compared with measured confirmatory specimen strengths, confirmed that these methods can predict strengths in specimens with very diverse sizes and multiaxial stress states.

Surface strength predictions had moderate success. Strength results indicate that consistent surface strength properties could not be produced in different specimen geometries. Therefore, it was generally not useful to predict confirmatory specimen surface strength from flexure and tensile specimen data. This inconsistency was not a result of oversight; considerable effort was made to produce consistent surface properties. This is more indicative of the general lack of understanding of the influences of machining practices on ceramic mechanical properties and the need for continued support of machining technology initiatives such as the DOE/ORNL Cost-Effective Ceramic Machining Program (ref. 1-1).

In the case where the test specimens and confirmatory specimens had similar surfaces, the surface strength predictions were accurate. For example, the tension-torsion specimens have surfaces that are similar to tensile specimens. The predictions of tension-torsion failure stresses are consistent with observed failure stresses. This also demonstrated that surface strength can be predicted for tension-compression multiaxial stresses.

The inconsistent surface properties also made life predictions more difficult. Subcritical crack growth lives are based on predicting the time for initial flaws to grow to a critical size. This is based on the assumption that the distribution of surface flaws in flexure and tensile specimens are the same as the confirmatory specimens, which, in general, was not true. However, when confirmatory specimen strength data were used to define the

initial flaw size distribution, the measured slow crack growth lives for the notched tensile specimens and spin disks were in fair agreement with the predictions. This demonstrates that slow crack growth lives can be predicted when specimen properties are consistent with the properties in the component. Additional work is planned under the Phase II Ceramic Life Prediction Program to develop and confirm methods that can predict the scatter in slow crack growth lives.

At 2500F, creep and environmentally-enhanced crack growth are the controlling failure modes. As described previously, a stress rupture model [based on the Orr-Sherby-Dorn (OSD) parameter] was developed that correlates a wide range of stress-temperature-life tensile test results. However, this model has not been expanded into a component prediction tool to account for multiaxial stress, competing failure modes, and size effects. To assess the significance of these component complications, life predictions were made with this model for the notched tensile and spin disk specimens tested at 2500F. The prediction of lives of the notched tensile specimen was moderately successful, although it was apparent that the creep stress relaxation that occurred during testing should be considered in the life prediction. The spin disk life predictions, however, were many orders of magnitude greater than observed during the actual hot spin pit testing. Life prediction using a crack growth approach, based on the observed surface damage, was successful in narrowing the discrepancy between observed and predicted lives. This indicates that surface condition plus size effects and multiaxial stresses are more important than previously recognized in creep rupture life prediction. Additional work in this area is planned under the Phase II Ceramic Life Prediction Program.

1.5 Nondestructive Evaluation (NDE)

NDE development and application included three tasks: 1) Development and fabrication of reference standards for NDE evaluation and calibration; 2) Application of selected NDE methods to ceramic specimens used for testing mechanical properties; and 3) Correlation of NDE with fractography to quantify detection capabilities.

NDE standards were successfully fabricated using three processes: laser machining, photolithography, and seeded inclusions. Laser drilling produced holes with diameters of 10 to 600 microns (μm) and depths of 5 to 200 μm . Photolithography was used to etch patterns in the surface of some standards. The etched surface was then bonded to another surface to produce internal voids corresponding to the etched pattern. Voids as small as 2 μm in diameter and 0.2 μm deep were successfully produced with this method. Seeded volume defects were produced by adding titanium nitride and tungsten carbide particles to Si_3N_4 powder. There was some difficulty controlling the distribution of seed sizes and shapes but 50 to 150 μm defects were achieved. This work demonstrated three viable techniques for fabricating NDE standards.

NDE methods evaluated included: visual examination, fluorescent penetrant inspection (FPI), acoustic microscopy (AM), computed tomography (CT), and microfocus radiography (MFXR). From these assessments,

acoustic microscopy was found to be more sensitive to some flaws than radiography. Computed tomography looked promising from seeded specimens, but showed no correlation with other NDE or destructive tests. Computer enhancement of X-ray film images improved detection for nonspecialists interpreting the films, but not for specialists. Computer enhancement will offer more benefit as systems with improved resolution are developed.

Inspection results from specimens that were destructively tested showed that the average size of inherent flaws are at or beyond the detection limit for the NDE methods applied in this program. However, the real usefulness of these methods will be dictated by how reliably they screen out the larger flaws in the tail of the flaw distribution curve. These larger flaws are particularly important in three cases: 1) Component design stresses are much lower than specimen failure stresses, and the flaw size that needs to be screened to prevent premature failure is correspondingly larger; 2) Larger components are predicted to have larger flaw sizes, particularly in the tail of the distribution; 3) Production components still tend to have larger flaws not normally seen in test specimens. Future work should be focused on reliability studies to quantitatively define the probability of detection for various flaw types and sizes.

1.6 Conclusions

Phase I of this program made significant advances in defining the state-of-the-art of ceramic component life prediction and NDE methods. This program has demonstrated that:

- Mechanical properties can be reliably generated from a wide range of specimen tests
- Today's Si_3N_4 materials such as NT154 are very stable, and are largely unaffected by aging or oxidation
- Accurate stress-temperature-time models can be defined through understanding of time-dependent mechanisms
- Advanced statistical methods can be combined into a single analysis code to manage the numerous complications of estimating strength and life parameters as well as component reliability with confidence intervals
- Component strength can be accurately predicted if specimens can be fabricated with properties that are consistent with components

- Component life prediction must also include consideration for size, multiaxial stress, and competing failure modes
- Laser drilling, photolithography, and seeded inclusions are viable techniques for fabricating NDE standards
- Several NDE techniques are available for screening flaws in ceramics, but reliability studies are needed to quantify capabilities.

The results from Phase I of this program have provided tools and technology to design ceramic components with improved reliability, as well as a proven approach and framework for further life prediction advancements in the ongoing Phase II Ceramic Life Prediction Program efforts.

REFERENCES - SECTION 1.0

- (1-1) Blau, Peter J., "Cost-Effective Ceramic Machining Program", Sponsored by U.S. Dept. of Energy, Office of Transportation Materials, Ceramic Technology Project, Contract DE-A05-84OR21400 with Martin Marietta Energy Systems, Oak Ridge National Laboratory, Oak Ridge, TN. Proceedings of the 1992 Automotive Technology Development Contractors Coordination Meeting, Society of Automotive Engineers, Warrendale, PA 1993.

2.0 INTRODUCTION

2.1 The Need For Ceramic Life Prediction Methodology Development

The use of advanced ceramics in heat engines can reduce or eliminate blade cooling, reduce containment structure and overall engine weight, and permit operation at higher temperatures and efficiency, resulting in reduced fuel consumption, improved performance, and reduced operating costs. However, full-scale production of ceramic components requires improvements in life prediction methodology that can ensure ceramic component integrity in field applications.

Phase I of the Life Prediction Program has encompassed the development of a large data base on an advanced silicon nitride structural ceramic, material behavior models, and probabilistic design tools. The program approach and execution, and the outline of this final report are described in the following subsections.

2.2 Approach

The AlliedSignal team's approach to developing life prediction methodology for ceramic heat engine components combined nondestructive evaluation (NDE), materials characterization, behavior modeling, and advanced statistical techniques with component risk integration tools. Figure 2-1 illustrates the approach adopted in this program to develop ceramic life prediction methodologies for gas turbine applications.

The elements of the approach are described in more detail in the following sections.

2.3 Material Selection And Processing

The material selected for the program was an advanced silicon nitride, designated NT154 from Norton Advanced Ceramics, Worcester, Massachusetts. To ensure material consistency for model development, strict controls were imposed during specimen fabrication, including fabrication of all test specimens from a single batch of powder. The rationale for material selection, and the processing considerations are described in Section 3, Material Selection and Processing.

2.4 Material Characterization

An extensive data base was generated on the most predominant failure modes anticipated for advanced heat engine applications: fast fracture, subcritical crack growth (SCG), creep rupture, and oxidation. Fourteen types

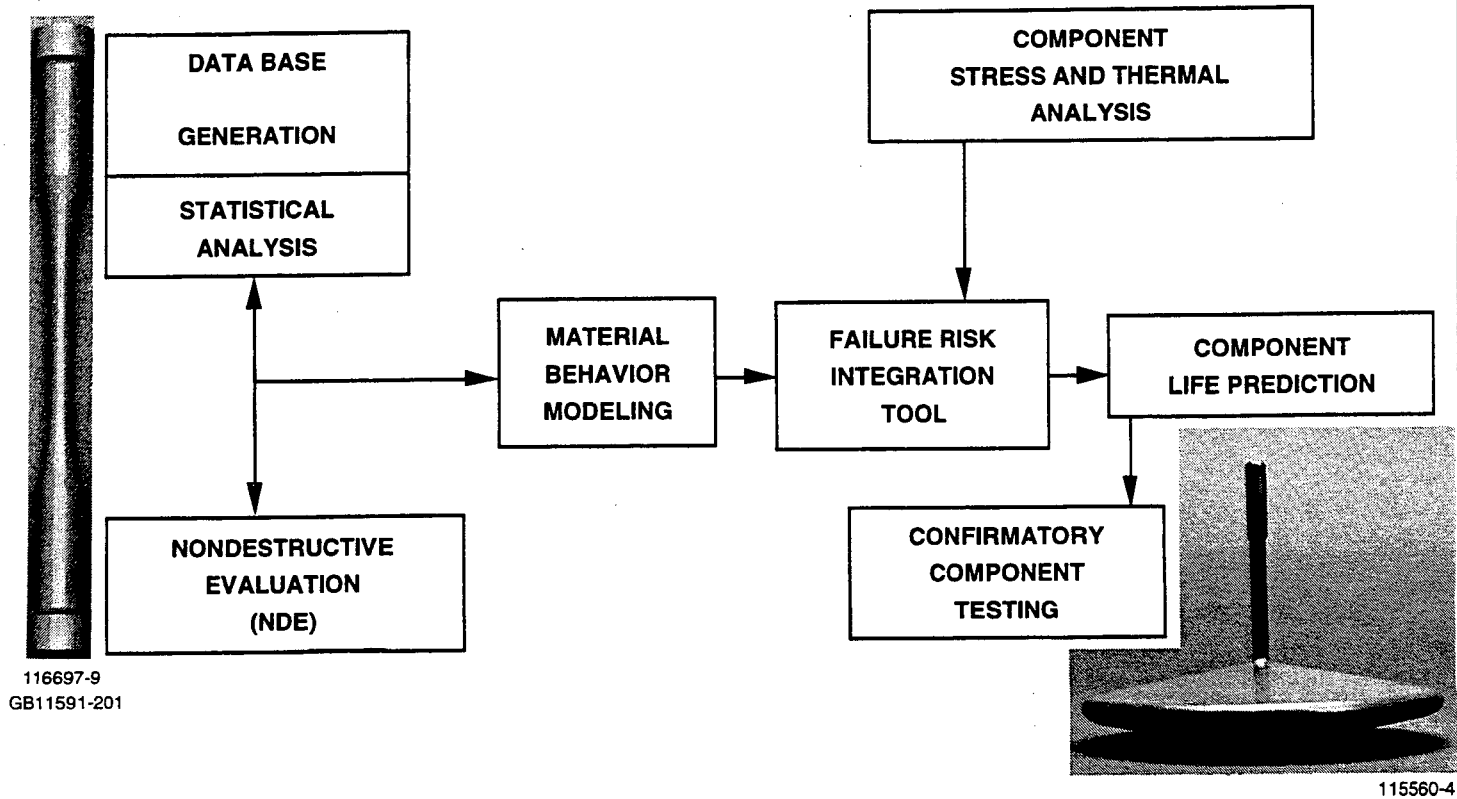


Figure 2-1. AlliedSignal Approach For Ceramic Life Prediction Methodology Development.

of discriminating tests employing more than 1000 specimens were conducted to characterize the failure mechanisms and to generate data for material behavior and statistical model development. Extensive microstructural characterization and post-failure fractography were conducted to identify failure mechanisms. Specimen testing procedures and results, as well as microstructural and fractographic observations are presented in Section 4.

2.5 Life Prediction Methods And Verification

Material degradation modes, such as aging, fast fracture under multiaxial loading, creep deformation, and creep rupture, were assessed through material characterization testing and analysis. Material behavior models were established from the test data, microstructural characterization, and fractographic observations. These are described in Section 5.1.

Statistical methods and tools were developed in the program to statistically treat specimen test data and to make component life predictions. These included:

- (1) Effective size methods to account for stress state, stress gradient, and the physical size of specimens and components, thus enabling the pooling of specimen test data from different sizes, types, and loading configurations
- (2) Confidence interval predictions methods based on likelihood ratio and bootstrap approaches
- (3) Temperature-scaling methods for combining test data from multiple temperatures
- (4) A multiaxial and anisotropic risk integration tool that integrates finite element component thermal and stress distributions to arrive at effective sizes for component failure predictions.

These methods are described in Section 5.2.

Using the methods described in Sections 5.1 and 5.2, strength and life parameters were estimated from test data in the data base. The derivation of these strength and life parameters are described in Section 5.3.

The validity of the new methodologies were assessed by using the strength and life parameters (Section 5.3) to predict the strength and life of confirmatory specimens that more closely simulate heat engine components in terms of stress state and physical size. The results of comparisons of the predictions versus the confirmatory test data are described in Section 5.4.

2.6 NDE Methods Development And Application

An integral part of the insertion of ceramic components in advanced heat engines is the development of NDE techniques that can detect and screen inherent flaws in components. NDE development and application in this program included three tasks:

- (1) Development and fabrication of NDE reference standards
- (2) Application of selected NDE methods to ceramic specimens
- (3) Correlation of NDE with fractography.

These tasks are described in more detail in Section 6.

2.7 Appendices

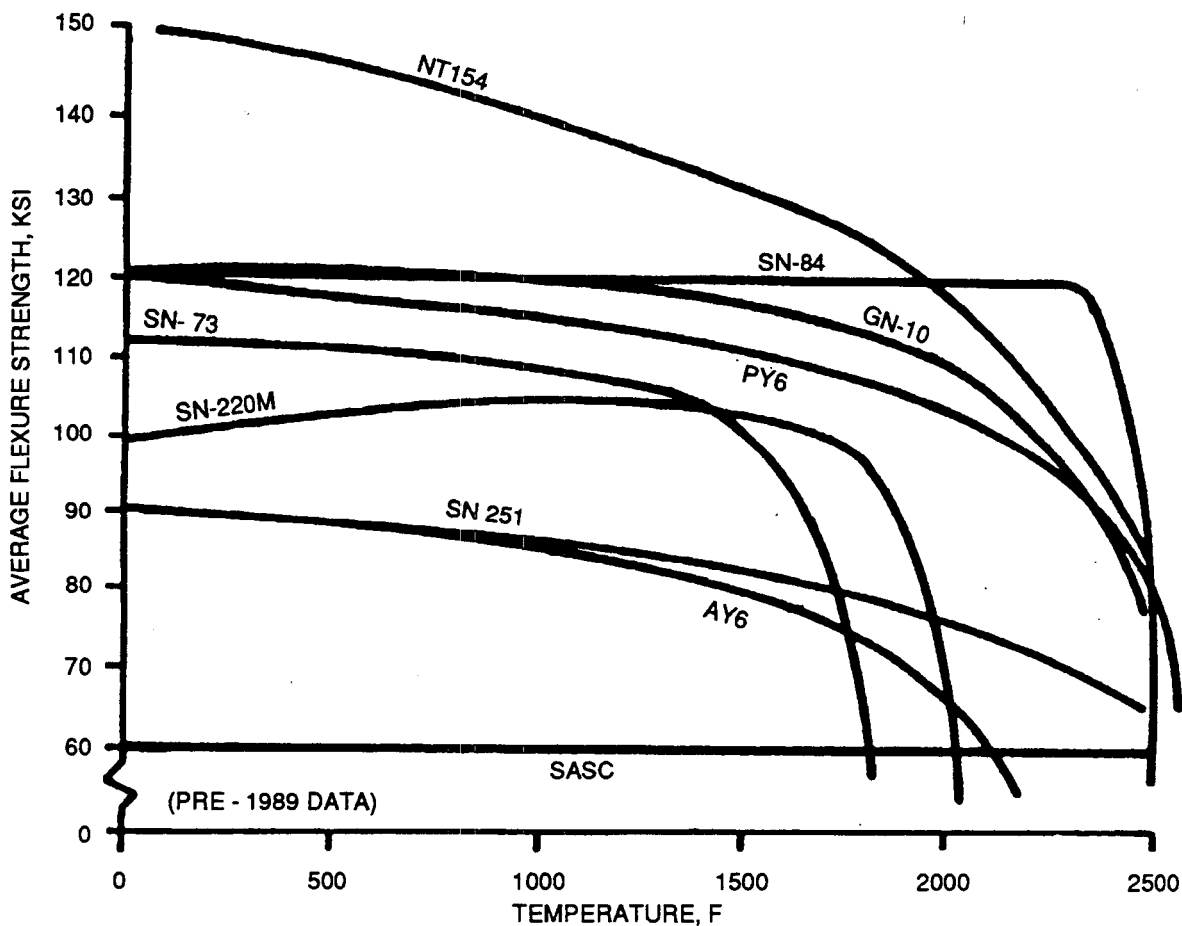
The supporting documents for the data base and methods development efforts in this program can be found in the Appendices, bound as Volume Two of this report:

Appendix No.	Title
I	Specimen Geometries
II	Subcontractor Report from the University of Utah: Studies of Mixed-Mode and Biaxial Stress Fracture of Structural Ceramics for Advanced Vehicular Heat Engines
III	Subcontractor Report from Brown University: Mode I/Mode III Fracture Toughness and Tension/Torsion Fracture Strength of NT154 Si ₃ N ₄
IV	Strength and Fractography Tables From Mechanical Tests
V	Fractographs From Tested Specimens
VI	Derivation Of Statistical Models
VII	Weibull Strength Plots For Fast Fracture Specimens
VIII	Effective Size Functions For Specimens Employed

3.0 MATERIAL SELECTION AND PROCESSING

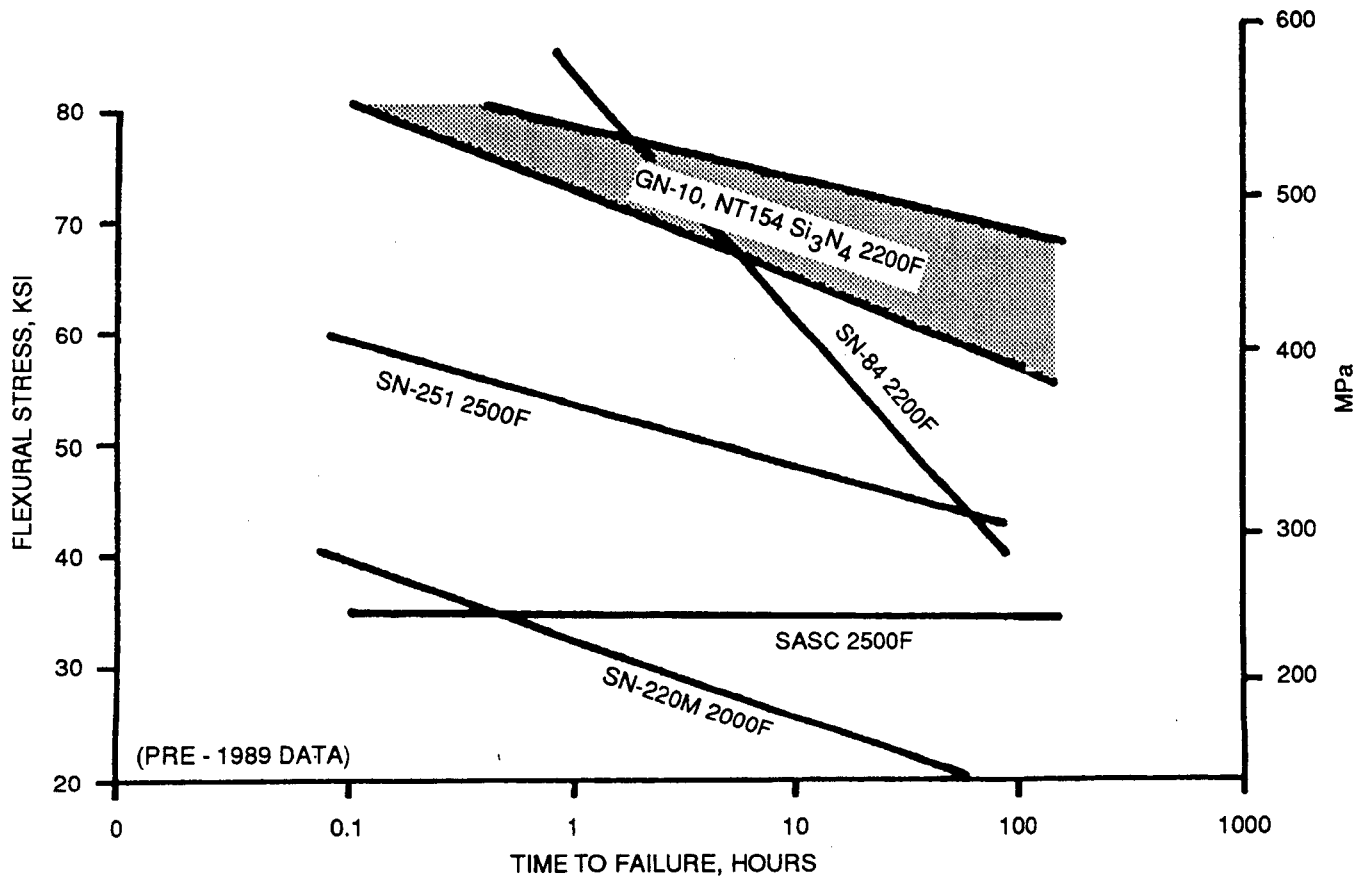
3.1 Material Selection

NT154 silicon nitride (Si_3N_4) produced by Norton Advanced Ceramics (NAC), Worcester, MA was selected for detailed characterization in this program. A comparison was made with other candidate commercially-available ceramics developed for engine applications and NT154 was selected, based on development maturity, high strength, high-temperature mechanical properties, quality (uniformity and consistency), and NAC experience in processing diverse sizes and shapes. NT154 also fulfilled the requirements of being in domestic production in the U.S. and of being a material suitable for engine components used in the concurrent DOE/NASA-funded Advanced Turbine Technology Application Project (ATTAP) underway at AlliedSignal Engines. Figures 3-1 and 3-2 illustrate the baseline fracture strength and rupture life advantages of NT154, relative to alternative candidate materials.



GC11591-301A

Figure 3-1. Strength Comparison Of Candidate Ceramic Materials.



GC11591-302A

Figure 3-2. Comparison Of Candidate Materials Stress Rupture Properties.

3.2 Processing Procedures And Sequence

Consistent material quality was required to generate a statistically significant specimen test data base and to ensure that all of the test specimens contained the same flaw populations. Achieving consistent material properties was complicated by the varying requirements for more than 1400 specimens of 14 different geometries. Specimen sizes ranged from the small 1.5 x 2 x 20mm MIL-A flexure bars to the 150mm diameter spin disks. Consequently, considerable effort was invested to ensure that specimens with consistent material properties were produced.

Figure 3-3 shows a flowchart of the NT154 processing sequence. All the specimens were processed from a single master lot of raw Si₃N₄ powder and sintering additives to ensure chemical consistency. Blending and ball milling of the powders was performed as a single batch, i.e., using the same equipment over a continuous period of time. The milled powders were cold isostatically pressed (CIPped) into billets and sintered to full density using the proprietary NAC ASEA glass encapsulation, hot isostatic press (HIP) process.

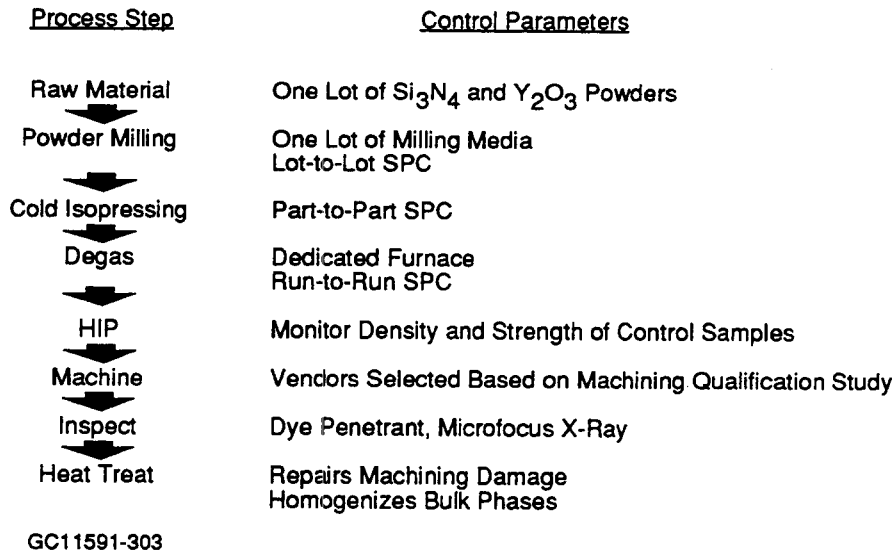


Figure 3-3. Material Uniformity Was Assured By Selected Processing Methods.

To ensure that material nonuniformities due to billet sizes and shapes were minimized, only three types of billets (Figure 3-4) were used to machine all the specimens. Square plates, approximately 57 x 57 x 7.6mm size, were used as the starting billets for the MIL-A and MIL-B flexure bars, long-beam chevron notched bars, diametral compression disks, and plate bending disks. Cylindrical billets were used for all the buttonhead tensile, tension/torsion, and E-Size flexure specimens. Special MIL-B and 10 x 13 x 100mm-size flexure bars were machined from spin disk billets, to verify consistency of surface and internal properties. Following HIPing, a proprietary NAC heat treatment was applied to all the billets to promote crystallization of grain boundary phases.

All specimen surfaces were 100 percent machined using identical surface grinding parameters, with the exception of the spin disks and some special flexure bars. Machining vendors were selected following a study (described in section 3.3) that assessed vendor capability to machine specimens with consistent properties. To maintain consistency within specimen classes, BOMAS, Somerville, MA, was contracted to machine all the flat specimens including the flexure bars, chevron notched bars, diametral compression disks, and plate bending disks. Allied Manufacturing, Worcester, MA, machined all the tensile specimens, and the Norton/TRW Valve Division in Salem, NH, machined all the spin disks.

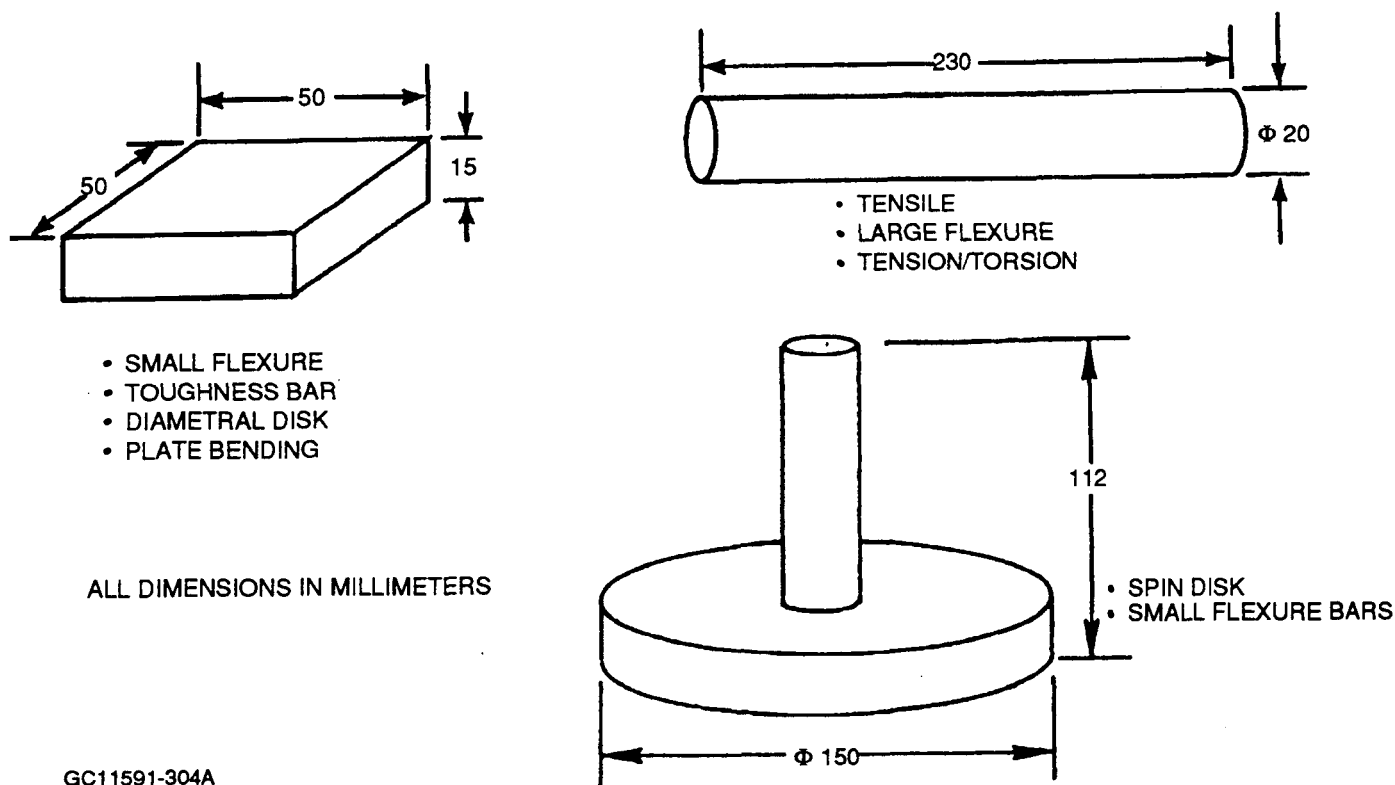


Figure 3-4. Test Specimens Were Processed From One Of Three Billet Geometries.

A postmachining heat treatment at 1000C for 20 hours in air was applied by NAC to all the specimens to improve surface strength. However, it was later discovered that this heat treatment was not as effective as the postmachining heat treatment of 1400C for 1 minute, used in the machining study. The 1000C heat treatment did not eliminate excessive (up to 90 percent) chamfer corner failures on the flexure bars. A new heat treatment was subsequently developed during this program, based on oxidation study results. This heat treatment increased the transverse-machined MIL-B flexure bar strength by 38 percent and drastically reduced the number of chamfer failures.

3.2.1 Inspection Process

In-process FPI, X-ray, and visual inspections were performed by NAC. However, to avoid applying inconsistent acceptance criteria, all specimens (including those rejected by NAC inspectors) were delivered to AlliedSignal for subsequent reinspection (described in section 3.4).

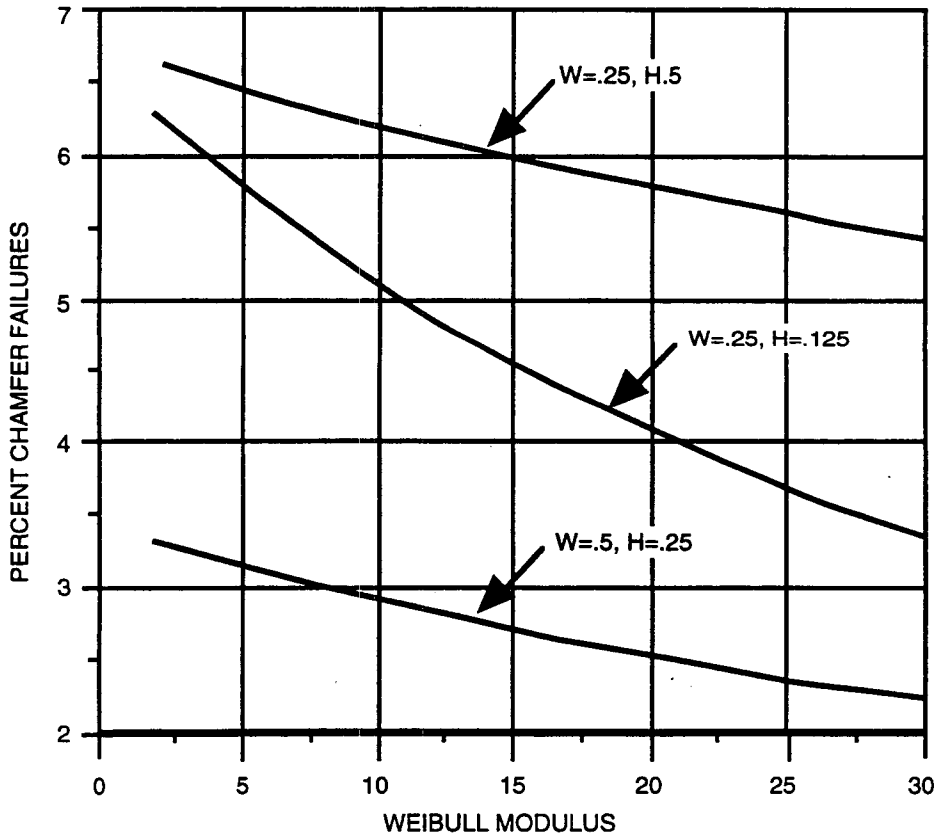
3.2.2 Certification Process

Each specimen was accompanied by certification test results from NAC. The certification tests consisted of fast fracture and stress rupture tests performed on MIL-B bars machined from square plates processed from the same milled powder and HIP batch. All test data were within NAC standard process control chart limits.

3.3 Machining Study And Vendor Evaluation

NT154 is a high-strength silicon nitride with a typically clean, uniform microstructure. Its properties are strongly dependent on the size of the microscopic flaws produced during machining. Consequently, a study evaluating machining parameters and machining vendor capabilities was performed, with the objective of achieving consistently high quality within the constraints of acceptable cost and manufacturing time.

From previous AlliedSignal experience with machined NT154 specimens, it was recognized that excessive crack initiation at chamfer corners (Figure 3-5) on flexure specimens and at buttonheads on tensile specimens had the potential to reduce the usefulness of the test specimen data base. Failures initiated by machining damage at these locations are undesirable, because the measured strengths are not indicative of the actual material capability.

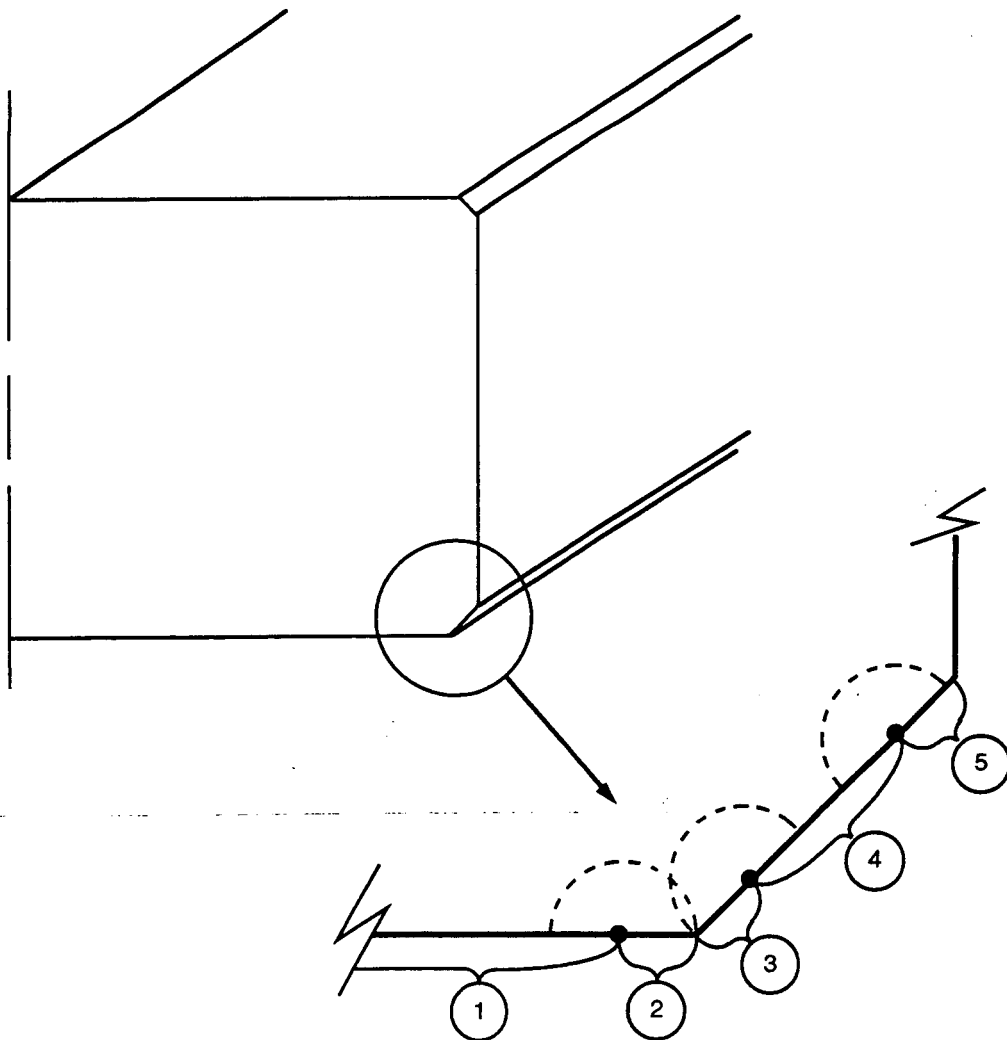


GC11591-305

Figure 3-5. Less Than 10 Percent Of The Surface Failures Were Expected In The Chamfer Areas (W And H Are Flexure Bar Dimensions In Inches).

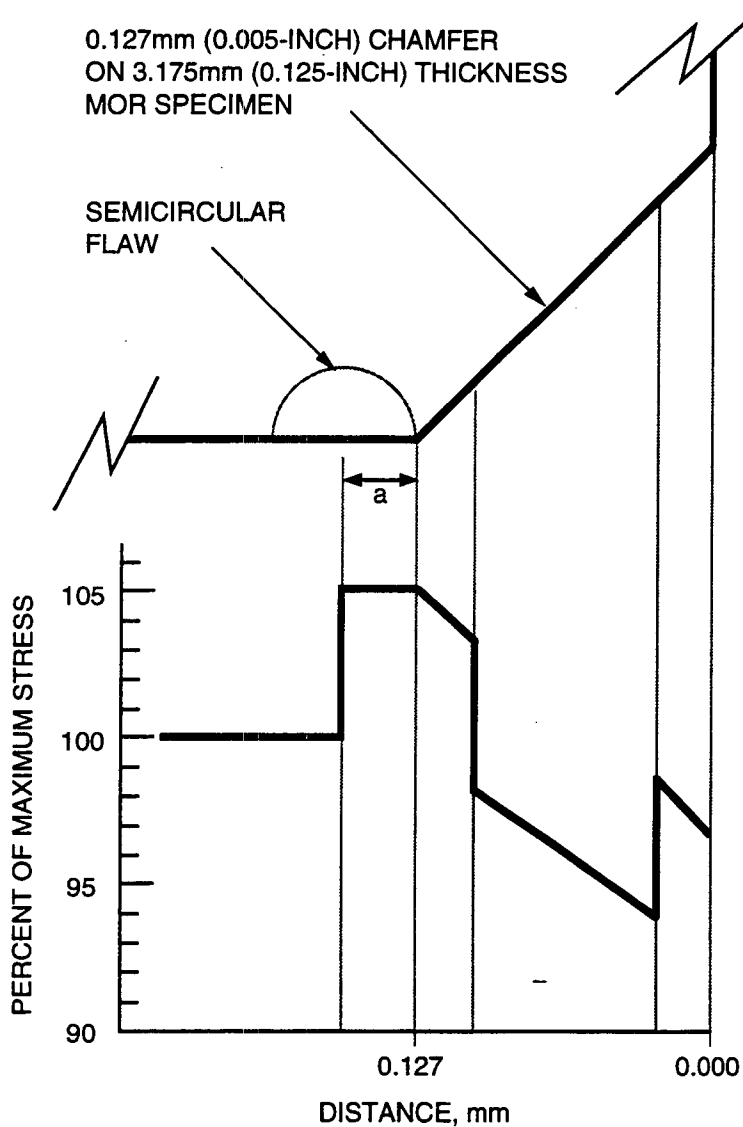
Analyses were performed to provide a means of determining when ceramic flexure data is contaminated by chamfer failures that are not representative of the remainder of the specimen tensile surface. The probability of failure was calculated for the five regions across the width of a flexure specimen shown in Figure 3-6. The length of regions 2, 3, and 5 is equal to the average flaw radius, calculated to be 38.1 μm for NT154. Any flaws located in regions 2 through 5 were assumed to be chamfer failures.

Stresses were assumed to be higher in regions 2, 3, and 5 to account for the possibly increased stress intensity of a corner crack. Calculations for semicircular cracks (ref 3-1, 3-2, 3-3) show cracks on 90-degree corners have zero to 10 percent higher stress intensity than cracks on flat surfaces. Stresses at 45-degree corners were assumed to be zero to 5 percent higher than beam theory predicts for regions 2, 3, and 5. The assumed stress distribution in the chamfer region for a 5 percent stress concentration is shown in Figure 3-7.



GC11591-306

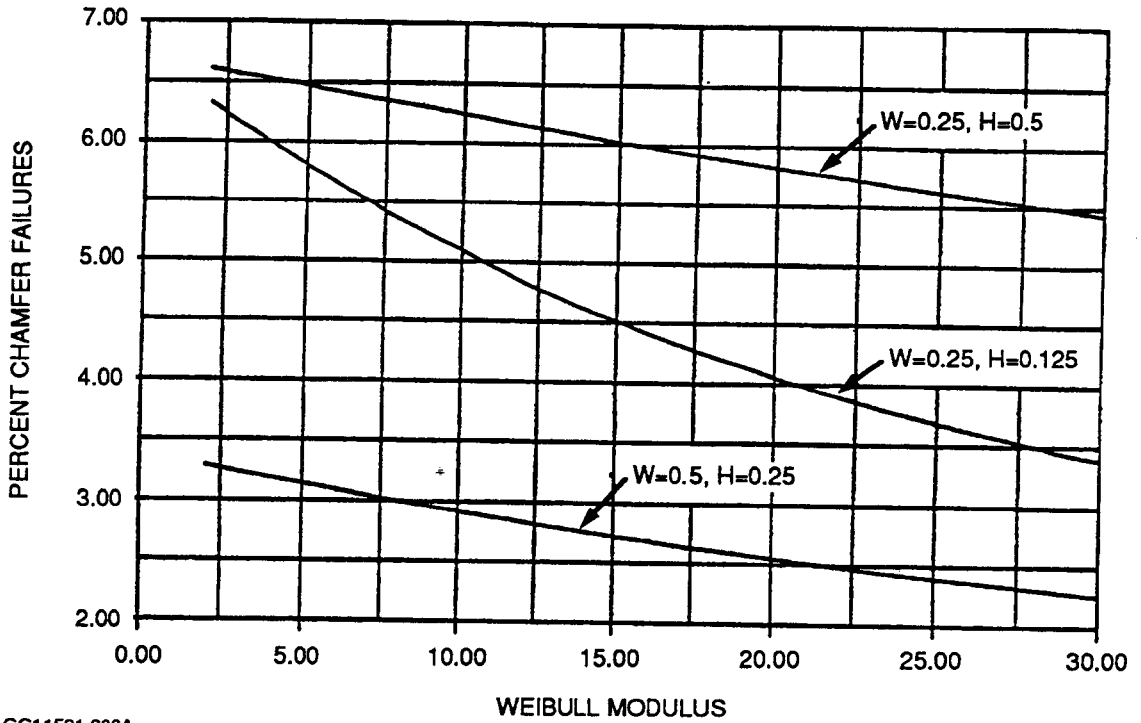
Figure 3-6. Failure Probabilities Were Calculated For The Five Regions Indicated.



GC9-11591-307B

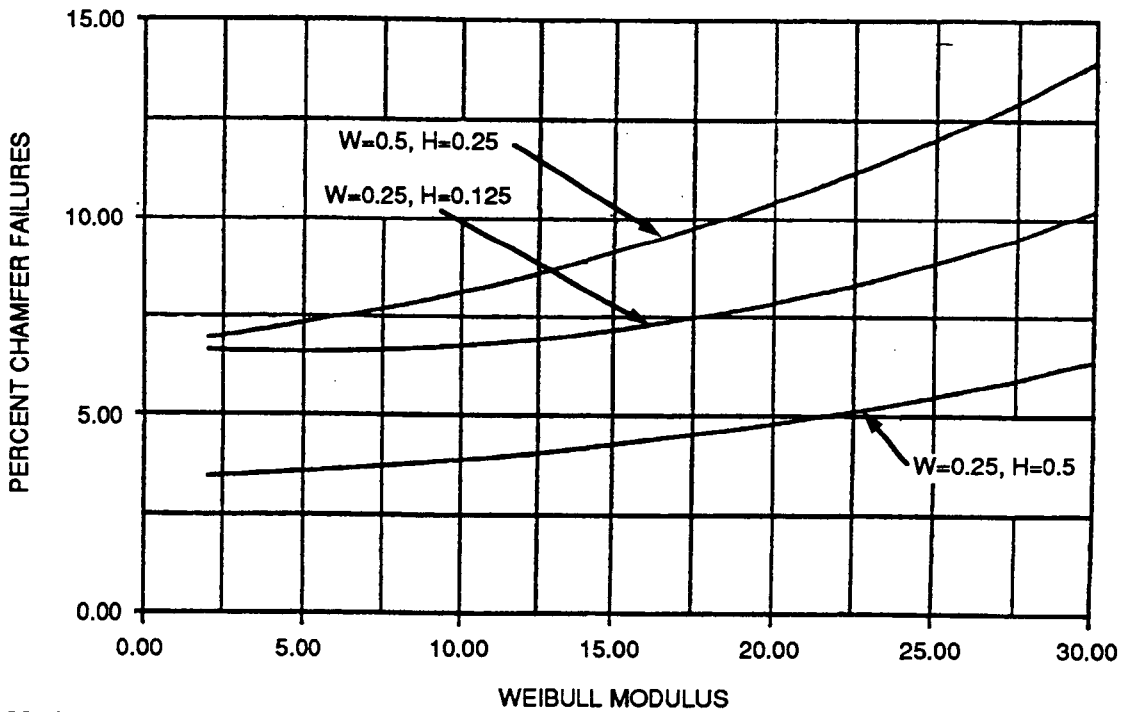
Figure 3-7. Stresses In The Chamfer Region Were Modified As Shown When A Stress Concentration Of Five Percent Was Used For Corner Flaws.

The expected percent chamfer failures were calculated using Weibull size-scaling methods. The fraction of failures expected in the chamfers is the combined probability of failure in regions 2 through 5, divided by the combined probability of failure in regions 1 through 5. The percent chamfer failures were calculated for Weibull moduli (m) ranging from 2 to 30, and are plotted in Figures 3-8 and 3-9. The corner stress concentration was assumed to be zero for Figure 3-8, and five percent for Figure 3-9. The indicated percent chamfer failures should be observed if the chamfer has the same flaw distributions as the tensile face of the specimen. As would be expected, the five-percent corner stress concentration causes the percent of chamfer failures to increase with increasing Weibull modulus, because the material becomes more sensitive to peak stresses in the chamfer as Weibull modulus increases.



GC11591-308A

Figure 3-8. Predicted Percent Chamfer Failures For A Corner Stress Concentration Of 1.00 (W And H Are Flexure Bar Dimensions In Inches).



GC11591-309A

Figure 3-9. Predicted Percent Chamfer Failures For A Corner Stress Concentration Of 1.05 (W And H Are Flexure Bar Dimensions In Inches).

Results from these analyses were used to guide machining vendor qualification, with the objective of selecting a vendor that could provide surfaces that will not have excessive (greater than ten percent) chamfer failures. These results were also used to determine if chamfer failures should be combined with surface failures when estimating strength parameters (discussed in section 5.3.2).

Prior to machining the data base specimens, a statistically-designed Taguchi experiment was conducted with four vendors to evaluate the influence of the following critical machining and heat treatment parameters:

- **Machining Parameters**
 - (1) Standard removal rate = 2.5 μm per pass to 50 μm minimum depth
 - (2) Rapid removal rate = 12.7 \pm 2.5 μm per pass to 50 μm minimum depth

- **Grinding Orientation**
 - (1) Longitudinal
 - (2) Transverse

- **Postmachining Heat Treatment**
 - (1) None
 - (2) 1400C/1 minute/air

Following machining and heat treatment, NT154 MIL-B specimens were tested by NAC at room temperature in four-point bending. Fractography was performed by AlliedSignal using a 40X stereoscopic microscope on all the flexure bars tested in the machining study. Special efforts were made to determine whether fractures originated from a chamfer corner.

The best results in the machining study were achieved by BOMAS*, the vendor selected to machine flexure specimens for the remainder of the program. No chamfer failures were observed on specimens machined in the longitudinal direction using the standard removal (feed) rates. Severe (rapid) feed rates, in combination with a postmachining heat treatment resulted in chamfer initiations for 6 percent of the failures. Heat-treated transverse-machined specimens using standard removal rates exhibited 11 percent chamfer failures.

To facilitate processing, NAC conducted an ATTAP-funded study to optimize the postmachining heat treatment. Based on the NAC results, a 1000C/20 hours/air heat treatment was subsequently adopted for the postmachining heat treatment.

*BOMAS Machine Specialties, Inc., 334 Washington Street, Somerville, MA 02143.

3.4 Specimen Quality

All machined specimens were initially inspected visually and dimensionally at NAC. The specimens were then delivered to AlliedSignal and visually inspected at 7X to 40X magnification using a stereo optical microscope. Visually acceptable specimens were then laser marked to facilitate traceability during subsequent nondestructive evaluation (NDE) and testing. The location and size of the laser marking was carefully chosen to avoid possible damage to the specimens. Most of the specimens were evaluated for cracks with fluorescent penetrant inspection (FPI). Selected specimens were also inspected by other NDE techniques, including radiography (RT), acoustic microscopy (AM), and computed tomography (CT).

Visual inspection of the tensile specimens revealed that most specimens had chips at the top and underside of the buttonhead. The chips at the underside of the buttonhead were of concern since contact with the split collet in the grip mechanism during testing might produce stresses sufficient to initiate buttonhead failures. The chips occurred during machining and were greatly reduced after corrective action was taken by the machining vendor.

Visual inspection of the tensile specimens also revealed that fourteen specimens had grind marks or scratches in the gage section. The scratches were either transverse or near-transverse to the longitudinal machining direction of the gage section. Based on prior AlliedSignal test experience with NT154, these marks or scratches were believed to be severe enough to cause failure. Consequently, these specimens were remachined to remove the flaws. The exact cause(s) of the flaws is unknown, but are believed to be accidental or atypical to the standard fabrication procedure. These flaws were only observed on specimens in the early deliveries, and none were seen on any of the 88 specimens in the last delivery batch.

It should be noted that inspection of prototype and "first article" machined specimens and communication with the machining sources greatly facilitated the process of procuring high-quality ceramic test specimens with complex geometries. This approach facilitated the identification and resolution of potential problems before machining of the rest of the specimen order was accomplished.

3.5 Heat Treatment

All the NT154 specimens tested in this program had at least two heat treatments. The first heat treatment was applied to the HIPed billets to promote crystallization of the grain boundary phase(s). While the details of this heat treatment are proprietary, NAC has indicated that the temperature was higher than the test temperatures

used in this program. A second heat treatment of 1000C for 20 hours in air was used to improve the machined surface strength.

Selected specimens received an additional heat treatment to further increase surface strength. The spin disks and some MIL-B bars received an AlliedSignal-developed heat treatment (1215C for 20 hours in air) to improve the transverse-machined surface strength. In the oxidation study this heat treatment was shown to increase transverse-machined MIL-B flexure bar strength by 38 percent and to drastically reduce the number of chamfer failures from as high as 90 percent to approximately 10 percent.

4.0 MATERIAL CHARACTERIZATION

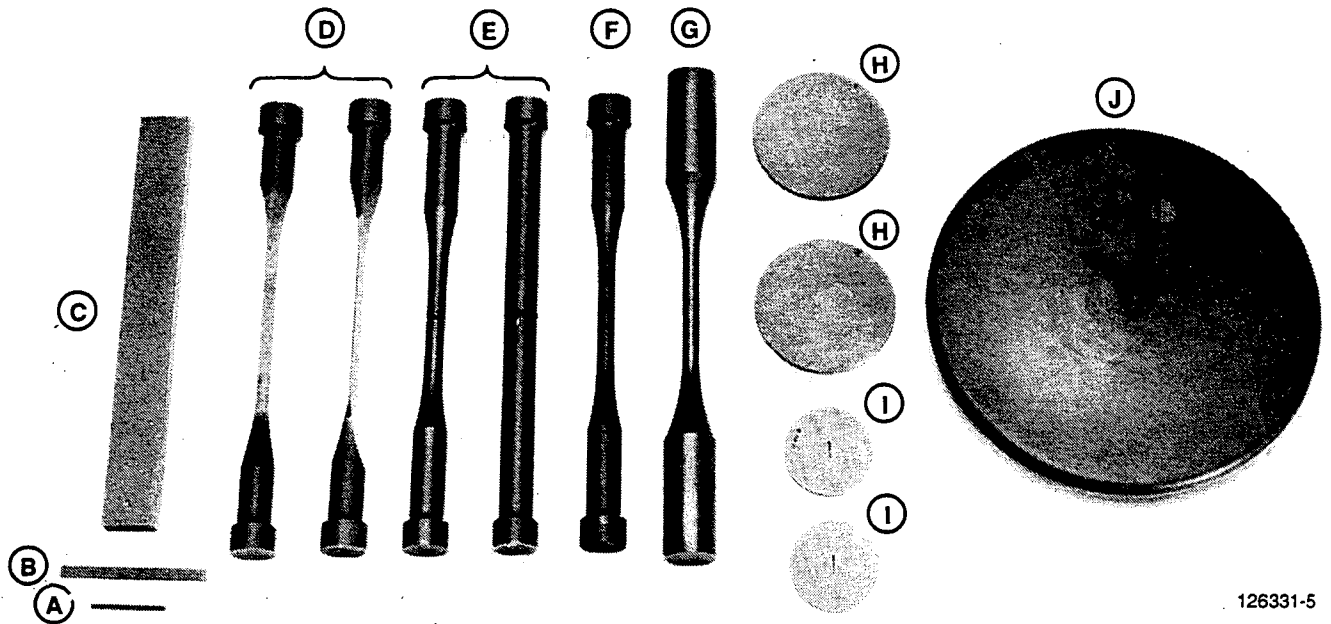
During the Phase I program, more than 1400 ceramic test specimens of 14 different geometries were fabricated and tested to generate a statistically significant sampling of mechanical properties. The objective was to obtain distinct surface and volume flaw distribution information representative of the confirmatory specimens so that life and behavior could be predicted. The temperatures, stresses, and atmospheric conditions during the tests were carefully selected to create conditions that would isolate the different failure modes and separate out the effects of fast fracture, subcritical crack growth, oxidation, and creep. Microstructural characterization was performed with the most appropriate tools and techniques to verify material uniformity, and similarity in flaw population, and to provide microstructural insights that would provide the basis for the failure and deformation mechanisms expected to occur.

All tests were performed using specimens made of the selected structural ceramic material, NT154 silicon nitride from Norton Advanced Ceramics, Worcester, MA, as described in detail in section 3.0. For consistency, all specimens were fabricated from the same raw powder lot by cold isostatic pressing, densification by glass encapsulated hot isostatic pressing (HIPping), and final machining.

4.1 Test Matrices And Specimen Geometries

The test matrices, including the number of specimens, stress concentration (K_t), test conditions, and the relative size and shape of the specimens are shown in Figures 4-1 and 4-2 and Tables 4-1 and 4-2. The test matrices were designed to cover the widest range of test conditions with the least number of specimens and to generate reliable data with good confidence.

To aid in finalizing the test matrices, a number of experts in ceramic behavior modeling and testing were consulted. Drs. C. Johnson and W. Tucker at the General Electric Corporate Research and Development Center (GE-CRDC) and Dr. D. Shetty at the University of Utah aided in determining the quantities and geometries required to accurately model material behavior and predict component lives. Drs. M. Ferber and M. Jenkins of the Oak Ridge National Laboratory High Temperature Materials Laboratory (ORNL-HTML), Dr. S. Wiederhorn of the National Institute of Standards and Technology (NIST), and Dr. N. Hecht of the University of Dayton Research Institute (UDRI) were consulted regarding test methods to help ensure that accurate results were obtained. In addition, reviews of material processing and machining plans to provide uniform material properties throughout the test matrix were held with Norton Advanced Ceramics (NAC).



126331-5

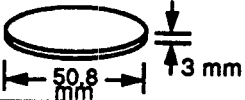
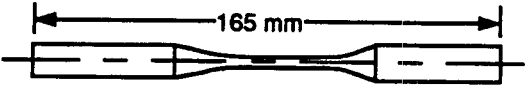
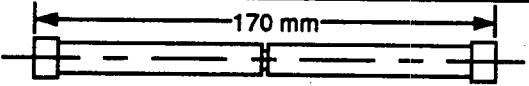
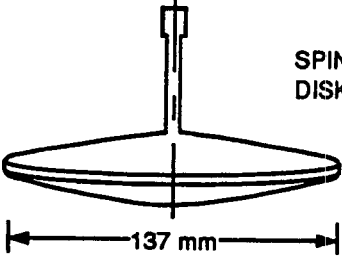
CODE	SPECIMEN TYPE	ROOM TEMP.	ELEVATED TEMP.*
		NO. SPECIMENS	
A	MIL-A	60	—
B	MIL-B	300	180
C	LARGE FLEXURE	100	—
	CHEVRON NOTCHED	60	10
I	DIAMETRAL COMPRESSION	30	42
E	NOTCHED TENSION-TORSION	20	—

* 980-1400C

GB11591-401C

CODE	SPECIMEN TYPE	TEST TYPE	ROOM TEMP.	ELEVATED TEMP.*
		NO. OF SPECIMENS		
F		TENSILE FAST FRACTURE	100	25
		TENSILE STRESS RUPTURE	—	130 (1-500 HRS)
D		ENVIRONMENT		
		AIR	—	6
		N ₂	—	6

Figure 4-1. Test Matrix For Data Base Included 1069 Specimen Tests.

CODE	SPECIMEN TYPE	TEST MATRIX		
		TEMPERATURE, C		
		ROOM	1204	1371
H	PLATE BENDING 	40	--	--
G	 TENSION - TORSION	30	--	--
E	 NOTCHED TENSILE	10 (FF)	10 (SR)	
		10 (FF)	10 (SR)	
J	 SPIN DISK	14 (FF)	8 (FF)	--
			8 (SR)	6 (SR)

(FF) = FAST FRACTURE

(SR) = STRESS RUPTURE

GC11591-402B

Figure 4-2. Test Matrix For Confirmatory Test Specimens.

TABLE 4-1. SMOOTH TENSILE RUPTURE TEST MATRIX

	<u>Number of Specimens</u>	<u>Temperature, C</u>	<u>Stress Range, MPa</u>
	9	1400	85 - 150
	12	1371	125 - 210
	16*	1371	180
	16*	1371	145
	8	1315	225 - 250
	3	1295	200 - 375
	9	1260	250 - 325
	13	1204	300 - 415
	20*	1204	375
	7	1149	425 - 450
	21*	1149	445
	<u>9</u>	<u>982</u>	<u>450 - 475</u>
Total/Range	143	982 - 1400C	85 - 475 MPa

*Replicate tests performed at a single combination of temperature and stress.

TABLE 4-2. NOTCHED TENSILE RUPTURE TEST MATRIX

<u>Number of Specimens</u>	<u>K_t</u>	<u>Temperature, C</u>	<u>Stress Range, MPa</u>
7	1.6	1204	240 - 300
10	1.6	1371	115 - 145
10	2.15	1204	175 - 260
11	2.15	1371	115 - 135

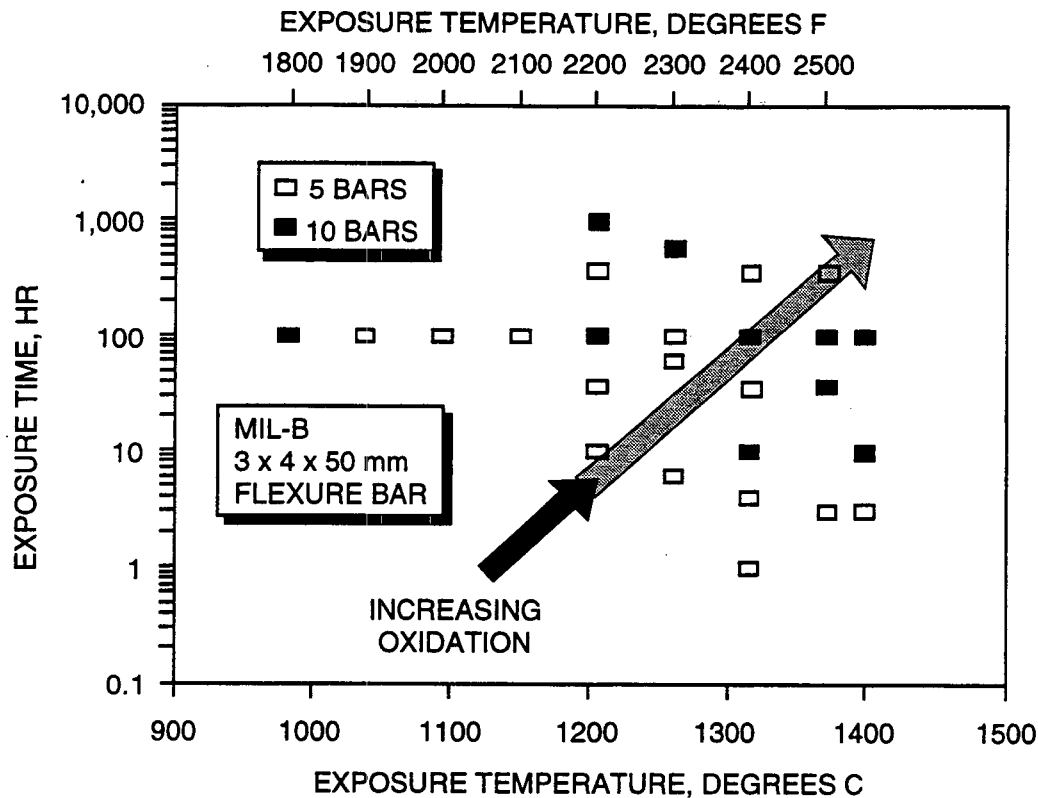
Multiple types of specimen geometries were used to generate the various special stress field or stress intensity conditions required. Special test specimens, including spin disks and notched tensile, flaw growth, and the E-size flexure bars, were designed for specific test purposes. The MIL-A and MIL-B flexure bars are MIL-STD/ASTM specimens, while the chevron notched K_{IC} fracture toughness bars and the ORNL buttonhead tensile specimens are popular industrial test specimen designs. The diametral compression and plate bending disks were either designed or adapted by the University of Utah.

4.1.1 Test Matrix - Data Base Specimens

The two test matrices for the data base specimens are given in Figures 4-1 and 4-2. The oxidation test specimens are listed separately, in Figure 4-3, because an additional range of oxidation heat treatment conditions were applied. The data base test matrices required a total of more than 1400 specimens. Test temperatures and stresses were based on previous AlliedSignal experience with automotive and aerospace heat engine applications, along with the known capabilities of NT154 silicon nitride. Test data sources included AlliedSignal, ORNL, ORNL-HTML, NIST, and UDRI. A smaller-scale test plan was first used, to verify that the temperature and stress levels selected were in the desired creep rate and slow crack growth ranges. Since these three types of tests generated the most comprehensive stress/temperature/time-to-failure data to date, it was extremely important that the tests were performed at the best combinations of stress and temperature.

4.1.2 Test Matrix - Confirmatory Specimens

Test results obtained on "confirmatory specimens" were used to verify the prediction tools and models developed from results obtained from the data base test specimens. The test matrix for the confirmatory specimens is listed in Figure 4-2. The two elevated temperatures for the notched tensile stress rupture tests, as well as the fast fracture and stress rupture conditions for the spin disks were selected based on results from the buttonhead tensile creep/rupture tests.



GC11591-431

Figure 4-3. Static Air Furnace Exposure Test Conditions.

4.1.3 Specimen Geometries

Drawings or schematics of some of the following specimens are presented in Appendix I: MIL-A, MIL-B, and E-size bars for flexural strength; buttonhead tensile specimens for fast fracture strength and creep/rupture tests; buttonhead tensile specimens with a polished rectangular gage section for flaw growth experiments; and notched tensile, smooth tension-torsion, and spin disk specimens for confirmatory tests. The cut-up plan for machining MIL-B flexure bars with the spin disk surfaces is presented in Appendix I. A photograph of the specimens is shown in Figure 4-1 (top). Specimens of various shapes and sizes were adapted to generate the required mechanical properties test data. Shown in Figure 4-1 (top), from left, are: (A) MIL-A Flexure, (B) MIL-B Flexure, (C) E-Size Flexure, (D) Tensile Flaw Growth, (E) Notched Tensile, (F) Smooth Tensile, (G) Smooth Tension/Torsion, (H) Plate Bending, (I) Diametral Compression Disk, and (J) Spin Disk specimens.

Different sizes of flexure and tensile specimens were selected to generate surface and internal flaw based strength distribution parameters and to evaluate methods for predicting size effects. The three sizes of flexure specimens used were: MIL-STD-A and -B, American Society for Testing and Materials (ASTM) Standard C1161, and a much larger specimen given the designation of E-Size. The dimensions of these specimens and loading distances (height, width, inner span, and outer span) were: MIL-A, 1.5 x 2 x 10 x 20 mm; MIL-B, 3 x 4

x 20 x 40mm; and E-Size, 18 x 9 x 63.5 x 127mm. The E-Size specimens were purposely tested on edge (i.e., the loading pins contacted the 9mm wide surfaces) to increase the ratio of stressed volume to stressed area. A drawing of the ORNL cylindrical buttonhead tensile specimen is shown in Appendix I. It has a 35mm long by 6.3mm diameter gage section.

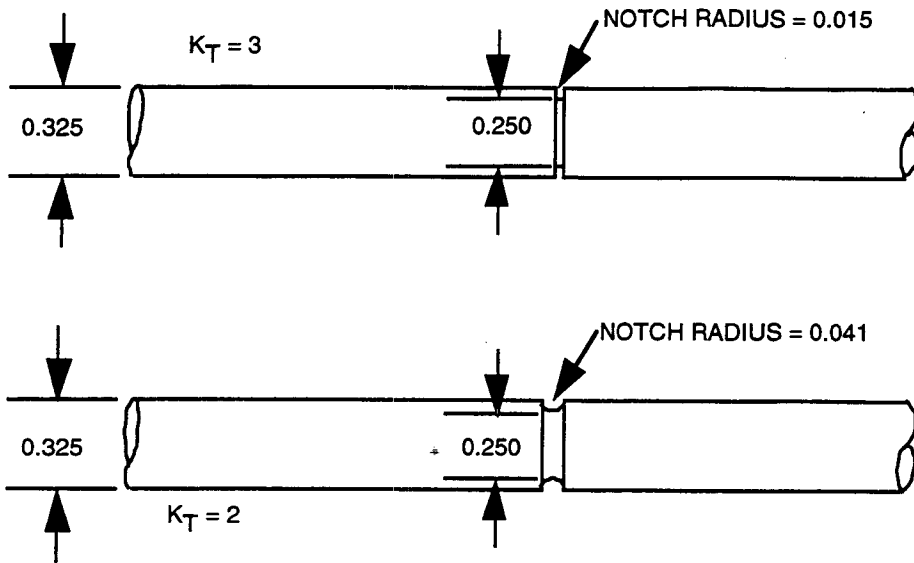
Three types of specimens were used to measure various modes of fracture toughness for developing the multiaxial model. These included the long-beam chevron notched bar for K_{IC} , shown in Appendix I; the diametral compression disk for $(K_I/K_{II})_C$, shown in Appendix I; and the cylindrical notched tension-torsion specimens for $(K_I/K_{III})_C$. A precracking technique for diametral compression disks was developed at the University of Utah by Dr. D. Shetty. The cylindrical notched tension-torsion specimens were circumferentially precracked by the cyclic compression technique developed by Dr. S. Suresh at Brown University.

The buttonhead tensile specimens designed by ORNL were used to generate uniaxial fast fracture and stress rupture data. The same buttonhead design was also adopted for the notched tensile specimens, in which a thin circumferential notch was machined in the middle of the gage section. This design was also used for the rectangular flaw growth specimens, in which the gage section was a polished flat rectangular strip.

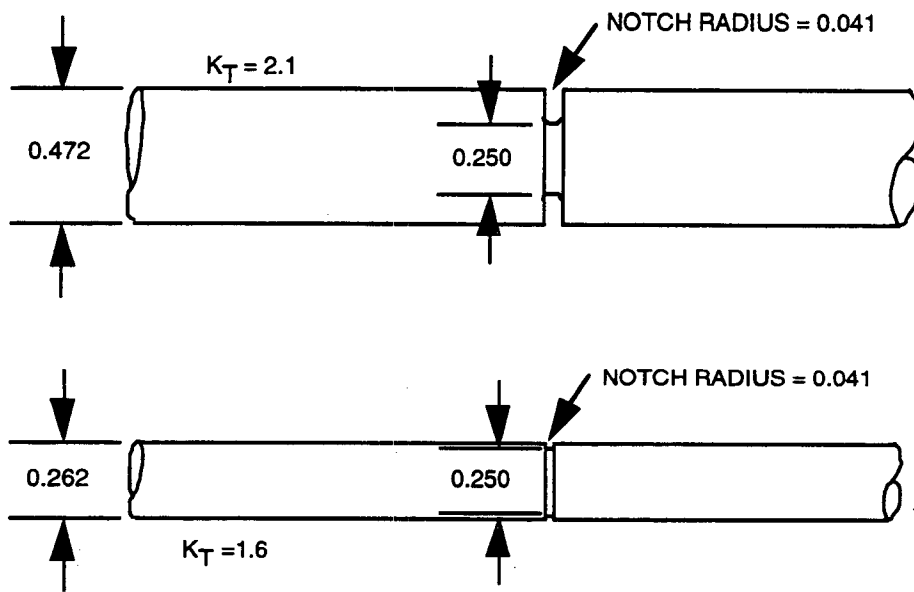
The original notched tensile specimens were designed to have identical gage sections but with notches of different width, as shown in Figure 4-4(a). However, examination of the two prototype specimens indicated that the different diamond wheels used to machine these notches generated significantly different surface finishes at the notch root, shown in Figure 4-5. This condition was undesirable, so the specimens were redesigned [Figure 4-4(b)] to allow use of the same diamond wheel to machine the notches on different diameter gages.

The spin test disk was originally designed to simulate the size and multiaxial stress conditions of an integral turbine rotor. An initial disk geometry was established, to produce higher volume than surface stress. Later, the disk design was modified after further analyses using NT154 tensile properties from UDRI showed the original design had higher surface failure risk than volume failure risk. The new design (Figure 4-6) has the same volume as the previous disk; however, the disk thickness was decreased at the rim and increased at the center, to achieve higher volume failure probability. A higher volume failure probability was desired, to more accurately simulate rotor conditions and to test volume failure prediction methods.

Increased volume failure probability was achieved by increasing the volume stresses, relative to surface stress. The previous disk design had 2 percent higher volume stress than surface stress; the new design has 17 percent higher volume stress. Reduced surface stress was primarily achieved through two design changes: 1) decreased rim thickness and increased centerline thickness; and 2) a change from a simple fillet to a compound



(a) ORIGINAL DESIGN

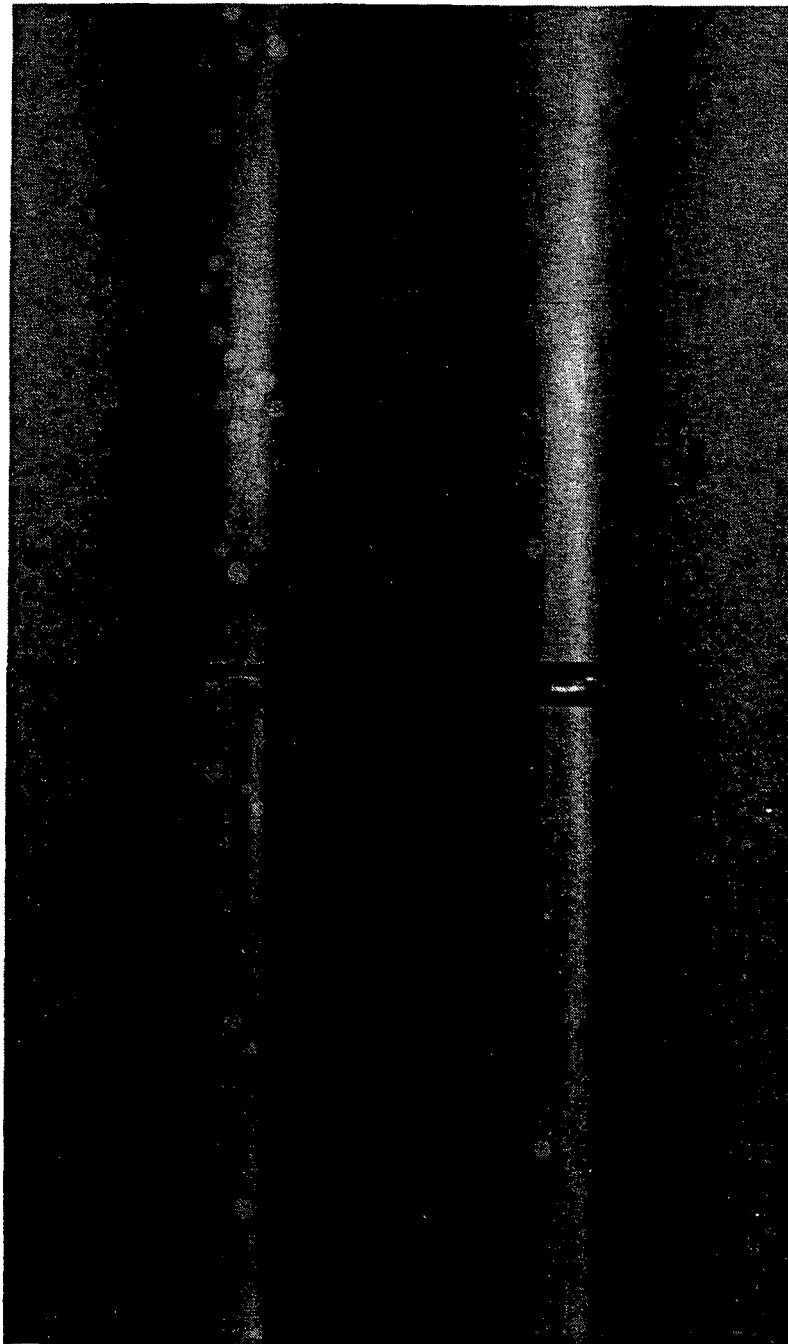


(b) IMPROVED DESIGN

ALL DIMENSIONS IN INCHES

GC11591-403

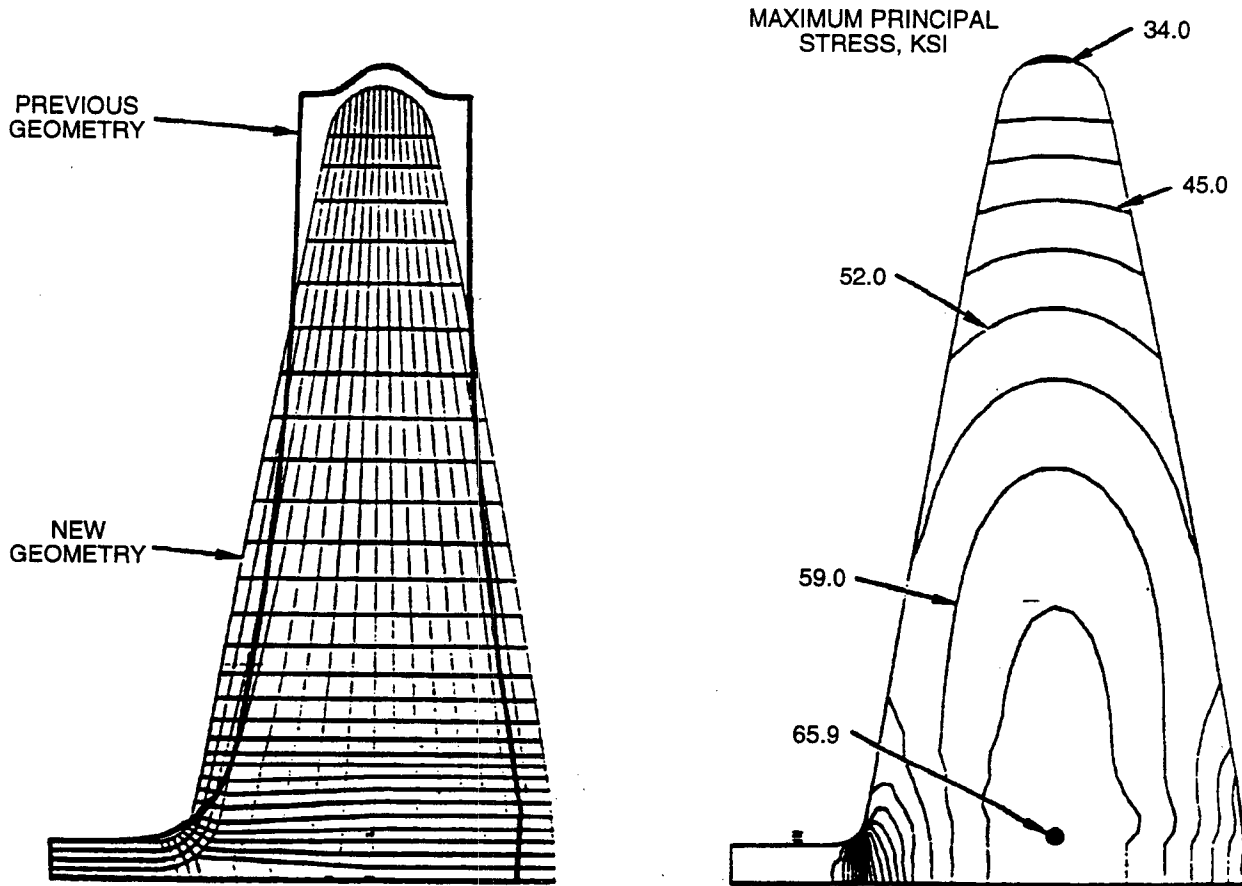
Figure 4-4. Notch Test Specimens Were Redesigned To Eliminate Notch Radius Surface Finish Differences.



GB11591-404

116697-11

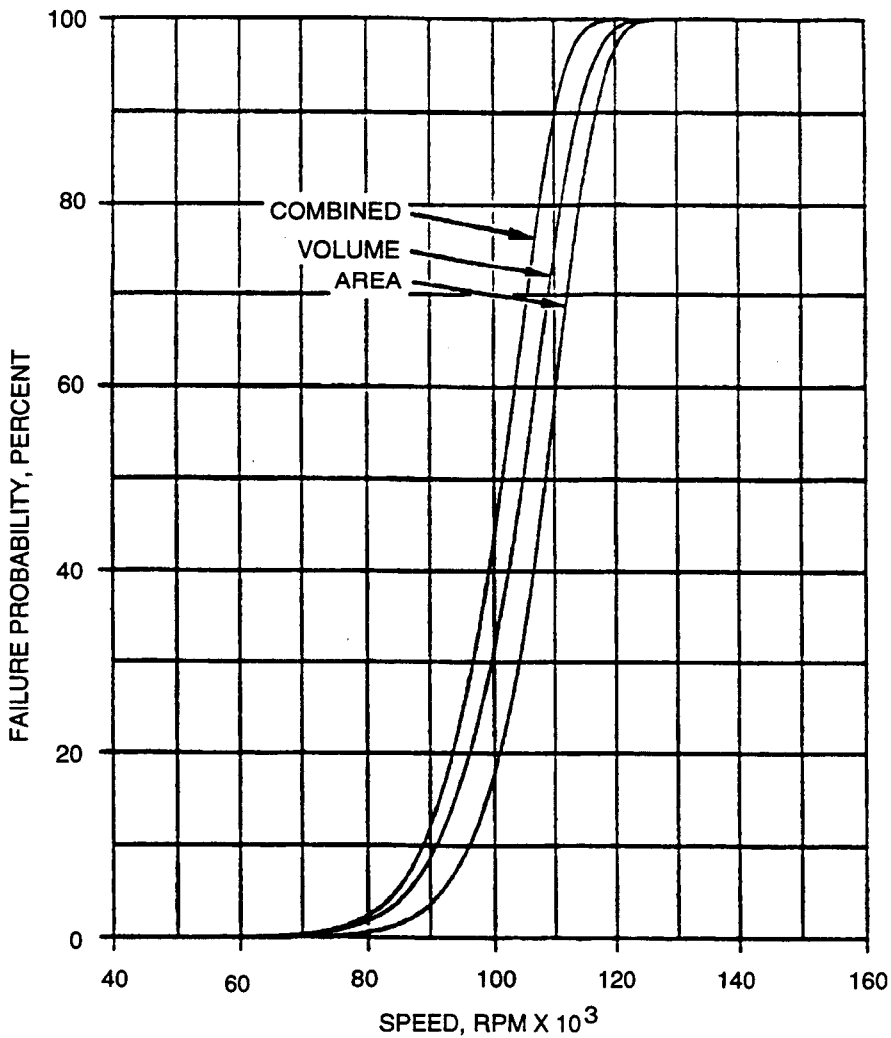
Figure 4-5. Prototype Of Early Design Notch Test Specimens Showed Unacceptable Differences In Surface Finish In The Notch Radius.



GC11591-405

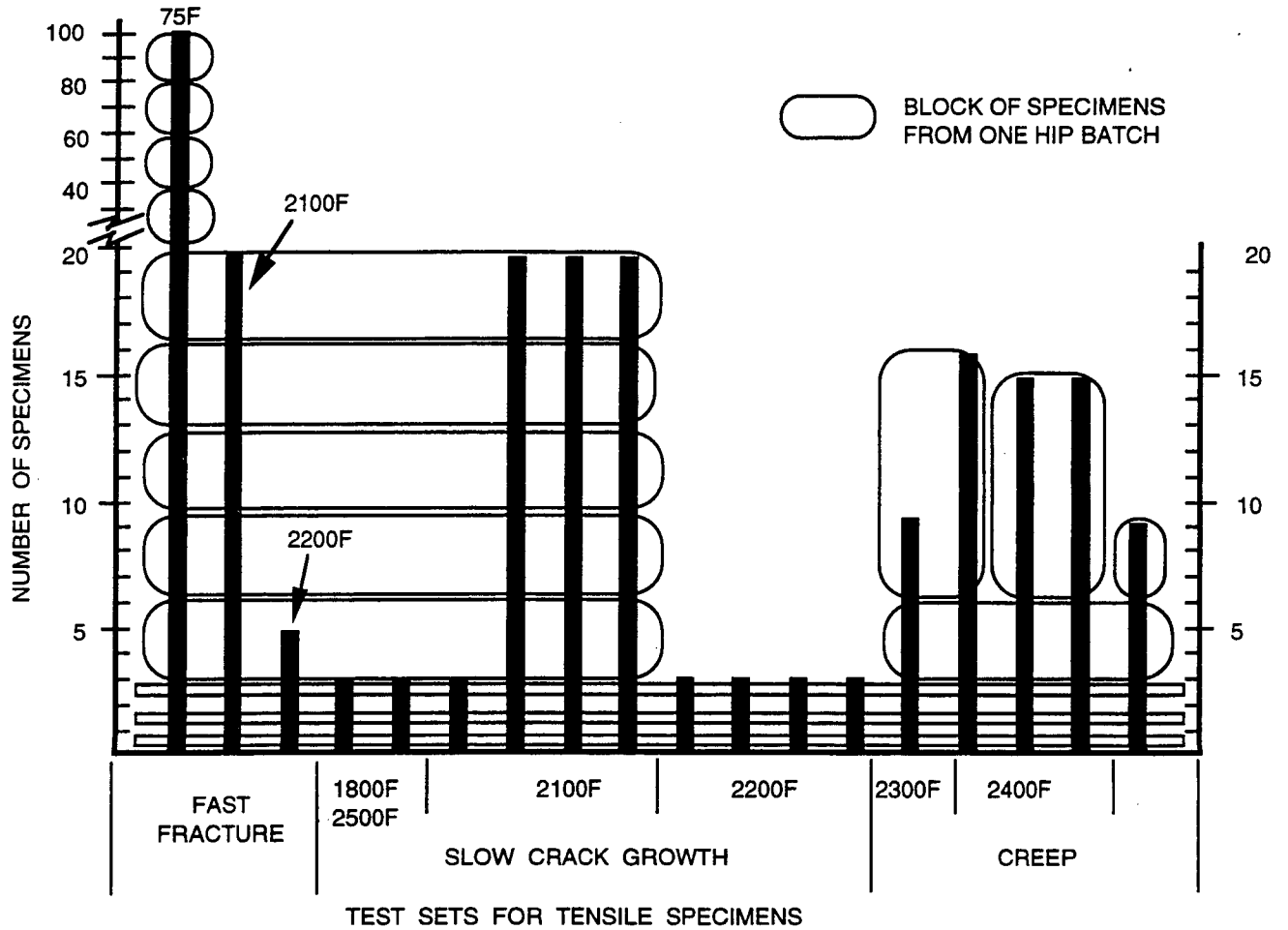
Figure 4-6. Spin Disk Geometry Was Modified To Increase Maximum Volume Stress Relative To Maximum Surface Stress. Stresses Shown Are For 100,000 rpm Cold Rotation.

fillet between the disk profile surface and the shaft. Figure 4-6 shows the maximum principal stresses in the new design. Higher speeds are required to spin test this design, but the predicted failure speed was successfully achieved with available high-speed motors. The surface, volume, and combined failure probabilities are plotted against rotational speed in Figure 4-7. Significantly higher volume failure probability, based on predictions with UDRI data, were achieved. The redesigned spin disk was successfully fabricated and tested in this program.



GC11591-406

Figure 4-7. Spin Disk Risk Analyses Show The New Geometry Has Higher Volume Failure Risk Than Area Risk And Required Test Speeds Up To 120,000 rpm.



GC11591-408

Figure 4-9. More Detailed Specimen Allocation Plan Was Devised For Cylindrical Tensile Test Specimens.

4.2.1 Data Base Specimen Testing

4.2.1.1 Flexural Strength

Flexure strength testing was performed in four-point bending test fixtures with pins capable of rolling freely. For room-temperature testing, the MIL-B bars were tested using a steel test fixture identical to those used in the International Energy Agency (IEA) round-robin flexure testing (ref. 4-1). The MIL-A bars were tested in the same fixture body but with specially-modified top and bottom load blocks to accommodate the smaller spans. The E-size bars were tested in a special fixture designed to accommodate the high loads associated with testing these large specimens on edge. For high-temperature flexural testing, hot-pressed SiC fixtures were used. Both the longitudinal and transverse load uniformity of all of the fixtures was verified with strain-gaged NT154 flexure bars and were within the acceptable range (5 percent).

4.2.1.2 Tensile Testing

4.2.1.2.1 Tensile Fast Fracture Strength

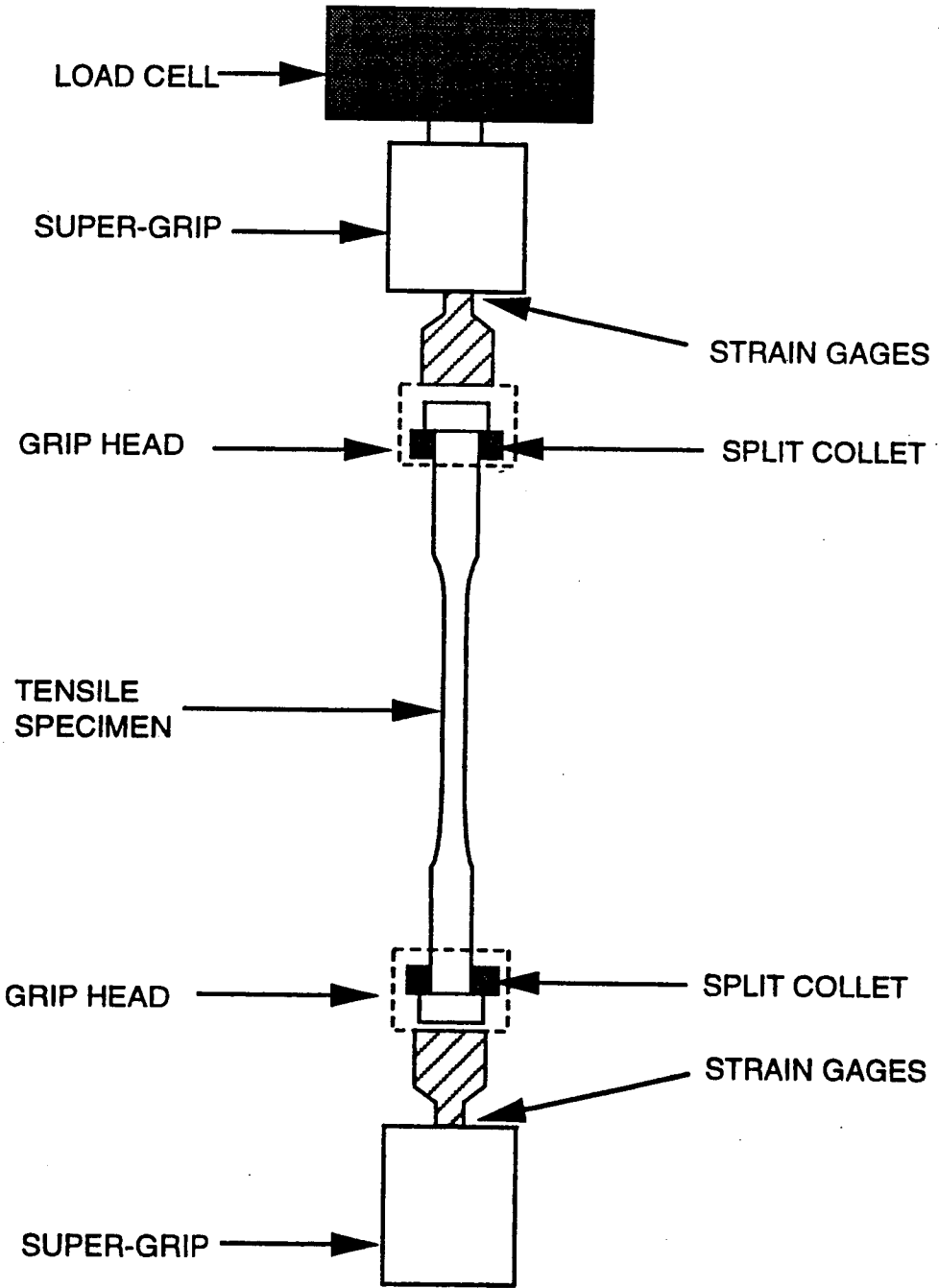
The tensile test setup consisted of an Instron Model 1380 machine with self-aligning Supergrips. The grips were attached to the load frame using self-aligning hydraulic couplers to minimize bending moments. Test procedures designed to minimize bending and avoid buttonhead failures were previously developed during the IEA Round-Robin Tensile Test Program (ref. 4-1), which used strain-gaged tensile specimens.

Excessive bending in tensile test specimens has been of historical concern. Although the Instron Supergrips are designed to minimize bending, monitoring the setup as well as each test was the only way to ensure that other factors were not entering into the test and causing unacceptable bending. Due to the large number of specimens (125) that were to be tested, cost and schedule limitations prevented strain gaging every specimen. As a result, an alternative technique to facilitate the setup and monitor bending in each test was successfully developed.

As shown schematically in Figure 4-10, the top and bottom load rods were machined to a reduced midsection and strain gages were then attached. Data obtained under an AlliedSignal-funded independent research and development (IR&D) program demonstrated that the maximum bending output from the load rods correlated with maximum bending as measured by strain gages attached to tensile test specimens. Output from the load rod strain gages were used for specimen setup and to monitor specimen bending during testing. An added advantage of this approach is that the leads from the strain gages do not have to be changed after each specimen test, which can be a very time-consuming task for specimens with eight strain gages.

Nickel-based superalloy IN718 collets were initially used, since preliminary testing indicated that they provided lower specimen bending and better correlation between load rod and tensile specimen strain gage outputs. However, buttonhead failures occurred after the collets were reused and it was cost prohibitive to replace the IN718 collets after each test. Subsequently, a new pair of oxygen-free, fully-annealed copper collets was used for each test. Care was taken to inspect the collets, collet holder, and collet holder plates prior to each test and to remove scratches and specimen debris that could cause buttonhead failures.

A special procedure was developed to seat the copper collets, which reduced bending and prevented buttonhead failures. The procedure involved loading to 1500 pounds and then checking the bending. The specimen was then unloaded, rotated to a different position and loaded again. This was repeated, and testing was initiated when the bending on both load rods was below 8 percent at 1500 pounds.



GC11591-409

Figure 4-10. Pull Rods Were Equipped With Strain Gages To Monitor Bending.

Testing was performed in the load control mode at 900 lb/min loading rate. A Daytronic/PC system with the Daytronic Logger program* was used to collect data at 0.5-second intervals up to specimen failure. The data included date, time, load, individual gage outputs, and percent bending.

The same procedure was used for high-temperature testing at 1148C and 1204C, except a resistance-heated furnace was used to heat the specimen between the collet holders. The soak time at temperature was 15 to 30 minutes.

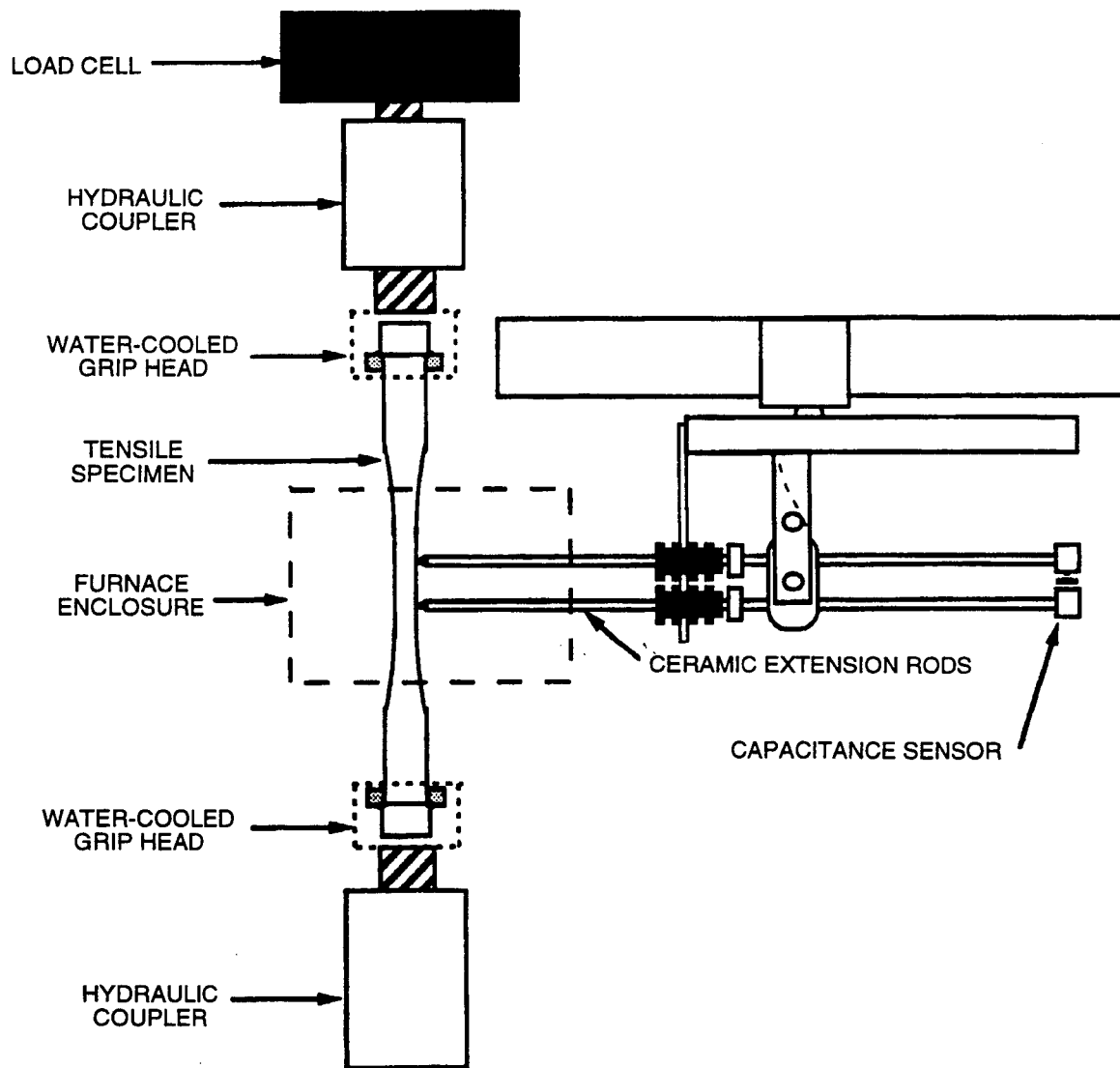
4.2.1.2.2 Tensile Creep/Stress Rupture

Creep/stress rupture testing was conducted in uniaxial tension under constant load on commercial electromechanical tensile test machines in ambient air. As shown in Figure 4-11, the specimen grips, with copper collets configured for buttonhead specimens, were located outside the compact, two-zone resistance-heated furnace, which was capable of generating a maximum temperature of 1600C. The grips were attached to the load frame using self-aligning hydraulic couplers to minimize bending moments. The percent bending was measured at room temperature using strain-gaged specimens to ensure that minimum bending was imposed on the specimens during the creep tests. In all cases, maximum bending was estimated to be on the order of three percent of the uniaxial stress.

Specimen displacements were measured over a 25mm gage length with direct-contact extensometers employing SiC probe arms and capacitive sensors. A resolution of 1 μ m displacement could be achieved with this setup. Personal computers (PCs) equipped with electronic data acquisition systems were used to monitor and store various output signals, including displacement, load, and test temperature.

Creep rates were large enough to be reliably measured only in the range of 1204C to 1400C. All tests were conducted either without interruption and taken to failure, or interrupted after approximately 500 hours. Because of possible complications that may arise from viscoelastic effects, procedures involving temperature or stress excursions, which are often recommended for obtaining estimates of activation energy or stress exponent, were not employed in these experiments.

*Daytronics Corporation, 2589 Corporate Place, Miamisburg, OH 45342.



GC11591-410

Figure 4-11. Loading Configuration For Creep Measurements.

4.2.1.3 Fracture Toughness

Long-beam, chevron-notched bar testing was conducted at both room and elevated temperature in the same hot-pressed SiC fixture used for the MIL-B flexural bars, but at a lower crosshead speed of 0.0005 inch/min. Only data from specimens showing stable crack growth (as indicated by the load deflection curves) was used for later analysis.

4.2.1.4 Diametral Compression

Chevron-notched diametral compression disks were used to generate mixed-mode fracture toughness parameters K_{IC} and K_{IIIC} , as shown in Appendix II, Figure 5. The precracking technique for the diametral compression disks was developed at the University of Utah, under subcontract with Professor D. Shetty. Details of the precracking and test techniques are described in the University of Utah report in Appendix II. The final successful precracking technique involved preloading the notched disks to 97 percent of the average failure load and then exposing precrack inside the notch by surface grinding and polishing the flat faces. (Figure 4-12).

4.2.1.5 Notched Tension/Torsion Testing

Notched tension/torsion tests to evaluate room temperature Mode I/Mode III (K_I/K_{III}) fracture toughness were completed under subcontract by Dr. S. Suresh at Brown University, Providence, Rhode Island. More test information is given in the Brown University report in Appendix III. The specimens were 115 x 19mm diameter circumferentially notched silicon nitride cylinders. Cyclic compression fatigue was used to precrack the specimen in the notch. It was demonstrated for the first time that stable cyclic compression fatigue precracks, 100 microns or more in depth, can be introduced in Si_3N_4 . An Instron Model 1322 servo-hydraulic biaxial testing machine was used for the K_I/K_{III} fracture testing. Three special tension/torsion specimens were strain gaged to verify proper equipment alignment.

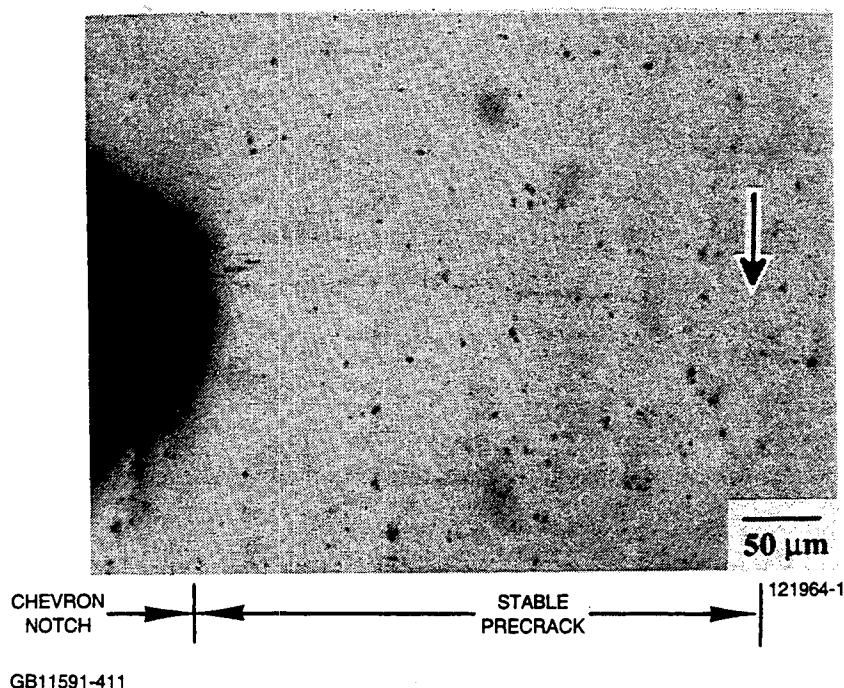


Figure 4-12. Successful Precracking Was Achieved By Preloading Followed By Surface Grinding.

4.2.1.6 Flaw Growth Testing

Twelve rectangular gage section flaw growth specimens were tested in stress rupture conditions at 1148C, 1205C, and 1260C, in air and nitrogen atmospheres. This work was performed under subcontract by A. Nagy at the SouthWest Research Institute (SWRI) in San Antonio, Texas. The rectangular gage sections were polished and the tests were periodically interrupted so that surface replicas could be taken to record any possible subcritical crack growth. After the specimens failed and fracture origins were identified, the replicas were analyzed with SEM to measure crack growth. Fractography of the specimens and review of the replicas are planned to be performed in the upcoming Phase II efforts of this program.

4.2.2 Confirmatory Specimen Testing

4.2.2.1 Notched-Tensile Stress Rupture

Thirty-eight specimens, notched to provide two stress concentrations (K_t) of 1.6 and 2.1, were tested at room temperature in fast fracture and 1204C and 1371C in stress rupture. Extensometry was employed on a few of the stress rupture specimens to record the strains occurring at the notch in the case of the higher K_t specimens, or at the notch and the gage together in the case of the lower K_t specimens. Here also, the tests were continued until fracture or until approximately 500 hours of testing was accumulated. The specimens whose testing was terminated when the creep exposure time exceeded approximately 500 hours were subsequently loaded to failure at room temperature to determine the retained fast fracture strength.

4.2.2.2 Smooth Tension/Torsion

Detailed test procedures for the smooth tension/torsion specimens are presented in Appendix III in the Brown University subcontractor report by A. Kim and Dr. S. Suresh.

4.2.2.3 Plate Bending

Detailed test procedures for the plate bending disks are presented in Appendix II, in the University of Utah subcontractor report by L. Chao and D. Shetty.

4.2.2.4 Spin Disk Testing

Fast fracture spin disk testing was performed at room temperature and 2200F. In addition, stress rupture testing was performed at 2200F and 2500F. The disks were spun to failure in air using an air-driven turbine motor. Figure 4-13 shows the room-temperature spin pit in the AlliedSignal Engines test facilities. Absorbing materials were used to line the inside of the room-temperature spin pit so that the fracture debris could be collected to identify the fracture origin(s).

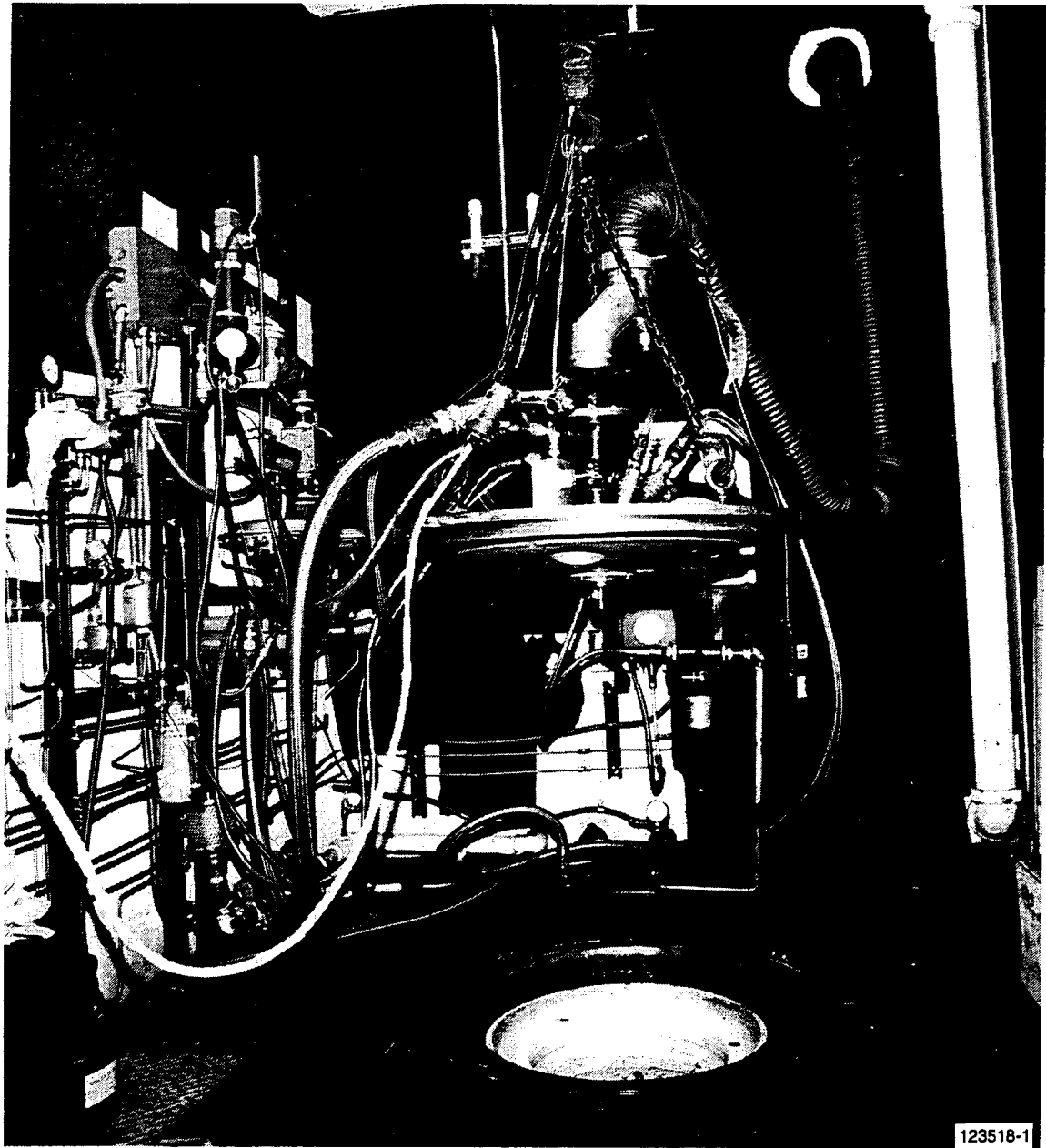
Figure 4-14 shows the interior of the spin pit following a test burst, with debris penetrating the paper cushioning liner. The disk fragments were carefully collected, cleaned, and inspected, and the fracture origin was identified and characterized. Figure 4-15 shows fragments from a typical burst collected and arranged by size; the failure origin documented was the small fragment resting on the "Disk 30" label. For some tests, high-speed photography was used to verify whether the disk failed in a true burst, and to show the approximate failure location (Figure 4-16). However, this method cannot determine the exact failure location and was less effective than fractography.

The spin pit layout for the high-temperature tests is shown in Figure 4-17. The ceramic fiber insulation furnace liner served as the absorbing material for the burst fragments. Heating was accomplished with SiC heating rods. The temperature inside the furnace was monitored with thermocouples, and an optical pyrometer was used to measure the temperature at the bottom of the disk through a viewing port.

4.2.3 Fractography

Both visual and scanning electron microscopic (SEM) fractographic analysis of failed specimens was performed to identify fracture origin locations, types, and other characteristics. The fractography information is vital for performing censored Weibull analyses of the data. MIL-HDBK-790 (ref. 4-2) was used as a guide in performing the fractography.

The fracture surfaces resulting from creep tests were first visually examined at 7 to 40X magnification with an optical stereoscopic microscope. This enabled determination of the location of the failure origin and the identification of any differences, on a macro scale, in the morphology of the fracture surfaces in different temperature regimes. This was followed by SEM of the failure origin on the fracture surface for evidence of flaws or defects. Detailed SEM of the original fracture surfaces for the purpose of observing cavitation was somewhat prohibited by the oxide scale produced when these surfaces were exposed to the high-temperature environment upon failure of the specimens. However, observation of cavitation was facilitated by generating



GB11591-412

Figure 4-13. AlliedSignal Room-Temperature Whirlpit Used For Ceramic Spin Disk Tests.

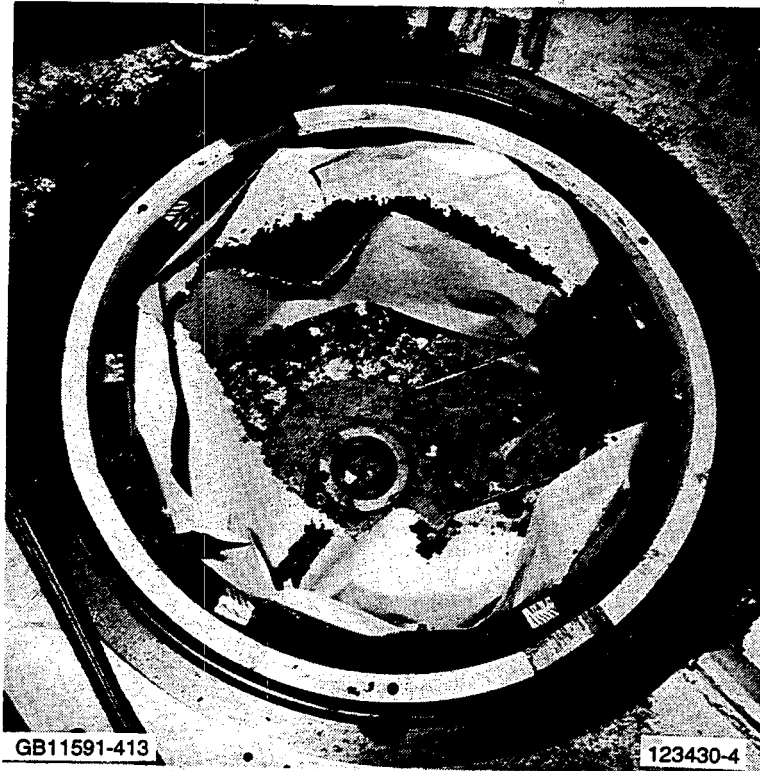


Figure 4-14. Spin Pit Was Lined With Absorbing Material To Collect Fragments.

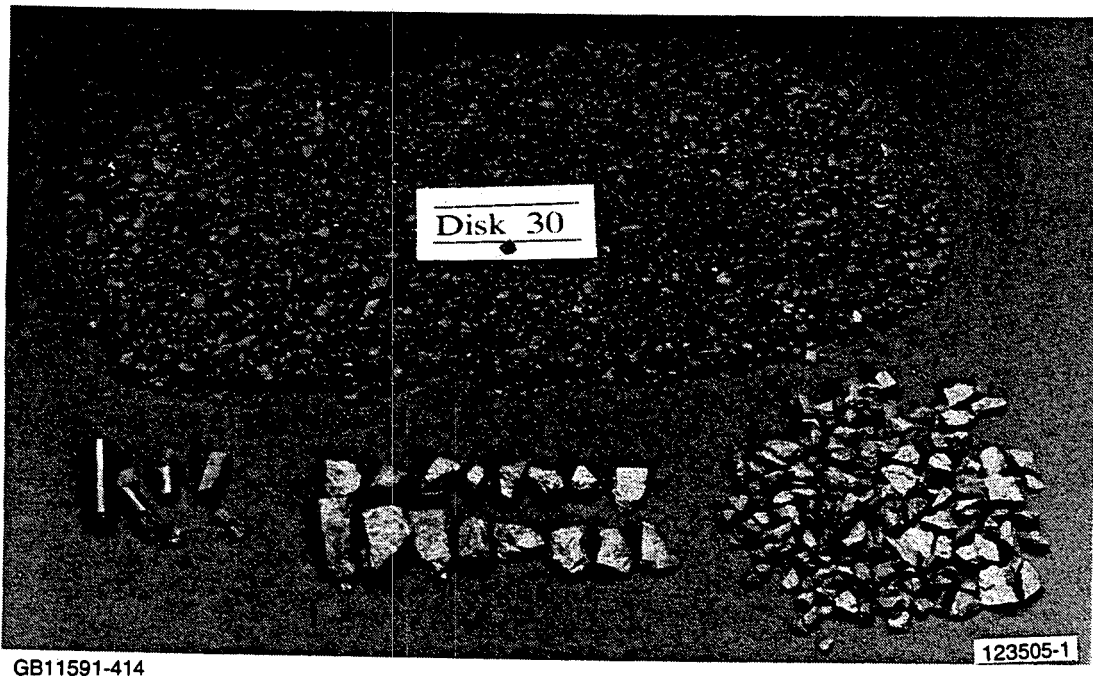
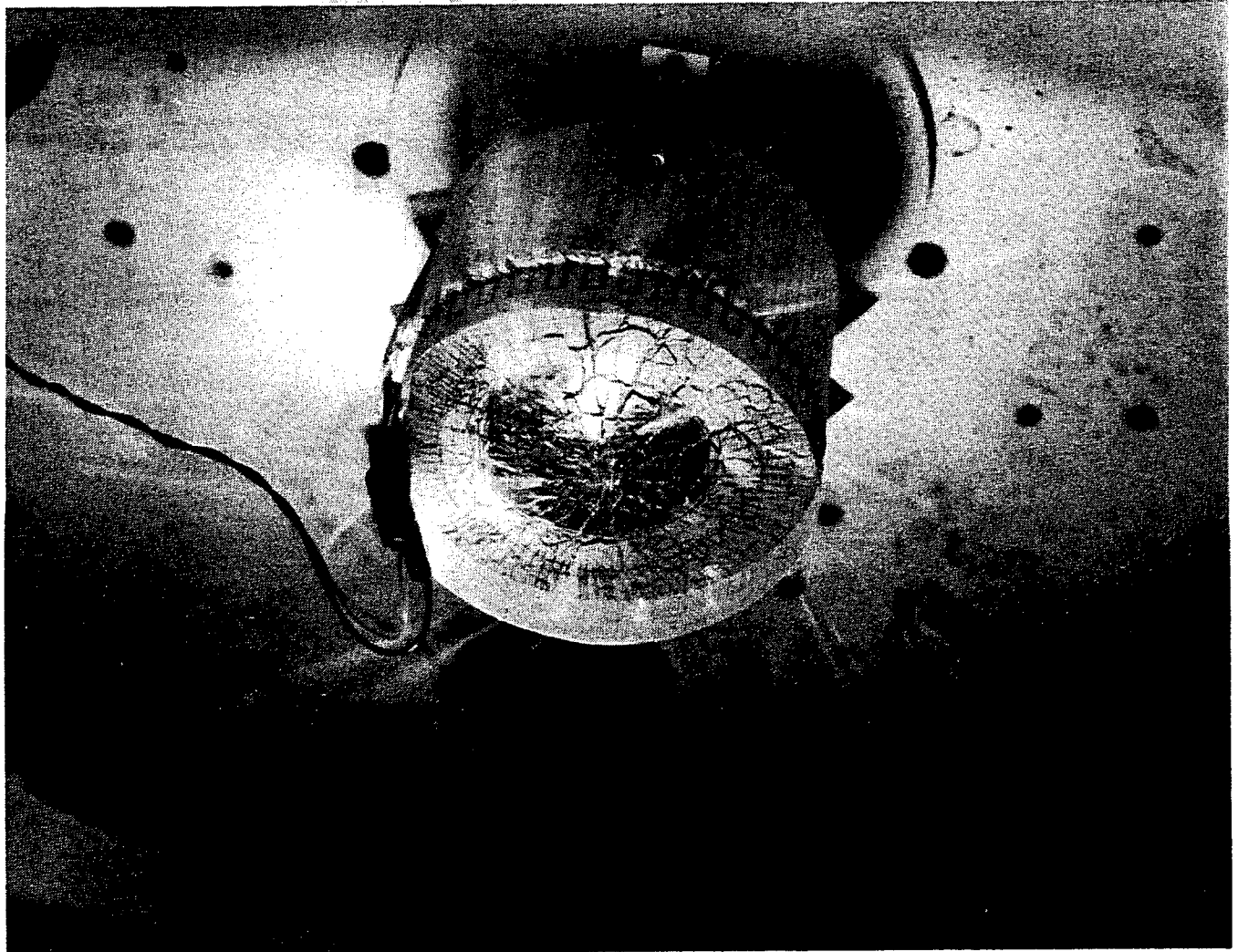


Figure 4-15. Following A Test Burst, The Fragments Were Collected For Determination Of The Failure Origin.

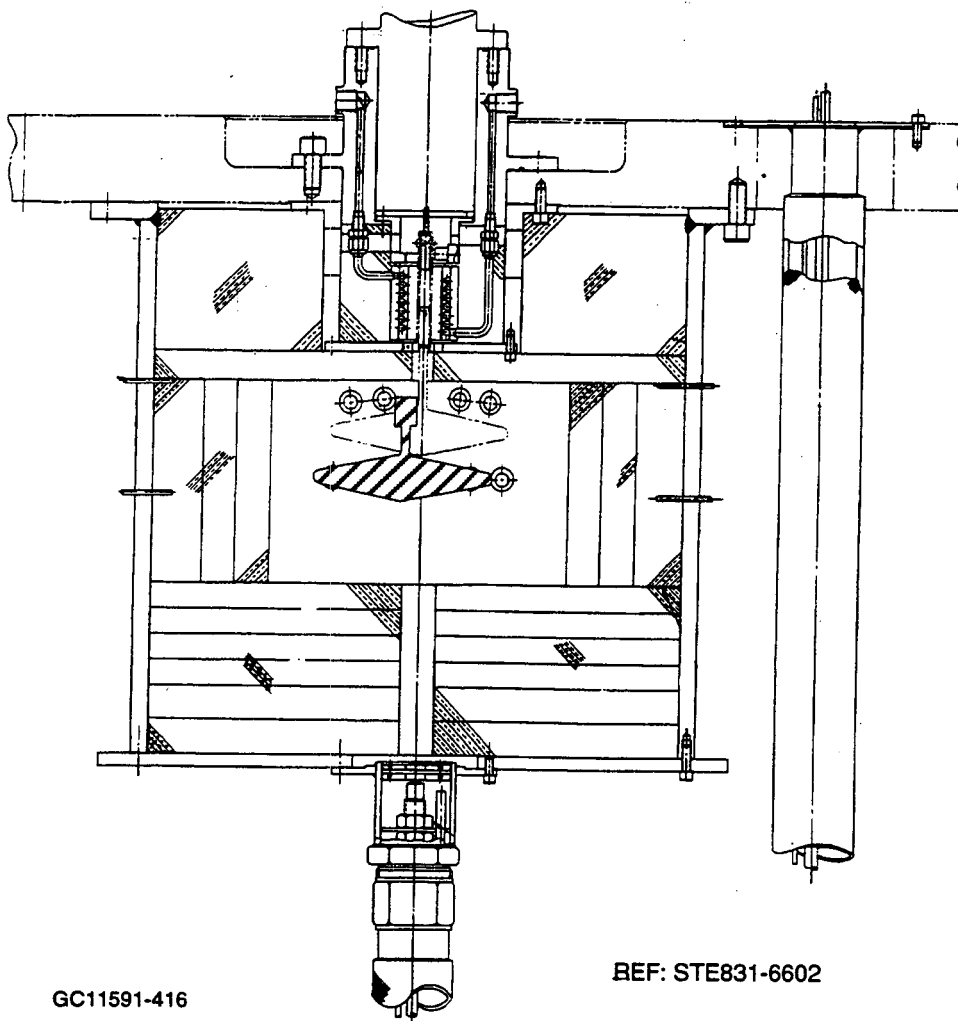


GB11591-415

88,500 RPM

123754-1

Figure 4-16. High-Speed Photography Verified Successful Disk Burst And Showed Possible Impacts Of Fragments Following Burst.



GC11591-416

REF: STE831-6602

Figure 4-17. Hot Spin Pit Layout For 2200F and 2500F Tests.

room-temperature secondary fractures parallel to the original fracture surface in the gage section. This procedure enabled observation of cavities on the two-grain junctions oriented perpendicular to the specimen axis.

In order to obtain a better overall assessment of triple-junction cavitation, longitudinal sections from the gage sections were polished using 6-, 3-, and 1- μ m diamond paste and then carbon coated for SEM observations.

4.2.4 Microstructural Characterization

The microstructure of the as-received and creep-tested specimens was studied using SEM and high-resolution transmission electron microscopy (TEM). Elemental compositions were determined using X-ray

diffraction (XRD) and scanning transmission electron microscopy (STEM). To obtain good representations of grain size and grain aspect ratios, sections of as-received material were polished and then etched in molten potassium hydroxide (KOH) at 400C for 15 minutes. The etchant attacks only the grain boundary phases, leaving the grains in relief. The etched specimens were then gold coated and examined in the SEM. An additional assessment of the grain structure was obtained from SEM of room-temperature fracture surfaces.

Thin sections for TEM analysis were sectioned from the buttonheads and the gage sections following tensile creep testing. The specimens prepared from the buttonheads were representative of the as-received material, since the water-cooled grips kept the temperature of the buttonhead below 200C. The specimens prepared from the gage sections were cut in the longitudinal direction (parallel to the stress axis) to allow viewing a maximum number of grain boundaries subjected to tensile stress. The edge-on views of the tensile boundaries were particularly useful for characterization of lenticular cavities.

Crystalline phases in the bulk samples were identified using XRD. This technique was also used to measure changes in the phase composition resulting from long-term creep exposure. These changes were differentiated by comparing the diffraction pattern from the buttonhead regions to those from the gage sections. This approach minimized uncertainties arising from specimen-to-specimen variations. The elemental compositions of the crystalline triple-junction phases and the amorphous intergranular phase were determined by means of STEM, EDX, and WDX techniques.

4.3 Test Data

Testing and fractography data are presented in the following sections. Section 4.3.1 presents the mechanical property testing results, including fast fracture flexure strength, uniaxial tensile strength, multiaxial strength, unimode and multimode fracture toughness, and tensile stress rupture. The data are in the form of tables or plots with individual raw data points. The combined data and analysis are presented in section 5.3.2. Detailed reports on tests that were performed by subcontractors Brown University and the University of Utah are included in the Appendices.

In section 4.3.2, the fractographic data is presented and discussed, including fracture origin type, location on the fracture plane, and chemistry (when applicable). For the E-Size and tensile test specimens, the fracture plane location relative to the length of the specimen were also included. The fractography data are based on 100 percent optical microscopy and extensive SEM fractography of selected specimens.

4.3.1 **Testing**

4.3.1.1 **Flexure Testing**

The following numbers and sizes of flexure bars were tested: 60 MIL-A, 487 MIL-B and 100 E-Size. All the bars were tested in four-point bending at room temperature and, for 177 randomly selected MIL-B bars, at 980C, 1148C, 1204C, 1260C, 1315C, and 1371C. Test results for longitudinally-machined bars are plotted in Figure 4-18. The 487 MIL-B bars tested also included 180 oxidation study specimens and 80 specimens with different surface machining directions (transverse and 45 degrees). As an example of the data, the average flexure strength of longitudinally machined MIL-B bars is 916 ± 164 MPa at room temperature, 670 ± 26 MPa at 1204C, and 630 ± 26 MPa at 1371C.

Additional MIL-B bars consisting of 30 transverse machined bars, and 30 machined at 45 degrees were tested at room temperature. Strength and Weibull parameter data from these specimens were used in developing the multiaxial failure mode model. A plot of the data is shown in Figure 4-19.

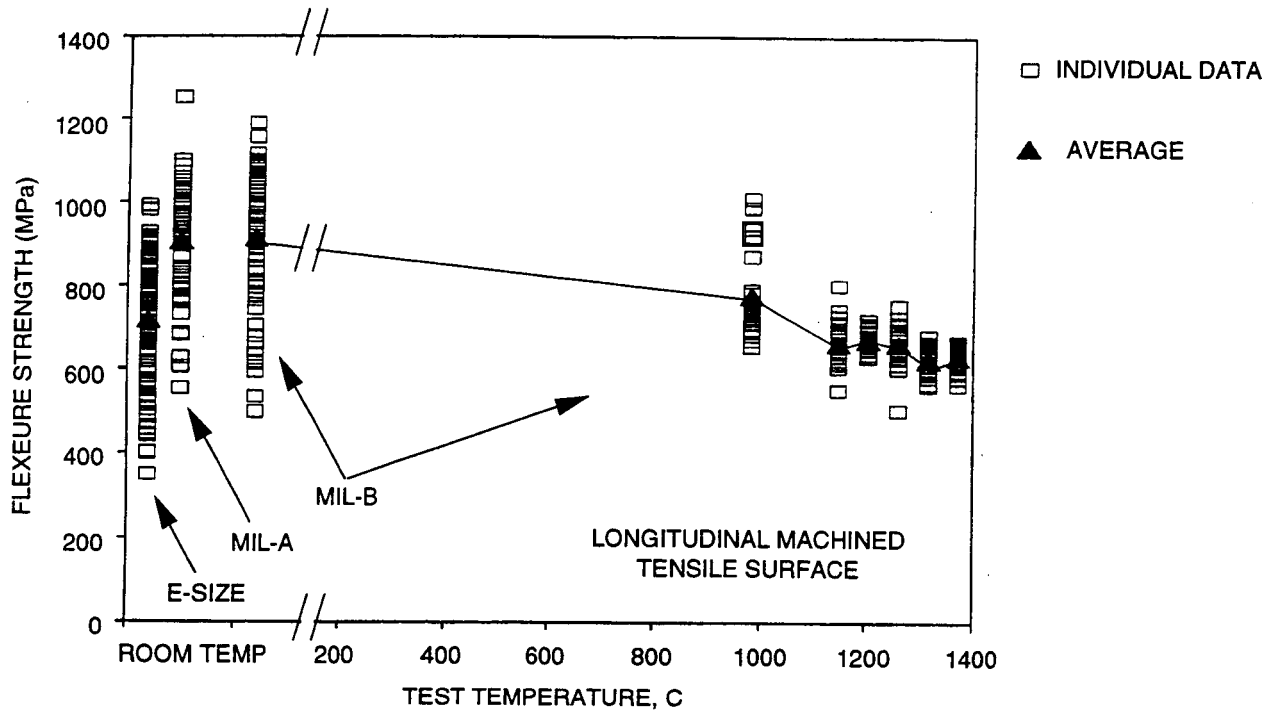
4.3.1.1.1 **Cutup Bars**

Several additional groups of flexure bars were tested during the later part of this program. The first group consisted of 108 MIL-B bars cut from special spin disk blanks, having two surfaces machined flat on the same five-axis CNC machine using the same machining parameters as the actual spin disks. The surfaces of these MIL-B bars had machining directions approximating longitudinal, 45 degrees, and transverse. Strength data for these bars is listed in Table 3 of Appendix IV.

The second additional group of flexure test bars were large 0.525 x 0.400 x 4.0 inch flexure bars machined from the interior of spin disk blanks, to evaluate spin disk volume properties. The size of the specimens was specially chosen to maximize the probability of internal failures. Strength data for these bars is listed in Table 3 of Appendix IV.

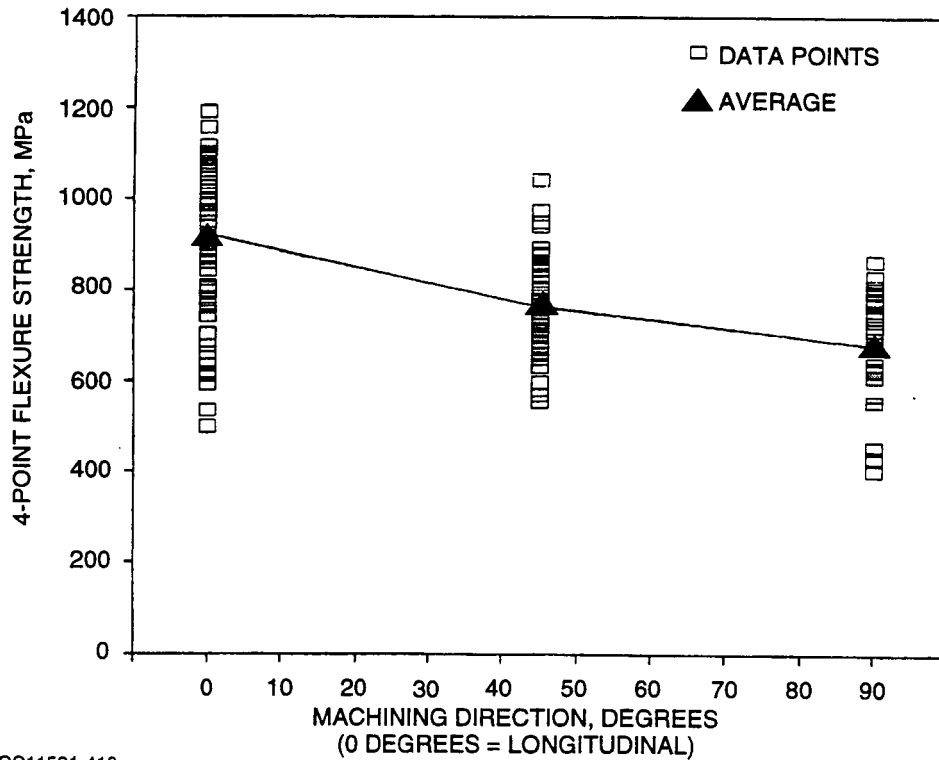
4.3.1.1.2 **Re-Heat Treated Bars**

Most of the baseline flexure bars failed from chamfer corners, which rendered the results virtually useless. The reason and evidence for this result is presented in more detail in the fractography section (4.3.2). Additional MIL-B flexure bar data were generated by applying the AlliedSignal heat treatment to the remaining unused bars. Results for these re-heat treated bars are presented in Table 4 of Appendix IV.



GC11591-417

Figure 4-18. Four-Point Flexure Strength Of NT154.



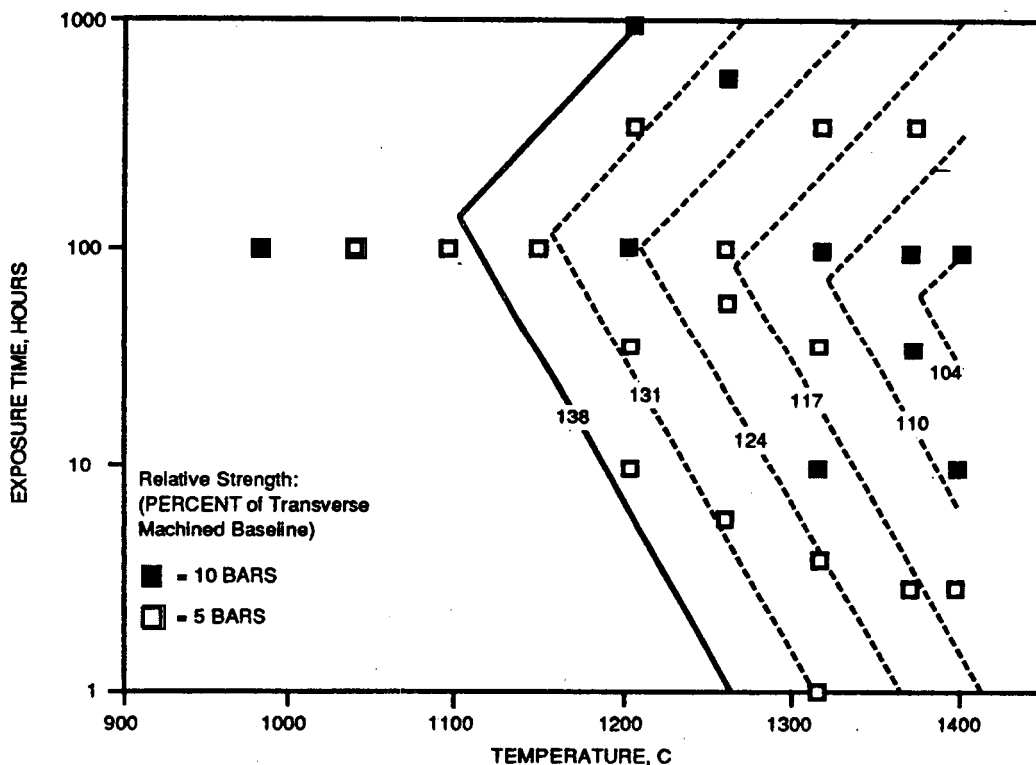
GC11591-418

Figure 4-19. Dependence Of Flexure Strength On Surface Machining Direction.

4.3.1.1.3 Oxidation Flexure Bars

Test results are shown as lines of relative strength in Figure 4-20 and in Appendix IV Table 9. Unexpectedly, exposure of 100 hours in the 980C to 1100C range and 10 hours at 1200C resulted in a significant improvement in strength, relative to as-received specimens which had the standard Norton preoxidation heat treatment; i.e., the average strength of oxidized specimens increased by 38 percent. For longer exposure times (> 100 hours) in the 1100C to 1400C temperature range, specimen strength decreased as expected.

Figure 4-20 also illustrates unusual behavior for exposures longer than 100 hours in the 1100C to 1400C temperature range; the average specimen strength increased with additional exposure time. This behavior was unexpected, since it was not observed in an earlier evaluation of NT154 specimens oxidized in a cyclic 1260C (2300F) Mach 0.3 burner rig environment (conducted by AlliedSignal under DOE/NASA Contract No. DEN3-27) (ref. 4-3). Following exposure to this cyclic burner rig test environment, which more closely simulates the conditions found within gas turbines, measured room-temperature flexure strength continued to decline for exposures up to 1000 hours. The rate of strength reduction after 1000 hours in the burner rig environment was comparable to that observed in the furnace-exposed specimens for times less than 100 hours.



GC11591-420

Figure 4-20. Air Furnace Oxidation Exposures Initially Improved Strength Of Transverse Machined NT154 Specimens.

The results of this study indicated that oxidation at temperatures below 1400C strengthened the surface of NT154. This exposure also reduced the severity of machining-induced surface flaws. Consequently, it may be concluded that oxidation (in the absence of corrosive salt deposits) is beneficial and will not adversely affect predicted component lives in the temperature range of interest for gas turbine applications.

It is speculated that the increase in flexure strength is a consequence of oxidation-induced compressive stresses. Examination of fracture surfaces indicated that oxidation in this temperature range does not occur as a plane-front process; i.e., an oxygen gradient exists below the surface, which is thought to imply preferential oxidation within grain boundaries (and microcracks from machining). Compressive stresses develop when the grain boundary volume expansion (from conversion of silicon nitride to silicon oxynitride) is constrained by unoxidized silicon nitride grains. Maximum strength is anticipated when oxidation-induced stresses are not relaxed by deformation in the oxynitride grain boundary phase. Creep in the oxynitride phase may be responsible for the decreasing benefit of oxidation at temperatures in the 1200C to 1400C range.

Growth of the oxygen-enriched surface layer exhibited logarithmic kinetics in this temperature range. Non-parabolic behavior in this temperature range is potentially attributable to oxidation-induced compressive stresses: i.e., compressive stresses reduce the lattice spacing [by inhibiting thermal expansion of the lattice], which will retard oxygen permeability in the oxynitride grain boundary phase. If this mechanism is correct, oxidation resistance of silicon nitride will be strongly dependent upon the creep resistance (composition) of the intergranular phase.

4.3.1.2 Smooth Tensile Testing

4.3.1.2.1 Tensile Fast Fracture

A total of 125 specimens were tested in tensile fast fracture. One hundred specimens were tested at room temperature, five at 1148C, and twenty at 1204C. The individual strength data points are plotted in Figure 4-21. The average tensile strength was 762 ± 112 MPa at room temperature, 559 ± 37 MPa at 1148C, and 500 ± 69 MPa at 1204C. There were no buttonhead failures using copper collets.

4.3.1.2.2 Smooth Tensile Creep/Stress Rupture Tests

Table 4-3 provides the results of the smooth tensile creep/stress rupture tests. The information includes the specimen identification number, test temperature and applied stress, time-to-failure, minimum creep rate as measured by the last segment of the creep data/curve, the total strain to failure, and the failure classification as to whether the origin of failure was internal or at the surface of the specimen. Figure 4-22 shows the results of the tests conducted on two machines at 1371C and at 1204C at various stresses. The plot does not show any systematic or detectable machine-to-machine variation in the failure times of the creep-tested specimens.

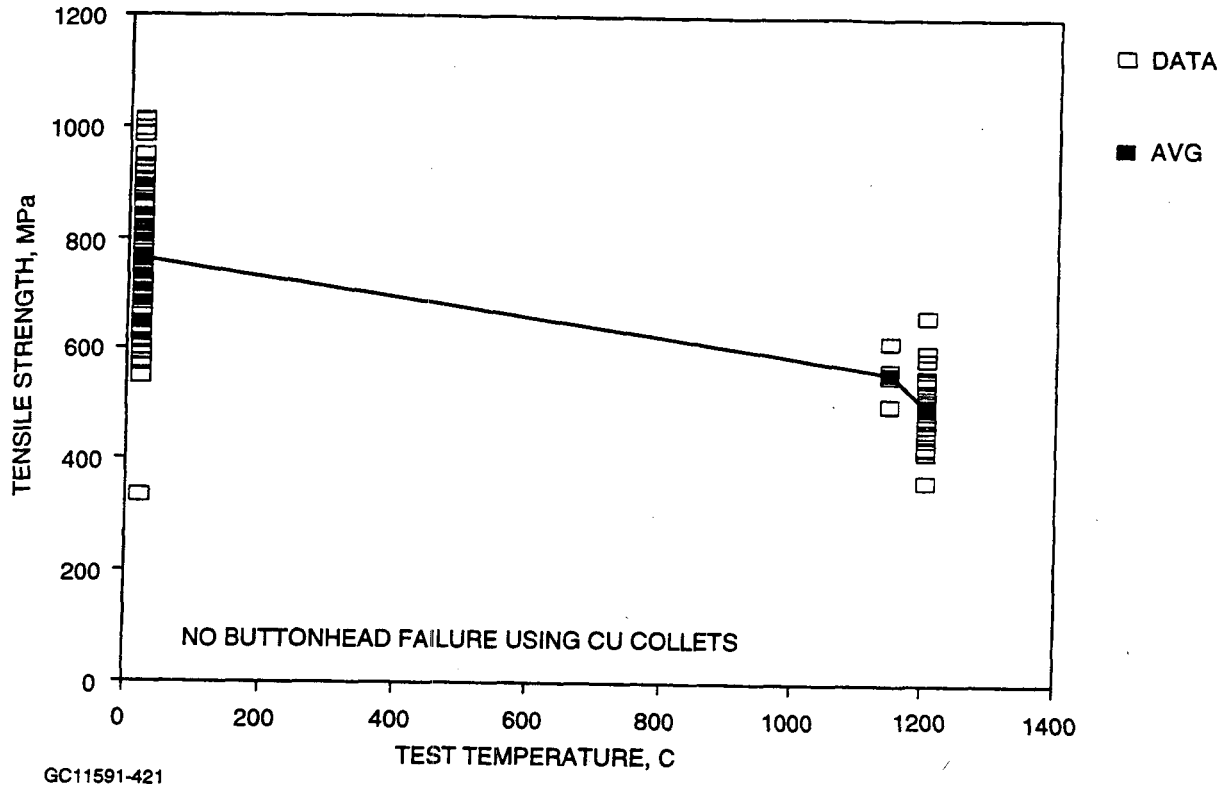


Figure 4-21. Tensile Strength Of NT154 ORNL Buttonhead Specimens.

Table 4-4 provides a further summary of the failure types for these specimens. An interesting point to note in this table, which is only an overall summary and which does not distinguish variability due to different applied stresses, is the increasing percentage of internal failures as the temperature is lowered. Note the results at 1149C, 1204C, and 1371C where statistically significant samples were tested.

4.3.1.2.2.1 Retained Strength After Creep Exposure

Figure 4-23 shows the room-temperature retained strength of smooth tensile specimens that accumulated approximately 500 to 600 hours of creep exposure at different temperatures. The horizontal line indicates the average room-temperature strength of as-received specimens (averaged over 100 samples). It is clear from this figure that the retained strength degrades significantly as a result of creep exposure in the range 1204C to 1400C, which is also the temperature range in which extensive cavitation is observed (see section 4.4.3).

TABLE 4-3. SUMMARY OF SMOOTH TENSILE CREEP/RUPTURE TEST RESULTS

No.	Minimum† Strain Rate, sec ⁻¹	Specimen ID No.	Test Temperature, C	Applied Stress, MPa	Time to Failure, hrs	Total Strain to Failure, µε	Failure Classification	RT FF Strength, MPa
1	3.2 x 10 ⁻⁸	3-29	1400	150	80	16,350	I	--
2	3.3 x 10 ⁻⁸	1-21	1400	140	96	18,270	S	--
3	2.4 x 10 ⁻⁸	1-10	1400	130	192	21,930	S	--
4	2.3 x 10 ⁻⁸	2-125	1400	130	139	16,500	I	--
5	1.4 x 10 ⁻⁸	1-4	1400	125	341	22,820	S	--
6	1.3 x 10 ⁻⁸	2-114	1400	110	411	24,570	S	--
7	1.1 x 10 ⁻⁸	2-68	1400	100	462	25,800	S	--
8	5.9 x 10 ⁻⁹	2-123	1400	90	476*	15,110	--	323
9	5.0 x 10 ⁻⁹	2-35	1400	85	597*	14,970	--	385
10	4.6 x 10 ⁻⁷	2-55	1371	210	1.4	3,510	S	--
11	2.3 x 10 ⁻⁸	1-9	1371	190	68	10,920	I	--
12	3.0 x 10 ⁻⁸	1-6	1371	180	62	13,450	S	--
13	2.6 x 10 ⁻⁸	3-32	1371	180	64	12,430	S	--
14	4.2 x 10 ⁻⁸	2-118	1371	180	28	9,280	I	--
15	4.7 x 10 ⁻⁸	2-140	1371	180	25	8,960	I	--
16	5.7 x 10 ⁻⁸	2-60	1371	180	19	8,850	I	--
17	7.1 x 10 ⁻⁸	1-8	1371	180	14	8,440	S	--
18	9.7 x 10 ⁻⁸	2-91	1371	180	8.6	7,510	S	--
19	7.4 x 10 ⁻⁸	1-7	1371	180	6.8	6,600	S	--
20	1.1 x 10 ⁻⁷	2-116	1371	180	6.8	6,370	S	--
21	1.2 x 10 ⁻⁷	2-34	1371	180	5.6	5,700	S	--
22	3.7 x 10 ⁻⁷	3-69	1371	180	1.8	4,060	I	--
23	3.6 x 10 ⁻⁷	1-19	1371	180	1.6	4,380	S	--
24	8.2 x 10 ⁻⁷	1-16	1371	180	0.84	3,750	S	--
25	2.4 x 10 ⁻⁶	2-77	1371	180	0.24	2,390	S	--
26	1.6 x 10 ⁻⁶	2-69	1371	180	0.24	1,620	S	--
27	3.4 x 10 ⁻⁶	2-109	1371	180	0.14	1,880	S	--
28	1.3 x 10 ⁻⁸	1-20	1371	160	209	14,410	S	--
29	4.0 x 10 ⁻⁸	2-126	1371	155	24	7,790	I	--
30	1.4 x 10 ⁻⁸	2-113	1371	150	208	17,210	S	--
31	1.7 x 10 ⁻⁸	2-134	1371	150	171	15,420	S	--
32	2.3 x 10 ⁻⁸	3-33	1371	150	75	11,060	S	--
33	1.0 x 10 ⁻⁸	3-50	1371	145	443	19,355	S	--
34	1.1 x 10 ⁻⁸	2-120	1371	145	385	20,420	--	--
35	1.0 x 10 ⁻⁸	2-7	1371	145	373	18,940	S	--

†As determined by HTML from the last segment of the creep curve

*Test Stopped

**Failed during loading

>=Ongoing test

Uniaxial tension, gage section 6.35 mm diameter, 35 mm length

Failure Classification:

-- = Not applicable

I = Internal

S = Surface

TABLE 4-3. SUMMARY OF SMOOTH TENSILE CREEP/RUPTURE TEST RESULTS (Contd)

No.	Minimum† Strain Rate, sec ⁻¹	Specimen ID No.	Test Temperature, C	Applied Stress, MPa	Time to Failure, hrs	Total Strain to Failure, µε	Failure Classification	RT FF Strength, MPa
36	1.1 x 10 ⁻⁸	1-12	1371	145	368	20,460	S	--
37	1.1 x 10 ⁻⁸	2-92	1371	145	368	19,400	S	--
38	1.5 x 10 ⁻⁸	2-63	1371	145	293	17,670	S	--
39	1.4 x 10 ⁻⁸	1-13	1371	145	266	18,900	S	--
40	1.6 x 10 ⁻⁸	3-35	1371	145	236	17,470	S	--
41	1.1 x 10 ⁻⁸	2-57	1371	145	364	20,200	S	--
42	2.4 x 10 ⁻⁸	2-136	1371	145	122	15,020	S	--
43	2.8 x 10 ⁻⁸	2-162	1371	145	117	17,200	S	--
44	2.3 x 10 ⁻⁸	2-101	1371	145	112	14,170	S	--
45	2.2 x 10 ⁻⁸	1-17	1371	145	111	13,840	S	--
46	3.2 x 10 ⁻⁸	2-50	1371	145	90	15,470	S	--
47	2.5 x 10 ⁻⁸	2-46	1371	145	73	11,930	S	--
48	2.7 x 10 ⁻⁸	2-45	1371	145	57	11,170	S	--
49	6.8 x 10 ⁻⁹	2-124	1371	140	586	21,250	S	--
50	6.3 x 10 ⁻⁹	2-117	1371	135	587	18,780	S	--
51	1.4 x 10 ⁻⁸	2-130	1371	135	280	18,450	S	--
52	8.7 x 10 ⁻⁹	2-119	1371	130	588	21,230	S	--
53	5.0 x 10 ⁻⁹	2-121	1371	125	728	16,950	S	--
54	2.2 x 10 ⁻⁸	1-2	1315	250	24	3,640	S	--
55	1.5 x 10 ⁻⁷	1-24	1315	240	2.9	2,360	I	--
56	1.5 x 10 ⁻⁷	2-64	1315	235	52	6,960	S	--
57	4.5 x 10 ⁻⁹	2-111	1315	232.5	297	10,660	S	--
58	5.7 x 10 ⁻⁹	2-37	1315	230	244	10,870	S	--
59	7.2 x 10 ⁻⁹	2-112	1315	230	168	9,100	S	--
60	3.2 x 10 ⁻⁸	2-128	1315	227.5	20	5,260	S	--
61	2.2 x 10 ⁻⁹	1-15	1315	225	675*	10,300	--	489
62	3.8 x 10 ⁻⁷	1-11	1295	375	0.35	--	S	--
63	2.2 x 10 ⁻⁷	1-23	1295	300	0.40	--	S	--
64	No extenso	2-66	1295	200	530*	--	--	--
65	8.0 x 10 ⁻⁸	2-102	1260	325	1.2	1,420	S	--
66	1.4 x 10 ⁻⁸	2-142	1260	305	46	4,460	I	--
67	1.2 x 10 ⁻⁸	1-36	1260	300	58	5,150	S	--
68	1.9 x 10 ⁻⁹	3-44	1260	295	560	8,190	I	--
69	2.3 x 10 ⁻⁹	2-145	1260	285	379	6,910	I	--
70	2.6 x 10 ⁻⁹	3-112	1260	275	474*	6,960	--	607

†As determined by HTML from the last segment of the creep curve

*Test Stopped

**Failed during loading

>=Ongoing test

Uniaxial tension, gage section 6.35 mm diameter, 35 mm length

Failure Classification:

-- = Not applicable

I = Internal

S = Surface

TABLE 4-3. SUMMARY OF SMOOTH TENSILE CREEP/RUPTURE TEST RESULTS(Contd)

No.	Minimum† Strain Rate, sec ⁻¹	Specimen ID No.	Test Temperature, C	Applied Stress, MPa	Time to Failure, hrs	Total Strain to Failure, µε	Failure Classification	RT FF Strength, MPa
71	1.2 x 10 ⁻⁸	3-89	1260	285	379	6,910	I	--
72	4.8 x 10 ⁻⁸	1-46	1260	275	6.1	1,130	S	--
73	1.0 x 10 ⁻⁹	3-120	1260	250	838*	7,430	--	571
74	1.1 x 10 ⁻⁸	2-56	1204	415	1.3	1,430	I	--
75	No extenso	3-73	1204	400	1.1	--	I	--
76	No extenso	3-121	1204	385	501*	--	--	686
77	1.5 x 10 ⁻⁹	3-75	1204	375	252	3370	S	--
78	No extenso	3-48	1204	375	525*	--	--	662
79	4.1 x 10 ⁻⁹	3-118	1204	375	120	3,620	S	--
80	3.3 x 10 ⁻⁹	3-116	1204	375	141	3,310	I	--
81	6.3 x 10 ⁻⁹	2-149	1204	375	66	2,690	I	--
82	5.1 x 10 ⁻⁹	3-54	1204	375	43	2,060	S	--
83	8.7 x 10 ⁻⁹	3-66	1204	375	24	1,980	S	--
84	9.4 x 10 ⁻⁹	3-34	1204	375	19	1830	I	--
85	1.0 x 10 ⁻⁸	2-146	1204	375	12	1,590	I	--
86	2.3 x 10 ⁻⁸	2-164	1204	375	0.84	1,250	I	--
87	No extenso	2-72	1204	375	0.5	--	I	--
88	No extenso	1-38	1204	375	528*	--	--	799
89	1.5 x 10 ⁻⁹	3-83	1204	375	266	2,920	I	--
90	2.3 x 10 ⁻⁹	3-76	1204	375	253	3,776	S	--
91	2.7 x 10 ⁻⁹	3-71	1204	375	153	3,400	I	--
92	No extenso	3-93	1204	375	80	--	S	--
93	7.8 x 10 ⁻⁹	2-93	1204	375	40	2,390	I	--
94	8.3 x 10 ⁻⁹	3-124	1204	375	7	1,360	S	--
95	1.1 x 10 ⁻⁸	3-95	1204	375	6	1,390	S	--
96	4.3 x 10 ⁻⁷	1-43	1204	375	0.40	1,240	I	--
97	9.0 x 10 ⁻¹⁰	2-28	1204	350	612*	5,190	--	639
98	4.4 x 10 ⁻⁹	2-71	1204	350	2.3	1,330	I	--
99	No extenso	3-39	1204	345	636*	--	--	757
100	No extenso	2-30	1204	340	566*	--	--	774
101	2.2 x 10 ⁻⁹	3-37	1204	340	177	3,550	S	--
102	3.9 x 10 ⁻¹⁰	2-36	1204	337	593*	3,800	--	611
103	1.1 x 10 ⁻⁹	3-19	1204	335	469	4,420	S	--
104	5.0 x 10 ⁻⁹	2-74	1204	325	68	2,900	I	--
105	6.8 x 10 ⁻¹⁰	2-31	1204	315	594*	3,630	--	589

†As determined by HTML from the last segment of the creep curve

*Test Stopped

**Failed during loading

>=Ongoing test

Uniaxial tension, gage section 6.35 mm diameter, 35 mm length

Failure Classification:

-- = Not applicable

I = Internal

S = Surface

TABLE 4-3. SUMMARY OF SMOOTH TENSILE CREEP/RUPTURE TEST RESULTS(Contd)

No.	Minimum† Strain Rate, sec ⁻¹	Specimen ID No.	Test Temperature, C	Applied Stress, MPa	Time to Failure, hrs	Total Strain to Failure, με	Failure Classification	RT FF Strength, MPa
106	1.8 x 10 ⁻¹⁰	1-3	1204	300	517*	1,580	--	--
107	No extenso	3-41	1149	450	7.0	--	I	--
108	No extenso	2-47	1149	450	0.08	--	I	--
109	No extenso	2-75	1149	445	0.02	--	I	--
110	No extenso	2-32	1149	440	376	--	S	--
111	No extenso	3-31	1149	435	594*	--	--	787
112	No extenso	3-109	1149	425	509*	--	--	806
113	No extenso	2-62	1149	425	32	--	I	--
114	No extenso	2-61	1149	425	**	--	I	--
115	No extenso	2-153	1204	445	3.2	--	S	--
116	No extenso	1-26	1204	445	**	--	I	--
117	No extenso	1-41	1204	445	1.0	--	I	--
118	No extenso	2-39	1204	445	503*	--	--	705
119	No extenso	2-94	1204	445	649*	--	--	928
120	No extenso	2-139	1204	445	277.6	--	I	--
121	No extenso	2-147	1204	445	503*	--	--	834
122	No extenso	2-150	1204	445	513*	--	--	785
123	No extenso	3-20	1204	445	501*	--	--	949
124	No extenso	3-59	1204	445	39.6	--	I	--
125	No extenso	3-61	1204	445	17.6	--	I	--
126	No extenso	3-64	1204	445	6.4	--	I	--
127	No extenso	3-77	1204	445	125.4	--	I	--
128	No extenso	3-87	1204	445	2.3	--	I	--
129	No extenso	3-79	1204	445	500*	--	--	768
130	No extenso	3-88	1204	445	0.4	--	I	--
131	No extenso	3-90	1204	445	**	--	I	--
132	No extenso	3-129	1204	445	0.1	--	I	--
133	No extenso	3-115	1204	445	20.4	--	I	--
134	No extenso	3-132	1204	445	**	--	I	--
135	No extenso	2-70	982	475	21	--	I	--
136	No extenso	2-38	982	470	512*	--	--	747
137	No extenso	2-73	982	465	**	--	I	--
138	No extenso	2-51	982	465	**	--	I	--
139	No extenso	2-54	982	460	602*	--	--	805
140	No extenso	2-44	982	460	**	--	I	--
141	No extenso	3-18	982	455	808*	--	--	884
142	No extenso	3-27	982	455	336	--	S	--
143	No extenso	3-40	982	450	631*	--	--	685

†As determined by HTML from the last segment of the creep curve

*Test Stopped

**Failed during loading

>=Ongoing test

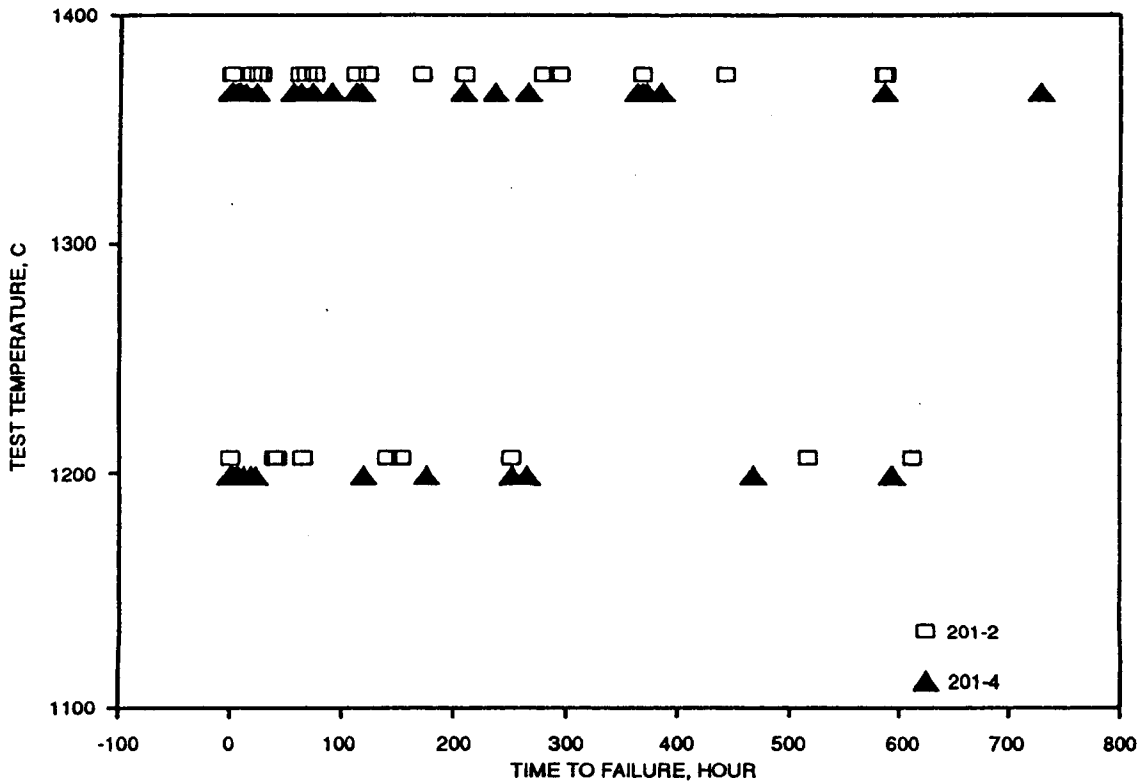
Uniaxial tension, gage section 6.35 mm diameter, 35 mm length

Failure Classification:

-- = Not applicable

I = Internal

S = Surface



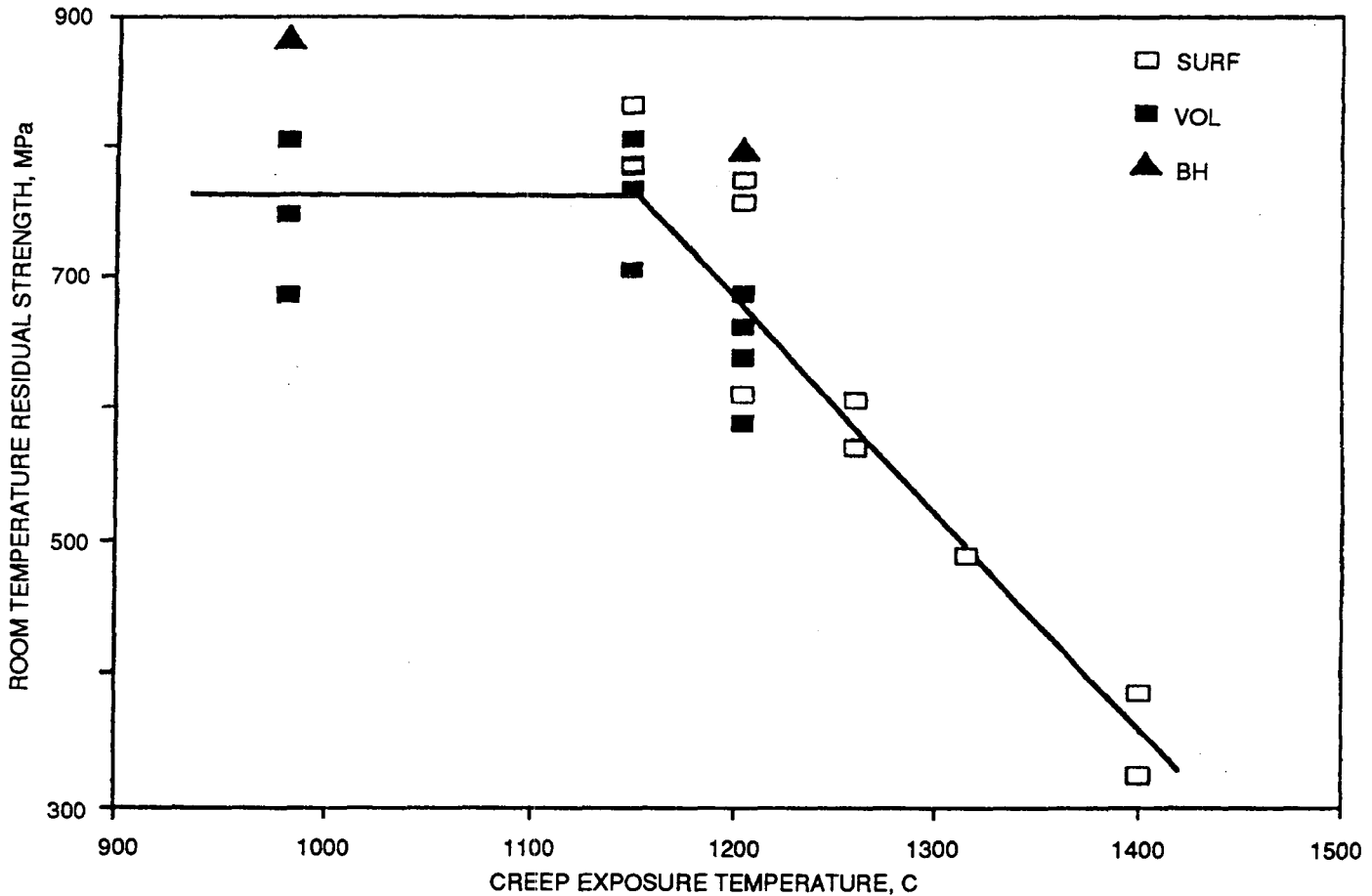
GC11591-422

Figure 4-22. Effect Of Test Machine On Failure Time.

TABLE 4-4. SUMMARY OF FAILURE TYPES AT EACH TEMPERATURE

Temperature, C	Total No.	F.O.L.*	Run-Outs	Failure in Creep	Type of Initiation		Percent Internal
					Internal	Surface	
1400	9	0	2	7	2	5	29
1371	44	0	0	44	6	38	14
1315	8	0	1	7	1	6	14
1260	9	0	2	7	3	4	43
1204	33	0	9	24	14	10	58
1149	28	4	8	16	14	2	88
982	9	3	4	2	1	1	50

*F.O.L. = Failed On Loading.



GC11591-423

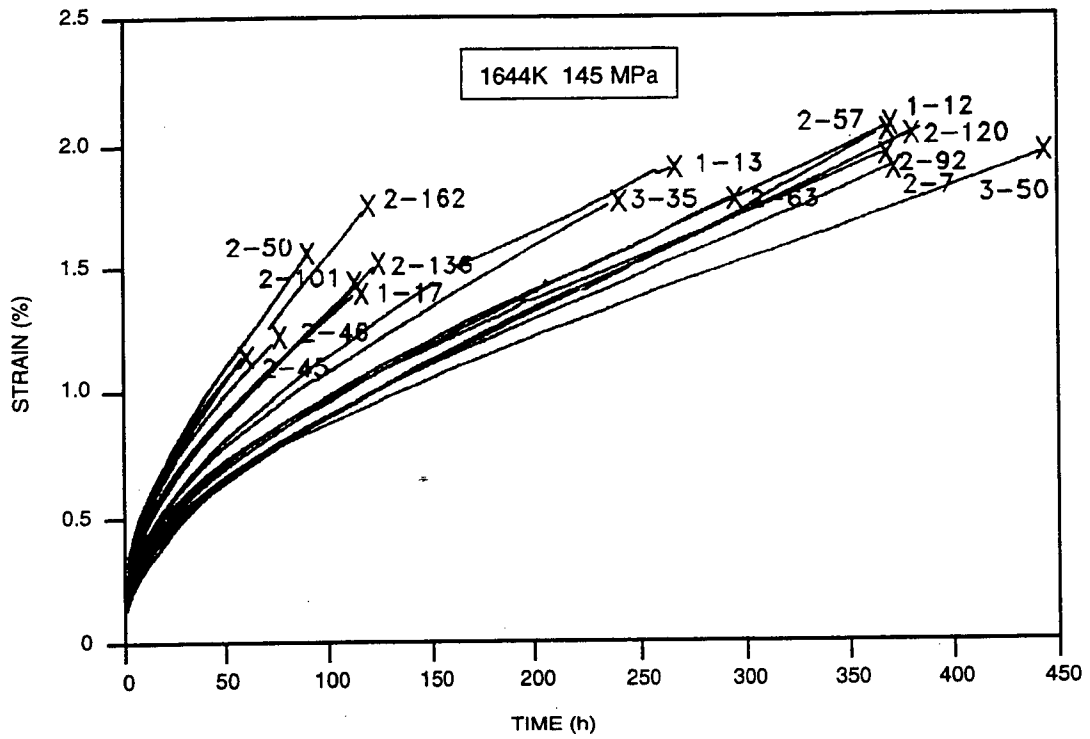
Figure 4-23. Residual Strength Of Creep-Tested Specimens.

4.3.1.2.2.2 Creep Regimes in NT154

All creep-tested specimens showed only two creep regimes, primary and secondary. This is consistent with previous observations of creep behavior of yttria-sintered silicon nitrides (ref. 4-4, 4-5). Figures 4-24 through 4-26 show the strain-versus-time data obtained in the replicate tests conducted at 1371C/145 MPa, 1371C/180 MPa and 1204C/375 MPa, respectively. In all the curves, a significant primary and a small secondary regime can be seen. These figures provide a visual depiction of the scatter that can be expected in creep rates and rupture times in this material.

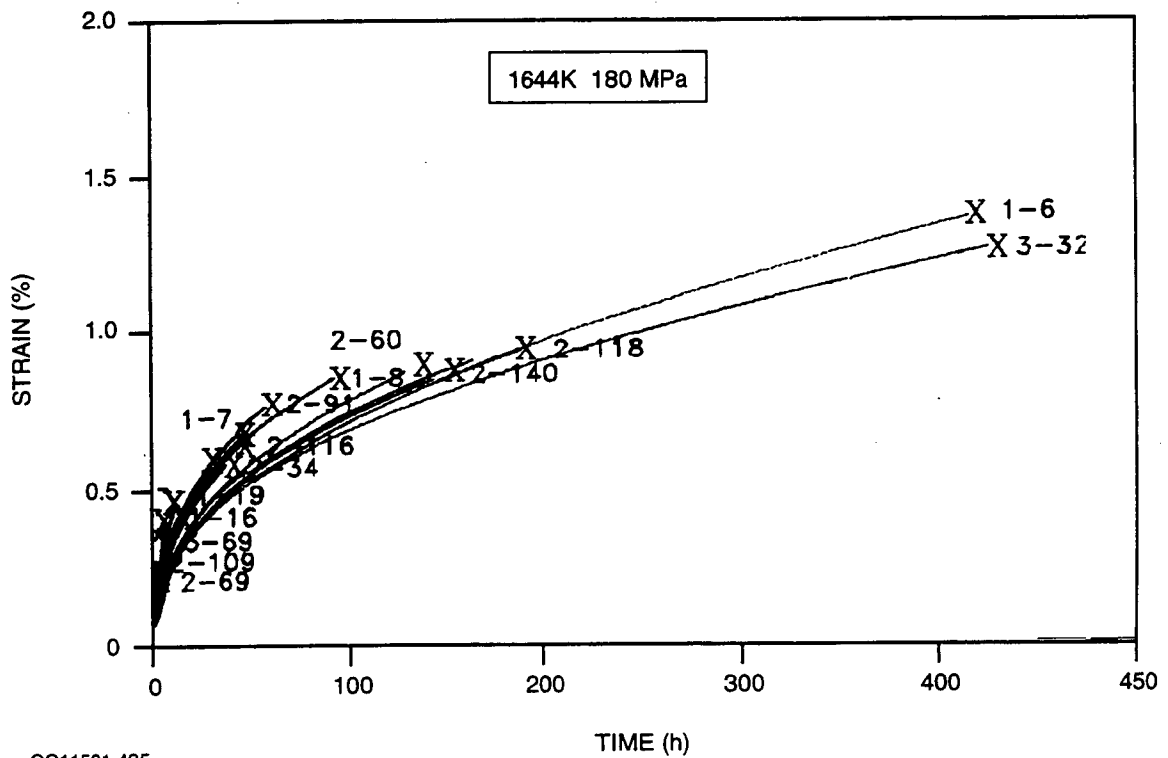
4.3.1.2.2.3 Secondary/Minimum Creep Rates

The secondary or minimum creep rates, $\dot{\epsilon}_s$, derived from the empirical data for specimens which had lives larger than 10 hours, are plotted as a function of stress in Figure 4-27. The data show the extent of scatter



GC11591-424

Figure 4-24. Strain Versus Time For NT154 Replicate Creep Tests At 1371C/145 MPa.



GC11591-425

Figure 4-25. Strain Versus Time For NT154 Replicate Creep Tests At 1371C/180 MPa.

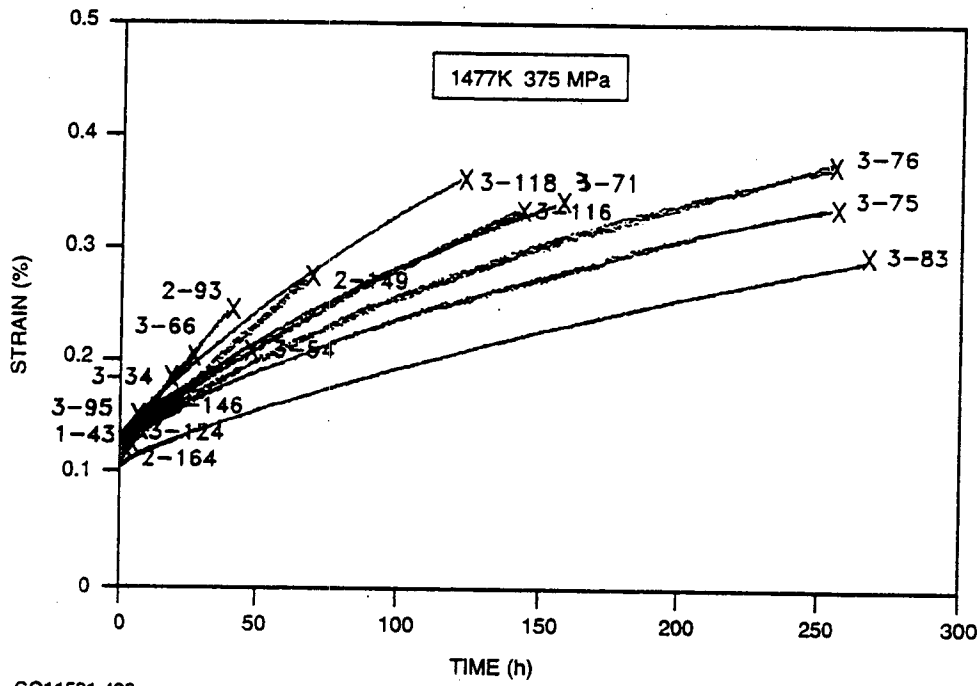


Figure 4-26. Strain Versus Time For NT154 Replicate Creep Tests At 1204C/375 MPa.

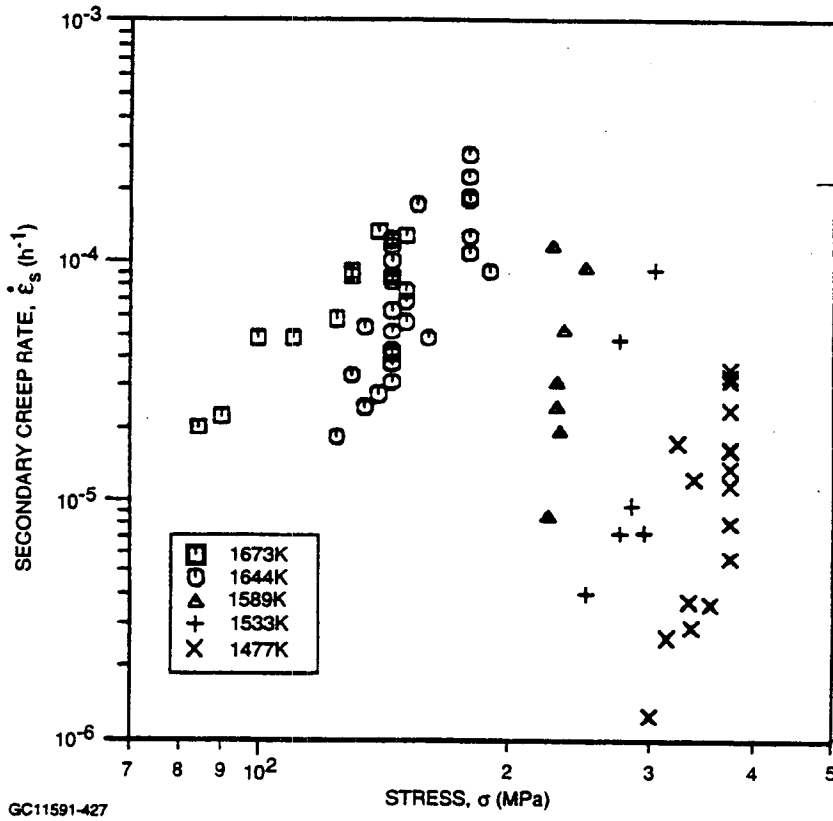


Figure 4-27. Secondary (Minimum) Creep Rate Versus Stress At Various Replicate Test Temperatures. Note Scatter In Replicate Tests At 1371C And 1204C.

present in the measured creep rates in this material. The replicate tests at 1371C and 1204C seem to indicate that a scatter of approximately a factor of three about the mean can be expected in secondary creep rates in the temperature range tested. The data also show a change in stress dependence in creep rate, which occurs around 1315C. The modulus of NT154 is nearly constant (3×10^5 MPa) in the temperature range 1149C to 1400C.

4.3.1.2.2.4 Monkman-Grant Plots Of Rupture Life

Figure 4-28 summarizes the rupture data in the form of a Monkman-Grant plot (ref. 4-6), in which rupture life is plotted against measured secondary creep rate. In their original work, Monkman and Grant showed that for many metallic materials an unique relationship existed between t_f and $\dot{\epsilon}_s$ independent of temperature and stress, which can be expressed in the following form:

$$t_f = K(\dot{\epsilon}_s)^{b_1} \quad [4-1]$$

where K and b_1 are constants independent of temperature or stress. The data for NT154 in Figure 4-28 shows that only at a specific temperature can the rupture life be correlated with the secondary creep rate. There is a stratification for this correlation with respect to temperature. For the same value of creep rate, specimens at the lower temperatures show lower lives. The results do not show a single master curve independent of

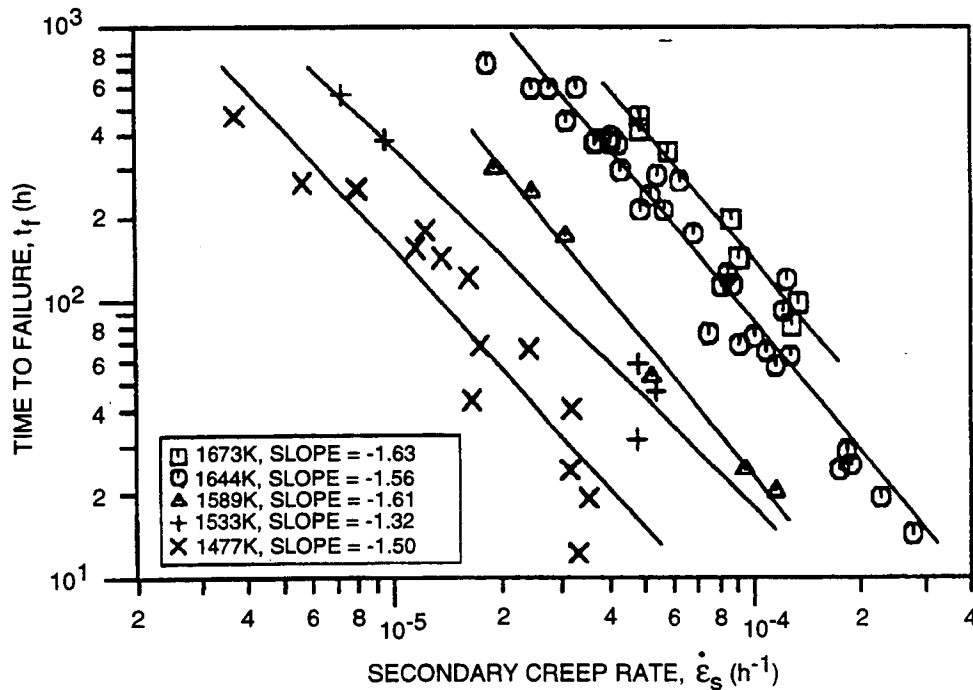
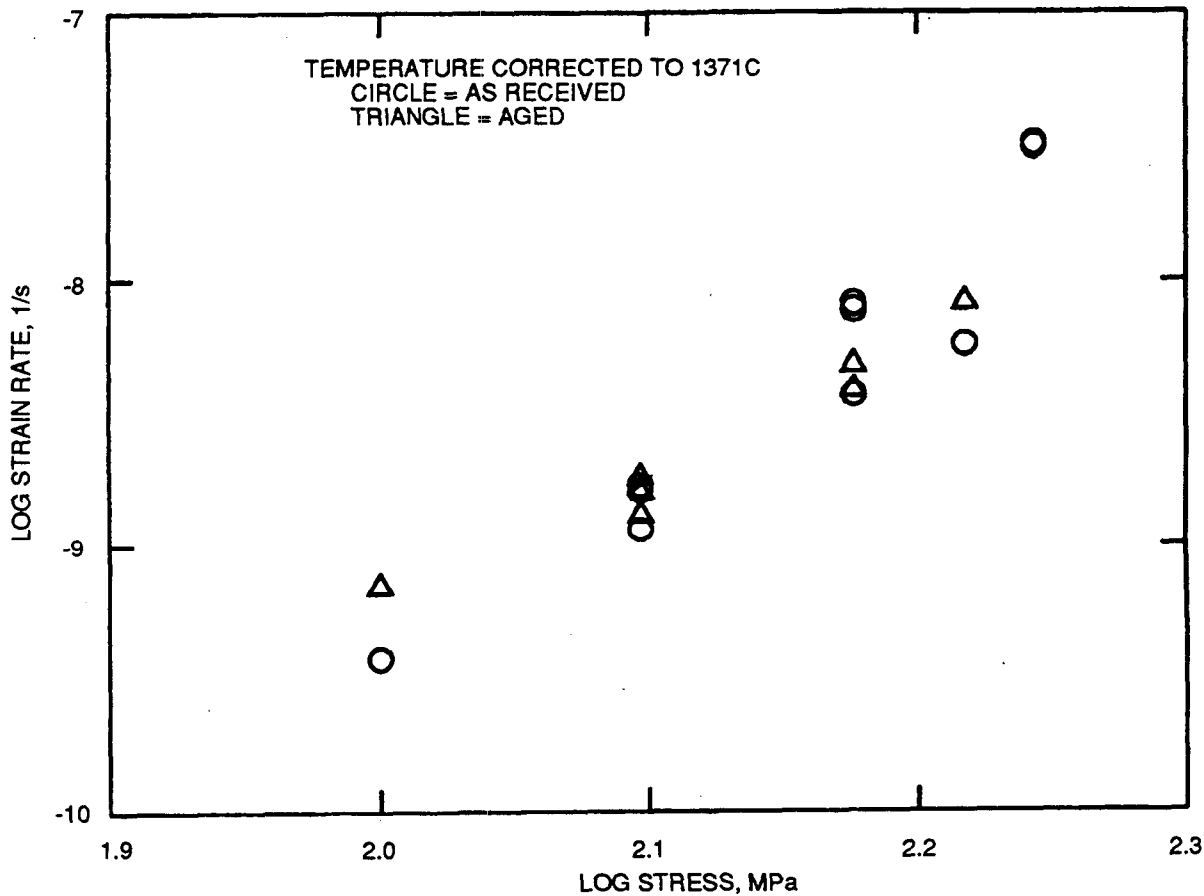


Figure 4-28. Monkman-Grant Plot Of Rupture Life Data.

temperature. This means that for NT154, the Monkman-Grant relationship which is arrived at by using data from one temperature cannot be used for the prediction of rupture life at another temperature. The stratification with respect to temperature has been observed by previous investigators in advanced silicon nitrides (ref. 4-4 and 4-7). The strain rate exponent, b_1 , in Figure 4-28 seems to have approximately the same value at all temperatures, the average value being near -1.55.

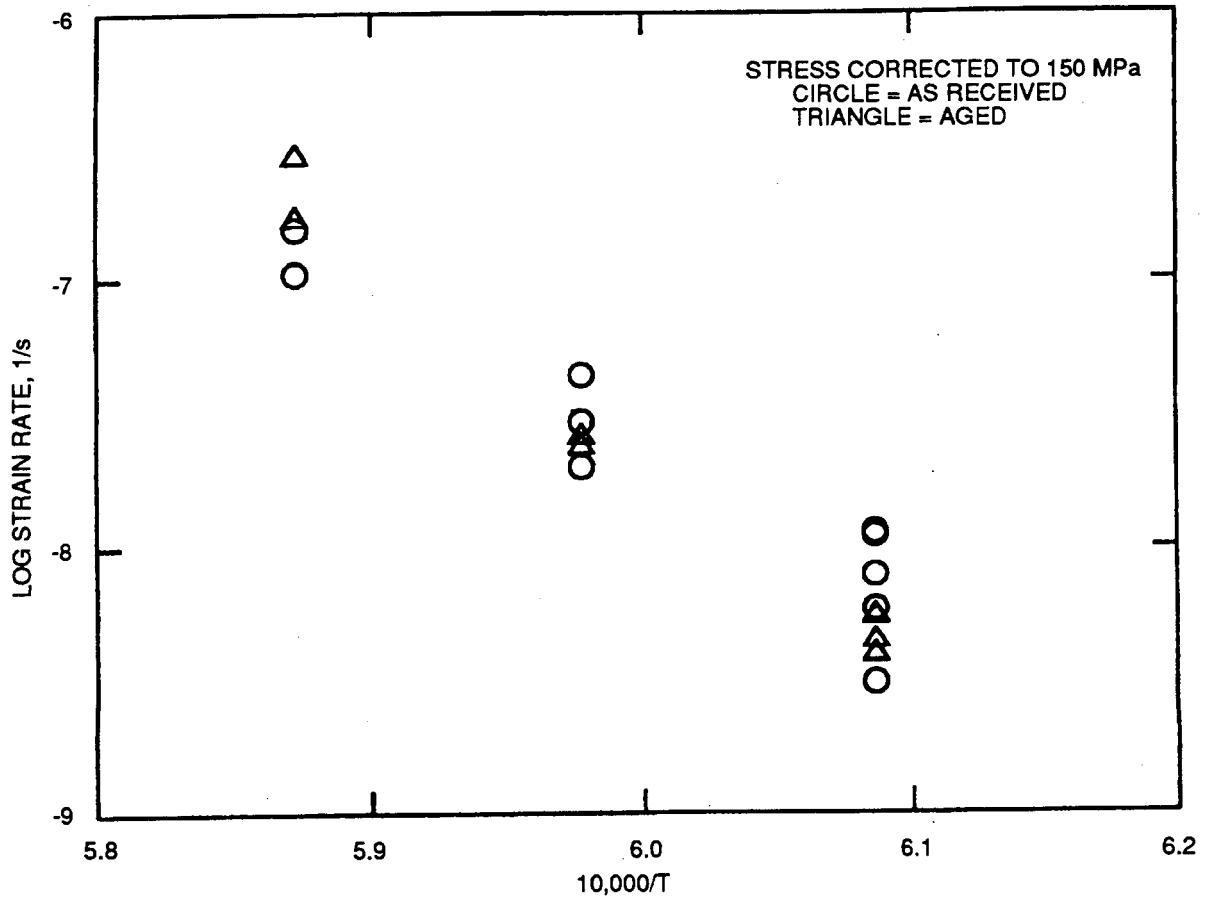
4.3.1.2.2.5 Effect Of Aging On Creep Behavior

Figures 4-29 and 4-30 show the plots supplied by NIST on the effect of aging at 1371C for 1000 hours on the creep rates of NT154. The plots include the as-received as well as the aged material. No significant difference in creep rates is observed between the two versions of the material.



GC11591-429

Figure 4-29. Effects Of Aging On NT154 Tensile Creep Rate. Log-Log Plot Of Stress Versus Strain. (NIST Data By S. Wiederhorn.)



GC11591-430

Figure 4-30. Effects Of Aging On NT154 Tensile Creep Rate. Log Strain Versus Temperature. (NIST Data By S. Wiederhorn.)

4.3.1.3 Fracture Toughness

4.3.1.3.1 K_{IC} Long-Beam Chevron-Notched Bars

Fracture toughness (K_{IC}) was measured at the same seven temperatures at which the flexure tests were conducted. Test data from 70 long-beam, chevron-notched specimens is plotted in Figure 4-31. Ten specimens were tested at each temperature, but only data from specimens showing stable crack growth (as indicated by the load deflection curves) was included. The average K_{IC} was $5.0 \pm 1.25 \text{ MPa}\cdot\text{m}^{1/2}$ at room temperature, $6.14 \pm 0.19 \text{ MPa}\cdot\text{m}^{1/2}$ at 982C, increasing to a maximum of $6.37 \pm 0.08 \text{ MPa}\cdot\text{m}^{1/2}$ at 1148C, then decreasing to $5.79 \pm 0.46 \text{ MPa}\cdot\text{m}^{1/2}$ at 1371C.

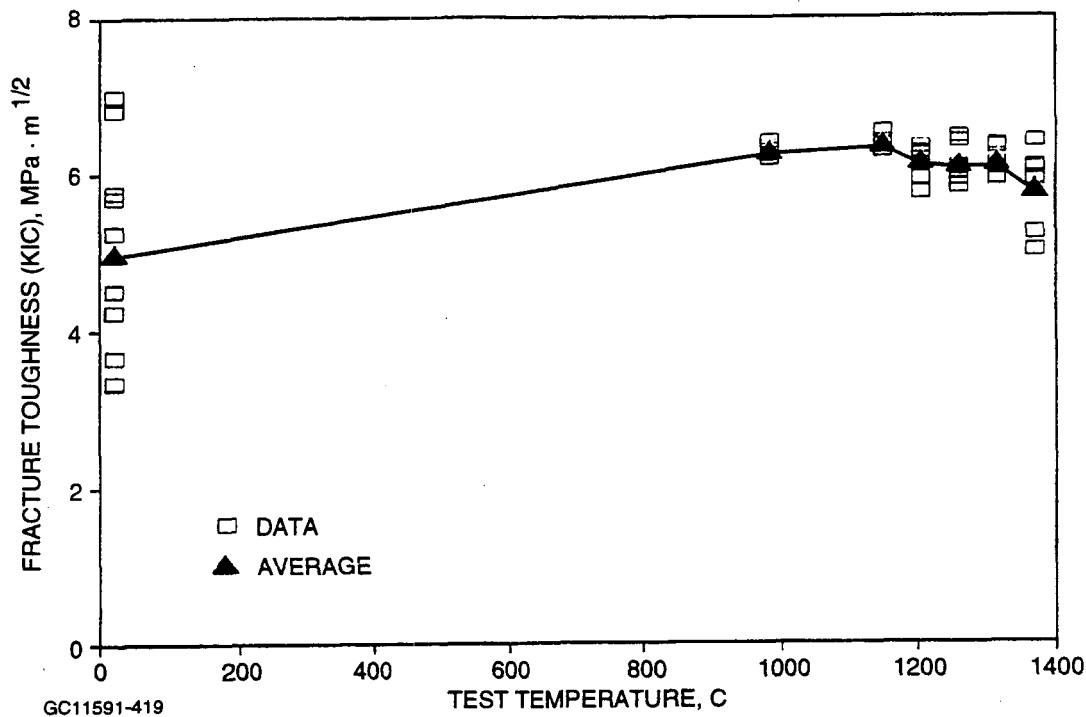


Figure 4-31. Fracture Toughness (K_{IC}) Test Results.

4.3.1.3.2 Diametral Compression Disks

The diametral compression data were used to determine the K_I/K_{II} shear sensitivity of NT154 silicon nitride. Detailed test data are presented in Appendix II. The effect of temperature and loading rate on shear sensitivity were evaluated and the results showed that the shear sensitivity factor, C , was not significantly affected by the loading rate (crosshead speed) or test temperature. Figures 10, 12, 13, and 16 in Appendix II compares the K_I/K_{II} fracture toughness envelope for tests performed at temperatures and crosshead speeds of 70F, 0.05 inch/min; 2200F, 0.05 inch/min; 2200F, 0.0005 inch/min, and 2500F, 0.05 inch/min, respectively. The C factor values were 2.1, 2.0, 1.7, and 1.8, respectively.

The average room temperature K_{IC} generated from using this method was $4.8 \text{ MPa}\cdot\text{m}^{1/2}$. This value is lower because it was calculated from failure loads of disks that failed in the precracking stage.

Figure 10 in Appendix II also shows that there was very little difference in K_I/K_{II} fracture toughness between disks with precracks outside of the chevron notch and disks with precracks inside the chevron notch.

4.3.1.3 Notched Tension/Torsion Specimens

A total of 29 specimens were successfully tested at room temperature to obtain a complete fracture toughness envelope spanning from negative mode I, to pure mode I (tension), then to pure mode III (torsion), with in-between data corresponding to combined tension/torsion conditions. Detailed test data are presented in Appendix III. The room-temperature purely mode I fracture toughness (K_{IC}) value generated from this work was $4.35 \text{ MPa}\cdot\text{m}^{1/2}$, comparable to the long-beam, chevron-notched K_{IC} results generated at AE. The apparent Mode III fracture toughness was found to be $8.98 \text{ MPa}\cdot\text{m}^{1/2}$, a factor of 2.1 times the Mode I fracture toughness. The higher value of the Mode III fracture toughness suggests occurrence of crack face abrasion and interlocking crack face asperities.

4.3.1.4 Notched Tensile Tests

The notch tensile fast fracture test results are provided in Appendix IV, Table 10. Table 4-5 provides a summary of the notched tensile rupture test data.

The results are plotted in Figure 4-32. Two tests (curved arrows in the figure) at 1371C were interrupted for TEM evaluation. The symbols with straight arrows represent specimens whose testing was interrupted at about 500 hours.

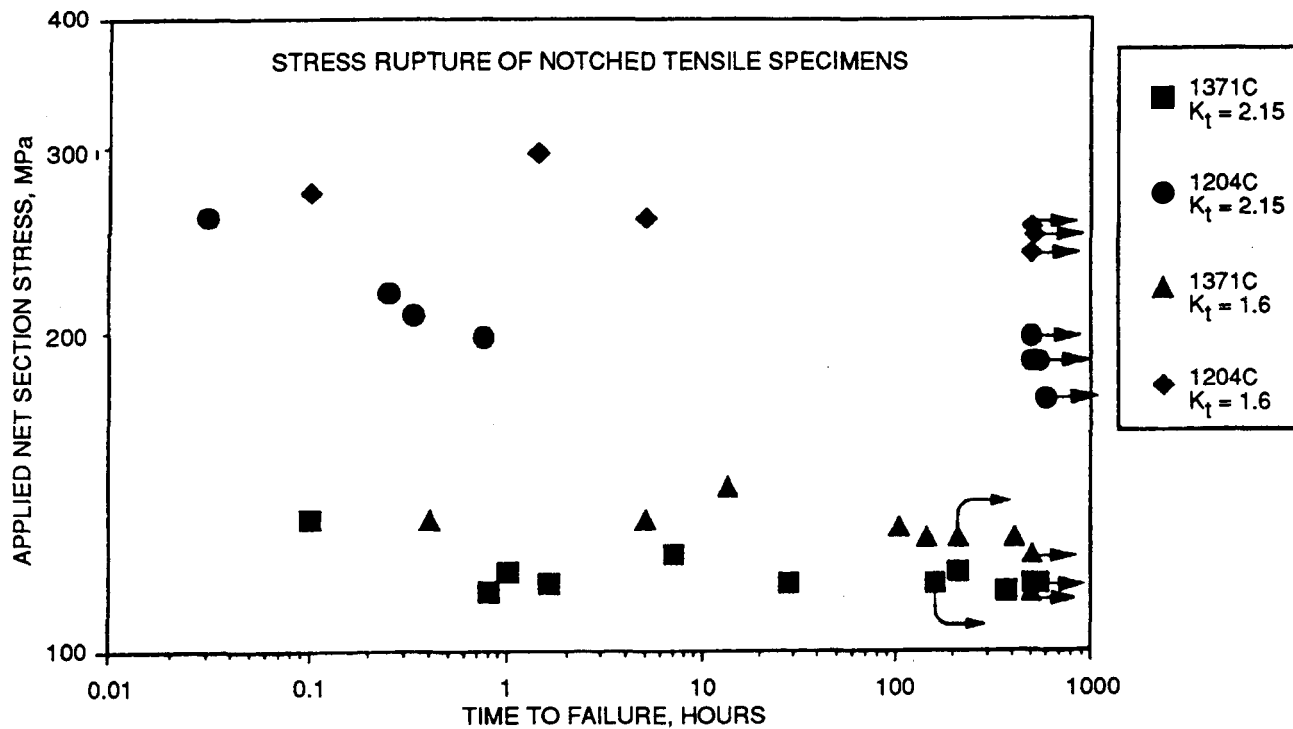
4.3.1.5 Plate Bending Tests

The University of Utah tested 37 plate bending specimens. Detailed test data are presented in the subcontractor report in Appendix II and in Table 6, Appendix IV. Fracture strain was calculated from the fracture pressure using a strain calibration plot (Figure 19, Appendix IV) and the values were converted to fracture stress using $E = 330.5 \text{ GPa}$. The room temperature elastic modulus, E , was measured on actual plate bending disks using the Grindo-Sonic* technique.

*J.W. Lemmens, Inc., St. Louis, MO.

TABLE 4-5. SUMMARY OF NOTCHED TENSILE RUPTURE TEST DATA

Specimen ID	Temp., C	Test Machine No.	Applied Stress, MPa	Outer Diameter, mm	Inner Diameter, mm	Stress Concentration	Time to Failure, hrs	Remarks
N-21	1204	TT-L201-4	300	6.67	6.34	1.6	1.4	
N-8	1204	TT-L201-4	275	6.65	6.33	1.6	≈0.1	
N-17	1204	TT-L201-7	260	6.67	6.30	1.6	5	
N-42	1204	TT-L214-3	240	6.68	6.30	1.6	503	25C F.F. strength = 474 MPa
N-45	1204	TT-L201-3	250	6.67	6.32	1.6	521	25C F.F. strength = 442 MPa
N-3	1204	TT-L201-7	255	6.49	6.14	1.6	502	25C F.F. strength = 603 MPa
N-22	1204	TT-L201-7	260	6.68	6.33	1.6	482	25C F.F. strength = 713 MPa
N-40	1371	TT-L201-4	115	6.65	6.31	1.6	500	25C F.F. strength = 262 MPa
N-38	1371	TT-L214-2	125	6.66	6.32	1.6	504	25C F.F. strength = 167 MPa
N-26	1371	TT-L201-4	135	6.66	6.34	1.6	0.4	
N-49	1371	TT-L201-4	135	6.65	6.33	1.6	5	
N-6	1371	TT-L201-4	145	6.66	6.34	1.6	13.6	
N-9	1371	TT-L201-7	130	6.66	6.34	1.6	144	
N-7	1371	TT-L201-7	130	6.66	6.34	1.6		No. 7 suffered load loss, fractured
N-35	1371	TT-L201-8	130	6.66	6.32	1.6		Test interrupted at 211 h (TEM)
N-30	1371	TT-L201-7	132.5	6.66	6.34	1.6	103	
N-12	1371	TT-L201-8	130	6.63	6.33	1.6	408	
K-15	1204	TT-L201-6	260	12.00	6.35	2.15	0	Severe machine damage evident
K-25	1204	TT-L201-4	260	11.97	6.37	2.15	0.033	
K-27	1204	TT-L201-4	200	11.97	6.32	2.15	0.75	
K-29	1204	TT-L201-4	175	12.00	6.38	2.15	593	25C F.F. strength = 427 MPa
K-47	1204	TT-L201-4	190	12.01	6.38	2.15	≈500	25C F.F. strength = 413 MPa
K-39	1204	TT-L201-4	200	12.01	6.38	2.15	500	25C F.F. strength = 367 MPa (TEM)
K2-52	1204	TT-L201-3	220	12.01	6.40	2.15	0.25	
K-37	1204	TT-L201-3	210	12.01	6.38	2.15	0.33	
K-5	1204	TT-L201-4	190	12.01	6.39	2.15	547	25C F.F. strength = 338 MPa
K-6	1204	TT-L201-4	200	12.01	6.35	2.15		Failed during loading
K-41	1371	TT-L201-4	115	11.96	6.31	2.15	372	Str to failure = 23,700 μ strain
K-30	1371	TT-L201-4	120	11.96	6.36	2.15	210	Str to failure = 20,010 μ strain
K-8	1371	TT-L201-4	125	11.95	6.33	2.15	7	Str to failure = 4,050 μ strain
K-52	1371	TT-L201-4	135	11.97	6.38	2.15	0.1	
K-11	1371	TT-L201-3	117	11.98	6.34	2.15	28	Str to failure = 16,280 μ strain
K-28	1371	TT-L201-3	117	11.97	6.33	2.15	505	25C F.F. strength = 214 MPa
K-10	1371	TT-L201-7	120	11.97	6.36	2.15	1	
K-12	1371	TT-L201-8	117	11.98	6.35	2.15	1.6	
K-9	1371	TT-L201-3	117	11.98	6.33	2.15	546	25C F.F. strength = 203 MPa
K-24	1371	TT-L201-2	117	11.97	6.35	2.15		Test interrupted at 160 h (TEM)
K-51	1371	TT-L201-7	115	12.01	6.40	2.15	0.8	



GC11591-432

Figure 4-32. Notch Stress Rupture Lives Versus Average Net Section Stress.

4.3.1.6 Smooth Tension/Torsion Strength Tests

Brown University tested 36 smooth tension/torsion specimens. Tests were performed at pure torsion, maximum possible tension (as dictated by the limits of the testing machine) followed by torsion, and two points between the limits. Detailed test data are presented in the subcontractor report in Appendix III and in Table 7, Appendix IV. The average maximum shear strength with no applied normal stress was 796.8 MPa. Under an applied normal stress of 105.4 MPa, the average shear strength was 800.4 MPa, with normal stress of 210.8 MPa, the average shear strength was 742.5 MPa, and with normal stress of 334.8 MPa, the average shear strength was 624.3 MPa.

4.3.1.7 Spin Disk Tests

Detailed spin disk test data are presented in Table 8, Appendix IV. Note that stepped stress rupture was applied on the first few disks to quickly determine the suitable speed/stress regime for desired failure times at that test temperature. For example, a disk with failure speed listed as 75, 80, 85, and 88.4 krpm and failure times of 50, 10, 10, Burst hours means that the disk survived 50 hours at 75,000 rpm, 10 hours at 80,000 rpm, 10 hours at 85,000 rpm, and failed by bursting at 88,400 rpm during a speed increase to the next higher speed interval.

4.3.2 Fractography

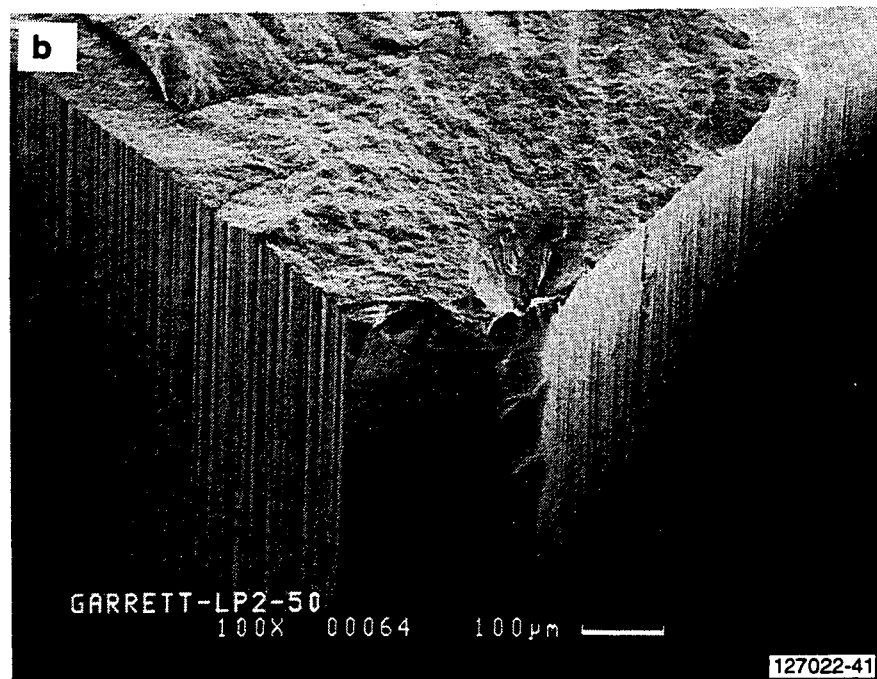
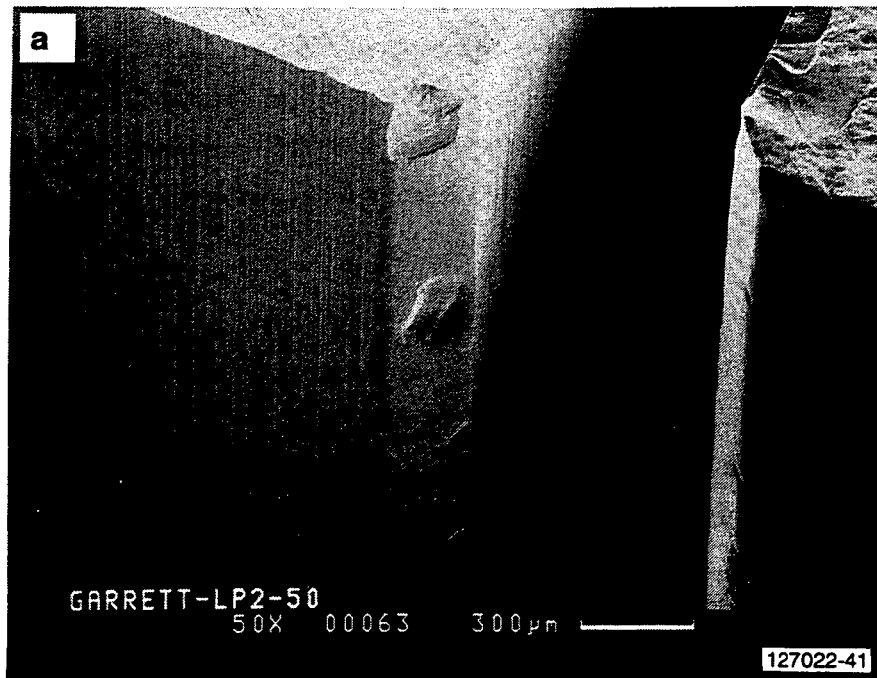
Fractographic analyses of the failed specimens were performed to identify fracture types, origin locations, and other characteristics. The fractography information is vital for performing Weibull analysis of the data. The visual and SEM/EDX/WDX fractographic techniques used for these bars are similar to those used previously by AlliedSignal in the International Energy Agency (IEA) round-robin flexure and tensile testing, and as specified by MIL-HDBK-790.

The characteristics of the internal failure origin flaws are very similar, regardless of whether the specimen billets were small plates, long cylindrical billets, or spin disks. Most of the internal flaws were dark carbon (C) inclusions with surrounding clusters of small iron (Fe) particles. Sometimes chromium (Cr), nickel (Ni), and cobalt (Co) were also detected in smaller amounts with the Fe. In a few cases, the inclusions contained aluminum (Al) or titanium (Ti) only. The most useful technique for determining the chemical content and size of the inclusion is the elemental X-ray dot maps generated by EDX. Carbon would have been missed without using this technique, due to the relatively low X-ray emission intensity of carbon. It is also more effective to perform most SEM analysis on room-temperature test specimens, because the carbon inclusions are oxidized when the specimens are tested to failure at elevated temperatures in the hot furnace. However, it is also essential to perform SEM fractography on a large number of specimens spanning a variety of specimen types and geometries, because some phenomena are hard to explain or confirm until a sufficient number of cases are studied.

Surface failures were difficult to generalize, because of the various combinations of specimen geometries, machining parameters, and heat treatments. An example is the chamfer corner failures caused by machining damage, which is unique to the flexure bars and not applicable to the other specimen types.

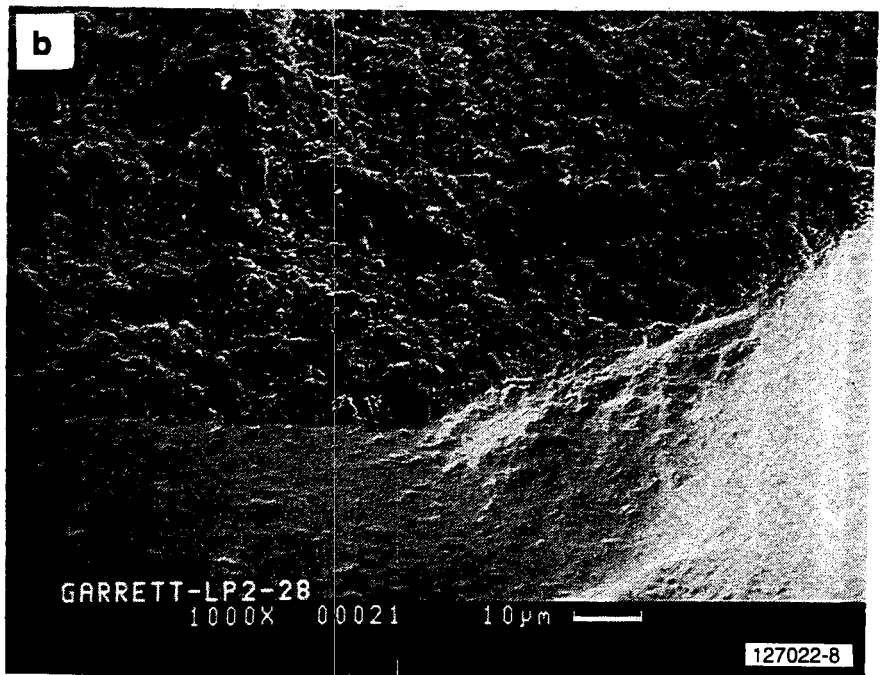
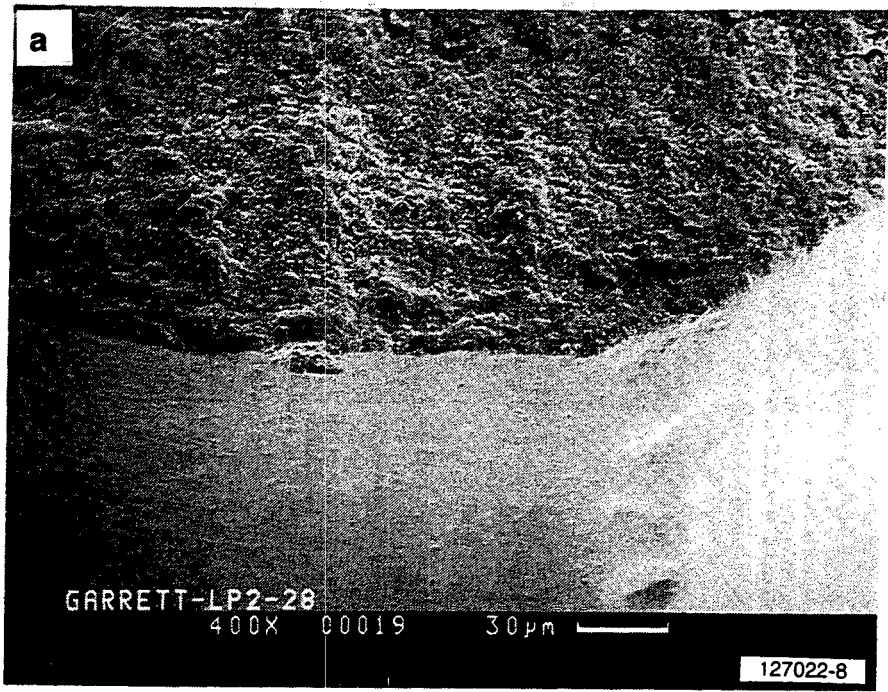
4.3.2.1 Flexure Bars

The fractography results for MIL-A, MIL-B, and E-Size flexure bars are presented in Table 1-2, Appendix IV. Surface failure at the chamfer corner location is the most frequently observed failure mode, especially in MIL-A and MIL-B bars. The cause of the chamfer corner failures is machining damage and the inability of the as-received heat treatment to heal this damage. The chamfer corner is the most likely location for machining damage to occur, because the corners are unconstrained and unsupported. Direct evidence of large machining damage such as chips can be seen in Figures 4-33 and 4-34. The smaller, but nevertheless significant, microcracks cannot be observed directly but were highlighted during some of the oxidation conditions, as seen at the fracture origin in Figure 4-35. Supporting evidence for the heat treatment effect can be found in the later section on re-heat treated flexure bar results, in which chamfer corner failures were nearly eliminated by the AlliedSignal heat treatment.



GB11591-433

Figure 4-33. Flexure Bar Failure Originating At Machining Chip On Chamfer Corner. Chips Could Be Removed By Polishing. MOR= 66.0 ksi.



GB11591-434

Figure 4-34. Flexure Bar Failure Originating At Machining Chip on Chamfer Corner. Chips Too Severe To Be Removed By Polishing. MOR= 134.5 ksi.

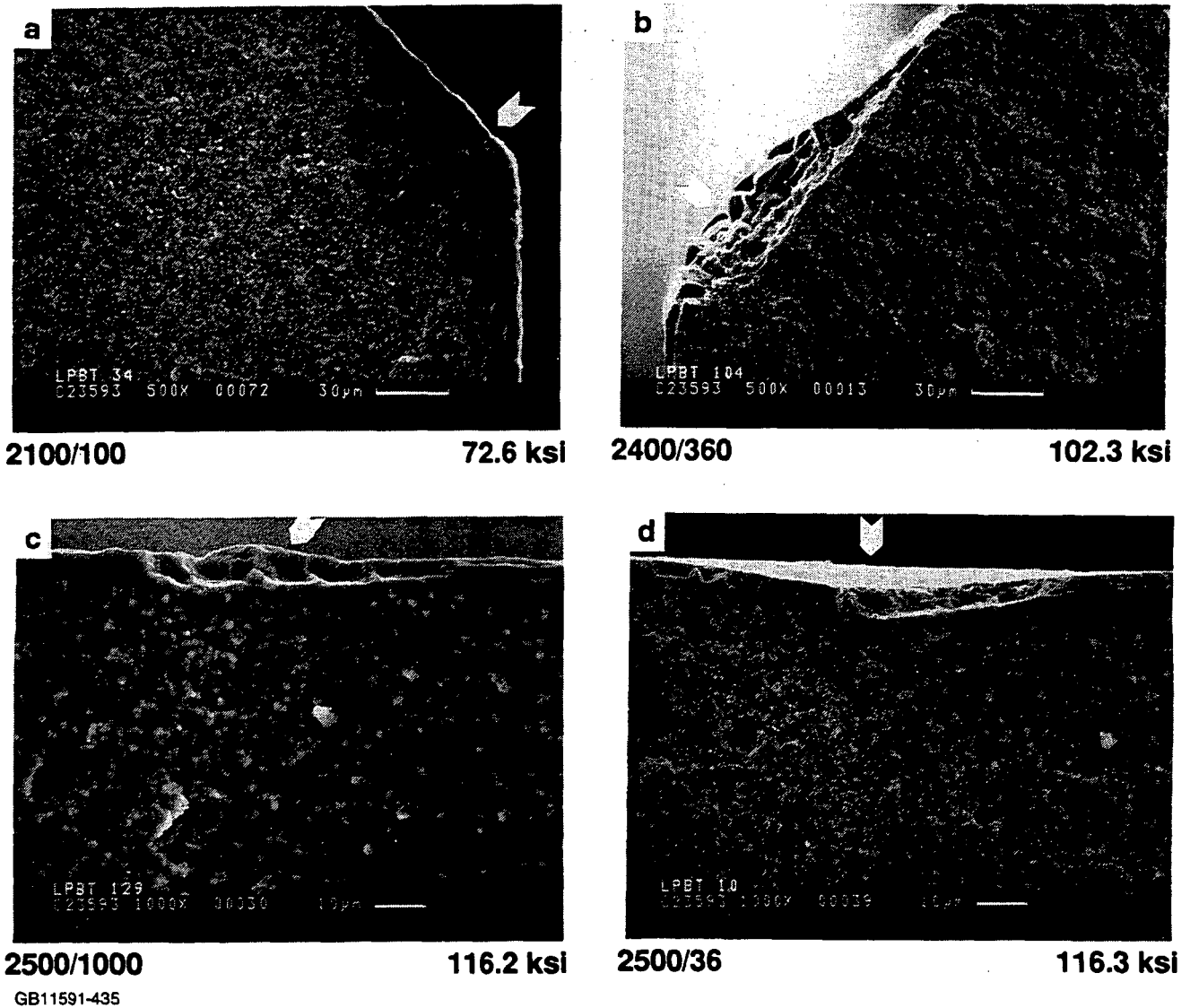


Figure 4-35. Failure Origins Of Oxidized Specimens.

Despite the chamfer corner failures, some internal failures were observed. The E-Size bars had about 10 percent of internal failures, and there was an internal inclusion failure in one of the MIL-A bars.

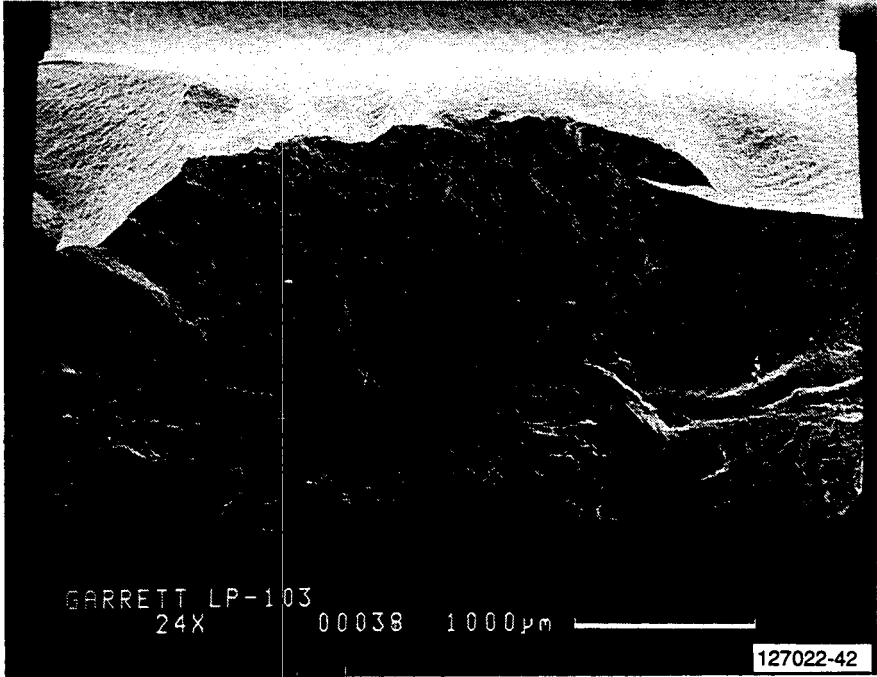
The E-Size specimens provided the most useful fractography data for the flexure bars because of the much larger surface and volume tested, which exposed more flaws. There were also less chamfer corner failures in these specimens, because the corners on the tensile sides were polished to a radius to remove machining damage. However, some large chips remained and caused failures, as shown in Figures 4-33 and 4-34. Examples of the inclusions found at the internal failure origins of E-Size bars are presented in Appendix V, Figures 1-3, showing typical elemental content of C, Fe, Ni, and Cr. The inclusions are very similar to those observed in the tensile specimens, which is not surprising because they were both machined from the same type of cylindrical billets.

Figure 4-36 shows a representative internal failure origin from a Cr inclusion in a MIL-B bar. A closeup view of the inclusion is shown in Figure 4-37(a), with elemental X-ray dot maps of the same area in Figures 4-37(b)-(d), showing the inclusion contained Fe, Ni, and Cr. However, since this specimen was tested at 2100F, the carbon portion of the inclusion would have been oxidized. A rather unusual type of flaw is shown in Figure 4-38 for interest. This is a closed crack or fold that intercepted the surface. The fractography results for MIL-A bars were based on 40X optical microscopy only, due to program time constraints.

4.3.2.1.1 MIL-B And 4-Inch Spin Disk Cutup Flexure Bars

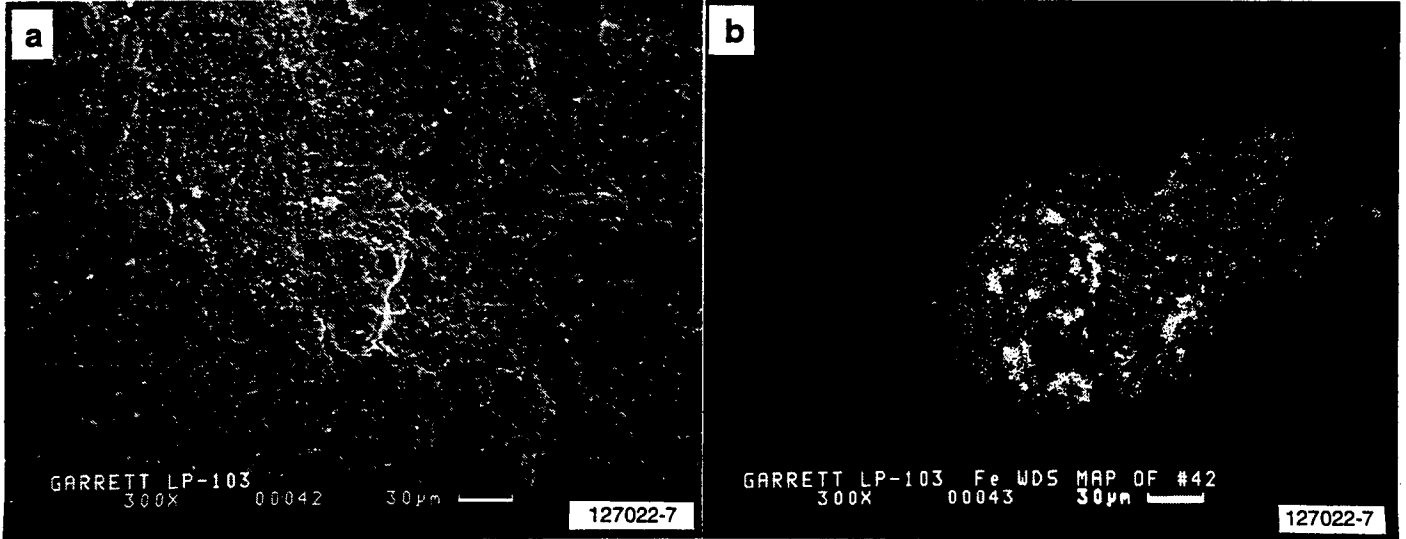
The fractography data for these specimens are presented in Appendix IV, Table 3 and were generated to support development of the anisotropy model.

Three groups of flexure bars were included in this set. Specimens numbered LPD-1 to -108 were MIL-B flexure bars machined from four disks that were concentrically ground flat on the same five-axis grinder using the same procedure and parameters as the actual spin disks. The cutup plan for these MIL-B bars was to include one tensile surface with representative longitudinal, 45-degree, or transverse machining. A schematic of the specimen cutup plan is given in Appendix I.

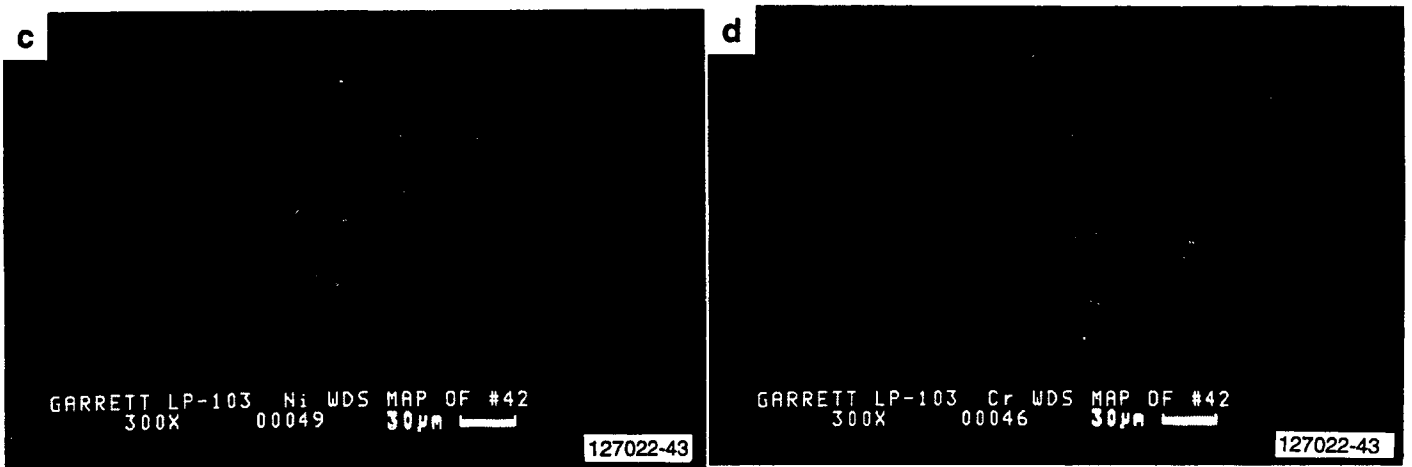


GB11591-436

Figure 4-36. Internal Failure Originating At Inclusion In MIL-B Flexure Bar Tested At 2100F. MOR = 105.6 ksi.

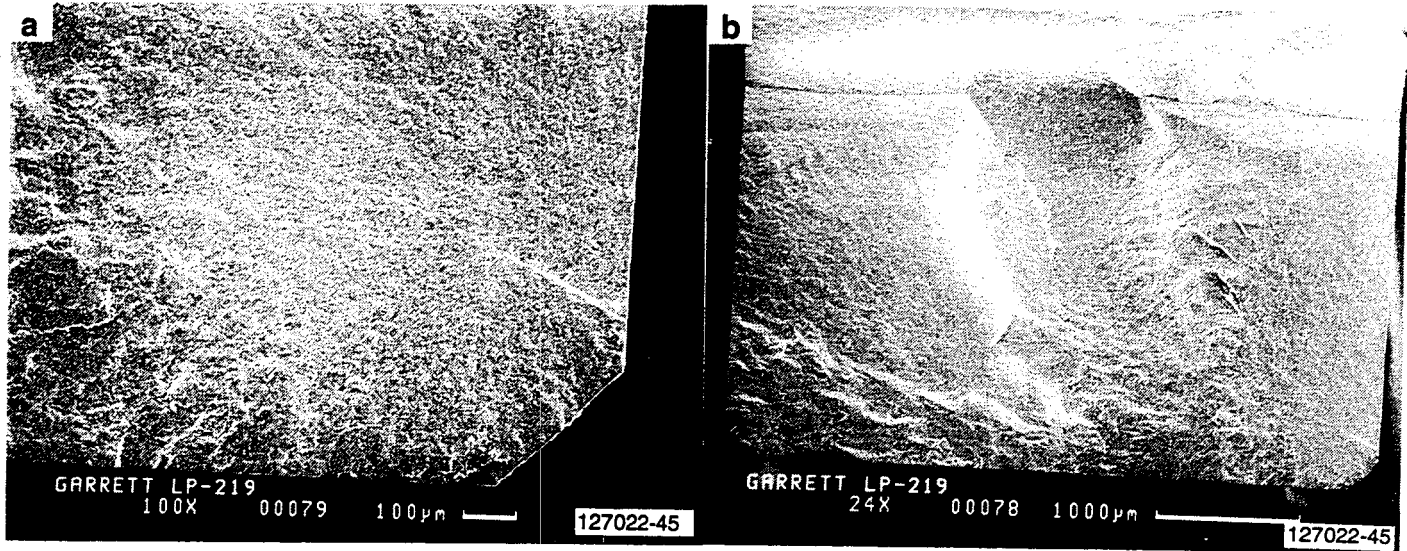


[GB11591-437]

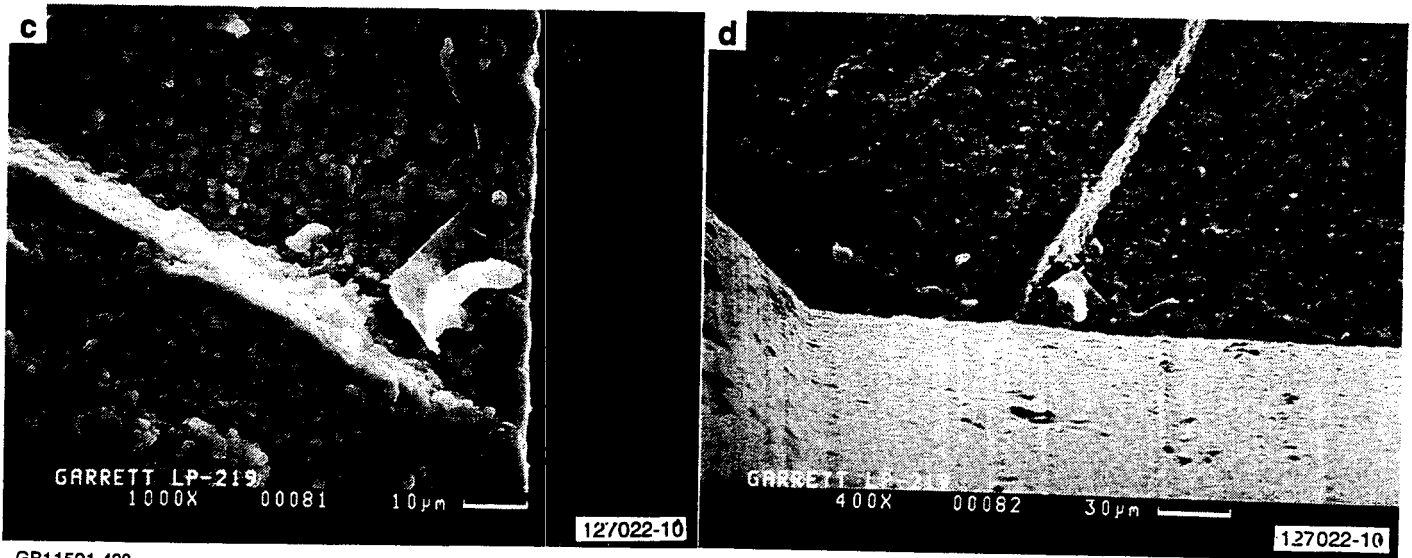


GB11591-437

Figure 4-37. (a) Closeup View Of Internal Failure Site In Figure 4-36; (b) Through (d) Fe, Ni, And Cr WDX Maps.



[GB11591-438]



GB11591-438

Figure 4-38. Failure Originating From A Surface Crack Or Fold In MIL-B Flexure Bar Tested At 2300F. MOR = 72.7 ksi.

Unfortunately, since the surface machining directions on the disks were actually concentric circles, there were very few true longitudinally-oriented directions on the surface as indicated in the cutup plan. The situation was the worst for bars cut from the innermost position, i.e., having the smallest radius (0.626 inch). The observed machining direction that intercepted the fracture origins were in many cases quite different from what was planned.

The 4-inch bars were cut from the inside of disks G22, G34, G47, and G51. The purpose of these bars was to sample internal flaws, and from the large number of internal inclusions observed (6 out of 24), the results gave good indications. The inclusions are probably C and Fe inclusions similar to those observed in the spin disk and tensile specimens. SEM/EDX/WDX was not performed on these specimens, due to program time and cost constraints.

4.3.2.1.2 Re-Heat Treated MIL-B Flexure Bars

Appendix IV, Table 4 shows the final fractography results for re-heat treated MIL-B flexure bars tested at room temperature in fast fracture. This data was acquired in support of the anisotropy model development.

This set of specimens contained 42 longitudinally machined, 30 45-degree machined, and 18 transversely machined MIL-B flexure bars. The different machining directions were on the tensile surfaces only; other non-tested surfaces were longitudinally machined. These bars were remaining, unused test bars that had their tensile surface chamfer corners radiused by polishing and were re-heat treated with the newly-developed AlliedSignal in-house heat treatment.

The reason for testing these additional specimens with a new heat treatment was because the MIL-B bars originally tested mostly failed from chamfer corners, which rendered the data quite useless for the anisotropy model. The improvement due to the chamfer polishing and new heat treatment is very dramatic, as shown by the virtual elimination of the undesirable chamfer corner failures.

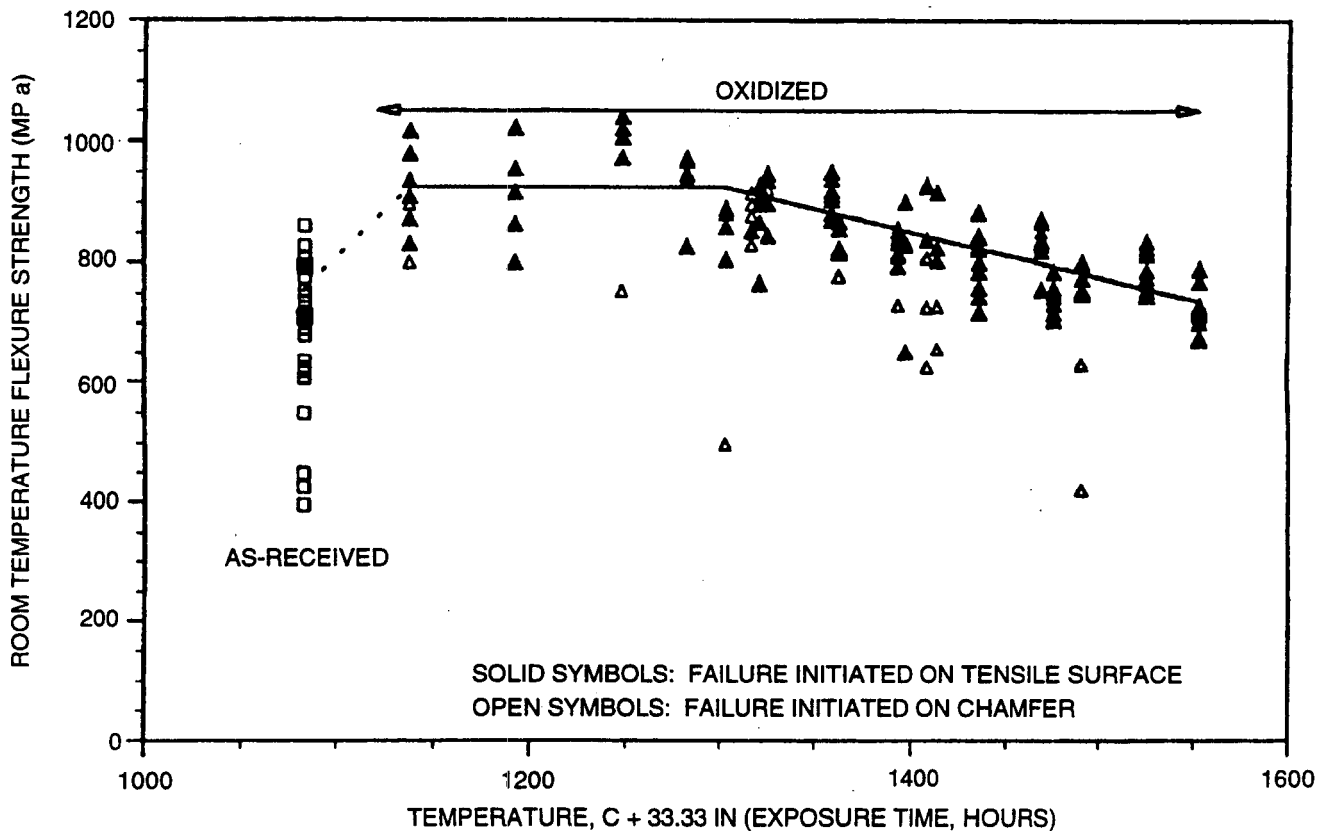
4.3.2.1.3 Oxidization Study Flexure Bars

Fractures in the as-received specimens, which were preoxidation heat treated by Norton, typically initiated in the chamfered edge of the specimen. Only seven percent of the as-received transverse machined specimens failed on the tensile surface. This result implies that machining damage was more severe on the chamfer than on the transverse machined surface.

Exposure to the high-temperature oxidizing environment reduced the severity of chamfer damage; over eighty percent of the environmental exposed specimens failed on the tensile surface. When specimens associated with chamfer failure are eliminated from the data base, scatter in the data is reduced, as shown in Figure 4-39.

Failure origins of selected oxidized specimens are illustrated in Figures 4-35(a) through (d). A large oxidized chamfer crack [Figure 4-35(a)] initiated a low-stress failure. This crack was attributed to machining damage. Other cracks in this figure were associated with oxidation-induced roughening of the surface. In a few instances, glassy silicate defects were associated with crack initiation [Figure 4-35(a)]. These defects appeared to be the result of dust particles reacting with the NT154 surface.

Fracture surfaces were examined on the SEM to determine the thickness of the oxidation-affected layer. It was found that growth of the oxidation-affected layer of these specimens followed logarithmic instead of parabolic growth behavior (Figure 4-40). Wavelength dispersive X-ray (WDX) maps indicated that oxygen (O) was typically present as a gradient in the surface of the silicon nitride [Figures 4-41(a) and (b)]. WDX analysis also indicated that the concentration of nitrogen (N) in the oxygen-affected zone remained high -- almost to the level present below the oxygen-affected zone.



GC11591-439

Figure 4-39. Oxidation Increased Flexure Strength Of Transverse-Machined Specimens And Reduced Incidence Of Chamfer-Initiated Failures.

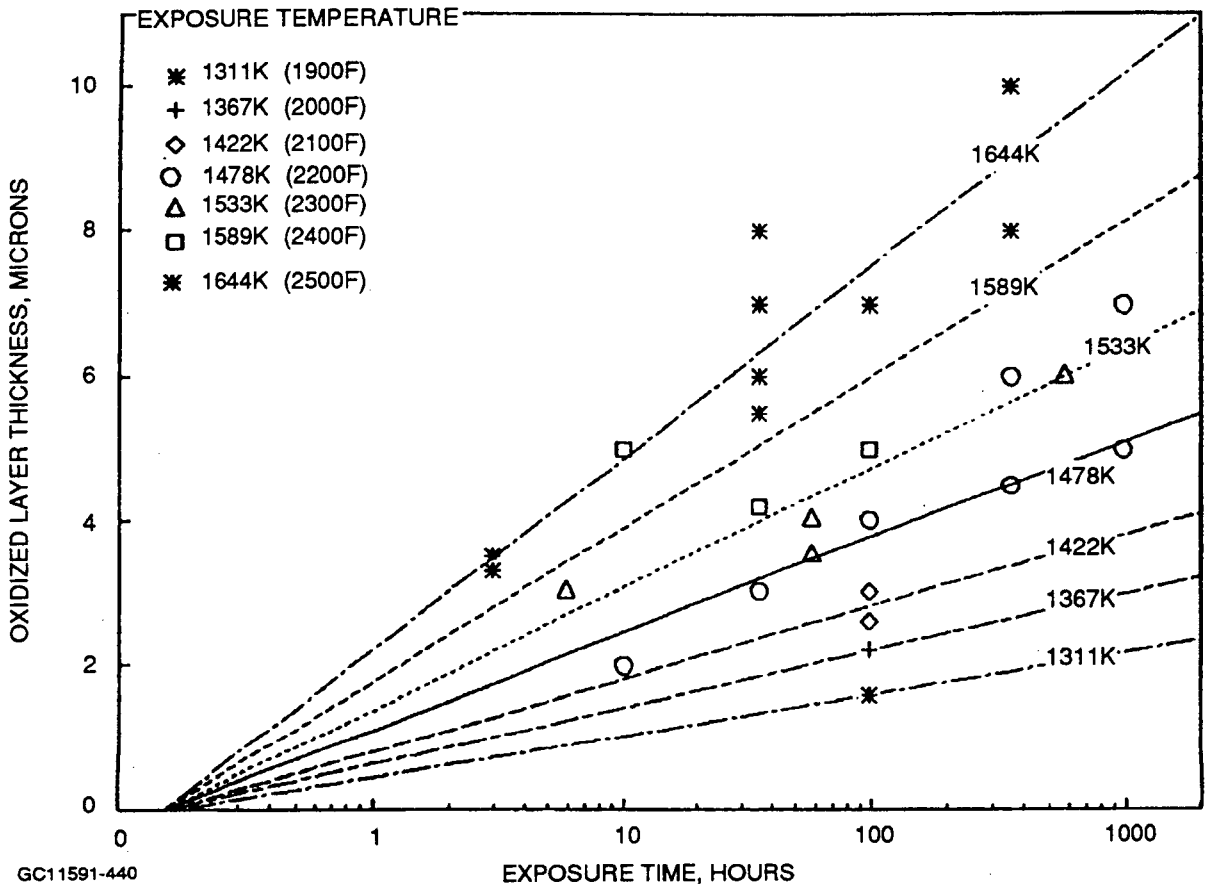
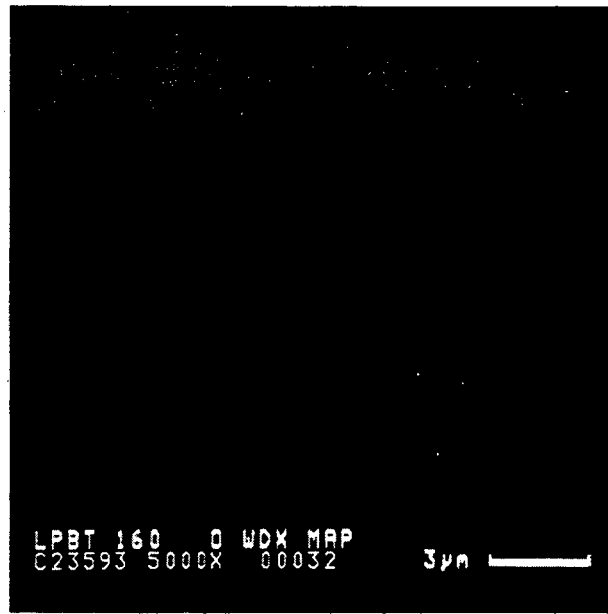
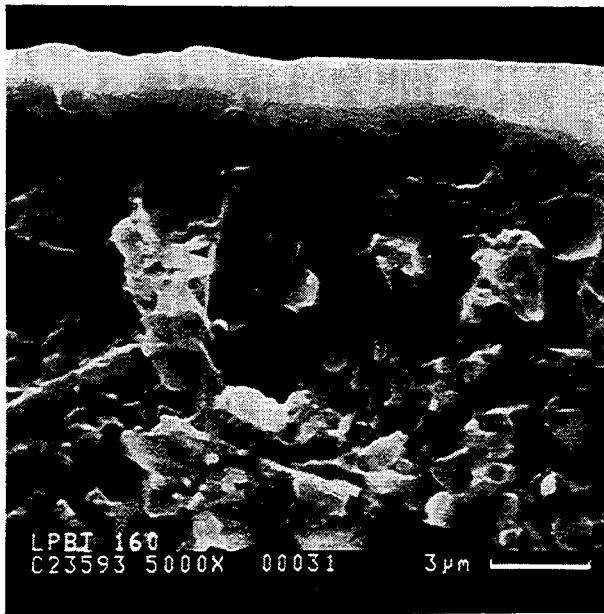


Figure 4-40. NT154 Exhibited Logarithmic Oxidized Layer Growth Below 1371C (2500F).



OXYGEN
GRADIENT

SEM PHOTOGRAPH

WDX OXYGEN MAP

GB11591-441

**EXPOSURE: 1260C/100 HOURS/AIR
POST-EXPOSURE RT STRENGTH = 920 MPA**

Figure 4-41. Oxygen Gradient Exists At The Surface of Oxidized Specimens.

Specimens were weighed before and after exposure to the furnace oxidation environment. In general, exposure to the static air environment produced negligible changes in specimen weight -- within measurement error. This result was duplicated in static oxidation tests of NT154 conducted by AlliedSignal under the DOE/NASA ATTAP program.

4.3.2.2 Smooth Tensile Test Specimens

4.3.2.2.1 Fast Fracture

The fractography results for the fast fracture tested smooth tensile specimens are presented in Table 5, Appendix IV. This set of specimens contained new, unique fractographic features which were assigned new designations after extensive discussion and analysis by AlliedSignal. The major issue was the need to include a new fracture origin classification of Internal/Volume and the ramifications of 100-percent scanning electron microscopy (SEM) examinations for internal features in tensile-tested NT154 specimens. The results showed that SEM findings significantly altered the original fractographic information previously determined by 40X optical microscopy alone. Twenty-four Internal/Inclusion fracture origins were reclassified as Internal/Volume, which were defined as internal failures without distinct features or elemental indications. SEM micrographs of such examples are shown in Figures 4-42(a) through (d) and Figures 4 and 5 in Appendix V. EDX spectra and elemental X-ray dot maps of C, O, and N were taken for the area at the center of the fracture origin but did not detect any differences compared with the Si_3N_4 matrix.

The inclusions observed in these tensile specimens were also very similar to those observed in other specimens, especially the E-Size flexure bars. Some typical examples of the inclusions are shown in Figures 6-11, in Appendix V. The lowest-strength room-temperature specimen, LPTEN2-21, failed at 48.7 ksi, from an elongated surface inclusion that contains Al as shown in Figure 4-43(a) through (d).

It was decided by AlliedSignal to describe the fracture origin type as what would be experienced by the stress field. For example, the void shown in Figures 4-44(a) through (d), with a cluster of Fe particles scattered on the void surface [Figure 4-44(d)], should be labeled as a void rather than an inclusion because a void imposes a more severe stress field effect than an inclusion. In addition, it was also decided not to use observations from other sets of specimens to label the flaw. This void was most probably left behind when the typical C inclusions that were frequently observed in room-temperature specimens were oxidized. But such information would not have been available if only one specimen or component was analyzed.

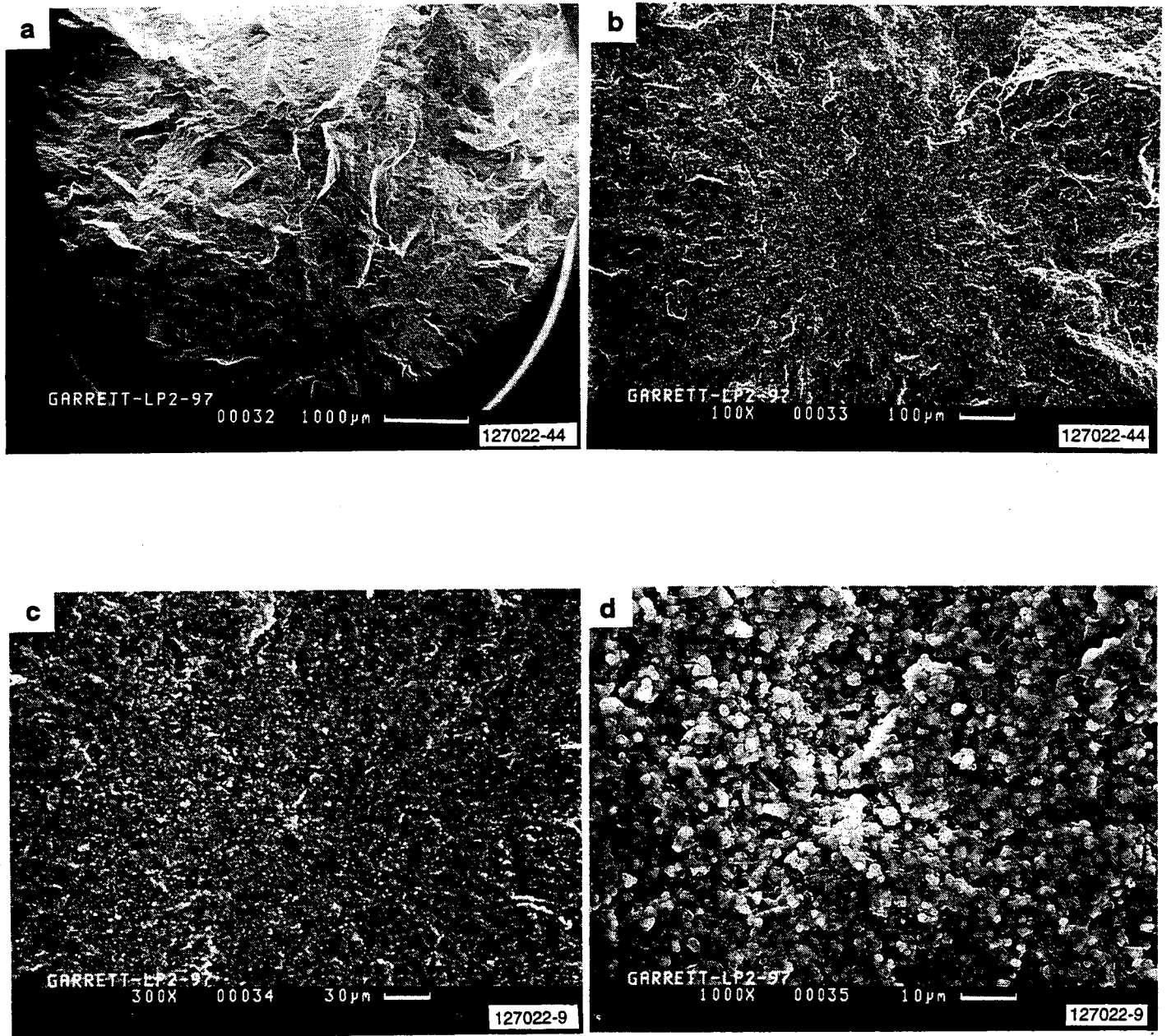
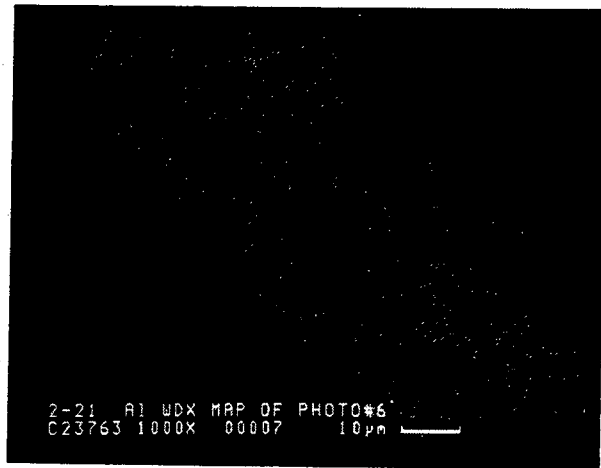
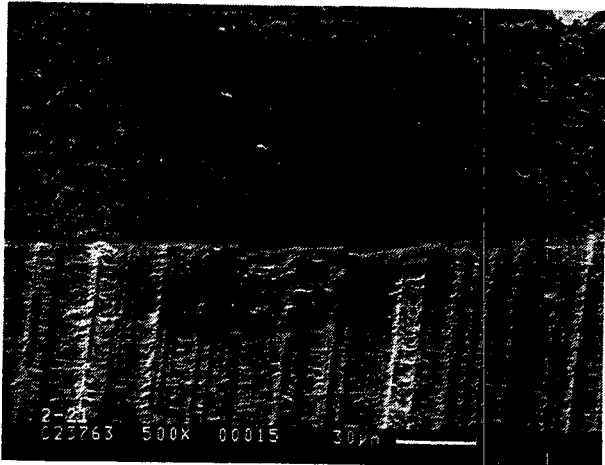
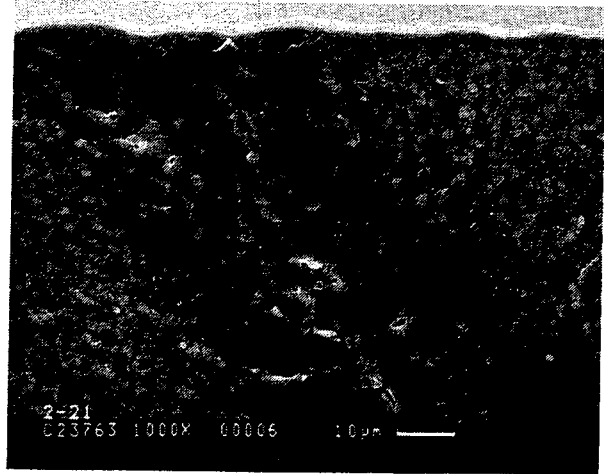
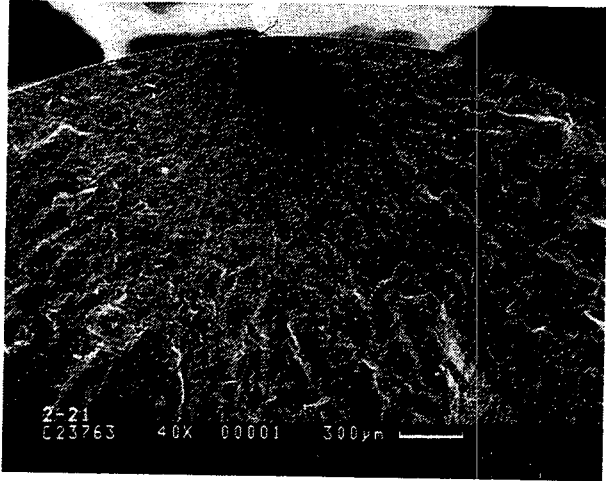
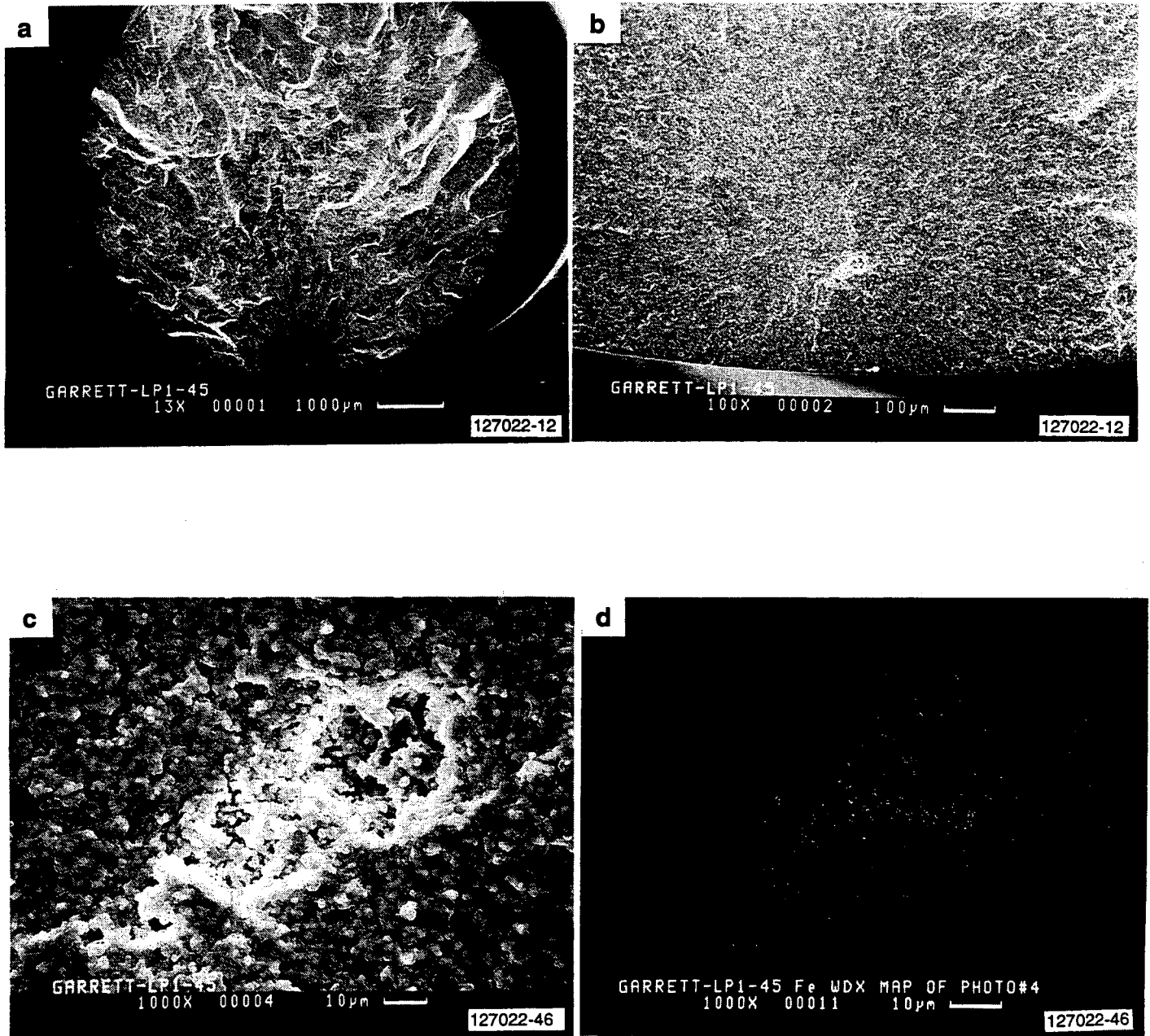


Figure 4-42. Internal Failure Of Room-Temperature Tensile Specimen Showed No Elemental Indications.



GB11591-443

Figure 4-43. Lowest Strength (336 MPa) Tensile Specimen Failed From Aluminum (Al) Surface Inclusion.



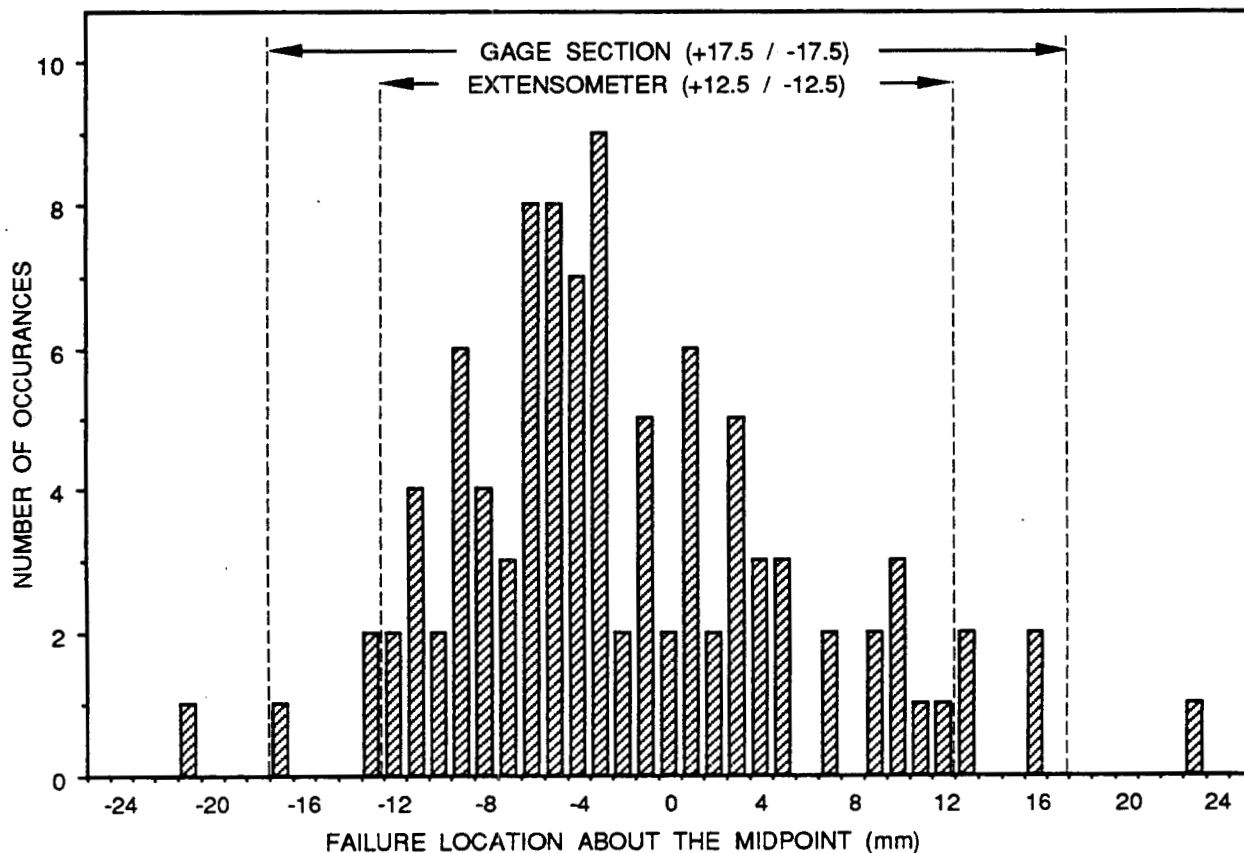
GB11591-444

Figure 4-44. Void At Failure Origin of Tensile Specimen Tested At 2200F. WDX Fe Map (d) Shows Cluster of Iron Particles In Void.

4.3.2.2.2 Smooth Tensile Creep/Stress Rupture

Figure 4-45 is a histogram showing the distribution of the locations of the creep fractures with respect to the midpoint in the gage section for those tests which were run to failure. Figure 4-45 shows that all but two failures were within the gage section, and that there were no concentration of failures at the location where the extensometer probes contacted the specimen. The two failures outside the gage section were associated with flaws. This data shows that contact probe extensometry is well suited for measuring creep strain in advanced silicon nitride specimens.

Fracture initiation in all specimens was either internal or at the surface of the specimens. On the fracture surface of all failed specimens, a sharply demarcated region, which was rough in topography compared to the region adjacent to and surrounding it, could be identified at the failure initiation. It has been suggested that this type of topography represents a region of subcritical crack growth (SCG) sometimes referred to as slow crack growth. SCG precedes catastrophic fracture. Optically, the SCG regions were more easily visible in specimens tested at the higher temperatures (lower stresses) because of their larger size. However, it could be identified in all specimens by means of SEM. Typical fractures showing the crack growth regimes in internal and surface initiations are shown in Figures 4-46(a) and (b), respectively. The internal initiations had circular SCG zones,



GC11591-445

Figure 4-45. Histogram Of Failure Locations About The Midpoint Of The Gage Section Of Tensile Creep Rupture Specimens.

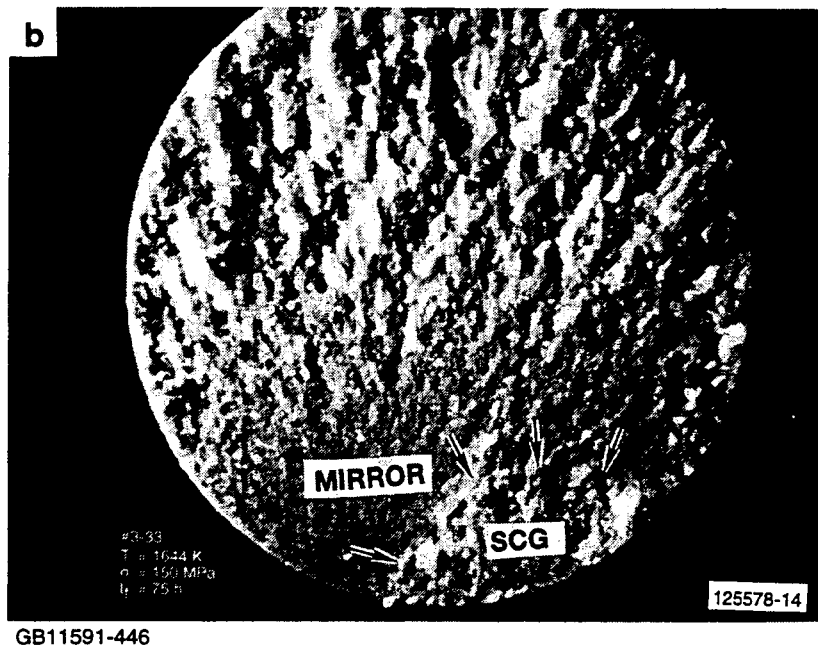
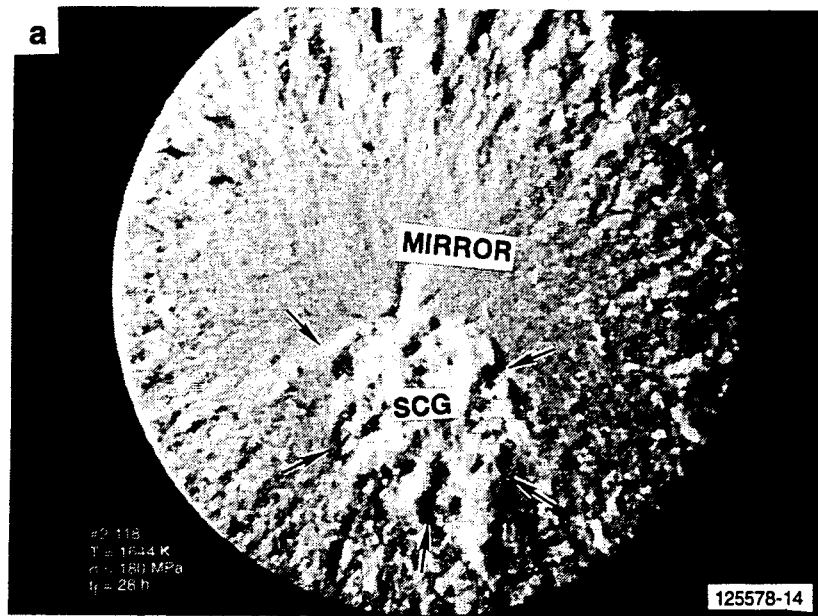


Figure 4-46. Optical Photomicrographs Of Fracture Surfaces From (a) Internal Initiation, And (b) Surface Initiation.

whereas, those pertaining to surface initiations were crescent-shaped. At higher magnifications, radiating fracture features emanating from the initiation could be observed within the SCG region. Surrounding the SCG region is the so-called "mirror" region (ref. 4-2, 4-7), abruptly starting where the SCG ends, and indicative of fast fracture. The mirror region, which appeared smoother than the SCG region, transitions into a rougher topography farther away from the SCG region. These observations are similar to those on PY6 silicon nitride reported by Ferber and Jenkins. (ref. 4-4)

In the internal failure initiations in many specimens, flaws or defects which appeared dark under optical microscopy could be identified at the center of the SCG zones. Most of these defects were found to be rich in Fe (by EDX). Cr, Ni, Al and Y were detected in some others. A few showed voids, which are believed to have been formed when the carbon particles oxidized during the time the specimen was left in the high-temperature environment after fracture. Support for this belief comes from observations made on room temperature tensile fast fracture specimens, in which carbon could be readily identified at many inclusions. In addition, no internal voids were observed in the room-temperature fast fracture specimens. Given also the fact that all internal failures (65 in a sample of 100) in the room-temperature fast fracture tests showed some form of inhomogeneity at the center of the initiation, the absence of detectable flaws in some of the internal initiations under creep testing could mean that the material constituting the flaws may have oxidized or transformed during exposure in the high-temperature environment soon after fracture occurred.

In contrast, at surface initiation sites, no flaws or defects could be identified optically or by means of SEM. Another important observation was related to the frequency of internal versus surface initiations in creep-tested specimens. The ratio of internal to surface initiation sites decreased notably with an increase in temperature. For example, for the three temperatures at which the largest number of specimens were tested (Table 4-4), approximately 88 percent of the specimens failed from internal initiation at 1149C, 58 percent at 1204C, and only 14 percent at 1371C. This observation is also reflected in the summary of the replicate tests alone, given in Table 4-6. In addition, it was noted that the ratio also decreased when stress was decreased from 180 to 145 MPa in tests at 1371C. No specimens failed from internal flaws at 145 MPa. This is an important observation to note, and may reflect the tendency for internal defects to become inoperative through crack blunting under conditions of increasing creep.

TABLE 4-6. SUMMARY OF PERCENT INTERNAL FAILURE INITIATION SITES IN REPLICATE TESTS

Test Conditions	Total No. Specimens	True Failures	Internal Failures	Percent Internal Failures
1371C/145 MPa	16	16	0	0
1371C/180 MPa	16	16	4	25
1204C/375 MPa	20	18	10	56
1149C/445 MPa	21	12	10	83

4.3.2.2.3 Correlation Of The SCG Zone Size With Stress Intensity

The sizes of the SCG regions increased in a systematic manner with decreasing applied stress. Figures 4-47(a) and (b) show SEM fractographs showing crack initiation and growth regions in internal initiations in specimens tested at 1204C, 1260C, 1371C, and 1400C. The arrows indicate the periphery of the SCG region, which is circular in shape. In each case, the SCG region is followed by a "mirror" region, the latter indicative of fast fracture. On a selected number of specimens where the size of the SCG zone could be accurately measured, the quantity $\sigma a^{1/2}$ was calculated, where σ is the stress and a is the radius of the zone. This is plotted in Figure 4-48.

It is interesting to note that the quantity $\sigma a^{1/2}$ remains approximately constant for a variety of temperatures and stresses, indicating that failure occurs when the SCG region grows to a size corresponding to a constant stress intensity. No attempt was made to calculate precisely the stress intensity factor, since it depended on the proximity of the SCG zone to the surface, and also for the reason that the fracture seemed to emanate from a particular location on the periphery in some cases.

Figure 4-49 is an SEM fractograph of the surface shown in Figure 4-46(b) [125578-14] of a specimen tested at 1371C. The fast fracture characterized by the mirror seems to emanate from the region where the crack (SCG zone) meets the surface. This is somewhat obvious even in the optical photograph of the same fracture, shown in Figure 4-46(b), and was typical of all surface-initiated cracks. Using a formulation for stress intensity given by Raju and Newmann (ref. 4-8) for circumferential cracks in rods under tension, the stress intensity at the depth of the crack or at the intersection where the crack meets the surface can be calculated. Since our observations show that the fast fracture initiated at the intersection where the SCG region meets the surface in all surface-initiated failures, an estimation of the stress intensity at this point would be of interest. Figure 4-50 shows such a plot with respect to failure time for 25 specimens tested at 1371C, and stresses ranging from 125 to 180 MPa. The average was similar to that obtained in fracture toughness testing at 1371C for chevron-notched bend test specimens of dimensions 6.4 x 6.4 x 51 mm.

These observations show that failure in NT154 occurs by subcritical growth of a single crack at all the tested conditions, and that the final fracture event is governed by the fracture toughness of the material.

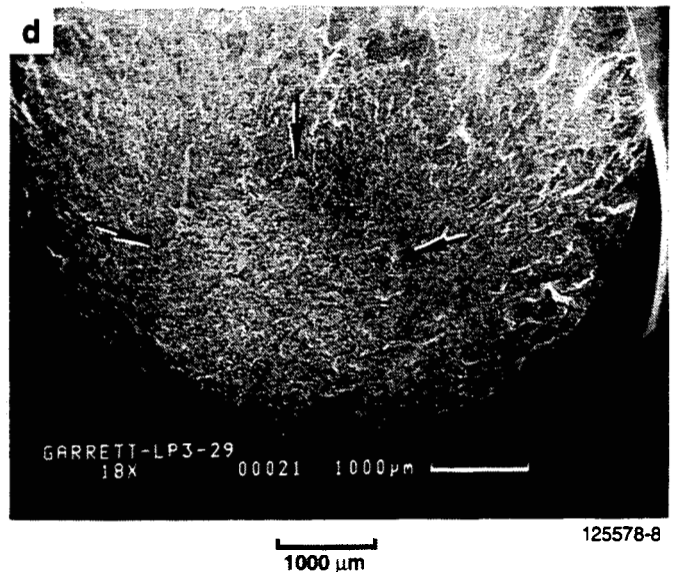
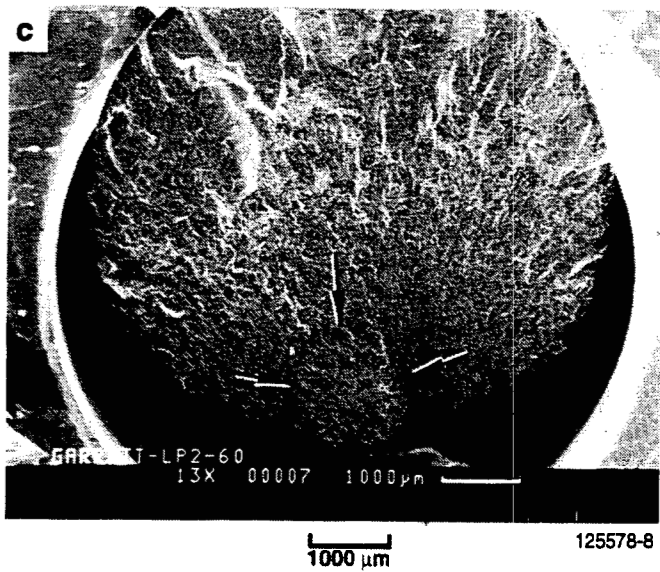
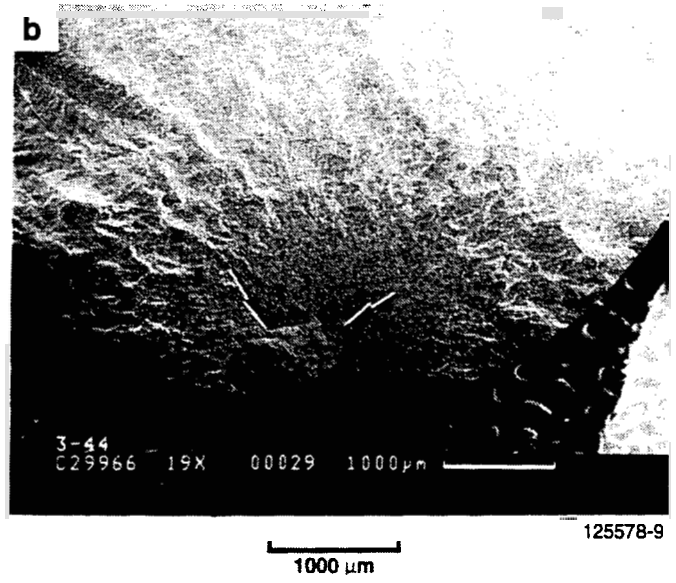
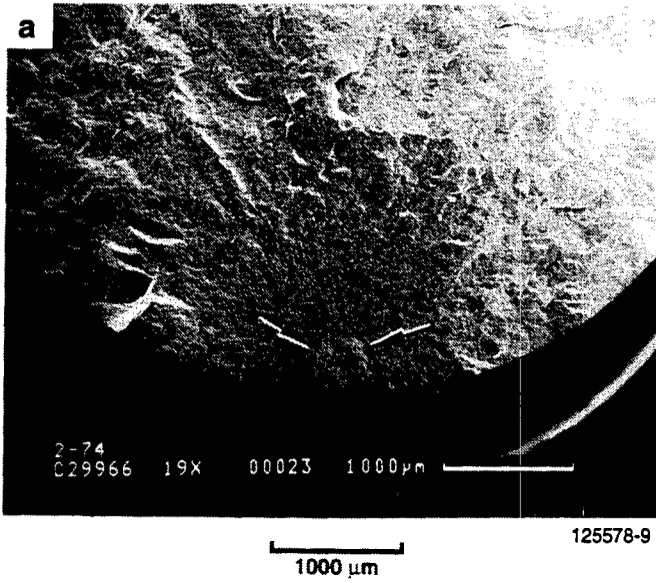


Figure 4-47. SEM Photomicrographs Showing Subcritical Crack Growth Zones Increased With Decreasing Applied Stress. (a) 1204C/325 Mpa/68 hr; (b) 1260C/295 MPa/560 hr; (c) 1371C/180 MPa/19 hr; (d) 1400C/150 MPa/80 hr.

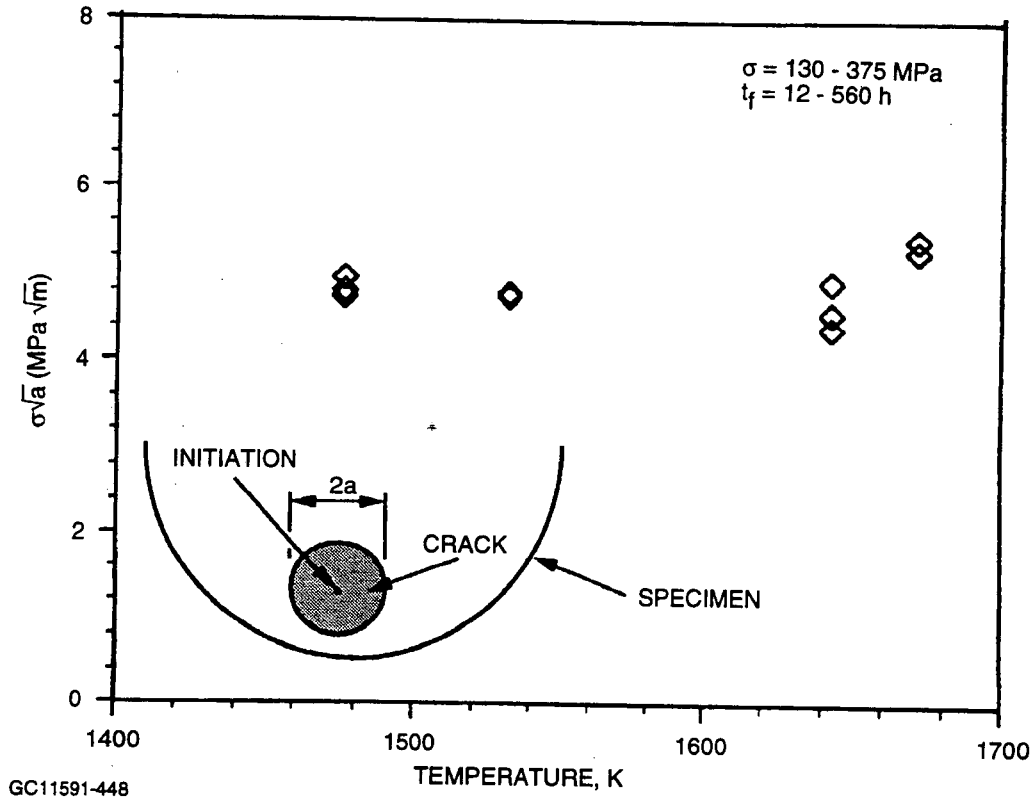


Figure 4-48. Plot of $\sigma a^{1/2}$ Versus Temperature Shows Relatively Constant Value.

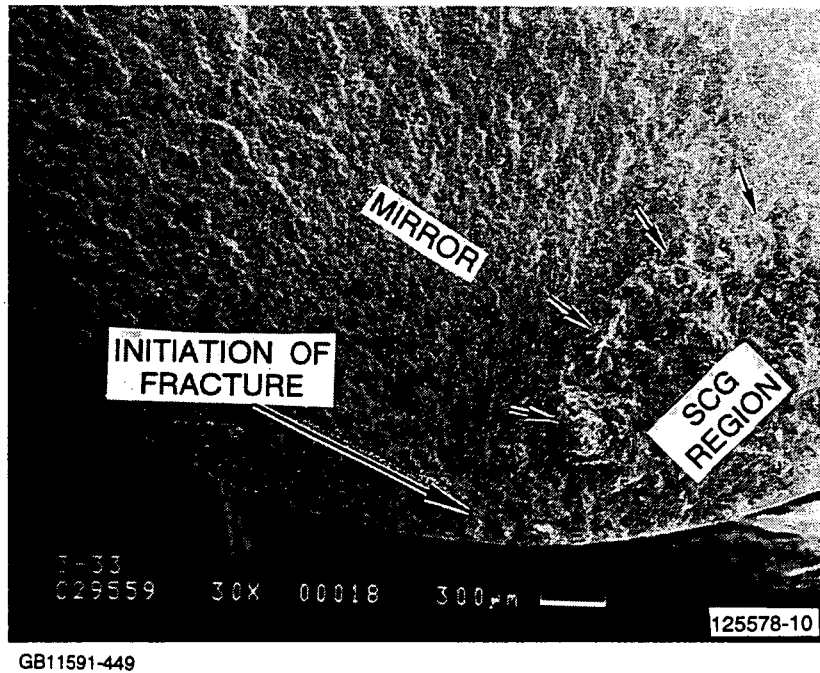


Figure 4-49. SEM Photomicrograph Of Fracture Surface In Surface-Initiated Failure At 1371C [Also Shown in Fig. 4-46(b)].

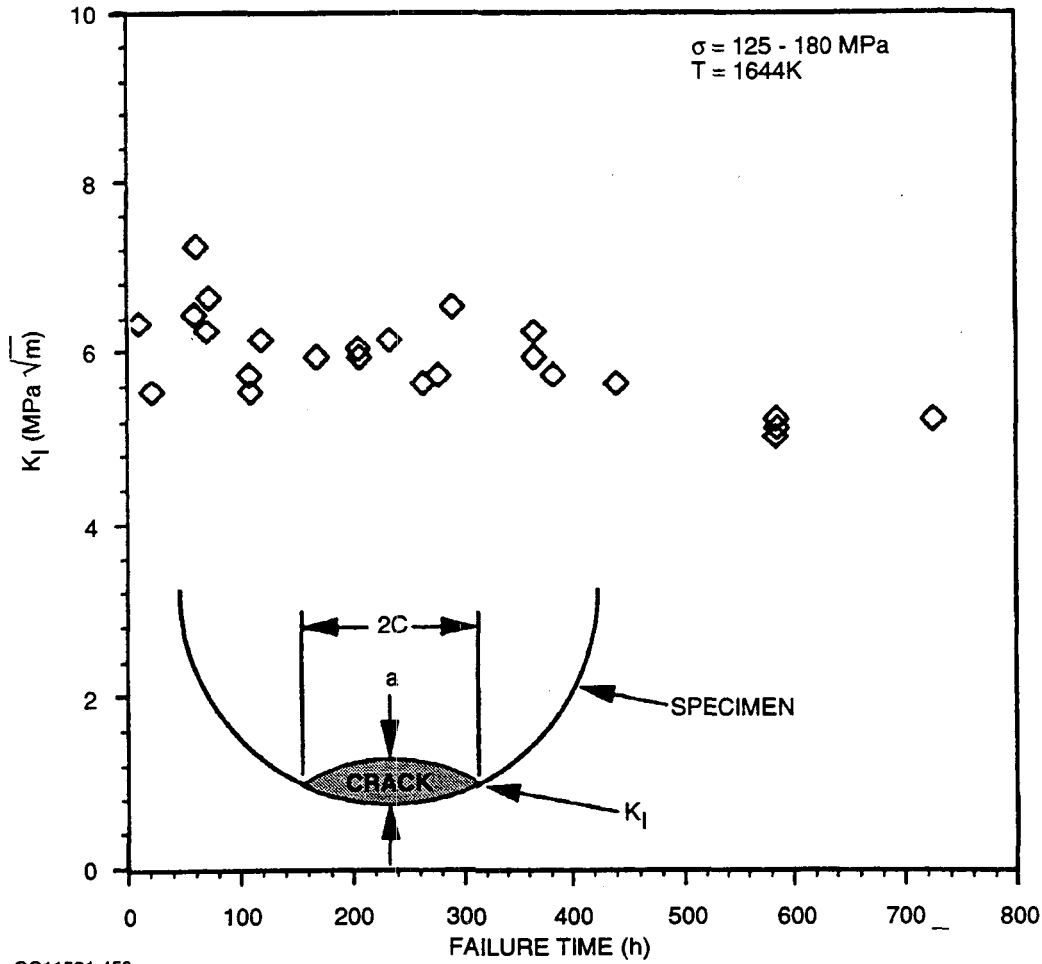


Figure 4-50. Plot of Stress Intensity (On Fracture) Versus Time At Edge Of SCG Region.

4.3.2.3 Fracture Toughness

4.3.2.3.1 Diametral Compression Disk

The diametral compression disks were tested at the University of Utah. A new precracking technique was developed, because the original method developed for alumina would not work for NT154 silicon nitride. Photos of a successful precrack can be seen in Appendix II, Figures 5-6. Appendix II, Figures 8-9 show the fracture patterns of two disks tested in mixed-mode loading. The cracks were noted as always fracturing in the K_I direction even when they were rotated to initiate in K_I/K_{II} or K_{II} conditions. Some fractography data are presented in the subcontractor report in Appendix II.

4.3.2.4 Notched Tension/Torsion

The notched tension/torsion specimens were tested at Brown University. Photographs of the fracture surfaces of specimens tested in pure mode I, pure mode III, and three combinations of mode I/mode III are presented in the subcontractor report in Appendix III.

4.3.2.4.1 Notched Tensile Fast Fracture And Stress Rupture

The fractography data are presented in Appendix IV, Table 10. All failures, except one in fast fracture and possibly one in stress rupture, were surface initiated (it is possible that failure initiation in specimen K-10 was from a subsurface site). In addition, all failures originated at or very near the tip of the notch, except the fast fracture specimen that failed from an internal void in the gage section away from the notch. In all specimens tested at 1371C, SCG zones were clearly visible. In those specimens tested at 1204C, no clear demarcation of any zone was evident at the failure initiation. In the room-temperature residual-strength tested specimen (K-9, 1371C), which had accumulated 546 hours under load, a small zone which may be associated with SCG was visible. Examples of SCG zones found in fracture initiations in notch rupture tests at 1371C at K_{Ic} of 1.6 and 2.1 are shown in Figures 4-51 and 4-52, respectively.

4.3.2.5 Plate Bending

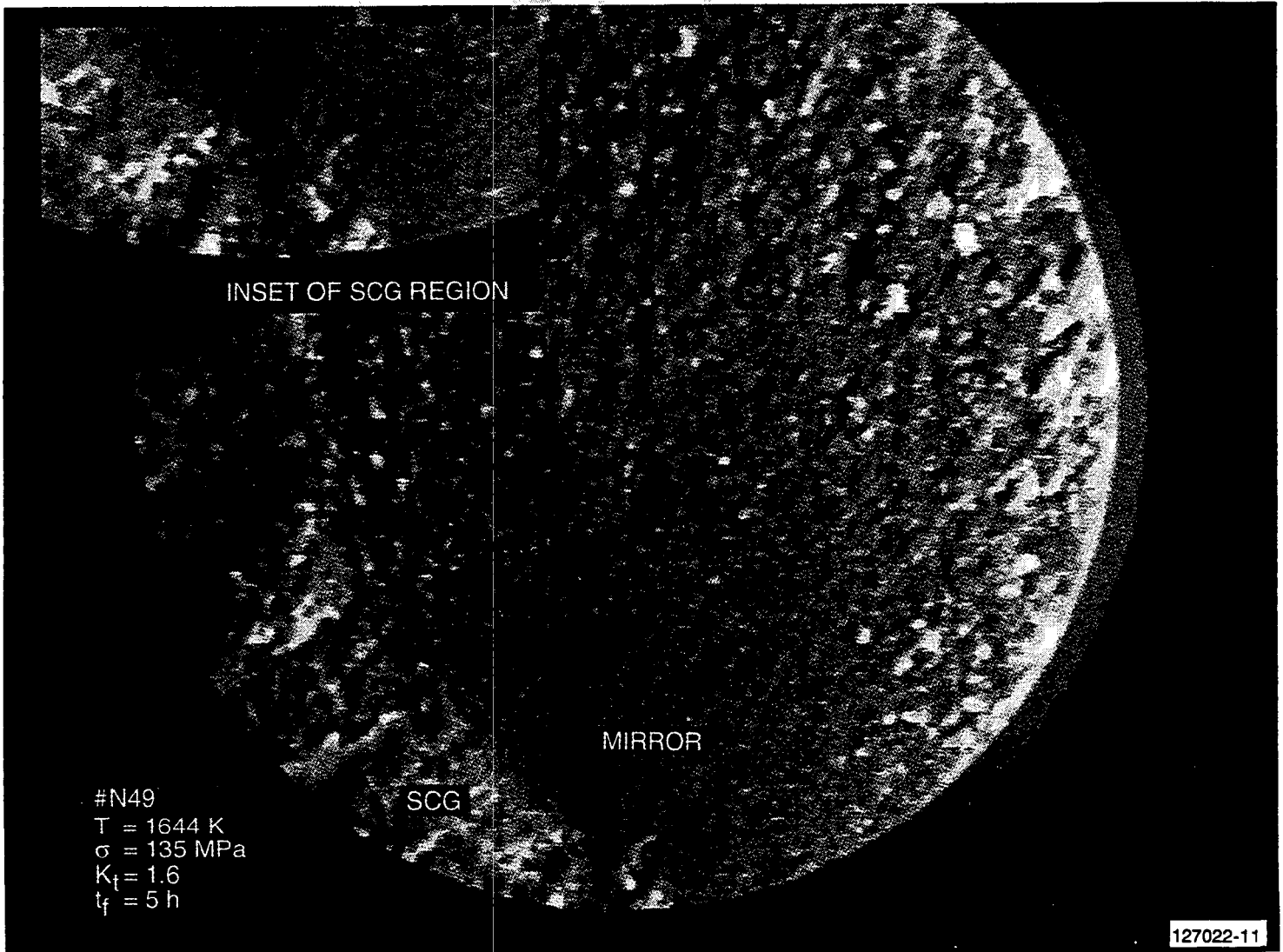
The University of Utah tested 36 plate specimens at room temperature. Note that specimens LPPB-1, -2, -3, -33, -34, and -36 were tested with a larger (24.765 mm) supporting radius fixture, and specimens LPPB-33, -34, and -36 were not re-heat treated with the AlliedSignal proprietary heat treatment. Detailed fractography data are presented in Appendix IV, Table 6.

The flat surfaces of these plates were surface ground in a single direction. The fracture angle values included in the data below are the smallest measured angle between the fracture origin plane and the machining direction of the surface. It is interesting to note that there was a distribution of fracture angles, rather than the specimen failing mainly from the transverse direction as was first expected. This is a good indication of the effectiveness of the AlliedSignal heat treatment in healing machining damage.

4.3.2.6 Smooth Tension/Torsion

Fractography of these specimens was very difficult, because the specimens failed and shattered into many fragments that were virtually impossible to reassemble. The fracture origins were also mostly on very small fragments that were hard to handle. These reasons also accounted for the high ratio (3 of 36) of fracture origins that were missing. The fracture origins for the missing specimens were estimated to be Surface/Surface, based on expert judgment. Detailed fractography data are presented in Appendix IV, Table 7.

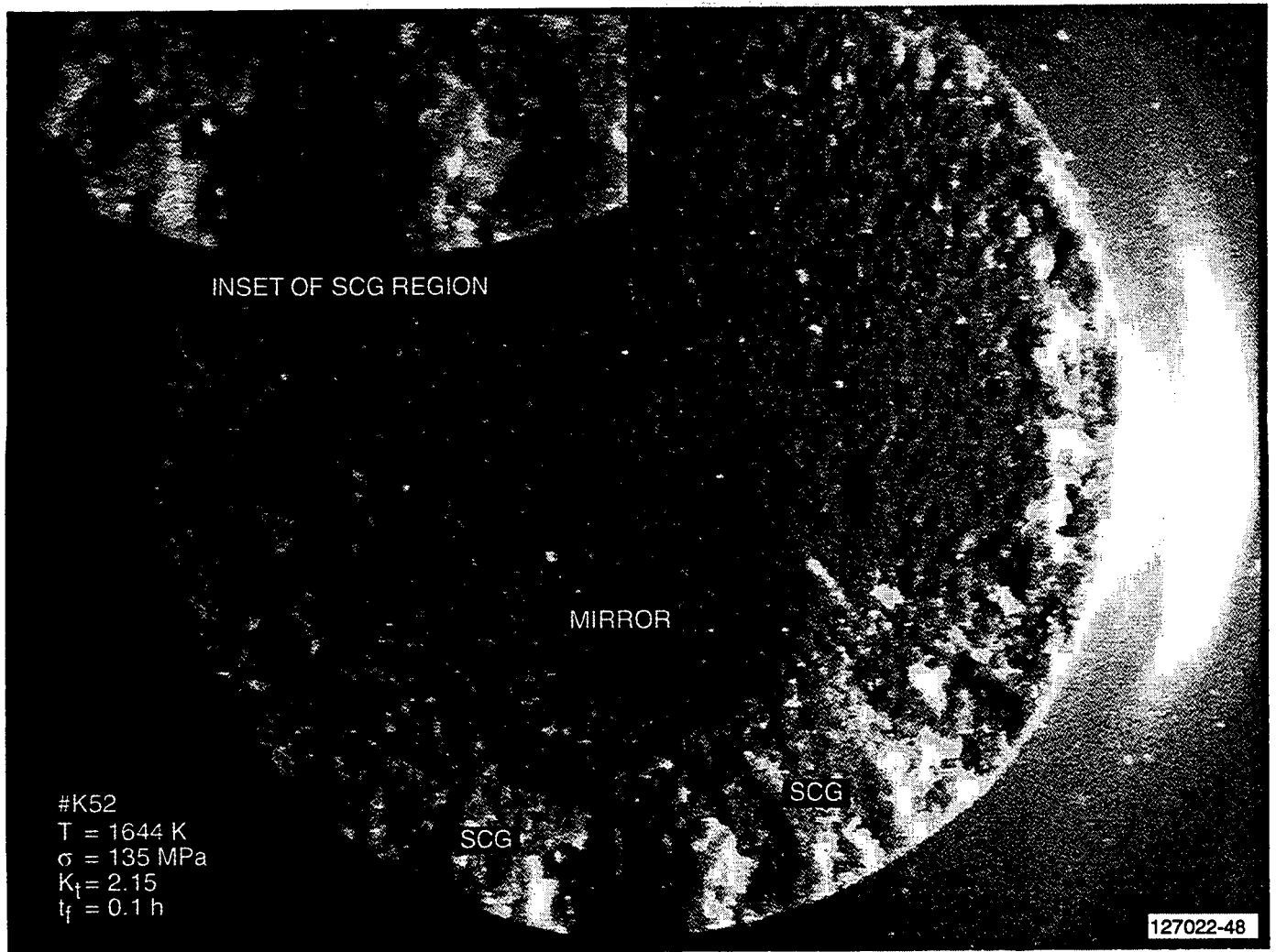
N49-135MPa/1371 C-K1.6(1.75X)



GB11591-451

Figure 4-51. SCG Zone In Specimen Tested at 1371C. $K_t = 1.6$.

K52-135MPa/1371C K2.15(1.75X)



GB11591-452

Figure 4-52. SCG Zone In Specimen Tests at 1371C. $K_t = 2.1$.

Brown University tested 36 specimens at room temperature. The specimens had longitudinally-machined gage sections and transversely-machined shank/grip regions. Data for the strain-gaged calibration specimens and specimens associated with machine and operator error were not included in the Appendix.

4.3.2.7 Spin Disk

Detailed spin disk test results are presented in Appendix IV, Table 8. with the fractography results in Appendix IV, Table 8. Fractography of the spin disks was the most difficult among all the Life Prediction specimens, because the spin disks failed and shattered into many fragments. There were also some secondary impacts, as shown by the high-speed photographs of the burst event and secondary origins and witness marks. Despite these difficulties, most of the important remnants were collected and 25 fracture origins were identified, out of the 26 spin disks tested. The only failure that could not be confirmed, Disk no. 26, tested at 2500F stress rupture condition, was determined to be a Surface/Surface failure based on expert judgment of the available evidence.

By locating and reassembling some of the fragments, the exact location of most of the fracture origins could be measured relative to the disk surface and centerline. Note that all identified origins were within 1.36 inches from the centerline and mostly on the stem side of the disk. This is possibly due either to higher stress due to the influence of the stem, or to occurrence of more machining damage because the two sides of the disks could not be fixtured or machined exactly to the specified disk shape. There is also a change in the radius of curvature near that location, which may have required a slight variation in grinding wheel movement.

After testing the first four spin disks (Disks nos. 30, 38, 27, and 16), the new AlliedSignal heat treatment was applied to the remaining spin disks to increase the strength of the transverse machined surface, to increase the possibility of internal failure. The subsequent occurrence of internal failures verified the success of the new heat treatment.

The characteristics of the internal failure origins observed in the spin disks are similar to those observed in the smooth tensile specimens. Inclusions containing C, Fe, Cr, Ni, or Al were observed. Examples of these inclusions are shown in Figures 12-14 in Appendix V. Many of the surface failures originated from surface machining damage, such as the deep scratches shown in Figures 15 and 16 in Appendix V or surface pits as shown in Figures 17 and 18 in Appendix V. Neither of these failure-originating flaws was observed in other specimens, possibly due to the combination of different machining, heat treatment, stress, and testing conditions unique to these spin disks.

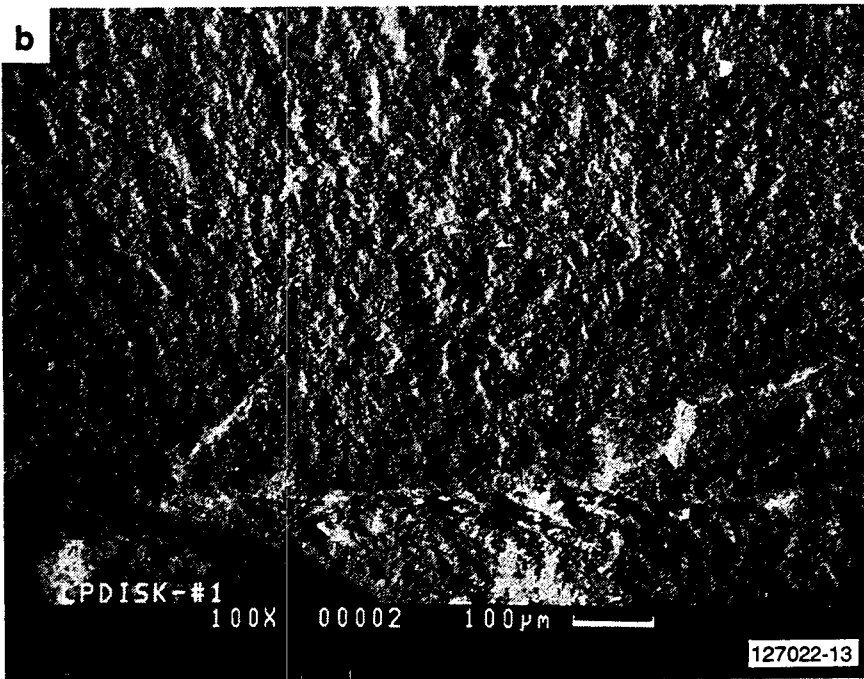
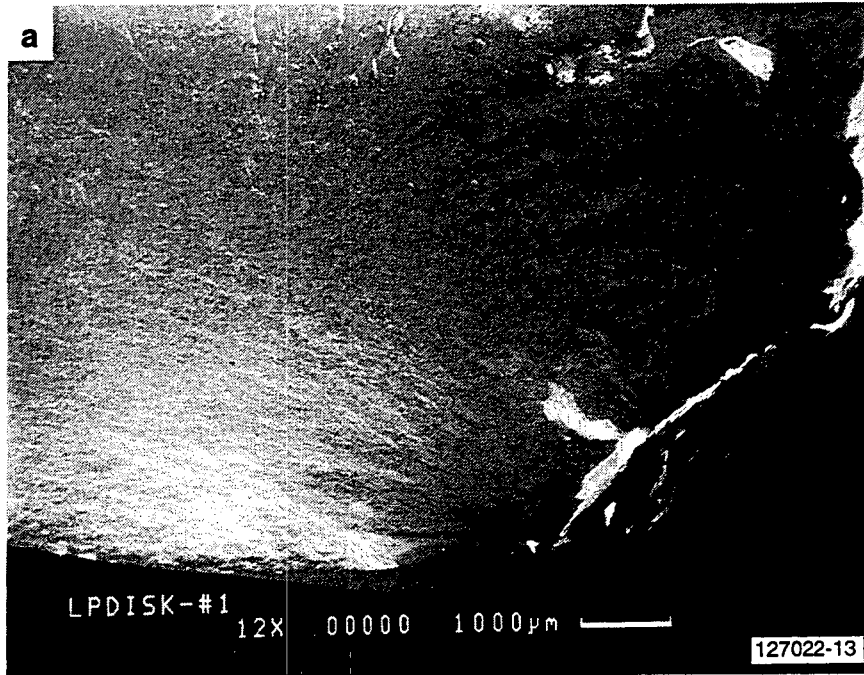
Three failure origins of interest are shown in Figures 4-53, 4-54, and 4-55, demonstrating internal flaw and fast fracture failures from possible cracks generated during the stress rupture testing.

4.4 Microstructural Characterization

4.4.1 Microstructure Of The As-Received Material

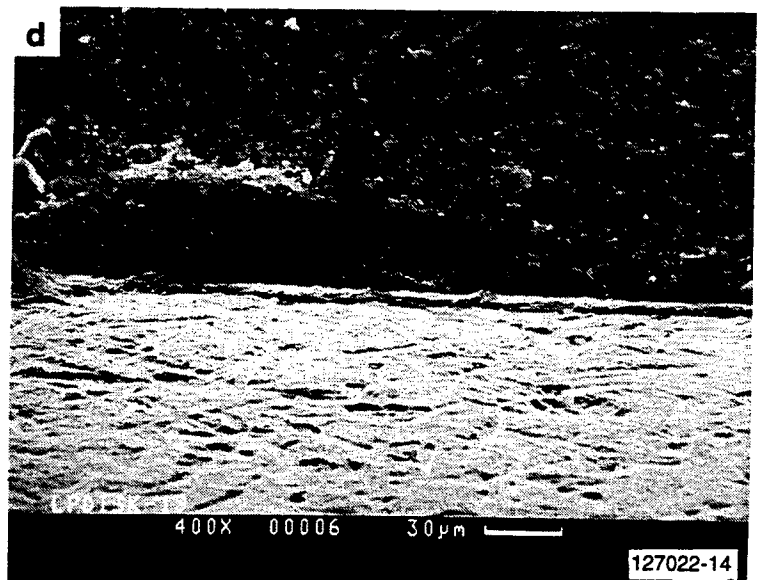
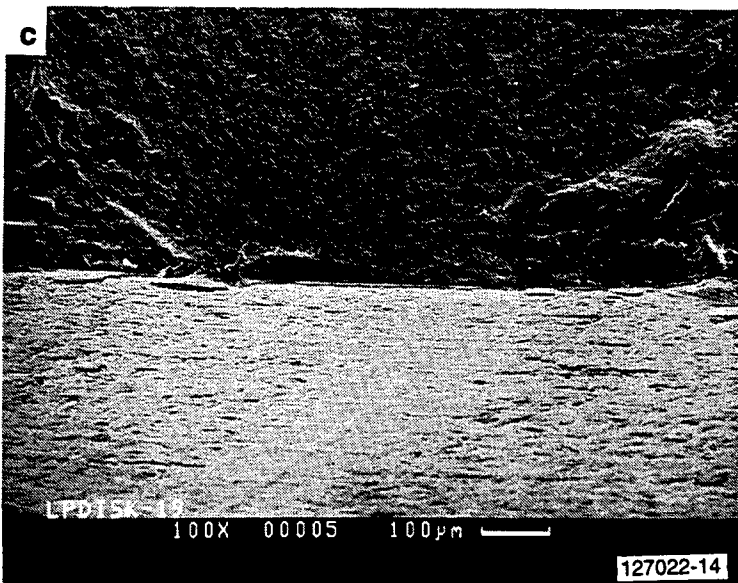
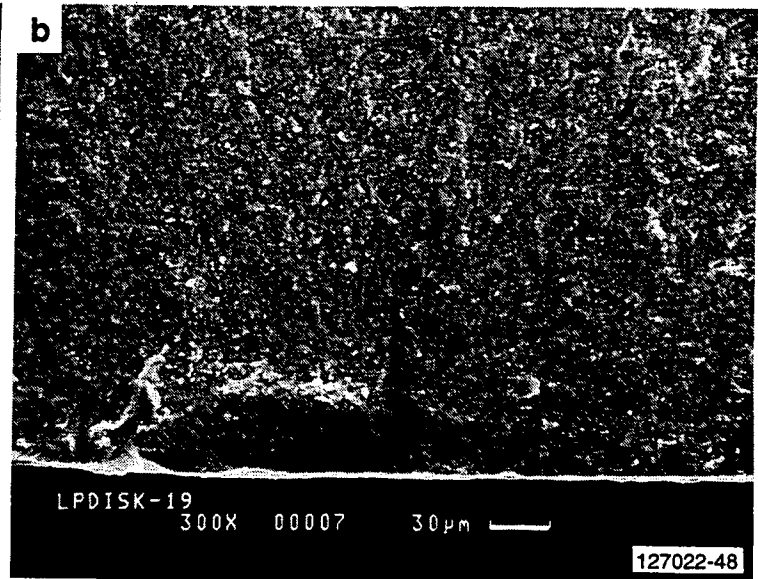
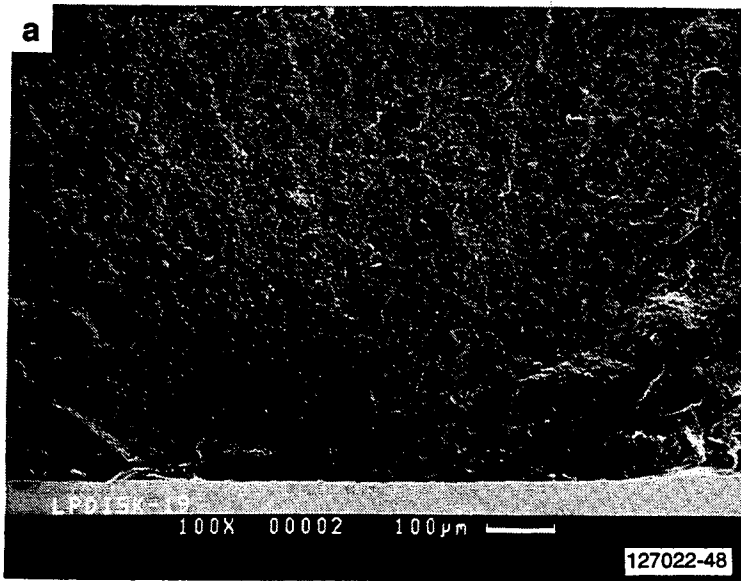
A representative view of the morphology of the grain structure of the as-received material is shown in Figures 4-56(a) and (b). Figure 4-56(a) is an SEM micrograph of the polished and etched surface, and Figure 4-56(b) is an SEM micrograph of a room-temperature tensile fracture surface. The SEM observations, with detailed TEM examinations, have shown that the microstructure consists of acicular grains, generally about 2 to 6 μm long and about 1 to 2 μm in width, and equiaxed grains, approximately 0.5 to 2 μm in diameter. In Figure 4-56(a), equiaxed grains seem to be concentrated in pockets and surrounded by acicular grains. The XRD results showed that silicon nitride grains were primarily of the beta- (β)-phase. The XRD results also confirmed the existence of 6 to 10 percent residual alpha-silicon nitride ($\alpha\text{-Si}_3\text{N}_4$) in the as-received material. TEM showed that some of the triple junctions contained other crystalline phases, small in size and rich in yttrium. These are shown in Figure 4-57 [supplied photo]. Yttrium, being a heavy element, gives a darker shade to these phases in the TEM microphotographs. The triple-junction phases were identified by XRD as either alpha-yttrium disilicate ($\alpha\text{-Y}_2\text{Si}_2\text{O}_7$) or N-apatite ($\text{Y}_5\text{N}[\text{SiO}_4]_3$). Both the residual $\alpha\text{-Si}_3\text{N}_4$ grains and the yttrium-rich crystalline phases were located primarily in the pockets of smaller, equiaxed grains.

Extensive TEM examinations were conducted to determine the morphology of the amorphous phase in this material. The results showed that an amorphous phase, rich in yttrium and varying in thickness, existed between Si_3N_4 grains, or between single Si_3N_4 grains and a triple-junction crystalline phase. In general, the amorphous phase was thinnest between two Si_3N_4 grains; the largest measured thickness being about 1.0 nanometer (nm), as shown in Figure 4-58, and the smallest being almost zero, or undetectable. The amorphous phase was thickest between a triple-junction crystalline phase and an Si_3N_4 grain; here the smallest measured thickness was about 0.6 nm, and the largest, 2.3 nm. The larger thickness of the amorphous phase in the triple-junction areas is to be expected, since these would be the regions where the phase would last devitrify (during the devitrification treatment) into the crystalline forms.



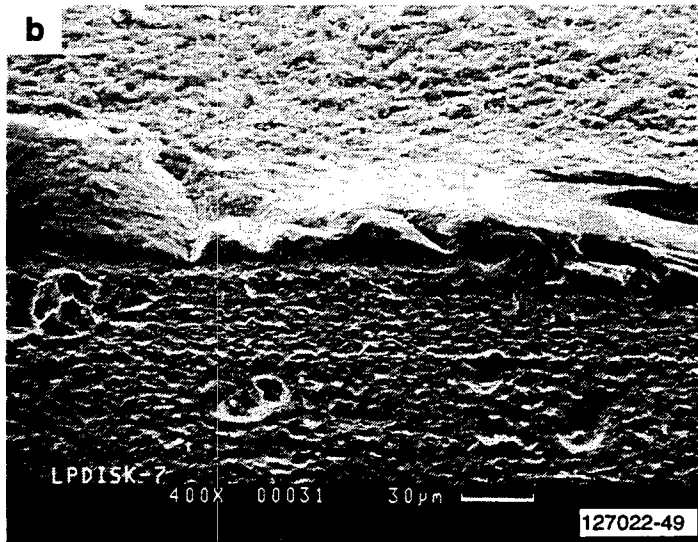
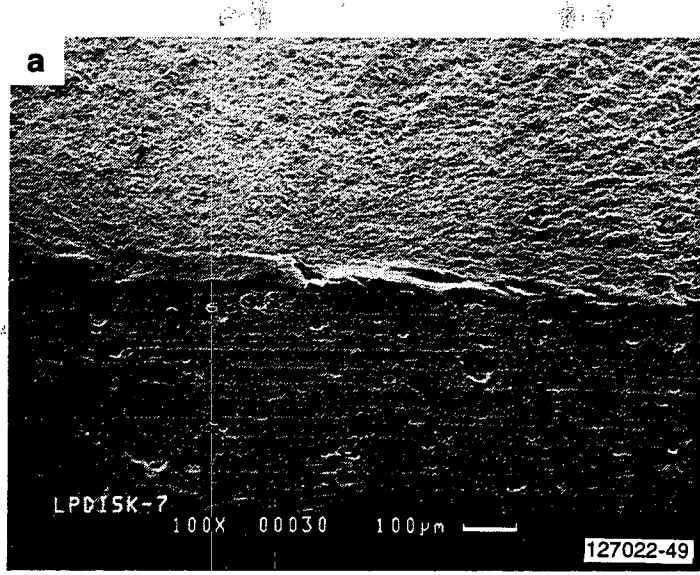
GB11591-453

Figure 4-53. Spin Disk Stress Rupture Failure From Internal Volume Flow At 2200F.



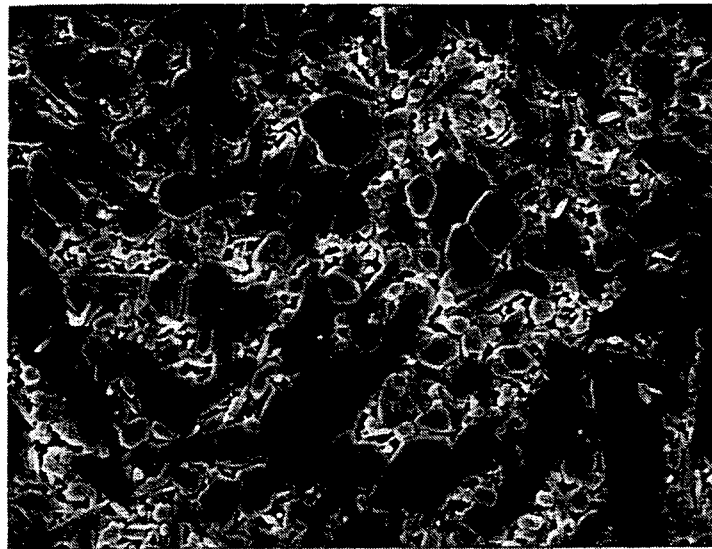
GB11591-454

Figure 4-54. Possible Crack Generated During 50 Hours Spin Disk Stress Rupture Testing At 75,000 rpm/2200F; Fracture Initiated on Speed Increase To 84,500 rpm. (a),(b) Surface Views; (c),(d) Edge On Views.

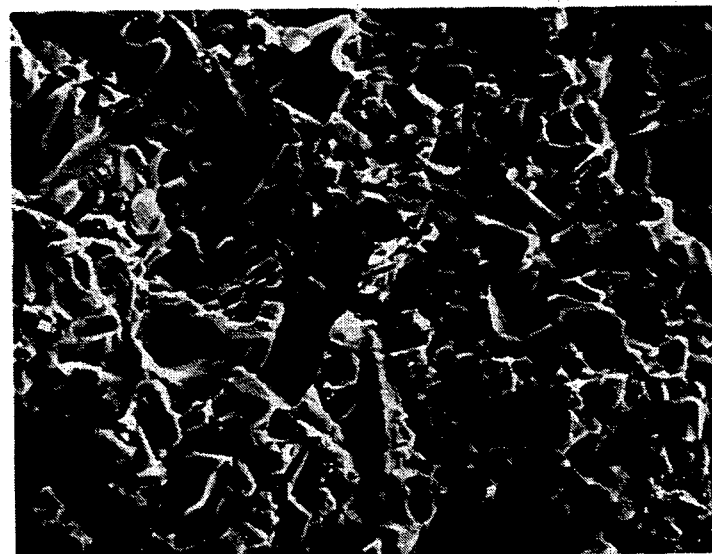


GB11591-455

Figure 4-55. Fracture Origin and Possible Crack Generated During Initial Spin Disk Stress Rupture Testing At 71,000 rpm/100 hrs Plus 75,000 rpm/10 hours. Disk Burst Occurred At 82,000 rpm.



125578-2
3 μm



125578-2
3 μm
GB11591-456

Figure 4-56. (a) SEM Photomicrograph Of Polished And Etched Surface Shows Acicular Grains Enveloping Pockets Of Smaller Equiaxed Grains; (b) SEM Of Room-Temperature Fracture Surface Showing Acicular Grains.



Figure 4-57. TEM Photomicrograph Of NT154 Microstructure, Showing Yttrium-Rich Triple-Junction Crystalline Phases (Arrows).

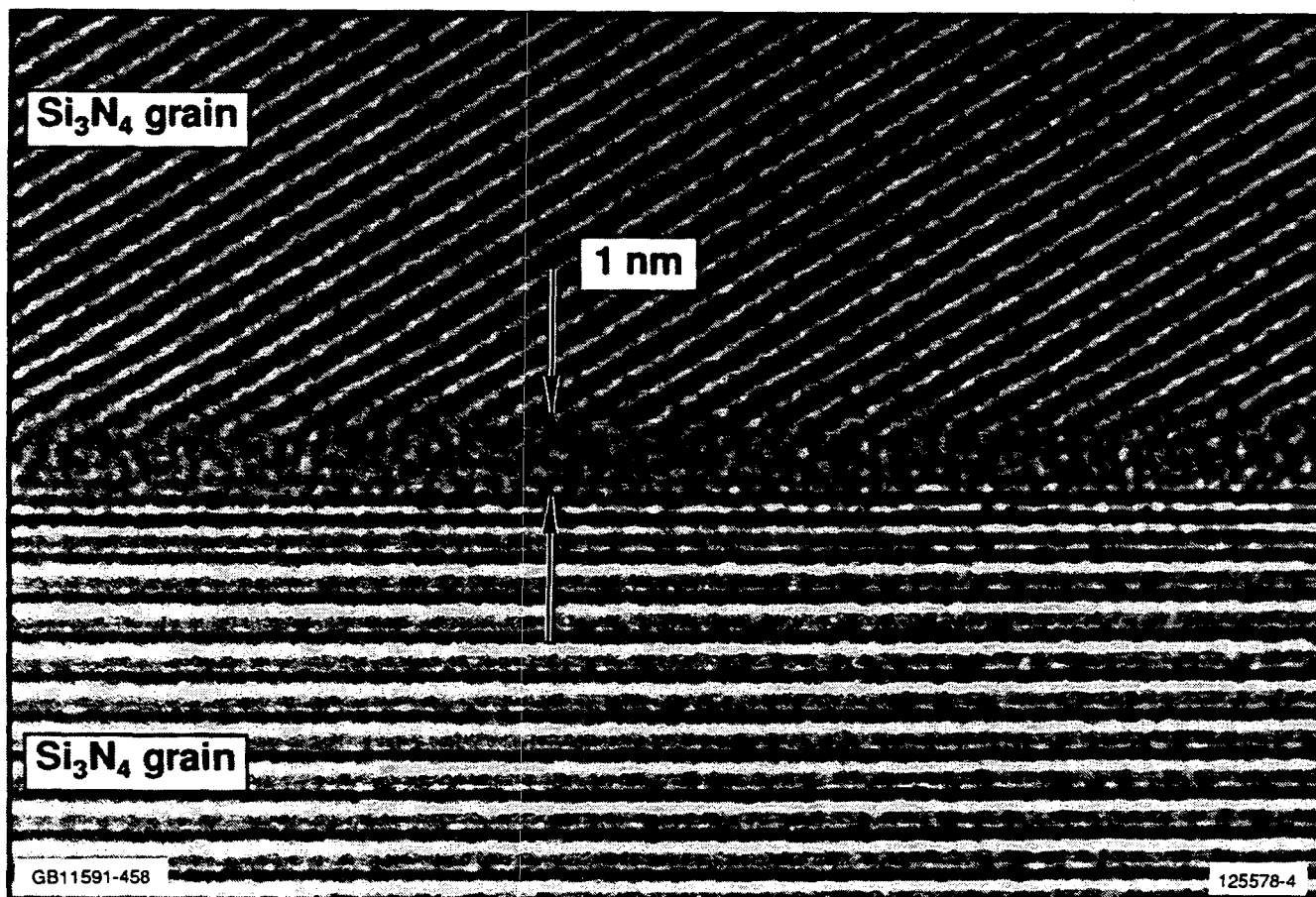


Figure 4-58. TEM Photomicrograph Of Amorphous Phase (Between Arrows) Separating Two Si_3N_4 Grains.

4.4.2 Phase Changes in Creep

Table 4-7 lists the results from X-ray analyses of four specimens tested at 1260C, 1315C, 1371C, and 1400C. The analyses were conducted on the gage sections which experienced creep, and on sections from the buttonhead, which were relatively cool during the test and therefore represented the as-received material. The results showed that the as-received material contained a small amount (6 to 10 percent) of residual α - Si_3N_4 , as determined by means of XRD (ref. 4-9). During creep at 1260C, the residual α - Si_3N_4 content remained the same as in the as-received material. At 1315C, the content changed slightly, and it changed significantly at 1371C and above. At 1371C, the residual content of α - Si_3N_4 was only 0.5 percent; at 1400C, it was not detectable. On the other hand, the results could not confirm or deny any significant changes in the quantities of crystalline triple-junction phases after creep testing at even the highest temperature. As a final point, it is believed that the results at 1260C would also hold true for temperatures below 1260C.

TABLE 4-7. RESULTS OF X-RAY ANALYSIS ON THE RATIO OF α/β NT154 PHASES

Specimen ID No.	Temperature, C	Stress/Time in Creep	Ratio of α/β NT154	
			(Buttonhead)	(Gage)
2-68	1400	100 MPa/411 hr	0.064	0.000
3-50	1371	145 MPa/443 hr	0.074	0.005
1-15	1315	225 MPa/675 hr	0.096	0.068
2-145	1260	285 MPa/379 hr	0.068	0.074

4.4.3 Creep Cavitation

A significant observation was the presence of lenticular cavities on two-grain junctions perpendicular to the tensile axis in specimens tested at all temperatures. SEM micrographs of typical grain facets with two-grain junction cavities in specimens tested at four temperatures are shown in Figures 4-59(a)-(d). Even in specimens tested at 1149C, very small cavities [on the order of only 0.02 μm in size; see Figure 4-59(a)] could be observed after 500 hours of testing. While the cavity size was found to increase with increasing temperature and time, the density of these lenticular cavities was much higher in the lower temperature range (1149C to 1315C). This was evident even with TEM, which provided much less area for observation. At 1400C, the density of the two-grain junction cavities was the lowest, although the sizes were the largest [Figure 4-59(d)].

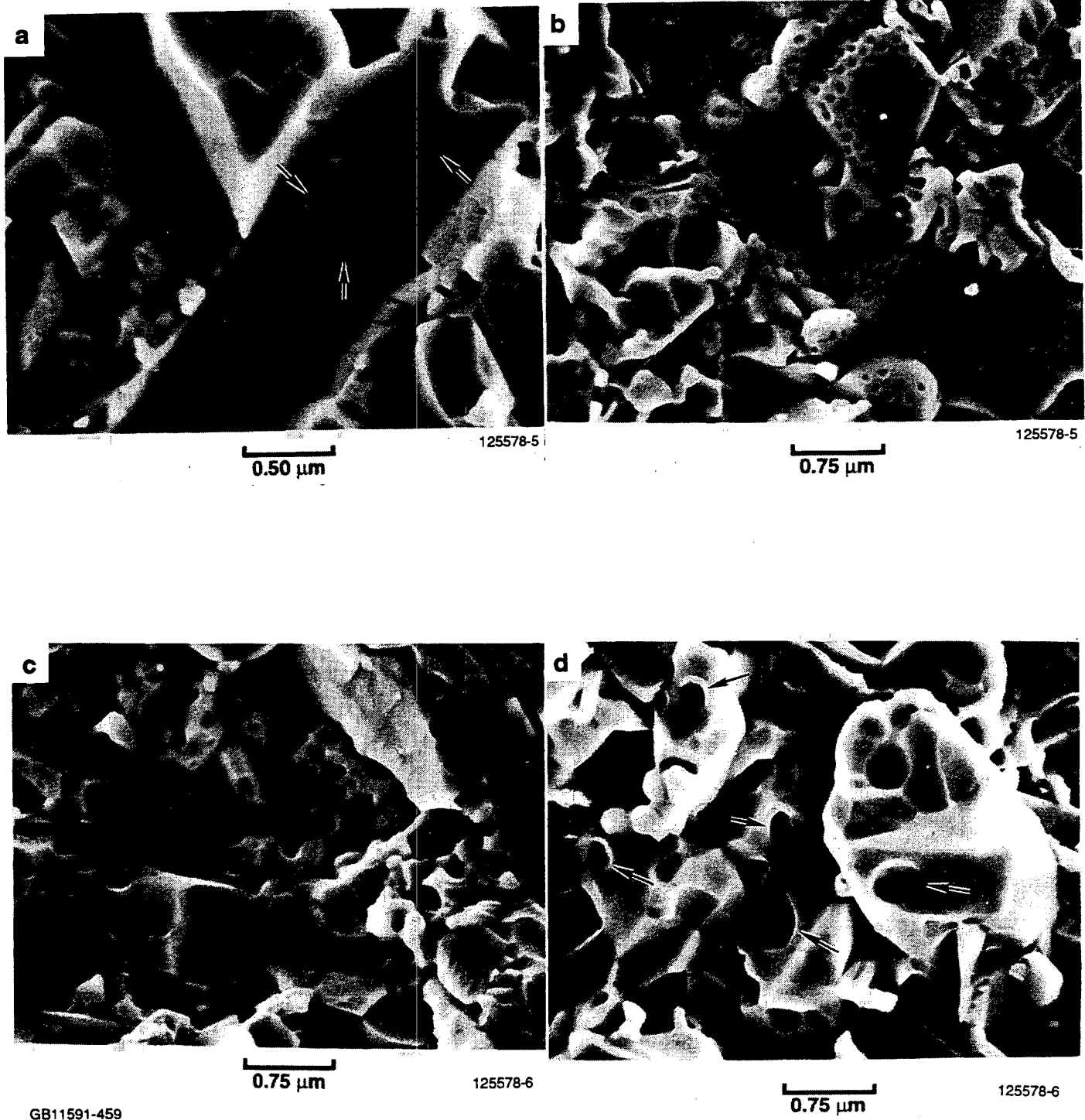
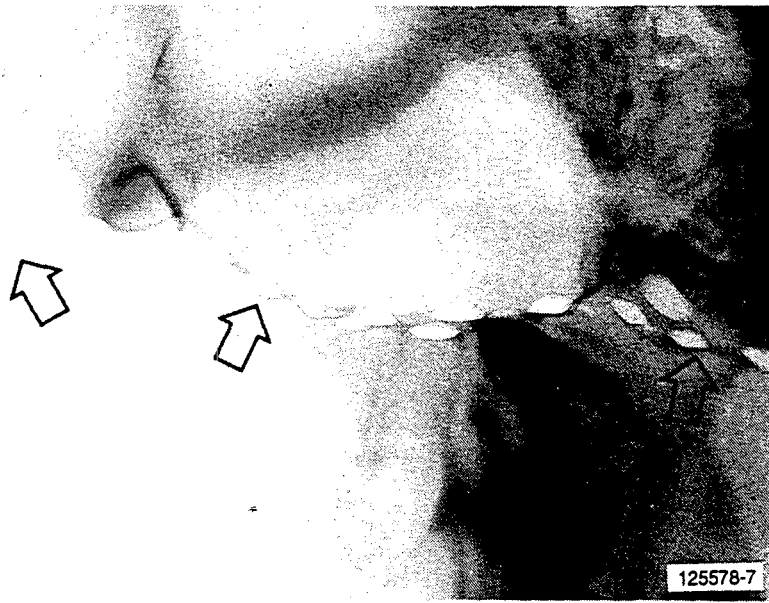


Figure 4-59. SEM Photomicrograph Of Two-Grain Junction Cavities In Specimens Tested At (a) 1422K/425 MPa/509 hrs; (b) 1477K/337 MPa/593 hrs; (c) 1589K/233 MPa/297 hrs; (d) 1673K/100 MPa/462 hrs.

As observed by other investigators (ref. 4-4, 4-5, 4-10), TEM examination showed that the two-grain junction cavities penetrated into the silicon nitride grains. Figure 4-60 shows the high-density cavitation of this type at 1204C. At temperatures above 1533K, these cavities were clearly faceted, but not always in both grains. Even with SEM, faceting could be identified but only in specimens tested at the higher temperatures [Figure 4-59(d)], because of the larger size of the cavities. TEM analysis showed that the bottom facets within the silicon nitride grains had a distinct orientation, parallel to {1120} type Si_3N_4 planes, as illustrated in Figure 4-61. No evidence of full-grain-boundary faceted cavitation, as observed in earlier versions of silicon nitrides (ref. 4-11), where the cavity is contained exclusively within the vitreous grain boundary phase, was found in the present study.

Using SEM, it was difficult to determine the actual extent of triple-junction cavitation on the secondary fractures produced for the purpose of observation of two-grain junction cavities. This was because of the difficulty in distinguishing between the true triple-junction cavities and the voids left by crystalline phases pulling off during fracture. It was possible, however, to image and identify triple-junction cavities with TEM, which provided an assessment of the triple-junction cavity sizes relative to those of the two-grain junction cavities. The triple-junction cavities seemed to be concentrated in areas or pockets where smaller grains predominated. Both the size and the number of triple-junction cavities increased with an increase in temperature. The relative size of triple-junction cavities compared to the two-grain junction cavities could be noted, and the ratio of their sizes seemed to increase from 1.0 or 1.5 at 1204C to about 10 at 1400C. Figures 4-62(a), (b), and (c) show the triple-junction cavitation identified by TEM at temperatures of 1204C, 1315C, and 1400C, respectively. Note the relative sizes of the two types of cavitation in these photographs, and also the increase in size of the triple-junction cavity with increased temperature. It should be mentioned that although cavities were observed at triple points at lower temperatures (e.g., at 1204C), the frequency was very low compared to those of the two-grain junction type, although the sizes were the same. Yet, it is worth noting the cavities could form even at the lower temperatures.

A quantitative assessment (frequency) of the triple-junction cavitation could not be undertaken with TEM because of the small area available for observation. Hence, a comprehensive SEM examination using polished surfaces of longitudinal sections was undertaken, to obtain a better assessment of the propensity and the extent of triple-junction cavitation as a function of temperature. The results were quite revealing and showed that triple-junction cavitation occurs extensively at 1400C and 1371C. It was less extensive at 1315C, and almost nonexistent at 1204C. Figures 4-63(a), (b), and (c) show the extensive triple-junction cavitation at 1400C compared to that at 1315C and 1204C.



GB11591-460

200 nm

Figure 4-60. TEM Photomicrograph Of Two-Grain Junction Cavitation In A Specimen Tested At 1477K And 315 MPa. Note Lenticular Shape(s) And High Density.

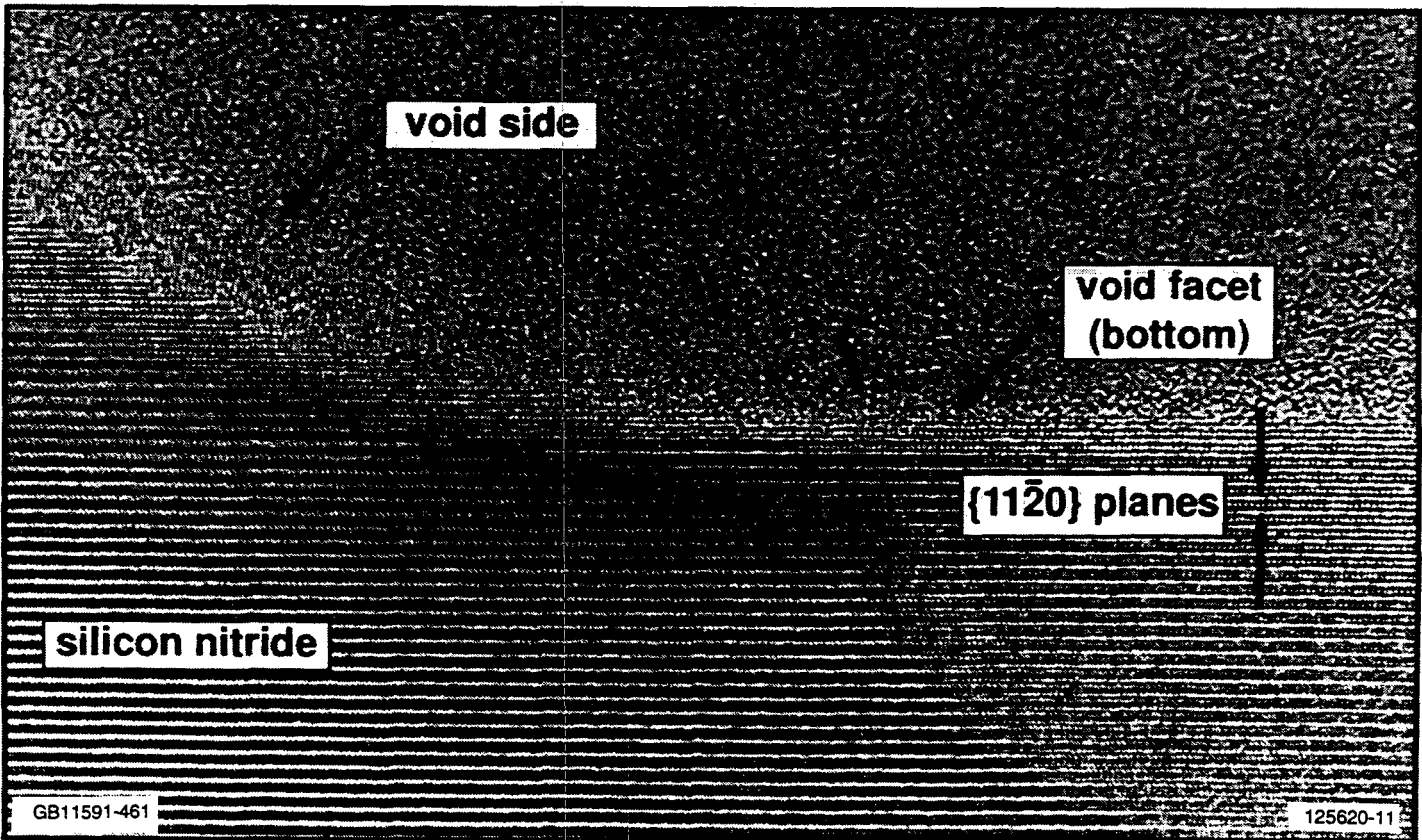
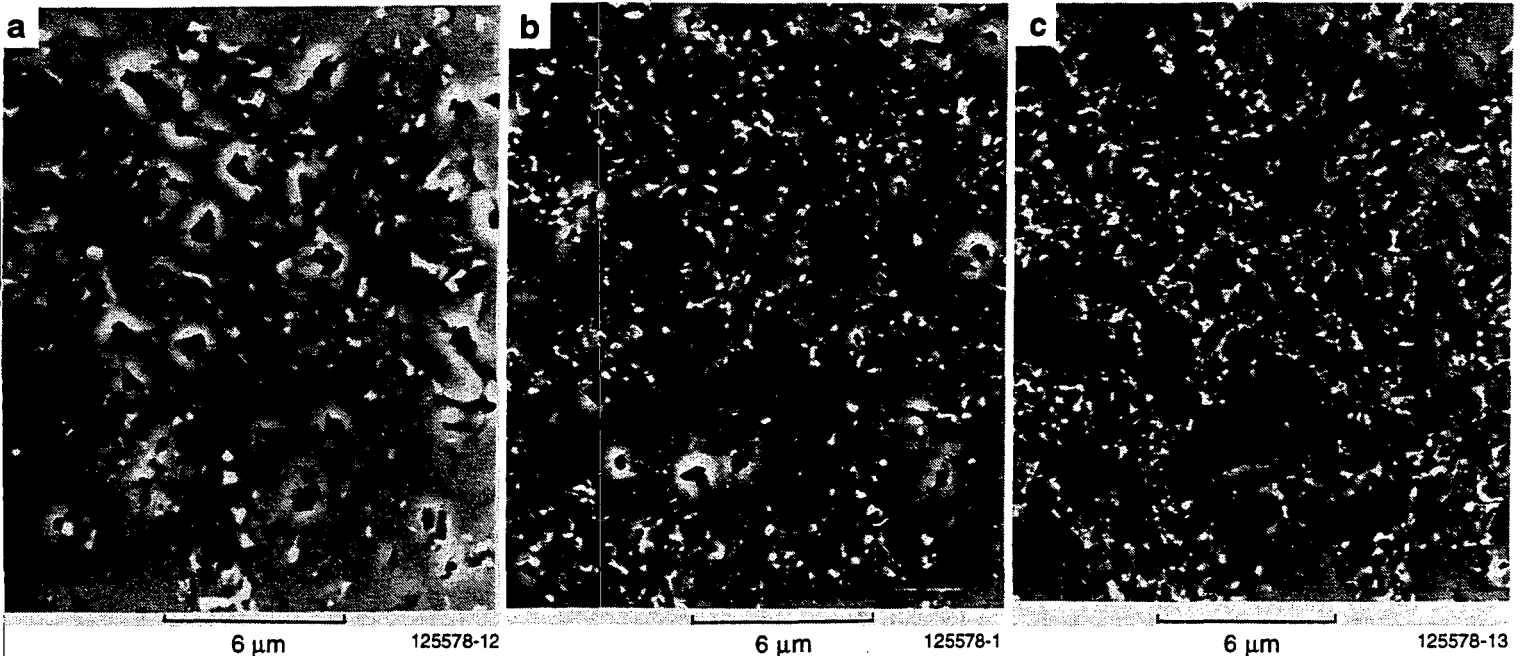


Figure 4-61. TEM Photomicrograph Showing An Enlarged View Of A Facet Of A Two-Grain Junction Cavity In A Specimen Tested At 1533K And 285 MPa.



Figure 4-62. TEM Photomicrograph Of Triple-Junction Cavitation(s) In Specimens Tested At (a) 1477K; (b) 1589K; And (c) 1673K. Note Size Of Triple-Junction Cavities (C₃) Relative To The Size Of The Two-Grain Junction Cavities (C₂).



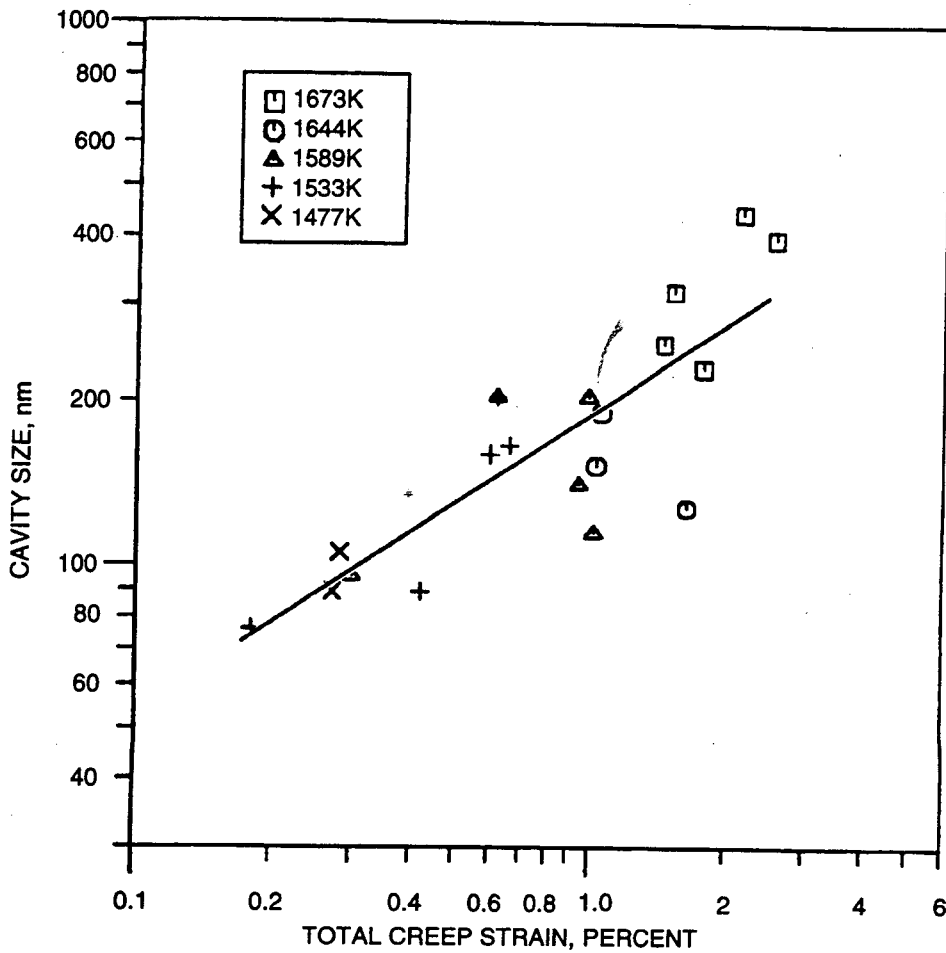
GB11591-463

Figure 4-63. Representative SEM Photomicrographs Of Polished Surfaces Of Longitudinal Sections Showing Triple-Junction Cavitation: (a) Extensive At 1673K; (b) Less Extensive At 1589K; And (c) Least Extensive At 1477K.

4.4.4 Correlation Of Cavitation With Creep

An estimate of the triple-junction cavitation was conducted on one of the specimens tested at 1400C. Note that the triple-junction cavitation was most prominent at this temperature. The specimen had accumulated about 2.5 percent strain at fracture. The polished surface was examined with SEM for representative areas and an image analysis was performed. An area fraction of 5.5 percent was obtained for triple-junction cavities, which was about twice the value of accumulated linear creep strain in the specimen. This observation is consistent with that of Luecke, et. al. (ref. 4-7), and shows that in NT154 triple-junction cavitation can account for most of the creep strain in the high-temperature range.

A more detailed study of the two-grain junction cavitation was conducted in NT154 material by means of SEM. The study concerned the growth rate of the cavities, rather than their nucleation rate. Each specimen that was selected for observation was refractured in the gage section, perpendicular to the specimen axis. The whole fractured surface was then scanned in the SEM for a period of about two hours. Representative areas showing the largest-sized cavities were documented, and an average value for the cavity size was computed. The average cavity sizes thus determined are plotted in Figures 4-64 and 4-65 against total accumulated creep strain and secondary creep rate ($\dot{\epsilon}_s$), respectively.



GC11591-464A

Figure 4-64. Two-Grain Junction Cavity Size Increases With Increase In Creep Strain.

Although this method is subject to error, and is restricted to two-grain junction cavities only, it provides an approximate relationship that exists between cavity size and the two variables. Plotting of Figure 4-64 was straightforward; however, in arriving at Figure 4-65, an equational form for cavity growth had to be assumed, since the specimens failed at different times in the secondary regime. The following equation was used and all data were plotted normalized to 100 hours:

$$d(\text{Cavity Size})/dt = A'(\dot{\epsilon}_s)^u(t)^{-w} \quad [4.4-2]$$

or:
$$\text{Cavity Size} = A''(\dot{\epsilon}_s)^u(t)^{[1-w]} \quad [4.4-3]$$

The time dependence in Equation [4.4-3] is similar to that proposed by Page and Chan (ref. 4-12). Figure 4-64 shows that on a log-log scale the cavity size is approximately a linear function of accumulated creep strain with a slope of 0.55. Given the scatter in the data, at 95 percent confidence, the slope can range from 0.36 to

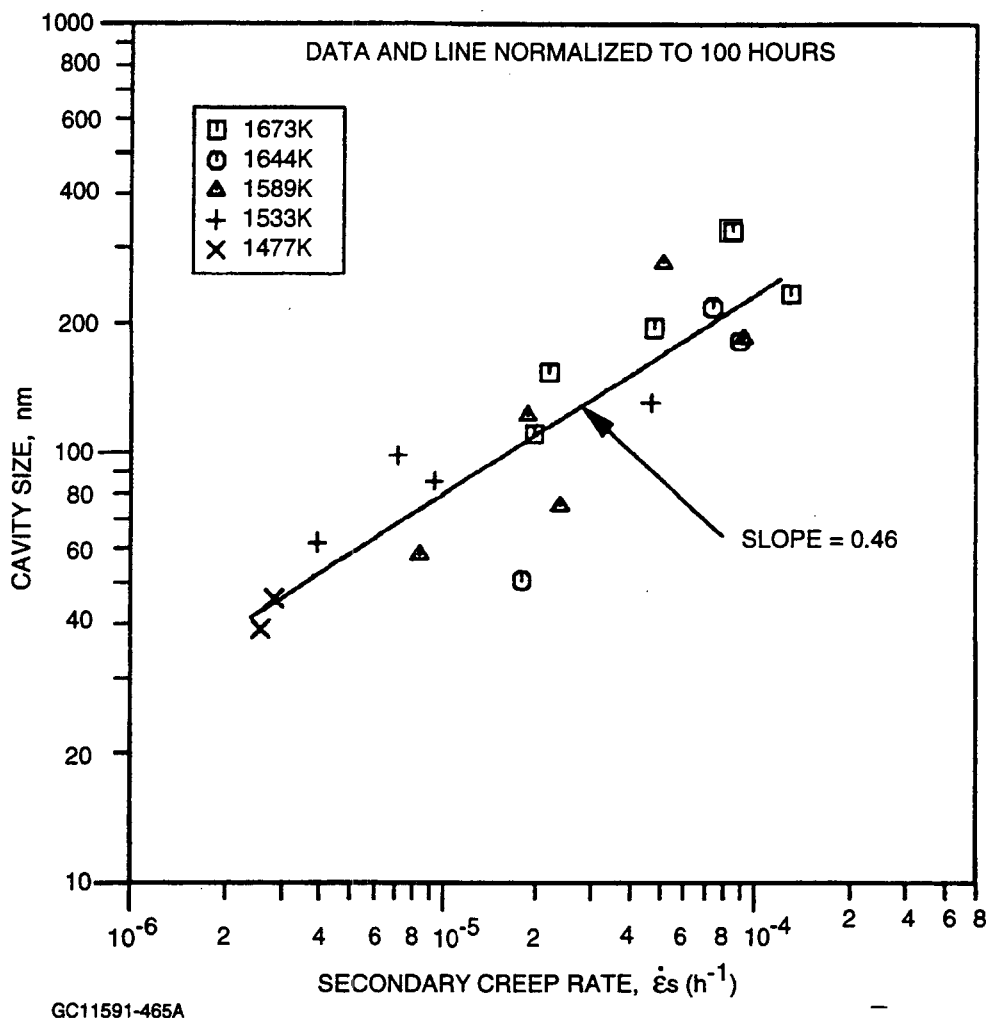


Figure 4-65. Two-Grain Junction Cavity Size Increases With Increase In Secondary Creep Rate.

0.74. The cavity size also plots approximately linearly against secondary creep rate on a log-log scale with a slope, u , of 0.46, and a value for time exponent, w , of 0.54.

The interesting point to note here is that the relationship between cavity size and strain or strain rate is independent of temperature. This observation is consistent with that of Luecke, et. al. (ref. 4-7), in which the relationship between the volume fraction of all cavities, at two- and three-grain junctions together, with strain was found to be independent of temperature. The absolute value of the slope in that plot would be 1.0 on a log-log scale. If the volume fraction is taken approximately as a cubic function of cavity size and if the rate of growth of the two-grain junction cavities is assumed to be the same as that of the three-grain junction type (since both are controlled by diffusion), then a slope near 0.33 would be expected in Figure 4-64. However, in view of the uncertainties involved in the SEM analysis and also the assumptions involved in the above comparison, the slope of 0.46 in Figure 4-64 could be considered as being consistent with the conclusions of Luecke, et. al. (ref. 4-7).

In summary, observations from the present program, taken together with those in the literature, seem to suggest that cavitation is part of the net creep process, and could account for most of the creep strain.

4.4.5 Microstructure Analysis Of Oxidized Specimens

As-received and exposed specimens were examined with the scanning transmission electron microscope (STEM) and by X-ray diffraction (XRD). The as-received material was fine grained, with an average grain size of approximately 1 μm . Volume fraction of the grain boundary phase was about five percent. Grain boundary pockets were crystalline and consisted of apatite and $\text{Y}_2\text{Si}_2\text{O}_7$ phases. The N-apatite phase was identified with XRD; however, with the energy dispersive system (EDX), only Oxygen (O) and no Nitrogen (N) was noted in virtually all grain boundary pockets.

Interior microstructure of oxidized samples LPBT60 (1204C for 10 hours) and LPBT102 (1315C for 360 hours) remained essentially unchanged. There did not appear to be an increase in the grain size or the volume fraction of the grain boundary phase at the locations examined. Unfortunately, attempts to prepare samples in the 2- to 10- μm thickness oxidized surface layer, which is of primary interest, were unsuccessful.

XRD analysis of the surface of the oxidized samples showed that, in addition to the alpha-yttrium disilicate and apatite phases, cristobalite had formed. The X-ray diffraction pattern of the surface of sample LPBT102 indicated that a strong peak for beta-yttrium disilicate was present. -

REFERENCES -- SECTION 4.0

- (4-1) (Anon.), ORNL Ceramic Technology Newsletter No. 23, Oak Ridge National Laboratory, Oak Ridge, TN, April-June, 1989.
- (4-2) (Anon.), "Fractography And Characterization Of Fracture Origins In Advanced Structural Ceramics," Military Handbook 790 (MIL-HDBK-790), U.S. Dept. of Defense, U.S. Army Research Laboratory, Materials Directorate, AMSRL-MA-S, Watertown, MA 02172-0001, 1 July 1992.
- (4-3) L.J. Lindberg, "Cyclic Oxidation of Advanced Silicon Nitrides," Proceedings of the Annual Automotive Technology Development Contractors Coordination Meeting October 1990, Dearborn, MI, Published By Society of Automotive Engineers, Warrendale, PA, 1991.

- (4-4) M.K. Ferber and M.G. Jenkins, "Evaluation of the Strength and Creep-Fatigue Behavior of Hot Isostatically Pressed Silicon Nitride", *J. Am. Ceram. Soc.*, **75** [9], 453-2462 (1992).
- (4-5) S.M. Wiederhorn, B.J. Hockey, D.C. Cranmer, and R. Yeckley, "Transient Creep Behavior of Hot Isostatically Pressed Silicon Nitride", *J. Mater. Sci.*, **28** [2], 445-453 (1993).
- (4-6) F.C. Monkman and N.J. Grant, "An Empirical Relationship between Rupture Life and Minimum Creep Rate in Creep-Rupture Tests", *Proc. Am. Soc. Test. Mater.*, **56**, 593-620 (1956).
- (4-7) W. Luecke, S.M. Wiederhorn, B.J. Hockey, and G.G. Long, "Cavity Evolution During Tensile Creep of Si_3N_4 ", pp. 467-472 in Silicon Nitride Ceramics - Scientific and Technological Advances, Proceedings of the Material Research Society Symposium, Boston, MA, Nov-Dec 1992, **287**, Edited by I-W Chen et al., Materials Research Society, Pittsburgh, PA, 1993.
- (4-8) I.S. Raju and J.C. Newman, Jr., "Stress-Intensity Factors for Circumferential Surface Cracks in Pipes and Rods Under Tension and Bending", NASA Technical Memorandum TM-87594, NASA-Langley Research Center, Hampton, VA, August, 1985.
- (4-9) D.J. Devlin and K.E. Amin, "A Method for Quantitative Phase Analysis of Silicon Nitride by X-ray Diffraction", *Powder Diffr.*, **5** [3], 121-124 (1990).
- (4-10) R.L. Yeckley and K.N. Siebein, "High Temperature Cavitation of HIP Silicon Nitride", pp. 751-765, in Proceedings of the Third International Symposium on Ceramic Materials and Components for Engines, Edited by V.J. Tennery, 1988.
- (4-11) J.E. Marion, A.G. Evans, M.D. Drory, and D.R. Clarke, "High Temperature Failure Initiation in Liquid Phase Sintered Materials", *Acta Metall.*, **31** [10], 1445-1457 (1983).
- (4-12) R.A. Page and K.S. Chan, "Stochastic Aspects of Creep Cavitation in Ceramics", *Met. Trans.*, **18A** [11], 1843-1854 (1987).

5.0 LIFE PREDICTION METHODS AND VERIFICATION

5.1 Material Behavior Models

5.1.1 Aging

Aging effects were observed in earlier vintages of NT154 silicon nitride -- i.e., the mechanical properties were affected by static exposure to elevated temperatures. This was apparently a result of changes occurring in the grain boundary phase. However, the later-vintage NT154 specimens used in the present program were subjected to an additional heat treatment by Norton Advanced Ceramics that resulted in devitrification and stabilization of most of the amorphous phase. This was experimentally verified as reported in Section 4.3.1.2.2.5. Since no significant aging effects were observed for the NT154 material in this program, no modeling was necessary.

5.1.2 Mixed-Mode Fracture/Flaw Shear-Sensitivity

Mixed-mode fracture envelopes were used in this program to assess the sensitivity of flaws in NT154 to shear stresses. Two types of tests, diametral compression and notched tension-torsion, were conducted to determine the $K_I - K_{II}$ and the $K_I - K_{III}$ fracture envelopes, respectively. The test setup and test procedure have been described in Section 4.2.1 with further details given in Appendices II and III. The mixed-mode fracture envelope has been successfully described by the following empirical equation (for the case of mode I and II loading):

$$K_I/K_{IC} + (K_{II}/CK_{IC})^2 = 1 \quad [5-1]$$

where: C is an empirical constant, the ratio of the fracture toughness in pure mode II (or mode III) loading to that in pure mode I loading. Palaniswamy and Knauss (ref. 5-1) have shown that $C = 0.816$ gives a very good fit in their rigorous analysis based on the maximum energy release rate criterion for crack extension under combined mode I and mode II loading. For polycrystalline ceramics, experimental values of C have ranged from 1.0 to 2.0 (ref. 5-2, 5-3).

From the fracture envelope, an effective stress formulation can be derived for component risk integration:

$$\sigma_E = 1/2 [\sigma_N + (\sigma_N^2 + 4\sigma_\tau^2/C^2)^{1/2}] \quad [5-2]$$

The effective stress formulation assumes that the strength of a given material is governed by inherent flaw sensitivity to the combined normal and shear stresses. If the flaws are not shear-sensitive (i.e., $C = \infty$), the effective stress becomes identical to the normal stress.

5.1.2.1 Mode I - Mode II Fracture Envelope

Four sets of diametral compression tests were conducted under the conditions listed in Table 5-1.

TABLE 5-1. DIAMETRAL COMPRESSION DISK TEST CONDITIONS

Temperature, F	Crosshead Speed, inch/min	No. of Specimens
70	0.05	20
2200	0.05	8
2200	0.0005	8
2500	0.05	7

5.1.2.2 Room Temperature Behavior

The $K_I - K_{II}$ fracture envelope is shown in Figure 5-1. The measured K_{IC} of $4.79 \text{ MPa}\cdot\text{m}^{1/2}$ was very close to the average of the long-beam chevron-notched specimens at $5.0 \text{ MPa}\cdot\text{m}^{1/2}$. The best fit value of C for the data was 2.07. The data at higher temperatures showed similar trends, as given in Table 5-2.

The effect of crosshead speed (strain rate) at 2200F was minimal. It is interesting to note that the elevated-temperature K_{IC} values determined from the diametral compression tests were less than the room-temperature K_{IC} values, whereas the reverse was true with the long-beam tests. The values of C also showed a gradual decline as the temperature was raised. It is worthy of note, however, that all the elevated temperature tests were conducted with a limited number of specimens, and the trends noted earlier could easily be due to data scatter.

5.1.2.3 Mode I - Mode III Fracture Envelope

The Mode I - Mode III tests were conducted with circumferentially notched and precracked specimens tested under tension-torsion loading. Only room-temperature tests were performed. The test results are shown in Figure 5-2.

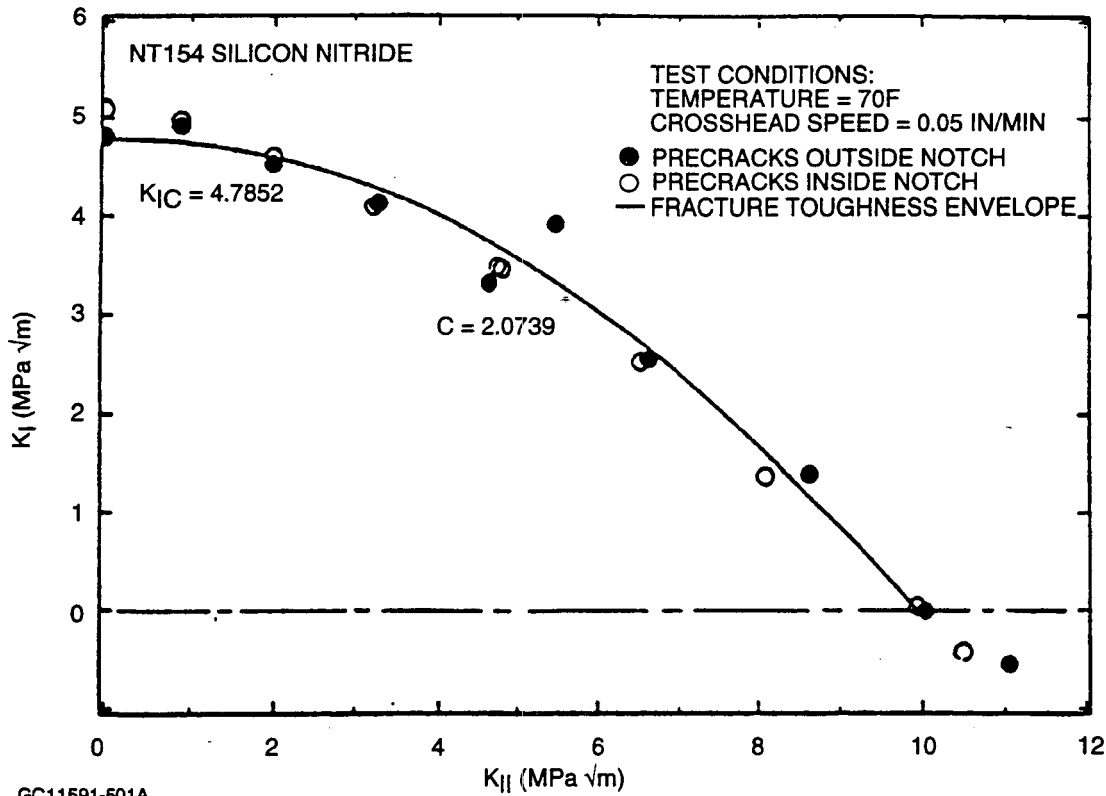
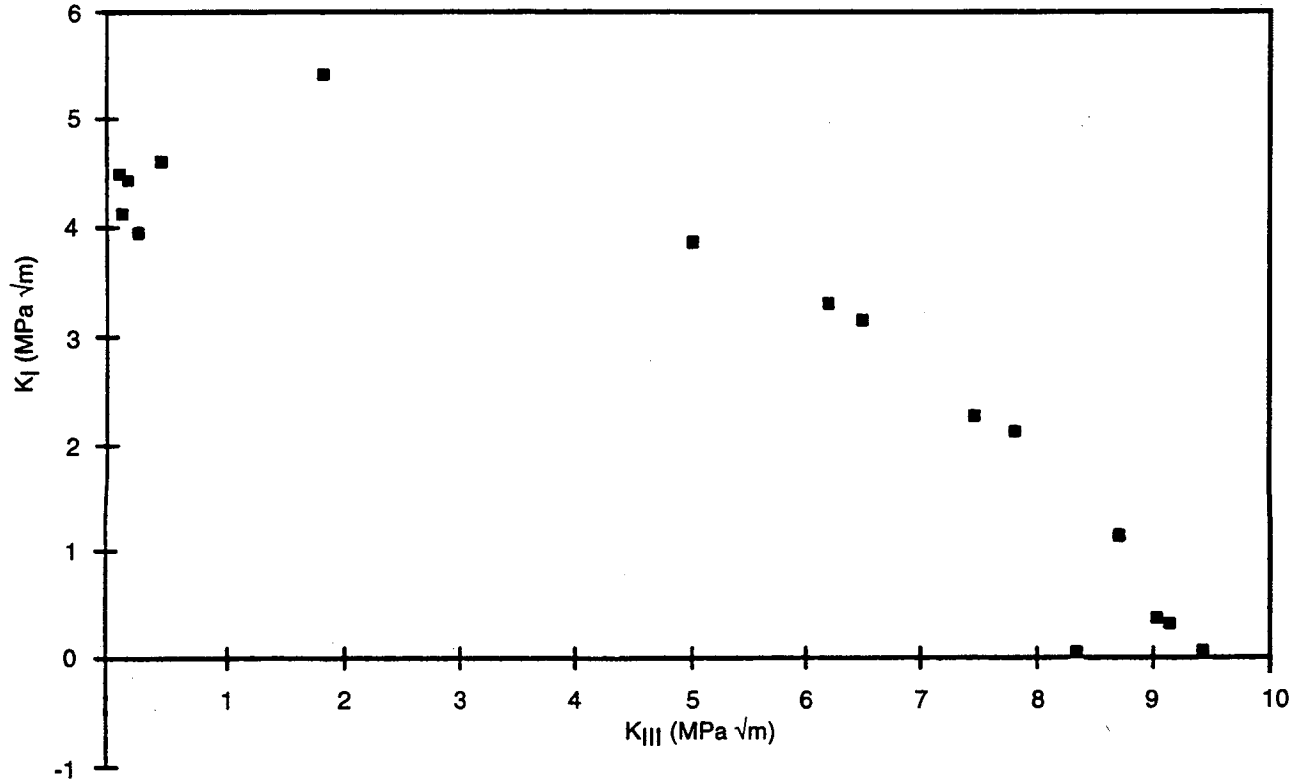


Figure 5-1. Modes I And II Stress Intensity Factors For Mixed-Mode Fracture Of Silicon Nitride Disks In Diametral Compression Tests. $C = 2.0739$. (Data From D. Shetty, U. Of Utah)

TABLE 5-2. LONG-BEAM K_{IC} TEST DATA

Temperature, F	Crosshead Speed, inch/min	K_{IC}	Long-Beam K_{IC}^*	C
70F	0.05	4.7	5.0	2.07
2200F	0.05	4.43	6.14	1.97
2200F	0.0005	4.65	6.14	1.78
2500F	0.05	4.3	5.79	1.68

* All the long-beam K_{IC} tests were carried out at a crosshead speed of 0.0005 inch/min.



GC11591-502A

Figure 5-2. Modes I And II Stress Intensity Factors/Fracture Envelopes For Mixed-Mode Fracture Of Notched Bars Tested Under Tension-Torsion Loading. $C = 2.10$.

The average K_{IC} value from pure tension loading was $4.35 \text{ MPa}\cdot\text{m}^{1/2}$, slightly lower than the values from the diametral compression or the long-beam chevron-notch specimen tests. The best estimate of the value of C (2.1) is very close to the value (2.07) from the diametral compression tests.

5.1.2.4 Applicability Of Long-Crack Fracture Envelope To Inherent Flaws

Both diametral compression and notched tension-torsion tests were conducted with specimens having cracks that were "long" or "large" compared to inherent flaws in the material. Some considerations need to be kept in mind in applying these data to inherent flaws:

- (1) **Fracture Surface Roughness** - in long-crack specimens, fracture surface asperities tend to increase the apparent material toughness. This is especially true under pure shear loading and/or with compressive normal loads. Since inherent flaws are much smaller, the contribution of this roughness-induced closure would be proportionately reduced.
- (2) **Crack Development** - in long-crack specimens, the cracks are well developed and a fracture mechanics description of the crack tip stress field is valid. With the inherent flaws, the applicability of a fracture mechanics description of the flaw-tip stresses is less applicable, due to factors such as size, shape, and tip acuity.

5.1.3 **Oxidation**

Based on the results of this study, oxidation at temperatures below 1400C strengthens the surface of NT154, and also reduces the severity of machining-induced surface flaws. Consequently, oxidation (in the absence of corrosive salt deposits) is beneficial and will not adversely affect predicted component lives in the temperature range of interest for gas turbine applications.

5.1.3.1 **Effect Of Oxidation Exposure On NT154 Room Temperature Strength**

Post-exposure room temperature flexure strength of NT154 silicon nitride (from transverse-machined specimens) was modeled as a function of exposure time and temperature, using data with exposures less than or equal to 100 hours; i.e.,

$$\text{Average Flexure Strength} = 1690 - 0.614 * (T + 33.33 * \ln[t]) \leq 925 \text{ MPa} \quad [5-3]$$

where: T is the temperature in degrees C, and t is the time in hours. This time-adjusted temperature function adequately describes the data, as shown in Figure 4-39.

5.1.3.2 **Thickness Of Oxidation-Affected Layer**

The thickness of the oxidation-affected surface layer was modeled as a function of exposure time and temperature:

$$\text{Oxidized Layer Thickness } (\mu\text{m}) = \exp(7.024 - 9966 / [T + 273]) * 0.435 * (\ln[t] + 1.9) \geq 0.85 \mu\text{m} \quad [5-4]$$

where: T is in degrees C, and t is in hours. This model for growth of the oxidation-affected surface layer of NT154 specimens is illustrated in Figure 4-40.

5.1.4 Creep Behavior

Creep curves and creep regimes have been described in Section 4.3.1.2.2.2. The modeling of creep rates is described in the following sections.

5.1.4.1 Secondary Creep

5.1.4.1.1 Modeling Of Secondary Creep Rate

The change in stress dependence in $\dot{\epsilon}_s$ becomes evident when it is modeled using an activation energy approach. This approach (ref. 5-4, 5-5) involves use of the familiar equation given below:

$$\dot{\epsilon}_s = A(\sigma/E)^n e^{-(Q/RT)} \quad [5-5]$$

where: A is a constant and σ , E, n, Q, R, and T are, respectively, stress, elastic modulus, stress exponent, activation energy, universal gas constant, and absolute temperature. Assuming a single activation energy for the creep rate throughout the temperature regime, a "global" regression procedure was adopted, which maximized the confidence level in the estimates of the activation energy and the stress exponents. The equation chosen was as follows:

$$\ln(\dot{\epsilon}_s) = a_0 + a_1/T + a_2 \ln(\sigma/E) + a_3 \sqrt{(\ln(\sigma/E) - \tau)^2} \quad [5-6]$$

where: a_0 , a_1 , a_2 , and a_3 are constants estimated through a multi-linear regression procedure, and τ is an optimized constant. Note that Equation [5-6] represents two linear regions meeting at a value of $\ln(\sigma/E)$ equal to τ . When $\ln(\sigma/E) > \tau$, the power-law stress exponent, n, in Equation [5-5] is the sum of the coefficients, a_2 and a_3 ; otherwise, n would be equal to their difference. Combining the two regimes in one bilinear equation is justified, so long as the temperature dependence is due to only one mechanism, represented by a single value of activation energy. Note that $a_1 = -(Q/R)$. The use of bilinear function in Equation [5-6] is somewhat analogous to the use of the hyperbolic sine function, often recommended (ref. 5-6) for obtaining a single overall expression for creep rate models for metals.

The average line predicted by Equation [5-6] for $\dot{\epsilon}_s$ along with the temperature-modified creep rate values from each specimen are shown in Figure 5-3. The ordinate in this figure represents the natural log of the temperature-modified secondary creep rate, determined by dividing the actual value of the rate by $e^{-(Q/RT)}$. Table 5-3 provides the values for a_0 , a_1 , a_2 , a_3 , and τ for the model for $\dot{\epsilon}_s$.

TABLE 5-3. REGRESSION ESTIMATES FOR $\dot{\epsilon}_s$

Rate Parameter	a_0	a_1	a_2	a_3	τ
$\dot{\epsilon}_s$	115.0	1.179×10^5	7.130	2.904	-7.19

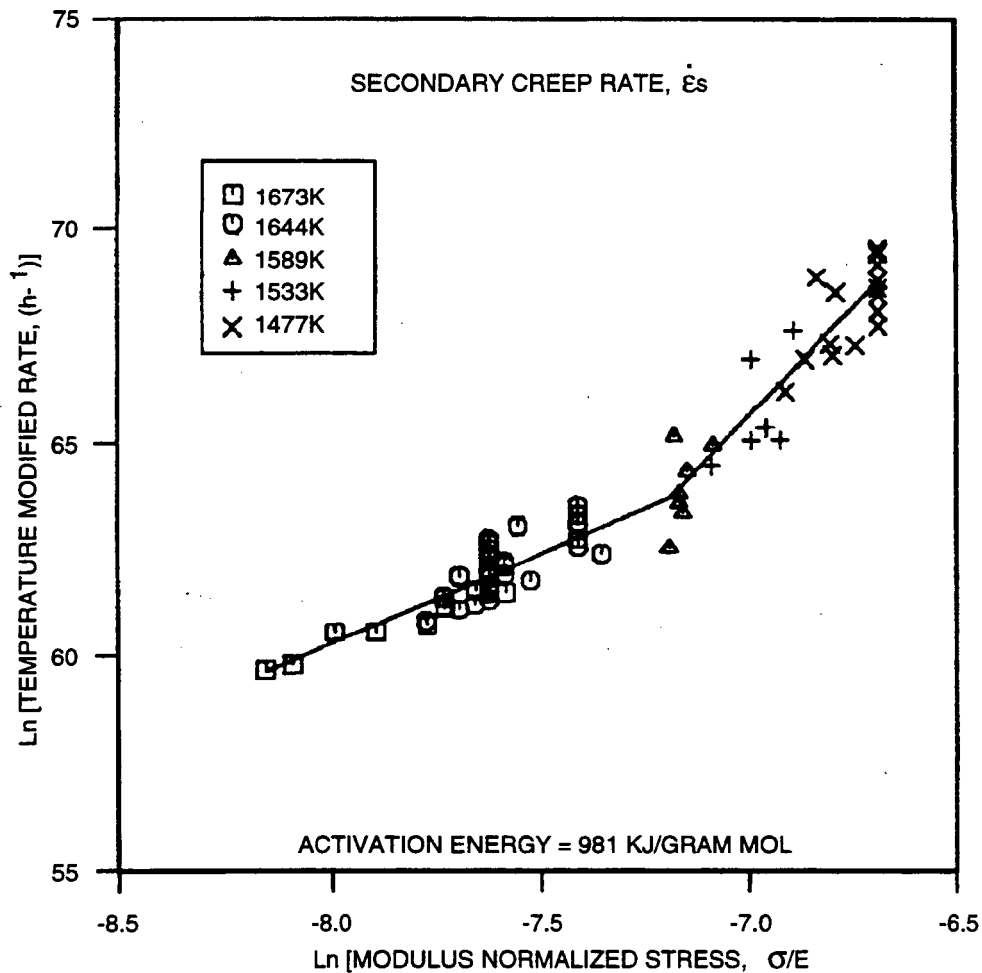
Figure 5-3 shows that there is a definite transition in the stress dependence of the secondary creep rate, demarcated at a temperature in the neighborhood of 1315C. The stress exponent in the lower-temperature regime is 10, whereas it is 4.2 in the higher-temperature regime. The figure also provides a better visual depiction of the scatter observed in this material for $\dot{\epsilon}_s$. The extent of scatter for the replicate tests at 1204C is about the same as the overall scatter found in the lower-temperature regime for the non-replicate tests. Similarly, the results of the tests at 145 MPa and 1371C show about the same scatter as in the non-replicate tests in the higher-temperature regime. Figure 5-4 shows the predicted lines from the above equation for the individual temperature sets along with the unmodified data.

Figure 5-5 shows the ratio of predicted to observed creep rates calculated from Equation [5-6]. This ratio is seen to fall within a factor of two for all specimens. Figures 5-3 and 5-5 show that the scatter is slightly larger in the low-temperature regime than in the high-temperature regime. The standard error of estimate (SEE) for $\ln(\dot{\epsilon}_s)$ for the whole regression was 0.61, and the maximum deviation of data points from the predicted average line is from -2.1 to +2.5 times SEE. The average of the tolerance intervals for all data for 99-percent exceedence or inclusion at the 95-percent confidence level for $\ln(\dot{\epsilon}_s)$ is $(\pm) 2.9$ times SEE.

The temperature and stress dependence of secondary creep rate, the temperature dependence of the Monkman-Grant lines, and the microstructural observations on cavitation and subcritical crack growth provide critical insights into the nature of the underlying mechanisms for creep and failure of NT154. In the following sections, more detailed discussions are provided on these important observations.

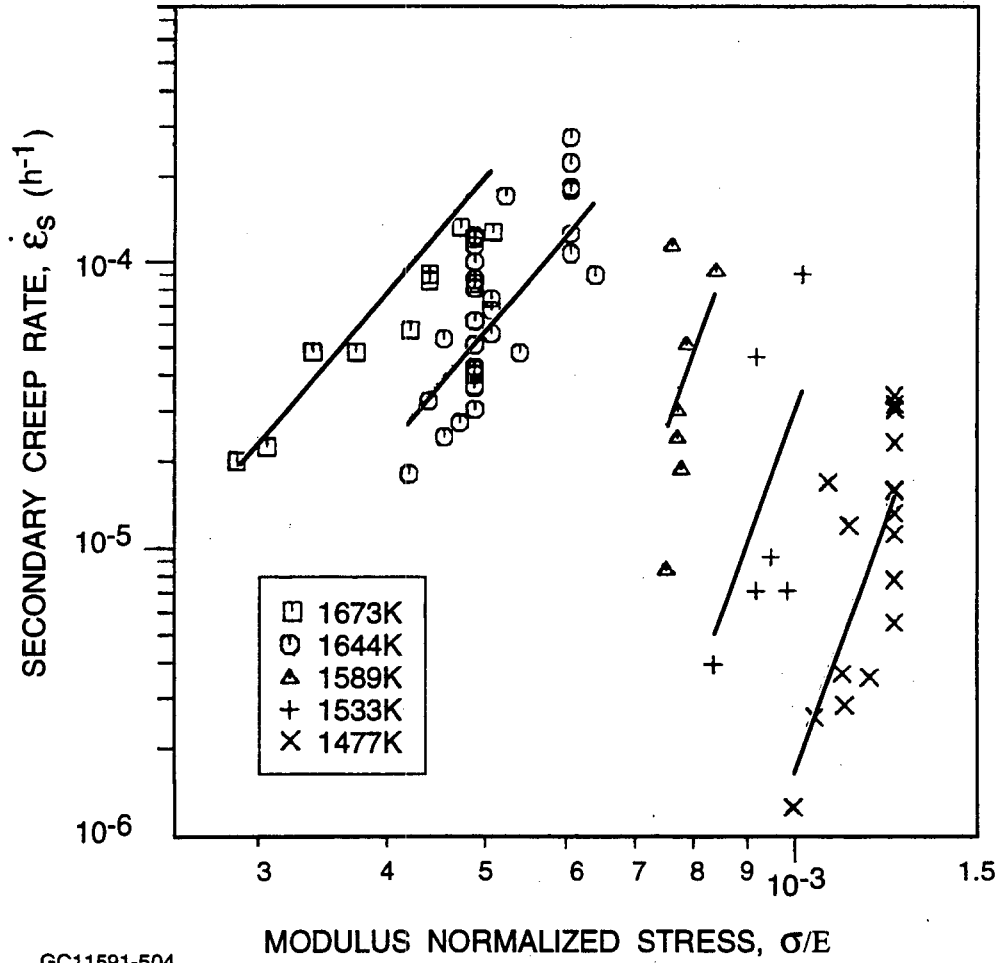
Any proposed mechanism for creep behavior of NT154 must consider the following key observations:

- (a) A single activation energy seems to be sufficient to account for the temperature dependence of the creep rate.
- (b) A decrease in the stress dependence of the minimum creep rate is observed near 1315C, as the temperature is increased.



GC11591-503

Figure 5-3. Temperature-Modified Secondary Creep Rate Plotted Against Modulus Normalized Stress.



GC11591-504

Figure 5-4. Secondary Creep Rate As A Function Of Modulus Normalized Stress.

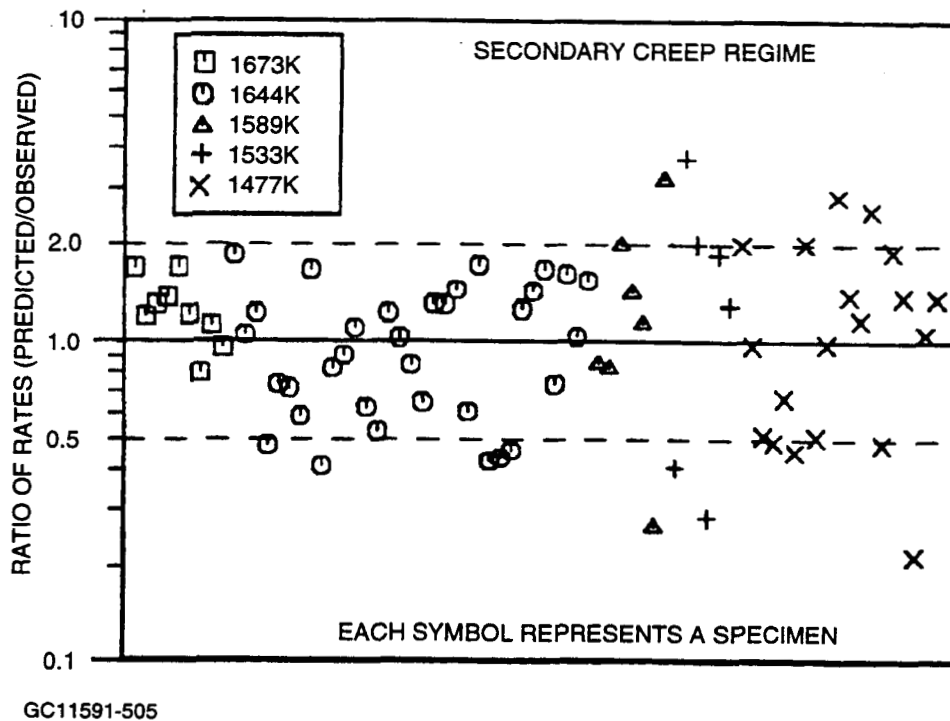


Figure 5-5. Scatter And Predictability Of Secondary Creep Rates.

- (c) Lenticular two-grain junction cavitation is observed in the whole temperature range of 1149C to 1400C, and is more numerous in the lower than in the higher temperature regime. Further, triple-junction cavitation is observed, which is most extensive in the higher temperature regime.

5.1.4.1.2 Temperature Dependence Of Secondary Creep Rate

Since cavitation penetrating into the silicon nitride grains depends on removal of silicon and nitrogen away from the cavity location, diffusional transport of matter through the amorphous phase has to be considered as a mechanism occurring across the whole temperature range. In view of the fact that triple-junction cavities could be observed at 1204C, although fewer in number but of the same size as the two-grain junction type, matter transport needs to be considered as a requirement for the growth of triple-junction cavities as well. In addition, if cavitation is responsible for creep strain, then the temperature dependence of the creep rate is due to this matter transport.

The present observations seem to support such a conclusion, which is the same as that reached by previous investigators who have studied creep behavior of advanced silicon nitrides (ref. 5-4, 5-5, 5-7) having an amorphous phase that is highly refractory. Although grain boundary sliding is often cited as a deformation mechanism in creep of silicon nitrides, it is not expected to be rate controlling in the present case. This is because, first, the amorphous phase is very thin in NT154. Second, an analysis by Lange (ref. 5-8), shows that sliding in the presence of an amorphous intergranular phase is faster than the rate of grain deformation required to accommodate sliding. In other words, the grain boundary sliding that occurs in NT154 at the temperatures tested can only be that which is necessary to preserve the compatibility and continuity of the polycrystalline aggregate (ref. 5-9).

An activation energy of 981 kJ/g.mol was obtained from regression analysis for secondary creep rate, which is close to the value of 930 kJ/g.mol reported by Ferber et. al. (ref. 5-10) on another batch of NT154 that underwent similar heat treatments, but much lower than the value of 1260 kJ/g.mol reported by Wiederhorn et. al. (ref. 5-5) for a version of NT154 which did not undergo the crystallizing heat treatment. The value for Q in this program is somewhat lower than the value of 1102 kJ/g.mol reported by Ferber and Jenkins for PY6 (6-percent yttria as sintering aid) silicon nitride material (ref. 5-4), but higher than the values reported by Arons and Tien (ref. 5-11) for NC132 (722 kJ/g.mol) which is a hot-pressed silicon nitride from Norton Advanced Ceramics, Worcester, MA containing MgO as the sintering aid, and by Bouarroudj et. al. (ref. 5-12) on a silicon nitride containing yttria and silica (720 kJ/g.mol). NT154 is considered to have an intergranular amorphous phase more refractory than that in NC132 or in the material used by Bouarroudj et. al. (ref. 5-12). Therefore, if diffusion of matter through the amorphous phase is rate controlling, then a higher value of activation energy than those found in the above-mentioned studies can be expected in NT154. It is important to note that the present data base includes many more specimens and test temperatures than any of the other above-mentioned studies.

The two sequential steps that have to occur for diffusion-assisted creep in silicon nitrides, whether as the main mechanism for creep or accommodative to cavitation, are: (i) solution - re-precipitation (ref. 5-13), and (ii) transport of matter through the amorphous phase (ref. 5-14). Of the two, the latter is likely to be the rate controlling mechanism in the present case. This follows from the observation by Wiederhorn, et. al. (ref. 5-5) that the estimated heat of solution of crystalline Si_3N_4 in amorphous phase is only 400 kJ/g.mol (ref. 5-15), whereas, the measured values of activation energy for viscosity of oxynitride glasses (ref. 5-16) can range up to 1000 kJ/g.mol. This conclusion is further supported by the results of a recent study by Ferber et. al. (ref. 5-10), on a new version of NT154 silicon nitride, designated as NT164, whose increased creep resistance is believed to be related to the lower thickness of the amorphous intergranular phase, resulting in lower flux of the diffusing species.

Our conclusion, therefore, is that the temperature dependence of the creep rate derives from the temperature dependence of the matter transport through the amorphous phase, which in turn would justify the assumption of a single activation energy in Equation [5-6].

5.1.4.1.3 Stress Dependence Of Secondary Creep Rate

The plot of secondary creep rate in Figure 5-3 shows a change in slope with stress, indicating a change in the stress-dependent part of the mechanism for creep. The slope is 4.2 in the higher temperature range, above 1315C, and 10.0 in the lower temperature range, below 1315C. These results are consistent with the findings of Ferber and Jenkins (ref. 5-4) on PY6 silicon nitride, in which an increase of stress exponent from 5.0 in the temperature range 1260C - 1371C to 16.1 at 1149C was noted.

The abruptness of the change in the stress dependence raises a question as to whether, in the temperature regime below 1315C, the low stress extrapolation of creep rate would follow the lower temperature part of the model, i.e., with the higher stress dependence. In other words, although all the data have been combined into a single model, which was justified because of the assumption of a single mechanism for temperature dependence (i.e., a single activation energy), the two regimes may need to be considered as distinctly separate, demarcated by temperature, from the point of view of creep rate prediction. Such a conclusion would follow if the change in stress dependence at the transition is brought about by a change in some microstructural or deformation characteristic resulting exclusively from a temperature change alone and independent of the time duration. If true, then, for prediction of creep rates in the lower temperature regime to stresses lower than which have been tested in the present case, the equation with the higher stress exponent would have to be used. Also, higher stress extrapolation in the higher temperature regime would follow a similar reasoning, but is not of interest since it would result in lives much less than ten hours. Tests of longer duration (2000 to 5000 hrs) at low stresses in the temperature regime 1260C to 1315C could provide insight into whether the two regimes need to be treated separately, demarcated by temperature alone.

The change in α - Si_3N_4 content observed in specimens tested at temperatures of 1371C and above may signify certain changes occurring in the amorphous phase. If the α phase is undergoing transformation to β , it has to dissolve through the amorphous phase to re-precipitate as β - Si_3N_4 crystals. This has the potential of increasing the amount of the glassy phase during creep, resulting in higher creep rates. Another possibility is an abrupt change in the thickness of the amorphous phase in this material in the neighborhood of 1315C as the temperature is increased. An increase in thickness of the intergranular phase with temperature has been reported in NC132 by Clarke (ref. 5-17) at a temperature above 1000C. It is probable that such a transition temperature could be higher for a more refractory amorphous phase like the one which exists in NT154. Even a small

increase in the thickness of the amorphous phase could contribute to a significant increase in the creep rate, since the flux of diffusing species would be changed dramatically through the larger cross section of the diffusion path. However, in the present case, another important consequence of an increased quantity of intergranular amorphous phase would be the increased propensity for triple-junction cavity nucleation (ref. 5-18, 5-19), which has been observed in the SEM and TEM evaluations of the present material. It is important to note that triple-junction cavitation can result in easier strain accommodation and lower compatibility requirements as well, in turn resulting in a lower stress dependence for creep rate at the higher temperatures compared to that at the lower temperatures.

This leaves then the explanation of the high stress dependence in the lower temperature regime as the key to understanding of the unique stress dependence of the creep behavior of NT154. It is not unreasonable to suppose that at the lower temperatures, two-grain junction cavitation alone accounts for most of the creep strain, since at 1204C the creep strains are only about one-tenth that at 1371C. If so, the high stress dependence may be due to the mechanism involved in nucleation of the lenticular cavities. Note that the two-grain junction cavities were more numerous in the lower temperature regime than in the higher temperature regime, although smaller in size. The nucleation rate of two-grain junction cavities may have a high stress dependence. This possibility cannot be ruled out in the present case, and it will be shown in section 5.1.4.2 that there is sufficient justification to warrant further examination of this hypothesis.

5.1.4.1.4 Proposed Creep Mechanism

Consistent with our findings, we propose that both two-grain junction cavitation and triple-junction cavitation are part of the net creep process, and are believed to account for the major part of the observed strain. The diffusional transport of matter which has to accompany cavitation, is solely responsible for the temperature dependence of the creep rate. Even for growth of triple-junction cavities, matter transport is believed to be a requirement. Support for this comes from (i) the observation of a small number of triple-junction cavities at 1204C, that are of the same size as that of two-grain junction type, and (ii) in constrained cavitation, which will be proposed for the strain-hardening part of the primary creep in section 5.1.4.2, there would be expected a limit to the contribution from physical pulling of grains towards growth of triple-junction cavities. The high stress dependence of the creep rate in the low-temperature regime is due to stress dependency of two-grain junction cavitation; the lower stress dependency at the higher temperatures is due to the contribution to creep from triple-junction cavitation.

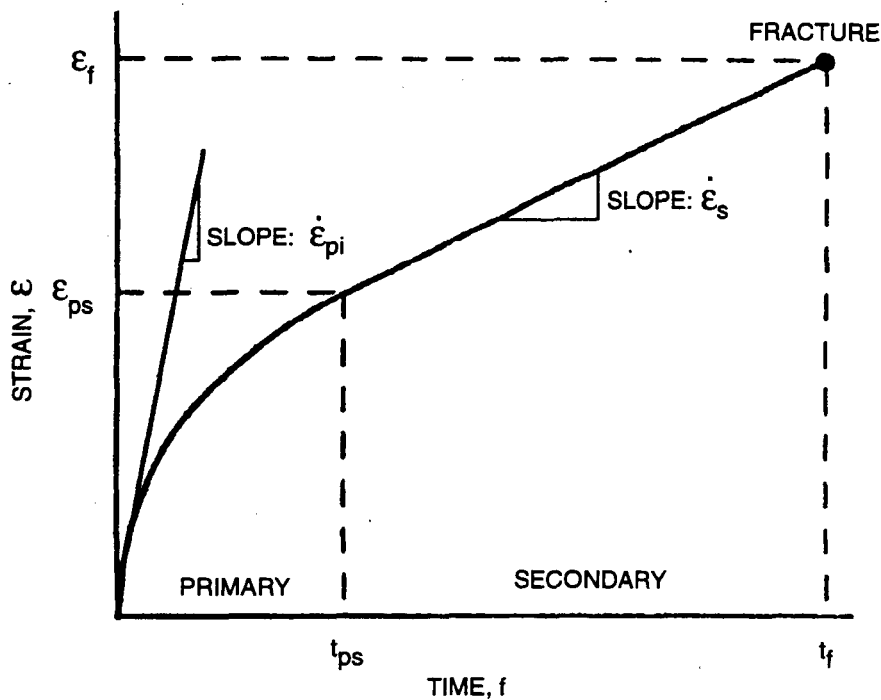
5.1.4.2 Primary Creep

5.1.4.2.1 Introduction

In the sections following, the primary creep rate behavior of NT154 is described by means of a comprehensive phenomenological model, employing an activation energy approach. In addition, the mechanisms that are likely to be responsible for the transient nature of the primary creep and for the unique stress dependence of the primary and minimum creep rates are discussed.

5.1.4.2.2 Creep Rate Equations

Advanced silicon nitrides having high creep strength typically show only two stages in creep: primary and secondary (ref. 5-4, 5-5). A typical curve depicting these two stages in a strain (ϵ) versus time (t) plot is shown in Figure 5-6. The primary creep begins at loading with a high initial creep rate, $\dot{\epsilon}_{pi}$. The creep rate, $\dot{\epsilon}_p$, in the primary regime continuously decreases until it reaches a constant or minimum value ($\dot{\epsilon}_s$) at the primary-to-secondary (P/S) transition time, t_{ps} , and the P/S transition strain, ϵ_{ps} . Secondary creep continues until fracture at time t_f .



GC11591-506

Figure 5-6. Schematic Of A Typical Creep Curve For A Material Showing Only Primary And Secondary Regimes.

Due to the transient and more complex nature of the primary and tertiary creep, secondary creep rates have been studied most extensively. The secondary creep rate is usually modeled through temperature- and stress-dependent terms, using an activation energy approach (ref. 5-4, 5-5), as shown in Equation [5-5] in section 5.1.4.1.1. This equation and variations of it can be found in general purpose finite element programs such as ANSYS (ref. 5-20). Also available in ANSYS are models for primary creep, as shown in Equation [5-7]:

$$\dot{\epsilon}_p = B \sigma^n \epsilon^H e^{-(Q/RT)} \quad [5-7]$$

where: B and H are constants. However, the primary creep models are not provided as coupled to the secondary creep models. A continuous creep rate model that couples the primary creep rate to the secondary creep rate at the P/S transition point, with a unique definition of the P/S transition point, is highly desirable.

The most notable previous attempt to model the entire creep curve is the Theta (θ) Projection Concept (ref. 5-21, 5-22), described by Equation [5-8]:

$$\dot{\epsilon} = \theta_1(1 - e^{-\theta_2 t}) + \theta_3(e^{\theta_4 t} - 1) \quad [5-8]$$

The basic premise of the θ Projection Concept is that normal creep curves can be envisaged as the sum of a decaying primary and an accelerating tertiary component. The terms θ_1 and θ_3 scale the primary and tertiary stages, respectively, while θ_2 and θ_4 are the respective rate parameters which define the rate at which the primary creep decays and the tertiary creep accelerates with time. The θ Projection Concept defines a minimum creep rate at a single point, and therefore does not incorporate an extended minimum or steady-state creep regime.

Since the advanced silicon nitrides do not exhibit tertiary creep, a modification of the θ Projection Equation was proposed recently by Evans, et. al. (ref. 5-23) for describing compression creep curves of a yttria-bearing silicon nitride. The modified equation involves a Taylor series expansion of the second term in Equation [5-8]. However, the modified equations seem to complicate the traditional interpretations of the creep behavior based on stress exponents and activation energies, which are so widely used in attempts to understand creep mechanisms of materials. An alternate approach to the θ Projection Concept, which was recently developed by Menon (ref. 5-24), is proposed in the next section. This method will be shown to have the ability to account for any gradual and systematic variation in stress and temperature dependencies of creep rate throughout the primary regime, from the initial high rate at loading to the transition to a constant or minimum value at the P/S transition time.

It is generally agreed (ref. 5-21, 5-22, 5-23) that the shape of creep curves in any regime is controlled by the physical mechanisms underlying that regime. However, when the understanding of the mechanisms are still under development, such as is the case for advanced silicon nitrides, a phenomenological or empirical approach with as much physical basis as can be incorporated into the model might prove to be an effective tool for analyzing creep behavior and for providing insight into the operative mechanisms. Such an approach is developed in the following sections.

5.1.4.2.3 Modeling Of Primary Creep

The creep rate modeling involves two steps, the first being derivation of rate parameters from modeling of empirical data and the second, modeling of the rate parameters using the activation energy approach.

5.1.4.2.3.1 Modeling Of Experimental Data

The first step involves modeling of experimental data from creep tests of each specimen (ref. 5-24). These data consist of a series of monotonically increasing strain (ϵ) versus time (t) data points at a specific stress (load) and temperature. Three forms of equations, which have been used in the past and which can be considered as having the capability to empirically express the strain hardening characteristic of the primary creep, were tried for fitting a curve to the creep strain (ϵ) versus time (t) data in the primary regime. They were logarithmic [$\epsilon = \beta \ln(\alpha t + 1)$], time fraction [$\epsilon = \beta(t)^{\alpha}$], and exponential [$\epsilon = \beta(1 - e^{-\alpha t})$]. The exponential form is the same as that used in the first term in the θ Projection Concept (Equation [5-8]). The logarithmic equation turned out to be the best form for fitting all the data. Accordingly, the primary regime is fitted with a logarithmic equation thus:

$$\text{Primary creep strain, } \epsilon_p = \beta \ln(\alpha t + 1) \quad 0 < t < t_{ps} \quad [5-9]$$

$$\text{Primary creep rate, } \dot{\epsilon}_p = \alpha\beta / (\alpha t + 1) \quad 0 < t < t_{ps} \quad [5-10]$$

where: α is a rate parameter which defines the curvature of the transient creep regime, and β is a scaling parameter. At $t=t_{ps}$, the primary creep rate, $\dot{\epsilon}_p$, and secondary creep rate, $\dot{\epsilon}_s$, are equal, thus providing a continuity condition, and an equation for the P/S transition time from Equation [5-10] as follows:

$$t_{ps} = ([\alpha\beta/\dot{\epsilon}_s] - 1) / \alpha \quad [5-11]$$

Also note that at $t=0$, the primary creep rate equals the product, $\alpha\beta$, which is the initial primary creep rate, $\dot{\epsilon}_{pi}$, at the onset of creep. Therefore, $\dot{\epsilon}_{pi} = \alpha\beta$. The strain in the secondary regime is given by the following equation:

$$\epsilon_s = \epsilon_{ps} + \epsilon_s(t-t_{ps}) \quad t > t_{ps} \quad [5-12]$$

The parameter α determines the rate of change of the primary creep rate with time, and will be shown to vary systematically with temperature and stress. It will also be shown in the next section that both ϵ_{pi} and α can also be modeled using an activation energy approach.

Shown in Figure 5-7 are the creep strain data and the predicted line from this part (Equations [5-9] through [5-12]) for a specimen tested at a temperature of 1260C and a stress of 285 MPa.

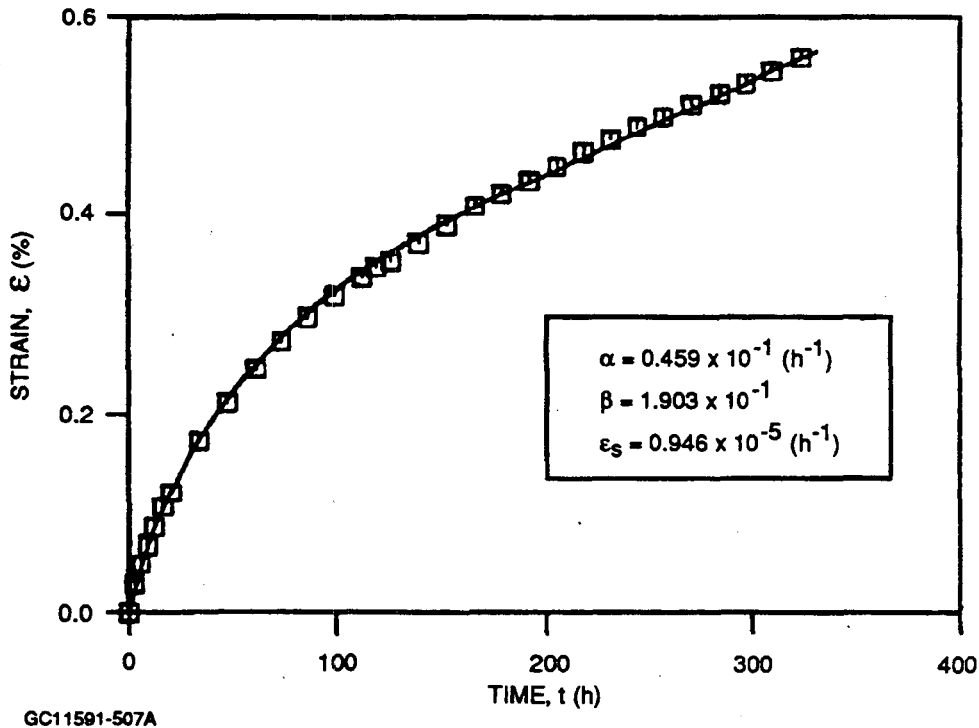


Figure 5-7. Creep Data For A NT154 Specimen Tested At 1533K And 285 MPa, With The Predicted Line From Equations [5-9] Through [5-12].

5.1.4.2.3.2 Modeling Of Rate Parameters

The rate parameters $\dot{\epsilon}_{pi}$ and α are modeled based on Equation [5-6] as follows (ref. 5-24):

$$\dot{\epsilon}_{pi}, \text{ or } \alpha = Ae^{-(Q/RT)}(\sigma/E)^n \quad [5-13]$$

As shown in section 5.1.4.1, the stress dependence of $\dot{\epsilon}_s$ was found to be bilinear when the temperature-modified creep rate is plotted against normalized stress on a log-log scale. This will be shown to be true also for $\dot{\epsilon}_{pi}$ and α . In other words, n assumes two different values, depending on the temperature regime in which the material is tested. We are assuming a constant activation energy in the whole temperature regime tested, because diffusion of matter will be shown to be the most likely mechanism responsible for temperature dependence of creep rate in the primary regime also. As a consequence, the two regimes that differ only in stress dependence can be represented by a single equation. A functional form was selected for stress dependence which would not alter the values of the stress exponents in the respective regimes, but, on the other hand, would add to the confidence in the multi-linear regression analysis, from which all rate parameters are estimated. This procedure would also define the demarcation point for bilinearity more precisely. The equation chosen for NT154 was as follows:

$$\ln(\dot{\epsilon}_{pi} \text{ or } \alpha) = a_0 + (a_1/T) + a_2[\ln(\sigma/E)] + a_3\sqrt{\{\ln(\sigma/E) - \tau\}^2} \quad [5-14]$$

where, a_0 , a_1 , a_2 , and a_3 are constants estimated through a multi-linear regression procedure, and τ is an optimized constant. Note that when $\ln(\sigma/E) > \tau$, the power-law stress exponent n is the sum (a_2+a_3), and when $\ln(\sigma/E) < \tau$, n is the difference (a_2-a_3). τ represents the transition point. The combining of the two regimes into a single equation is justified, as long as the temperature dependence can be represented by a single value of activation energy. In the regression analysis, the value of Q is found from the equality $a_1 = -(Q/R)$. This method also provides a better estimate of the activation energy, because all data, generated at various temperatures and stresses, are included.

The advantage of the present approach is that the data for all three parameters can be independently regressed. This would allow for any systematic variation with respect to time in temperature and stress dependences of creep processes to express themselves, while still preserving the equality and continuity of the primary creep rate to the secondary creep rate at the P/S transition point. Physically, this means that gradual changes in temperature and stress dependences with time which could be brought about by changes such as in the chemistry of the intergranular amorphous phase, as often observed in creep behavior of silicon nitrides (ref. 5-11, 5-25), can be reasonably incorporated in the above equations.

5.1.4.2.3.3 Results Of Modeling

Average lines predicted by the models along with the individual data points are shown for $\dot{\epsilon}_{pi}$ and α in Figures 5-8 and 5-9, respectively. In addition, Figure 5-10 shows the average line predicted for the primary creep rate $\dot{\epsilon}_p$ at time equal to half the t_{ps} . The average line for $\dot{\epsilon}_s$ was shown in Figure 5-3. The ordinate in these figures represents the natural log of the temperature-modified rate parameter, arrived at by dividing the actual value of the rate parameter by $e^{-(Q/RT)}$. Table 5-4 provides the values for a_0 , a_1 , a_2 , a_3 , and τ of Equation [5-12] for the models of the three parameters.

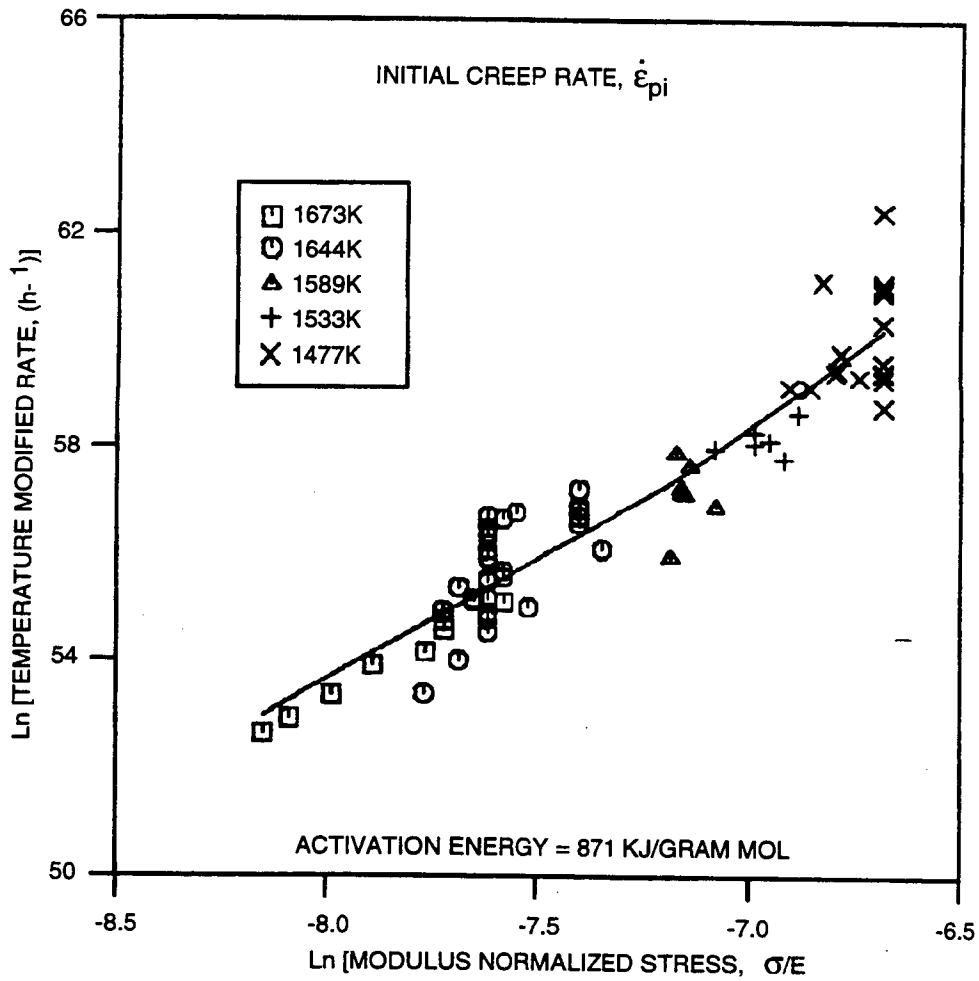
TABLE 5-4. REGRESSION ESTIMATES FOR RATE PARAMETERS $\dot{\epsilon}_s$, $\dot{\epsilon}_{pi}$, AND α

Rate Parameter	a_0	a_1	a_2	a_3	τ
$\dot{\epsilon}_s$	115.00	1.179×10^5	7.13	2.90	-7.19
$\dot{\epsilon}_{pi}$	4.08	1.035×10^5	5.11	0.60	-7.19
α	90.57	0.830×10^5	5.56	1.25	-7.19

Figures 5-8 through 5-10 also provide a visual depiction of the scatter for the respective rates. The extent of scatter for the replicate tests at 1204C or at 1371C seems to be a good measure of the overall scatter in the respective low- or high-temperature regimes for each of the rate parameters. As observed previously for $\dot{\epsilon}_s$, the scatter seems to be slightly larger in the low-temperature regime than in the high-temperature regime.

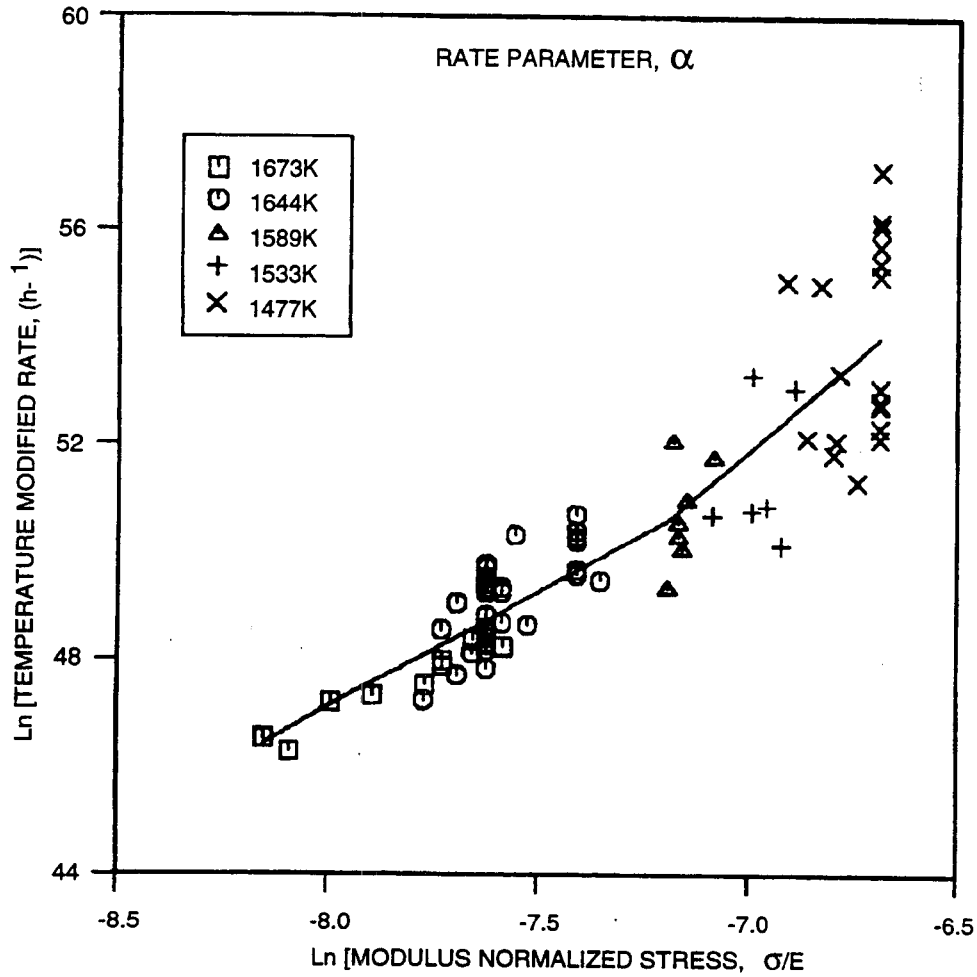
The creep rate model can be examined on the basis of its ability to predict creep rates in the primary regime. In Figure 5-11 [GC11591-511] each line connecting five symbols, staggered for clarity on the abscissa, represents a single specimen. The five symbols on each line represent ratios of predicted to observed creep rates calculated at five locations in the primary regime, namely at 0.125, 0.25, 0.50, 0.75, and 1.0 of the P/S transition time. For most of the specimens, the primary creep rate is predictable within a factor of two. In Figure 5-5 was shown a comparison of predicted versus observed rates for secondary creep rate. This ratio also fell within a factor of two. Figure 5-11 also substantiates the earlier observation from Figures 5-8 through 5-10 that the scatter in the low-temperature regime is slightly higher than in the high-temperature regime.

Equations [5-9] through [5-12] show that a knowledge of the three rate parameters and the P/S transition time is all that is needed for predicting creep rates and strains in the primary and secondary regimes. The value of β for calculating the primary creep strain in Equation [5-8] can be obtained from the equality, $\beta = \dot{\epsilon}_{pi}/\alpha$.



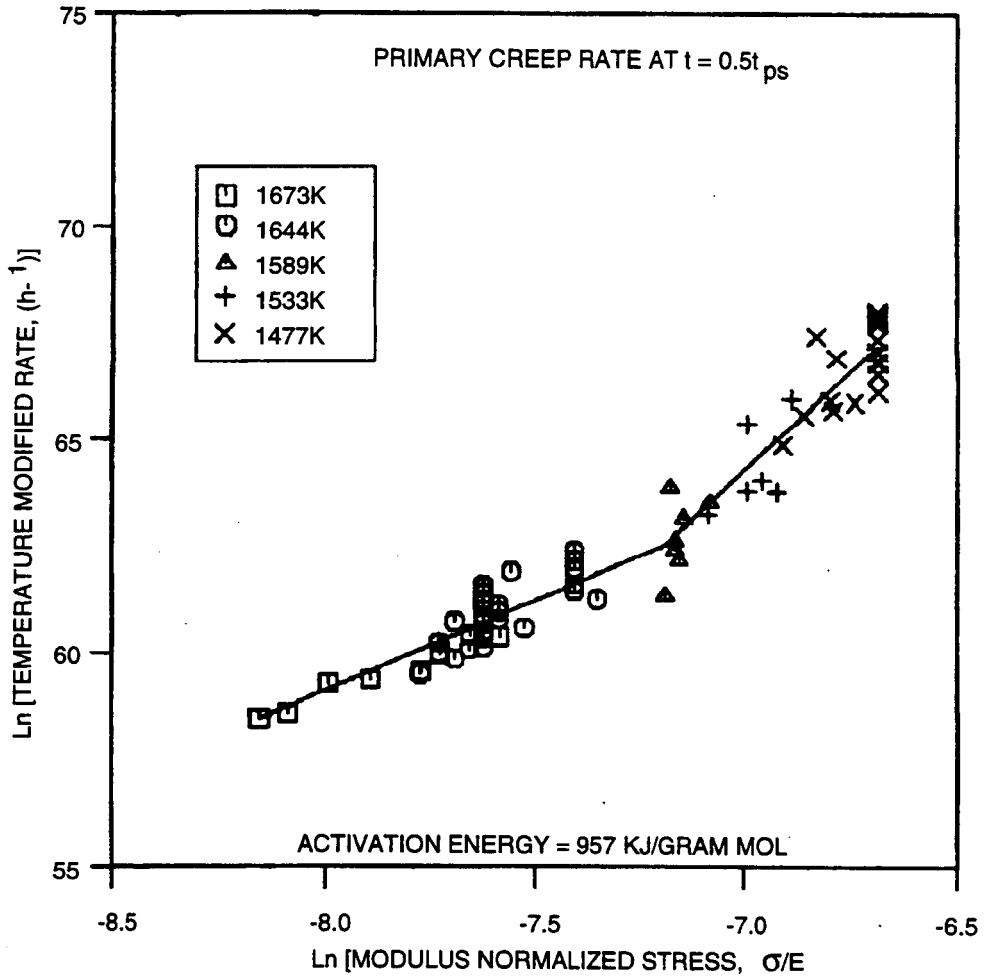
GC11591-508

Figure 5-8. Dependence Of Temperature-Modified Initial Primary Creep Rate On Normalized Stress.



GC11591-509

Figure 5-9. Dependence Of Temperature-Modified Rate Parameter, α , On Normalized Stress.



GC11591-510

Figure 5-10. Dependence Of Temperature-Modified Primary Creep Rate At $t = 0.5t_{ps}$ On Normalized Stress.

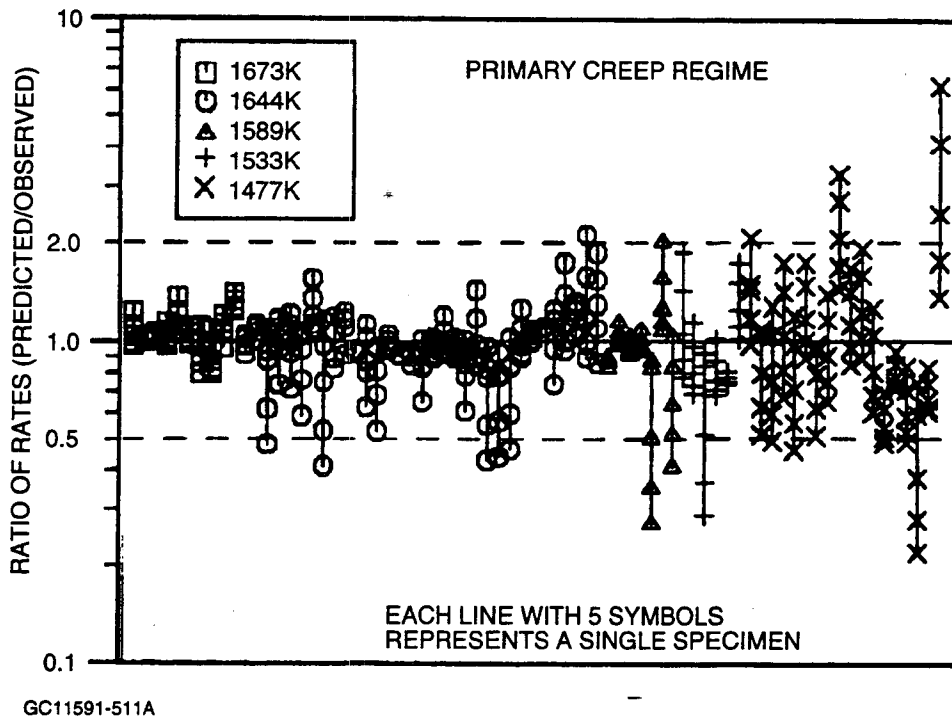


Figure 5-11. Scatter And Predictability Of Creep Rates In The Primary Regime.

5.1.4.2.4 Discussion

5.1.4.2.4.1 Model For Primary Creep Rate

The success of the present model to successfully predict creep rates in the primary regime is due to the fact that the rate parameter, α , which defines the rate of change of primary creep rate with time, varies systematically with stress and temperature, and can be modeled thus. This allows for the interpolation and

extrapolation of primary creep curves from a set of short-term data in the general temperature regime of interest, while still maintaining the traditional interpretations involving use of stress exponents and activation energies.

Table 5-5 provides values of activation energies and stress exponents in the primary creep regime, for $\dot{\epsilon}_{pi}$ and $\dot{\epsilon}_p$ at $t=t_p/2$, along with those for $\dot{\epsilon}_s$. For $\dot{\epsilon}_s$, an activation energy of 981 kJ/g.mol was estimated through the regression, and the stress exponents in the low- and high-temperature regimes were 10.0 and 4.2, respectively. It is interesting to note that the mean value of the activation energy increases slightly, from 871 to 981, from the beginning to the end of the primary regime. In addition, the value of one of the stress exponents also changes, significantly, during primary creep. The stress exponents in the high- and low-temperature regimes, n_1 and n_2 respectively, are 4.5 and 5.7 for $\dot{\epsilon}_{pi}$ -- that is, when the creep processes have just commenced upon initial loading. The values for the two stress exponents become distinctly different, $n_1 = 4.2$ and $n_2 = 10.0$, as the primary regime transitions into the secondary. In other words, throughout the primary regime, the stress exponent for the higher temperature regime, >1315C, is essentially constant, but below 1315C, it increases twofold.

TABLE 5-5. VALUES FOR ACTIVATION ENERGY AND STRESS EXPONENTS

Rate Parameter	Q	n_1	n_2
$\dot{\epsilon}_{pi}$	871	4.5	5.7
$(\dot{\epsilon}_p)_{t=tp/2}$	957	4.2	9.3
$\dot{\epsilon}_s$	981	4.2	10.0

A steady increase in creep resistance with time has been reported previously by Lange, et. al. (ref. 5-25) in a study of primary creep in a MgO-sintered silicon nitride. Both an increase in activation energy and an increase in the stress exponent with an increase in strain or time were inherent in the observations of Arons and Tien (ref. 5-11) on primary creep in NC132 from Norton Advanced Ceramics, Worcester, MA. It is interesting to note that in the present case the stress exponents in the two temperature regimes are affected differently with time.

5.1.4.2.4.2 Comparison To Previous Studies On Primary Creep

The earliest studies on primary creep were conducted on silicon nitrides hot pressed with MgO (ref. 5-11, 5-25), which are known to contain a larger amount of intergranular amorphous phase than NT154. The glassy phase was known to be much less refractory in those silicon nitrides than that present in yttria-sintered silicon

nitrides. In an extensive study of compressive creep of NC132, Lange, et. al. (ref. 5-25) concluded that transient creep in the primary regime could arise from (i) viscoelastic response of the amorphous phase itself, (ii) sliding of grain boundaries accommodated by elastic deformation of the material adjacent to the asperities on the grain facet, or (iii) due to a strengthening from progressive compositional change of the amorphous phase resulting from oxidation. The transient viscoelastic response was also reported later by Arons and Tien (ref. 5-11) in tensile creep of NC132. In their work, the strain hardening effect was explained by a model in which continued grain boundary sliding would result in a continuous increase in contact area between grains, offering increasing resistance to sliding with time.

The contribution from viscoelasticity is not believed to be significant in creep of NT154. Viscoelasticity would result in further recoverable strain in addition to the instantaneous elastic strain in an experiment in which the load is removed after a certain amount of creep strain has accumulated while the specimen is still kept at temperature. This has been measured to be very small in NT154, about 5 percent of the primary creep strain, and could not possibly explain the extensive primary creep in this material.

Similarly, there is not sufficient evidence in the present case to hypothesize a scenario in which strain hardening in primary creep could be explained by progressive strengthening of the amorphous phase through oxidation. The compositional changes resulting in progressive strengthening of the amorphous phase in NC132 occurs because of the instability of the amorphous phase with respect to oxidation. During oxidation, diffusion of oxygen into the interior and of nitrogen, magnesium, and impurities out of the interior takes place, all through the amorphous phase (ref. 5-13). In NT154, there may be similar changes occurring as a result of surface oxidation, but these are believed to be very minor. Ytria-containing silicon nitrides are known to be much superior in oxidation resistance (ref. 5-26). In addition, the present batch of material was given a high-temperature heat treatment specifically designed to crystallize most of the amorphous phase. Such heat treatments are known to result in increased resistance to diffusion and grain boundary shear (ref. 5-27). Note that the amorphous phase in NT154 was found to be extremely thin.

Percolation was a mechanism proposed by Drucker (ref. 5-28), and later by Lange (ref. 5-8) to explain creep rates in earlier versions of silicon nitrides, which contained larger amounts of amorphous phase with lower viscosity. The percolation mechanism involves grain separation rather than grain boundary sliding, and is accommodated by flow of the viscous phase from boundaries under compression to boundaries under tension. The deformation rate is therefore controlled by the flow characteristics of the glassy phase. The contribution from this mechanism also is considered to be insignificant in the present case, since the TEM studies have shown that, first, the amorphous phase is very thin in this material to begin with, and second, no significant differences in thickness of the phase between tensile and non-tensile boundaries were apparent. Therefore,

contact between grains can be expected to be established early in creep in NT154. This was also the conclusion reached by Wiederhorn, et. al. (ref. 5-5) in their analysis of transient creep in another version of NT154.

5.1.4.2.4.3 Importance Of Cavitation In Creep Of NT154

The above discussion leaves grain boundary cavitation and the accompanying diffusion of matter as the major possible mechanism for primary creep. It was noted in Section 4.4.3 that cavitation in NT154 consists of both two-grain junction and triple-junction types. Below 1315C, the two-grain junction type was more numerous, although this type was observed also at the high temperatures but in lower concentrations. The triple-junction cavities were extensive mainly at temperatures above 1315C, and were much larger than the two-grain junction type. At 1204C, the size of the triple-junction cavities were of the same order as that of two-grain junction cavities, and their number was very small.

In a recent study of cavity evolution during tensile creep of the same batch of NT154, Luecke et. al. (ref. 5-7) concluded that most of the creep strain can be accounted for by cavitation in this material. Cavities accounted for approximately 85 percent of the total strain at any point during creep. The volume fraction of cavities was estimated using density measurements employing a sink-float technique, and was found to vary linearly with strain. The present study, employing a different method (Section 4.4.3), points to the same conclusion.

5.1.4.2.4.4 Proposed Mechanism For Primary Creep In NT154

(a) Strain Hardening Effect In the Primary Regime

Observations on two-grain junction and triple-junction cavitation seem to support the conclusion reached by Luecke, et. al. (ref. 5-7) that cavitation could account for most of the creep strain in NT154. However, we would like to make a distinction between the high- and low-temperature regimes. It is proposed that two-grain junction cavitation alone is responsible for most of the creep strain at temperatures below 1315C, and that triple-junction cavitation is primarily responsible for creep strain at temperatures above 1315C. This would be in accordance with our experimental observations. It is hypothesized further that cavitation is constrained and this constraining effect is partly responsible for the strain hardening effect in primary creep. If it were unconstrained, tertiary creep would be expected to be manifested towards the end of each test, which was clearly not the case.

There may be two reasons for the constraint on cavitation. First, the constraint may occur due to the fact that diffusion is slow in the amorphous phase and, therefore, the material tends to be deposited close to the cavities, which can reduce the local grain boundary normal stress in the vicinity of the cavities. The local volume increase would generate a back stress from the surrounding material, as suggested by Riedel (ref. 5-29). This back stress on the grain boundary facet will have to adjust itself until the local rate of volume increase by diffusive cavitation is compatible with the deformation of the surrounding material. Thus, constrained cavitation forces the initial strain rate to slow down with time.

Second, the constraint may arise as a result of the geometrical aspects of the microstructure itself. The microstructure can be described as pockets of smaller equiaxed grains being walled by larger, acicular grains. It is reasonable to suspect that in such a configuration, the motion of the acicular grains is highly restricted. Contribution from the acicular grains towards accommodative strains, which are needed for compatibility in creep, will have to arise primarily through the two-grain junction cavitation, and only to some extent through their elastic deformation. This would have a tendency to restrict creep deformation within the pockets, the walls of acicular grains providing the constraint.

Evidence seem to point to this possibility of constraint arising from the unique microstructure of NT154. In the SEM evaluation, many of the acicular grains were seen to be completely or extensively decorated with two-grain junction cavities on their long facets. An example is shown in Figure 5-12. In this figure, one long grain (A) is seen to be highly cavitated, and a longitudinal path (C) of cavities beginning from this long grain is left on a series of small grains adjacent to it. The path seems to indicate that there was probably a long grain which was pulled off to the other side of the fracture surface. Note the pocket (P) of smaller grains enveloped by these two long array of cavities. In addition, TEM showed that the majority of the triple-junction cavities were concentrated within these pockets of smaller size grains, indicating that it was easier for creep to occur within these pockets. However, the creep within the pockets can continue at the same initial rate only if the acicular grains could deform at the same rate. Since, two-grain junction cavitation is the most likely mode of deformation for the acicular grains, and also since this mode is the slowest, the creep rate within the pockets will have to decrease with time.

A consequence of such a mechanism would be increased creep resistance for a material if the grains within the pockets can also be converted into an acicular structure. Recent efforts involved in improvement of creep resistance of advanced silicon nitrides seem to point to the possibility of such a type of microstructure providing lower creep rates (ref. 5-30).



GB11591-512

125620-2

Figure 5-12. Two-Grain Junction Cavitation On An Acicular Grain (A) At 1477K.

In addition to constrained cavitation, a gradual increase in contact between grains at the asperities as the grains move and rearrange in creep may play a role in the observed hardening in the primary regime.

(b) Stress Sensitivity Of Creep Rate

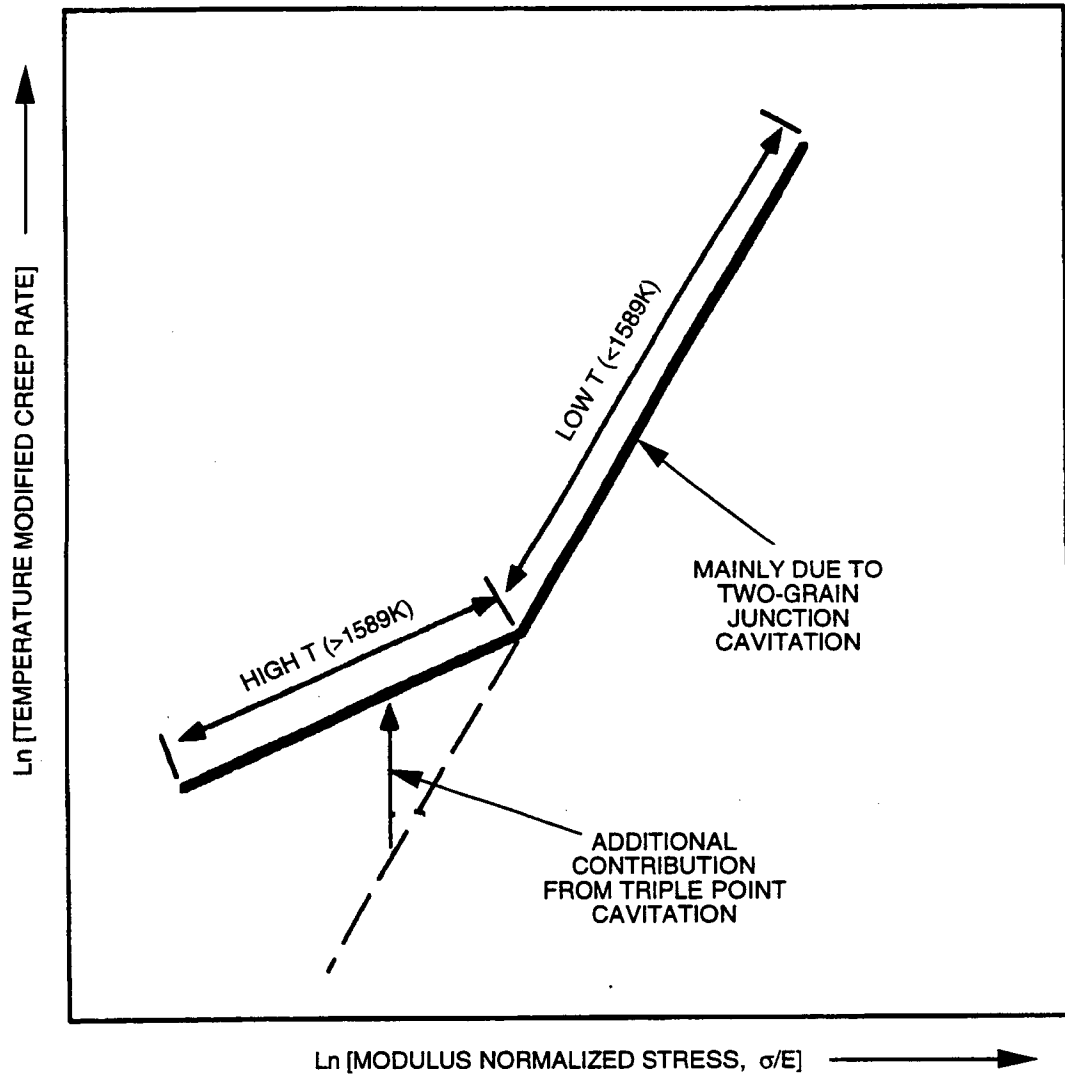
It is to be noted that cavity growth in NT154 is different from that in NC132 or other lower grades of silicon nitrides which contain much larger amounts of glassy phase and which are also of lower viscosity (ref. 5-11, 5-25). In the latter materials, cavitation occurs only in the amorphous phase, and failure is by propagation of cavitation through the amorphous phase (ref. 5-18, 5-19). Therefore, models for stress dependence of creep rate based on processes involving void growth exclusively in the glassy phase (ref. 5-11) will not suffice for explaining the behavior of NT154.

On the other hand, a high stress dependence for nucleation of two-grain junction cavities could explain the stress dependence for secondary creep rate in the low-temperature regime, and as a result, also the stress dependence of the high-temperature regime. In the lower temperature regime, cavitation was almost exclusively of the two-grain junction type, and was also more numerous than at 1371C and above. Consistent with the suggestions of previous investigators (ref. 5-5, 5-11, 5-25), contact between ledges between adjacent grains is hypothesized as the driving force for nucleation of cavities. This mechanism is well recognized in the literature for lenticular cavitation (ref. 5-29). Cavitation is believed to initiate at ledges of multiple interplanar height, when dissolution of material becomes energetically favorable for releasing the concentrated stresses at the asperities. This mechanism should be considered as the most likely one in the present case, since our examinations with TEM have provided evidence of both strain whorls (ref. 5-5, 5-18) as well as dislocation pileups punched in from the grain boundaries (ref. 5-31) in creep tested samples of NT154, indicating highly stressed asperities.

Thus a high stress dependence for nucleation of cavities could account for the high stress exponent in the low-temperature regime. This would of course require continuous nucleation. It is reasonable to assume that continuous two-grain junction nucleation occurs in creep of NT154, since both constrained cavitation and rearrangement of the grains in creep would tend to force cavitation at newer sites.

The lower stress exponent in the higher temperature regime can then be explained, based on the observations described in earlier sections. Both SEM and TEM examinations have shown that at 1371C and 1400C, there is significant triple-junction cavitation, a phenomenon which can be accentuated by an increase in the thickness of the amorphous phase (ref. 5-18, 5-19). Note that the triple-junction cavitation can account for most of the linear strain measured in creep in this temperature range. As graphically explained in Figure 5-13, this means that in the higher temperature regime there is an additional strain component arising from the triple-junction cavitation. The reason for the increased triple-junction cavitation in NT154 at higher temperatures is believed to be due to an increase in the thickness of the amorphous phase and not its viscosity, since the latter would be expected to affect the activation energy significantly. The value in the neighborhood of four for stress dependency for nucleation of triple-junction cavities may be consistent with the model proposed by Marion, et. al. (ref. 5-18).

One final point to be discussed is the gradual increase in stress dependence observed at lower temperatures from the beginning of the primary to the end of the primary regime (Table 5-5). It is interesting to note that the stress exponent in the high-temperature regime does not change with time; it changes only in the low-temperature regime. We believe that it is due to the time required for the grain contact to occur, which is necessary for the two-grain junction nucleation to begin. In other words, substantial grain-to-grain contact



GC11591-513B

Figure 5-13. Schematic Of Model Explaining Change In Stress Dependence Of Creep Rate In Low- And High-Temperature Regimes.

occurs only after the material has had time to deform, and consequently the grains have had some time to "pack". Contact of ledges between grains is not a requirement for nucleation of triple-junction cavities, which can start immediately on loading.

The above explanations thus justify (i) use of a single activation energy in the model for creep rates, independent of temperature, (ii) a global regression procedure for determining more precisely the stress dependencies of creep rates and the demarcation point between the two temperature regimes, and (iii) a phenomenological approach to modeling of primary creep which has proved helpful in delineating possible mechanisms and in quantifying changes in stress and temperature sensitivities of primary creep rate as a function of time.

5.1.4.2.5 Conclusions

A phenomenological approach to predicting creep rates in the primary and secondary creep regimes of NT154 silicon nitride is presented. The model is shown to predict the creep rates within a factor of two. Two-grain junction and triple-junction cavitation are primarily responsible for creep deformation. The unique stress dependency observed in creep rate is postulated to be due to the stress dependency of cavity nucleation. The temperature dependency is due to matter transport through the amorphous phase. It is shown that the creep behavior of NT154 is unlike that of earlier versions of silicon nitrides which contain larger amounts of glassy phase.

5.1.5 Stress Rupture

5.1.5.1 Introduction

In order to circumvent the prohibitive cost and time involved in generating long-time creep rupture data, several empirical approaches have been developed in the past (ref. 5-32, 5-33) for predicting the long-term creep rupture life of materials. In most of these, data from short-term tests are used to derive a relationship between the test stress and a parameter which incorporates both the rupture life and the test temperature. This relationship is then used to predict long-term lives. The underlying assumption is that the mechanisms responsible for short-term failures are the same as that to be expected in tests of longer duration. Furthermore, it is assumed that these mechanisms are independent of temperature, and that the relationship between the time-temperature parameter and stress adequately preserves both these assumptions.

The Monkman-Grant relationship (ref. 5-34) is one among these empirical approaches and is often cited as one that also lends to prediction of long-term rupture life of materials. Although it does not incorporate a temperature-time parameter, its simpler basis has led to attempts at utilizing it for stress rupture life prediction. Originally developed for metals, it has also been examined from the point of view of its ability to predict rupture life of ceramic components (ref. 5-4, 5-5, 5-7). In this section, the applicability of the Monkman-Grant

relationship as a stress rupture life prediction tool for advanced silicon nitrides is examined. Also in this section, an empirical approach based on a time-temperature parameter is presented.

5.1.5.2 Monkman-Grant Relation Between Rupture Life And Creep Rate

The Monkman-Grant relationship states that the rupture life, t_f , is uniquely related to secondary or minimum creep rate, $\dot{\epsilon}_s$, independent of temperature or stress. The relationship was described by Equation [4-1] in Section 4.3.1.2.2.4:

$$t_f = K(\dot{\epsilon}_s)^{b_1} \quad [4-1]$$

where: K and b_1 are constants. For many metallic materials (ref. 5-34), b_1 is close to, but slightly less than -1, and the relation has been found to be independent of temperature and stress. This has been interpreted as support for a mechanism of stress rupture in which the bulk creep response is a good indicator of the rate of damage accumulation leading to failure. When b_1 is equal to -1, the relationship could be thought of as a strain criterion for failure under circumstances where the strains involved in the transient part of the creep are small or relatively constant. Then, depending on whether there is transient creep or not, a fraction of the strain given by $t_f \dot{\epsilon}_s$ [referred to as the Monkman-Grant Product (MGP)], or the total creep strain, respectively, could be a constant in tests at different temperatures or stresses.

Often, the value of b_1 is other than -1. It has been noted that for cast MarM-247, which is a high-temperature nickel-based superalloy, expressions similar to that given by Equation [4-1] relating even the transition times, such as secondary to tertiary, or tertiary to quaternary, to the secondary creep rate hold independent of temperature or stress (ref. 5-24). This has been found to be true for some other equiaxed high-temperature turbine blade materials as well, and in each case, the value of b_1 is close to but slightly less than -1.0.

The advantage of using the Monkman-Grant relation is that once the relationship is established from short-term tests, all that is needed for estimating failure time for a new set of conditions is the value of the secondary creep rate. Since the time to reach the secondary creep regime generally comprises a smaller portion of the failure time for many materials, relatively short tests can be used to arrive at this information.

Departures from the uniqueness of the Monkman-Grant relationship have been noted by previous investigators in metallic as well as ceramic materials. Castillo, et. al. (ref. 5-35) observed that Monkman-Grant lines are stratified with respect to temperature for the nickel-based superalloy IN738. This stratification is seen

to be even more conspicuous in the case of the single-crystal nickel-based alloy CMSX-3 (ref. 5-36), and also, as recently noted, in the case of the single-crystal alloy SC-180 (ref. 5-37). In these cases, however, for a specific value of secondary creep rate, specimens at the lower temperature show a longer life. For ceramic materials, a reversal of this trend has been noted. Ferber and Jenkins (ref. 5-4) found, for example, that for PY6 silicon nitride, the Monkman-Grant lines are stratified with respect to temperature, but with the higher-temperature tested specimens showing longer lives at the same value of creep rate. This was also the observation by Luecke, et. al. on NT154 (ref. 5-7). Our observations in section 4.3.1.2.2.4 show that the Monkman-Grant lines are stratified with respect to temperature in NT154 in the range 1204C to 1400C, consistent with the observations of Ferber and Jenkins (ref. 5-4) on PY6 and Luecke, et. al. (ref. 5-7) on NT154.

In creep rupture of metallic materials, an increase in temperature is accompanied by an increased propensity for intergranular or interdendritic crack growth and fracture, which is primarily brought about by increased environmental influence. Since crack growth is more affected by environment than creep rate, the latter being dislocation assisted, the environmental influence becomes both a significant and additional factor, which degrades life further than a correlation with creep rate alone would predict, as the temperature is increased. Hence we see a lower rupture life for the same value of creep rate as the temperature is increased. Modifications have been proposed to account for this stratification in the Monkman-Grant relation with respect to temperature in metallic materials. For example, in improving predictions for IN738, Castillo, et. al. (ref. 5-35) employ additional parameters from the creep curves, such as tertiary times. Obviously this cannot apply to NT154, first, since it does not show tertiary creep, and second, the stratification is reversed.

No attempt has been made so far to explain the reasons for the departures in the Monkman-Grant relationship in ceramic materials. In the following sections, we will analyze the applicability of the Monkman-Grant relationship to prediction of creep rupture life of NT154 silicon nitride, examine the fractographic and other evidence in the hope of sorting out possible failure mechanisms and reasons for the observed stratification, and suggest modifications to the present form of the Monkman-Grant relation for the purpose of prediction of rupture life in advanced ceramic materials.

5.1.5.3 Examination Of Monkman-Grant Relation For NT154

As shown in Figure 4-28, when the stress rupture life was plotted against the minimum creep rate on a log-log scale, a unique master curve was not obtained. The data were found to be stratified with respect to temperature in such a way as to suggest that K in Equation [4-1] is an increasing function of temperature. It was obvious from the trend in the plot that the data could be correlated using an additional temperature term. An

inverse function of temperature is one that can be used to correlate the data. It will become evident in the forthcoming discussion that use of an inverse temperature term would provide insight into the stress dependence of the Monkman-Grant relationship. The modified equation based on this term is given below:

$$\ln(t_f) = b_0 + b_1 \ln(\dot{\epsilon}_s) + b_2/T \quad [5-15]$$

where: b_0 and b_2 are constants, and T is absolute temperature. Comparing to Equation [4-1], the first and the last terms of Equation [5-15] would equal $\ln(K)$ in Equation [4-1]. The results of the modification of the Monkman-Grant relation by the third term in Equation [5-15] are shown in Figure 5-14. The data at different temperatures are collapsed reasonably well. In this figure, both the average line and the data had to be normalized to a particular temperature (1260C) for all to be shown in one plot. Figure 5-15 shows the prediction from Equation [5-15] for the individual temperatures along with the unmodified data. The values for b_0 , b_1 , and b_2 in Equation [5-14] for NT154 silicon nitride are 15.87, -1.53, and -4.21×10^4 , respectively. Note that b_2 is negative, which means that rupture life increases with an increase in temperature for the same value of creep rate.

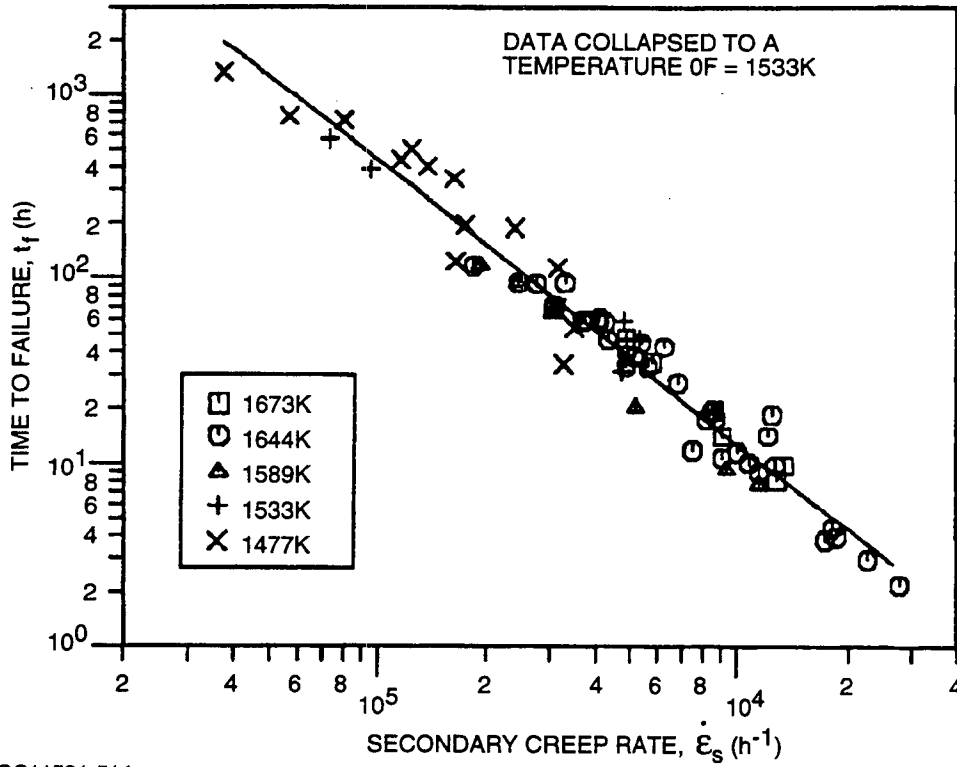
On the other hand, stress, σ , is uniquely related to $1/T$ at a constant value for creep rate, $\dot{\epsilon}_s$, by the following relation:

$$\ln(\dot{\epsilon}_s) = \ln(A) + n \ln(\sigma/E) - (\bar{Q}/R)(1/T) \quad [5-16]$$

where: A , n , σ , E , Q , and R are, respectively, a constant, stress exponent, stress, elastic modulus, activation energy and the universal gas constant. Equation [5-15] can be derived from Equation [4-1]. This relationship between σ and T through $\dot{\epsilon}_s$ means that the stress rupture data could be correlated by means of a stress term as well, thus:

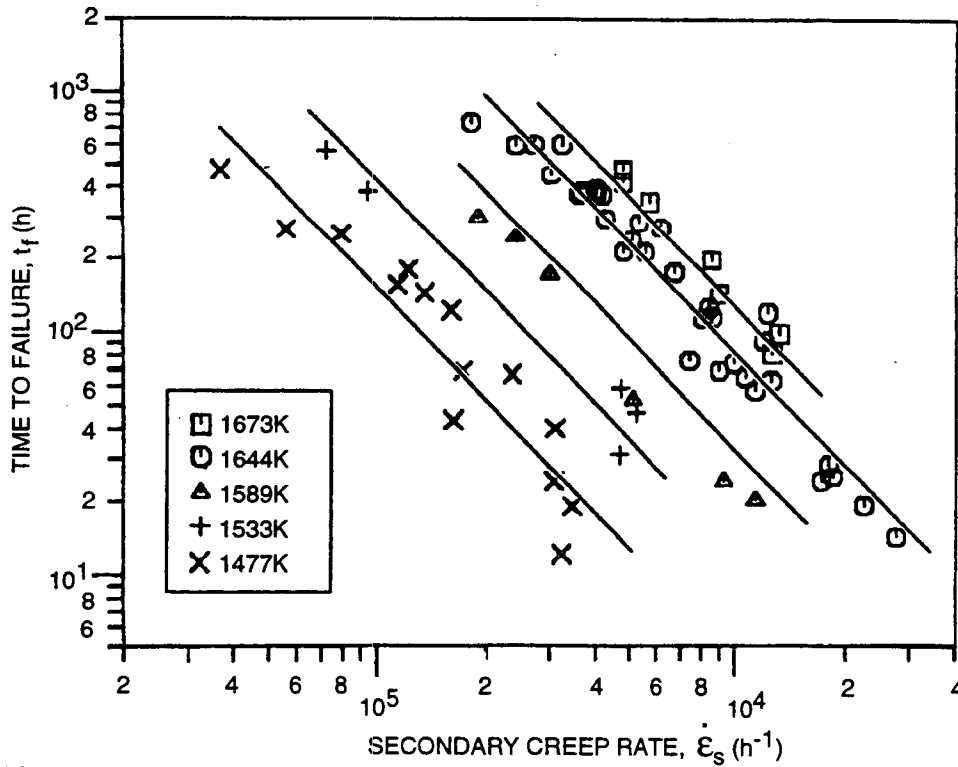
$$\ln(t_f) = c_0 + c_1 \ln(\dot{\epsilon}_s) + c_2 \ln(\sigma/E) \quad [5-17]$$

Equations [5-15] and [5-16] are thus equivalent. Figure 5-16 shows the correlation of rupture life to secondary creep rate by means of the modification proposed in Equation [5-17]. The values for c_0 , c_1 , and c_2 are, respectively, -27.79, -1.27, and -2.71. Note that c_2 is negative, which indicates that rupture life decreases with increase in stress for the same value of creep rate.



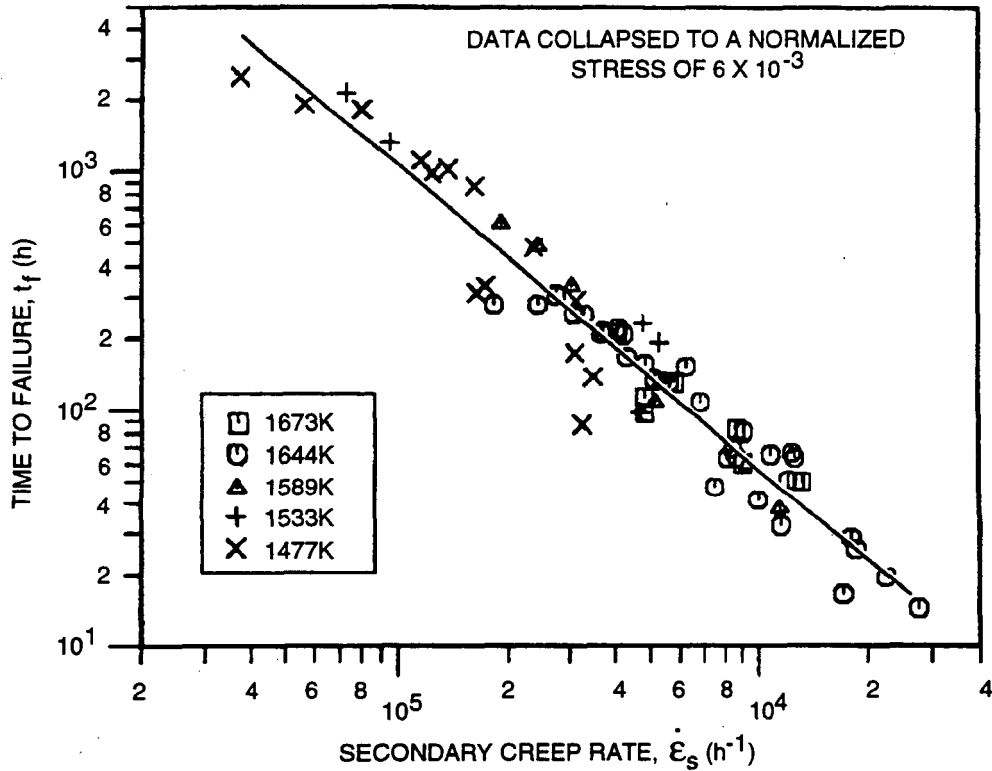
GC11591-514

Figure 5-14. Temperature Dependence Of The Monkman-Grant Lines Correlated With An Additional Temperature Term.



GC11591-515

Figure 5-15. Comparison Of The Average Lines Predicted Versus The Unmodified Data.

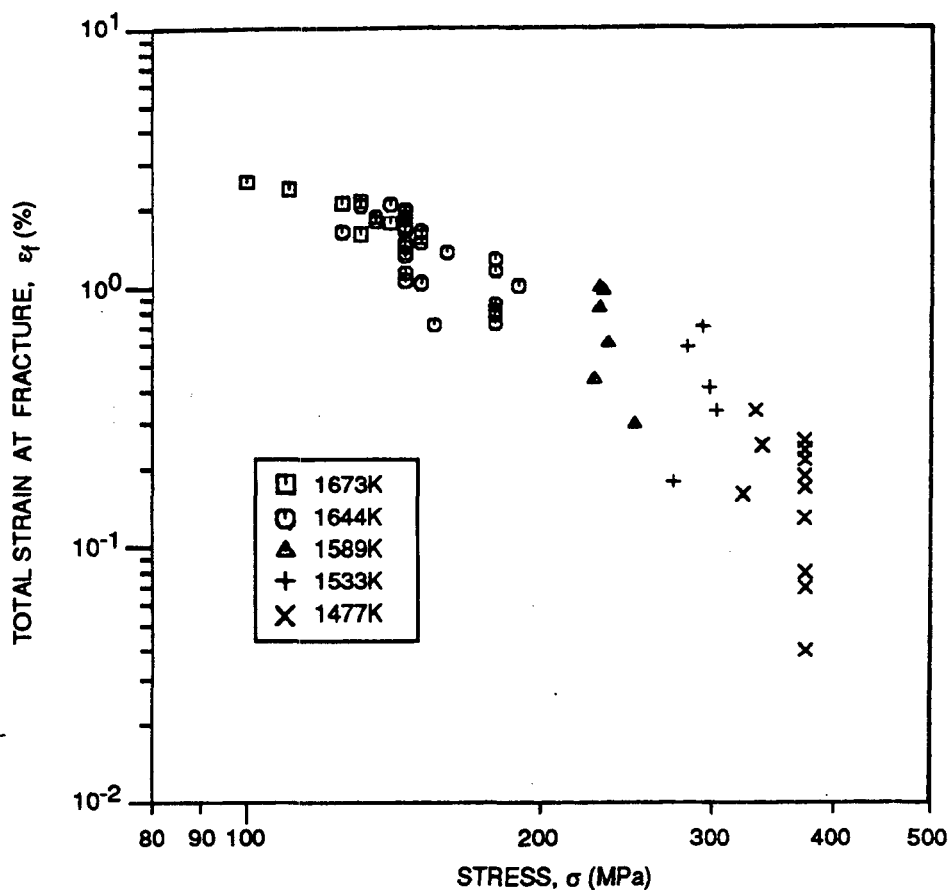


GC11591-516

Figure 5-16. Stratification Of The Monkman-Grant Lines Can Be Correlated With An Additional Stress Term.

It must be intuitively obvious from the data shown in Figure 5-15 that the slope c_1 , which would represent slope in constant-stress tests, should always be smaller than the slope b_1 in a constant-temperature test. This is indeed so in the present case. As in Figure 5-14, the data in Figure 5-16 also had to be plotted in a normalized form, but at a constant value of (σ/E) . Equations [5-15] and [5-17] also suggest that when there is an additional stress dependence in the Monkman-Grant relation, an additional temperature dependence can also be expected, and vice versa.

A plot of the creep failure strain against stress, Figure 5-17, shows a definite and significant trend, the failure strain decreasing with increasing stress. This is visible even at 1371C, where we have data from replicate tests at two stresses. A similar trend can also be shown to be exhibited by the MGP value. It is therefore evident that NT154 does not follow a strain criterion for failure in creep, i.e., failure does not occur at a constant accumulated strain.



GC11591-517

Figure 5-17. Dependence Of Creep Failure Strain On Applied Stress.

5.1.5.4 Subcritical Crack Growth In NT154

An observation that stands out in fractography of NT154 failure specimens is that the damage area for failure is localized. A well-demarcated region showing subcritical crack growth (SCG) is observed on the fracture surface. This has already been discussed in section 4.3.2. The evidence points to SCG being the mechanism causing failure in creep and stress rupture of NT154.

5.1.5.5 Crack Blunting

Crack tip blunting is a possibility that needs to be considered in examining creep rupture failure by subcritical crack growth in NT154. This possibility is supported by the observation (see Table 4-6) in replicate tests that 83 percent of the specimens tested at 1149C failed from internal initiations associated with defects. At 1204C, the percentage was only 56. At 1371C, the overall percentage was 13; however, none failed from internal initiations at 1371C and 145 MPa. All the other failures, which were all surface initiated, showed no indication of flaws or defects at the initiation sites. In comparison, the room-temperature tensile fast fracture tests on specimens of identical geometry (a total of 100 specimens) showed 65 percent failures initiating internally at flaws. The lower number of failure initiations at inherent flaws as the temperature is increased indicates a tendency for the inherent flaws to become less competitive with surface-initiated cracks in failure of NT154. One of the concepts that would be consistent with this phenomenon is crack blunting. The other is environmentally induced surface degradation.

However, recent studies reported on PY6 silicon nitride (ref. 5-38) at different temperatures in which the stressing rate was varied (dynamic fatigue) suggest that crack blunting may be occurring under the reported conditions. PY6 silicon nitride, which contains 6 percent yttria as a sintering aid, was tested by Lin, et. al. (ref. 5-38) at 1149C, 1260C, and 1371C at stressing rates between 10^{-4} and 10^2 MPa/sec. The specimens, which were of the same geometry used in the present tests, were machined from the same batch of material which was previously used by Ferber and Jenkins (ref. 5-4) in determining the material static fatigue capability. While the strength normally decreased with a decrease in the stressing rate, a transition in the form of an increase in strength was observed at 1260C and 1371C, in the neighborhood of a stressing rate of 10^{-2} MPa/sec. Below and above the transition rate, the normal behavior continued. The observations were explained based on a slow crack growth model, in which crack blunting or healing competed with crack growth from flaws, as the stressing rate was lowered. Crack blunting must, therefore, be considered as an important phenomenon that can occur in creep rupture of silicon nitrides, since the results on the stress rate dependence of strength of PY6 (ref. 5-38) near the transition rate cannot be explained by environmental degradation.

5.1.5.6 Comparison With GN-10 Silicon Nitride

It would be interesting to compare the results of the present program on NT154 to that on GN-10 silicon nitride from AlliedSignal Ceramic Components, Torrance, CA recently reported by Liu, et. al. (ref. 5-39) and Schienle (ref. 5-40). GN-10 has a larger amount of the amorphous phase at the grain boundaries and less creep resistance than NT154. Tests on GN-10 were conducted at 1204C, 1260C, and 1315C on specimens of identical geometry. When the data were plotted, as shown in Figure 5-18, the rupture life was found to be a function of strain rate, but independent of temperature. Note that the slope has a value of -0.83. The cavity evolution in GN-10 is distinctly different from that observed in NT154. Hockey and Wiederhorn (ref. 5-41) have found in their extensive studies employing transmission electron microscopy (TEM) that, in GN-10, cavitation is confined to the amorphous layer alone. None of the specimens in References (ref. 5-40, 5-41) showed internal initiation or initiation at flaws. On the other hand, these specimens showed a SCG region, which had initiated at

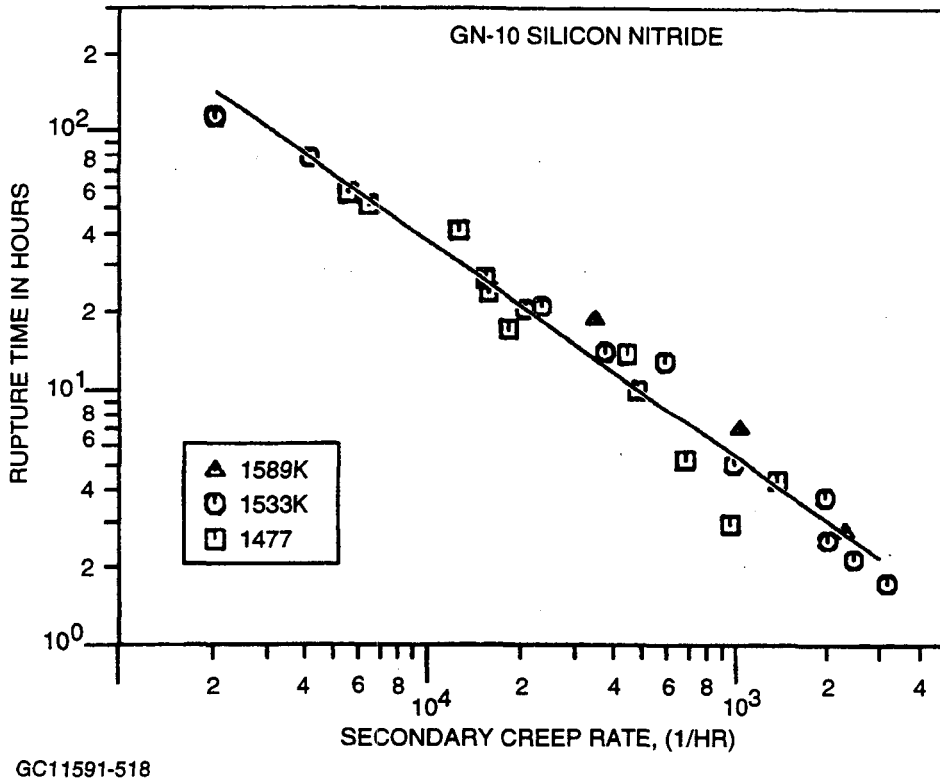


Figure 5-18. Monkman-Grant Plot For GN-10 Silicon Nitride.

the surface. However, unlike NT154, crack initiation at the surface was associated with a bubble-like morphology indicating extensive viscous flow activity of the amorphous phase, reminiscent of the finger-like morphology reported by Marion, et. al. (ref. 5-18) in failure of lower strength silicon nitrides.

The evidence thus indicates that failure in GN-10 is due to cavitation which takes place exclusively in the amorphous phase, leading to coalescence of these full-grain-facet cavities or cracks. It is therefore similar to that reported in earlier versions of silicon nitrides such as NC-132 (ref. 5-18, 5-19, 5-25) in which creep fracture has been ascribed to nucleation of holes within the amorphous phase, followed by growth by viscous flow or diffusion, leading to full-facet cavitation. This is then followed by development and coalescence of microcracks. It is interesting and very important to note that in these materials, creep strain has been attributed to boundary separation resulting from the same mechanism (ref. 5-8, 5-42). In other words, the mechanism responsible for creep strains and that causing failure are identical in GN-10.

The above observations thus suggest that GN-10 is a material in which the failure mechanism and the creep mechanism are closely allied to each other. Although a crack growth region can be identified in both NT154 and GN-10, in the latter, the mechanisms involved in crack advance are identical to that involved in producing creep strain. This would then explain the existence of a master curve for the Monkman-Grant lines in GN-10. It may also be suspected that the two mechanisms are less closely allied in NT154.

5.1.5.7 Failure Mechanism

The observations presented in previous sections clearly point to cavitation as the main mechanism responsible for creep deformation in NT154. Correlation of rupture life with creep rate at any particular temperature would seem to indicate that the mechanisms responsible for failure are related in some way to mechanisms responsible for creep. If the failure process was closely allied to processes responsible for producing creep strain, which is the case for GN-10, an increase in stress or increase in temperature would be expected to accelerate creep rate and the failure rate by the same proportion. If it were not so, the differences could manifest as an additional stress or a temperature dependence in the expression relating failure time to creep rate.

The mechanism proposed for specimen failure is the following: failure occurs by growth of a crack. The crack initiates at an existing flaw, or at a grain boundary that is undergoing either extensive cavitation or degradation through surface oxidation. The crack grows intergranularly. The mechanism of crack advance involves matter transport at the crack tip. While an increase in temperature or stress would nominally result in an increase in the rate of crack growth, this increase could be partially retarded by the possibility of increased

crack tip blunting. A consequence of blunting may be the increased tendency for crack linking at or ahead of the crack tip as a part of the crack growth process as temperature is increased. It may even be possible that at very high temperatures, for $T \gg 1400\text{C}$, when crack tip blunting becomes severe and cavitation would become so extensive as to result in a general material degradation at a faster rate than the propagation rate of a single crack, specimens may fail from general creep damage, exhibiting then a unique relationship between t_f and $\dot{\epsilon}$, independent of temperature.

5.1.5.8 A Phenomenological Approach To Understanding Of The Failure Process

The objective of the following discussion is to examine the failure process through a phenomenological approach, to see if this approach would provide a basis for the empirical expressions given in Equations [5-14] and [5-16], which are proposed as modifications to the Monkman-Grant relationship. The approach to be used will be based on crack growth, which will be consistent with the observations on this material. It is to be noted that lack of explicit crack growth information as a function of temperature necessitates simplistic assumptions in the formulation to be discussed below, which is somewhat similar to that put forward in explaining static fatigue of glass by Charles [ref. 5-43]. A detailed and more accurate formulation of the mechanism will have to wait until more information on crack initiation and growth is forthcoming.

A crack that has initiated on a grain facet advances by diffusion of material away from the crack tip. The growth rate, da/dt , is a function of temperature and the local stress, σ_{loc} , at the crack tip:

$$da/dt = A_1 e^{-(Q'/RT)} f(\sigma_{loc}) \quad [5-18]$$

where: A_1 is a constant, and Q' is the activation energy for matter transport away from the crack tip. Let us assume that Q' equals Q , the activation energy for matter transport involved in creep. It is also assumed that the function $f(\sigma_{loc})$ accounts for all the stress dependence in the failure process. We will discuss the implications of Q' being different from Q later. The function $f(\sigma_{loc})$ is assumed to be of the power-law type, $(\sigma_{loc})^z$. In this specific formalism, it will be shown that stratification of the Monkman-Grant lines would occur, if $z > n$, the stress exponent for creep. When $n = z$, a unique Monkman-Grant relation will be obtained.

The function σ_{loc} is related to macroscopic stress, σ . We use the Inglis criterion (ref. 5-44) for relating σ_{loc} to σ through the radius of curvature, ρ , of the crack tip:

$$\sigma_{loc}/\sigma = 2(a/\rho)^{0.5} \quad [5-19]$$

Equation [5-19] was intended for use in linear elastic fracture mechanics. However, NT154 silicon nitride is a creep brittle material, in which deformation is primarily a grain boundary phenomenon. Hence, the use of Equation [5-19] in the present case may be justified. As will become clear later in the discussion, for the present derivation, all that is needed is an expression that relates local stress to the average macroscopic stress, and not necessarily the Inglis criterion. Substituting Equation [5-19] in Equation [5-18], and rearranging gives:

$$da/dt = A_2 e^{-(Q/RT)} (2\sigma)^z (a/\rho)^{z/2} \quad [5-20]$$

where: A_2 is a constant. To a first approximation, crack blunting is assumed to be a function of creep rate. Hence ρ also would be a function of creep rate. The blunting may be assumed to occur primarily when the crack enters or encounters smaller-grained pockets undergoing extensive creep or cavitation. In the following discussion, the contributions from general material degradation ahead of the crack tip and crack linkage, both of which would increase with increase in crack blunting or creep rate is neglected. For simplicity, ρ is assumed to be only a function of $\dot{\epsilon}_s$ and not of time or crack length. As will become clearer later in the discussion, even if ρ were not a function of creep rate, our conclusions on the cause of stratification will still be borne out. The integral $\int [da/(da/dt)]$, integrated from an initial flaw size of a_0 to the final crack length of a_f provides a value for time spent in crack propagation, t_p :

$$t_p = A_3 e^{(Q/RT)} (\sigma)^{-z} \rho^{z/2} a_0^{(1-z/2)} \quad [5-21]$$

where A_3 is a constant. Assuming ρ to be proportional to $(\dot{\epsilon}_s)^m$, i.e., to $[e^{-(Q/RT)} \sigma^n]^m$, where n is stress exponent for $\dot{\epsilon}_s$, we obtain:

$$t_p = A_4 (e^{-Q/RT})^{[mz/2 - 1]} (\sigma)^{mz/2 - z} \quad [5-22]$$

where A_4 is a constant. Dividing both sides by $(\dot{\epsilon}_s)^{[mz/2 - z/n]}$ and rearranging, an expression similar to Equation [5-17] can be obtained as follows:

$$t_p = A_5 (\dot{\epsilon}_s)^{[mz/2 - 1]} (\sigma/E)^{[n-z]} \quad [5-23]$$

A comparison with Equation [5-17] shows that $z > n$. When n equals z , i.e., when the stress dependencies of the failure mechanism is the same as that of creep, Equation [5-23] becomes similar to the original Monkman-Grant relation. The above discussion thus shows that if the the stress dependence of the failure process is greater than that for creep, stratification of the Monkman-Grant lines can be expected.

Note that m is a small but a positive quantity. If there was no crack blunting, m equals zero, and the creep rate exponent would equal -1.0 . With crack blunting, Equation [5-23] would always predict a creep exponent, c_1 , slightly more positive than -1.0 . However, as seen from the results from Equation [5-17], the value of c_1 is -1.27 . This difference between the regressed value of c_1 and its corresponding value in Equation [5-22] is believed to be due to the inadequacy of the simple assumptions underlying Equation [5-23] to incorporate all the essential elements of the failure process. For example, one of the factors that was neglected in the derivation was the general material degradation ahead of the crack tip, which will be proportional to creep rate. Also, the more the crack blunting, the more the degree of this degradation. The additional factor which would bring Equations [5-17] and [5-23] in line can be written as $(\dot{\epsilon}_c)^{-y}$ where y is small. Note also that the regression (Figure 5-16) used the actual creep rates, whereas, Equation [5-23] implies the predicted values.

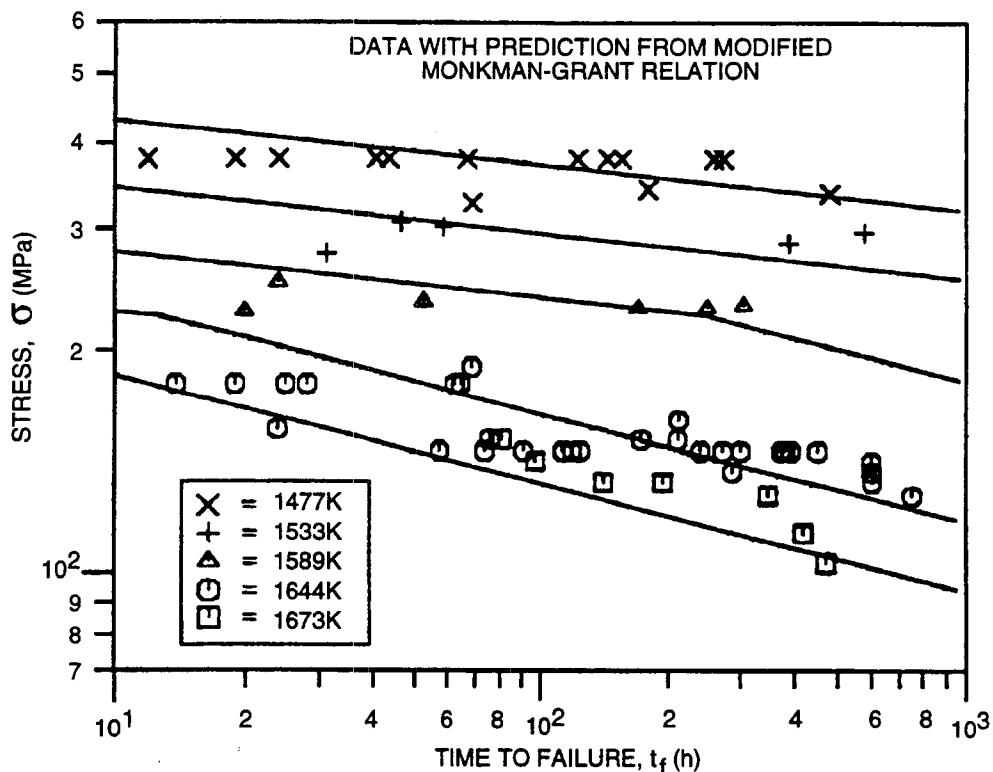
Another assumption involved in the above derivation was that all life is propagation and that there is no initiation period for the flaws or defects before they begin to propagate. It is quite conceivable that, except for cases involving large flaws, there is a "crack initiation" period in NT154, which could involve development of "subcracks", first, within the pockets of smaller equiaxed grains (see section 4.4.1 for microstructural details) where creep damage and crack openings could occur more easily, before the formation of a well-defined crack. However, even if the basic assumption of crack propagation from the beginning of loading may need to be modified in the future, the present results emphasize that the processes leading to crack initiation may follow a similar equational form since the overall equation explains the stratification in Monkman-Grant lines. Thus, until the crack growth mechanisms are more fully understood, the modified Monkman-Grant relations (Equations [5-15] and [5-17]), may serve as adequate interim expressions for prediction of NT154 stress rupture life.

It is possible to arrive at Equation [5-15] by assuming that the temperature dependence, instead of the stress dependence, of the failure process is different from that for creep, i.e., Q' is less than Q . This can easily be shown by substituting Q' for Q in Equation [5-21], and assuming that z is equal to n . The high local stresses at the crack tip could lower the effective activation barrier for matter transport. As mentioned earlier, however, the two assumptions are related and not independent of each other, if creep rate is used for correlation of the stress rupture life. Note that our results and the Monkman-Grant lines comprise both surface-initiated as well as internally-initiated failures, the latter taking place under an inert environment. It is less likely for the stress dependence to be affected by the environment than the temperature dependence, since the latter involves diffusion. Activation energy is more likely to be affected by such processes as oxidation.

The purpose of the above discussion was simply to show that a crack-growth-based approach is consistent with the empirical modifications suggested in Equations [5-15] and [5-17]. It was not meant to be, by any means a rigorous formalism, as it involved many assumptions. It is interesting to note that at least the general form of the equations, proposed as modifications of the Monkman-Grant relation (Equation [5-15] or [5-17]), is justified. The above reasoning thus provides the explanation for the stratification in the Monkman-Grant lines, which is as follows: For the specific value of creep rate, lives are higher at the higher temperatures because stresses are lower. Because the stress dependence of the failure process is higher than for creep, creep rate alone is insufficient for correlating the rupture life. Thus, lower stresses at the higher temperatures should result in higher lives, or alternatively, the higher stresses at the lower temperatures should result in lower lives, than a correlation with creep rate alone would predict. Note that crack blunting is not a requirement for the stratification to occur. However, it would explain the extra term $(\dot{\epsilon}_c)^{-\gamma}$ needed to reconcile Equations [5-17] and 5-23], if it is assumed that damage ahead of the crack tip is a substantial contribution to crack growth.

The above discussion brings to light the distinction that is often made in the literature (ref. 5-45 through 5-47) between SCG and creep as being two distinct regimes for silicon nitrides. A change in slope in a plot of stress versus failure time is often taken as an indication of a possible change in failure mode and a support for this distinction. Figure 5-19 shows the prediction from the modified Monkman-Grant relation, Equation [5-15], along with the unmodified rupture data. The data shows a change in slope between the two regimes, i.e., at $< 1315\text{C}$ and at $> 1315\text{C}$. The average lines predicted by the modified MG relation also show this change in slope in the same temperature regime. Since the MGP lines are linear with creep rate (Figure 5-15), a change in stress dependence of secondary creep rate at a temperature $> 1315\text{C}$ ought to effect a change in slope in the predicted lines also in Figure 5-19. This is what is, in fact, observed. These results also suggest that the stress dependence of the crack growth process is related to that of creep.

Traditionally, failure by creep would have meant a specimen failing from general and uniform degradation involving cavitation or microcracks, or from creep straining. In either case, the fracture is considered to follow the criterion of limit load. The evidence gathered on NT154 shows that even under creep conditions, subcritical crack growth could manifest as the failure mode. SCG was the failure mode under all the conditions tested in the present case, although creep deformation is occurring concurrently. The localization of damage in the form of a crack is what seems to prematurely cause failure in NT154. Hence, the distinction often made between an SCG regime and a creep regime would be arbitrary for NT154, and creep cannot be considered as a true "failure mode" in the range of temperatures tested in the present case.



GC11591-519

Figure 5-19. Rupture Data Plotted Versus Predictions From The Modified Monkman-Grant Relation.

Since the Monkman-Grant relationship has been cited by many authors (ref. 5-4, 5-5, 5-7) as applicable to prediction of rupture life in silicon nitrides, it may be worthwhile to recap the conditions under which the relationship may be expected to hold. First, if the processes leading to failure are general and non-localized in nature, such as general and uniform cavitation, the material may obey an unique relationship, and may follow a strain criterion as well, barring slight differences due to differences in the applied stresses. Here, the failure need not occur by SCG of a well-defined crack. Second, for a specimen failing by SCG, if there is no difference, in essence, between the processes leading to creep strain and that contributing to SCG, then also the Monkman-Grant relationship may be expected to hold. Where there is a difference in the mechanisms between the two, however, a stress as well as a temperature dependence of the Monkman-Grant lines can in general be expected.

5.1.5.9 Stress Rupture Prediction Using Empirical Time-Temperature Parameters

In addition to the Monkman-Grant relation, attempts to correlate empirically the stress rupture data by means of some of the time-temperature parameters (ref. 5-32) may prove equally successful, in view of the fact that some of these parameters is related to or can be derived from a modification of the Monkman-Grant relation itself. Conway (ref. 5-32) explains the basis for some of these parameters, and Jones (ref. 5-33) uses one of these for correlation of flexure data for silicon nitrides.

In this section, an approach which uses one of these parameters will be examined from the point of view of its ability to predict stress rupture life of NT154.

5.1.5.9.1 Orr-Sherby-Dorn Parameter

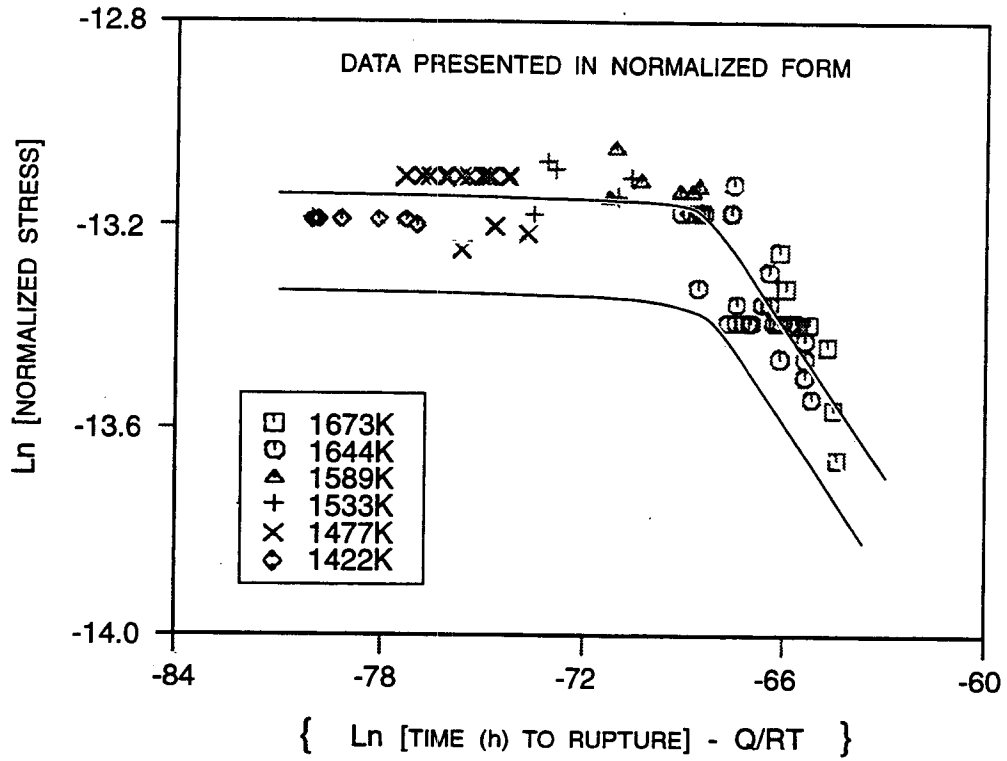
The Orr-Sherby-Dorn (OSD) parameter is defined as $t_r e^{-Q/RT}$ (ref. 5-48, 5-32). In creep of metals, where this parameter was first employed, Q referred to the activation energy for creep, which dictated the time to a particular level of creep, as well as to rupture. Then, a plot of stress, σ , versus OSD parameter involving rupture time is supposed to provide a unique curve independent of temperature. This, in fact, would be true only if no other mechanism intervenes in the rupture of the material. We have noted, however, in Section 5.1.5 that mechanism of rupture in NT154 is SCG, which has a different stress dependence than that for creep. Hence, a modification to the original form of the OSD parameter would be necessary to correlate the failure times, similar to the one employed for modifying the original Monkman-Grant relation in Section 5.1.5.3. The equation that correlates σ to t_r and T will have the following form:

$$\ln(\sigma/E) = A_0 + A_1 \Psi + A_2 \sqrt{[(\Psi - \Psi_1)^2] + \Psi_2} + A_3/T \quad [5-24]$$

where: Ψ is the log of the OSD parameter value, defined as: $\Psi = [\ln(t_r) - (Q/RT)]$. Ψ_1 and Ψ_2 , along with A_0 , A_1 , and A_2 are constants. Ψ_1 defines the value of Ψ in the plot at which bilinearity occurs. This bilinearity in the OSD plot is believed to be due to the bilinearity in the stress dependence of creep rate.

5.1.5.9.2 Results

Figure 5-20 shows the correlation. The plot includes not only all the data shown in Figure 5-19, but also the data generated at 1149C, for which creep strains could not be reliably measured. Figure 5-21 shows the predicted lines for the individual temperatures and the unmodified data. Table 5-6 provides the regression values for the constants. SEE is the standard error of estimate on $\ln(\sigma/E)$ for the regression.



GC11591-520

Figure 5-20. Model Based On OSD Parameter For Rupture Strength.

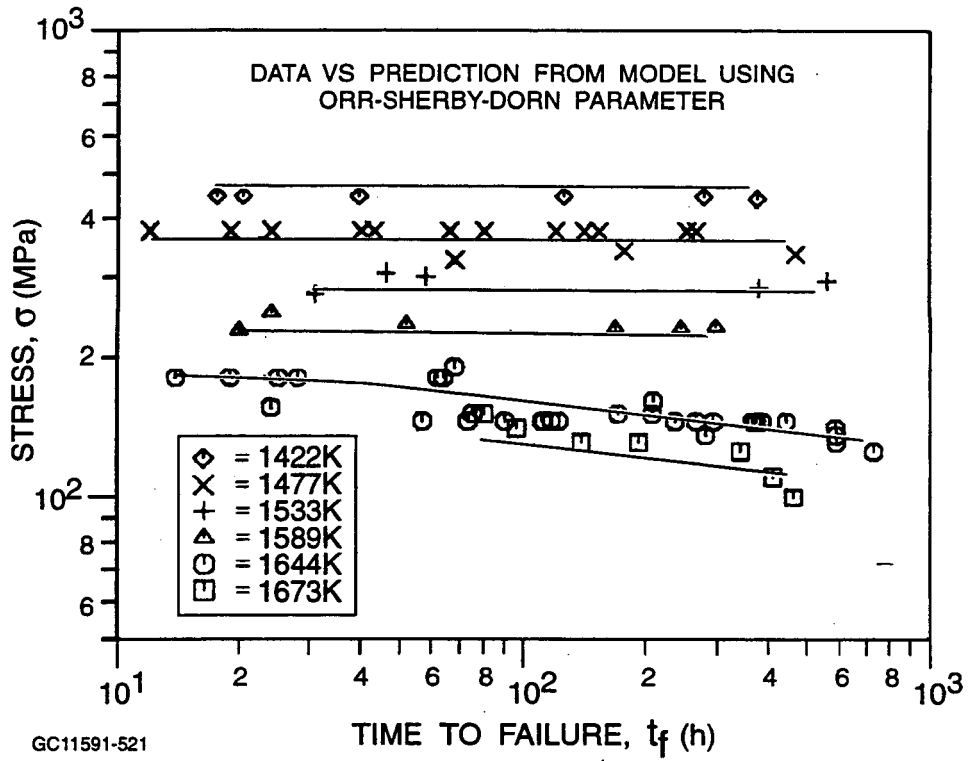


Figure 5-21. Comparison Of Stress Rupture Data With Model Based On OSD Parameter.

TABLE 5-6. COEFFICIENTS FOR THE OSD MODEL

A_0	A_1	A_2	A_3	Ψ_1	Ψ_2	SEE	Q
-16.553	-0.0497	-0.0488	9484	-68.5	0.4	0.066	981

Overall, the OSD parameter is able to correlate the data well. Note that the prediction from the OSD model fits well even the data generated at 1149C. The microstructural observations described in section 4.4.3 showed the presence of lenticular cavities, indicating that creep was occurring even at 1149C. Therefore, the correlation at the lower temperature can be expected.

Figure 5-22 shows a comparison of stress rupture lives predicted by the two models. The lines represent predictions using the OSD parameter; the symbols represent predictions using the modified Monkman-Grant (Equation [5-15]) relation. The agreement between the two models is good.

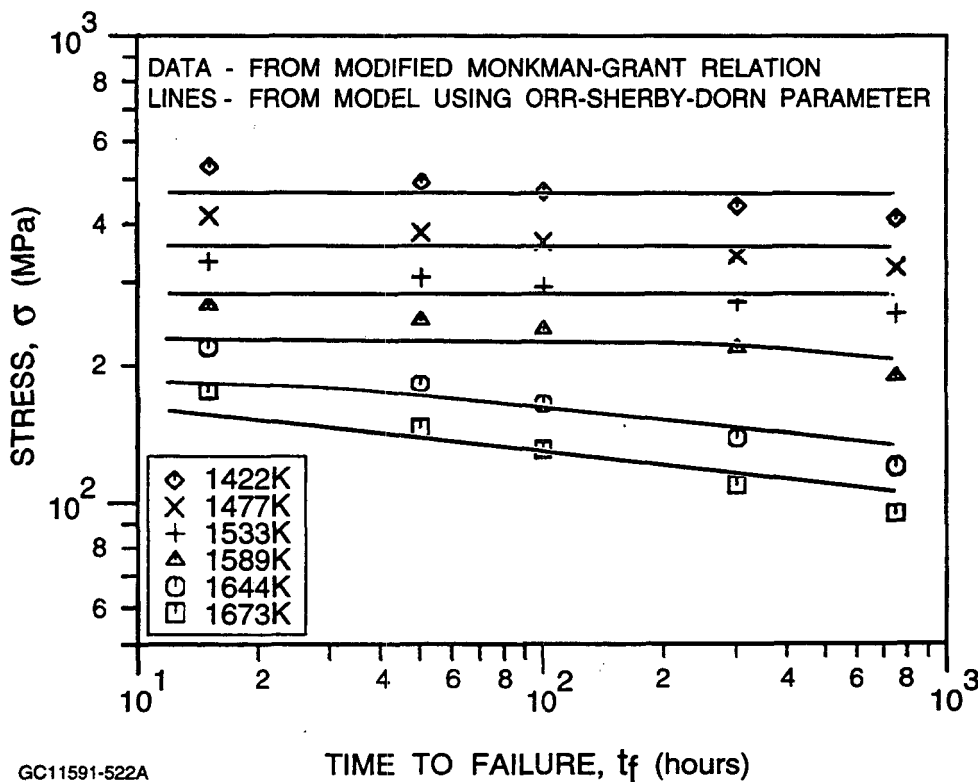


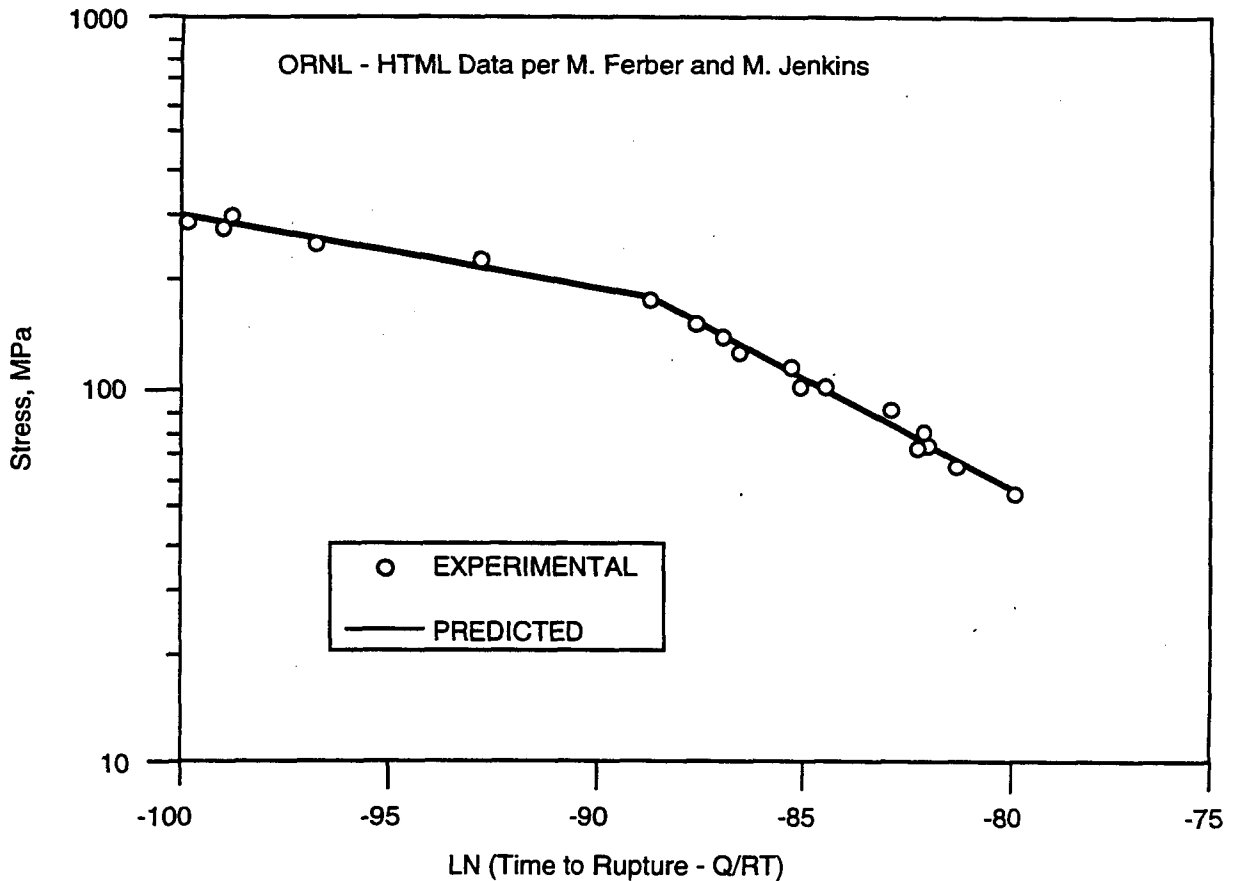
Figure 5-22. Comparison Of Rupture Strength Predictions From Modified Monkman-Grant Relation Versus Model Based On OSD Parameter.

Ferber (ref. 5-49) has applied this approach to the rupture data generated on PY6 silicon nitride. Figure 5-23 shows excellent correlation of that data using the OSD parameter.

5.1.5.10 Stress Rupture: Additional Observations

5.1.5.10.1 Scatter in Stress Rupture Data

Stress rupture data at 1149C (2100F), 1204C (2200F), and 1371C (2500F) are shown in Figures 5-24 through 5-26. The scatter in the data is most easily observed in the constant-stress replicate tests. Scatter over three orders of magnitude at 1149C and 1204C was observed; at 1371C, the scatter was narrower than those at lower temperatures. In general, the scatter decreased with increasing temperature.



GC11591-523

Figure 5-23. Stress Rupture Model Based On OSD Parameter For PY6 Silicon Nitride (Ref. 5-49).

1149C (2100F) STRESS RUPTURE DATA

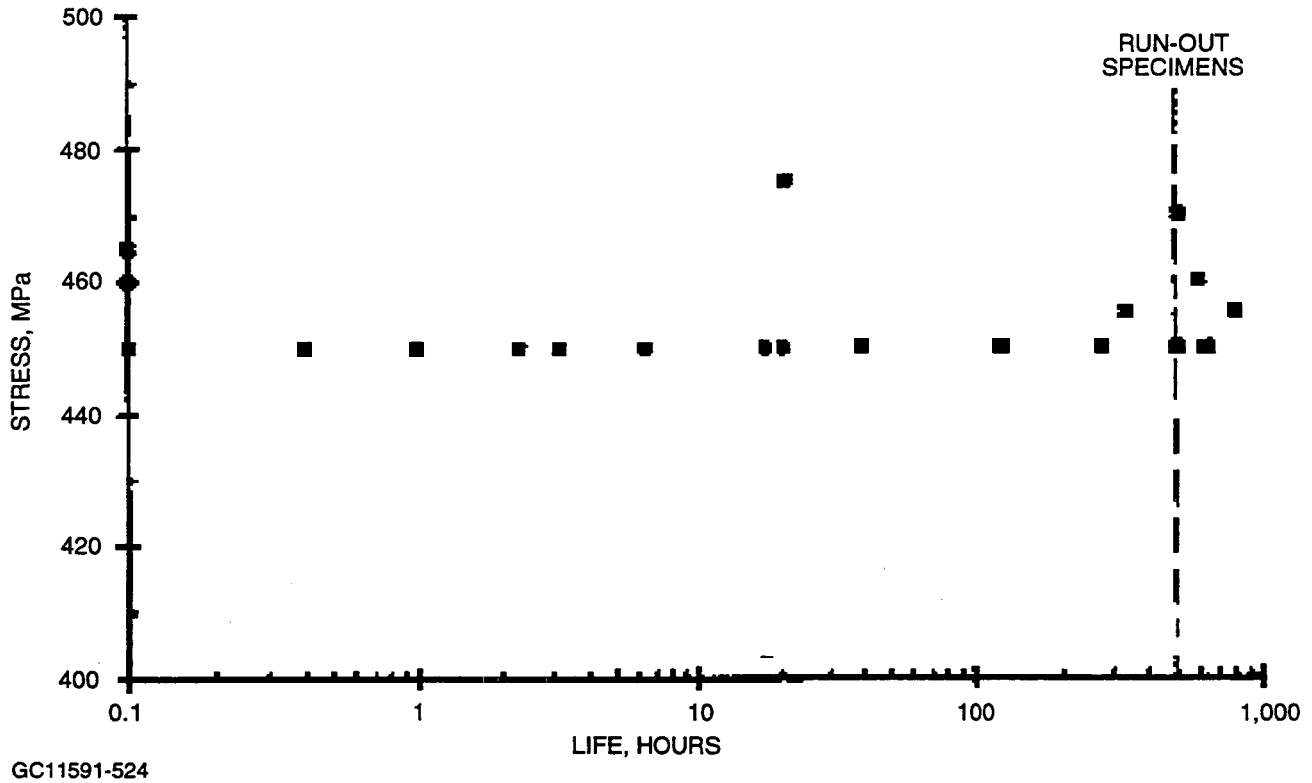


Figure 5-24. Stress Rupture Data At 1149C (2100F) Showing A Wide Scatter. (Replicate Tests Conducted At 450 MPa.)

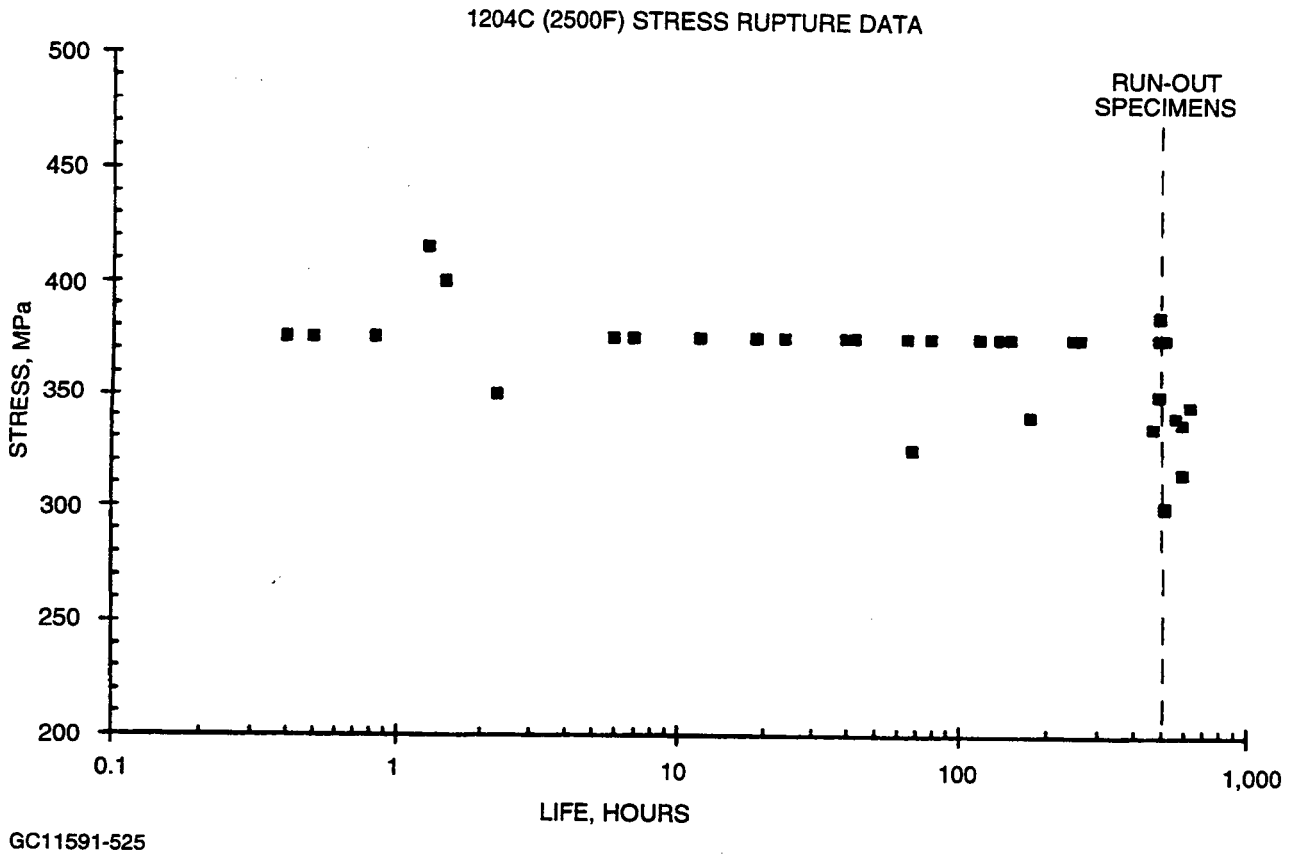
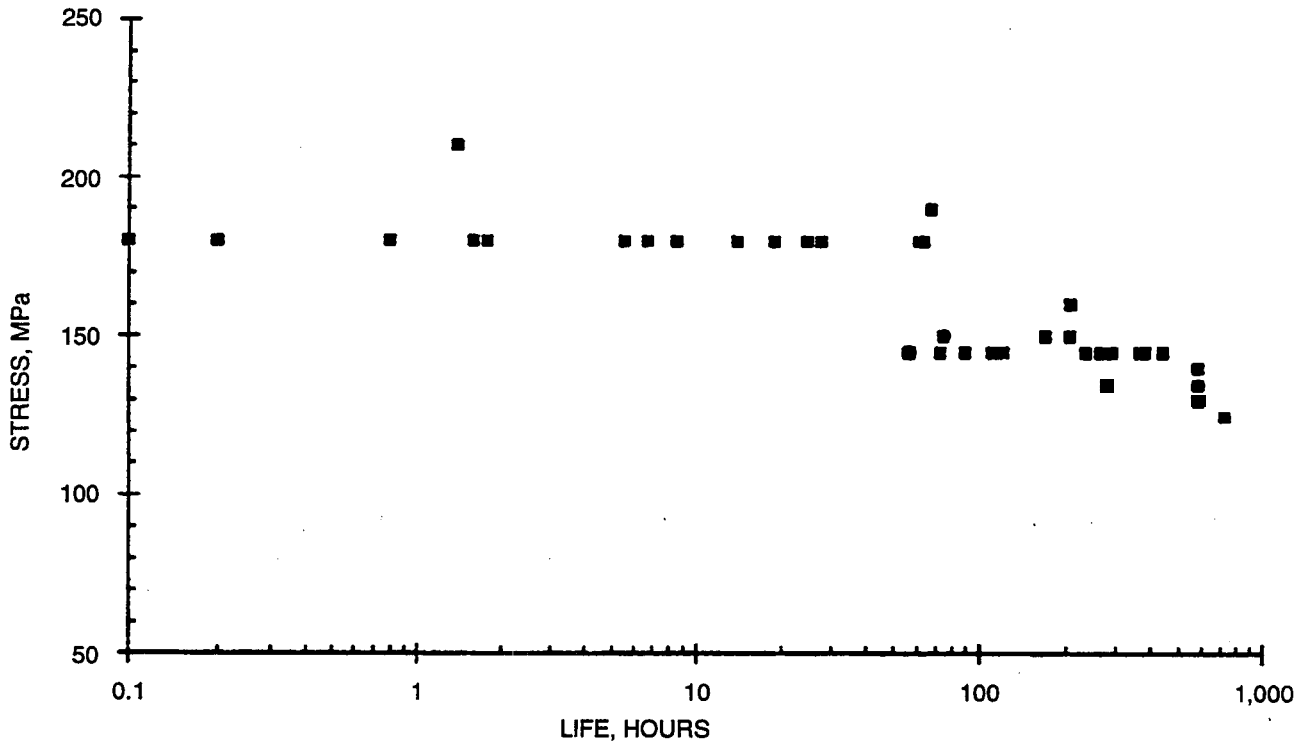


Figure 5-25. Stress Rupture Data At 1204C (2200F) Showing A Wide Scatter. (Replicate Tests Conducted At 375 MPa.)

1371C (2500F) STRESS RUPTURE DATA



GC11591-526

Figure 5-26. Stress Rupture Data At 1371C (2500F). (Replicate Tests Conducted At 180 And 145 MPa.)

The scatter in the stress rupture life can be correlated to the fast fracture strength if the same flaw population controls both fast fracture and stress rupture. This will be the basis for the Subcritical Crack Growth (SCG) approach to component stress rupture prediction discussed in Section 5.2.

5.1.5.10.2 Failure Strain Versus Stress Rupture Life

It was pointed out in Section 5.1.5.3 that NT154 does not follow a strain criterion for failure in creep; i.e., failure does not occur at a constant accumulated strain. Figure 5-17 showed that the failure strain is a function of the applied stress, independent of temperature. In addition, at a given temperature and stress, the failure life is a function of the accumulated strain. This is most evident in the failure strain vs. life data plot at 1371C (2500F) from the constant load replicate tests performed at 145 and 180 MPa, as shown in Figure 5-27. The data from the the two stress levels merge together, indicating that for a given specimen, the failure life is dependent on the amount of accumulated strain in the specimen. The role of applied stress is to determine the mean level of the accumulated strain. A composite plot of the data from 1204C (2200F) to 1371C (2500F) shows similar trends, as shown in Figure 5-28.

The above observation indicates that the scatter in lives at a given applied stress level may be a function of the strain capability variation in the specimens.

5.1.5.10.3 Surface Versus Volume-Initiated Failures

A summary of the failure origins in the stress rupture tests is shown in Tables 4-4 and 4-6. A similar table of failure origins in the smooth fast fracture tensile tests is shown in Appendix IV Table 5.

In the fast fracture tensile tests, the proportion of surface-initiated failures decreased with increasing temperature. However, in the stress rupture tests, the proportion of surface-initiated failures increased with increasing temperature. Furthermore, at least at 1371C (2500F), the proportion of surface-initiated failures increased with decreasing stress level (the replicate specimens tested at 180 MPa showed 75 percent surface failures, while 100 percent of the specimens tested at 145 MPa showed surface failures). This trend probably also holds true at other temperatures.

The different proportions of stress rupture surface and volume-initiated failures compared to those of room-temperature fast fracture tests may be caused by:

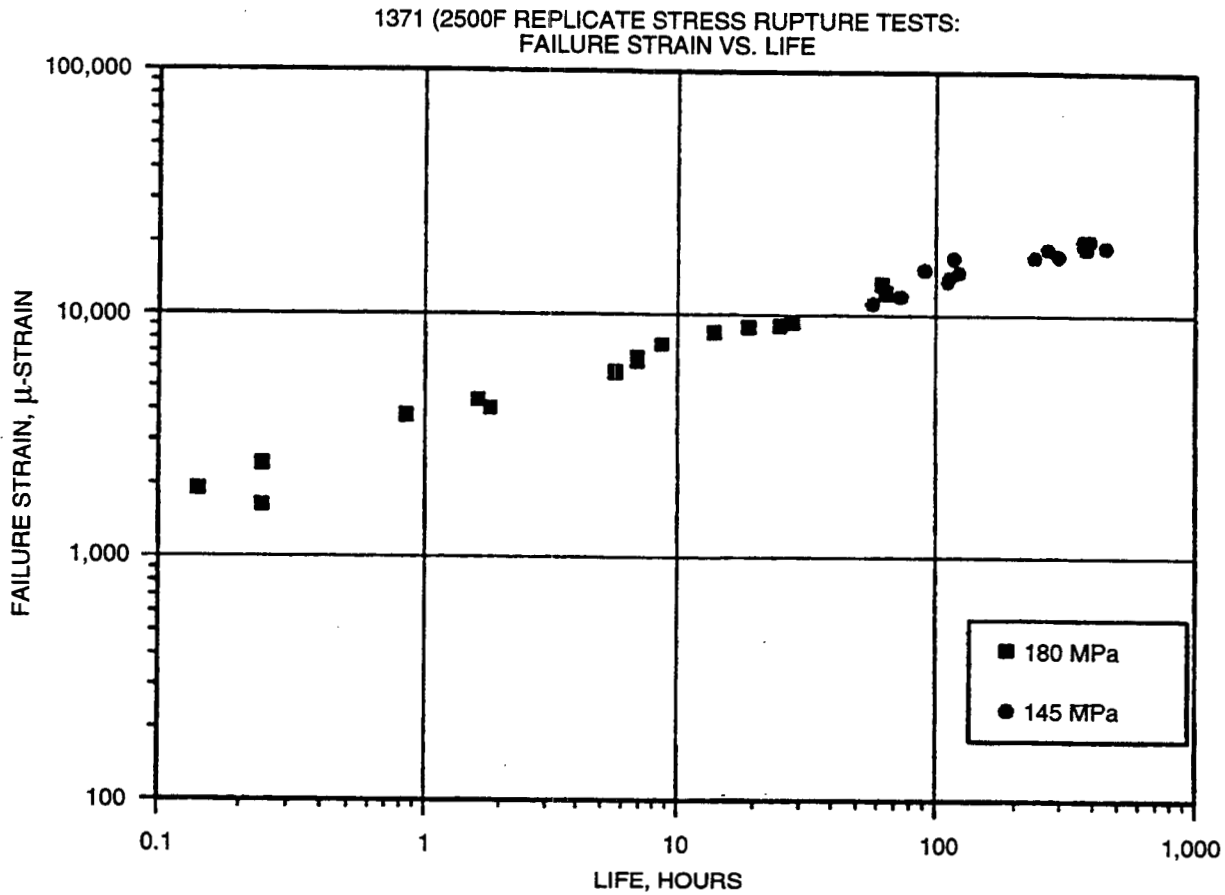
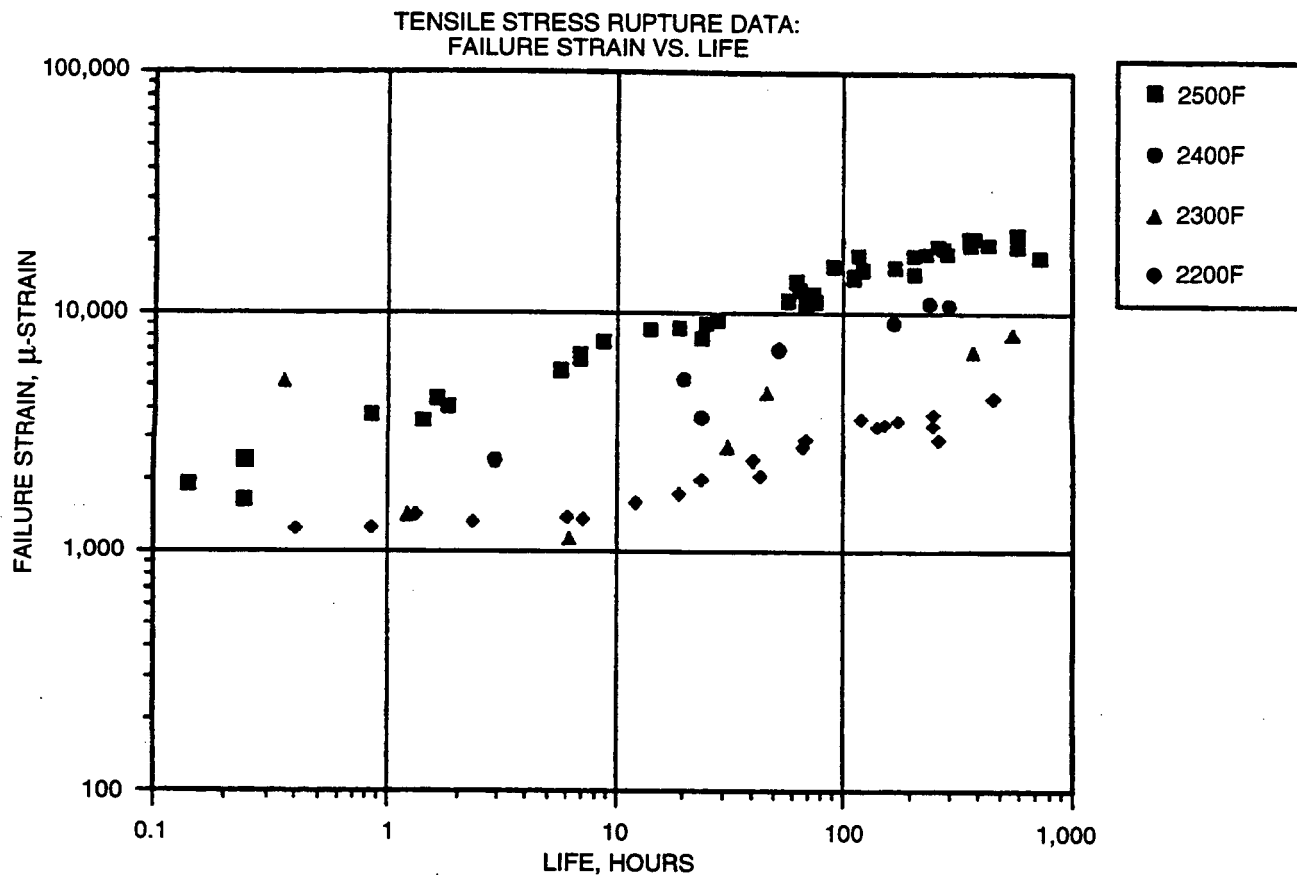


Figure 5-27. Failure Strain Versus Stress Rupture Life From The Replicate Tests Conducted At 1371C (2500F).



GC11591-528

Figure 5-28. Failure Strain Versus Stress Rupture Life Over Temperature Range 1204C To 1371C (2200F To 2500F).

- (1) Different active flaw populations under fast fracture and stress rupture, especially at higher temperatures where creep takes place, e.g., volume flaws may be rendered inoperative due to crack blunting;
- (2) Different rates of surface and volume flaw growth.

The second possibility can be addressed via censoring of fast fracture and stress rupture data to obtain true estimates of fast fracture and stress rupture distributions that can be used to derive the slow crack growth parameters. This approach will be discussed in more detail in Section 5.2.

5.1.5.11 Conclusions

The Monkman-Grant relationship was examined from the point of view of its applicability to the prediction of stress rupture life of NT154 silicon nitride. It was found that the Monkman-Grant relation for NT154 is a function of both temperature and stress, and that the original Monkman-Grant expression needs to be modified for application to rupture life prediction for the present material. The stratification in the Monkman-Grant lines can be explained based on a crack-growth-based approach. The results point to a failure process in which the stress dependence of the failure process is higher than that for creep.

The modified Orr-Sherby-Dorn (OSD) parameter, a time-temperature parameter, was also successful in modeling the mean behavior of the NT154 stress rupture specimen data over the time-temperature regime tested.

Both the Monkman-Grant and the modified Orr-Sherby-Dorn approaches consider only material behavior under uniaxial loading and in the size ranges of the specimens tested. The predictions from the models would not be applicable when component stress states and sizes are significantly different from that of the specimens. For component design, the mean behavior, the scatter in material response, and size scaling need to be considered. The insights gained from the material behavior observations and modeling will be utilized. This will be discussed further in Section 5.2.

5.2 Life Prediction Methods And Verification

5.2.1 Weibull Strength Model Applied To Structural Ceramics

The increasing use of ceramics as structural components places an ever-more important emphasis on the development of theories and tools for life prediction and reliability assessment of ceramic components.

Ceramic materials are noted for their wide variability of strength amongst seemingly identical specimens and on the dependence of strength on the size of the specimen tested. Based on these observations, in 1939 Weibull developed the first theory of brittle fracture (ref. 5-50). In that paper, Weibull introduced models for uniaxial and multiaxial states of stress. The uniaxial model described by Equation [5-25] received wide acceptance; however, the multiaxial model raised controversy and opened the door to an extensive wave of ideas that followed. The most important of these ideas are addressed in the following section.

$$P_f = 1 - \exp - \int_V \left(\frac{\sigma}{\sigma_o} \right)^m dV \quad [5-25]$$

Weibull developed his theory based on the notion that material strength was not a constant, that instead, strength was a random variable, as shown by the strength of otherwise identical specimens. Furthermore, by applying the weakest-link theory, Weibull showed that the strength of a component should be a function of its size. These developments provided the solid ground on which the Weibull Brittle Strength theory now stands.

In weakest-link theory it is assumed that failure may be caused by independent and mutually exclusive events, each with a given probability of failure. This can be described as a system that looks and behaves like a chain; each of the chain links would be considered a possible event and the failure of any of the links in the chain would cause failure of the whole system. Now assume that a large number of (seemingly) identical chains are tested and failure of each one of the chains occurs from the weakest of the links in the chains. Then the statistics and distribution of these chain failures will be those for the distribution of the weakest links. The Weibull distribution has been proven to represent the distribution of a broad range of brittle materials very successfully. The Weibull distribution is a type II extreme value distribution of minima, and as such has the proper limiting conditions to represent the distribution of the weakest-link system.

5.2.2 Multiaxial Fracture And Anisotropic Flaw Distribution

5.2.2.1 Multiaxial Fracture

Among the better-known theories of brittle fracture under multiaxial stresses are those developed by Batdorf and coworkers (ref. 5-51, 5-52) and Evans (ref. 5-53). The theories developed by Batdorf and Crose (ref. 5-51) and Batdorf and Heinisch (ref. 5-52) assume that the failure origins are from randomly-oriented and randomly-distributed microcracks. In contrast, Evans' theory assumes that the material has an elemental strength which characterizes the distribution of flaws in the material. These two different approaches have been proven to be

the same for the same fracture criterion, numerically by Chao and Shetty (ref. 5-54) and analytically by Tucker and Johnson (ref. 5-55). From this point on, the derivations based on Evans' approach will be followed, because this simplifies the formulation of the problem.

The theories of Evans and Batdorf and coworkers emphasized fracture for volume-distributed flaws; the mathematical formulation can be written in the form of Equation [5-26].

$$P_f = 1 - \exp \left\{ -\frac{1}{4\pi} \iiint_V \int_0^{2\pi} \int_{-\frac{\pi}{2}}^{\frac{\pi}{2}} \frac{\sigma_E^m(x, y, z, \phi, \psi)}{\sigma_o^m} \cos \phi d\phi d\psi dV \right\} \quad [5-26]$$

Later, Batdorf and Heinisch (ref. 5-56) developed an approach for fracture of surface-distributed flaws; the representation for this theory would be written in Evans formulation in the form of Equation [5-27].

$$P_f = 1 - \exp \left\{ -\frac{1}{2\pi} \iint_A \int_0^{2\pi} \frac{\sigma_E^m(x, y, \theta)}{\sigma_o^m} d\theta dA \right\} \quad [5-27]$$

By following the same approach employed for volume and surface failure modes, an expression can be developed for a corner (or edge) failure mode, and the probability of failure is represented by Equation [5-28].

$$P_f = 1 - \exp \left\{ -\int_L \int_0^{2\pi} \frac{\sigma_E^m(l, \theta)}{\sigma_o^m} \delta(\theta) d\theta dl \right\} \quad [5-28]$$

where $\int_0^{2\pi} \frac{\sigma_E^m(l, \theta)}{\sigma_o^m} \delta(\theta) d\theta = \frac{\sigma_E^m(l)}{\sigma_o^m}$ is from the definition of the delta function.

A corner failure mode has a dimensionality of one, as compared to two for surface and three for volume. Equation [5-28] is determined by representing the spatial integration of the corner failure mode by a point; a delta function representation, in contrast to a line integral for surface failure mode; and a surface integral for volume failure mode. The spatial integration, or orientation distribution, over a point is along only a single direction, which is the direction along the corner in question. Since the stress at a corner is parallel to the corner and its spatial integration is along this same direction, it integrates to unity in all cases, which can be effectively dropped from Equation [5-28] to yield a much simpler expression, Equation [5-29].

$$P_f = 1 - \exp \left\{ - \int_L \frac{\sigma_E^m(l)}{\sigma_o^m} dl \right\} \quad [5-29]$$

In order to simplify the above equations, using the notation of Evans and Batdorf, with the redefinition by Tucker and Johnson (ref. 5-55), define the following terms:

$$I_V = \frac{1}{4\pi V} \iiint_V \int_{-\frac{\pi}{2}}^{\frac{\pi}{2}} \int_0^{2\pi} \frac{\sigma_E^m(x, y, z, \phi, \psi)}{\sigma_{\max}^m} \cos \phi d\phi d\psi dV \quad [5-30]$$

$$I_A = \frac{1}{2\pi A} \iint_A \int_0^{2\pi} \frac{\sigma_E^m(x, y, \theta)}{\sigma_{\max}^m} d\theta dA \quad [5-31]$$

$$I_C = \frac{1}{L} \int_L \frac{\sigma_E^m}{\sigma_{\max}^m} dL \quad [5-32]$$

Equations [5-30] through [5-32] are referred to as the multiaxial and stress gradient factors. They summarize, in a single term, the effect of the multiaxial stress field, the stress gradient, and the chosen failure criterion on the reliability of a component. Note that these factors are a function only of the first Weibull parameter, m . With these definitions, Equations [5-26], [5-27] and [5-29] can be rewritten in the following manner:

$$P_f = 1 - \exp \left\{ -I_V V \left(\frac{\sigma_{\max}}{\sigma_o} \right)^m \right\} \quad [5-33]$$

$$P_f = 1 - \exp \left\{ -I_A A \left(\frac{\sigma_{\max}}{\sigma_o} \right)^m \right\} \quad [5-34]$$

$$P_f = 1 - \exp \left\{ -I_C L \left(\frac{\sigma_{\max}}{\sigma_o} \right)^m \right\} \quad [5-35]$$

The above equations deal with a term called the effective stress, σ_E , a transformation of a multiaxial stress field, a second order tensor, to a scalar quantity. The rules for transformation follow material behavior laws, the most commonly used ones are based on fracture mechanics and energy principles. An excellent compilation of the most commonly used ones is found in the CARES computer code users manual (ref. 5-57). In our analyses, we have used the form proposed by Shetty (ref. 5-58), Equation [5-36]:

$$\sigma_E = \frac{1}{2} \left[\sigma_N + \sqrt{\sigma_N^2 + \frac{4\sigma_\tau^2}{C^2}} \right] \quad [5-36]$$

Equation [5-36] is derived from fracture mechanic principles where σ_N is the stress normal to the crack plane and σ_τ is the stress parallel to the plane. Shetty's equation assumes failure of a crack-like flaw by a combination of modes I, II and/or III. Bounded values of C imply shear-sensitive materials; unbounded values, $C = \infty$, imply insensitive materials. Shear-sensitive materials are those that can fail in mode II and mode III, shear insensitive are those that will only fail in mode I. For a volume failure mode, the normal stress, σ_N , in Equation [5-36] can be described in terms of the principal stresses as shown by Equation [5-37], using spherical coordinates as shown in Figure 5-29(a).

$$\sigma_N = \sigma_1 \ell_1^2 + \sigma_2 \ell_2^2 + \sigma_3 \ell_3^2 \quad [5-37]$$

where: $\ell_1 = \cos \phi \cos \psi$

$$\ell_2 = \cos \phi \sin \psi$$

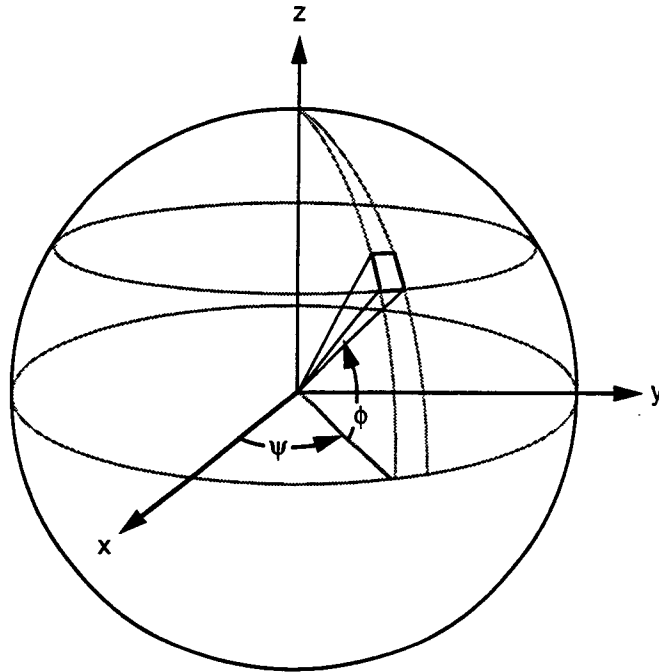
$$\ell_3 = \sin \phi$$

and $\sigma_1, \sigma_2, \sigma_3$ are the maximum principal stresses.

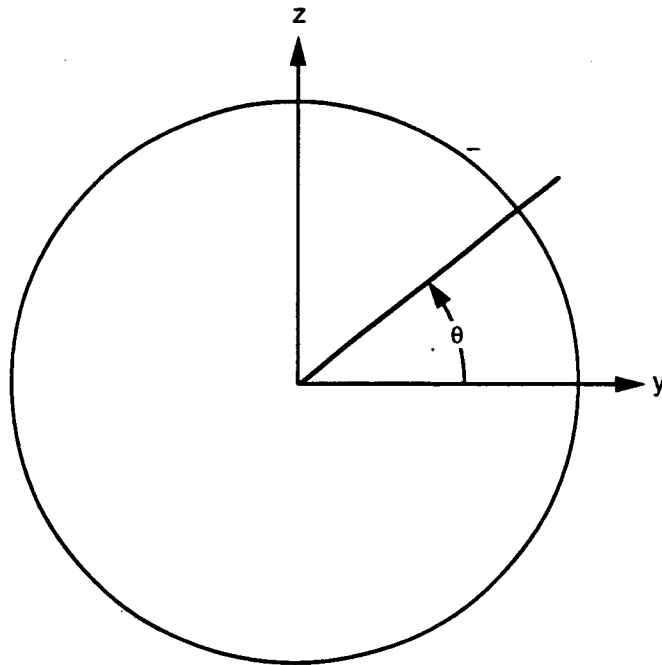
The mode II and mode III shear stress, σ_τ , can also be described in terms of the principal stresses, as shown in Equation [5-38]. For a surface failure mode, the normal and shear stresses are described by Equations [5-39] and [5-40] and the coordinate system in Figure 5-29(b).

$$\sigma_\tau^2 = (\sigma_1 \ell_1)^2 + (\sigma_2 \ell_2)^2 + (\sigma_3 \ell_3)^2 - [\sigma_1 \ell_1^2 + \sigma_2 \ell_2^2 + \sigma_3 \ell_3^2]^2 \quad [5-38]$$

which is equivalent to: $\sigma_\tau^2 = [(\sigma_1 - \sigma_2) \ell_1 \ell_2]^2 + [(\sigma_2 - \sigma_3) \ell_2 \ell_3]^2 + [(\sigma_3 - \sigma_1) \ell_3 \ell_1]^2$



A) VOLUME FAILURE MODE



B) SURFACE FAILURE MODE

GC11591-529A

Figure 5-29. Coordinate Axes For Spatial Integration. (a) Volume Failure Mode; (b) Surface Failure Mode.

$$\sigma_N = \sigma_1 \ell_1^2 + \sigma_2 \ell_2^2 \quad [5-39]$$

where: $\ell_1 = \cos \theta$

$$\ell_2 = \sin \theta$$

$$\sigma_r = (\sigma_1 - \sigma_2) \ell_1 \ell_2 \quad [5-40]$$

5.2.2.2 Anisotropic Flaw Distributions

Surface characteristics play an important role in the strength of ceramic components. It is well known that specimens with as-processed surfaces exhibit significantly different strength than specimens with machined surfaces. In the same manner, it is well known that bend test specimens (3- or 4-point) with surfaces machined in the longitudinal direction exhibit significantly different strength than specimens machined in the transverse direction. The developments described in this section are an attempt to describe the effect of machining on the surface strength of ceramic materials. The work by Rice and Mecholsky (5-59 and 5-60), explain that grinding produces two populations of surface flaws: one along the grinding direction and the second perpendicular to it. The surface flaws along the grinding direction tend to be larger and more severe than the flaws in the perpendicular direction.

Evans (ref. 5-53) defines anisotropic strength distributions and describes them as ellipsoidal in nature with relative lengths of the major and minor axes, depending on the distribution and orientation of flaws in each one of the axes directions. In the case of machining damage, flaws are predominantly in the machining direction with secondary flaws perpendicular to this, as described by Rice and Mecholsky (ref. 5-59 and 5-60). These two concurrent flaw orientations may be assumed to be independent; thus the probabilistic statement for a flaw distribution oriented in a single direction can be derived by replacing the uniformly-distributed flaw distribution function by a new function. The function must satisfy the following requirement: it must integrate to unity over its domain. A suitable function is the delta function. Using this function in Equation [5-27], or equivalently in [5-31], Equations [5-41] and [5-42] are obtained:

$$P_f = 1 - \exp \left\{ - \frac{1}{2\pi} \iint_A \int_0^{2\pi} \frac{\sigma_E^m(x, y, \theta)}{\sigma_o^m} \delta(\theta - \theta_o) d\theta dA \right\} \quad [5-41]$$

$$I_A = \frac{1}{2\pi A} \iint_A \int_0^{2\pi} \frac{\sigma_E^m(x, y, \theta)}{\sigma_{\max}^m} \delta(\theta - \theta_o) d\theta dA \quad [5-42]$$

Carrying the integration a step further, Equation [5-42] can be rewritten as follows:

$$I_A = \frac{1}{2\pi A} \iint_A \frac{\sigma_E^m(x, y, \theta_o)}{\sigma_{\max}^m} dA \quad [5-43]$$

Equation [5-43] indicates that the spatial integration does not need to be performed for the case of anisotropic flaw distributions. The probability of failure is only a function of the effective stress on the face of the flaw produced by the machining direction, θ_o .

5.2.3 Maximum Likelihood Parameter Estimation Methods

In this section, maximum likelihood methods are presented and used to estimate the parameters of the Weibull distribution. This is accomplished by determining those parameter values that maximize the sample likelihood or the sample log likelihood. For a detailed account of these methods, refer to Nelson (ref. 5-61). The likelihood is a function of the assumed distribution, the parameters of the distribution, and the data. It is defined as the product of the probability density function of the distribution for each observed strength value. The log likelihood is the logarithm of the likelihood function. The Weibull distribution for ceramic components using the form of Equations [5-33] through [5-35] is given by Equation [5-44]; the likelihood and log likelihood are given by Equations [5-45] and [5-46]:

$$f(\sigma_i) = m I_i V_i \sigma_o^{-1} \left(\frac{\sigma_i}{\sigma_o} \right)^{m-1} \exp \left\{ -I_i V_i \left(\frac{\sigma_i}{\sigma_o} \right)^m \right\} \quad [5-44]$$

$$L(m, \sigma_o) = \prod_{i=1}^n f(\sigma_i, m, \sigma_o) \quad [5-45]$$

$$l = \sum_{i=1}^n \ln I_i + \sum_{i=1}^n \ln V_i + n \ln m + (m-1) \sum_{i=1}^n \ln \sigma_i - nm \ln \sigma_o - \sum_{i=1}^n I_i V_i \left(\frac{\sigma_i}{\sigma_o} \right)^m \quad [5-46]$$

The parameters of the distribution, m and σ_o , that maximize the log likelihood function are known as the maximum likelihood estimates, \hat{m} and $\hat{\sigma}_o$. These estimates can be obtained by differentiating the log likelihood function and forming two equations, one with respect to m and the second with respect to σ_o and setting them equal to zero:

$$\frac{\partial l}{\partial m} = 0, \quad \frac{\partial l}{\partial \sigma_o} = 0 \quad [5-47]$$

The solution of these equations is presented in the following section.

5.2.3.1 Pooled Data Specimens With Multiple Sizes And Loadings

Testing of structural ceramics in an effort to determine material properties is an expensive undertaking, because of the cost of the individual specimens and the number that must be tested in order to obtain accurate and precise estimates of the distribution parameters. This is further exacerbated by the need to determine properties for volume failure modes and the one or more types of surface finishes that may be encountered in a component. Furthermore, it is possible that the more effective way of testing for each of these failure modes requires specimens of different shapes, sizes, and loading conditions. Hence, in the effort to estimate the distribution parameters as accurately as possible, it is necessary to make use of (combine) all available test data in these calculations. Combination of data implies that the distribution parameters are the same from specimen to specimen for a given failure mode. Section 5.2.1 states that specimens of different sizes have different strengths. To reconcile these two situations, the second Weibull parameter, σ_o , is defined as the characteristic strength of an effective unit size specimen.

The first efforts to combine test data from different specimens were accomplished by Batdorf and Sines (ref. 5-62), who used a least-squares analysis in their approach. In 1992, Johnson and Tucker (ref. 5-63) addressed the same problem. In this development, problems were categorized according to the type of loading and size combination. In the process, the following four classes of problems were defined:

- Class I, for data with uniform tensile stress and single specimen size
- Class II, for data with uniform tensile stress and multiple specimen sizes
- Class III, for data with common multiaxial and stress gradient factors and multiple specimen sizes
- Class IV, for data with different multiaxial and stress gradient factors and multiple specimen sizes.

Class IV encompasses Classes I through III and, as such, is the only one addressed here. Class IV problems can be solved by using the definition of the probability of failure as shown by Equation [5-33] where the multiaxial and stress gradient factor, I , captures the effect of the Class IV problems. Hence, in the log likelihood function, I_i represents the multiaxial and stress gradient factor for any specimen size and any loading condition. However, note that the multiaxial and stress gradient factor is a function of the first Weibull parameter, m , as shown in Equation [5-48], and should be treated as a variable in the Equation:

$$I = I(m) \quad [5-48]$$

The equations that result from performing the operations of Equation [5-47] are:

$$\frac{1}{\hat{m}} = \frac{1}{n} \sum_{i=1}^n \left\{ \left(\frac{\hat{I}'_i}{\hat{I}_i} + \ln \sigma_i \right) \left(\frac{n \hat{I}_i V_i \sigma_i^{\hat{m}}}{\sum_{i=1}^n \hat{I}_i V_i \sigma_i^{\hat{m}}} \right) \right\} \quad [5-49]$$

$$\hat{\sigma}_o = \left[\frac{1}{n} \sum_{i=1}^n I_i V_i \sigma_i^{\hat{m}} \right]^{\frac{1}{\hat{m}}} \quad [5-50]$$

where: \hat{m} and $\hat{\sigma}_o$ are the maximum likelihood estimates of Weibull modulus and the second Weibull parameter, respectively, and \hat{I}'_i is the first derivative of \hat{I}_i with respect to \hat{m} . A closed-form solution for \hat{m} from Equation [5-49] is not possible, and an iteration process must be used to find the solution. The solution for $\hat{\sigma}_o$ is straight forward through the use of Equation [5-50].

5.2.3.2 Censored Data

The previous section assumed that all of the specimens failed from the same failure mode, but it is very common to find that among the specimens tested two or more failure modes are present; e.g., failures originate from volume sources for some and from the surface for others. Johnson (ref. 5-64) describes a variety of possible flaw populations that can exist in a set of specimens. In this section, we are concerned only with concurrent flaw populations; those in which several flaw types are present in the same specimen and compete to cause failure.

The strength distribution associated with each of the different flaw populations is described with different sets of Weibull parameters. In order to determine the best estimates of Weibull parameters for a given failure mode, it is necessary to perform censored maximum likelihood analysis. Censored data analysis requires that the fracture origins for each specimen be identified. Identifying fracture origins is a time-consuming, difficult task that requires experience and sophisticated equipment.

Maximum likelihood analysis requires that the likelihood function be defined. The likelihood function for censored data contains the product of the probability density function of the non-censored data and the product of the cumulative density function of the censored data, as shown in Equation [5-51]:

$$L = \prod_{i=1}^r f(\sigma_i) \prod_{j=r+1}^n S(\sigma_j) \quad [5-51]$$

The log likelihood function is given by Equation [5-52]:

$$l = \sum_{i=1}^r \ln \left[m V_i I_i \sigma_o^{-1} \left(\frac{\sigma_i}{\sigma_o} \right)^{m-1} \exp \left\{ -V_i I_i \left(\frac{\sigma_i}{\sigma_o} \right)^m \right\} \right] + \sum_{j=r+1}^n \ln \left[\exp \left\{ -V_j I_j \left(\frac{\sigma_j}{\sigma_o} \right)^m \right\} \right] \quad [5-52]$$

where: r is the number of specimens failed by the flaw population under consideration, and n is the total number of specimens. The number of censored data points is the difference between n and r . $S(\sigma_j)$ is the probability of the flaw type under consideration surviving a stress level of σ_j .

Calculation of the Weibull parameters proceeds similarly to the derivation for the non-censored data. Applying the two parts of Equation [5-47] to Equation [5-52] results in Equations [5-53] and [5-54]:

$$\frac{1}{\hat{m}} = \frac{1}{\sum_{k=1}^n \hat{I}_k V_k \sigma_k^{\hat{m}}} \sum_{k=1}^n V_k \sigma_k^{\hat{m}} \left[\hat{I}'_k + \hat{I}_k \ln(\sigma_k) \right] - \frac{1}{r} \sum_{i=1}^r \left[\frac{\hat{I}'_i}{\hat{I}_i} + \ln(\sigma_i) \right] \quad [5-53]$$

$$\hat{\sigma}_o = \left[\frac{1}{r} \sum_{i=1}^r I_i V_i \sigma_i^{\hat{m}} \right]^{\frac{1}{\hat{m}}} \quad [5-54]$$

Again, a closed-form solution for \hat{m} from Equation [5-53] is not possible, and an iteration process must be used to find the solution. And again the solution for $\hat{\sigma}_o$ is straight forward. Note that non-censored data analysis can be derived from the censored data analysis by assuming that r equals n .

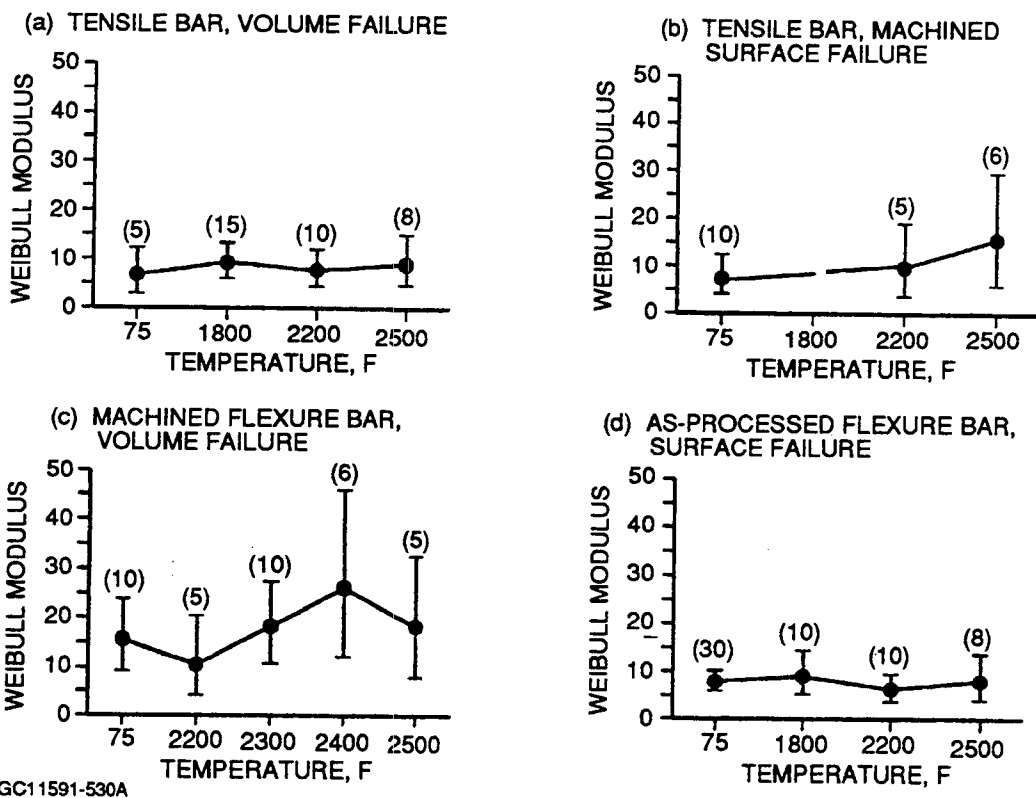
5.2.3.3 Pooled Data From Multiple Test Temperatures

Methods for modeling temperature-dependent strength are important for designing ceramic components for high-temperature engine applications. The method developed in this program is based on the important assumption that the Weibull modulus for a given strength distribution is independent of temperature under fast fracture conditions, and thus only the second Weibull parameter is a function of temperature. This assumption permits a single estimate of the Weibull modulus from data at several temperatures, instead of separate estimates at each temperature. This should provide more precise estimates of strength parameters, as well as more accurate strength-versus-temperature modeling. This new method also offers a practical solution to calculating failure probabilities with confidence intervals for engine components with temperature gradients. At this point, the method being described here only applies to isothermal components.

The assumption that m is independent of temperature is unconventional, but is supported in two ways. The first supporting argument is from analysis of NT154 fast fracture data at varying temperatures as measured by the University of Dayton Research Institute (UDRI) (ref. 5-65) and AlliedSignal Engines during the ATTAP program. Weibull moduli for each failure mode are plotted versus temperature in Figure 5-30. The variation of m with respect to temperature is well within the 95-percent confidence bands for each of the four failure modes analyzed. There is no obvious trend of m to increase or decrease with temperature except for the machined surface. The Weibull modulus for machined surface strength seemed to rise with temperature above 2200F.

Figure 5-31 summarizes Weibull moduli for internal and surface failures for all the specimen groups tested in this program. Here again, all the vertical data lines indicate the maximum likelihood estimate of Weibull modulus and the 95-percent confidence interval. The number of data points in each data group is indicated at the top of each data line. The horizontal axis represents the category of specimen groups. "70F POOLED" denotes the pooled data, consisting of all the room-temperature data points. Likewise, "70-2200F POOLED" denotes all the data from room temperature up to 2200F except the 2200F MIL-B data.

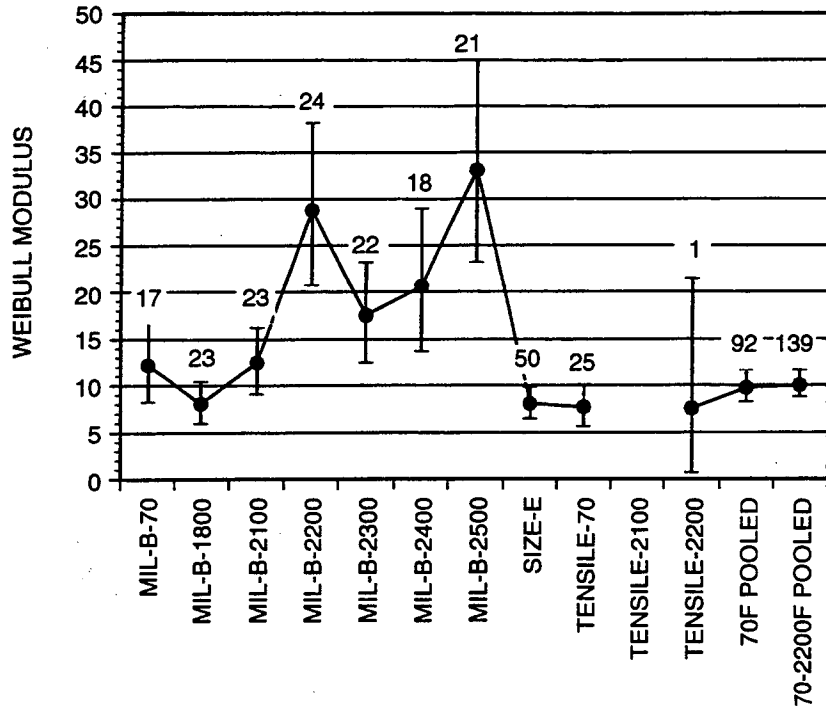
The Weibull moduli for volume failures are in the fairly close range of 8 to 9, except those data groups which had very small sample sizes. The plot for surface failures is more complicated. The surface flaw population from a typical machined surface apparently undergoes significant change at temperatures of 2200F and above. This observation corresponds to the indications from the ATTAP data. One plausible explanation is that some chemical process, most likely oxidization, takes place at a fairly high rate at temperatures above 2200F, and the machined flaws are significantly altered by this chemical process.



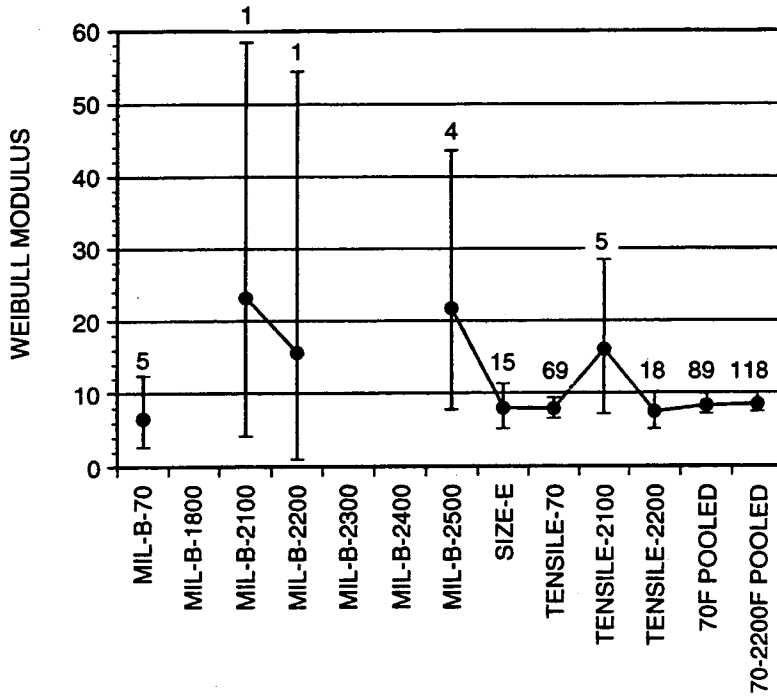
GC11591-530A

Figure 5-30. Weibull Moduli For Several Failure Modes Show No Apparent Temperature Dependence. (ATTAP NT154 Data.)

(A) SURFACE FAILURES



(B) VOLUME FAILURES



* THE NUMBERS ON THE PLOT INDICATE THE NUMBER OF DATA POINTS IN THAT SPECIMEN GROUP

GC11591-531

Figure 5-31. Weibull Moduli For Different NT154 Specimens And Test Temperatures.

The second supporting argument for the assumption of temperature independence of m results from consideration of strength-controlling flaw distributions in the absence of slow crack growth during strength testing, in a material that exhibits linear elastic fracture (no R-curve behavior, etc.). In this case, the m value of a given distribution and its variability are not expected to change by simply increasing the test temperature; therefore, m should not be temperature dependent.

Pooling fracture data from multiple test temperatures is greatly facilitated by this assumption of temperature independence of m . The above arguments support, but do not prove, the validity of the assumption. There are numerous examples of data sets in the literature that suggest a temperature dependence of m . In light of the above discussion, it is proposed that one or more of the following factors are the cause of such observations: slow crack growth during loading; lack of proper censoring of multiple strength distributions; creation of new flaws from oxidation, etc.; temperature-dependent R-curve behavior; and/or insufficient sample size.

Since the Weibull modulus is considered to be temperature independent, more precise parameter estimates can be obtained if the analysis is based on all the data at various temperatures, rather than the data from each temperature separately. In order to perform Weibull analyses with all the strength data pooled together, an additional variable, C , is introduced into the equivalent size and stress state factor I to account for the different characteristic strength at different temperatures. Thus I becomes a function of temperature.

Assume that there are a total of n specimens tested at k different temperatures in a fast fracture test data set and n_j is the number of data points at temperature T_j . I_{ij} is the equivalent stress state factor for the i th specimen at temperature T_j . I_{ij}^* is the temperature-scaled equivalent stress state factor for the i th specimen at temperature T_j . I_{ij}^* is defined as follows:

$$I_{ij}^* = I_{ij}(m)(C_j)^m \tag{5-55}$$

where: $C_j = \sigma_{or} / \sigma_{oj}$; σ_{or} is the characteristic strength at the reference temperature and σ_{oj} is the characteristic strength for the j th temperature.

Substituting I_{ij}^* for I_{ij} in the maximum likelihood derivation leads to Equations [5-56] and [5-57] for calculating \hat{m} and $\hat{\sigma}_{oj}$:

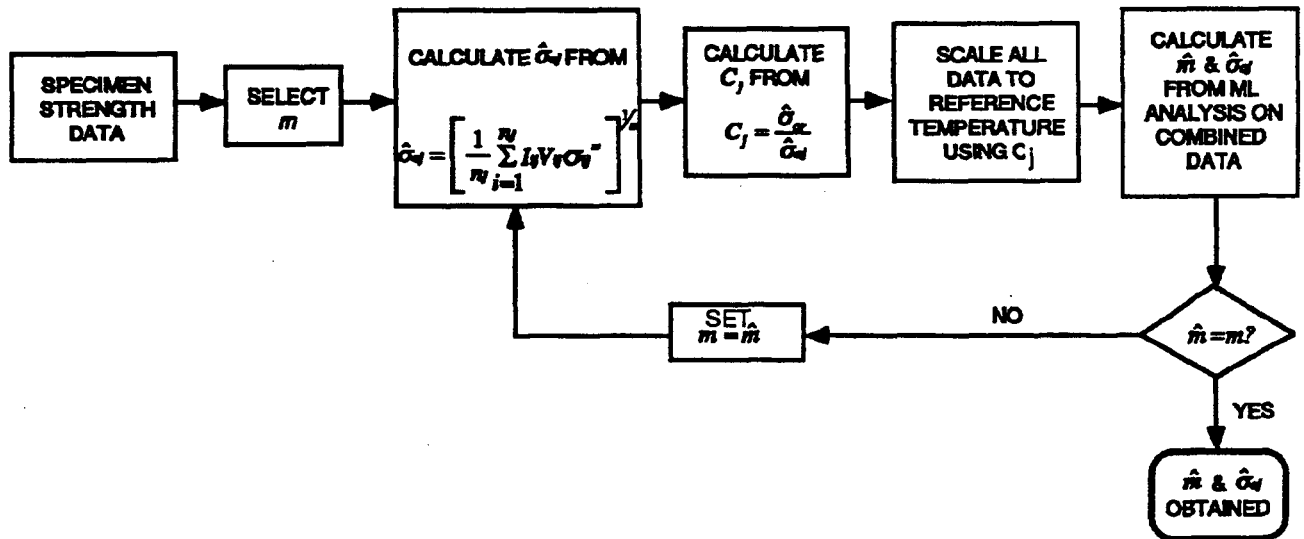
$$\frac{1}{\hat{m}} = \frac{1}{n} \sum_{j=1}^k \sum_{i=1}^{n_j} \left(\frac{\hat{I}_{ij}^*}{\hat{I}_{ij}^*} + \ln(\sigma_{ij}) \right) \left(\frac{n_j \hat{I}_{ij}^* V_{ij} \sigma_{ij}^{\hat{m}}}{\sum_{i=1}^n \hat{I}_{ij}^* V_{ij} \sigma_{ij}^{\hat{m}}} - 1 \right) \tag{5-56}$$

$$\hat{\sigma}_{oj} = \left[\frac{1}{n_j} \sum_{i=1}^{n_j} \hat{I}_{ij}^* V_{ij} \sigma_{ij}^{\hat{m}} \right]^{1/\hat{m}} \quad [5-57]$$

Equation [5-47] involves I_{ij}^* in calculating \hat{m} , but I_{ij}^* is calculated by Equation [5-55], which requires $\hat{\sigma}_{oj}$ from Equation [5-57]. Thus these two equations can only be solved iteratively. The algorithm is depicted by the flowchart in Figure 5-32.

Although the derivation is given for a single failure mode data set, this method was extended to data sets with competing failure modes and included in the computer code developed for specimen data analyses in this program.

A reference temperature must be chosen before the analysis is performed. The choice of reference temperature will not affect the value of \hat{m} and $\hat{\sigma}_{oj}$. Therefore, the choice of reference temperature is arbitrary when one needs only to calculate the estimates of Weibull modulus and characteristic strength from a multiple-temperature test data set. However, the choice of reference temperature does affect the location of the pinch



GC11591-532A

Figure 5-32. Floating-Point Temperature Scaling Scheme.

point for the confidence intervals in a failure probability prediction plot. Thus it is advisable to use a temperature of interest as the reference temperature. For predicting component failure probability, the component temperature should be used as the reference temperature.

It should be noted that each $\hat{\sigma}_{oj}$ is calculated from Equation [5-57] with data points at a given temperature only, and C_j is calculated from a set of discrete $\hat{\sigma}_{oj}$. This implies that the functional relationship of σ_o and T is represented in Figure 5-33 by the straight lines connecting the maximum likelihood estimate ($\hat{\sigma}_{oj}$) from each temperature group. This approach is referred to as the floating level approach.

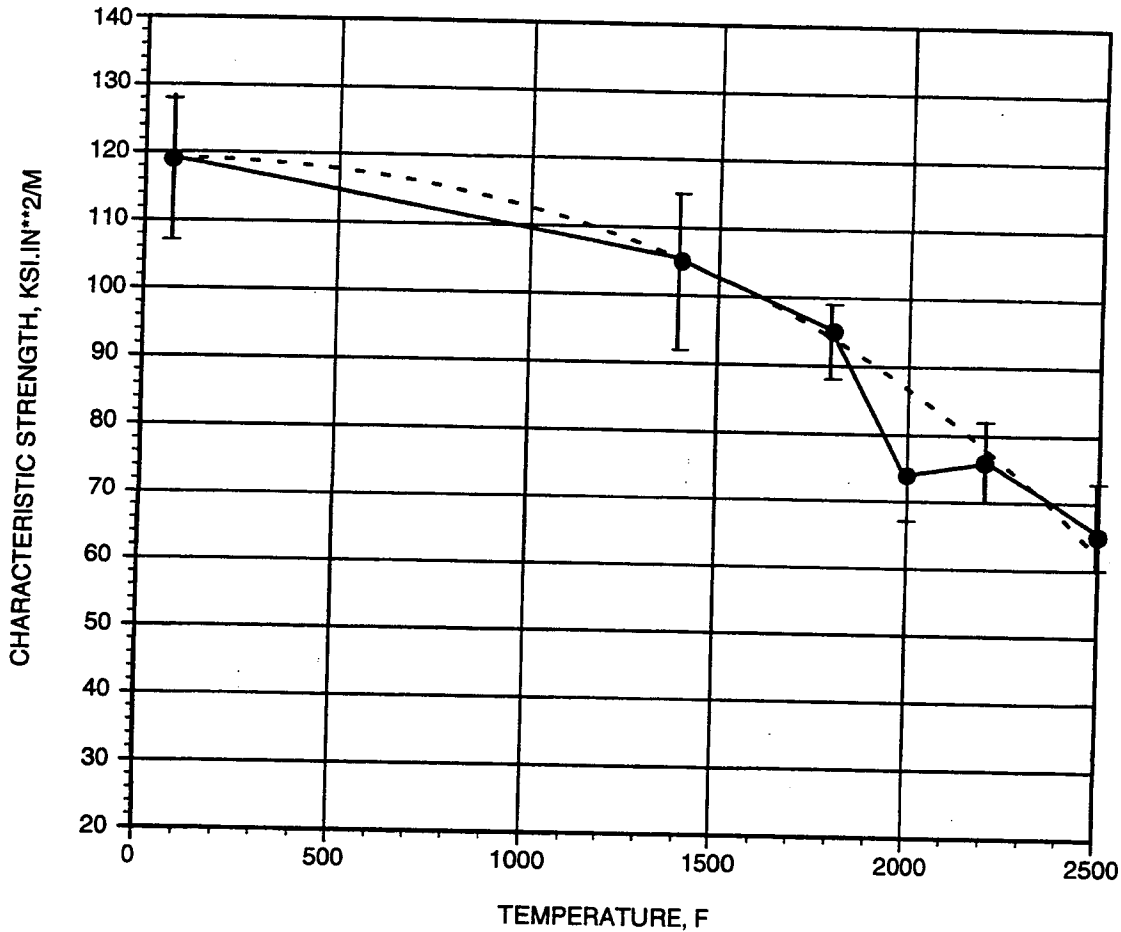
An alternative is to use a curve-fitting scheme to force a preassumed functional relationship between σ_o and T , as indicated by the dotted curved line in Figure 5-33. In the algorithm implementing the curve-fitting approach, a set of discrete $\hat{\sigma}_{oj}$ calculated from Equation [5-57] is used to determine the parameters in the preassumed function $\sigma_o = f(T)$. The updated C_j is calculated from Equation [5-55] using $\sigma_{oj} = f(T_j)$ instead of $\hat{\sigma}_{oj}$, as in the case of the floating level approach.

The curve-fitting approach is more efficient when characteristic strength is needed for a temperature which has no test data if the correct functional relationship $\sigma_o = f(T)$ is being used. How to select this functional relationship for a given material and an evaluation of bias when an incorrect function is being used in curve-fitting should be carefully studied. Serious numerical difficulties were encountered in implementing the curve-fitting scheme, mainly because data are only available at a few different temperatures. Although it was decided to use the floating level algorithm in the CERAMIC code for the time being, further development work in this area is planned for Phase II of this program.

5.2.3.4 Pooled Strength And Slow Crack Growth Data

If stress rupture failures are a consequence of subcritical crack growth (SCG), and if SCG and fast fracture both occur from the same flaws, the fast fracture strength and stress rupture data may be pooled to perform a combined likelihood analysis of the complete fast fracture and stress rupture data set. One implication from such an analysis is that the number of observations are increased significantly and thus may greatly increase the confidence of subsequent predictions. The derivation of the pooled likelihood function in the presence of competing failure modes is presented below.

The solution for the distribution of observations having strength degradation in the presence of slow crack growth under static loading and competing failure modes is derived for the situation in which each specimen tested to failure is treated. In this case, an observation is either a strength at failure or the time at which failure



GC11591-533

Figure 5-33. Characteristic Strength Versus Temperature For Floating Point and Curve-Fitting Schemes.

occurs. The former situation happens when failure occurs during loading to the static value, and the latter occurs when the static load has been safely reached and failure occurs after sufficient subcritical crack growth has taken place. The development is based on a classical Weibull treatment and, hence, does not cover multiaxial failure effects. Moreover, it is assumed that any crack growth is coplanar and that the initial "weakest" flaw grows to the final weakest flaw. This setup and assumptions give a first step in the development of analysis procedures that allow for subcritical crack growth in the presence of competing failure modes.

The following discussion will demonstrate the approach, using the simplest form of fracture mechanics description of SCG:

$$da / dt \cong A(K)^n \quad [5-58]$$

where: A and n are constants and:

$$K = Y\sigma\sqrt{a} \quad [5-59]$$

and where: Y denotes a geometry factor, σ is the applied load (stress), and a is the crack length. Then as shown in reference (5-66), Equation [5-59] can be substituted into Equation [5-58], and Equation [5-58] can be integrated and rearranged to yield:

$$(\sqrt{a_f})^{2-n} = (\sqrt{a_0})^{2-n} + \left(\frac{2-n}{2}\right) A(Y\sigma)^n t, \text{ for } (n \neq 2) \quad [5-60]$$

where: a_f denotes the final crack length ($\geq a_0$), a_0 denotes the initial crack length, and t is the time span over which the constant load, σ , is applied.

In view of the above assumptions and the fact that the setup is essentially uniaxial, Equation [5-60] can be used to transform an initial strength to a final strength at which failure occurs after the time span, t . In order to do this so as to determine the distribution, a substitution in Equation [5-60] for the crack lengths is made in terms of the critical stress via the relationship to K_{IC} given by:

$$K_{IC} = Y\sigma_c\sqrt{a} \quad [5-61]$$

where: σ_c is the stress that will just produce failure for the length a . When this substitution is carried out and some rearrangements are made, we obtain:

$$(\sigma_f)^{n-2} = (\sigma_0)^{n-2} - \left(\frac{n-2}{2}\right) \left(\frac{K_{IC}}{Y}\right)^{n-2} A(Y\sigma)^n t \quad [5-62]$$

where: $n > 2$ and the f and 0 subscripts denote the final and initial critical stresses, respectively. Equation [5-62] gives the degradation in strength for a particular failure mode; it is obvious that $\sigma_f < \sigma_0$ when t is greater than zero.

Now Equation [5-62] can be solved for t ; the critical stress, σ_c , of the flaw substituted for σ_0 ; and the load, σ , substituted for σ_f . The result gives the time that is required for the initial strength to be degraded to the load and hence failure then occurs and is:

$$t_j = B_j \left[(\sigma_{cj})^{n_j-2} - (\sigma)^{n_j-2} \right] \quad [5-63]$$

where the subscript j denotes the j th failure model (such as surface- or volume-initiated failure) and:

$$B_j = 1 / \left[(n_j - 2 / 2) (K_{Icj} / Y_j)^{n_j-2} A_j (Y_j)^{n_j} \right] \quad [5-64]$$

and where $\sigma_{cj} > \sigma$ in the case of subcritical growth. Equation [5-63] gives a one-to-one relationship of t_j to σ_{cj} and can be inverted to yield:

$$t_j^{-1} = \sigma_{cj} = \left[\frac{t_j}{B_j} + (\sigma)^{n_j-2} \right]^{\frac{1}{n_j-2}} \quad [5-65]$$

Equations [5-63] and [5-65] form the basis for the development of the distribution of an observed time.

A time is observed if and only if the minimum of $\{\sigma_{cj}\} > \sigma$ and thus all failure modes undergo subcritical growth. In this case the time that is observed is the minimum of the times computed by Equation [5-63] for each of the failure modes. Otherwise, a critical strength for at least one failure mode is less than or equal to σ and failure will occur on initial loading.

The distribution for a strength observation is derived by employing the probability of having a strength of less than or equal to x_i that is observed (the subscript i denotes the i th observation). Since at least one failure mode must have a critical strength less than or equal to σ (in order to observe strength upon failure), this probability is given by:

$$F(x_i) = 1 - S_1(x_i)S_2(x_i), \quad 0 \leq x_i \leq \sigma \quad [5-66]$$

where: for simplicity the setup is given for two competing failure modes; S denotes the survivor function (the probability that the critical strength is greater than x_i), and it is assumed that the failure modes act independently of each other. Differentiation of Equation [5-66] yields the probability density for a strength observation of x_i and is:

$$f(x_i) = f_1(x_i)S_2(x_i) + S_1(x_i)f_2(x_i) \quad [5-67]$$

From Equation [5-67] it follows that the joint probability density of a specimen failing from the first mode and at strength x_i is:

$$g_1(x_i) = f_1(x_i)S_2(x_i) \quad [5-68]$$

A similar expression holds for Mode 2. Since Equation [5-67] conditioned on $0 \leq x_i \leq \sigma$ must integrate to unity and the failure modes are independent of each other, the event of failure by one is mutually exclusive of the other, and both events are exhaustive. Thus, the likelihood for an observed strength and observed failure mode is given by either g_1 or g_2 .

The distribution for a time observation is derived by employing the probability of having a time less than or equal to y_i that is observed. Since all failure modes must have critical strengths greater than σ (in order to observe a time upon failure), this probability is given by:

$$F(y_i) = S_1(\sigma)S_2(\sigma) - S_1(\sigma_{cli})S_2(\sigma_{c2i}), \quad 0 < y_i \quad [5-69]$$

where: the dependency on y_i is given from Equation [5-65] by:

$$\sigma_{cji} = \left[\frac{y_i}{B_j} + (\sigma)^{n_j-2} \right]^{\frac{1}{n_j-2}} \quad [5-70]$$

Differentiation of Equation [5-69] yields the probability density for a strength observation of y_i and is:

$$f(y_i) = f_1(\sigma_{cli}) \frac{d\sigma_{cli}}{dy_i} S_2(\sigma_{c2i}) + S_1(\sigma_{cli}) f_2(\sigma_{c2i}) \frac{d\sigma_{c2i}}{dy_i} \quad [5-71]$$

The first term on the righthand side of Equation [5-71] covers the situation in which the observed time is due to failure mode 1 and the second covers the situation due to failure Mode 2. From equation [5-71] it follows that the joint probability density of a specimen failing from the first mode and at time y_i is:

$$h(y_i) = f_1(\sigma_{cli}) \frac{d\sigma_{cli}}{dy_i} S_2(\sigma_{c2i}) \quad [5-72]$$

A similar expression holds for mode 2. As in the case for a strength observation, since Equation [5-71] conditioned on $0 < y_i$ must integrate to unity and the failure modes are independent of each other, the event of failure by one is mutually exclusive of the other, and both events are exhaustive. Thus the likelihood for an observed time and observed failure mode is given by either h_1 or h_2 .

Now each observation is either a failure strength or a time at which failure occurred. Thus Equation [5-68] multiplied by dx_i gives the probability of an observed failure strength due to failure Mode 1 in the interval from x_i to $x_i + dx_i$. Likewise, Equation [5-72] multiplied by dy_i gives the probability of an observed time due to failure mode 1 in the interval from y_i to $y_i + dy_i$. This forms the basis for developing the overall likelihood function. Let:

$$\delta_{ji} = \begin{cases} 1, & \text{if the } i\text{th specimen fails from mode } j \text{ with a strength observation} \\ 0, & \text{otherwise} \end{cases} \quad [5-73]$$

$$\gamma_{ji} = \begin{cases} 1, & \text{if the } i\text{th specimen fails from mode } j \text{ with a time observation} \\ 0, & \text{otherwise} \end{cases} \quad [5-74]$$

where:

$$\delta_{1i} + \delta_{2i} + \gamma_{1i} + \gamma_{2i} = 1 \quad [5-75]$$

Then the likelihood for an observed strength x_i and observed failure mode, or an observed time y_i and observed failure Mode is:

$$\begin{aligned} L_i &= [f_1(x_i)S_2(x_i)]^{\delta_{1i}} [S_1(x_i)f_2(x_i)]^{\delta_{2i}} \left[f_1(\sigma_{c1i}) \frac{d\sigma_{c1i}}{dy_i} S_2(\sigma_{c2i}) \right]^{\gamma_{1i}} \left[S_1(\sigma_{c1i}) f_2(\sigma_{c2i}) \frac{d\sigma_{c2i}}{dy_i} \right]^{\gamma_{2i}} \\ &= \left[f_1(x_i)^{\delta_{1i}} S_1(x_i)^{\delta_{2i}} \left\{ f_1(\sigma_{c1i}) \frac{d\sigma_{c1i}}{dy_i} \right\}^{\gamma_{1i}} S_1(\sigma_{c1i})^{\gamma_{2i}} \right] \left[S_2(x_i)^{\delta_{1i}} f_2(x_i)^{\delta_{2i}} S_2(\sigma_{c2i})^{\gamma_{1i}} \left\{ f_2(\sigma_{c2i}) \frac{d\sigma_{c2i}}{dy_i} \right\}^{\gamma_{2i}} \right] \quad [5-76] \end{aligned}$$

from equations [5-68] and [5-72], the similar expressions for g_2 and h_2 , and the definitions of Equations [5-73], [5-74], and [5-75]. For future reference, note that the bracketed terms in the last line of Equation [5-76] each involve only failure Mode 1 or failure Mode 2. The log likelihood is by definition the logarithm of the likelihood of the complete data set, which under independence is the product of the L_i . This yields:

$$l = \sum_{i=1}^n \ln Li = \sum_{i=1}^n \ln \left[f_1(x_i)^{\delta_{1i}} S_1(x_i)^{\delta_{2i}} \left\{ f_1(\sigma_{c1i}) \frac{d\sigma_{c1i}}{dy_i} \right\}^{\gamma_{1i}} S_1(\sigma_{c1i})^{\gamma_{2i}} \right] \\ + \ln \left[S_2(x_i)^{\delta_{1i}} f_2(x_i)^{\delta_{2i}} S_2(\sigma_{c2i})^{\gamma_{1i}} \left\{ f_2(\sigma_{c2i}) \frac{d\sigma_{c2i}}{dy_i} \right\}^{\gamma_{2i}} \right] \quad [5-77]$$

as the log likelihood of the observed strengths or times and failure modes for the complete data set.

Since the bracketed terms of Equation [5-77] involve only a single mode, the maximum is obtained by maximizing individually each of the summed bracketed terms. But, due to the nature of the δ_{ji} and γ_{ji} , i.e., within a bracket one and only one is unity and the others are zero, the maximization of an individual sum of brackets is obtained from a censored data analysis. If the B_j and n_j are known, then the derivative terms in Equation [5-77] have no impact and the analysis becomes a standard censored data analysis based on strengths for each of the individual failure modes. However, if the B_j and n_j must be estimated from the data at hand, then this is no longer the case. The derivative terms then have an impact on the final solution through their dependency on B_j and n_j .

The above derivation for pooling fast fracture and slow crack growth data to obtain better fast fracture strength or subcritical crack growth life estimates was not incorporated in the present program, due to time and financial constraints. In this program, fast fracture and subcritical crack growth lives were compared, to obtain estimates of the subcritical crack growth parameters, as described in Section 5.3.4. The pooling of fast fracture strength and stress rupture life data will be pursued in Phase II of this program.

5.2.3.5 The CERAMIC Computer Code

The methods described in sections 5.2.3.1 through 5.2.3.3 have been automated in an AlliedSignal computer code named CERAMIC. The goal of this code is to provide an efficient and user-friendly tool for statistical analysis of ceramic fracture data and life prediction of ceramic components. The importance of this code lies in the capability to predict confidence intervals for the parameters of the distribution and tolerance level prediction for the reliability of a component with competing failure modes. The code uses maximum likelihood, likelihood ratio and bootstrap methods in the solution of the problem. See the CERAMIC Users Manual for code use (ref. 5-67).

Maximum likelihood methods are used in the calculation of the parameters of the distribution, as described in the previous section. These methods do not provide for a graphical representation of the data relative to the predicted distribution. On the other hand, the least-squares method provides for such comparison, because it uses the median ranks associated with the data for the prediction of the distribution. In order to provide the users of CERAMIC with this graphical capability, it was decided to plot the median rank along with the maximum likelihood prediction of the distribution, as shown in Figure 5-34. The data are plotted on Weibull paper by using the median ranks. The median ranks for non-censored data are calculated by Equation [5-78]:

$$MR = \frac{i - 0.5}{n} \quad [5-78]$$

where: i is the rank order of the specimen in the data, and n is the total number of specimens tested.

For censored data, the median ranks are calculated by the method of Johnson (ref. 5-68), which recommends adjusting the median ranks in the following way: First, place the data in ascending order. If the first data point is a failure, assign it a mean order number of one, $i = 1$, and continue assigning mean order numbers in ascending order until a censored (or suspended) data point is encountered. When suspensions are encountered, calculate an increment, Inc_1 , as shown in Equation [5-79]:

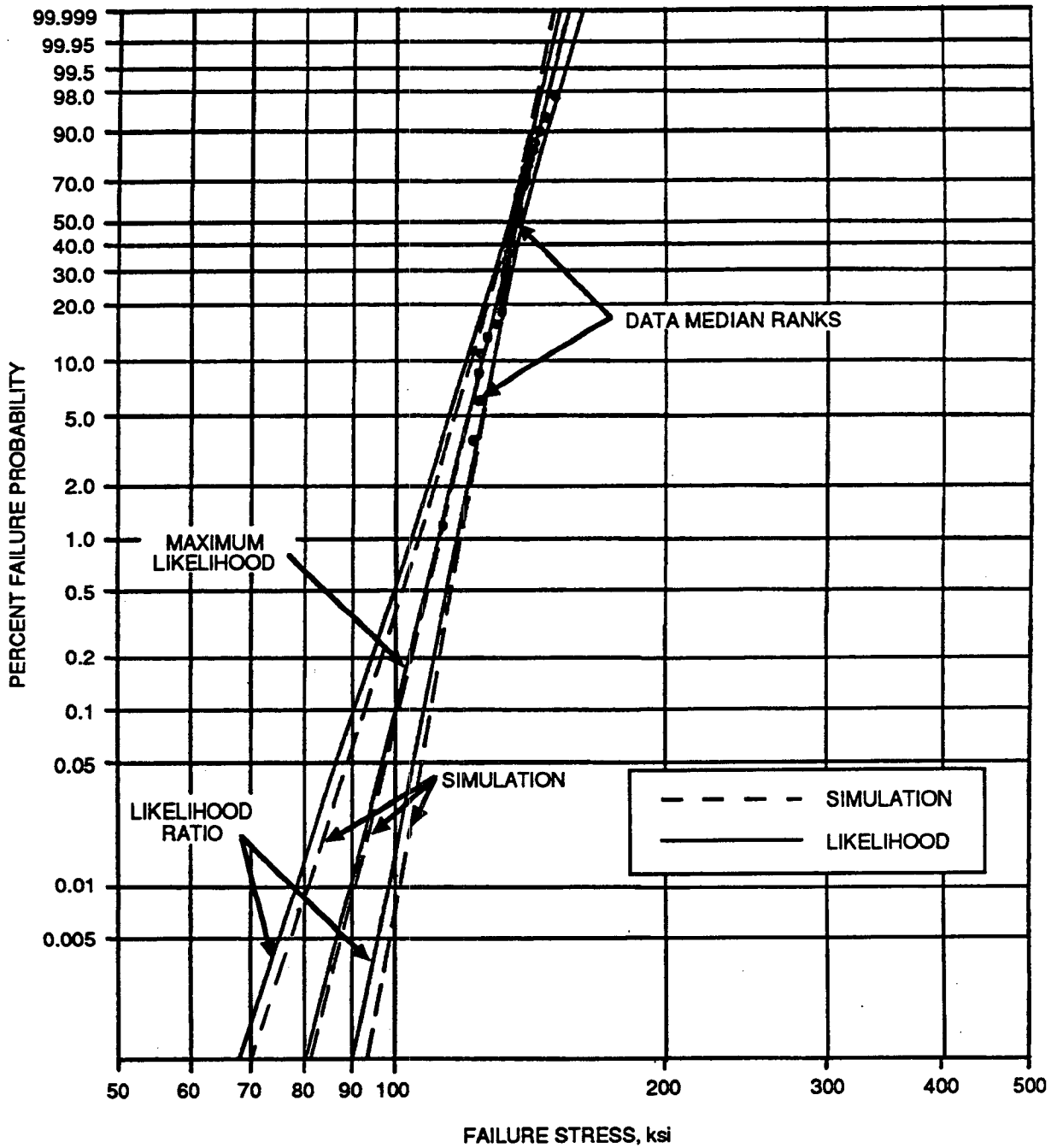
$$Inc = \frac{n + 1 - \text{Previous Mean Order Number}}{1 + \text{Number of Items Beyond Present Suspended set}} \quad [5-79]$$

Then calculate the mean order number of the next failure by adding this increment to the previous mean order number:

$$MON_2 = Inc_1 + \text{Previous Mean Order Number} \quad [5-80]$$

Calculate the mean order number of subsequent failures by adding Inc_1 to the previous mean order number until the next suspension is encountered. Then calculate the second increment by using Equation [5-79] and calculate the mean order number of the next failure using Equation [5-80] with the second increment. To calculate the median ranks, use Equation [5-78] with the mean order number in place of i , to yield Equation [5-81]:

$$MR = \frac{MON - 0.5}{n} \quad [5-81]$$



GC11591-534A

Figure 5-34. Example Of CERAMIC Code Graphic Capabilities To Plot Maximum Likelihood, Likelihood Ratio, Bootstrap, And Median Ranks.

Since the CERAMIC code has the capability to pool data and uses all of the information to calculate the Weibull parameters, it is necessary to plot all of the data with the best estimate of the Weibull distribution. Given that the data is of Class IV, it is necessary to place all of the data together in the same plot. In order to accomplish this, scaling each one of the specimens to a representative size is required. A representative specimen was chosen to be an effective size of unity. The effective size is the product of the multiaxial and stress gradient factor and the physical size of a component, i.e., IV . The scaling of the specimen data is done in terms of the probability of failure, as shown by Equation [5-82]:

$$\frac{\ln(1 - P_f)}{\ln(1 - P_f)_c} = \frac{IV}{(IV)_c} \quad [5-82]$$

where: C stands for the component, unity in this case. CERAMIC can scale to any size the user requires.

CERAMIC also has the capability to plot the probability of failure tolerance bounds. The tolerance bounds can be computed by two methods. The likelihood ratio method is represented in the plots with a solid line, while the bootstrap method is plotted with dashed lines. In the process of calculating tolerance bounds via the bootstrap method, a measure of the bias in the distribution and distribution parameters can be computed. By plotting the maximum likelihood prediction and the bootstrapped 50-percent line, the amount of bias can be observed. Note that these two lines still are biased. Methods need to be developed to unbiased the estimates of distribution functions.

5.2.4 Confidence Bounds On Predictions And Parameter Estimates

In section 5.2.3, a method was outlined to obtain the estimates of the Weibull parameters. It is observed that with a limited size test matrix, one can never exactly predict component reliability or determine the parameters which define the strength distributions. The uncertainty associated with the estimators can be quantified by the size of the confidence bounds. Two techniques for calculating confidence intervals are used: likelihood ratio (ref. 5-69 and 5-70) and bootstrap (ref. 5-69 and 5-71). These methods were extended to analyses of specimens with multiple sizes and loading conditions by Johnson and Tucker (ref. 5-63). Provided here are extensions of the bootstrap and likelihood ratio techniques to specimens and components with competing failure modes, and multiple-temperature test data.

5.2.4.1 Likelihood Ratio

The likelihood ratio method involves the statistics of the log of the ratio of the likelihood function of two distributions. Cox and Oakes (ref. 5-70), Chapter 3.3, describe the method for the two parameter Weibull distribution. The likelihood ratio method is based on the likelihood ratio statistic, Equation [5-83]:

$$W(m) = 2[l(\hat{m}, \hat{\sigma}_o) - l(m, \hat{\sigma}_{om})] \quad [5-83]$$

Where:

$l(\hat{m}, \hat{\sigma}_o)$ is the likelihood function given the maximum likelihood estimates of m and σ_o .

$l(m, \hat{\sigma}_{om})$ is the likelihood function of the maximum likelihood estimate of σ_o given m .

$W(m)$ has an approximate Chi-squared distribution with one degree of freedom, $\chi_{1,\alpha}^2$. To determine the $1 - \alpha$ confidence limits, one must compute the values of m for which Equation [5-84] holds. Two solutions can be found to this equation that gives an upper confidence bound and a lower confidence bound.

$$m: W(m) \leq \chi_{1,\alpha}^2 \quad [5-84]$$

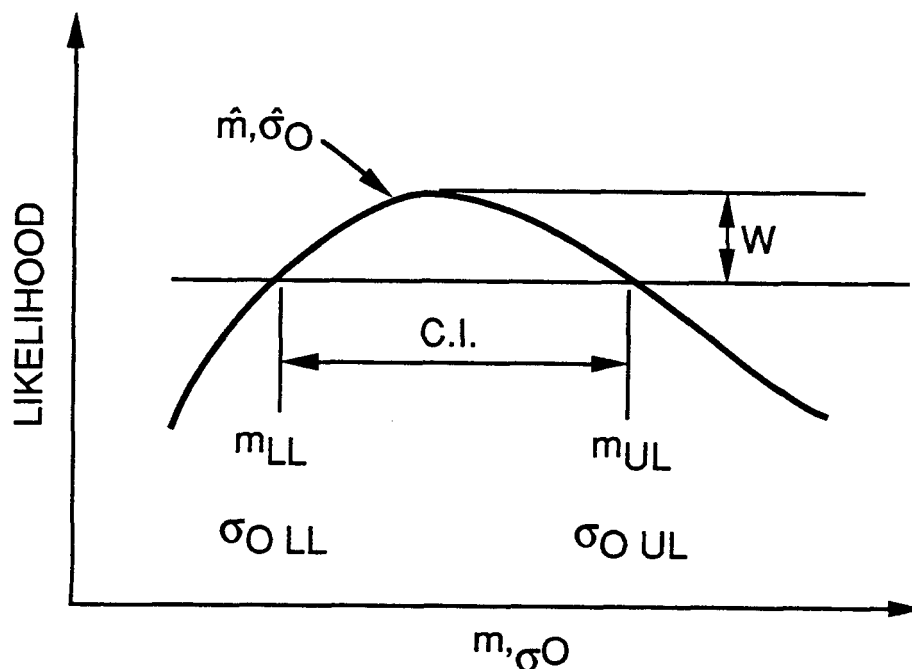
The inequality in Equation [5-84] is represented graphically in Figure 5-35.

Equation [5-83] is the likelihood ratio function for the first Weibull parameter, m ; Equation [5-85] is the likelihood ratio function for the second Weibull parameter, σ_o , with the accompanying bounds given by Equation [5-86].

$$W(\sigma_o) = 2[l(\hat{m}, \hat{\sigma}_o) - l(\hat{m}_{\sigma_o}, \sigma_o)] \quad [5-85]$$

$$\sigma_o: W(\sigma_o) \leq \chi_{1,\alpha}^2 \quad [5-86]$$

Equations [5-84] and [5-86] determine the value of m or σ_o for which the likelihood ratio statistic is less than or equal to the value of the Chi-square distribution with one degree of freedom and probability alpha. The first likelihood in equations [5-83] and [5-85] is the maximum likelihood function as given by equation [5-52]. The second likelihoods in these equations are derived and presented in Appendix VI, section 4.3.2.



GC11591-535

Figure 5-35. Confidence Interval Calculation Using The Likelihood Ratio Technique.

Having calculated the confidence intervals for the parameters of the distribution, we proceed to develop the formulation for the tolerance interval of the reliability prediction for a component. The derivation for the component reliability prediction for a single failure mode will not be presented here; we refer the reader to Appendix VI. Instead, we present the derivation for a component with more than one failure mode, three for the example used in the derivation.

The component combined reliability for all the competing flaw populations can be calculated by Equation [5-87] for a design stress level z :

$$R(z) = S_1(z)S_2(z)S_3(z) \quad [5-87]$$

where:

$$S_j = \exp\left(-I_{jc} V_{jc} \left(\frac{z}{\sigma_{oj}}\right)^{m_j}\right) \quad [5-88]$$

Define the log likelihood function by Equation [5-89]:

$$l = \sum_{i=1}^n \left[\ln \left\{ f_1(\sigma_i)^{\delta_{1i}} S_1(\sigma_i)^{\delta_{2i}} S_1(\sigma_i)^{\delta_{3i}} \right\} + \ln \left\{ S_2(\sigma_i)^{\delta_{1i}} f_2(\sigma_i)^{\delta_{2i}} S_2(\sigma_i)^{\delta_{3i}} \right\} + \ln \left\{ S_3(\sigma_i)^{\delta_{1i}} S_3(\sigma_i)^{\delta_{2i}} f_3(\sigma_i)^{\delta_{3i}} \right\} \right] \quad [5-89]$$

where: $f_j(\sigma_i)$ is the density function for strength σ_i for failure mode j , and $S_j(\sigma_i)$ is the survival probability of j^{th} failure mode to exceed strength σ_i . $\delta_{ij} = 1$ if the i^{th} specimen failed from mode j ; otherwise, $\delta_{ij} = 0$.

Furthermore, define $\gamma = \ln \left(\frac{1}{R(z)} \right)$ and $\gamma_{jz} = \ln \left(\frac{1}{R_j(z)} \right) = I_{jc} V_{jc} \left(\frac{z}{\sigma_{0j}} \right)^{m_j}$ and apply some algebra to Equation [5-88] to yield:

$$\gamma = \gamma_{1z} + \gamma_{2z} + \gamma_{3z} \quad [5-90]$$

Then write the probability density function in the following form:

$$f_j(z) = \frac{I_{j\hat{c}} V_{j\hat{c}}}{I_{jc} V_{jc}} \gamma_{jz} m_j \frac{\sigma_i^{m_j-1}}{z^{m_j}} \exp \left[- \frac{I_{j\hat{c}} V_{j\hat{c}}}{I_{jc} V_{jc}} \gamma_{jz} \left(\frac{\sigma_i}{z} \right)^{m_j} \right] \quad [5-91]$$

The likelihood ratio statistic then takes the form of Equation [5-92]:

$$W(R(z)) = 2 \left[l(\hat{m}_1, \hat{m}_2, \hat{m}_3, \hat{R}(z), \hat{\sigma}_{o2}, \hat{\sigma}_{o3}) - l(\hat{m}_{1,R(z)}, \hat{m}_{2,R(z)}, \hat{m}_{3,R(z)}, R(z), \hat{\sigma}_{o2,R(z)}, \hat{\sigma}_{o3,R(z)}) \right] \quad [5-92]$$

with the restriction that the quantities subscripted with $R(z)$ are values conditional on the current value of $R(z)$.

Determining the right-hand log likelihood in Equation [5-92] is equivalent to the constrained optimization problem:

$$\text{Maximize } \hat{l}_{R(z)} \text{ such that } \gamma = \gamma_{1z} + \gamma_{2z} + \gamma_{3z} \quad [5-93]$$

Using Lagrange multipliers changes the problem into the format of an unconstrained optimization problem with the additional parameter λ :

$$\text{Maximize: } L = \hat{l}_{R(z)} + \lambda(\gamma - \gamma_{1z} + \gamma_{2z} + \gamma_{3z}) \quad [5-94]$$

The confidence bounds are then determined from Equation [5-95]:

$$R(z): W(R(z)) \leq \chi_{1,\alpha}^2 \quad [5-95]$$

Iterating on estimates of $R(z)$ (or γ) eventually satisfies the equality in Equation [5-95]. Equation [5-94] must be maximized at each iteration. An efficient method of maximizing Equation [5-94] entails setting the partial derivatives of L equal to 0 and solving for the requisite m_j 's for a given $\lambda \neq 0$. This works well for $\lambda > 0$ and handily gives an upper bound on reliability. The lower bound is of much greater interest, however, and this corresponds to $\lambda < 0$, which tends to give numerical difficulties. The most promising approach attempted to date uses a quasi-Newtonian search algorithm in the space defined by the m_j 's.

5.2.4.2 Bootstrap

The bootstrap method consists of gathering information about estimates of variability and uncertainty by obtaining "observed" data sets via a Monte Carlo simulation method. Bootstrap techniques can be parametric or non-parametric. The parametric technique uses the original experimental estimates for the assumed distribution to generate a new data set. This data set is then employed to produce new estimates for the distribution parameters of the experimental data. The non-parametric technique generates a new data set from the original data set by sampling with replacements. In both methods, a number of specimens equal to the original data set is employed. This report describes only the parametric bootstrap approach. Bootstrap techniques are described by Cox and Oakes (ref. 5-70).

The confidence limits are calculated by generating new data sets and their respective Weibull parameters a sufficient number of times to accurately define the required confidence limits. Given that the bootstrap method relies heavily on evaluation, the approach is better described in a step-by-step basis. The calculation of the confidence limits of the Weibull parameters is illustrated in the following example; a more detailed discussion is found in Appendix VI.

- (a) The first step consists of estimating the Weibull parameters using the maximum likelihood method. The estimates are computed from Equations [5-49] and [5-50].

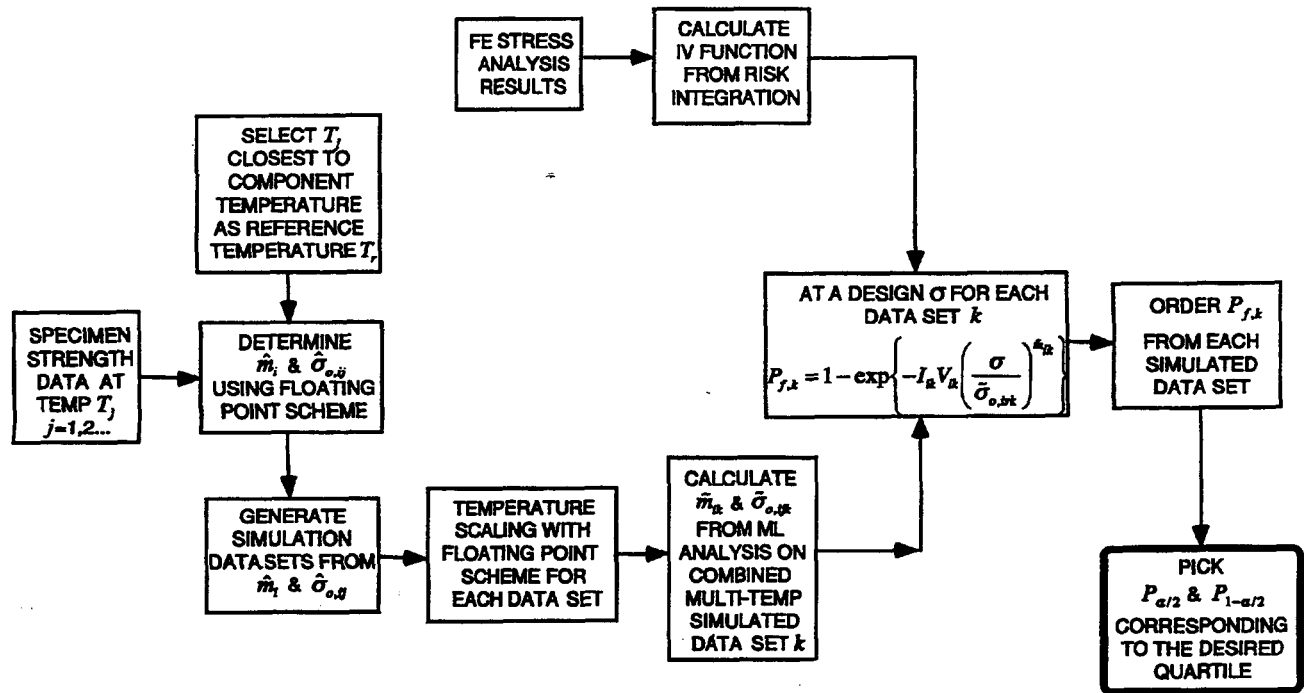
- (b) Second, choose a random number between zero and one, and pick this number to be a reliability value, R .
- (c) Third, select a specimen type from the original data set, with its corresponding V_i and I_i . Using the above \hat{m} and $\hat{\sigma}_o$, compute the fracture strength of this pseudo specimen, using Equation [5-96], given that it has the reliability equivalent to the value of the random number chosen in step (b).

$$\sigma_i = \hat{\sigma}_o \left(-\frac{\ln(R_i)}{\hat{I}_i V_i} \right)^{1/\hat{m}} \quad [5-96]$$

- (d) Repeat steps (b) and (c) for each specimen type and size a number of times equal to the number of specimens in the individual data set.
- (e) Calculate the Weibull parameters for this newly-generated data set using Equations [5-49] and [5-50] and save these values; calling them \tilde{m} and $\tilde{\sigma}_o$.
- (f) Repeat steps (b) through (e) s times.
- (g) Sort the \tilde{m} and $\tilde{\sigma}_o$ pairs in ascending order for \tilde{m} without losing the pair, and also for $\tilde{\sigma}_o$ without losing the pair.
- (h) To calculate the x confidence interval, pick the $(100-x)(s/2)(1/100)$ points from the upper and lower ends of the sorted values in step (g); these define the limits. For example, if the 95-percent confidence interval is required, substitute 95 for x to obtain 5, then multiply by the adjoining factor to get 25 when s equals 1000. Hence the 95-percent confidence interval is given by the 25th point from the lowest and the 25th point from the top of the sorted values \tilde{m} and $\tilde{\sigma}_o$ in step (g).

The procedure above describes the case in which the combined data is at a single temperature. For the cases in which data exist for more than one temperature, the procedure is illustrated in Figure 5-36. The flowchart in Figure 5-36 describes the bootstrap procedure used in failure probability confidence bound prediction when multiple-temperature data is present in the data set. This procedure only applies to the cases in which the component has a uniform temperature distribution.

With specimen strength data available at multiple temperatures (T_j), the specimen test temperature equal or closest to the component temperature should be selected as the reference temperature. Weibull analysis with pooled data from multiple test temperatures (described in Section 5.2.3.3) is performed to determine the



GC11591-536

Figure 5-36. Bootstrap Algorithm To Predict Confidence Interval For Components With Thermal Gradient Temperature Distribution.

combined best estimates, \hat{m}_i and $\hat{\sigma}_{o,ij}$. Subscript i denotes the i th failure mode and j denotes the j th temperature. This set of parameters will be used as the seeds to generate a large number of simulated data sets of similar composition in number of failure modes and number of data points for each failure mode.

For each simulated data set, a Weibull analysis with the floating-level temperature scaling is performed, again with the same reference temperature. The scaling factor C_{ij} is determined by the data points in each particular simulated data set; therefore, the scaling factor varies from data set to data set. For each simulated data set, a set of parameters \tilde{m}_i and $\tilde{\sigma}_{o,ijk}$ is obtained. Failure probability corresponding to a given design stress is calculated with the following equation:

$$P_{f,k} = 1 - \exp \left\{ -I_i V_i \left(\frac{\sigma}{\tilde{\sigma}_{o,ik}} \right)^{m_{ik}} \right\} \quad [5-97]$$

where: $\tilde{\sigma}_{o,ij}$ is the characteristic strength at the reference temperature for the k th simulated data set. $P_{f,k}$ for $k=1$, σ (σ is usually chosen to be 1000) are then ordered and the upper and lower bound of P_f are picked according to the confidence level desired following step (h) given previously. The term $I_i V_i$ is the effective size based on the component stress distribution and does not change for different simulated data sets.

If the component being analyzed has a thermal gradient (nonuniform temperature distribution), the procedure is more complicated. In this case, the risk integration over the whole volume or area will involve C_{ij} , the temperature scaling factors. C_{ij} will change from one simulated data set to another, and therefore the integration will have to be repeated for each simulation. That is impractical, given the amount of computation involved in each integration. If C_{ij} is treated as fixed throughout the bootstrap procedure, one will get a non-conservative prediction of confidence bounds for failure reliability. The need for a method capable of dealing with a component with a thermal gradient is obvious. Plans to find a solution are included in the Phase II Life Prediction Methodology program.

5.2.5 Component Predictions And Size Integration

The probability of failure of a component with k independent failure modes can be calculated with Equation [5-98]. This equation requires the multiaxial and stress gradient factor of the component for each failure mode, the parameters of the distribution which were computed using the CERAMIC code, and the maximum effective stress level in the component, z .

$$P_f(z) = 1 - \exp \left\{ - \sum_{j=1}^k I_j V_j \left(\frac{z}{\sigma_{o,j}} \right)^{m_j} \right\} \quad [5-98]$$

Computation of the tolerance limits for a component also requires the information for the reliability calculation plus the data used to compute the parameters of the distribution. The approach was described in section 5.2.4.

To compute the multiaxial and stress gradient factor requires the integration of Equations [5-30], [5-31], or [5-32], depending on the failure mode in question. A closed-form solution of these equations is not always possible; the stress fields, the geometry, and failure theory make the integration intractable. Solutions for standard test specimens are derived in Appendix VIII to show the functions that are coded into the CERAMIC program. To compute the multiaxial and stress gradient factor for an arbitrary specimen geometry and stress field the numerical integration code ERICA was developed.

ERICA is a finite element post-processor program for the ANSYS finite element code (ref. 5-72). It reads geometry and stress fields from the ANSYS results file (File12) and performs the numerical integration of Equations [5-30], [5-31], and [5-32]. The integration for the surface multiaxial and stress gradient factor has the option to integrate isotropic and anisotropic surface conditions. The volume and corner integrations support only the isotropic option. ERICA also has the option to calculate fast fracture and/or slow crack growth reliability predictions.

5.2.5.1 Volume Multiaxial And Stress Gradient Factor Calculation

ERICA accepts three types of ANSYS elements for calculating the volume multiaxial and stress gradient factor: STIF42, STIF25, and STIF45. The integration performed is that of Equation [5-30] with an effective stress defined by Equation [5-36] and the normal and shear stresses defined by Equations [5-37] and [5-38]. The numerical integration is performed using a Gauss-Legendre scheme (ref. 5-73) with 24 Gauss points in each of the spatial integration directions, ϕ and ψ . The integration over the volume of the element uses three Gauss points in each direction, x, y, and z and interpolated stresses from the values at the nodes on the element.

5.2.5.2 Surface Multiaxial And Stress Gradient Factor Integration

ERICA accepts the same elements from ANSYS to calculate the surface multiaxial and stress gradient factor as for the volume calculations. The integration performed is that of Equation [5-31] with the effective stress defined by Equation [5-36] and the normal and shear stresses defined by Equations [5-38] and [5-39]. The integration scheme has the same number of integration points as that of the volume integration with stresses interpolated also from those at the nodes.

The STIFF45 element integration accepts only isotropic surface conditions. STIFF42 and STIFF25 accept isotropic and anisotropic surface conditions. The anisotropic surface conditions are assumed to be generated by machining or grinding of the surface. The STIFF42 and STIFF25 elements are axisymmetric elements with the

axis of revolution aligned along the Y-axis. The machining flaw orientation is given by the angle θ_o . This angle is measured from the imaginary circle created by a machining tool that is cutting normal to the surface of the axisymmetric element.

Surface integration for the axisymmetric elements is performed using the stresses in the local coordinate system on the surface of the element. The local coordinate system is rotated on the $x - y$ plane by an angle α ; this angle is calculated by Equation [5-99]:

$$\alpha = \tan^{-1} \left(\frac{y_2 - y_1}{x_2 - x_1} \right) - 90 \quad [5-99]$$

where: x and y are the coordinates of the nodes. The stresses on the local coordinate system are given by Equations [5-100], [5-101], and [5-102].

$$\sigma_{y'y'} = \sigma_{xx} \sin^2(\alpha) + \sigma_{yy} \cos^2(\alpha) - 2\tau_{xy} \sin(\alpha)\cos(\alpha) \quad [5-100]$$

$$\sigma_{z'z'} = \sigma_{zz} \quad [5-101]$$

$$\tau_{y'z'} = -\sin(\alpha)\tau_{xz} + \cos(\alpha)\tau_{yz} \quad [5-102]$$

These equations are then used to define the normal and shear stresses needed for the effective stress, Equation [5-36]. The normal and shear stresses are given by Equations [5-103] and [5-104]:

$$\sigma_N = \sigma_{y'y'} \cos^2(\theta) + \sigma_{z'z'} \sin^2(\theta) + 2\tau_{y'z'} \sin(\theta)\cos(\theta) \quad [5-103]$$

$$\sigma_\tau = (\sigma_{y'y'} - \sigma_{z'z'}) \sin(\theta)\cos(\theta) + \tau_{y'z'} (\cos^2(\theta) - \sin^2(\theta)) \quad [5-104]$$

5.2.5.3 Corner (Or Edge) Multiaxial And Stress Gradient Factor Integration

In performing the corner integration, the effective stress is replaced by the maximum principal stress at the node. At a corner, there can only be a stress in the direction parallel to the corner, because of the free-surface condition that exists. The integration for the STIFF45 element uses a three-point Gauss integration along the length of the element. The integration for the axisymmetric elements reduces to Equation [5-105].

$$I_c = \left(\frac{\sigma_E}{\sigma_{\max}} \right)^m \quad [5-105]$$

5.2.5.4 Multiaxial Integration For Subcritical Crack Growth

The multiaxial integration for slow crack growth proceeds in the manner outlined in the above sections, with the exception of replacing the effective stress by Equation [5-106] which was derived from reference (5-74) and extended to competing failure modes (e.g., surface- and volume-initiated failures):

$$\sigma_E(t) = \sigma_E(0) \left(1 + D_j t \sigma_E^2(0) \right)^{\frac{1}{(n-2)}} \quad [5-106]$$

where: t is the time for which the probability of failure is to be calculated, and $\sigma_E(0)$ is the effective stress of the component at time zero, equivalent to Equation [5-36], and:

$$D_j = \frac{K_{IC}^{(n-2)}(n-2)}{2} A_j Y_j^2 \quad [5-107]$$

where:

K_{IC} = fracture toughness

n_j = subcritical crack growth exponent for failure mode j

A_j = subcritical crack growth constant for failure mode j

Y_j = flaw geometry factor

Y (surface flaw) = 1.282

Y (volume flaw -- penny shaped) = 1.128

The program actually calculates a multiaxial and stress gradient factor for subcritical crack growth, defined using the time-dependent effective stress. The probability of failure is calculated using Equation [5-108]:

$$P_{f_{SCG}} = 1 - \exp \left\{ -I_{SCG} V \left(\frac{\sigma_{\max}}{\sigma_o} \right)^m \right\} \quad [5-108]$$

5.3 Estimation Of Strength And Life Parameters From Specimen Data

5.3.1 Material Consistency

Great care was taken during the present program to produce material with consistent properties. However, due to the large number of specimens, variety of geometries, and test furnace size limits, it was inevitable that the specimens would be processed in multiple batches over a period of time. Due to the multilevel complications and time constraints on processing, it was not possible to totally randomize the specimens with regard to all processing variables. This resulted in a need to verify that the material properties were consistent among the different batches and over time.

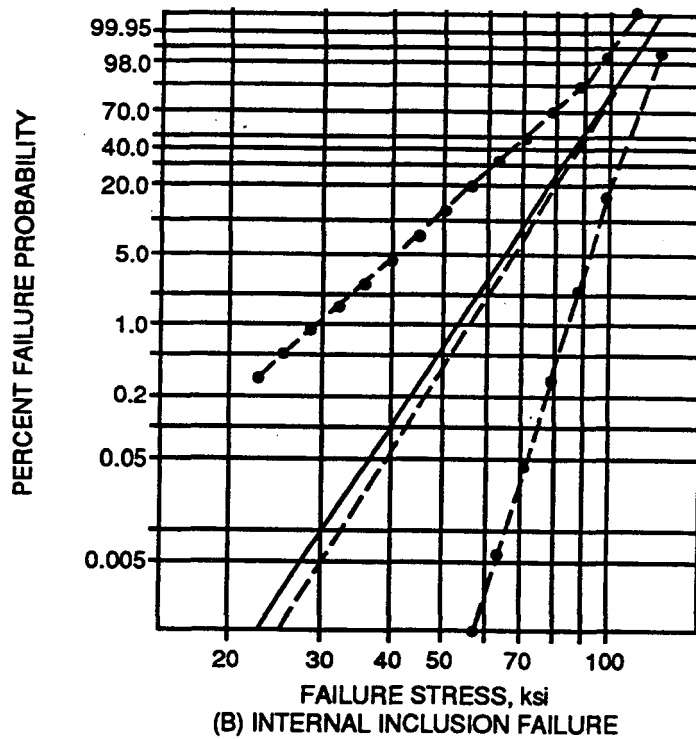
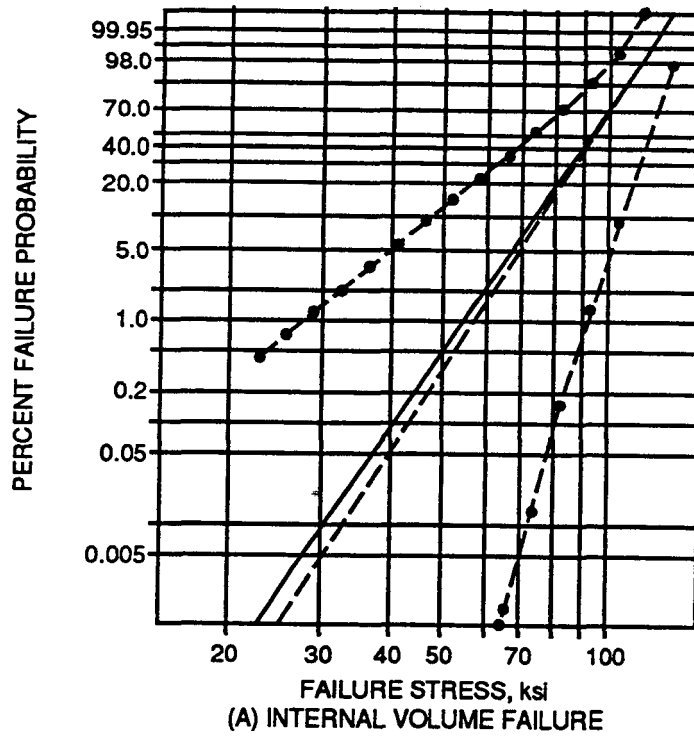
As discussed in section 4.1.4, a test plan was devised to allocate specimens to multiple HIP batches, to identify inconsistencies and minimize test risks. Specimens were processed in three groups, during the early, middle, and later phases of the program. Significant numbers of specimens were committed to each of the groups represented by the three time periods, so that meaningful statistical results could be obtained. Tensile and E-Size flexure specimens were employed, to give an adequate coverage of volume effects. Fast fracture testing was carried out at room temperature for each of the groups.

Specimens in each group were divided into three subgroups (E1, E2, E3, and T1, T2, T3, respectively) according to the processing dates. There were a number of failure modes identified by fractography among these specimens. The three major types, in terms of number of occurrences and importance to component design are: surface failure, internal volume, and internal void failures. Figure 5-37 indicates that inclusions and voids have similar strength distributions and can be combined into a single internal flaw population. As a result, the study only focused on surface and internal failure modes.

There is no established statistical technique for comparing the consistency of two or more strength distributions with competing multiple failure modes. However, two less-than-definitive methods were applied to check material consistency.

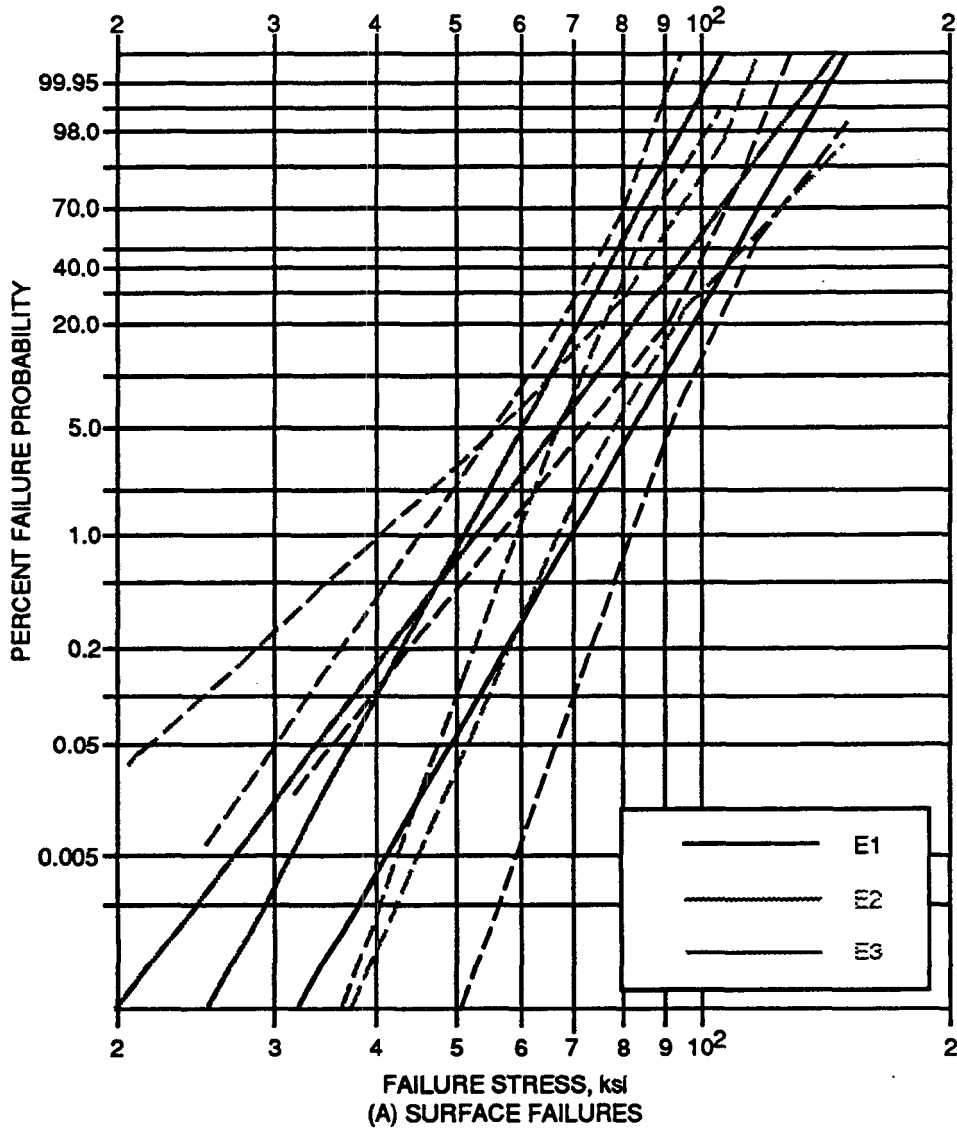
The first approach compared the failure probability and 95-percent confidence intervals, determined by each subgroup of specimens. The bootstrap method was used in calculating the confidence intervals for the two failure modes, censoring other failure data points.

A comparison of the reliability lines and confidence intervals calculated from specimen groups according to three processing dates are shown in Figure 5-38 for the E-size flexure specimens and Figure 5-39 for the tensile specimens. Surface and volume failure probabilities are plotted separately. The material is considered to be



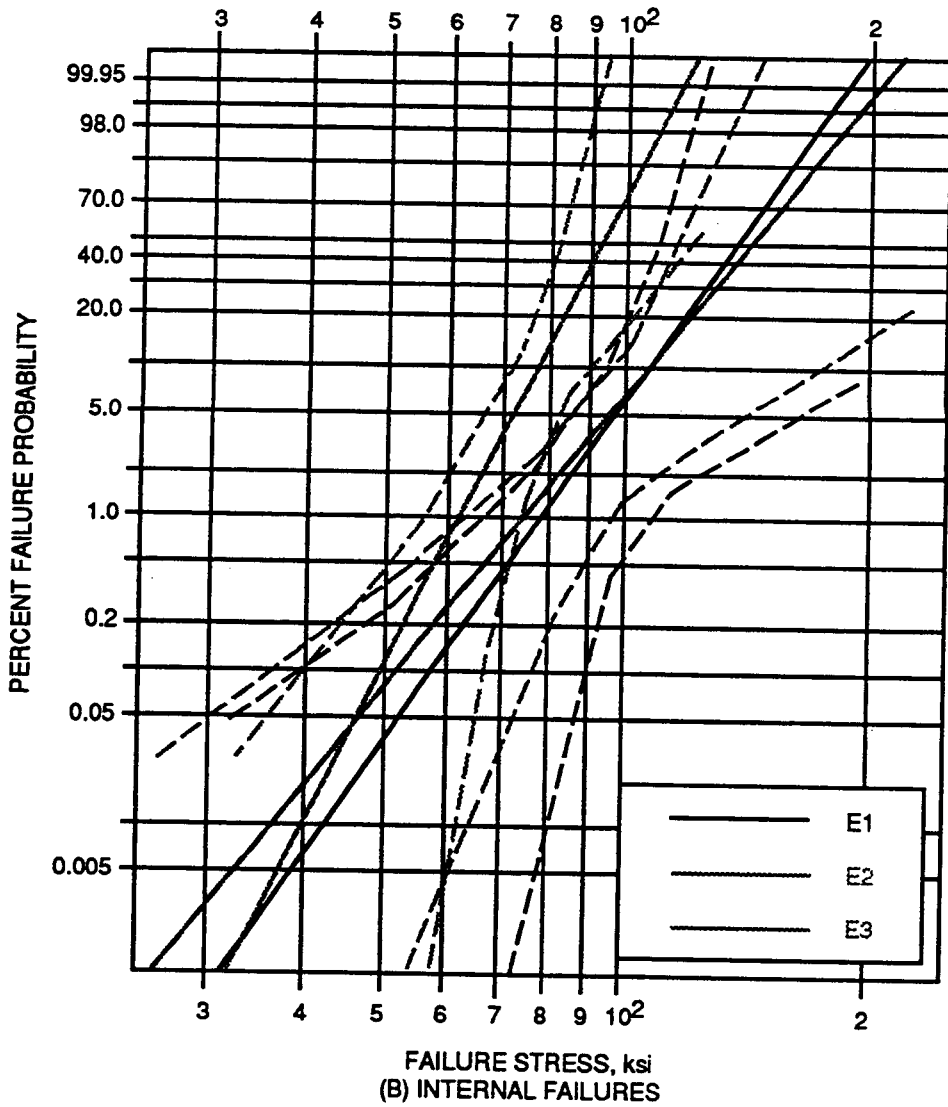
GC11591-537B

Figure 5-37. Similarity Of Internal Volume And Inclusion Failure Data Leads To Combining The Two Failure Modes.



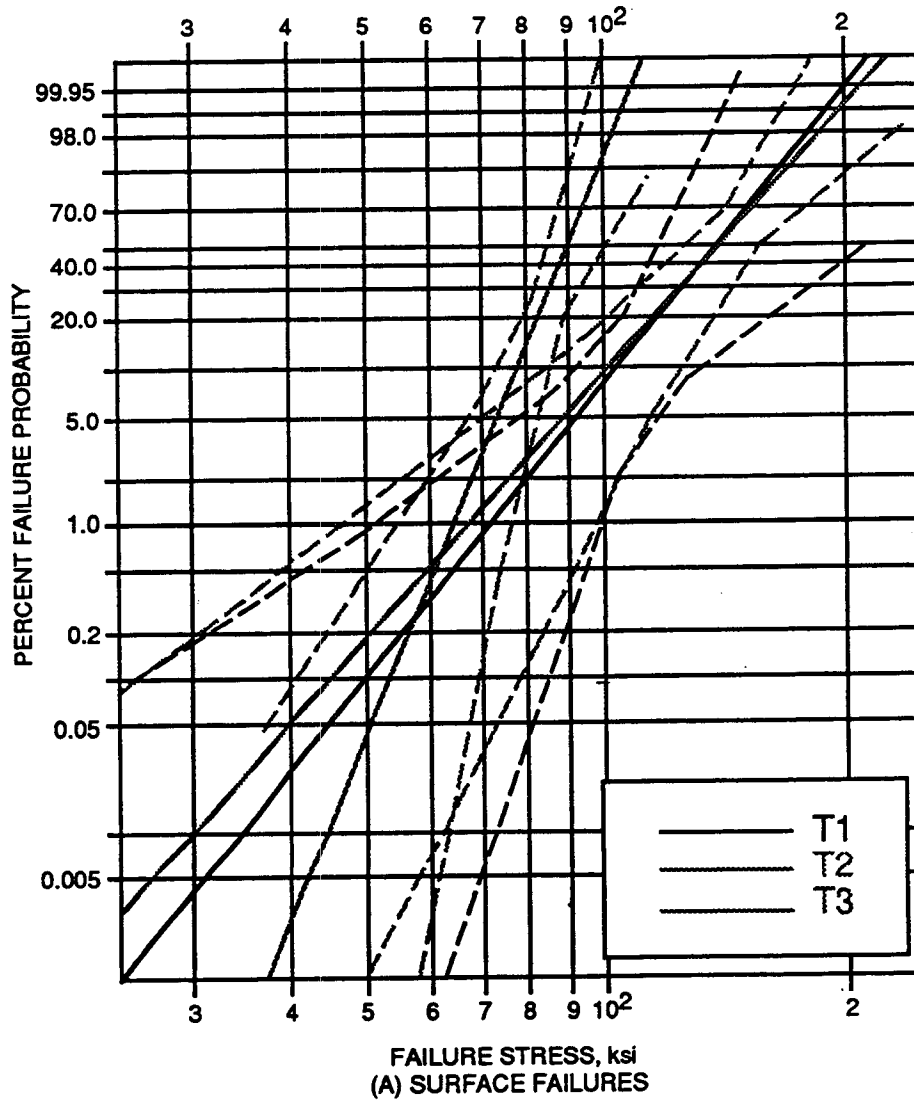
GC11591-538-1

**Figure 5-38. Material Consistency Comparison For E-Size Flexure Specimens.
(A) Surface Failures.**



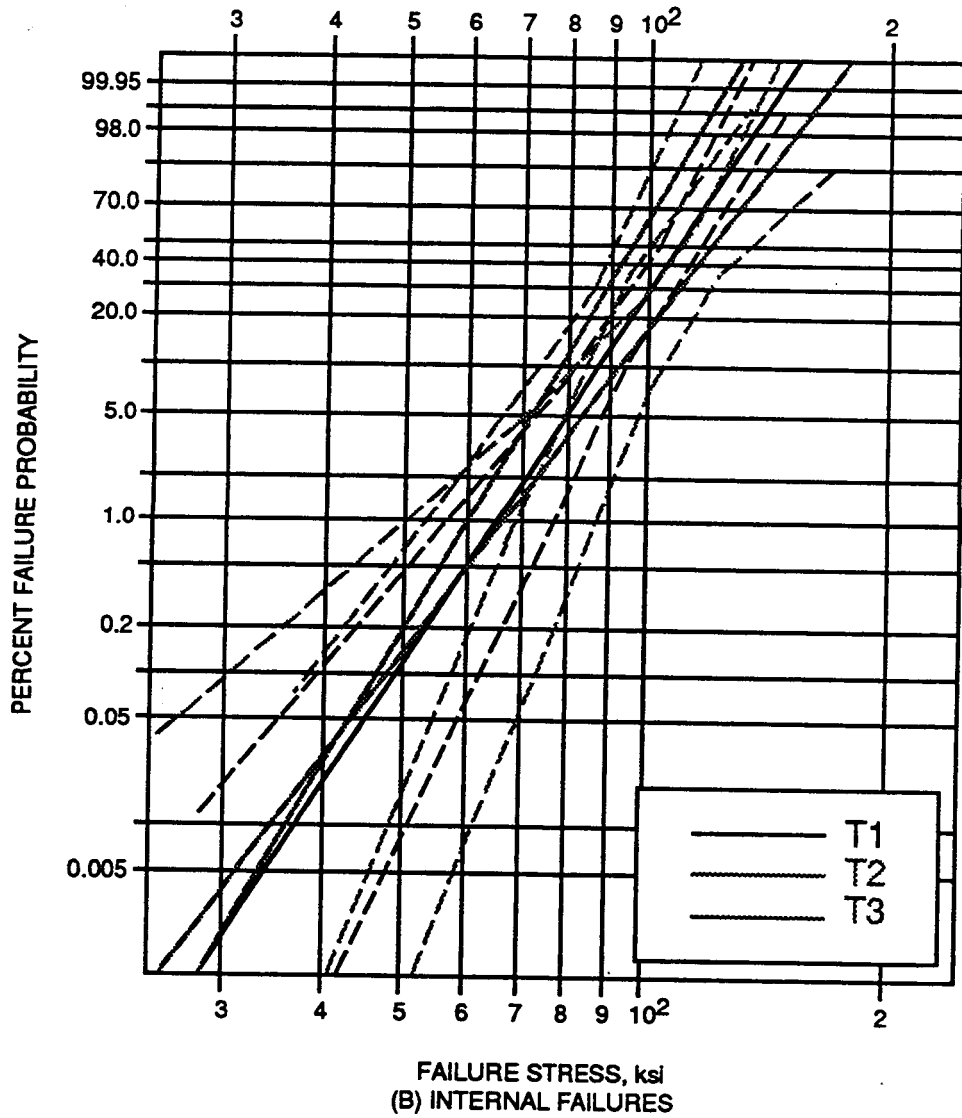
GC11591-538-2

**Figure 5-38. Material Consistency Comparison For E-Size Flexure Specimens. (Contd)
(B) Internal Failures.**



GC11591-539-1

**Figure 5-39. Material Consistency Comparison For Tensile Specimens.
(A) Surface Failures.**



GC11591-539-2

**Figure 5-39. Material Consistency Comparison For Tensile Specimens. (Contd)
(B) Internal Failures.**

consistent if a reliability line can be defined on these plots that is within all three sets of confidence intervals. Applying this criterion to the four cases plotted, the surface failure for tensile specimens failed the test. Although the comparison is qualitative, one can still make useful observations. The internal flaw population demonstrated much better consistency over processing dates compared with the surface flaw population.

Since the fast fracture distribution is not a normal distribution and it is further complicated by the presence of competing failure modes, the conventional analysis of variance (ANOVA) procedure does not apply. Therefore, a second test for material consistency was performed using nonparametric statistical methods based on ranks. The analyses were carried out by employing routines in the computer code SAS (ref. 5-75).

The results are presented in Tables 5-7 and 5-8. The tables give the results, from applying the Kruskal-Wallis method (ref. 5-76) for testing for differences among the location and scale (scatter) among the three groups for each specimen type. Each of the procedures was verified by carrying out an ANOVA on the ranks of the appropriate observation with essentially the same results as shown for the Wilcoxon tests (ref. 5-75). Thus the Chi-square approximation should be adequate. The Chi-square distribution is the limiting form for the Kruskal-Wallis test (ref. 5-76), as each group size approaches infinity. When the approximation is adequate, an ANOVA test based on ranks will generally agree with the results shown by the Chi-square approximation, and this is the case for the strength data for the three groups of specimens. The null hypothesis (H_0) being tested is that the three groups have the same distribution (location on scale). The results given in the tables show, at the usual significance levels, one would conclude there is statistical evidence that the underlying location and scale of the three groups of tensile specimens differ.

TABLE 5-7. NONPARAMETRIC TEST FOR THREE GROUPS OF E-SIZE FLEXURE SPECIMENS

Location Test:					
Code	N	Sum of Scores	Expected under H_0	Std Dev under H_0	Mean Score
1	26	1128.00	1313.00	127.251	43.385
2	47	2430.50	2373.50	144.793	51.713
3	27	1491.50	1363.50	128.796	55.241
Kruskal-Wallis Test					
$\chi^2=2.3672$		DF=2		$P > \chi^2=0.3062$	
Scale Test:					
1	26	1136.00	1313.00	127.253	43.692
2	47	2526.00	2373.50	144.795	53.745
3	27	1388.00	1363.50	128.798	51.407
Kruskal-Wallis Test					
$\chi^2=2.0460$		DF=2		$P > \chi^2=0.3595$	

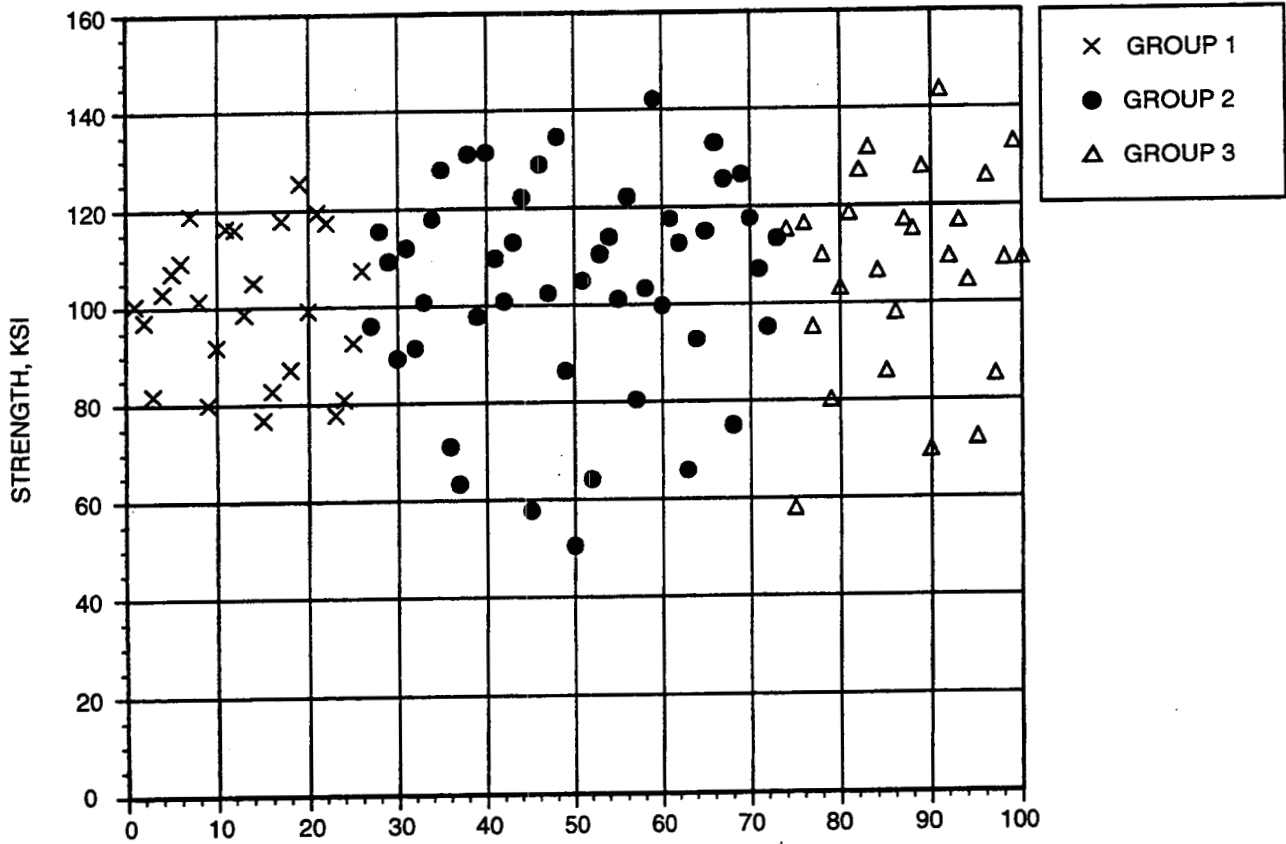
TABLE 5-8. NONPARAMETRIC TEST FOR THREE GROUPS OF TENSILE SPECIMENS

Location Test:					
Code	N	Sum of Scores	Expected under H_0	Std Dev under H_0	Mean Score
1	24	1711.50	2121.00	143.182	40.750
2	22	1139.50	1111.00	120.173	51.795
3	36	2199.00	1818.00	139.248	61.083
Kruskal-Wallis Test					
$\chi^2=9.5793$		DF=2		$P_f > \chi^2=0.0083$	
Scale Test:					
1	24	2133.00	2121.00	143.186	50.786
2	22	1392.00	1111.00	120.177	63.273
3	36	1525.00	1818.00	139.253	42.361
Kruskal-Wallis Test					
$\chi^2=7.1020$		DF=2		$P_f > \chi^2=0.0287$	

The largest shift in a mean value for a location test (on ranks of observations) occurs between the first and second group of tensile specimens. Likewise, the largest difference in a mean value for a scale test (on ranks of the absolute value of each observation corrected for its group mean) occurs between the second and third group of tensile specimens. Thus, the possible differences are related to the groupings in a complex way, with changes possibly occurring throughout the whole period of the program. (Also, the differences between the sum of scores and its expected value for the Wilcoxon test shows the same thing, but in a more subtle way.)

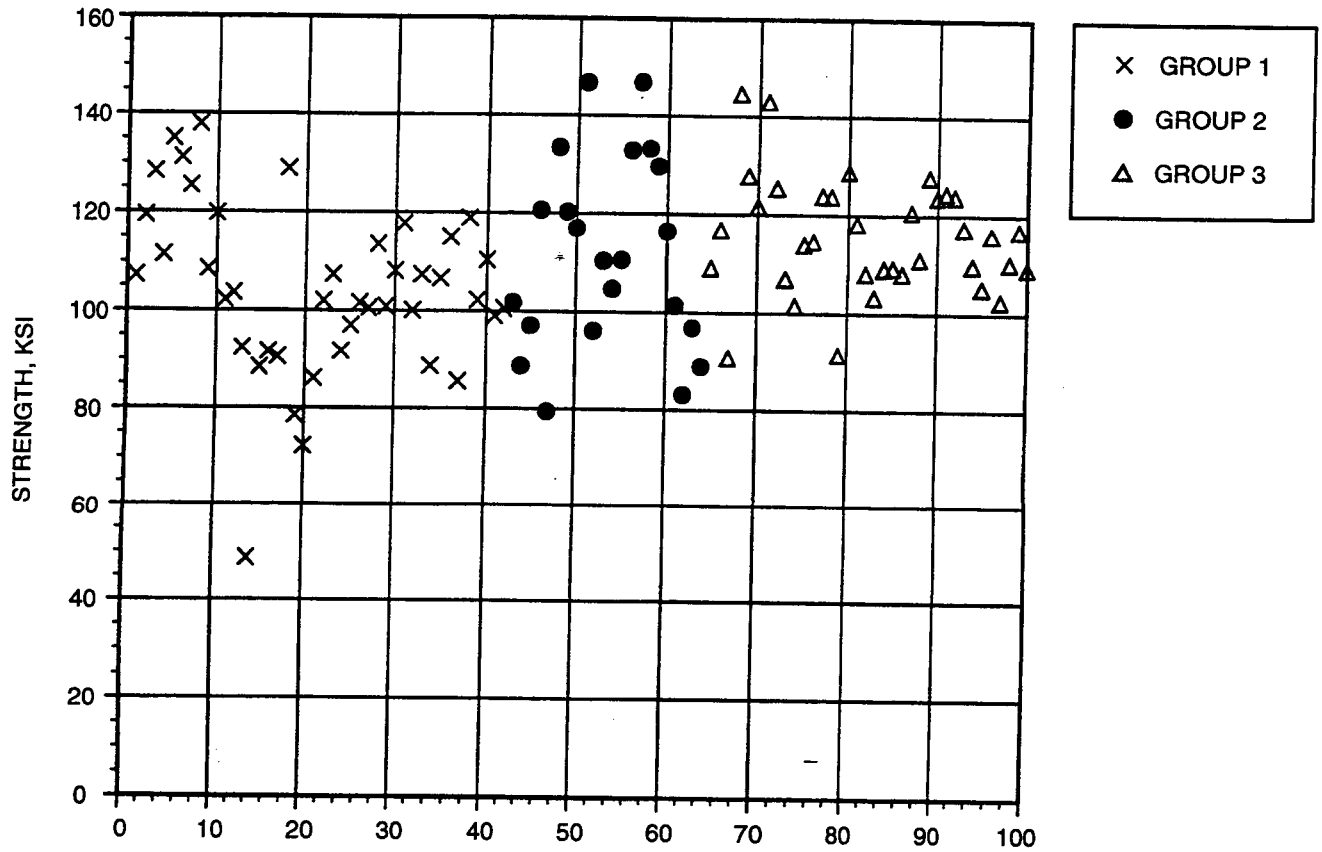
In the case of the E-size flexure specimens, there is no real sign of difference of any statistical significance. Consistent with this finding is the fact that there are no "large" shifts of mean values of the test statistics for the E-Size bar specimens.

Figures 5-40 and 5-41 give plots of the raw data. Any "time" implications within a group should be ignored. The only real difference is among the three groups denoting the three time periods. The strengths were plotted with respect to the order of observation. Perusal of the plots corroborates the analysis findings. Also, it appears that one observation in the first tensile group may be an outlier. This observation was removed and both tests performed again for the tensile data. While the observed significance levels increased or remained about the same as the earlier levels, the overall findings remained the same as when this observation was included. Thus, there are statistical grounds for believing that changes in the strength distribution may have occurred during the period of the program. Note that this does not mean that any changes did take place. And if a change did take place, the nonparametric method employed is not sensitive to which underlying failure mode is the root cause producing the change. For example, it could be that the strength distribution associated with volume failure modes remained constant during the program, while the strength distribution associated with surface failure modes due to machining flaws changed over time.



GC11591-540

Figure 5-40. Scatter In Fast Fracture Data For E-Size Flexure Specimens.



GC11591-541

Figure 5-41. Scatter In Fast Fracture Data For Tensile Specimens.

A more definitive conclusion on the material consistency test requires a more quantitative test method, which needs to be developed. For the present, it was decided to treat the material as being consistent with respect to processing date. The probability plots and associated confidence limits indicate that this should not have too serious an effect on the predictions (also see Section 5.3.2).

5.3.2 Weibull Strength Parameters Estimated From Pooled Data

Weibull strength parameters were estimated for each of the strength populations expected in the confirmatory test specimens. Several sets of data were pooled, to increase the confidence in the parameter estimates, and later, in the predictions of confirmatory specimen failure probabilities. The pooled data included 405 strength measurements from MIL-A flexure, MIL-B flexure, E-size flexure, and tensile specimens tested at multiple temperatures.

The maximum likelihood parameter estimation methods described in section 5.2.3 were used to calculate strength parameters from individual and pooled sets of strength data. To apply these methods, it is necessary to define the flaw populations that exist in each set of specimens and determine which of these populations are common between different groups of specimens. For example, if both E-size flexure and the tensile specimens were found to have the same volume flaw population, then these specimens would be pooled relative to volume strength. This means that volume flaws from both sets of data would be given the same name, and strength parameters would be calculated that maximize the likelihood for volume failures in the combined set of E-size and tensile specimen data. Conversely, if it was found that the MIL-A and E-size specimens did not have the same chamfer failure distributions, then different names would be assigned to the chamfer failure data sets, and strength parameters would be calculated separately.

No statistical methods are readily available to determine if strength distributions from specimens with different sizes and different degrees of censoring (due to competing failure modes) should be pooled. Therefore, some general guidelines were established to define which sets were to be pooled. These guidelines are based on:

- (1) Physical evidence from fractography showing similar origin features,
- (2) A common value of m that falls within the 95-percent bounds of \hat{m} 's that are estimated separately for each set of strength data,

- (3) A common value of σ_0 that falls within the 95-percent bounds of $\hat{\sigma}_0$'s that are estimated separately for each set of room-temperature strength data, and
- (4) The percentage of each strength population simulated during bootstrap analyses must be similar to the percentage observed in the original data set.

Physical evidence was used when available. If the origin of a surface failure was found to be a pit, it would be censored relative to the machining surface failures. Guidelines (2) and (3) were used to determine if similar types of flaw which occurred in different specimens should be pooled. Even when the first three guidelines are met, pooling sets of data can produce large enough changes in parameter estimates to significantly change the number of failures simulated during bootstrap analyses. This results in narrower or wider confidence bounds than are representative of the true specimen data. Guideline (4) addresses this potential problem. These guidelines are more likely to allow pooling of failure modes from sets of specimen data that should not be pooled than in indicating data that should be pooled. Since more definitive statistics are not available for making these comparisons, stringent guidelines were avoided that might overly reduce the size of the pooled data set being defined for confirmatory specimen predictions.

A list of the Weibull parameters estimated for each set of specimen strength data is given in Table 5-9. Included are parameter estimates from three groups of pooled data sets described later in this section. There are two sets of room-temperature tensile strength data. The set with 7 specimens was tested with steel collets and produced buttonhead failures that were not observed in the other group of 93 specimens tested with copper collets. The parameters listed in Table 5-9 were estimated with the maximum-likelihood censored analysis methods described in section 5.2.3. All strength distributions are assumed to be isotropic, as described in section 5.3.3. σ_0 is the second Weibull parameter, defined as the 63.2 percent strength for a unit size (in, in², or in³) under uniaxial tension for length, biaxial tension for surface, and triaxial tension for volume. Estimates of σ_0 from different specimens should be similar if the same flaw population exists in each.

Weibull strength plots were generated for each separate set of specimens, and each strength population. Weibull plots for surface, internal, and chamfer strength estimated from the E-size flexure data are shown in Figures 5-42 through 5-44. These plots include 95-percent confidence bounds calculated with the bootstrap method. The combined failure probability for all three failure modes is plotted in Figure 5-45. Single-failure-mode Weibull plots for each set of data listed in Table 5-9 are given in Appendix VIII.

TABLE 5-9. WEIBULL STRENGTH PARAMETER ESTIMATES AND 95 PERCENT CONFIDENCE BOUNDS FOR INDIVIDUAL AND POOLED DATA SETS

Specimen	Temp	Total No.	Surface							Volume							Chamfer						
			No.	s_0	-	+	m	-	+	No.	s_0	-	+	m	-	+	No.	s_0	-	+	m	-	+
Mil-A	70	60	10	126.2	114.3	134.3	25.7	16	38	1	27.5	0	81.6	4.1	0.26	15.7	49	140.9	136.2	145.9	8.46	6.87	10.82
Mil-B	70	60	17	119.2	107.4	128.3	12.2	8.24	16.7	5	49.3	18.8	1000	6.62	2.77	12.5	38	168.4	159.2	182.9	5.89	4.42	7.6
Mil-B	1800	30	23	78.3	67.9	87.1	8.07	5.97	10.4	0						7	158.4	139.7	222.8	6.47	3.33	10.38	
Mil-B	2100	30	23	75	67.6	80.7	12.5	9.09	16.26	1	713	27.2	1000	23.2	4.25	58.4	6	119.4	110.9	148	11.6	5.66	19
Mil-B	2200	30	24	86	81.5	89.3	28.8	20.7	38.2	1	60	0	68.2	15.7	1.05	54.4	5	107.7	103.9	120.5	27.2	12	48.7
Mil-B	2300	30	22	80.1	73.7	84.8	17.5	12.5	23.2	0						7	109	105.5	118	21.5	11.8	33.4	
Mil-B	2400	28	18	77.2	71	81.5	20.6	13.7	29	1	73.4	27.4	76.1	40	4.7	109.9	9	97.8	96	101.8	31.7	18.5	48.2
Mil-B	2500	29	21	78.3	82.5	85.4	33.1	23.2	45	4	59	33.5	66.3	21.7	7.81	43.6	4	100.2	96.5	115.4	25.8	9.6	50.7
Size-E	70	100	50	103.6	99.6	107.5	8.06	6.47	9.82	15	67.4	56.7	76.8	7.98	5.23	11.29	35	210.5	179.8	269.7	4.34	3.2	5.67
Tensile	70	7	1	120.1	87.5	1E+05	4.71	0.344	16.5	1	48.7	14.8	8770	3.58	0.24	12.9	4	Button head					
Tensile	70	93	24	118.4	112.8	126.2	7.6	5.52	9.98	68	63.2	56.6	69.1	7.97	6.63	9.4	1	Surface inclusion					
Tensile	70	100	25	118.7	113.1	126.5	7.69	5.6	10.1	69	62.9	56.5	68.8	7.89	6.58	9.32							
Tensile	2100	5	0							5	56.9	39.4	59.4	16.1	7.18	28.5							
Tensile	2200	20	1	96.6	78.9	26000	7.53	0.67	21.4	18	38.7	30	46	7.45	5.13	10.11	1						
Combined																							
Tensile		125	26	119.2	113.9	127	7.75	5.94	10.8	92	63.2	58.2	69.6	7.97	6.96	9.57							
ALL 70F		320	42	116.5	112.8	121.1	9.74	8.24	11.6	90	64.9	60.2	70.5	8.26	7.2	9.86							
70 to 2200F		405	89	116.7	113	120.6	9.99	8.78	11.63	114	65.7	61.4	70.9	8.45	7.45	9.85							

A comparison of σ_0 and m estimates from each set of data are plotted in Figures 5-46 through 5-48. The number of failures (surface, volume, or chamfer, respectively) in each set is shown above or below the 95-percent confidence bounds. The line in the center of each bar is the median parameter estimate from the maximum likelihood censored data analysis.

Surface strength parameters were calculated for machining surface strength. Other surface failures, such as pits, were censored. The surface parameter estimates shown in Figure 5-46 have very diverse values. The room-temperature estimates of m meet consistency Guideline (2), for MIL-B, E-size, and tensile specimens, but not for MIL-A specimens, which have a considerably higher estimated m for surface strength. With increasing temperature, we also see an increase of m estimated from MIL-B specimens; at 2200F, there was a considerable increase. This high m at 2200F was less pronounced for chamfer failures and was not evident in the volume parameter estimates from the tensile specimens. The increase in \hat{m} at 2200F is surprising, if it is related to the creep-induced stress redistribution that occurs in flexure bars.

Observing σ_0 's for the surface, it is seen that the E-size bars do not meet Guideline (3). They have significantly lower strength than the room-temperature tensile or MIL-B specimens. The resulting sets of surface strength data that met our pooling guidelines are MIL-B (room temperature), MIL-B (1800F), MIL-B (2100F), and tensile. The elevated-temperature tensile data was included, but there was only one surface failure.

The volume strength parameters in Figure 5-47 all meet the pooling guidelines. As expected, few volume failures were observed in the MIL-A and MIL-B specimens. The arrows in Figure 5-47 indicate insufficient data to calculate confidence intervals. The MIL-B data above 2100F were not pooled. If creep did affect the surface

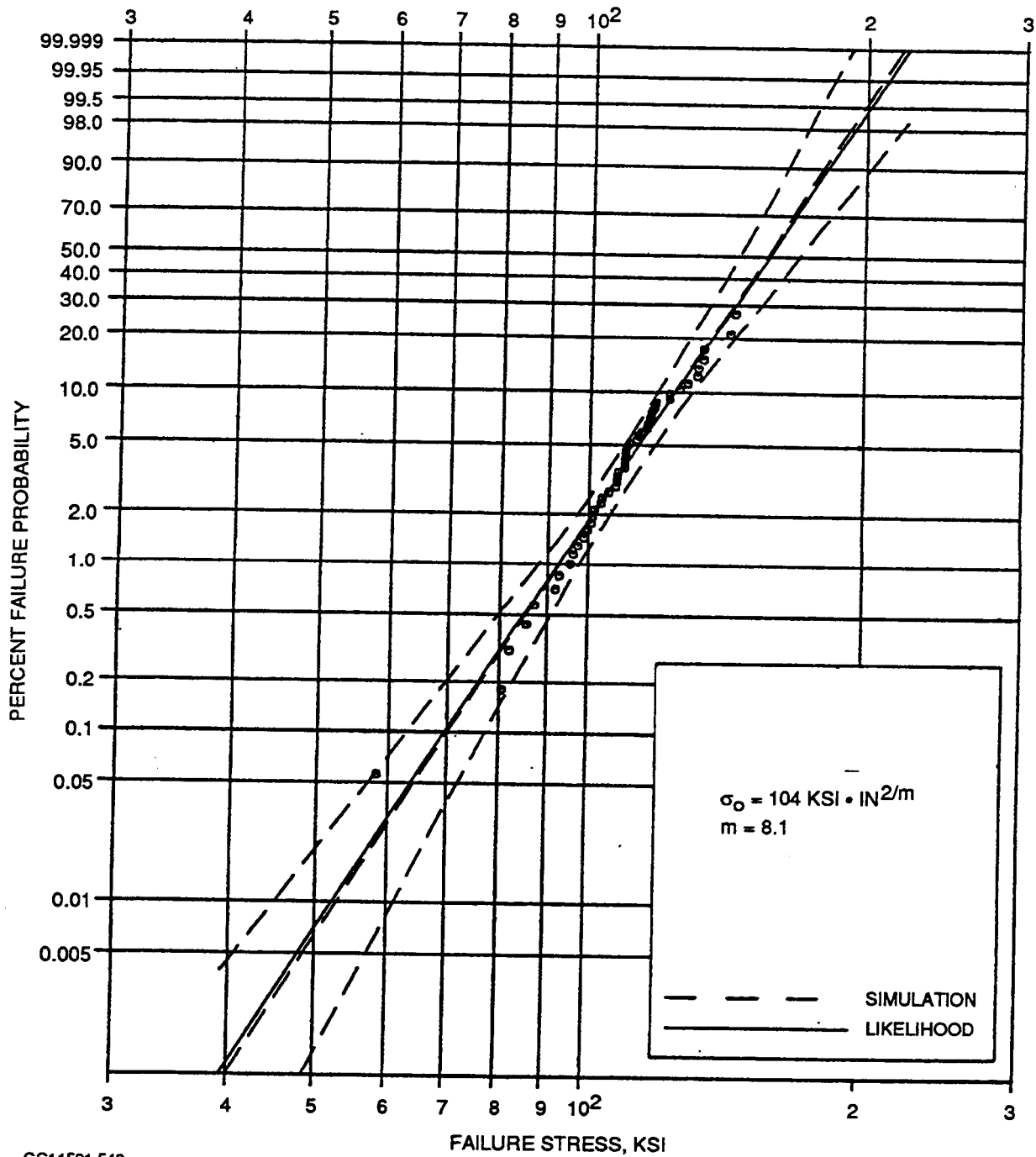
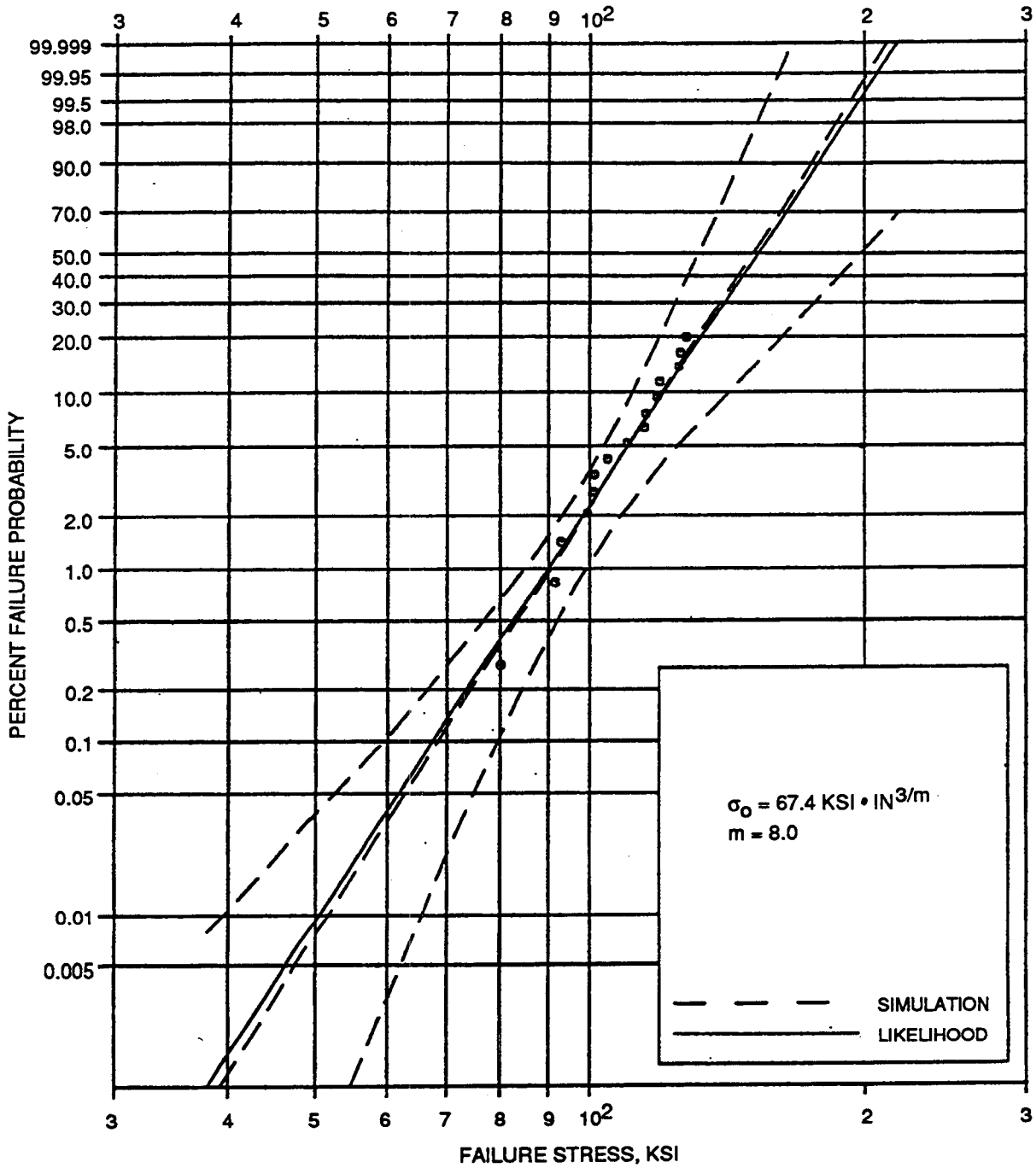


Figure 5-42. Weibull Plot Of Surface Strength From Room-Temperature E-Size Flexure Test Data. All Non-Surface Failures Are Censored.



GC11591-543

Figure 5-43. Weibull Plot Of Volume Strength From Room-Temperature E-Size Flexure Test Data. All Non-Volume Failures Are Censored.

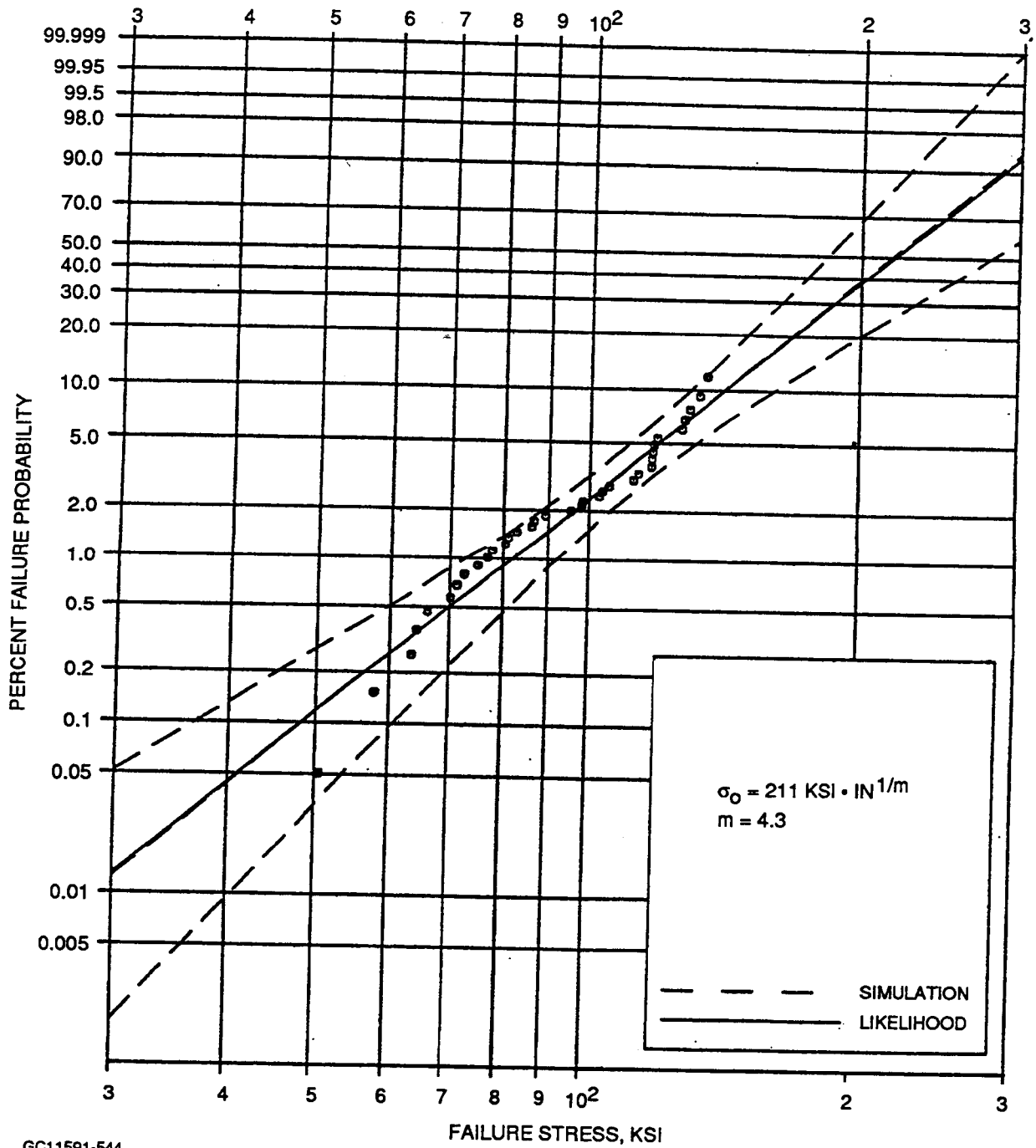
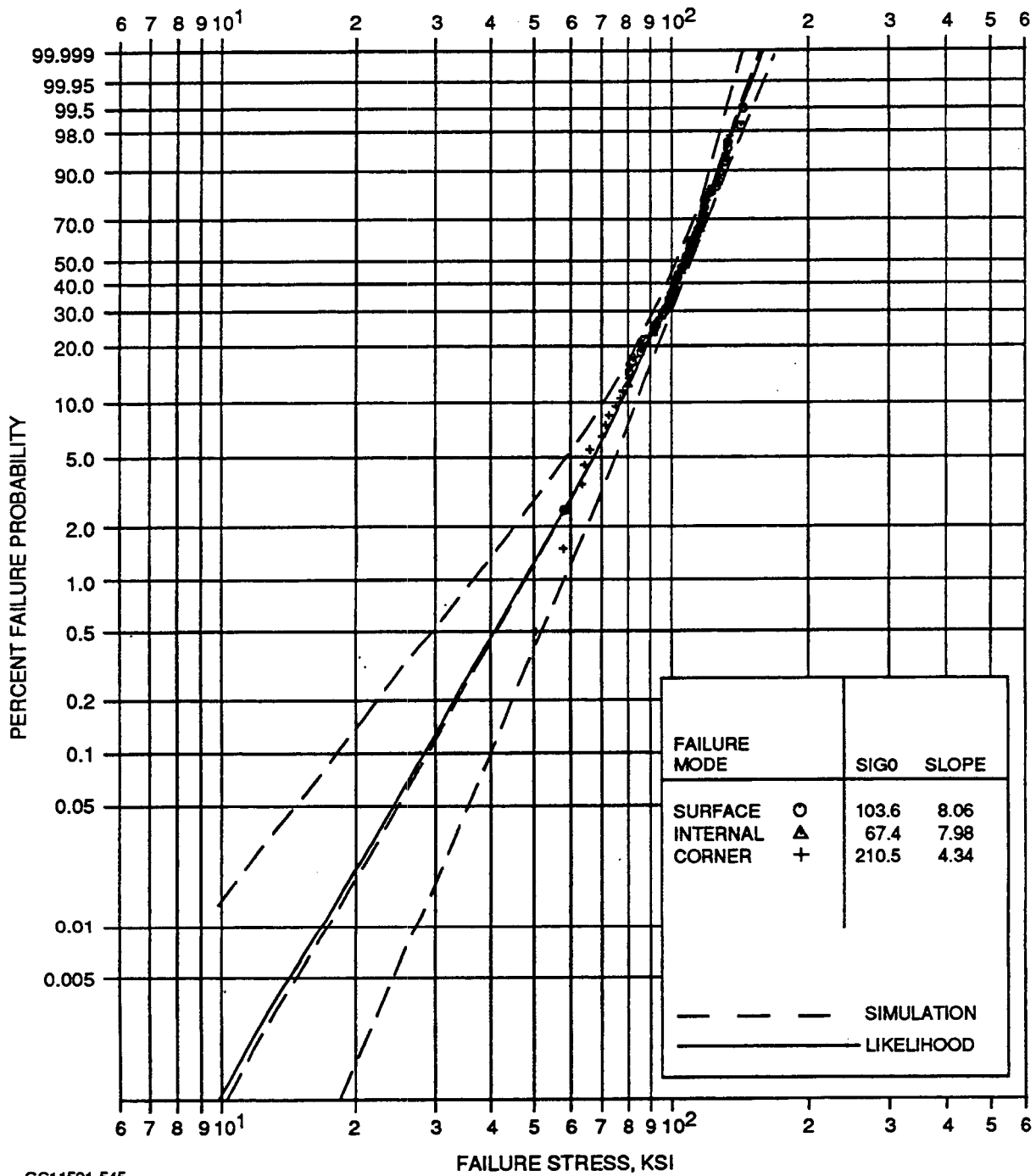
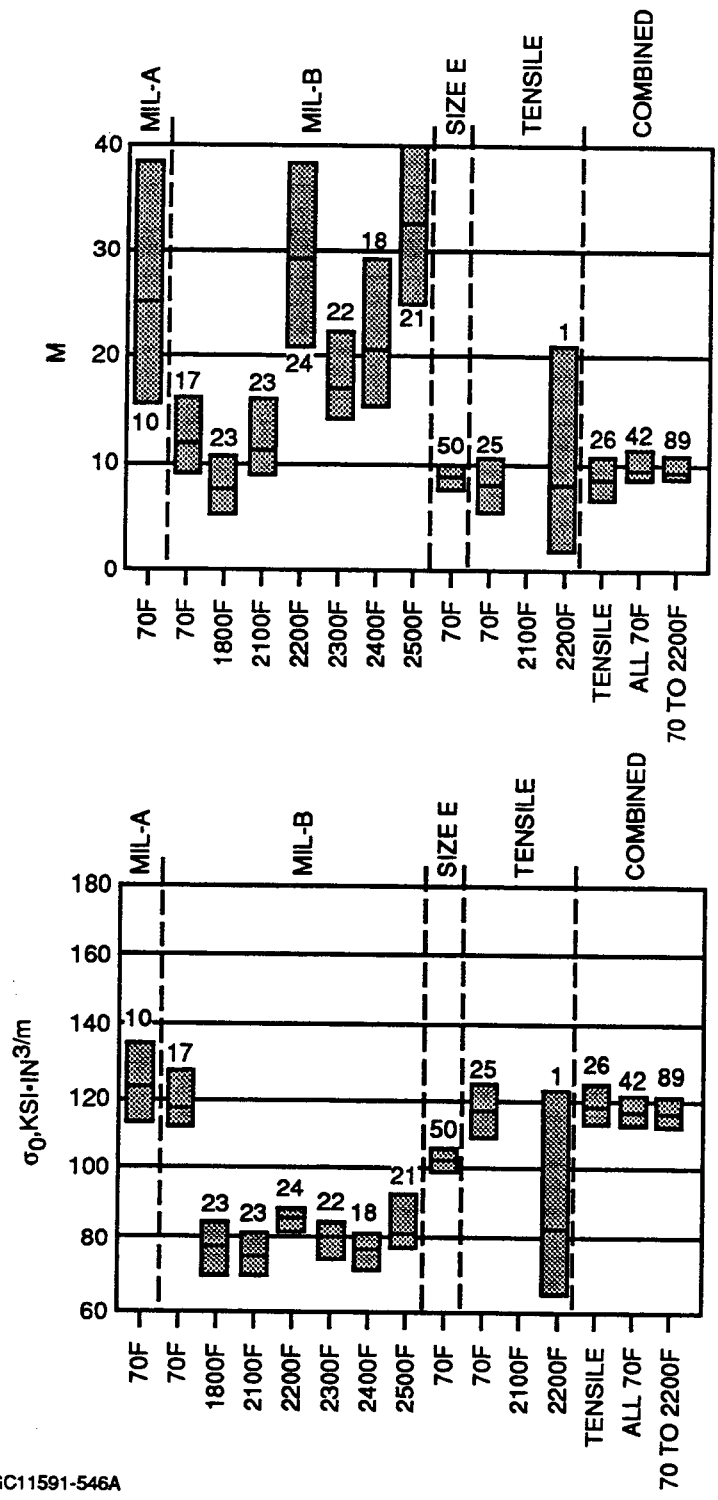


Figure 5-44. Weibull Plot Of Chamfer Strength From Room-Temperature E-Size Flexure Test Data. All Non-Chamfer Failures Are Censored.



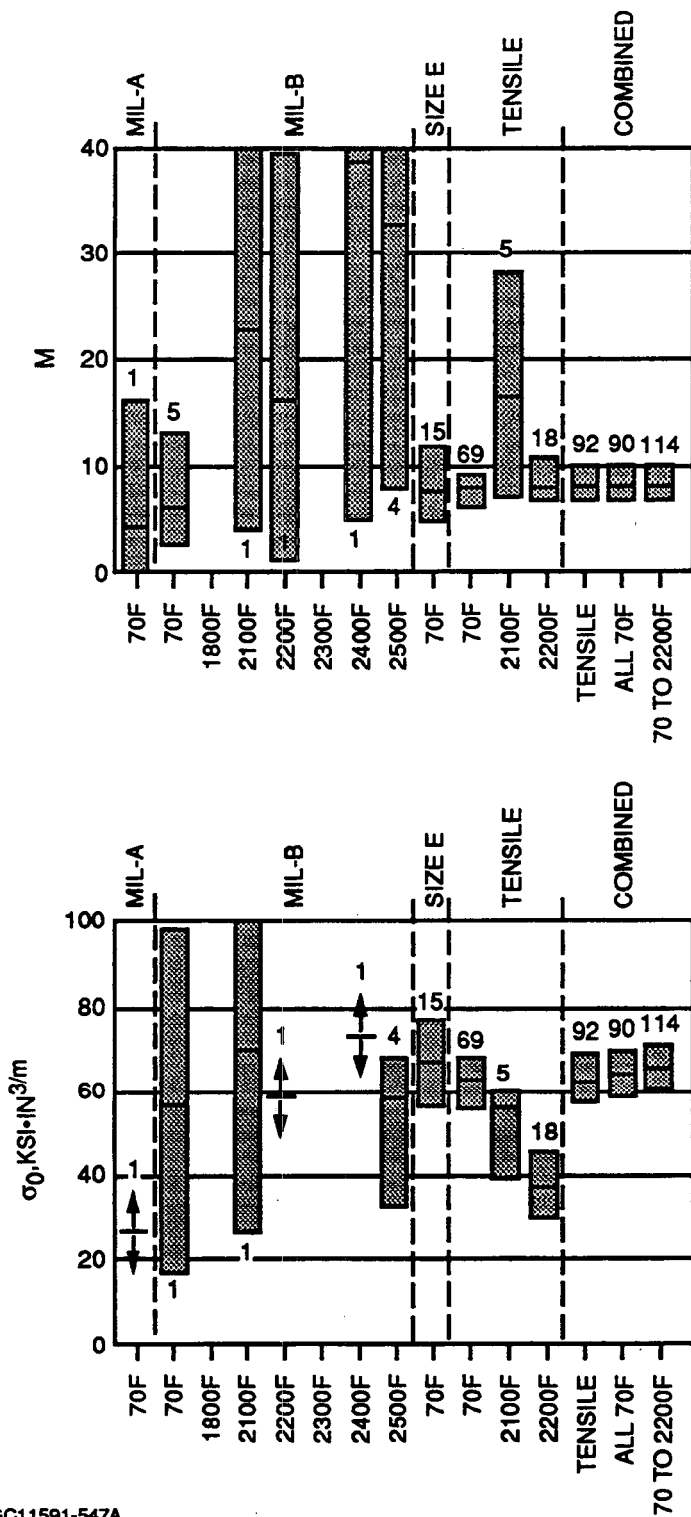
GC11591-545

Figure 5-45. Weibull Plot Of Combined Surface, Internal, And Chamfer Failures From Room-Temperature E-Size Flexure Test Data.



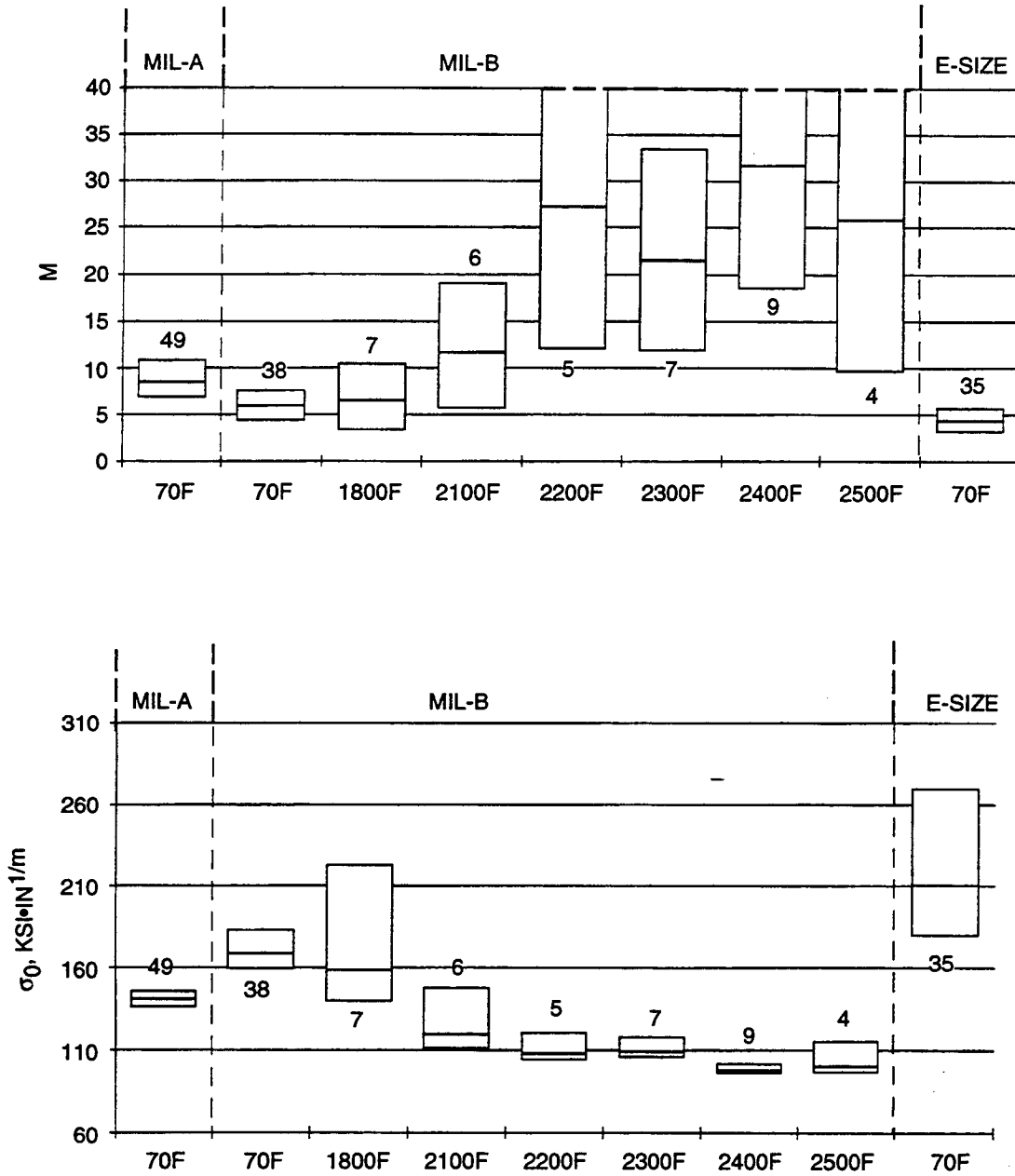
GC11591-546A

Figure 5-46. Surface Strength Parameter Estimates From Several Sets Of Specimen Data.



GC11591-547A

Figure 5-47. Volume Strength Parameter Estimates From Several Sets Of Specimen Data. Arrows Indicate Insufficient Data To Calculate Confidence Bounds.



GC11591-548

Figure 5-48. Chamfer Strength Parameter Estimates From Several Sets Of Specimen Data.

data in these specimens, then the volume data would also be influenced. Few volume failure data points were lost by excluding these sets of data.

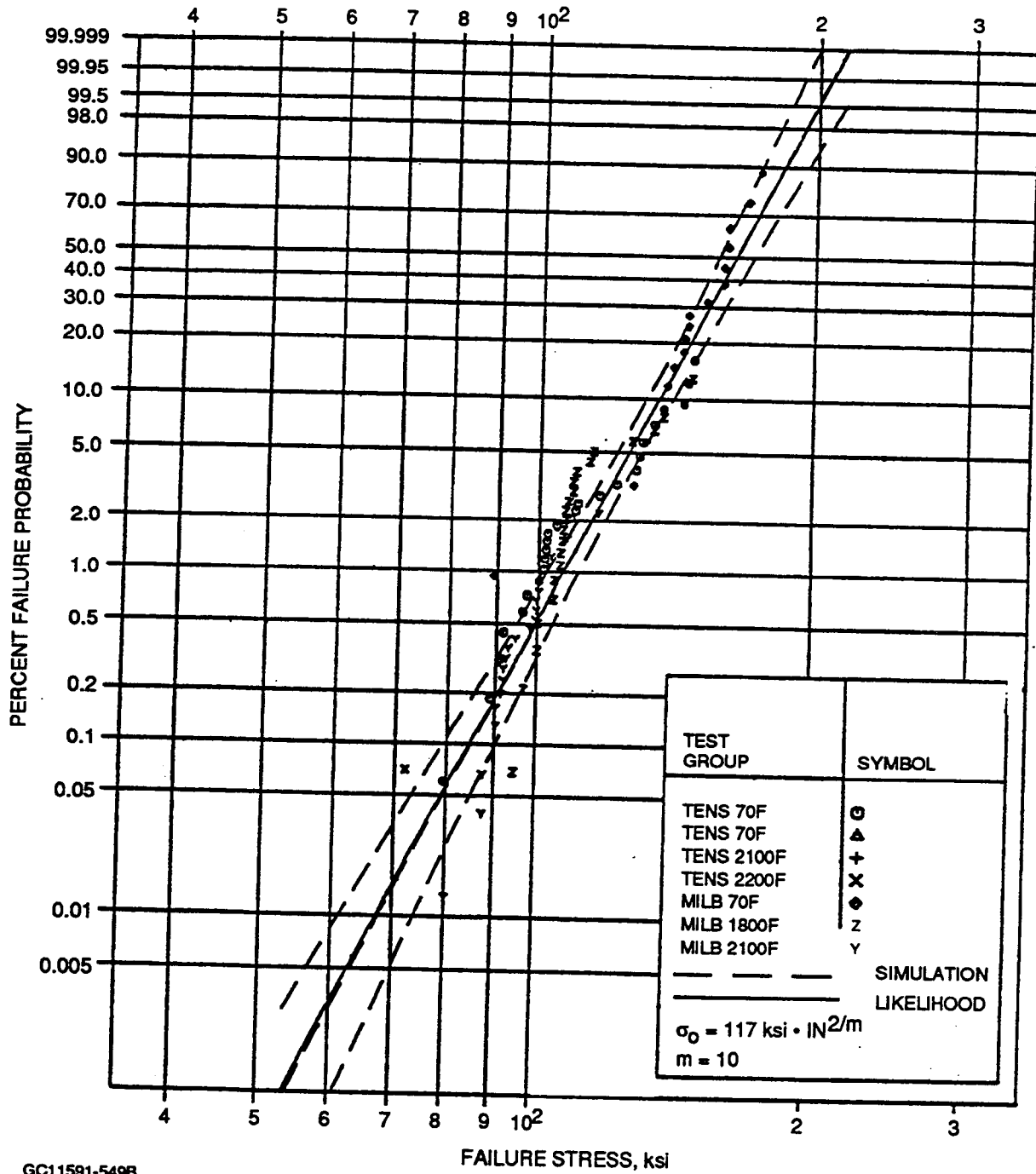
Chamfer strength parameters in Figure 5-48 show similar trends as the surface strength parameter, except for MIL-A, which does not have a significantly higher \hat{m} than the other sets of data. No confirmatory specimens have chamfers, so none of the chamfer failure sets were pooled. This ensures that the expected percentage of chamfer failures would be generated during the bootstrap confidence interval calculations for confirmatory specimen reliability.

The resulting pooled data for confirmatory specimen predictions includes nine sets of strength data. The strength/flaw types defined for each group of specimens are listed in Table 5-10. Some flaw types were defined which did not occur in the original data set. For example, no surface failures were observed in tensile tests at 1800F, but surface failures are included as a possible failure mode. Since surface failures were possible in these specimens, information is obtained during pooled data analyses from the censored non-surface failures.

The parameters estimated from this combined set of data are listed in Table 5-9 and are plotted in Figures 5-46 through 5-48. This pooled set of data also met the fourth guideline. The simulations generated to calculate confidence bounds produced similar percentages of each failure mode, as observed in the original data set. Also included in Table 5-9 and Figures 5-46 through 5-48 are parameters estimated from pooling all room-temperature test data, and from pooling all of the tensile data. Weibull plots of the estimated surface and volume strength reliability lines are plotted in Figures 5-49 and 5-50. Included are all of the non-censored data points for these two failure modes. Both plots have narrow confidence bounds, due to the large number of data points used to estimate these lines.

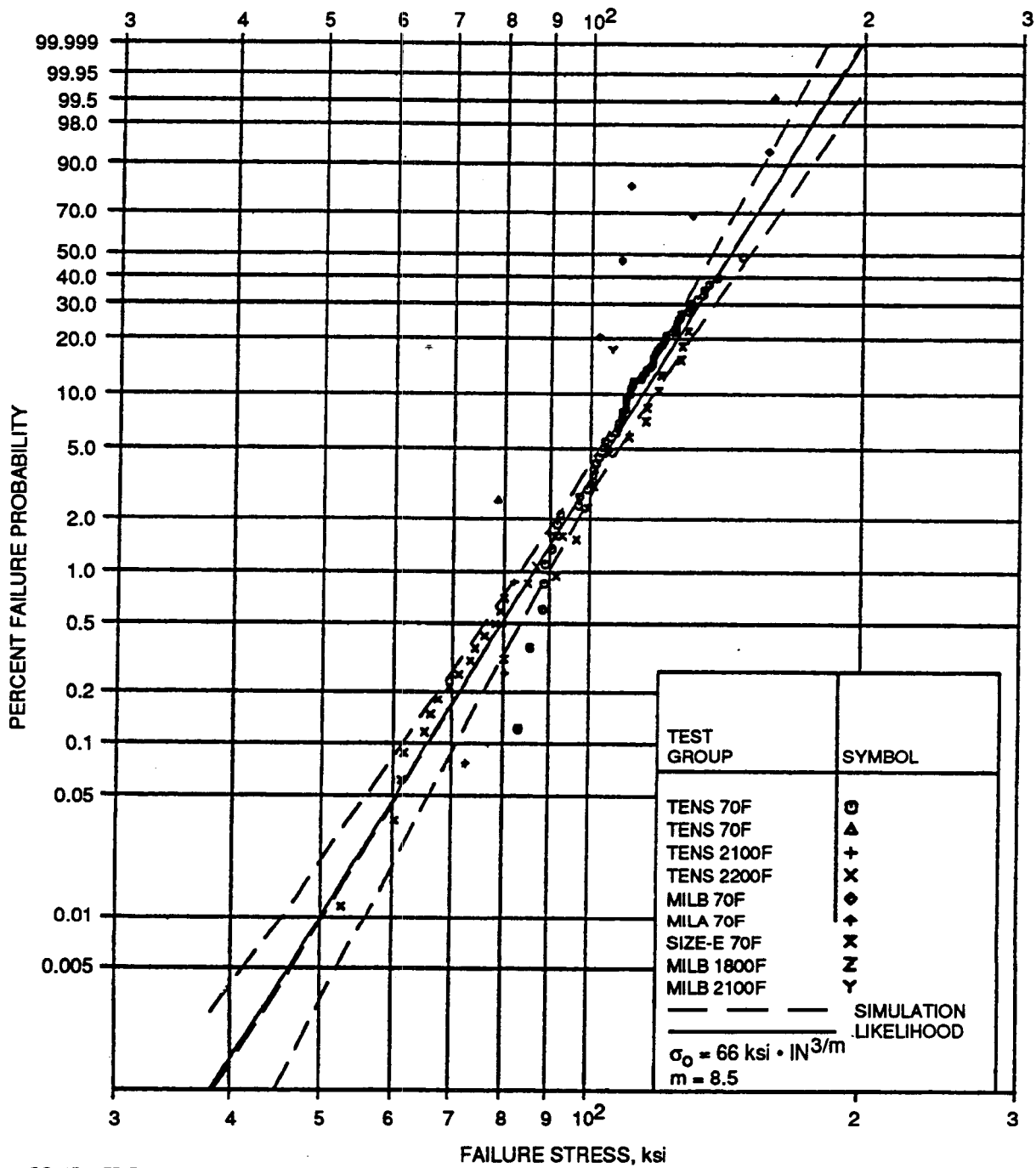
TABLE 5-10. FLAW/STRENGTH TYPES DEFINED FOR EACH SET OF SPECIMENS IN THE POOLED DATA SET

Flaw Populations	MIL-A	MIL-B 72F	MIL-B 1800F	MIL-B 2100F	E-Size Bend	Tensile	Tensile 1800F	Tensile 2200F
<u>Pooled</u>								
Machined surface		X	X	X		X	X	X
Volume	X	X	X	X	X	X	X	X
<u>Not pooled</u>								
Chamfer	X	X	X	X	X			
Machined surface	X				X			
Pit						X		X
Scratches						X		
Buttonhead						X		



GC11591-549B

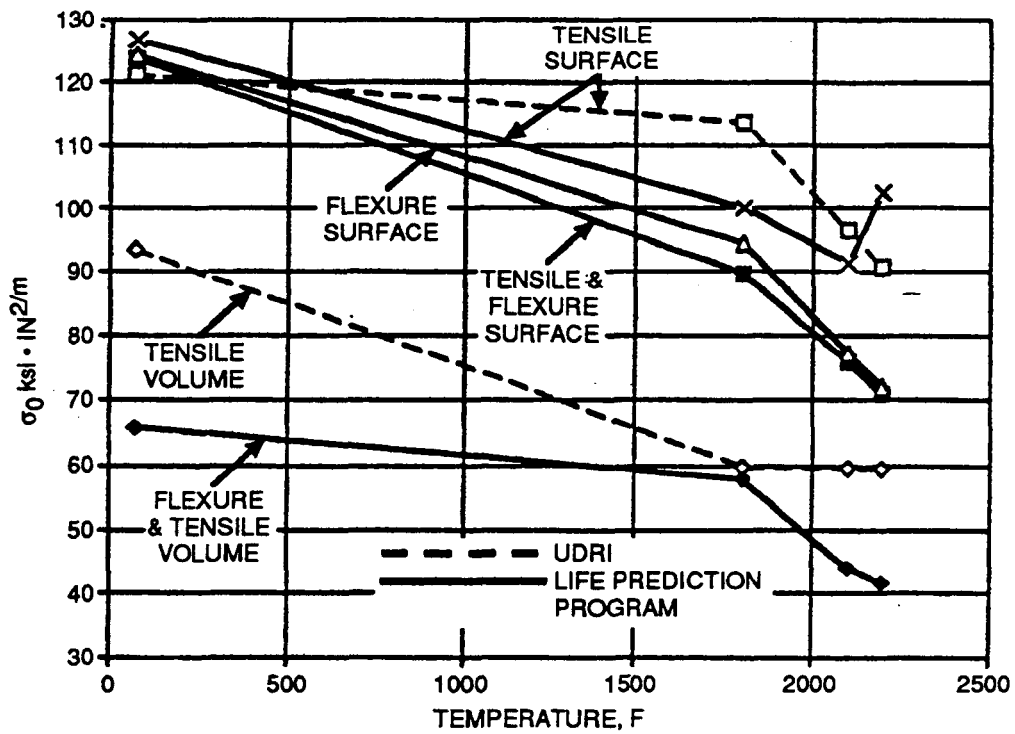
Figure 5-49. Weibull Plot Of Pooled Surface Strength From Tensile And MIL-B Specimens Tested At Multiple Temperatures.



GC11591-550B

Figure 5-50. Weibull Plot Of Pooled Volume Strength From All Specimens/ Types And Multiple Temperatures.

Strength at elevated temperature is used to predict failure probabilities of confirmatory specimens tested at elevated temperatures, and to calculate slow crack growth parameters as discussed in Section 5.3.4. A plot of the second Weibull parameter, σ_0 , versus temperature for surface and volume failures is given in Figure 5-51. These calculations were made with the maximum likelihood pooled data technique for multiple specimen sizes and test temperatures described in Sections 5.2.3 and 5.2.4. A single value of \hat{m} is calculated for each failure mode and is given in Table 5-9. The volume strength from the pooled data set (the line labeled "Flexure and Tensile Volume") does not have unusual characteristics. The surface failure strength, however, shows a significant increase at 2200F. This is shown by the line labeled "Tensile Surface", which was generated from tensile data only. The same strength-temperature trend occurs with the pooled surface data set, because the one surface failure at 2200F is from the tensile data.



GC11591-551A

Figure 5-51. Temperature Dependence Of The Second Weibull Parameter, Estimated For NT154 Surface And Volume Strength.

Additional NT154 tensile data from UDRI was also investigated to better understand the temperature dependence of NT154 surface strength. This is a different vintage of NT154, so the data could not simply be combined with data from this program; however, it does provide additional insight into temperature-dependent strength characteristics. The surface and volume σ_o from the UDRI data are included in Figure 5-51 as dashed lines. Also included are estimates of σ_o at elevated temperatures from MIL-B data pooled from 70F, 1800F, 2100F, and 2200F tests. Because the pooled-temperature maximum likelihood method finds a common \hat{m}' for all temperatures, the estimate of σ_o for 2200F is significantly different than the estimate of σ_o from the 2200F data only. The tensile data is considered to be more useful, because stresses in the gage section are not sensitive to creep deformation, unlike the flexure specimens, which can have significant stress redistribution.

Most of the lines in Figure 5-51 show similar strength reduction with increasing temperature, except the surface failure strength from this program (estimated from one data point) and the UDRI volume strength, which decreases to 1800F and then is flat to 2200F. From this information, we assumed that the reduction in σ_o with temperature for surface strength is proportional to the reduction in volume σ_o calculated from the pooled specimen data in this program. This assumed 2200F surface strength is represented by the solid line identified as "Tensile and Flexure Surface".

The result of these pooled data analyses is a combined set of 405 strength measurements, including 89 surface strengths and 114 volume strengths, for predicting confirmatory specimen strengths and assessing the predictive capabilities of the strength prediction methods developed in this program. The analyses of these strength data also demonstrate the difficulties in producing consistent surface properties in specimens with diverse sizes and shapes. Conversely, the volume properties of NT154 are much more consistent between these diverse specimens.

5.3.3 Anisotropy And Shear Sensitivity

Strength anisotropy and shear sensitivity can significantly influence the predicted failure stress of components with multiaxial stresses. Models for both anisotropy and shear sensitivity (i.e. mixed-mode fracture) were developed in Section 5.2.2. The validity of the anisotropy model and the degree of shear sensitivity are defined from analyses of the strength and fracture toughness tests performed in this program.

Anisotropy and shear sensitivity must be considered concurrently. A value for shear sensitivity can be calculated directly from the diametral-compression disk test results; however, the large precracks used in these specimens may not adequately represent the surface machining damage or internal inclusions which control the strength of the NT154 specimens studied in this program. Additional test data was generated to help determine

the shear sensitivity of these inherent flaws. Fast fracture flexure tests were performed on specimens with zero, 45, and 90 degrees machining directions relative to the flexure stress direction. Test results from torsion and plate bending strength tests also provide insight into the shear sensitivity of inherent flaws. Shear sensitivity can be calculated from these data if the orientation of the inherent flaws is known. Results from several toughness and strength tests were reviewed, to determine the applicability of the anisotropy model and the degree of shear sensitivity for NT154.

The bounds of shear sensitivity can be defined from fracture mechanics criteria and mixed-mode fracture toughness results. Fracture mechanics criteria based on theoretical cracks without closure effects should provide an upper bound for shear sensitivity. The shear sensitivity value calculated from the non-coplanar strain energy release rate criteria is $C = 0.816$ or $Q = 2.45$, where:

$$Q = 2 / C \quad [5-109]$$

The definitions of C and Q are given in section 5.2.2.

The results from diametral compression tests run at the University of Utah, with large cracks, should be indicative of the lower value of shear sensitivity, assuming that roughness-induced closure effects are exaggerated in these large precracks. Results from these tests are shown in Table 5-11.

TABLE 5-11. SHEAR SENSITIVITY ESTIMATED FROM DIAMETRAL COMPRESSION TEST RESULTS

Temperature	No. of Tests	Crosshead Rate	C	Q
Room	20	0.05 in/min	2.07	0.97
2200F	8	0.05 in/min	1.97	1.02
2200F	8	0.0005 in/min	1.78	1.12
2500F	8	0.05 in/min	1.68	1.19

If a material is completely insensitive to shear, i.e., shear stresses alone would never cause failure, then $C = \infty$ and $Q = 0$. The range of Q is therefore zero to 2.45, based on theoretical considerations, and 0.97 to 2.45 if we accept that the diametral compression data represent a lower value of Q for this material.

The plate bending specimens provide the only physical evidence of crack orientation. In these specimens, the fracture-initiating crack usually propagates a sufficient distance before bifurcating to allow the initial crack orientation to be measured. The tensile failure surface of these specimens was machined in a single direction,

and all of these specimens were re-heat treated to improve transverse surface strength. Figure 5-52 shows a histogram of the observed failure directions relative to the machining direction. These failure orientations show a small tendency toward zero degrees and no failures at 80 and 85 degrees, but generally these failures appear to be randomly oriented relative to the machining direction. A map of the fracture origins relative to the machining directions is shown in Figure 5-53. This map also indicates random orientation as well as location of fracture origins relative to the machining direction, with the exception of the three failures farthest from the center of the specimen. The stress away from the centerline is less biaxial and the failures are perpendicular to the maximum principal stress direction. These re-heat treated specimen failure observations indicate that the surface flaws and strength are isotropic.

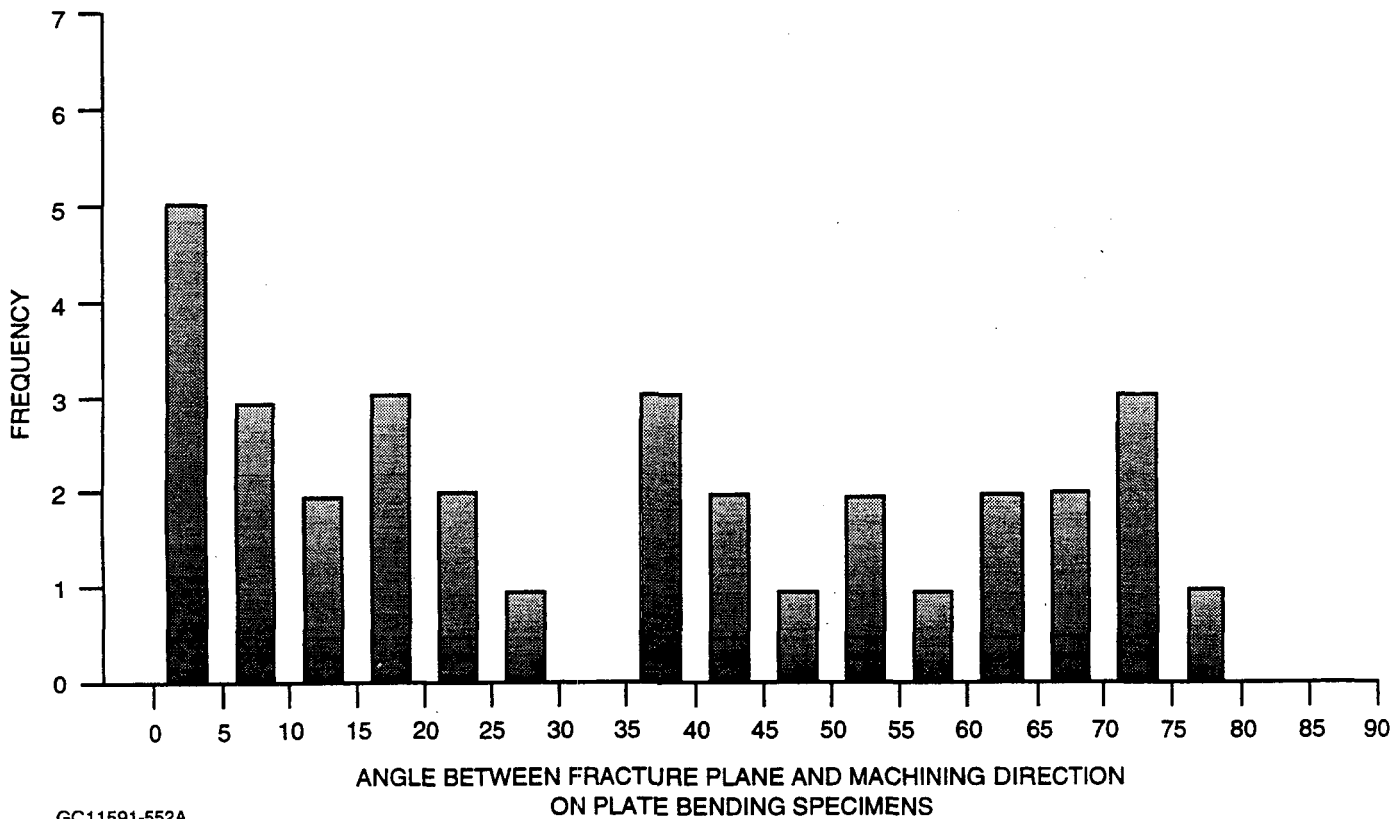


Figure 5-52. Angle Between Fracture Plane And Machining Direction On Plate Bending Specimens.

MAP OF PLATE BENDING SPECIMEN FRACTURE ORIGINS

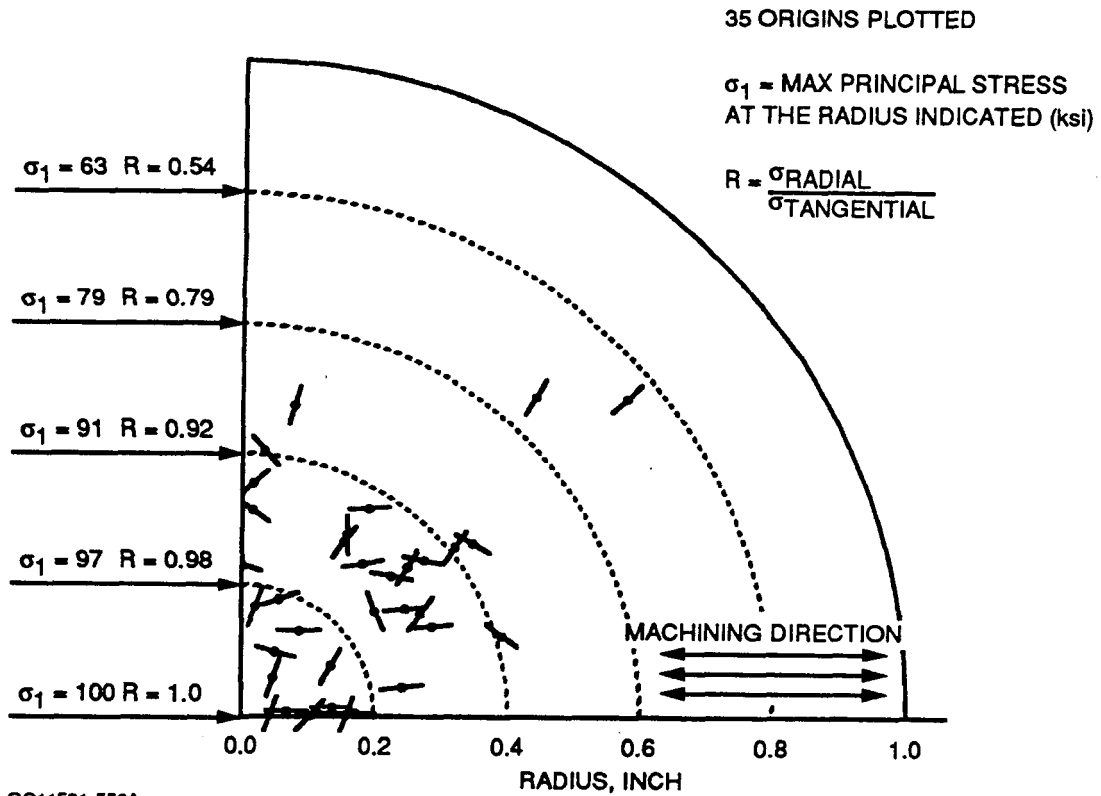


Figure 5-53. Location And Orientation Of Fracture Origins Relative To The Machining Direction In The Plate Bending Specimens.

Further information is available from three sets of flexure strength tests. These specimens were machined at three angles relative to the stress direction (zero, 45, and 90 degrees) to obtain more data on surface strength anisotropy. A summary of these data is given in Table 5-12. Set 1 shows a 16-percent lower average transverse strength compared to longitudinal, and no significant difference in estimates of Weibull modulus. However, Set 1 has limited value for modeling anisotropy, because no surface failures were observed at 45 degrees and only three transverse failures occurred.

The re-heat treated and polished chamfer bars in Set No. 2 produced significantly more surface failures than Set No. 1. This set of data also has a lower transverse strength, 14-percent lower average transverse strength compared to longitudinal. However, in Set No. 2 the Weibull modulus of the transverse flaws is significantly higher than the estimated m for zero and 45 degrees. This is difficult to explain. If the zero and 90 degree flaws are primarily unidirectional flaws (i.e., the delta model in section 5.2.2 applies) than the 45 degree test should have primarily sampled the lower strength, higher "m" transverse flaws. This would have produced a similar "m" to the transverse data, not the longitudinal. A possible explanation for this behavior is proposed after a review of Set No. 3.

TABLE 5-12. WEIBULL PARAMETER ESTIMATES FROM ROOM TEMPERATURE FLEXURE DATA USED TO EVALUATE SURFACE STRENGTH ANISOTROPY

Direction, Degrees	No. Total	No. Surf.	Analysis	σ_0 , (ksi, in)	σ_{50} , (ksi)	m	Comments
SET 1. MIL-B. baseline flexure data. not re-heat treated. chamfers not polished							
0	60	17	Isotropic	119.2	158	12.2	MIL-B only
0	320	42	Isotropic	116.5	164	9.7	Surface is MIL-B & Tensile
45	30	0					
90	30	3	Isotropic	97.5	89	13.6	MIL-B only
90	30	3	Anisotr.	102.2		13.6	MIL-B only
SET 2. MIL-B. re-heat treated. polished chamfers							
0	42		Isotropic	126.1	151	21.0	
45	30		Isotropic	122.2	146	21.3	
90	18		Isotropic	114.7	130	32.4	
SET 3. MIL-B. from flat spin disks. circumferential machining. re-heat treated. polished chamfers							
0	48	34	Isotropic	103.1	133	13.6	
45	30	14	Isotropic	107.4	135	15.9	
90	30	21	Isotropic	103.1	132	13.9	
DIRECTION = Angle between machining and stress directions σ_0 = Second Weibull parameter, normalized to unit size and triaxial tension σ_{50} = 50 percent failure stress relative to MIL-B flexure specimen size, i.e., not size scaled							

The re-heat treated specimens sectioned from spin disks, Set No. 3, showed very consistent average strength and Weibull modulus for all three machining directions. This set of data allows a closer look at the hypothesis that machining produced two orthogonal anisotropic flaw/strength distributions. Weibull plots of surface strength for these data are given in Figures 5-54, 5-55, and 5-56. Assuming that the longitudinal and transverse strengths have the same second Weibull parameter and modulus, we can calculate the Q required to produce the second Weibull parameter observed in the 45 degree tests. First, the effective stress equation for uniaxial loading at 45 degrees to a set of unidirectional flaws is:

$$\sigma_E = \frac{1}{2} \left[\frac{\sigma_x}{2} + \sqrt{\left(\frac{\sigma_x}{2}\right)^2 + Q^2 \left(\frac{\sigma_x}{2}\right)^2} \right] = \frac{\sigma_x}{4} [1 + \sqrt{1 + Q^2}] \quad [5-110]$$

This is obtained by substituting $\sigma_x / 2$ for τ in Equation [5-36] from section 5.2.2. Then two equations can be written for the probability of failure at 45 degrees. Assuming that the zero and 90 degree tests have equal orthogonal strength distributions, the expected failure probability at 45 degrees can be written:

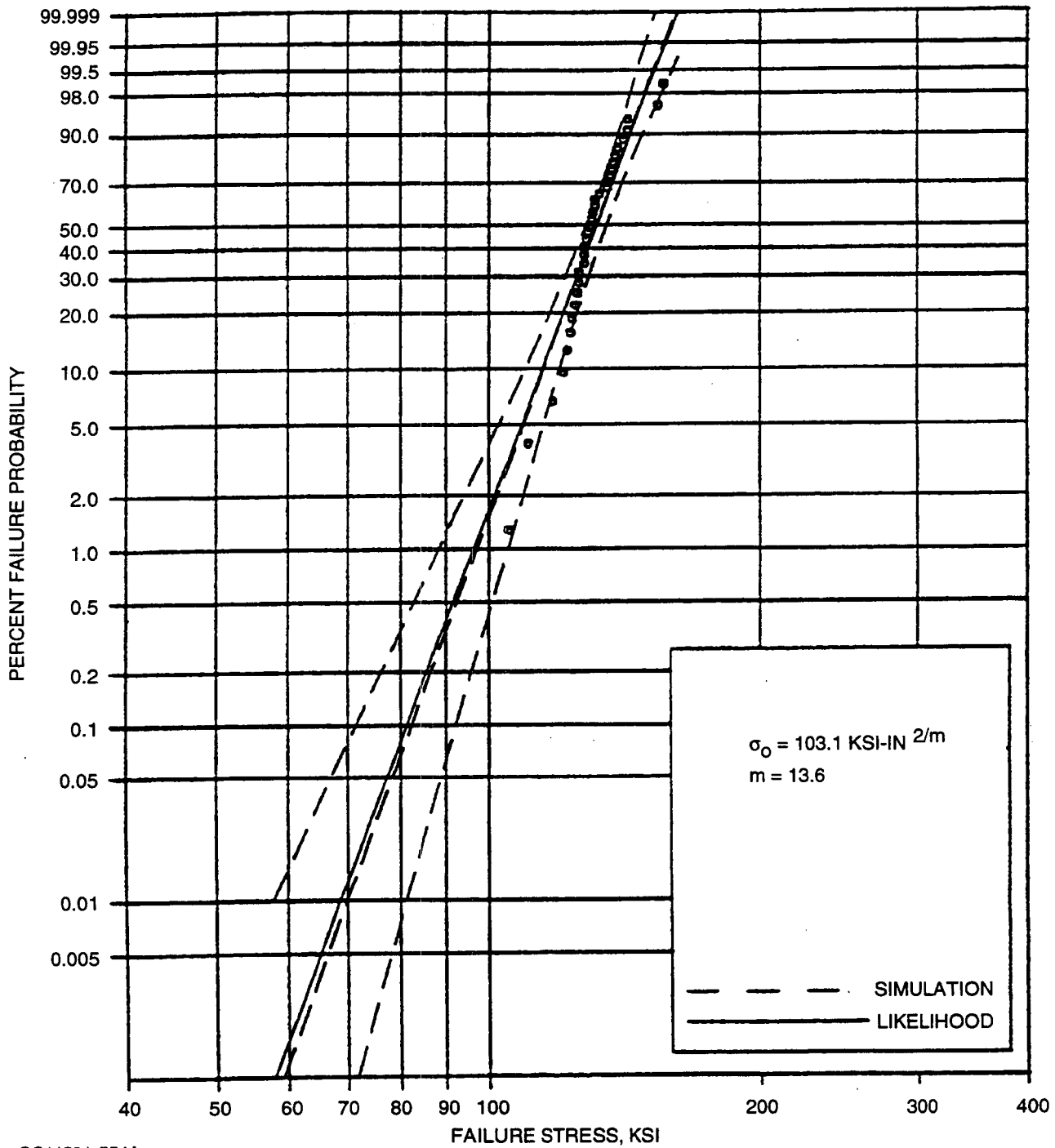
$$PS_{45^\circ} = \text{EXP} - \left[IA \left(\frac{\sigma_E}{\sigma_{o,0^\circ}} \right)^{m_{0^\circ}} + IA \left(\frac{\sigma_E}{\sigma_{o,90^\circ}} \right)^{m_{90^\circ}} \right] = \text{EXP} - \left[2IA \left(\frac{\sigma_E}{\sigma_{o,0^\circ}} \right)^{m_{0^\circ}} \right] \quad [5-111]$$

and the probability of survival determined directly from the 45 degree tests is:

$$PS_{45^\circ}^* = \text{EXP} - \left[IA \left(\frac{\sigma_x}{\sigma_{o,45^\circ}^*} \right)^{m_{45^\circ}} \right] \quad [5-112]$$

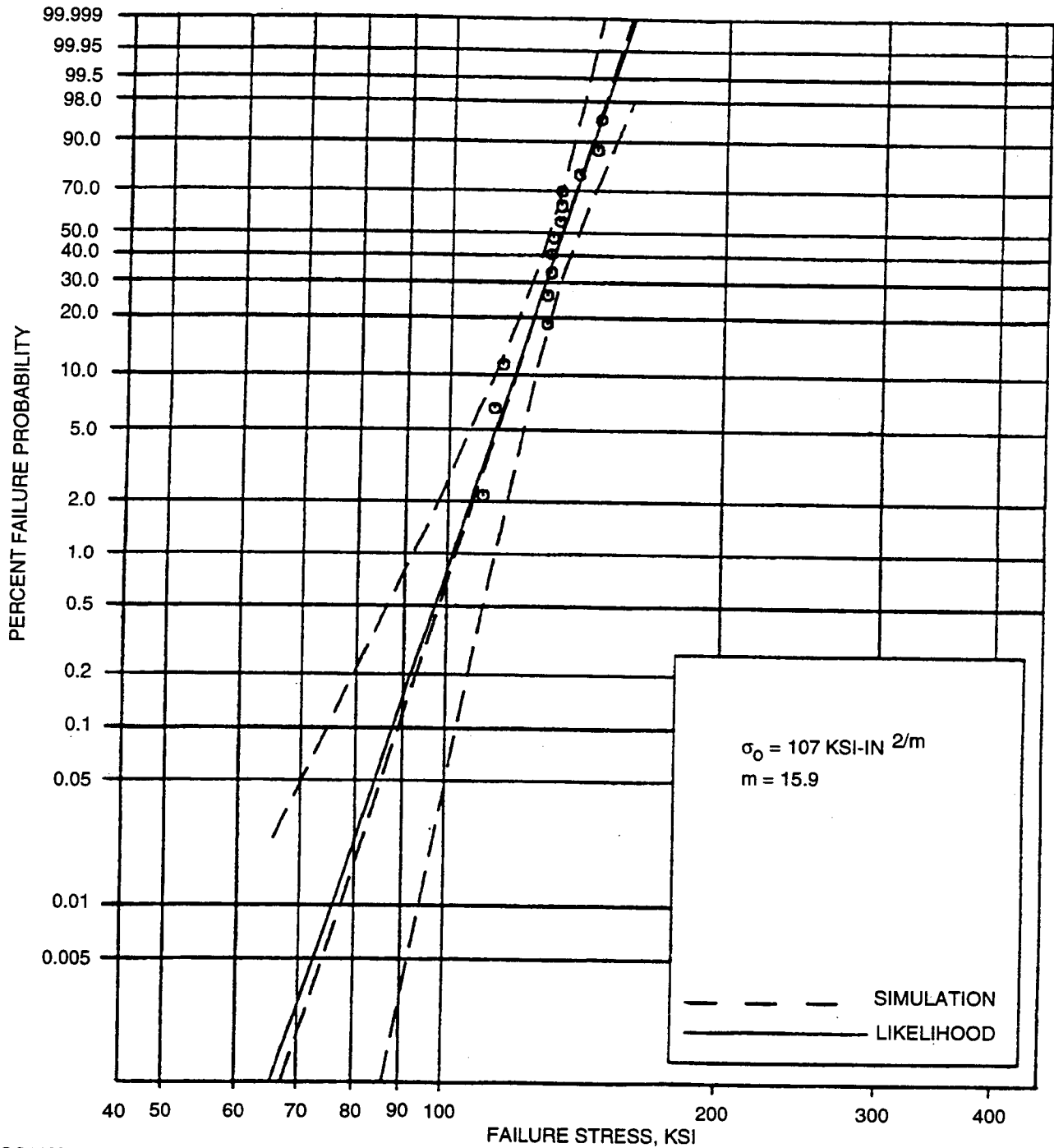
If only two anisotropic orthogonal distributions exist, then the probability of survival at 45 degrees (PS_{45°) calculated from zero and 90 degree data should be equivalent to the probability of survival measured at 45 degrees ($PS_{45^\circ}^*$). Therefore, by equating Equations [5-111] and [5-112], and assuming that all three distribution have the same m results in:

$$\sigma_E = \left(\frac{\sigma_{o,0^\circ}}{\sigma_{o,45^\circ}^*} \right) \sigma_x 2^{\frac{1}{m}} \quad [5-113]$$



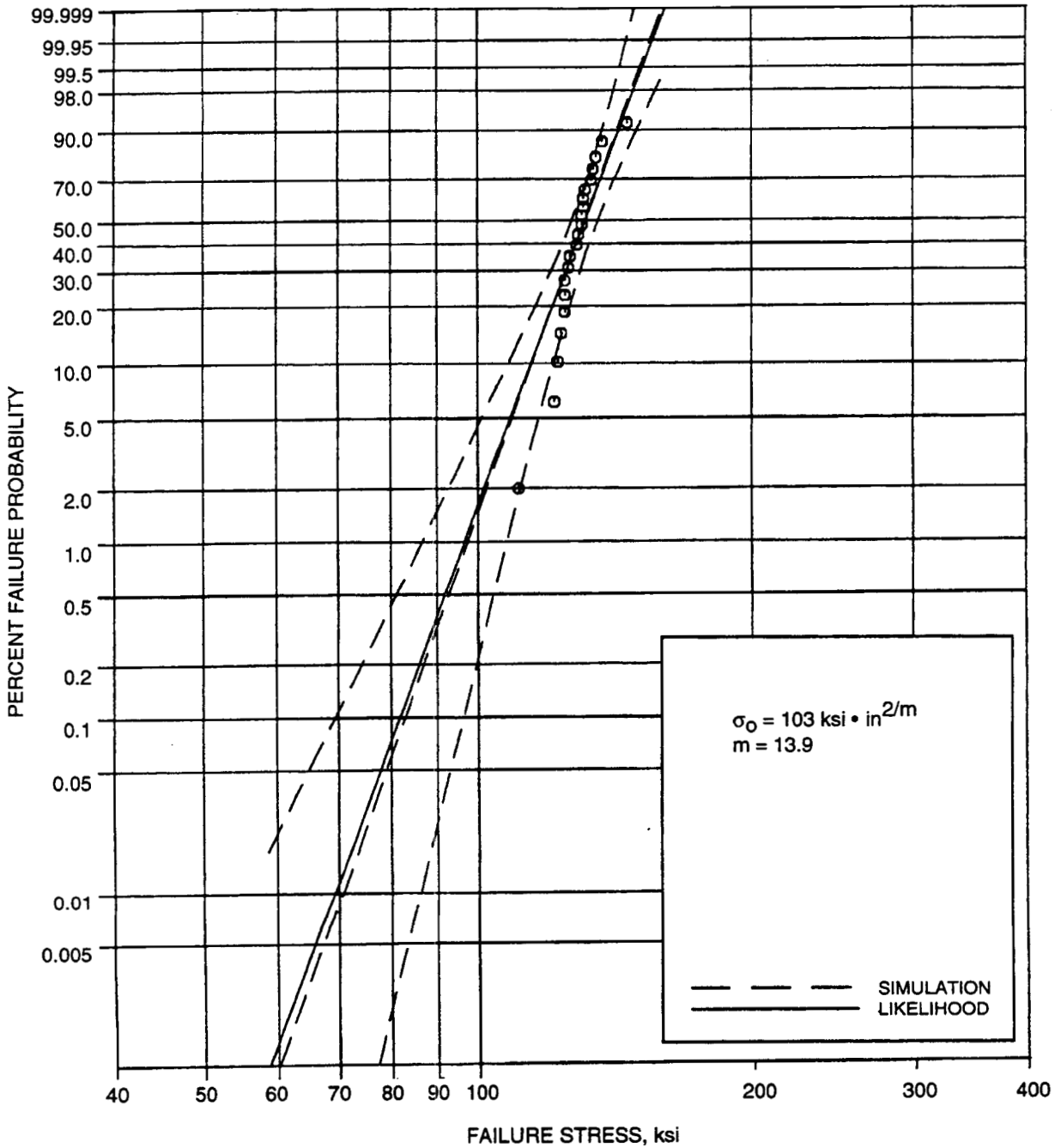
GC11591-554A

Figure 5-54. Weibull Plot Of Room-Temperature Surface Strength From MIL-B Specimens Sectioned From Flat Spin Disks With Longitudinal Machining. Non-Surface Failures Were Censored.



GC11591-555A

Figure 5-55. Weibull Plot Of Room-Temperature Surface Strength From MIL-B Specimens Sectioned From Flat Spin Disks Machined 45 Degrees To the Stress Direction. Non-Surface Failures Were Censored.



GC11591-556A

Figure 5-56. Weibull Plot Of Room-Temperature Surface Strength From MIL-B Specimens Sectioned From Flat Spin Disks Transversely Machined. Non-Surface Failures Were Censored.

Substituting Equation [5-110] into Equation [5-113] allows calculation of the Q needed to produce the σ_o calculated from the 45 degree specimen data if only unidirectional flaws were present at zero and 90 degrees.

$$Q = \left[\left\{ 4 \left(2^{-\frac{1}{m}} \right) \frac{\sigma_{o,0^\circ}}{\sigma_{o,45^\circ}} - 1 \right\}^2 - 1 \right]^{\frac{1}{2}} = 2.45 \quad [5-114]$$

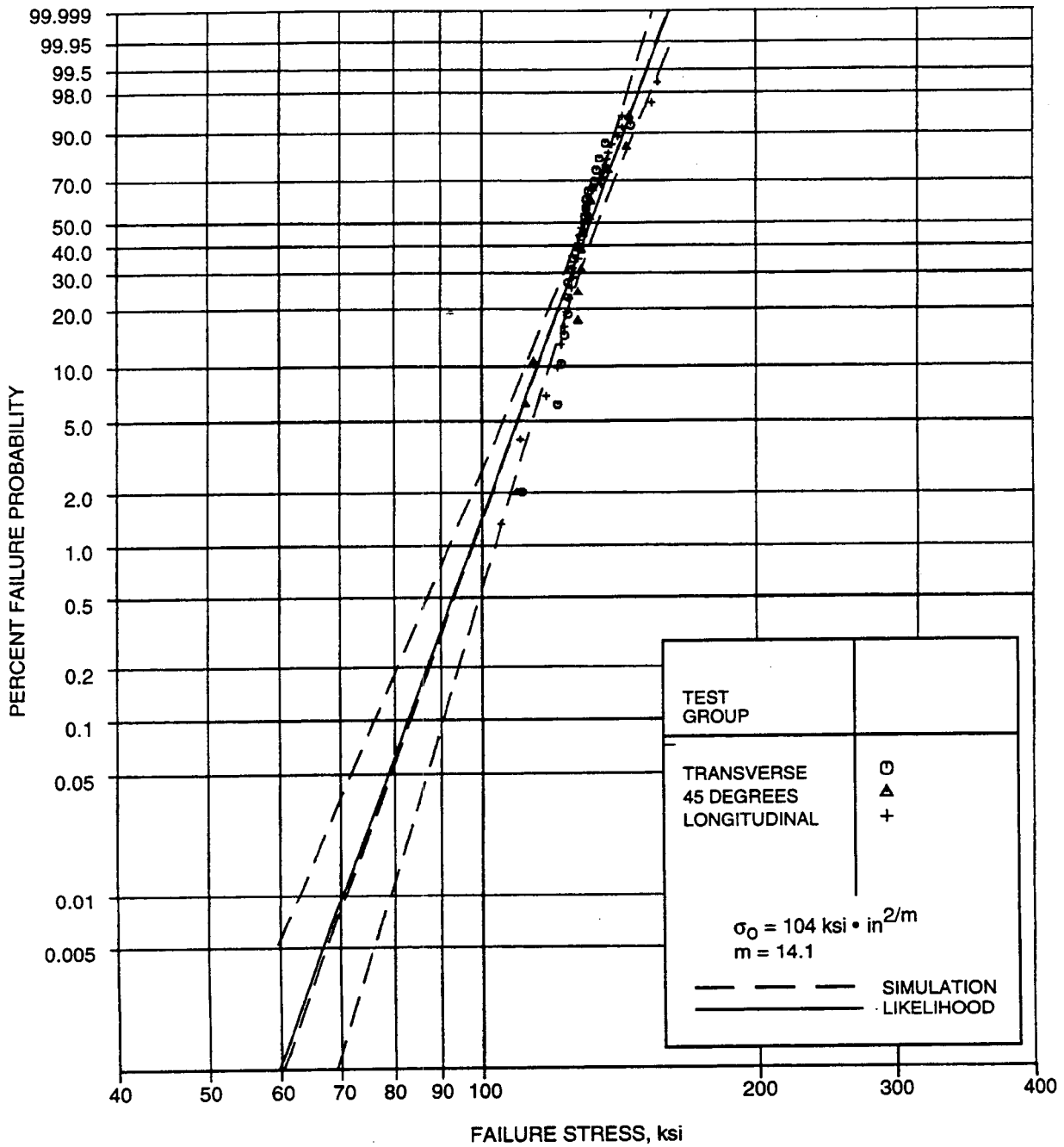
This value of $Q=2.45$ was obtained by using Set No. 3 parameters in Equation [5-114]. A value of 2.45 is unexpectedly large for Q , based on previously-described fracture mechanics criteria. As a result, it is very unlikely that the underlying machining flaws are two unidirectional orthogonal flaw distributions. A Weibull surface strength plot including all three data sets (zero, 45, and 90 degrees) is shown in Figure 5-57. Although anisotropic surface strengths were expected, the parameters from Set No. 3 appear to be a result of an isotropic strength.

Torsion testing provides additional information about anisotropy and shear sensitivity. These tests should provide a better measure of shear sensitivity. The surface of the torsion-specimen gage section is machined longitudinally, i.e., the grinding direction is parallel to the centerline. If flaws are oriented zero and 90 degrees to the machining direction, then these flaws will be subjected to shear stress only, and there is no normal stress acting on these flaws. This was not the case in the 45-degree flexure specimens, which would have a tensile stress normal to these flaws. Several possible values for the second Weibull parameter were calculated from these torsion specimens and are shown in Table 5-13. These tension and torsion specimens were not re-heat treated.

TABLE 5-13. COMPARISON OF σ_o ESTIMATES FROM TENSILE AND TORSION STRENGTH DATA

Ref. No.	Loading	Total	No. Surf.	Analysis	Q	σ_o (ksi, in)	m	Specimen
1	Tension	100	25	Isotropic	0	118.7	7.7	ORNL Tensile
2	Torsion	13	8	Isotropic	0	116.2	14.6	Tension-Torsion
3	Torsion	13	8	Isotropic	0.97	117.3	14.6	Tension-Torsion
4	Torsion	13	8	Anisotropic	0.97	47.4*	14.6	Tension-Torsion
5	Torsion	13	8	Anisotropic	2.45	103.7*	14.6	Tension-Torsion

* = Estimate of transverse strength from torsion loading
 σ_o = Second Weibull parameter, normalized to unit size and triaxial tension



GC11591-557B

Figure 5-57. Weibull Surface Strength Data Estimated From Pooled Longitudinal, 45-Degree, and Transverse-Machined MIL-B Specimens Sectioned From Flat Spin Disks.

These torsion data were used to evaluate three candidate models from machined surface strength:

- (1) Longitudinal and transverse strengths are anisotropic and orthogonal
- (2) One isotropic strength distribution is present
- (3) Longitudinal strength is isotropic and the transverse strength is anisotropic.

Rows 2 and 3 of Table 5-13 show the longitudinal σ_0 predicted from the torsion data. Two values of low shear sensitivity were used, and strength was modeled as being isotropic. Different estimates of σ_0 are obtained for the isotropic and anisotropic analyses, because the delta function used for modeling anisotropy produces a different I-m function as described in Section 5.2.2. Row 2 provides an estimate of σ_0 similar to the tensile specimen shown in Row 1. If we look at a more rational large value of Q in Row 3, we see very little change in the estimates of σ_0 . These calculations provide support for Models 2 and 3.

Parameter estimates in Rows 4 and 5 of Table 5-13 are calculated to evaluate surface strength from Model 1. If the surface has two anisotropic orthogonal surface strength distributions, then these torsion tests should have primarily sampled the lower strength longitudinal flaws (i.e., transverse strength). To test the applicability of Model 1, the transverse σ_0 was estimated from the torsion data with the assumption that the transverse strength is anisotropic. Since we have no transverse tensile data for comparison with these estimates, the MIL-B transverse σ_0 was used. Although this may be reasonable because the MIL-B and tensile specimens have similar longitudinal surface strength parameters, the transverse MIL-B data had only three machined surface failures. The analyses in Rows 4 and 5 show that we need an unreasonably high shear sensitivity to predict a transverse σ_0 similar to that from the transverse MIL-B data. Similar to previous data sets reviewed in this section, the torsion data does not support modeling surface strength as two orthogonal anisotropic strength distributions.

Since none of the data sets reviewed in this section provide sufficient proof to select one modeling approach, we need to look at the combined implications of all of these data sets. A summary of the conclusions from these data sets is given in Table 5-14.

The combination of all of this evidence supports Model 3, isotropic longitudinal strength and anisotropic transverse strength. The plate bending tests exhibited randomly oriented failures and showed no strong indication of anisotropy and supports Model 2. However, these specimens were re-heat treated and may not be indicative of the inherent machining flaws/strength. The re-heat treatment may heal cracks, produce residual stresses, or create a new flaw population that competes with or is more severe than the machining flaws. The flexure sets 2 and 3 were also re-heat treated. Set No. 2, however, still exhibits different zero- and 90-degree

TABLE 5-14. ASSESSMENT OF CANDIDATE SURFACE STRENGTH MODELS BASED ON SUPPORTING SPECIMEN DATA

Supporting Data	Model 1	Model 2	Model 3
Plate Bending*	-1	1	0
Flexure Set-1	1	-1	1
Flexure Set-2*	-1	-1	1
Flexure Set-3*	-1	1	0
Tension-Torsion	-1	0	1
* Re-heat treated <u>Rating</u> 2 strongly support 1 weakly support 0 provides no insight -1 weakly disproves -2 strongly disproves			

strengths and the 45-degree strength parameters are more consistent with the longitudinal strength parameters than the weaker 90-degree strength. Set No. 2 provides support only for Model 3. Set No. 3 flexure specimens, sectioned from spin disks, appear to have isotropic strength. Analyses of these data showed an unreasonably large shear sensitivity would be required for these strength parameters to be produced by two orthogonal anisotropic distributions. The non re-heat treated flexure specimens in Set No. 1 exhibit some anisotropy, and lower transverse strength than longitudinal. However, with only three transverse surface strength measurements this set of data is not convincing. The torsion specimens did provide several failures from non re-heat treated surfaces. These failures can be predicted from tensile specimen properties if we assume an isotropic distribution of flaws, and these failures are not predictable from MIL-B transverse machining properties. This also suggests Model 3 may be applicable. Model 2 is less likely for non re-heat treated specimens which appear to have lower transverse strength.

From these analyses of anisotropic behavior two modeling approaches will be used for confirmatory specimen predictions. The non re-heat treated tension-torsion specimens surfaces will be modeled with isotropic (longitudinal) strength and an anisotropic transverse strength. For the spin disk predictions, observations from the spin disk cutups, flexure Set No. 2 will be used. The spin disk surfaces will be modeled as having one isotropic surface distribution. These studies did not provide guidance in selecting a value of shear sensitivity that can be applied to inherent surface or volume flaws. The flaws will be considered to be insensitive to shear for consistency in the confirmatory specimen predictions.

5.3.4 Evaluation Of SCG Parameters

The stress rupture test matrix shown in Table 4-1 and the tensile fast fracture matrix shown in Figure 4-1 were both utilized to obtain subcritical crack growth (SCG) parameters. Since both the stress rupture and fast fracture tests sample inherent flaws, the derived SCG parameters would be appropriate for inherent flaw growth. Two primary methods were employed to obtain the crack growth description (ref. 5-74 and 5-77).

- (1) Multiple-stress-level stress-rupture tests, assuming median behavior at each stress level.
- (2) Multiple replicates of stress rupture and tensile fast fracture tests in which the scatter of strengths and lifetimes were treated statistically.

The simplest form of an SCG equation was the starting point for both approaches:

$$da / dt = AK^n \quad [5-115]$$

where K is the stress intensity factor, and A and n are SCG parameters. The appropriateness of the basic equation was examined in the course of the parameter estimations.

In method (1), only stress rupture data was utilized. At a given temperature, the log of the applied stress level was plotted against the log of the time to failure. If Equation [5-115] is appropriate, the well-known life-time relation results:

$$t_f = \frac{2}{\sigma^2 Y^2 A (2-n)} (K_{IC}^{2-n} - K_{II}^{2-n}) \quad [5-116]$$

Neglecting K_{IC}^{2-n} and substituting $K_{II} = \frac{\sigma}{S} (K_{IC})$, $t_f = BS^{n-2} \sigma^{-n}$ [5-117]

with:

$$B = 2 / AY^2(n-2)K_{IC}^{n-2} \quad [5-118]$$

where: S is the fast fracture strength, σ is the applied stress, Y is the geometry factor for the appropriate flaw, K_{ii} is the initial stress intensity, and K_{IC} is the fracture toughness. n can be obtained from the Log σ versus Log t_f plot. In this method, no distinction is made between surface and internal initiated failures; the SCG parameters are assumed to apply equally to surface and internal crack growth.

In method (2), a statistical procedure is employed to treat the scatter in strengths and lifetimes. In this procedure, the lifetime as well as the strength measurements must be and were performed with the same loading configuration.

In general, N samples are tested in fast fracture to determine the initial flaw size distribution; N samples are then tested in stress rupture to determine the lifetime distribution. In the simplest case, the i -th value of the lifetime is matched with the i -th value of the fast fracture strength, and the crack velocity as a function of the initial applied stress intensity for each specimen is obtained:

$$da / dt(K) = -2K_i^2 / (Y^2 S^2 t_f) * d(\ln \sigma / S) / d(\ln t_f) \quad [5-119]$$

where: K_i is the initial stress intensity at the onset of the stress rupture test and equals $= \sigma / S * K_{IC}$.

The technique can be refined by censoring both the fast fracture and stress rupture data for surface- and volume-initiation locations, fitting distribution functions such as Weibull to both strength and lifetime distributions, and estimating SCG parameters from the fitted functions.

Using the censored strength and life distributions, the median SCG parameters can be estimated by assigning median ranks to both the strength and life, to a virtual data set for both strength and life, and performing regression according to Equation [5-119]. In the case of Weibull strength and life distributions, an SCG equation of the form shown in Equation [5-115] results.

The virtual data set approach is also amenable to estimating the bounds of the SCG parameters. Simulation data using random numbers may be generated similar to that described earlier for Bootstrap simulation of strength distribution confidence bounds.

5.3.4.1 SCG Parameters From Method (1)

Some of the stress rupture data has been shown in Figures 5-24 through 5-26. The regressed SCG exponents at the temperatures are shown in Table 5-15. At 1800F, the data scatter was so great that meaningful exponents could not be obtained.

TABLE 5-15. REGRESSED "n" AS A FUNCTION OF TEMPERATURE

Temperature, F	No. of Specimens	No. of Replicate Specimens	Regressed "n"*
2100	29	21	17.6
2200	33	20	17.0
2300	9	--	21.9
2400	8	--	31.6
2500	43	32**	15.1
2550	9	--	3.4

* See discussion of regressed "n" in text. below.
 ** Two stress levels.

Regression was performed with "log life" as the dependent variable and "log stress" as the independent variable. Due to data scatter, if the regression were performed with "log stress" being the dependent variable and "log life" being the independent variable, and then taking the inverse of the slope, the values of "n" could be significantly different. Runout specimens were included in the regression.

In the discussion of creep rates in Sections 5.1.2 and 5.1.3, a demarcation between low- and high-stress dependence was noted at ~1315C (2400F). This was not observed in the n values shown in Table 5-15. Limited sample size and scatter in stress rupture lives at 2400F may be responsible.

5.3.4.2 SCG Parameters From Method (2)

The data set at 2200F, in which 20 fast fracture and 20 stress rupture tests (conducted at 54.4 ksi) were performed, was used extensively to evaluate the SCG parameters.

5.3.4.2.1 As-Generated Data

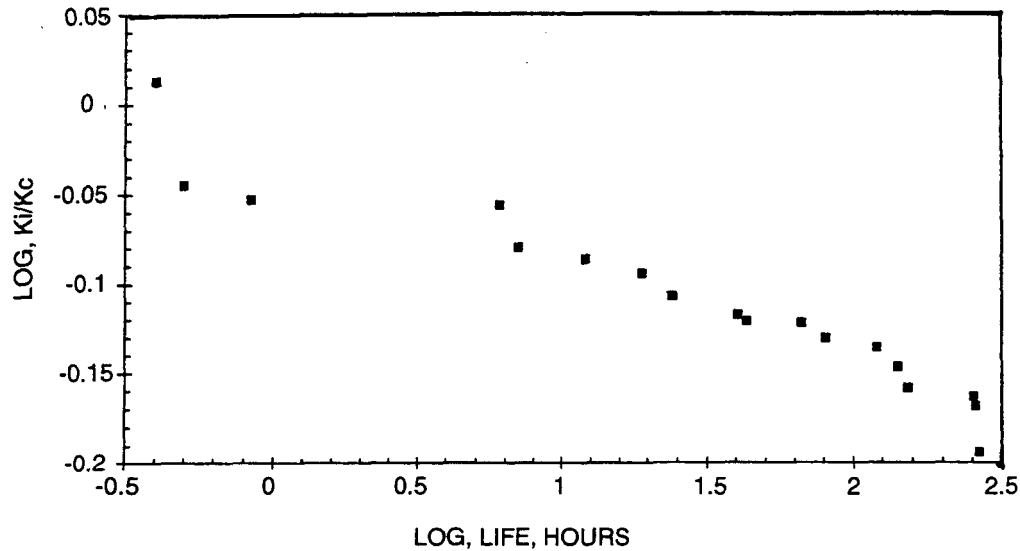
The as-generated stress rupture and fast fracture data can be used directly to derive the SCG parameters, A and n. The procedure employed was as follows:

- (1) The fast fracture (FF) and stress rupture (S/R) data were paired and ranked, with the lowest FF strength data paired with the shortest life data, as shown in Table 5-16. In the 2200F data set, the two runout S/R specimens and the two strongest FF specimens were not used.
- (2) A plot was made of $\log K_I/K_C$ (where K_I/K_C = applied stress in S/R tests/corresponding FF strength) vs. log life, as shown in Figure 5-58. A linear fit was made to the data points.
- (3) A calculation was made of da/dt via Equation [5-118]; in this case, all the stress rupture failures were assumed to be internally initiated, with flaw geometry factor $Y = 1.128$, and $K_{IC} = 5.54 \text{ ksi}\cdot\text{in}^{1/2}$.

TABLE 5-16. 2200F FAST FRACTURE STRENGTH AND STRESS RUPTURE LIFE PAIRS STRESS RUPTURE TESTS CONDUCTED AT 54.4 ksi

Strength, ksi	Failure Origin	Life, hours	Failure Origin
52.80	Internal	0.40	Internal
60.30	Internal	0.50	Internal
61.40	Internal	0.84	Internal
61.80	Internal	6.00	Surface
65.30	Internal	7.00	Surface
66.30	Internal	7.00	Surface
66.30	Internal	12.00	Internal
67.50	Internal	12.00	Internal
69.50	Internal	24.00	Surface
71.20	Internal	40.00	Internal
71.80	Surface*	43.00	Surface
72.00	Surface	66.00	Internal
73.40	Internal	80.00	Surface
74.30	Internal	120.00	Surface
76.20	Internal	141.00	Internal
78.30	Internal	153.00	Internal
79.30	Internal	253.00	Surface
80.10	Internal	257.00	Surface
85.00	Internal	266.00	Internal
86.90	Internal	Runout	
96.40	Internal	Runout	
*Failed from surface pit (atypical surface origin); data point censored.			

LOG (KI/KC) VS. LOG (LIFE); 2200F - 54.4 ksi DATA



GC11591-558

Figure 5-58. Stress Rupture (2200F/54.4 ksi) Test Data Compared To 2200F Fast Fracture Data. A Linear Fit Was Used To Derive The V-K Curve Shown In Figure 5-59.

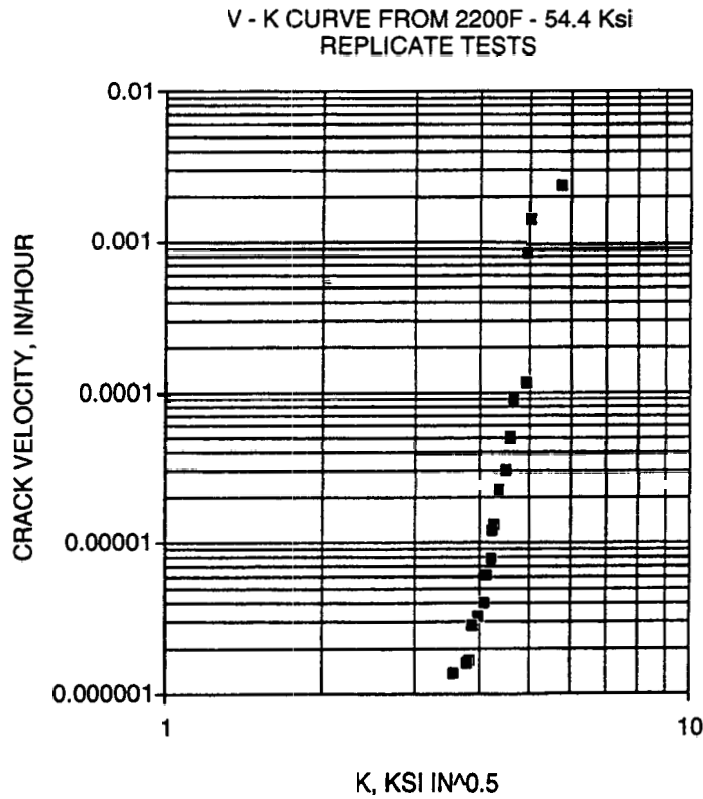
(4) A plot was made of da/dt against K_I , as shown in Figure 5-59. Linear regression yielded $A = 1.56E-17$, $n = 19.0$.

Since FF data was available, (Log Life) can be regressed against (Log FF strength) as indicated in Equation [5-116] for another estimate of n . This approach results in $n-2 = 18.2$, and $n = 20.2$, which is close to the value obtained from the V-K curve.

5.3.4.2.2 Censored Fast Fracture And Stress Rupture Data

5.3.4.2.2.1 2200F Test Data

By censoring both the fast fracture and the stress rupture data and fitting Weibull distribution to both the fast fracture strength and the stress rupture life, estimates of both the surface and internal SCG parameters can be determined. For 2200F, both the pooled (70F to 2200F) Weibull bend test and tensile strength distribution estimate and the 2200F tensile-only Weibull strength estimate, shown in Figure 5-44 and Table 5-9, were used.



GC11591-559

Figure 5-59. V-K Curve (Linear Fit) Plot Of 2200F/54.4 ksi Stress Rupture And 2200F Fast Fracture Test Data.

The Weibull fits to the censored surface- and internal-initiated stress rupture life data are shown in Figures 5-60 and 5-61, respectively. The Weibull life and fast fracture strength parameters used for SCG parameter evaluations are as shown in Table 5-17. (Note: in contrast to the rest of the report, all Weibull strength parameters were scaled to the actual size of the specimens with uniaxial tension as the reference stress state, to facilitate direct comparison with the stress rupture test results):

Using the maximum likelihood Weibull strength and life estimates, the following procedure was employed to derive the SCG parameters for each failure origin:

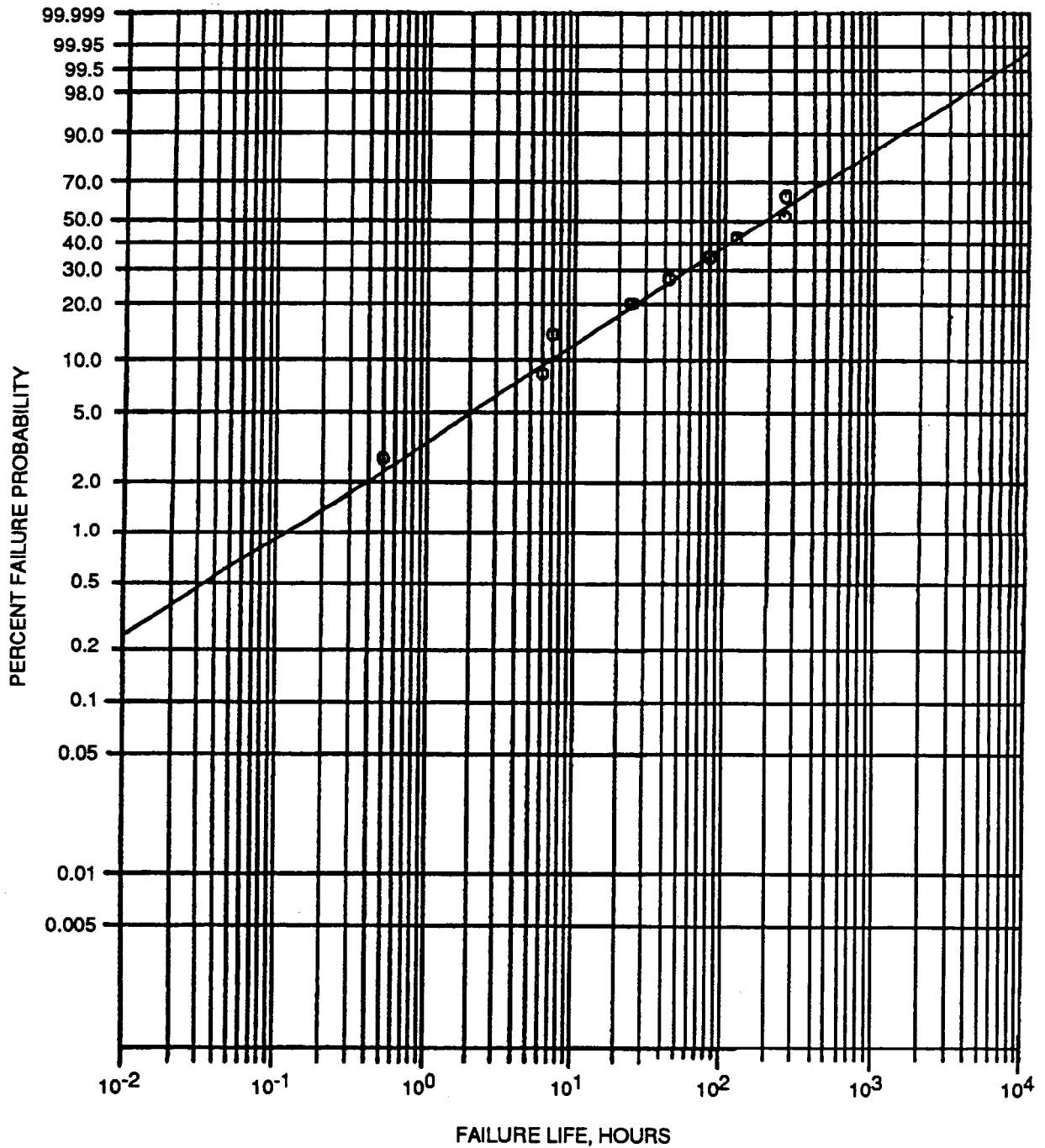
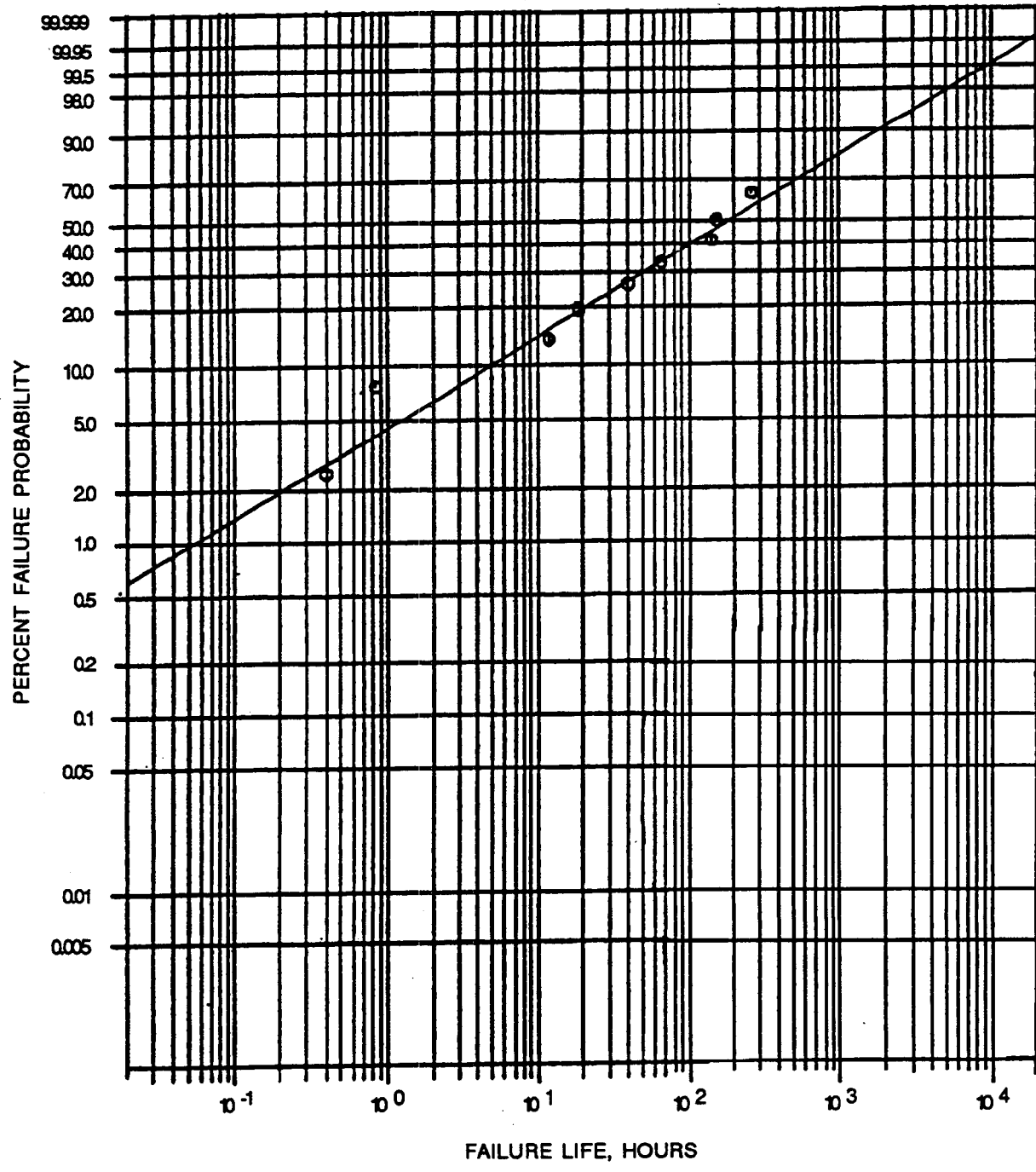


Figure 5-60. Weibull Plot Of Censored Surface-Initiated Stress Rupture Failures Tested At 2200F/54.4 ksi. Characteristic Life = 348.9 Hours; Slope = 0.58.



GC11591-561A

Figure 5-61. Weibull Plot Of Censored Internal-Initiated Stress Rupture Failures Tested At 2200F/54.4 ksi. Characteristic Life = 380.6 Hours; Slope = 0.52.

- (1) A virtual set of 20 fast fracture strengths and stress rupture lives were generated using median ranks
- (2) Steps 2, 3, and 4 as shown earlier were repeated for as-generated data.

The resulting SCG parameters, as well as the parameters generated using raw data only are shown in Table 5-18.

TABLE 5-17. 2200F LIFE AND STRENGTH PARAMETERS USED TO CALCULATE SCG PARAMETERS

	Charac. Life, Hours	Weibull Modulus	No. of Specimens
Volume	380.6	0.52	9
Surface	348.9	0.58	9
Runouts	--	--	2

Pooled Data	Charac. Strength, ksi	Weibull Modulus	No. of Specimens
Volume	80.51	8.45	N/A
Surface	78.75	9.99	N/A

2200F Data Only			
Volume	80.56	7.45	18
Surface	118.31	7.53	1

TABLE 5-18. SCG PARAMETERS FROM 2200F LIFE AND STRENGTH DATA

	Internal		Surface	
	A	n	A	n
Pooled Data	3.70E-17	18.23	4.88E-18	19.29
2200F Data Only	5.31E-16	16.33	4.33E-13	14.98
As-Generated Data	1.56E-17	19.0	---	---

The discrepancies, particularly in the surface SCG parameters, were due to differences in the fast fracture strength estimates. The tensile specimen surface characteristic strength, plotted as a function of temperature, showed a peak at 2200F, whereas the pooled bend and tensile strength did not, as shown in Table 5-17 and Figure 5-51. It was also encouraging to note that the value of the 2200F exponent "n" from stress rupture data only, (n= 17.0, see Table 5-15), was close to the values obtained from the paired fast fracture and stress rupture method.

5.3.4.2.2.2 2100F Test Data

Twenty replicate stress rupture tests were performed at a stress level of 65.3 ksi, along with five fast fracture tests. The five fast fracture tests were too small in number for adequate estimation of the strength characteristics at 2100F; however, they made a contribution to the pooled strength estimation.

The censored life distributions and pooled estimates of volume and surface fast fracture characteristics were used to calculate the SCG parameters. The Weibull life and fast fracture strength parameters and the resulting SCG parameters are shown in Table 5-19.

TABLE 5-19. 2100F LIFE, STRENGTH, AND SCG PARAMETERS

	Characteristic Life, hours	Weibull Modulus	No. of Specimens
Volume	992.8	0.20	11
Surface	4475.3	0.52	3
Runouts	---	---	7

	Characteristic Strength, ksi	Weibull Modulus
Volume	84.93	8.45
Surface	84.4	9.99

	A	n
Volume	1.71E-35	44.25
Surface	2.65E-21	21.21

The vast difference between the surface and volume "n" is due to the large difference in the Weibull moduli of the life distributions.

5.3.4.2.2.3 2500F Test Data

Even though a total of 32 replicate stress rupture tests were performed at two stress levels (16 at each stress), no fast fracture tests were performed. Since the vast majority of the failures observed in the tests performed at this temperature were surface initiated, the original flaw distribution was probably no longer failure-controlling. In the confirmatory specimens, life predictions would be made on the basis of a deterministic stress-life relationship.

5.3.4.2.3 Comparison Of SCG Parameters

The only complete set of data was that tested at 2200F; hence, this discussion will concentrate on the 2200F results.

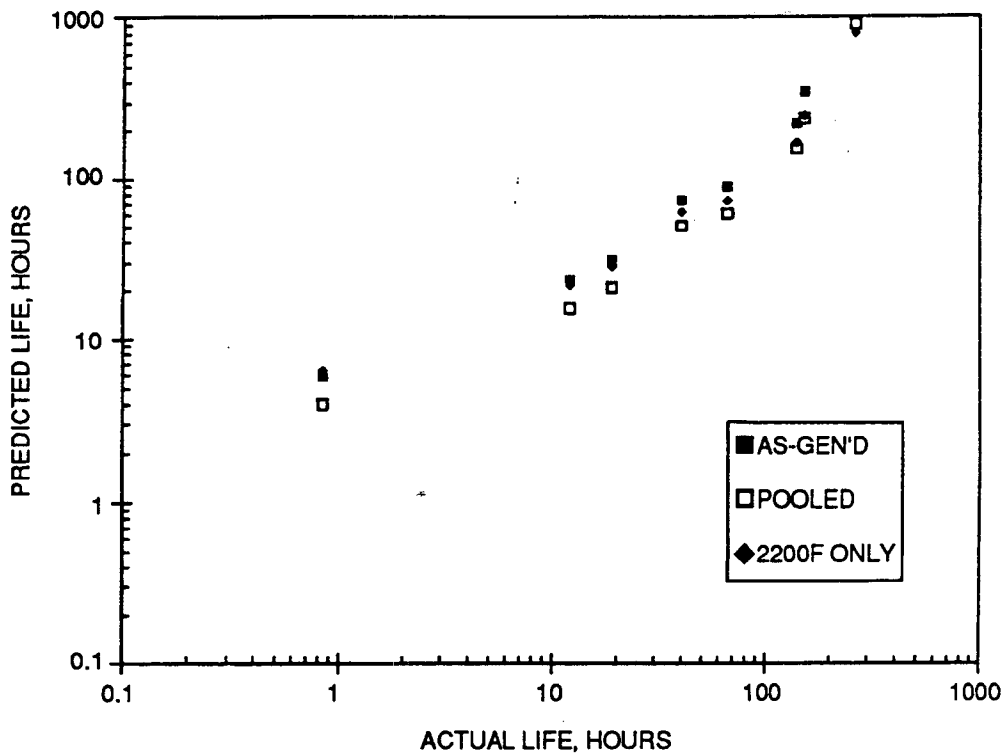
The only data from the core program that could be used to assess the SCG parameters were the same tensile and stress rupture data that were used to derive the parameters. Since the vast majority (18 of 20) of the failures observed in the fast fracture tests were volume initiated, and the two failures from surface flaws were in the middle of the group of 20 (ranking nos. 10 and 11), the following procedure was used:

- (1) The raw stress rupture and tensile data were again paired as done earlier; the pairs were then separated, based on whether the stress rupture failures initiated from volume (internal) or surface flaws. The assumption for the stress rupture failures initiated from surface flaws was that even though the fast fracture failures originated from volume flaws, in each specimen there were surface flaws just slightly smaller than the critical size under fast fracture loading.
- (2) Crack growth life predictions were then made for volume- and surface-initiated failures, based on the corresponding fast fracture strength, and the appropriate SCG parameters.

Comparisons of the predictions against actual data for volume and surface initiated failures are shown in Figures 5-62 and 5-63. The volume predictions using the three sets of "A" and "n" parameters were all very similar. On the other hand, the surface predictions showed wide disparity.

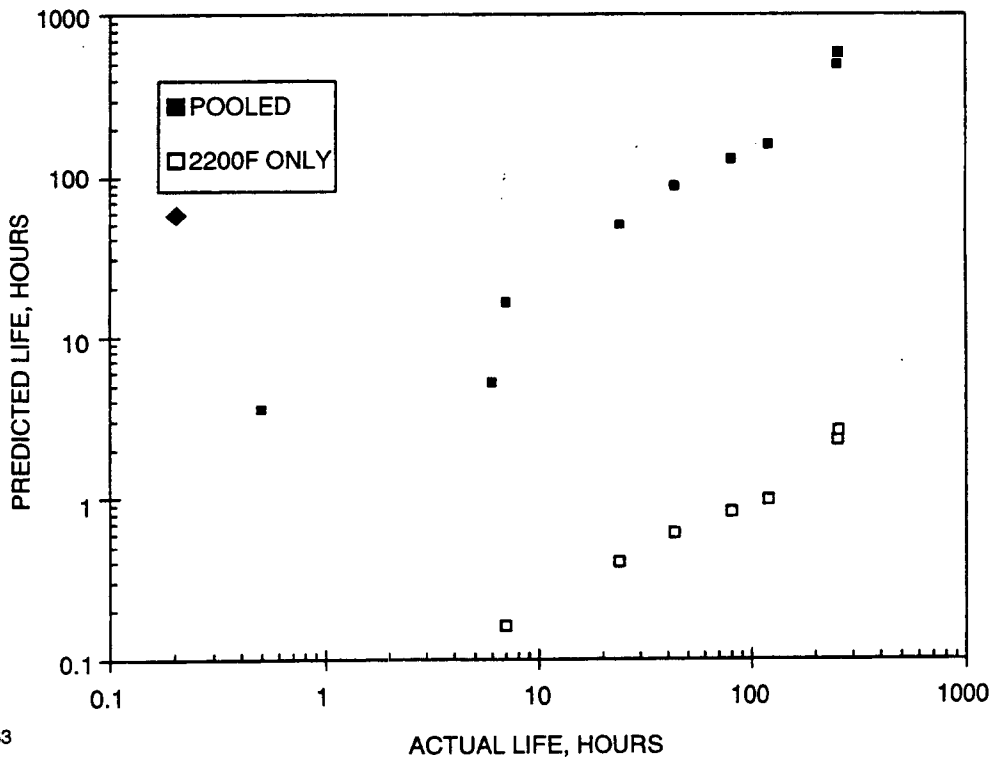
On cursory examination of Figure 5-63, it appears that the predictions based on parameters from the pooled fast fracture data were closer to the actual data than the predictions based on the 2200F fast fracture data alone. However, there are other considerations that need to be taken into account:

- (a) The surface life predictions based on pooled fast fracture data are, on average, higher than any of the volume predictions. This suggests that if the fast fracture failures originated predominantly from volume flaws, as in this case, the stress rupture failures should also be from volume flaws, which was not observed.



GC11591-562A

Figure 5-62. Comparison Of Predicted 2200F Volume Stress Rupture Failures, Utilizing Three Sets Of SCG Parameters.



GC11591-563

Figure 5-63. Comparison Of Predicted 2200F Surface Stress Rupture Failures, Using SCG Parameters From Pooled And 2200F-Only Fast Fracture Data.

- (b) The surface stress rupture predictions were based on the assumption that in the fast fracture tests there were surface flaws that were just smaller than the critical size and these flaws grew to surface-initiated stress rupture failure. If however, the initial surface flaws were much smaller than the critical size, they would have to grow much faster than volume flaws to result in surface-initiated stress rupture failures, as the SCG parameters based on 2200F fast fracture data would project.

Based on these considerations, the SCG parameters based on 2200F fast fracture data only were judged to give a better estimate than those from the pooled fast fracture data. Both sets of SCG parameters were used for the confirmatory test predictions. Moreover, the confirmatory tests would provide additional data to determine which set of SCG parameters provides a more representative description of the true SCG behavior.

5.4 Confirmatory Specimen Predictions

The strength and life prediction methods developed in this program were evaluated with test data acquired using three confirmatory test specimen types: notched-tensile, tension-torsion, and spin disks. An additional type, plate bending specimens, was initially intended to be used for methods confirmation. Later, it was learned that plate bending results were needed to model anisotropy and inherent-flaw shear sensitivity, hence this specimen type was not used for methods confirmation.

The other three confirmatory specimen designs included increasing levels of component complications. The notched-tensile specimens provided a stress gradient similar to the attachment stresses in inserted ceramic turbine blades. The tension-torsion specimens provided assessment of prediction methods in a tension-compression biaxial state of stress. The spin disks provided a very large area and volume, tension-tension biaxial stresses, and a higher volume stress than surface stress. Fast fracture tests were performed with all three specimen types. Stress rupture tests were performed with the notched-tensile specimens and the spin disks. These confirmatory specimens covered a wide range of potential ceramic engine component complications.

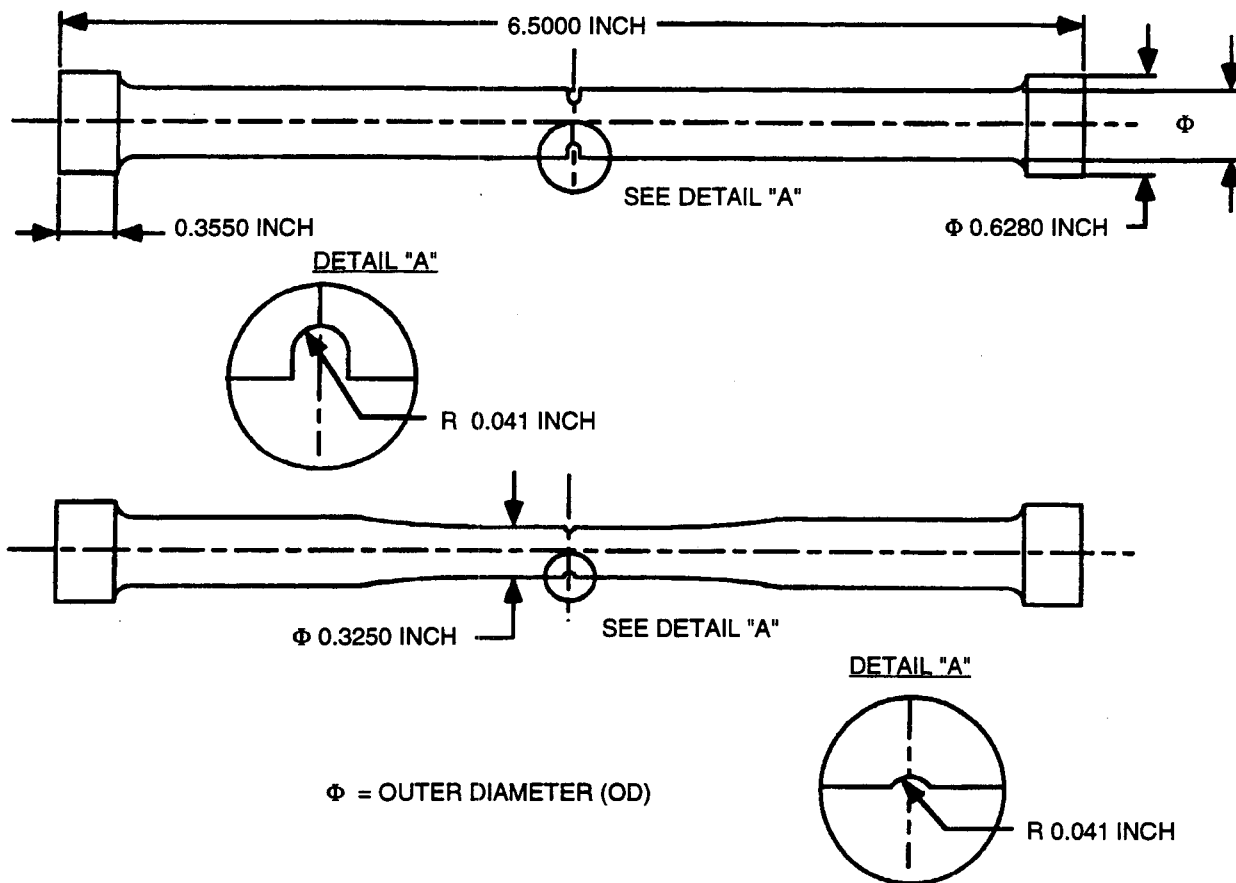
In all the confirmatory specimen tests described in the following subsections, the test data are compared against predictions based on the data base specimen test results and the methodologies described in Sections 5.2 and 5.3. In the fast fracture strength comparisons, the test data are compared against the maximum likelihood reliability lines and confidence bounds. The maximum likelihood line is an estimate of the population (i.e., true) reliability and the confidence intervals indicate the region we expect to find the true line 95 percent of the time. It is reasonable to plot and compare measured strengths to these predictions if a large sampling of strengths (>100) were obtained. The confirmatory test sets were smaller, so they do not give an accurate representation of the true reliability line. Therefore, we expect the strength data from the confirmatory tests to

be outside these confidence bounds more than 5 percent of the time. Some physical feeling for the expected deviation in plotted strength data compared with an estimation of a true line and confidence intervals can be obtained by reviewing the plots in Figures 5-50 and 5-51. Based on this, it should not be disturbing to see plotted data slightly outside the predicted intervals.

5.4.1 Notched Tensile Specimens

5.4.1.1 Specimen Designs

Two notched-tensile specimens (Figure 5-64) were designed for the purpose of verifying failure probability and life prediction capabilities developed in this program. It should be noted that the two specimen designs have the same notch root radius. However, the stress distribution is quite different in the two specimens because of the difference in notch depth.



GC11591-564

Figure 5-64. Two Notched-Tensile Specimen Designs (Differing In Notch Depth) Were Used For Confirmatory Tests.

Finite element stress analysis was performed for both specimen designs, and the stress contour plots are given in Figures 5-65 and 5-66. The stress concentration factors (K_t) were 1.61 for the shallow-notch specimen and 2.10 for the deep-notch specimen.

Since the notch roots were machined transversely, the surface flaw population at the notch roots is assumed to be the same as the transversely-machined MIL-B flexure specimens. The transversely-machined MIL-B specimens were pooled together with nine other specimen groups for Weibull analysis and failure probability confidence interval predictions using a bootstrap method. Transversely-machined surface failure and internal volume failure modes are considered to be the only significant failure modes actively competing in these specimens.

The equivalent volume (IV) and surface (IA) for the two notched tensile specimens were calculated from the stress analysis results using the ERICA computer code. Anisotropy was used in the surface integration and the shear sensitivity factor Q was taken to be zero. The IA(m) for the transverse-machined surface failure and IV(m) for the internal volume flaws were then used for size scaling and stress state/stress gradient scaling from the strength data for flexure specimens and smooth tensile specimens for the notched tensile specimens.

The confidence intervals of combined failure probability predicted for both notched tensile specimen designs are plotted in Figure 5-67. By combined failure probability is meant the total probability of the notch specimen to fail, either by the transversely-oriented surface flaw or by the internal volume flaw. To make the comparison, the fast fracture strength data points for the two confirmatory specimens are also plotted.

It should be noted that the confidence interval is rather wide and this is caused by insufficient data. There were only 3 surface failures in the group of 30 transversely-machined MIL-B specimens. Most of the specimens failed at an edge, due to inadequate chamfer treatment. Despite the small number of data points, the method managed to predict failure confidence intervals, largely relying on data censoring on data points from other failure modes.

The open circles in Figure 5-67 mark the confirmatory specimen test data. The shallow-notched specimen results showed very good consistency with the predictions made based on MIL-B flexure specimens. However, the deep-notch specimen test results showed a drastic difference. To investigate this discrepancy, the machining process for these two specimens was examined.

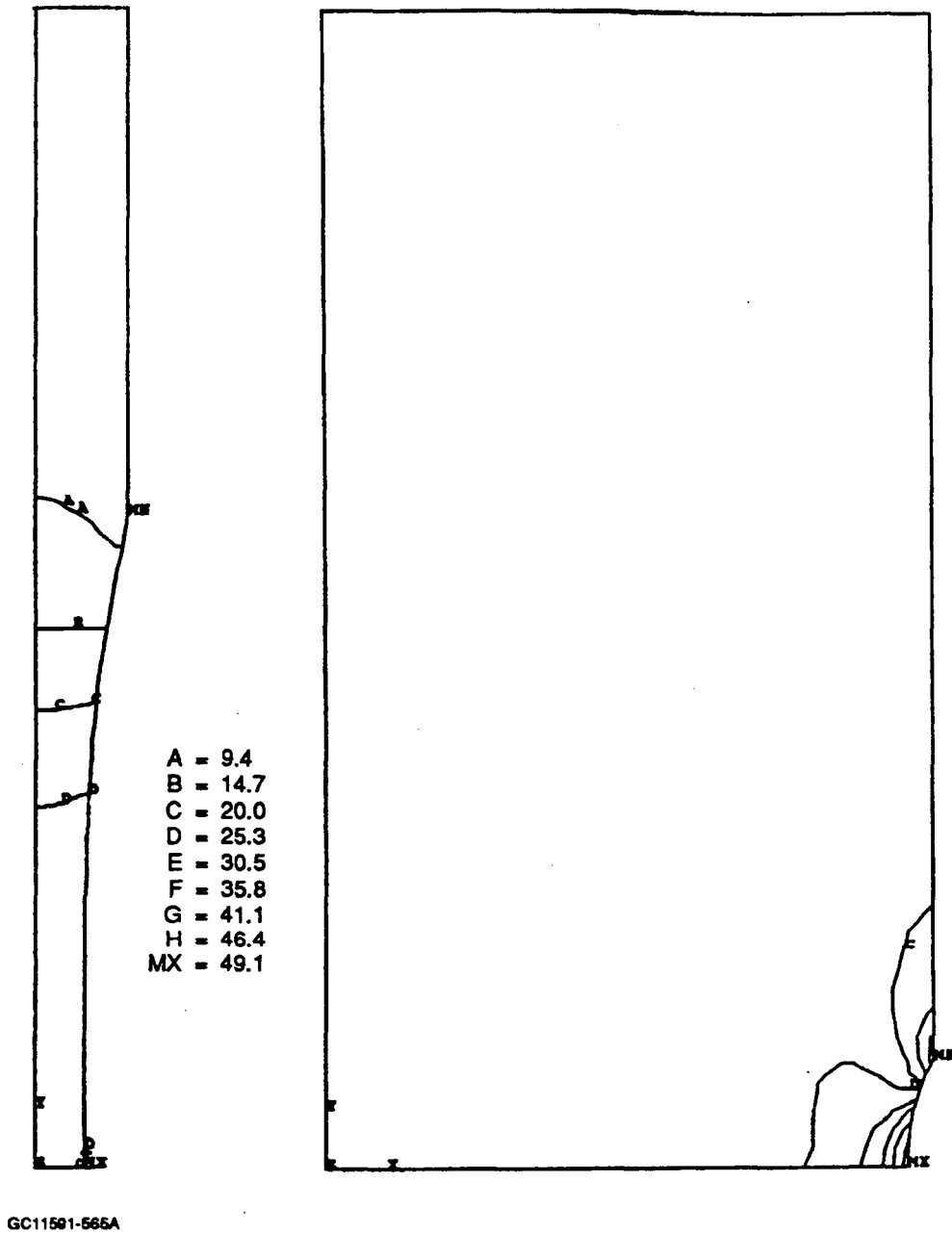
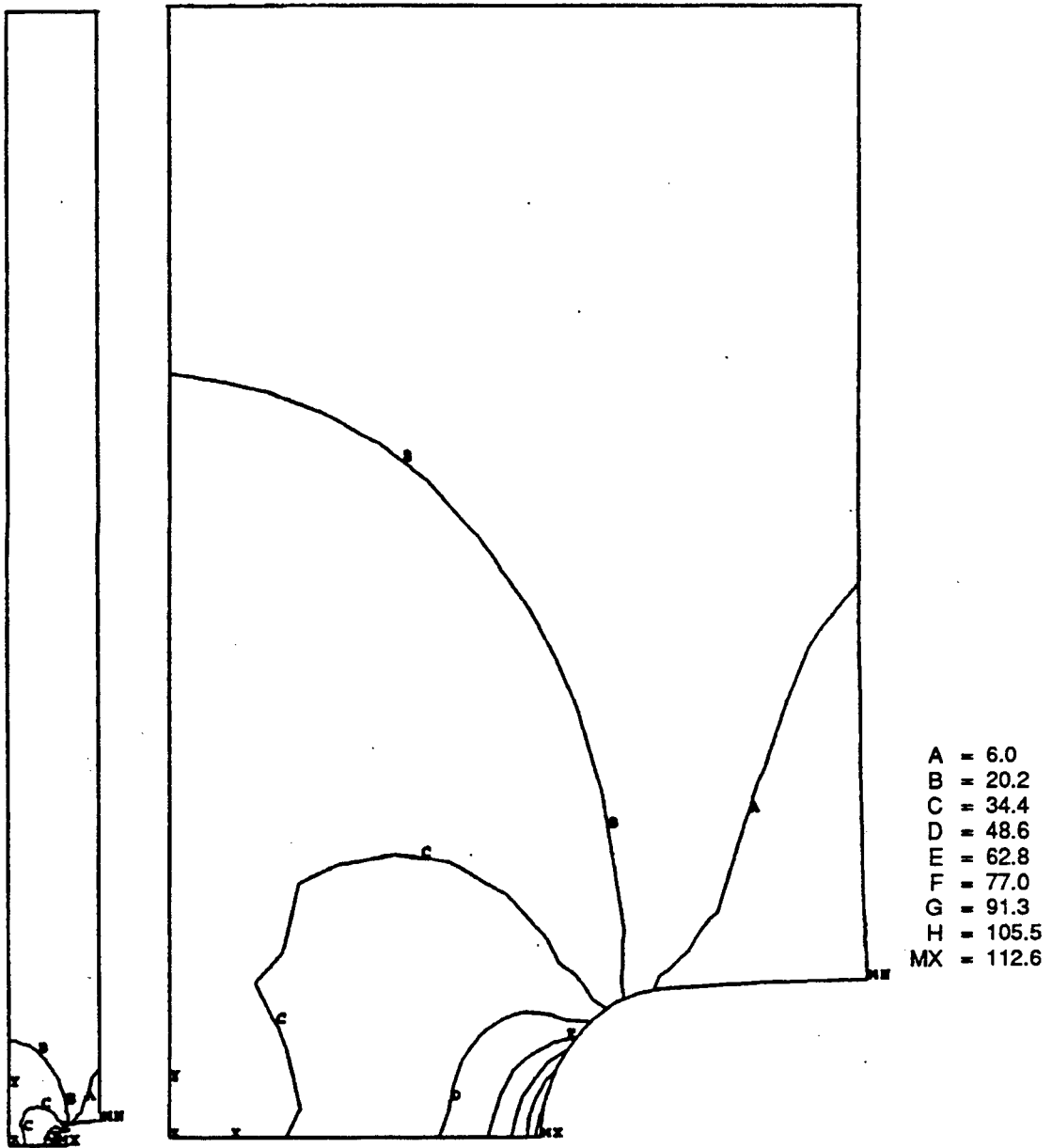
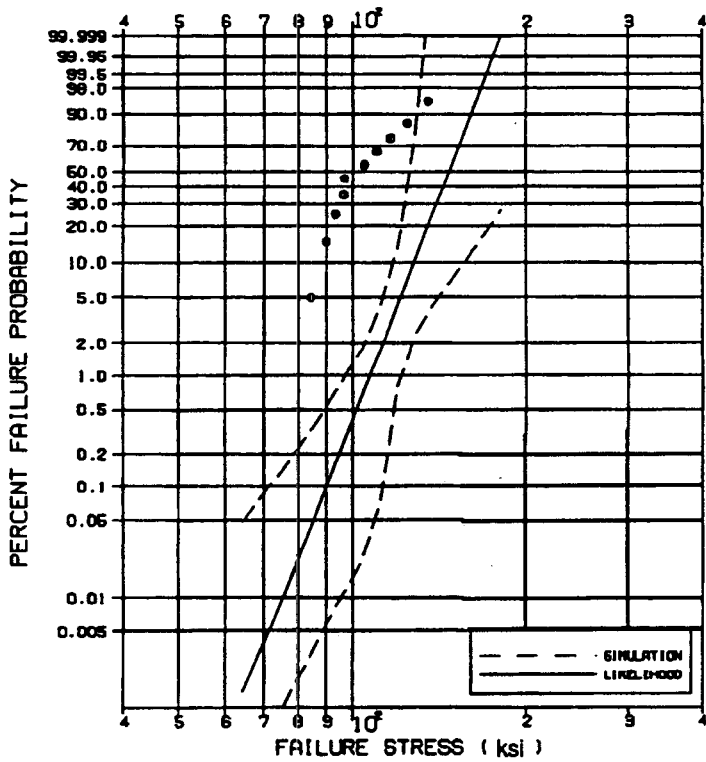
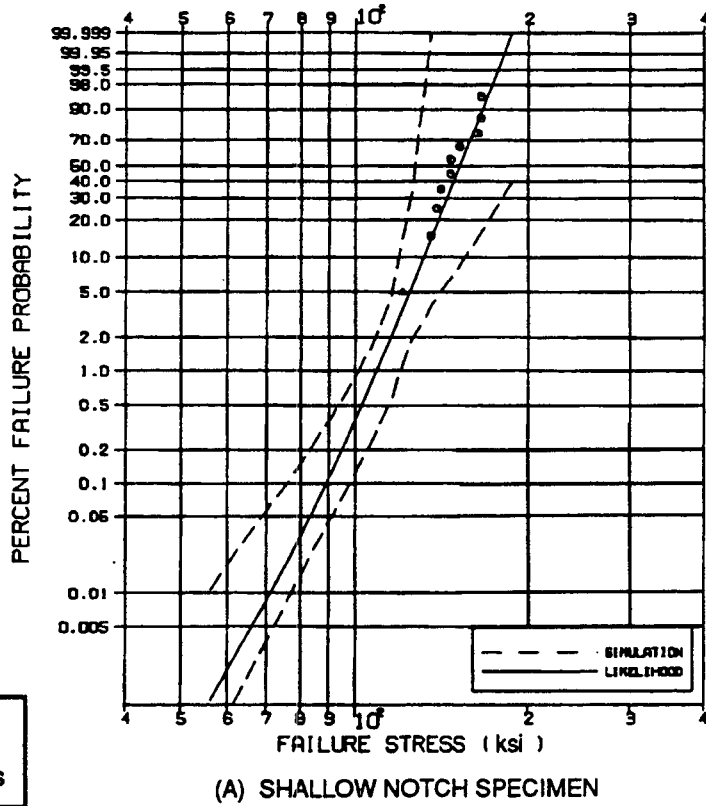


Figure 5-65. Finite Element Stress Analysis Stress Contours For The Shallow-Notch Tensile Test Specimens. (Units =ksi).



GC11591-568A

Figure 5-66. Finite Element Stress Analysis Stress Contours For The Deep-Notch Tensile Test Specimens. (Units = ksi).



GC11591-567A

(B) DEEP NOTCH SPECIMEN

Figure 5-67. Comparison Of Predicted Fast Fracture And Confirmatory Test Results For Notched Tensile Test Specimens.

To demonstrate the effectiveness of the predictive model for two different stress fields, the same flaw population was required at the notch roots for the two notched-tensile specimens. This required that the notch be machined before the outer diameter (OD) was machined to the blueprint specification in the middle of the part. It was found that the vendor had overlooked this request. All the specimens were machined to the net shape first, and then the notches were machined. Since the deep-notch specimens have a notch three times deeper than the shallow-notch specimens, the radial forces during machining were greater for the deeper notch, and for the same nominal load the local stresses during machining were much higher at the notch root for the deeper notch. Therefore, one would expect more severe surface flaws caused by machining for the deep-notch specimens.

Another factor also contributed to the significantly lower strength for the deep-notch specimens. As described in section 4.2.4, fractography revealed that failures originated at chemical reaction pits at the surface in some of the deep-notch specimens. This was not observed for the shallow-notch specimens. It is believed that machining fluid residue was not thoroughly cleaned away in the notch root areas of the deep-notch specimens, and chemical reaction pits were formed, which caused reduction of the surface strength. Typical notch surface topographies are shown in Figure 5-68.

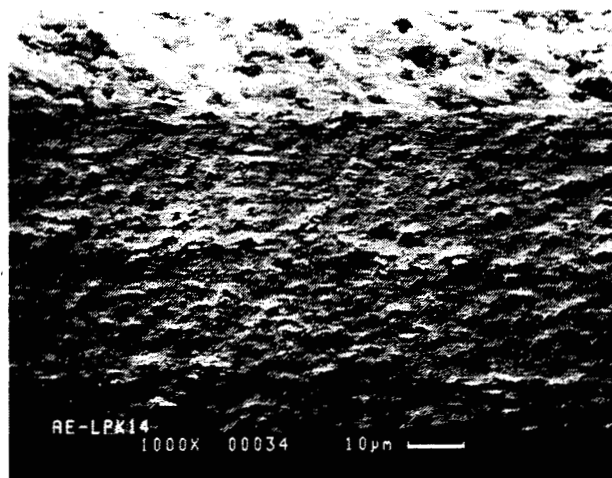
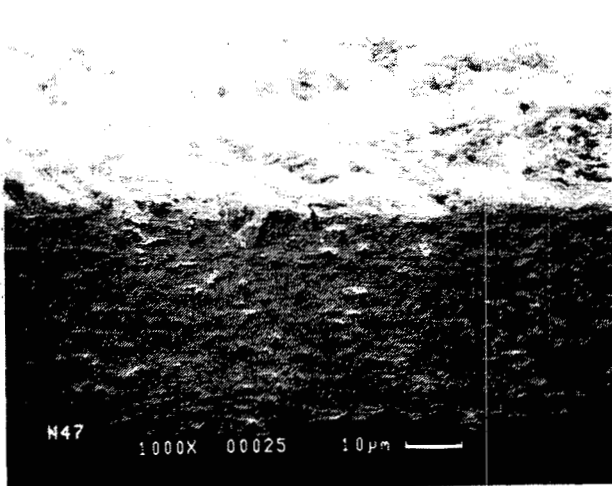
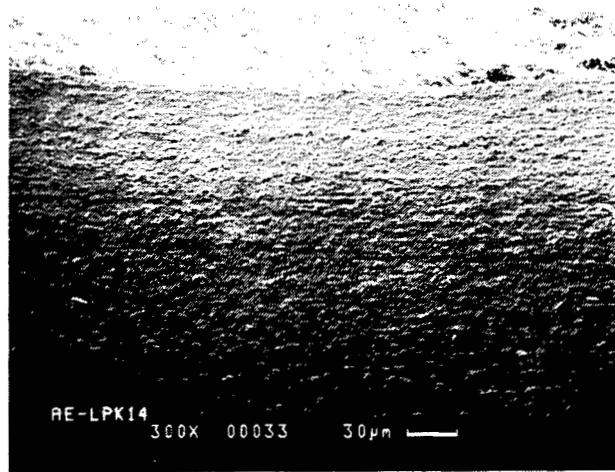
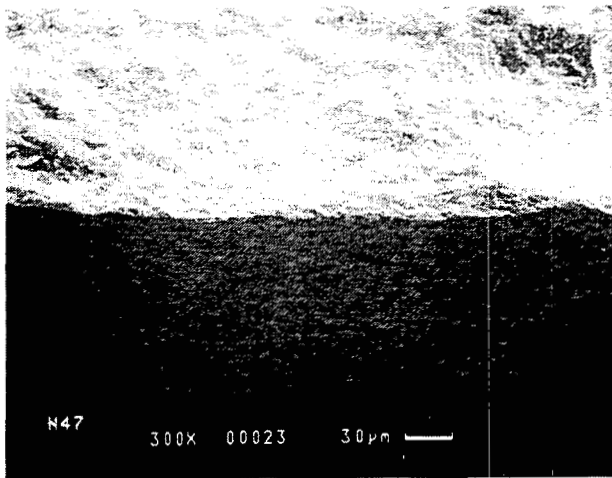
5.4.1.2 Notched Tensile Specimen Stress Rupture Tests

5.4.1.2.1 2200F Test Data

Two sets of SCG parameters (for surface and volume crack growth, see Section 5.3.4) derived from smooth bar fast fracture and stress rupture tests were used for the predictions. One set was based on pooled fast fracture data, and the other was based on 2200F tensile fast fracture results only. The SCG parameters were derived from median ranks of fast fracture and stress rupture data and hence were valid only for prediction of median ranks. An inherent assumption in the predictions is that the SCG parameters from longitudinally-machined specimens are applicable to the transversely-machined notch surface.

The failure probability prediction/risk integration was performed with the ERICA computer code. Failure probabilities as a function of time were produced at discrete load levels. The predictions were then compared against actual confirmatory test data.

All the observed failures were surface-initiated. The predictions were consistent with this observation. Between the two sets of surface SCG parameters, the set based on the pooled fast fracture data predicted much longer lives than observed. The set based on the 2200F tensile fast fracture results only produced reasonable



KT = 1.6

KT = 2.1

GB11904-17

Figure 5-68. Differences In Surface Finish Of Notched Specimens Could Account For Discrepancies In Observed Strength Values.

predictions, as shown in Figure 5-69. Note that the 5-percent and 95-percent lines are for probability of failure at 50-percent confidence, rather than confidence bounds as in the fast fracture predictions.

In both sets of predictions however, the predicted lives were longer than the observed lives at the higher stresses and shorter than the observed lives at the lower stresses. Possible reasons for this discrepancy are:

- (1) The SCG parameters were derived from longitudinally-machined specimens, whereas the notch surface was transversely-machined. The transversely-machined surfaces may have a different stress-dependence compared to that for the longitudinally-machined surfaces.
- (2) It was assumed that creep deformation and stress relaxation at the notch root was negligible; a more comprehensive analysis that includes creep deformation may be called for.
- (3) The SCG formulation employed in this program did not explicitly take into account the effect of cracks on the stress field (all the calculations were performed on the basis of the uncracked stress field). The differences in the stress field between the smooth and notched specimens, and the differences in the final crack sizes may have also contributed to the discrepancy between the observed and predicted lives.

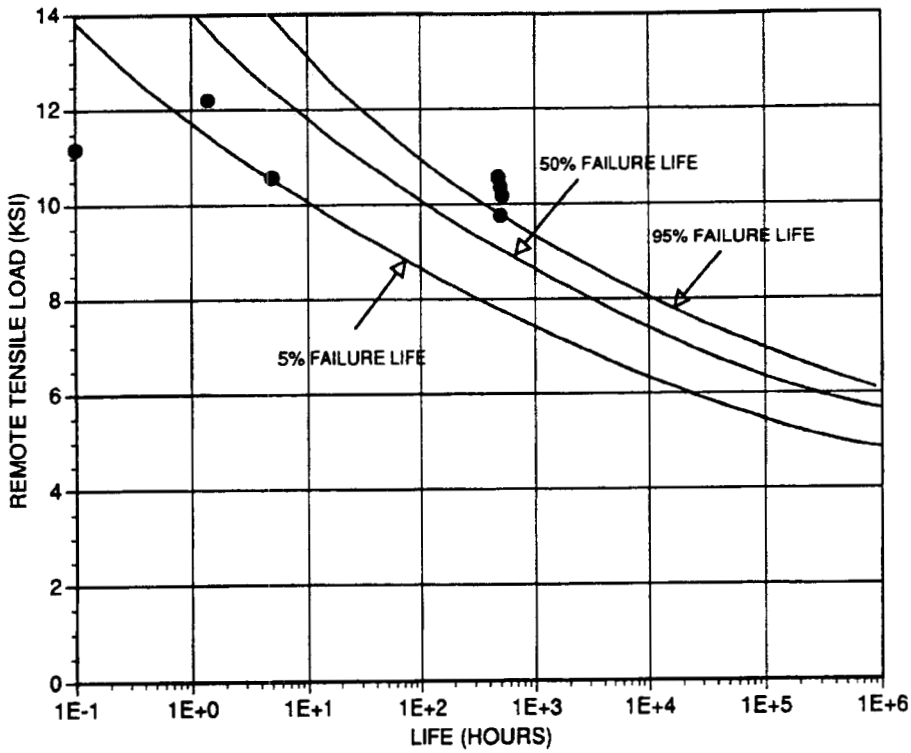
5.4.1.2.2 2500F Test Data

Since the vast majority of the 2500F smooth stress rupture specimens failed from the surface, it was reasoned that the inherent flaws no longer were failure-controlling. The predictions at 2500F were made on the basis of deterministic stress-life relationship derived from the 2500F smooth specimen stress rupture tests, as follows:

$$t_f = 1.66E + 22\sigma^{-15.10} \quad [5-120]$$

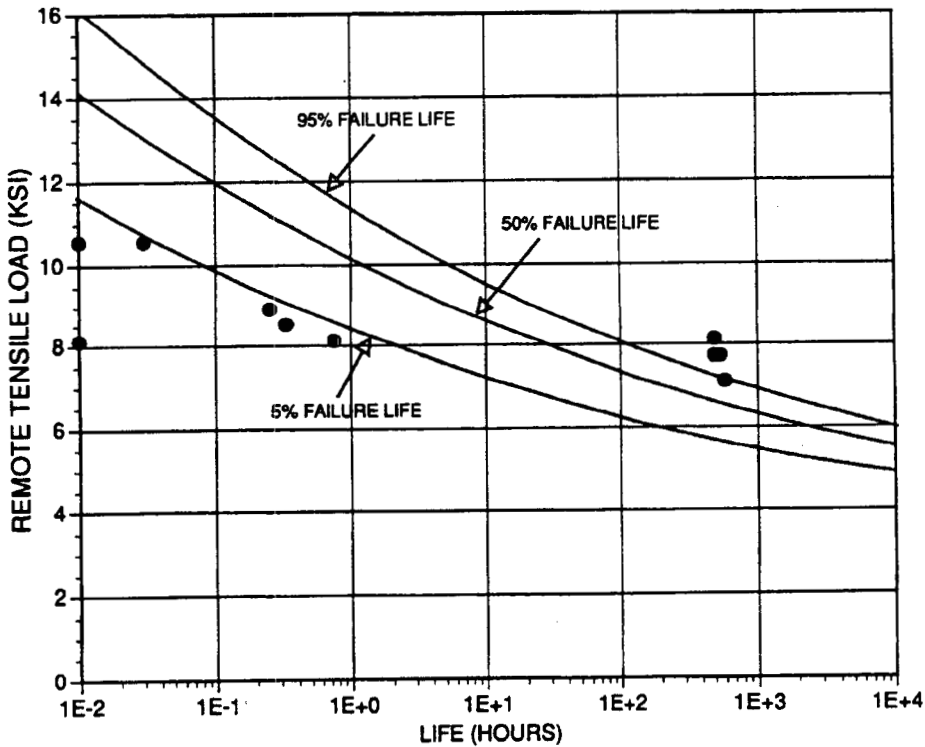
At 2500F, the elastic notch root stress field was no longer valid, since creep deformation would lead to stress redistribution. For the notched specimens, the upper bound would be the elastic stress, while the lower bound would be that from full relaxation (i.e., $K_t = 1$).

The predictions are shown in Figures 5-70 and 5-71. It can be seen that reasonable agreement was achieved between the predicted and observed lives. The modified Orr-Sherby-Dorn parameter model described in Section 5.1.5.9 was also applied to the notched tensile specimens; the predictions were comparable to those from Equation [5-120].



● TEST DATA POINTS

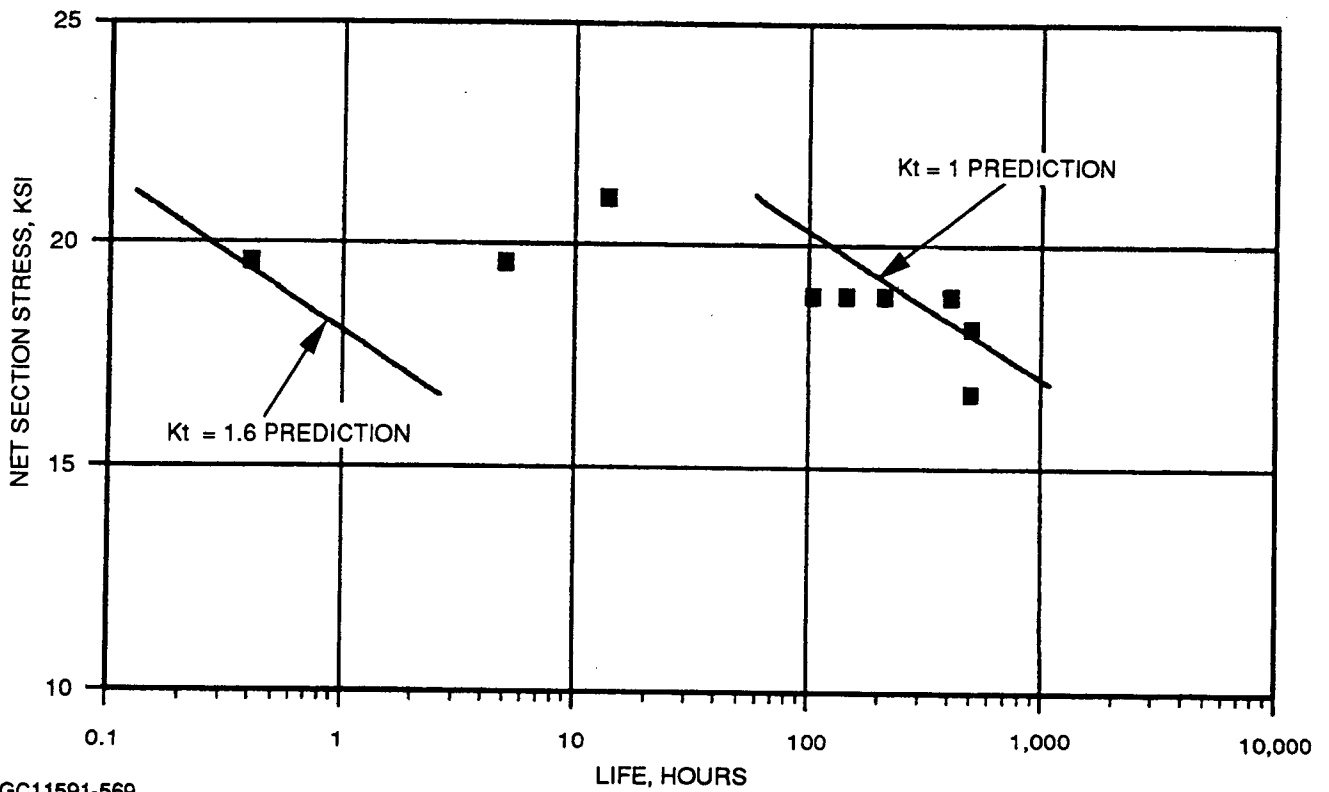
(A) SHALLOW NOTCH SPECIMEN



GC11591-568

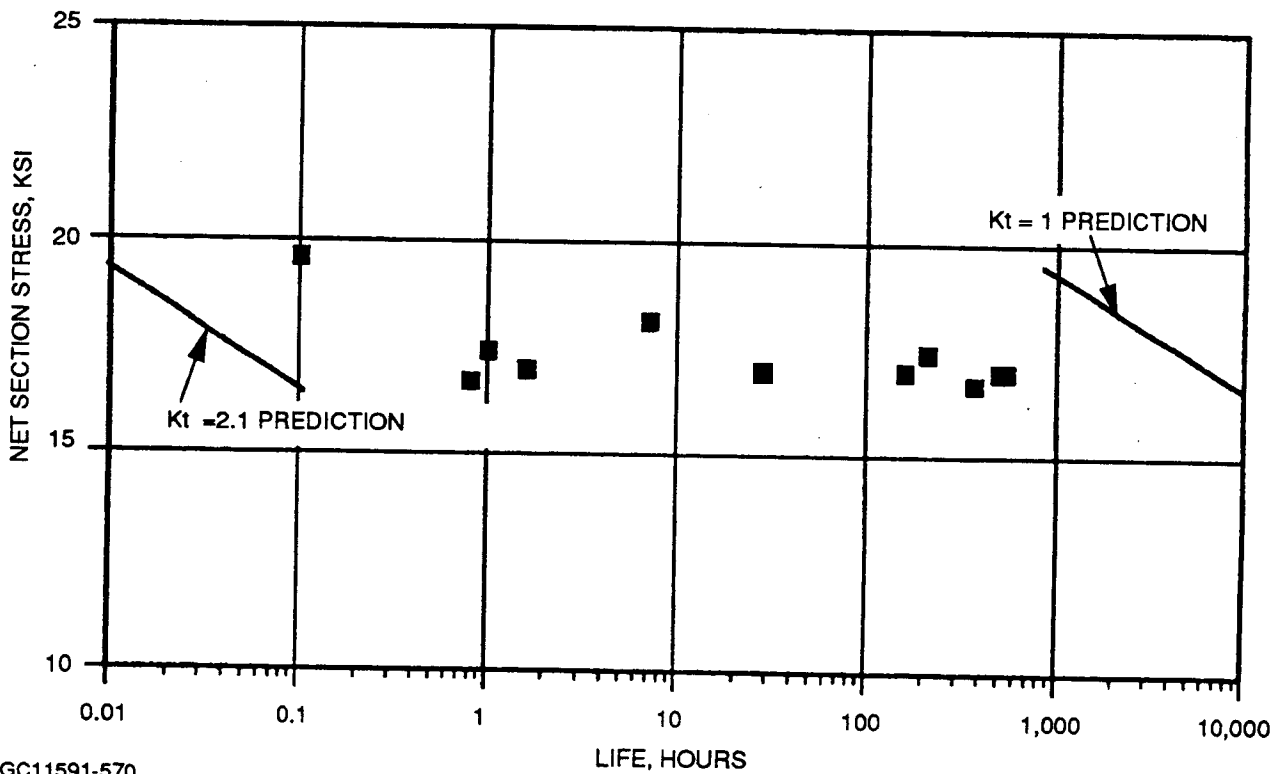
(B) DEEP NOTCH SPECIMEN

Figure 5-69. Comparison Of Slow Crack Growth Predicted Life And Actual Life For Notched-Tensile Test Specimens.



GC11591-569

Figure 5-70. Comparison Of 2500F Stress Rupture Test Data For $K_t = 1.6$ Notched-Tensile Test Specimen Geometry.



GC11591-570

Figure 5-71. Comparison Of 2500F Stress Rupture Test Data For $K_t = 2.1$ Notched-Tensile Test Specimen Geometry.

5.4.2 Plate Bending And Tension-Torsion Confirmatory Specimen Testing

Analysis of the plate bending data is reviewed in other sections of this report. The plate bending tests were designed to confirm multiaxial fracture prediction methods. However, it was later learned that the mixed-mode fracture data obtained from the diametrical compression tests and notched tension-torsion tests were not sufficient to define the shear sensitivity for predicting fracture under multiaxial loading. Both of these tests measured fracture behavior from relatively large precracks that may not be representative of inherent material flaws. The plate bending data was needed to determine the shear sensitivity for inherent flaws and to provide information for modeling surface anisotropy. These model development activities are reviewed in Section 5.3.3.

The tension-torsion confirmatory specimens were intended to assess the developed methodology in predicting the fast fracture strengths of components under tension-compression state of stress. Descriptions of the testing and analysis is included in the following sections.

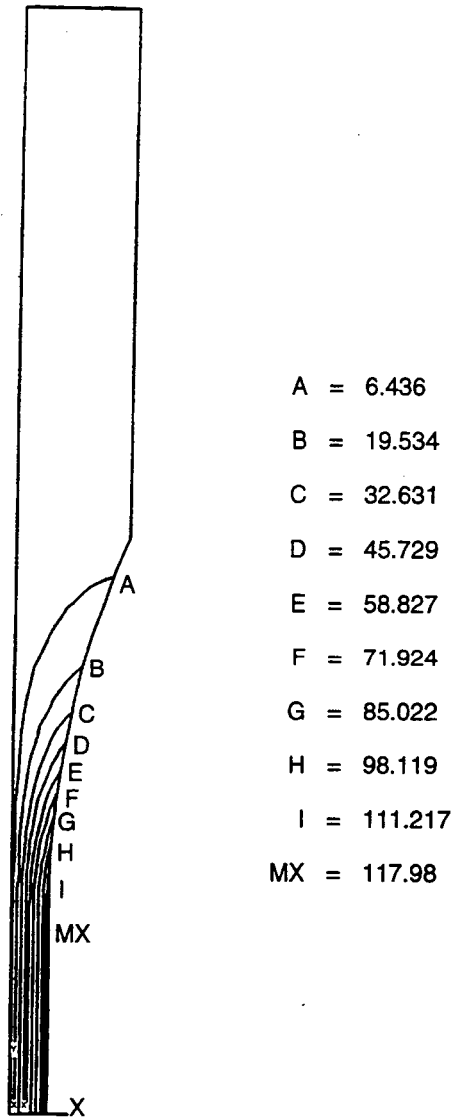
5.4.2.1 Specimen Tests

Tension-torsion confirmatory specimen testing and fractography are described in Section 4.2.2. The tension-torsion strength tests were conducted in four groups, with different mean axial stress/torsional stress ratios, as listed in Table 5-20.

TABLE 5-20. TENSION-TORSION CONFIRMATORY TEST SPECIMEN STRESS RATIOS

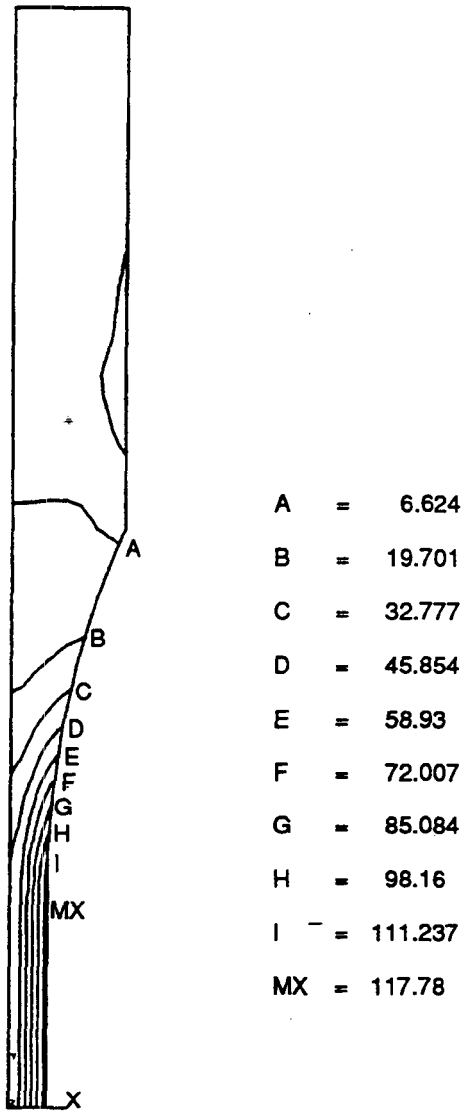
Group	Mean Axial/Torsional Stress Ratio
1	0.50
2	0.29
3	0.13
4	0.0

Finite element analysis was employed to determine the stress state in the tension-torsion specimens tested. An axisymmetric finite element model was created that models half of the entire specimen. The maximum principal stress distributions in two representative specimens, Specimen 9 under pure torsion (Group 4) and Specimen 15 from Group 1 under tension-torsion loading, are shown in Figures 5-72 and 5-73, respectively. The maximum principal stress at failure was chosen to be the basis of comparison between the predictions and test data.



GC11591-571

Figure 5-72. Maximum Principal Stress Distribution In Tension-Torsion Specimen No. 9 At Failure. Specimen Loaded In Pure Torsion (Units - ksi).



GC11591-572A

Figure 5-73. Maximum Principal Stress Distribution In Tension-Torsion Specimen No. 15 At Failure. Specimen Loaded In Axial Tension And Torsion. Nominal Tensile To Shear Stress Ratio = 0.5 At Gage Section Surface (Units = ksi).

The shear sensitivity and flaw distribution assumptions have been discussed in Section 5.3.3. The no-shear sensitivity ($Q=0$) and the isotropic flaw assumptions, along with the finite element stress solutions for the average specimen in each group, were used to calculate the specimen effective sizes for the four groups of tests. Within each group of specimens, there were some axial/torsional stress ratio variations at failure. This variation had a negligible effect on the effective sizes and was ignored. Representative effective size versus Weibull modulus data for the four groups of specimens and the finite element model employed in the stress analysis are given in Appendix VIII.

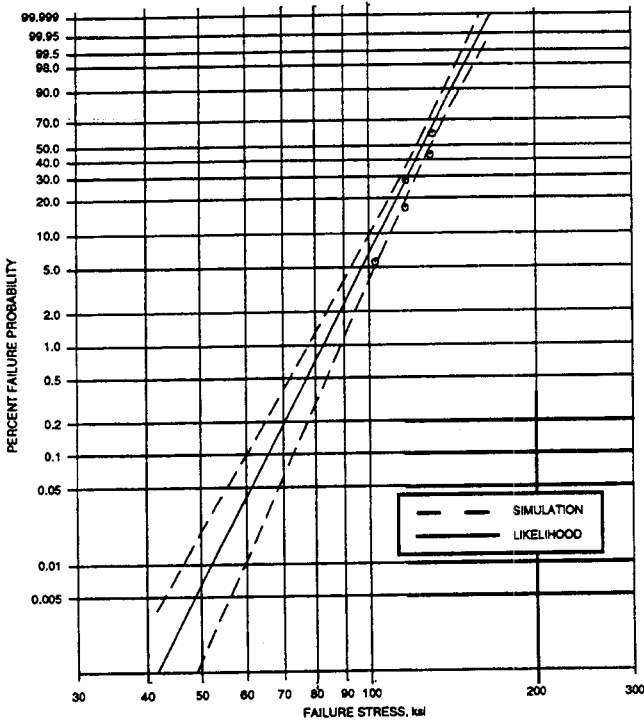
The effective sizes were then used with the reduced data from the data base tests (tensile and bend specimens) to produce predictions (maximum likelihood and 95-percent confidence bounds); the confidence bounds are tolerance limits on the reliability. The actual data were then overlaid on the predictions. For each specimen group, comparisons of the surface, internal, and combined predictions and test data on the basis of the maximum principal stress in the tension-torsion specimens were produced. These are shown in Figures 5-74 through 5-77.

5.4.2.2 Comparison Of Predictions With Test Data

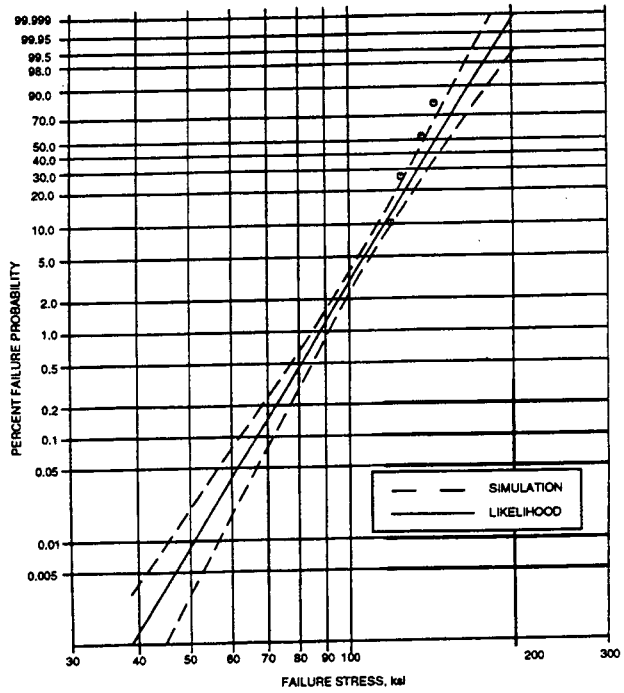
It can be seen that the surface predictions were reasonably close to the test data in all four groups, whereas the internal predictions consistently overestimated the volume strength of the specimens. The overestimation was the greatest under pure torsion loading and was the closest with Group 1, which had the highest tension/torsion ratio. The combined predictions were all reasonable, since these were dominated by surface failures.

The discrepancy between the internal predictions and test data may have been caused by the following:

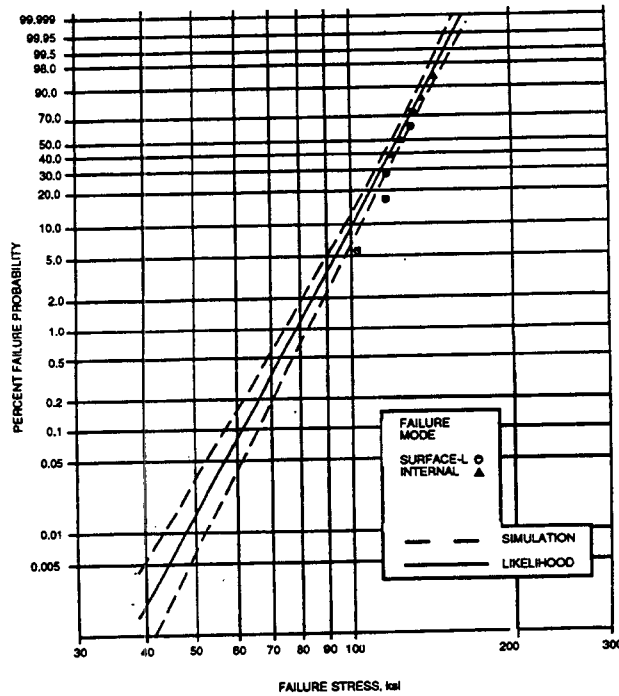
- (1) Mis-identification of internal-initiated fractures, since the internal-initiated failures were all very close to the surface. Furthermore, the internal- and surface-initiated failures showed similar load- and torque-carrying capability.
- (2) The volume flaws may be more shear-sensitive than the surface flaws. This is consistent with the observation that the greatest discrepancy was under pure torsion loading, while Group 1 specimens with the highest tension/torsion ratio showed least discrepancy. This possibility was evaluated; however, in the pure torsion specimens even with the highest degree of shear-sensitivity ($C = 0.816$), some discrepancy still existed between the predictions and test data. Furthermore, it would be difficult to



(A) SURFACE FAILURES



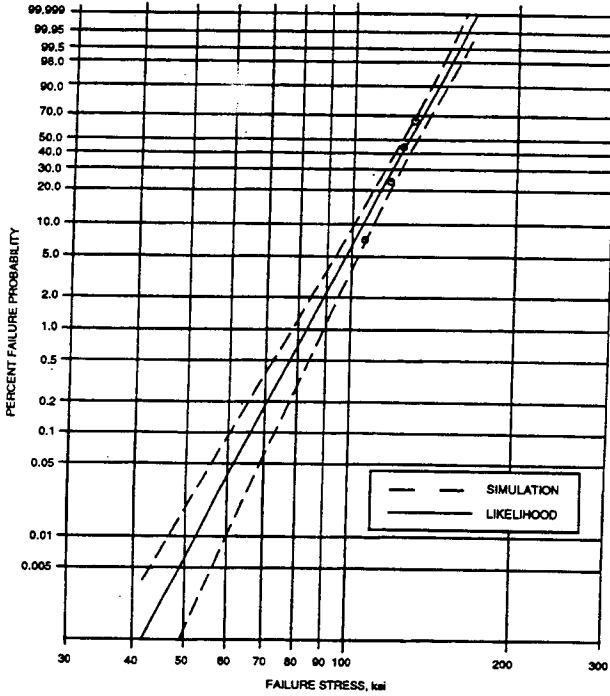
(B) INTERNAL FAILURES



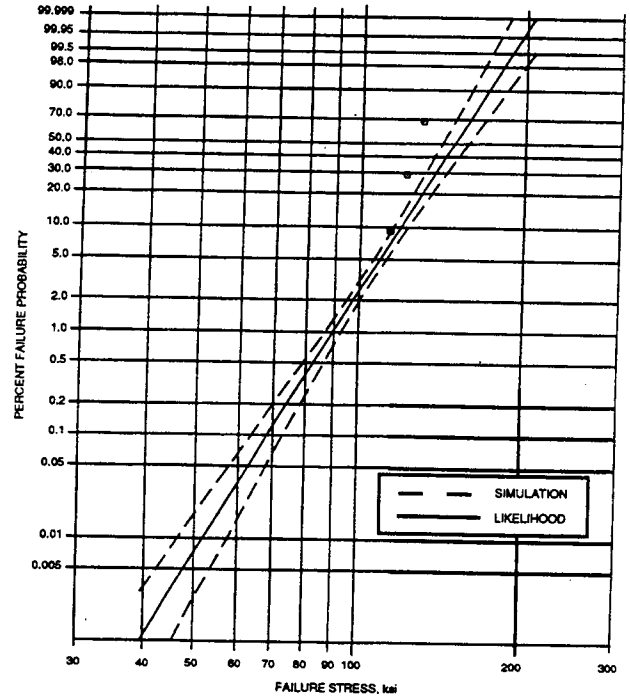
(C) COMBINED SURFACE AND INTERNAL FAILURES

GC11591-900

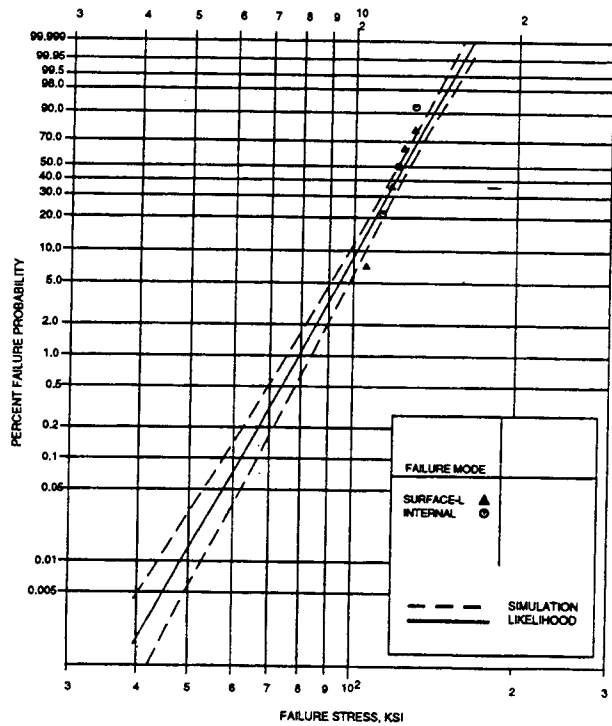
Figure 5-74. Comparison Of Group 1 Tension-Torsion Test Data ($\sigma_y/\sigma_{yz}=0.5$). (A) Surface Failures; (B) Internal Failures; (C) Combined Surface and Internal Failures With Maximum Likelihood (Solid Lines) and 95-Percent Confidence Bounds (Dashed Lines) Predictions.



(A) SURFACE FAILURES



(B) INTERNAL FAILURES



(C) COMBINED SURFACE AND INTERNAL FAILURES

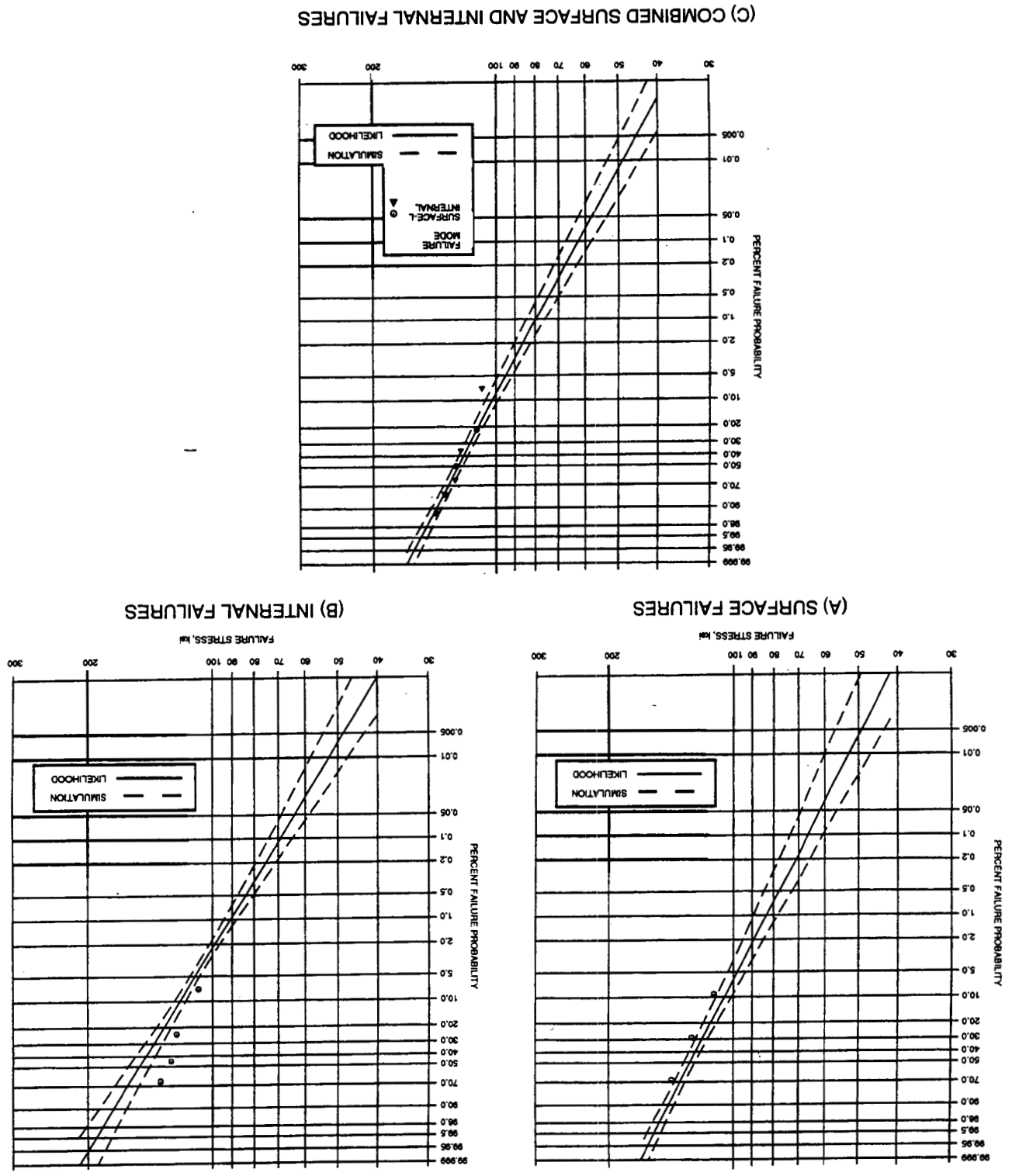
GC11591-901

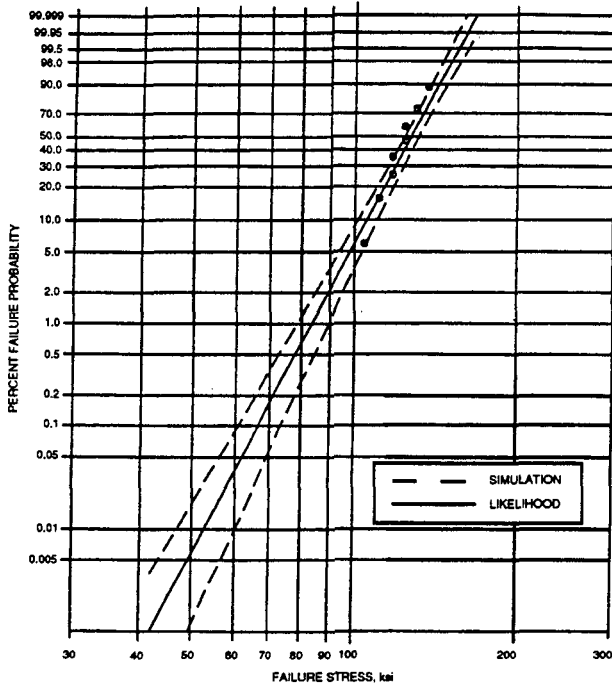
Figure 5-75. Comparison Of Group 2 Tension-Torsion Test Data. (A) Surface Failures; (B) Internal Failures; (C) Combined Surface and Internal Failures With Maximum Likelihood (Solid Lines) and 95-Percent Confidence Bounds (Dashed Lines) Predictions.

Figure 5-76. Comparison Of Group 3 Tension-Torsion Test Data. (A) Surface Failures; (B) Internal Failures; (C) Combined Surface and Internal Failures With Maximum Likelihood (Solid Lines) and 95-Percent Confidence Bounds (Dashed Lines) Predictions.

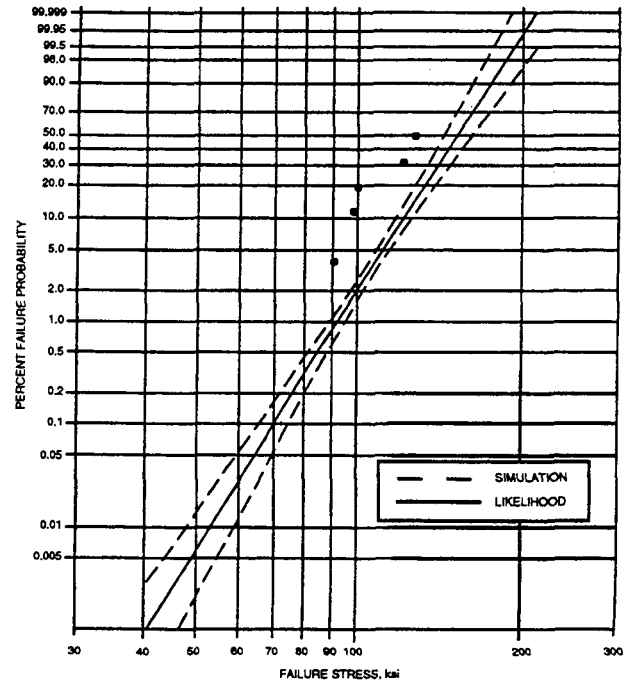
31-11591
5-159

GC11591-902

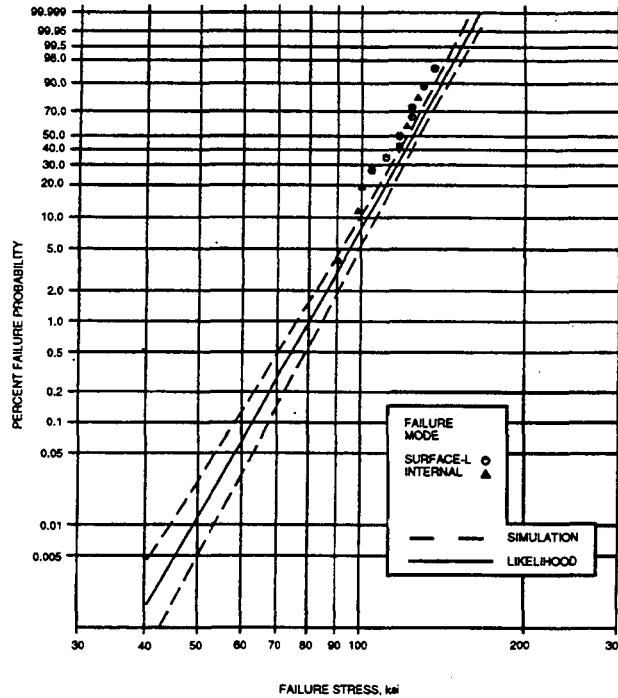




(A) SURFACE FAILURES



(B) INTERNAL FAILURES



(C) COMBINED SURFACE AND INTERNAL FAILURES

GC11591-903

Figure 5-77. Comparison Of Group 4 (Pure Tension) Test Data. (A) Surface Failures; (B) Internal Failures; (C) Combined Surface and Internal Failures With Maximum Likelihood (Solid Lines) and 95-Percent Confidence Bounds (Dashed Lines) Predictions.

reconcile the fact that the surface flaws were not shear-sensitive while the internal flaws have the highest level of shear sensitivity.

5.4.3 Spin Disk Test Results And Predictions

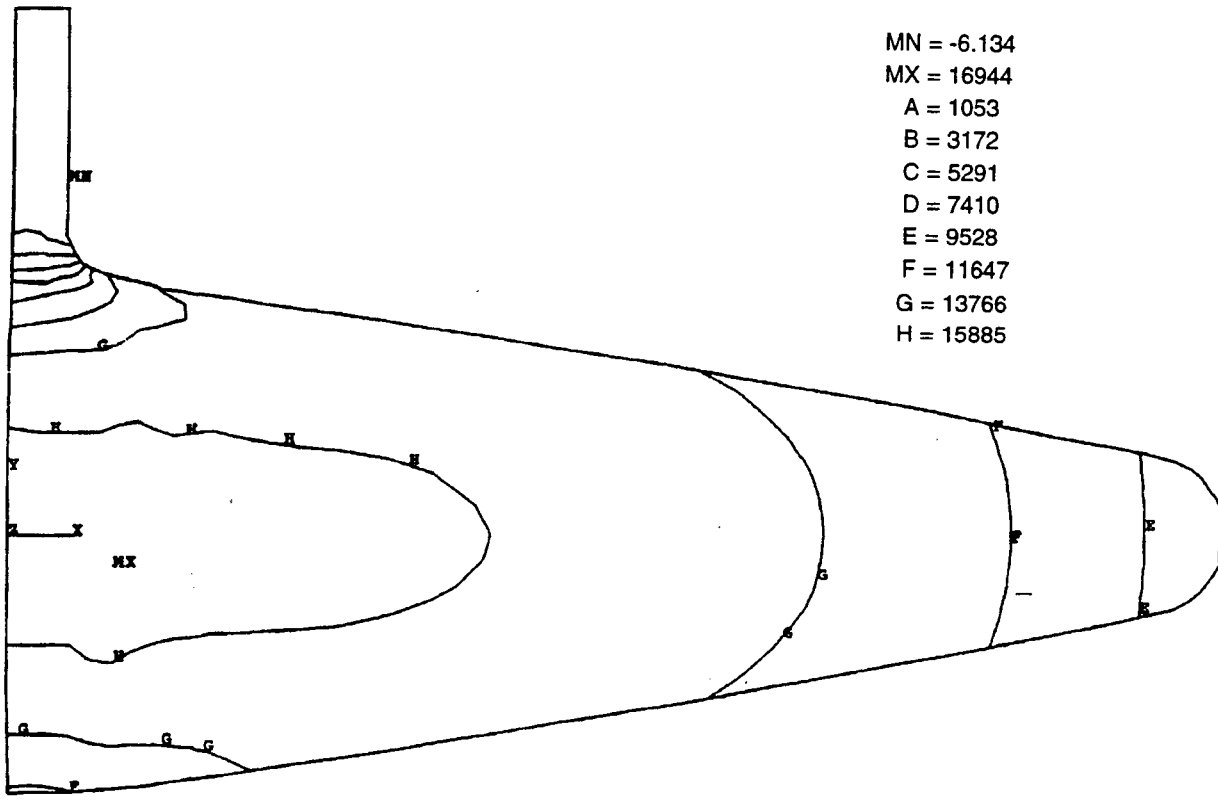
The spin pit disk confirmatory test specimens were designed with the purpose of verifying the underlying theory, including multiaxial effects; and to confirm the statistical and time-dependent methodologies developed during this program. The spin disks have a relatively large effective size, compared to the four-point bending and tensile test specimens; from one to four orders of magnitude larger. The size difference should prove the validity of size-scaled uniaxially-tested specimen data for components with complex multiaxial and stress gradient fields. The high-temperature testing at 2200F and 2500F should prove the capabilities of the time-dependent models and the usefulness of combining data at different temperatures to predict material Weibull parameters.

The deep- and shallow-notched test specimens addressed tensile-tensile multiaxial stress fields; the tension-torsion specimens addressed tensile-compression multiaxial stress fields. As described in the previous sections, the predictions are encouraging, but mainly address the applicability of the multiaxial stress theory, since the size scaling is relatively minor, and, because of the low percentage of volume failures in these specimens, the stress gradient effect was inconclusive. The spin disk tests address multiaxiality, stress gradient, and size complications concurrently; the surface and volume of the spin disks are orders of magnitude larger than the other test specimens, and have steep gradients and complex multiaxial stress fields.

Finite element stress analysis was performed for the spin disk at the various test conditions. The principal stress distribution at 50,000 rpm is shown in Figure 5-78. The stress at other speeds can be obtained by multiplying the stress at 50,000 rpm by the square of the speed ratio. The spin disk temperature distribution for the nominal 2200F tests is shown in Figure 5-79. The thermal stress distribution corresponding to the temperature distribution is shown in Figure 5-80. The combined thermal and centrifugal stress distribution is shown in Figure 5-81. Similar temperature and stress distribution plots for the nominal 2500F tests are shown in Figures 5-82 through 5-84.

5.4.3.1 Fast Fracture Prediction And Results

The spin disk fast fracture testing consisted of 14 disks tested at room temperature: 3 disks failed from internal flaws, 9 from surface flaws, and 2 from machining damage. These room-temperature tests yielded encouraging volume fast fracture results. Upon comparison of the predicted volume failure mode with the test

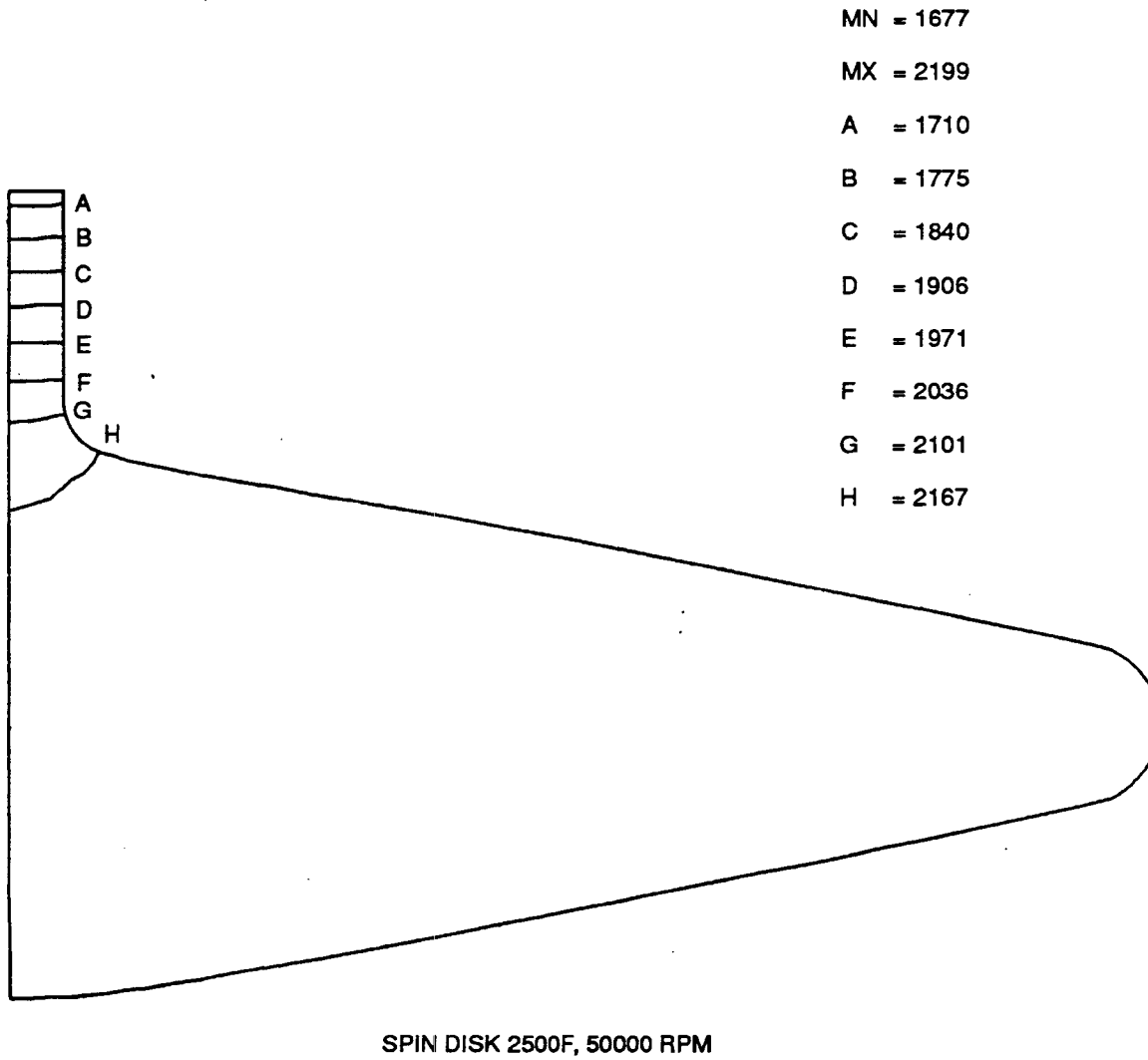


MN = -6.134
MX = 16944
A = 1053
B = 3172
C = 5291
D = 7410
E = 9528
F = 11647
G = 13766
H = 15885

SPIN DISK RT, 50,000 RPM

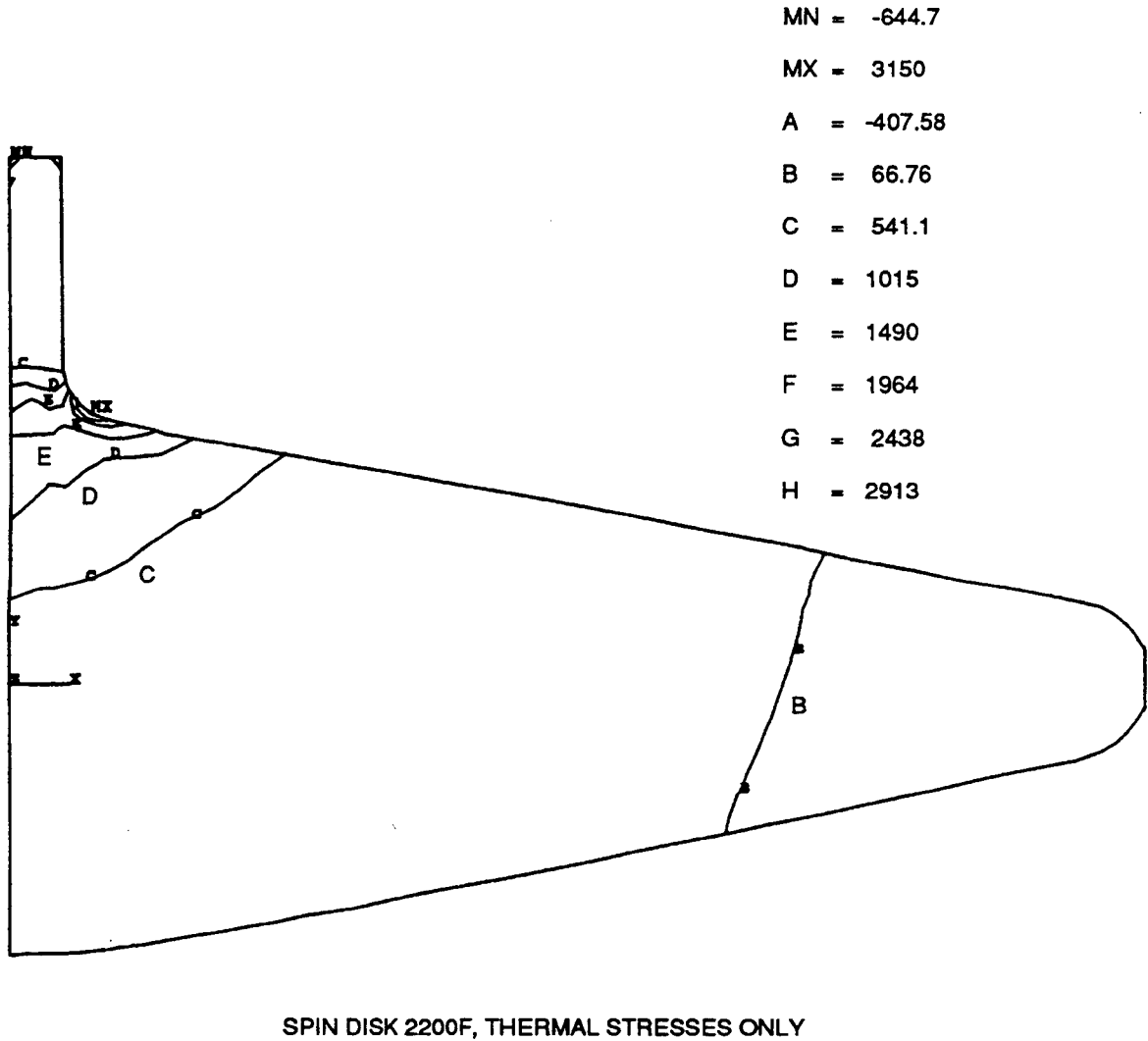
GC11591-594A

Figure 5-78. Spin Disk Maximum Principal Stress Distribution Under Centrifugal Loading Only, 50,000 rpm (Units = psi).



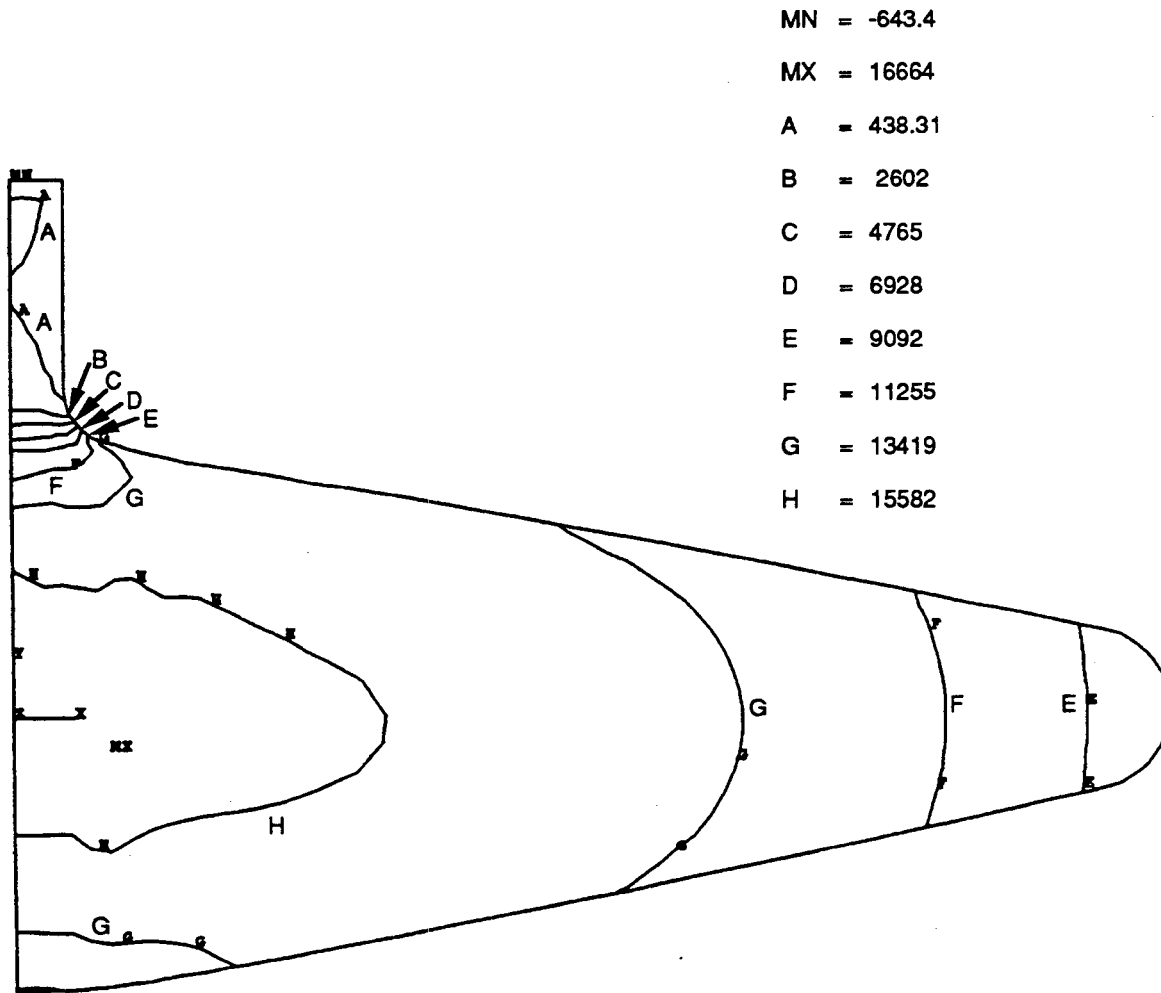
GC11591-595

Figure 5-79. Spin Disk Temperature Distribution At 2200F Test Condition, Thermal Loading And 50,000 rpm.



GC11591-596A

Figure 5-80. Spin Disk Maximum Principal Stress Distribution Under Thermal Loading Only, At 2200F Test Condition (Units = psi).



SPIN DISK 2200F, 50000 RPM AND THERMAL STRESSES

GC11591-597A

Figure 5-81. Spin Disk Maximum Principal Stress Distribution At 2200F Test Condition, Thermal Loading And 50,000 rpm (Units = psi).

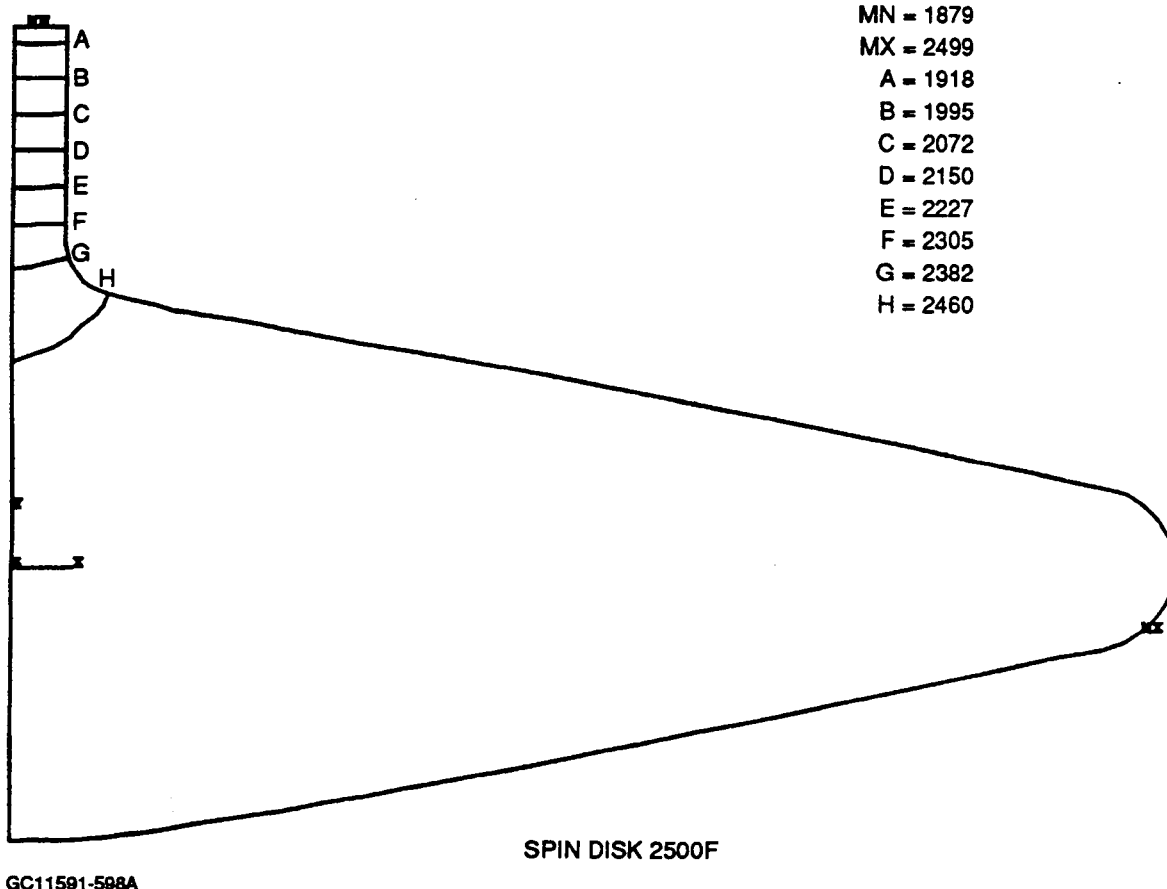
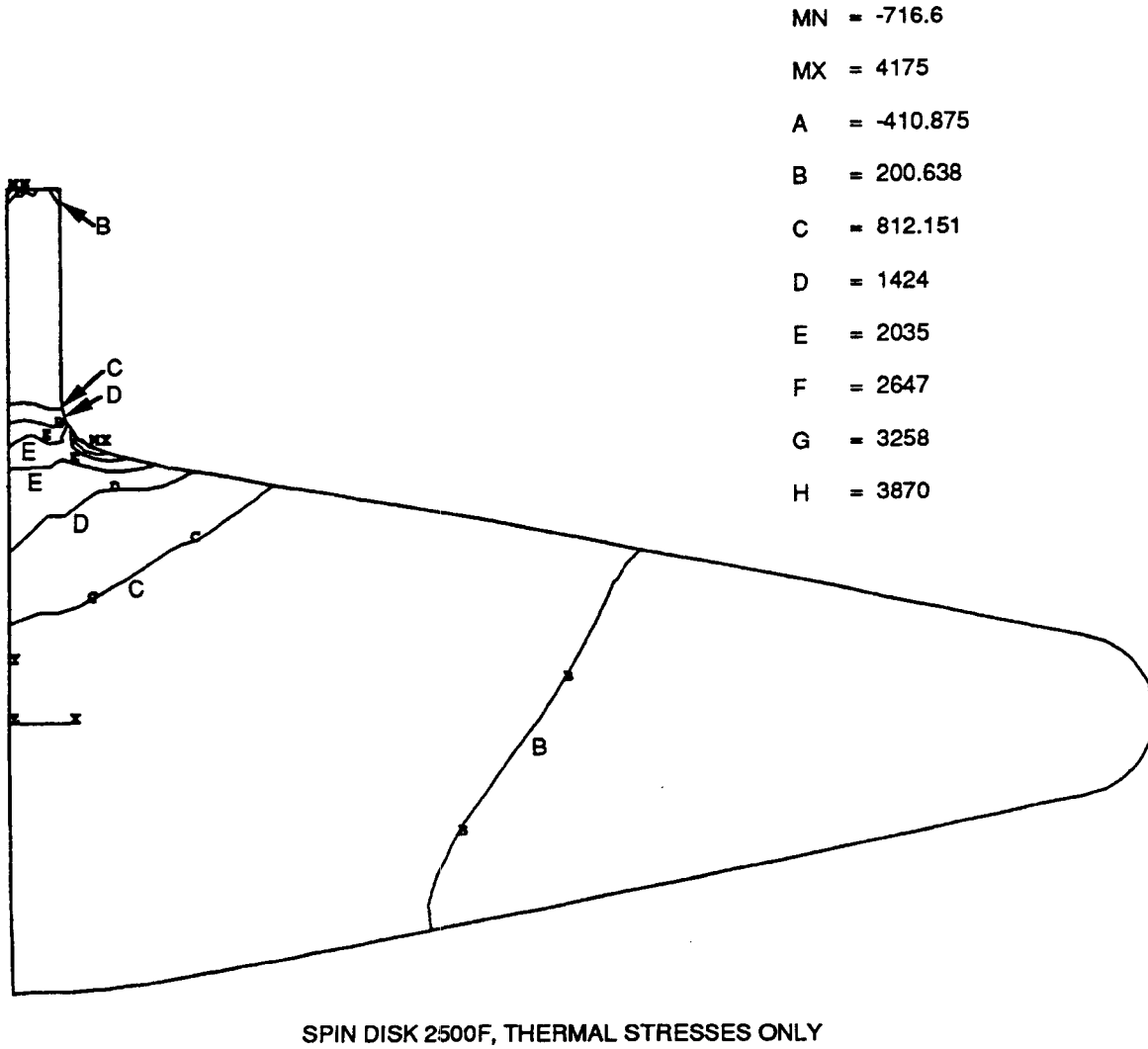
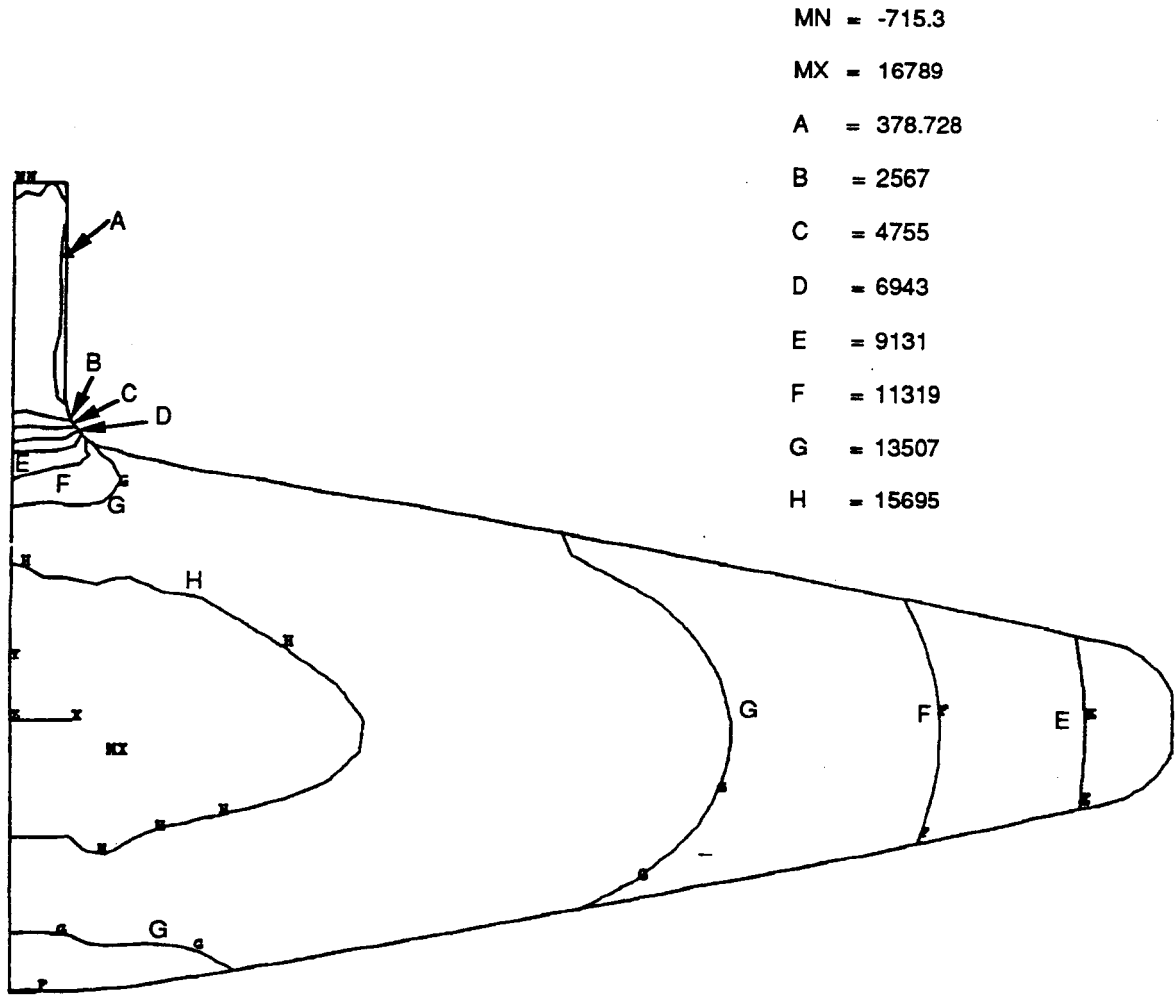


Figure 5-82. Spin Disk Maximum Temperature Distribution At 2500F Test Condition.



GC11591-599A

Figure 5-83. Spin Disk Maximum Principal Stress Distribution Under Thermal Loading Only, At 2500F Test Condition. These Stress Values Are Added To The Centrifugal Stresses To Obtain The Overall Stress Field At These Test Conditions (Units = psi).



SPIN DISK 2500F, RPM AND THERMAL STRESSES

GC11591-600A

Figure 5-84. Spin Disk Maximum Principal Stress Distribution At 2500F Test Condition, Thermal Loading And 50,000 rpm (Units = psi).

data, it was found that an excellent correlation was obtained. The volume prediction was made using the Weibull parameters obtained from pooling all of the fast fracture specimen data, including the high-temperature data. Figure 5-85 shows the volume prediction and the confidence interval of the predictions with the spin disk test data. The prediction of the surface failure mode was much less consistent, as shown by Figure 5-86.

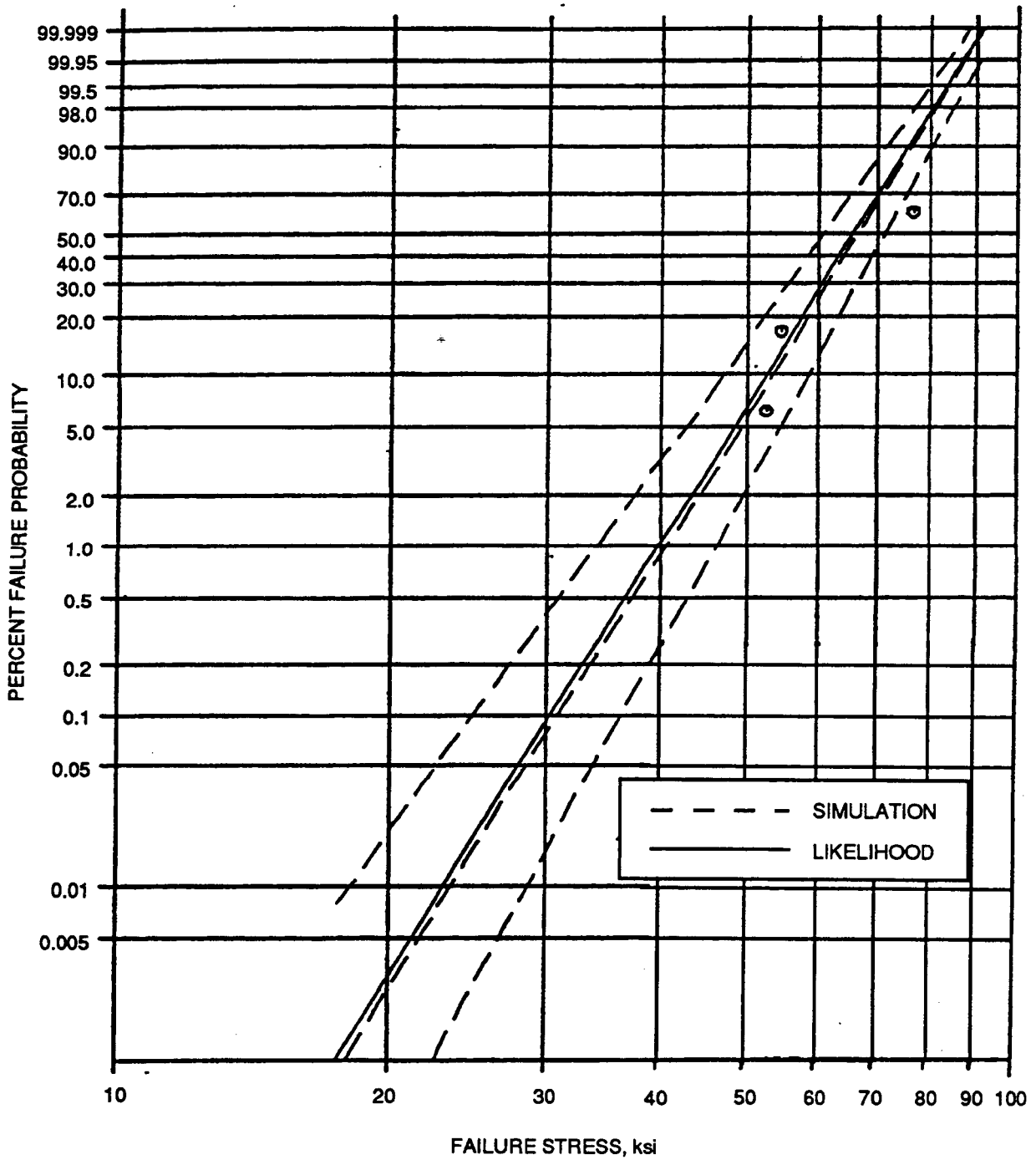
A second set of fast fracture data was obtained from a set of 11 spin disks tested at 2200F, of which 3 failed from internal flaws, 5 from surface flaws, and 2 from machining damage. Again, the volume predictions (Figure 5-87) proved encouraging, although the agreement was not as good as the room-temperature results. The volume prediction was made using the same set of data used for the room-temperature volume prediction that included the assumption that Weibull modulus is constant with temperature as described in Section 5.2.3.3. It is encouraging to see that the predictions are reasonably accurate even when the data from different temperatures was combined into a single data base. The surface predictions for the disks tested at 2200F were not made, because there were no flat disk specimen test data at 2200F.

As can be observed in Figure 5-86, the room-temperature surface predictions are questionable, which is a disturbing result, given that the volume prediction were so reasonable. The surface predictions were made using MIL-B bend test specimens cut from flat spin disks. These flat disks were machined to simulate the spin disk surface because it was anticipated that the surface conditions of the regular MIL-B specimens would be different from those of the spin disk surface properties. The only plausible reason for such a discrepant result is that the spin disks and the specimens had different surface strength properties.

Upon further investigation of this issue, it was found that all of the spin disk surface failures originated from the shaft side of the disk, inside a circle of radius no more than 1.5 inches. It was particularly disturbing that the failures were concentrated on the shaft side of the spin disk, given that the stress fields in the disks are almost the same between the two sides of the disk. Fractographic analysis (using SEM) showed that there was heavy machining damage at the failure locations. This damage is shown in Figure 5-88. The machining damage is uncharacteristic of the surface properties of the specimens used to predict the spin disk surface failure mode. It is hypothesized that the machining damage was the result of the proximity of the compound radius to the shaft. It is believed that the compound radius that transitions into the shaft presented machining difficulties because of the extra care the machining vendor made in ensuring the shaft was not broken during the machining process.

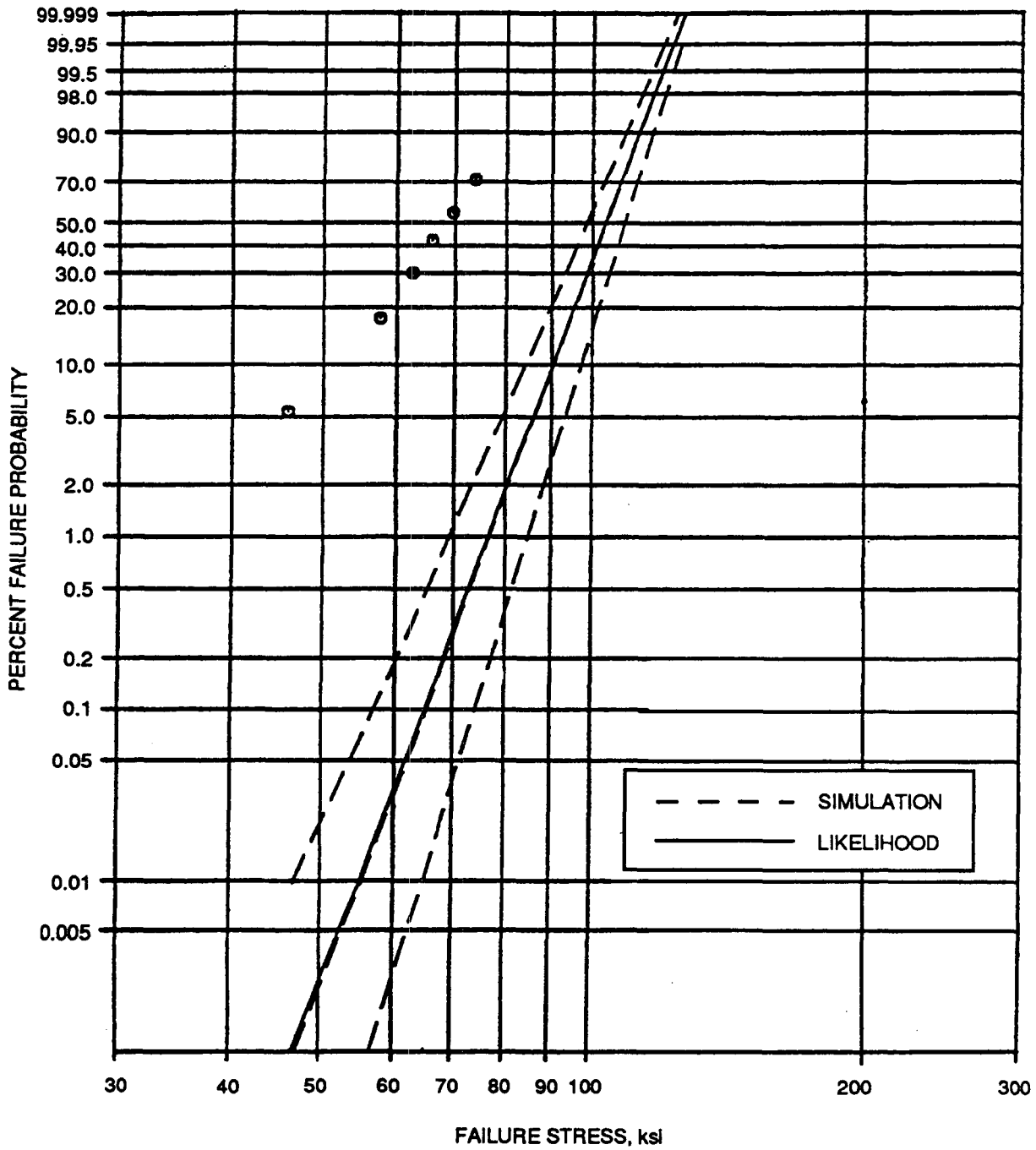
5.4.3.2 Stress Rupture Predictions And Results

The subcritical crack growth, time-dependent failure mode was investigated by testing 6 spin disks at 2200F, of which 1 failed from a volume flaw, 4 from surface flaws, and 1 from machining damage. An attempt



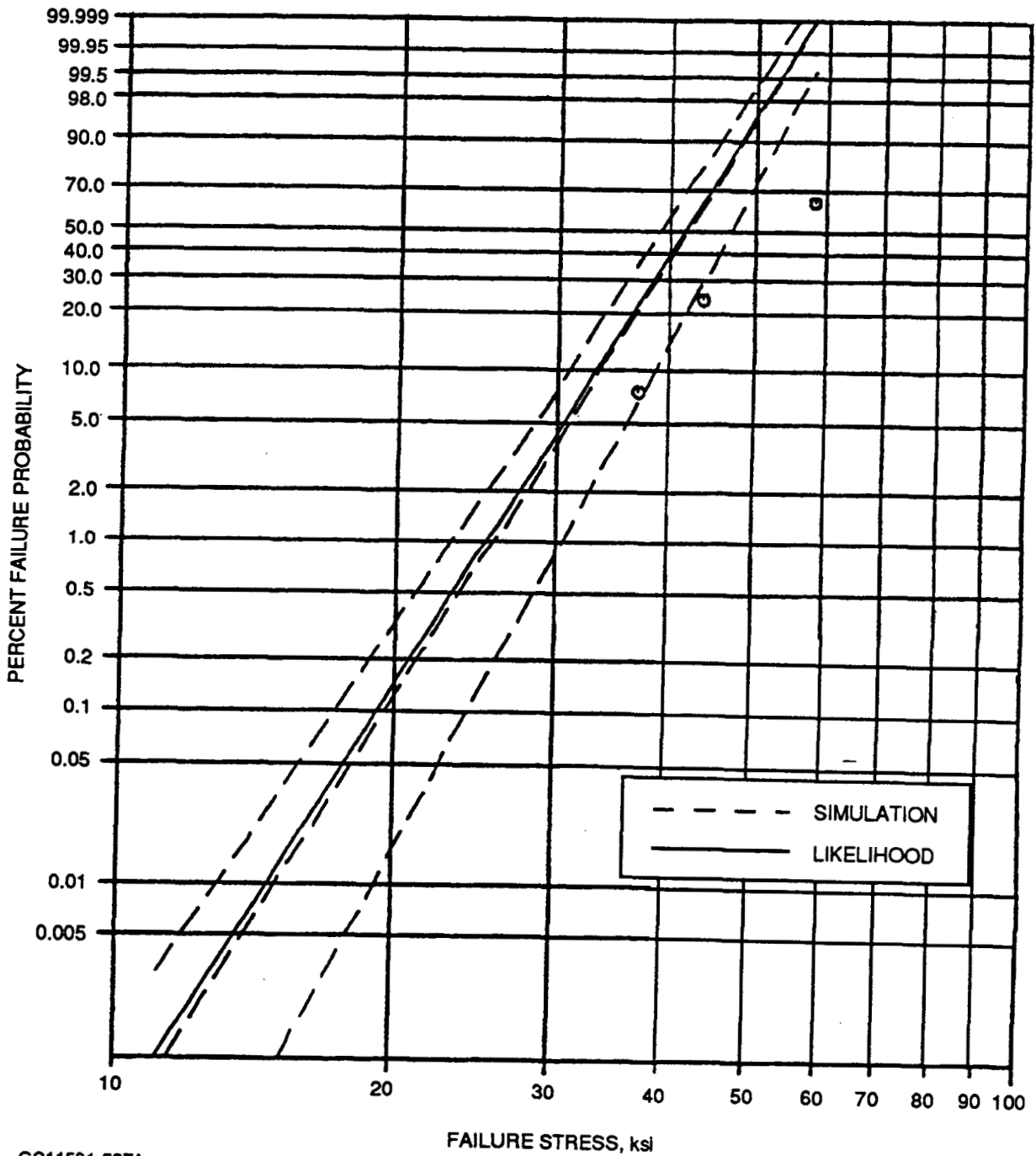
GC11591-585A

Figure 5-85. Spin Disk Room-Temperature Fast Fracture Volume Failure Predictions From Pooled Data Set.



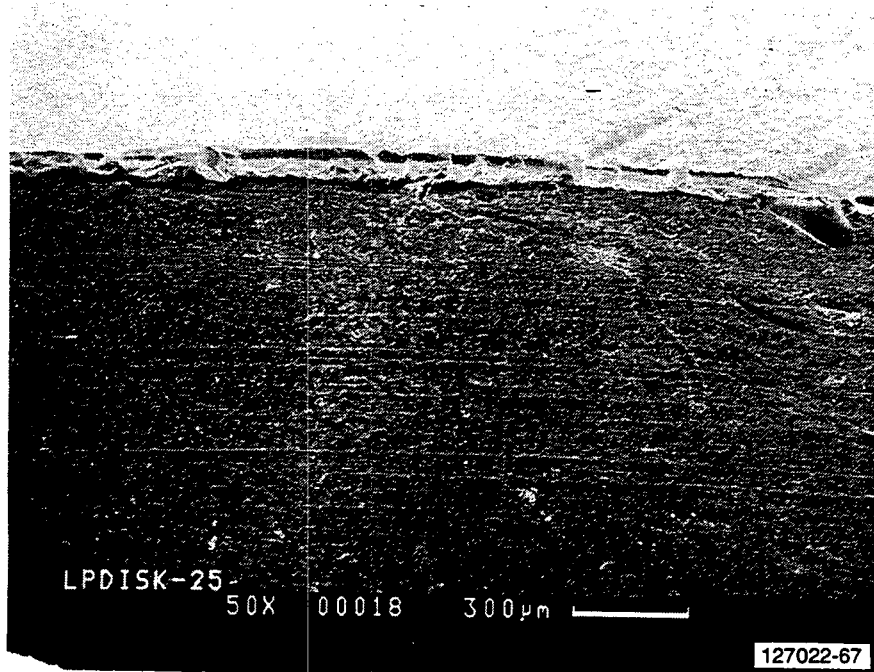
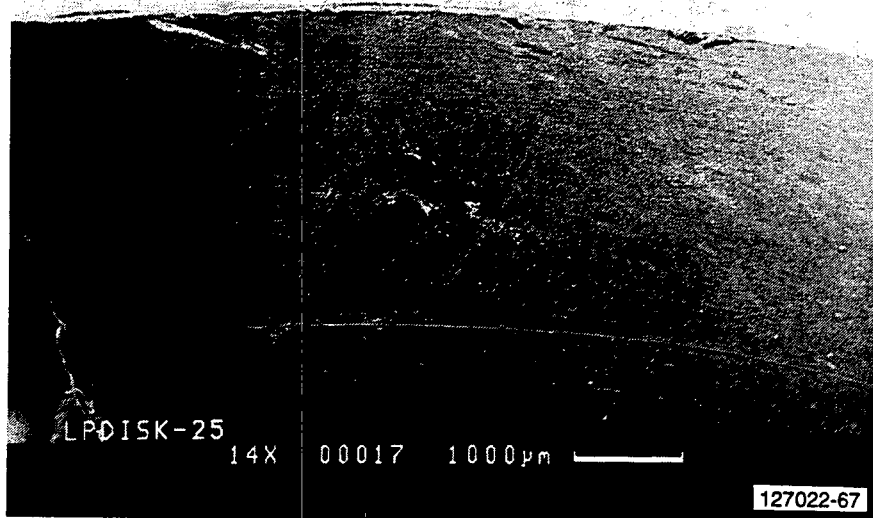
GC11591-586A

Figure 5-86. Spin Disk Room-Temperature Fast Fracture Surface Failure Predictions From Pooled Data Set.



GC11591-587A

Figure 5-87. Spin Disk 2200F Fast Fracture Volume Failure Predictions From Pooled Data Set.



GB11591-748

Figure 5-88. Failure Originated From Deep Surface Machining Line And Associated Damage On 2200F, Fast Fracture Tested Spin Disk (Burst Speed = 60,800 rpm). Machining Damage Was Typical Of Spin Disks Tested.

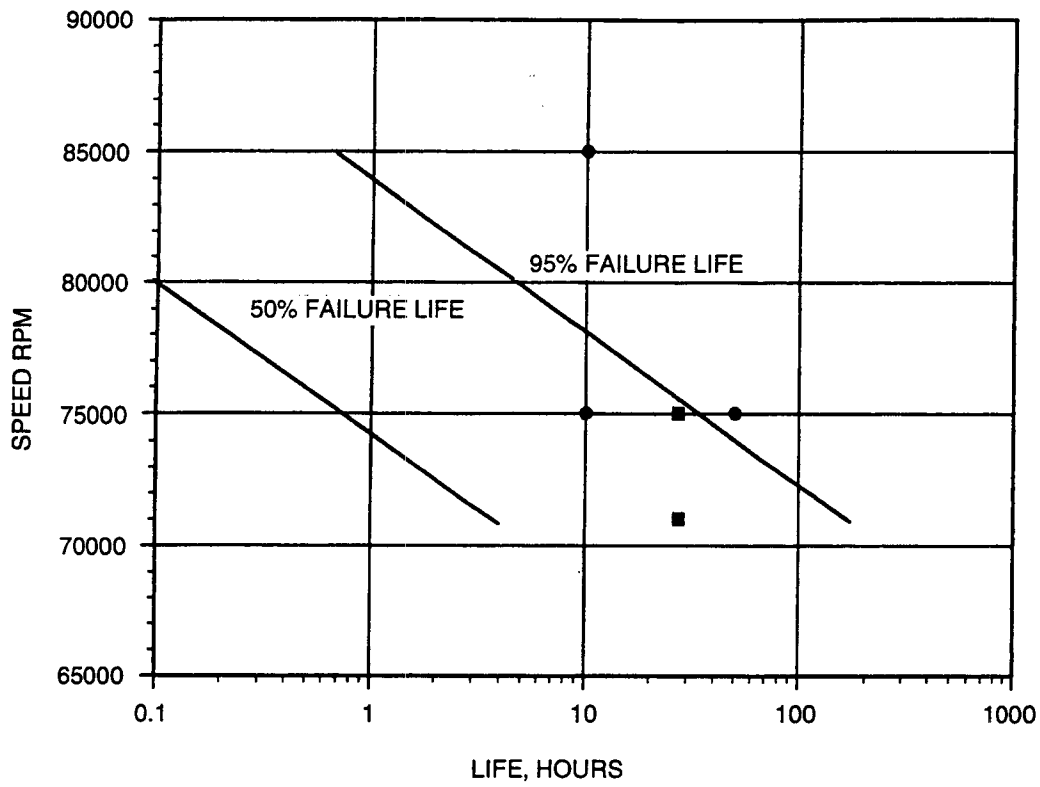
was made to predict the life of these disks using the slow crack growth model developed in Section 5.3.4 and Weibull strength properties from the multi-temperature pooled data. However, these predictions were very poor. In order to prove the accuracy of the subcritical crack growth parameter estimates, a compromise was made; it was decided to use Weibull parameters estimated directly from the spin disk data. The predictions based on SCG parameters obtained from 2200F fast fracture data only were very satisfactory; Figure 5-89 shows the volume failure mode predictions. There is only one failure, but it is inside the 5- and 95-percent quantiles of the life prediction interval. Figure 5-90 shows the surface failure mode predictions. The life tends to be under-predicted; the results are encouraging, since the data points are inside the 5- and 95-percent quantiles. Of the surface data only two are true subcritical crack growth failures; the other three disks were tested in a step-increment fashion. The Weibull analysis of the fast fracture spin disk failures is shown in Figures 5-91 through 5-94.

Creep rupture predictions were verified with five disks tested at 2500F. All failures were surface-initiated, consistent with the observations in the smooth and notched tensile stress rupture specimens, indicating that the inherent flaws were no longer failure-controlling. The same deterministic stress-life relationship (Equation [5-120]) used for the notched specimens and the Orr-Sherby-Dorn (OSD) model described in Section 5.1.5.9 was used to predict the creep rupture life in the spin disks.

The highest surface stresses at the appropriate speeds were used for the predictions. The location of the highest surfaces stresses corresponded with the observed failure location. The predicted and observed lives were as shown in Table 5-21.

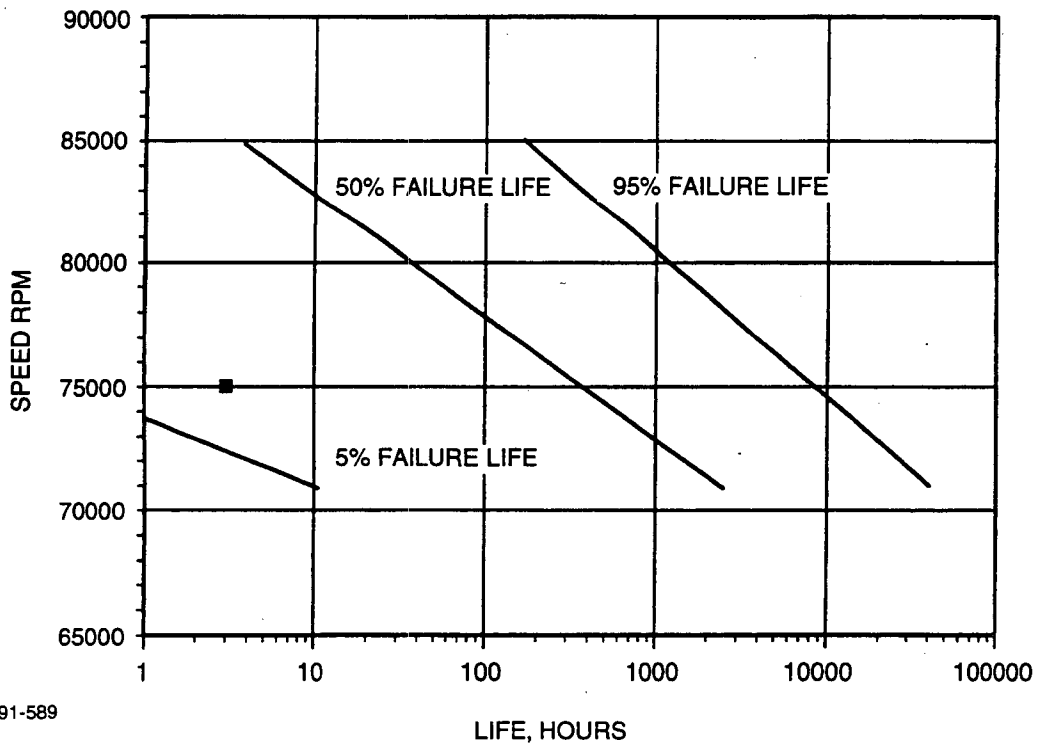
TABLE 5-21. SPIN DISK LIFE PREDICTIONS VERSUS OBSERVED DATA

Speed, rpm	Observed Life, hours	Predicted Life, hours		
		Equation [5-120]	OSD Model	Subcritical Crack Growth
41,800	7	1,390,000	123,400	5,800
45,000/50,000*	10/0.4*	--	--	--
50,000	0.017, 11	15,800	6,000	65
55,000	0.95	1,200	1,100	4
*Step test				



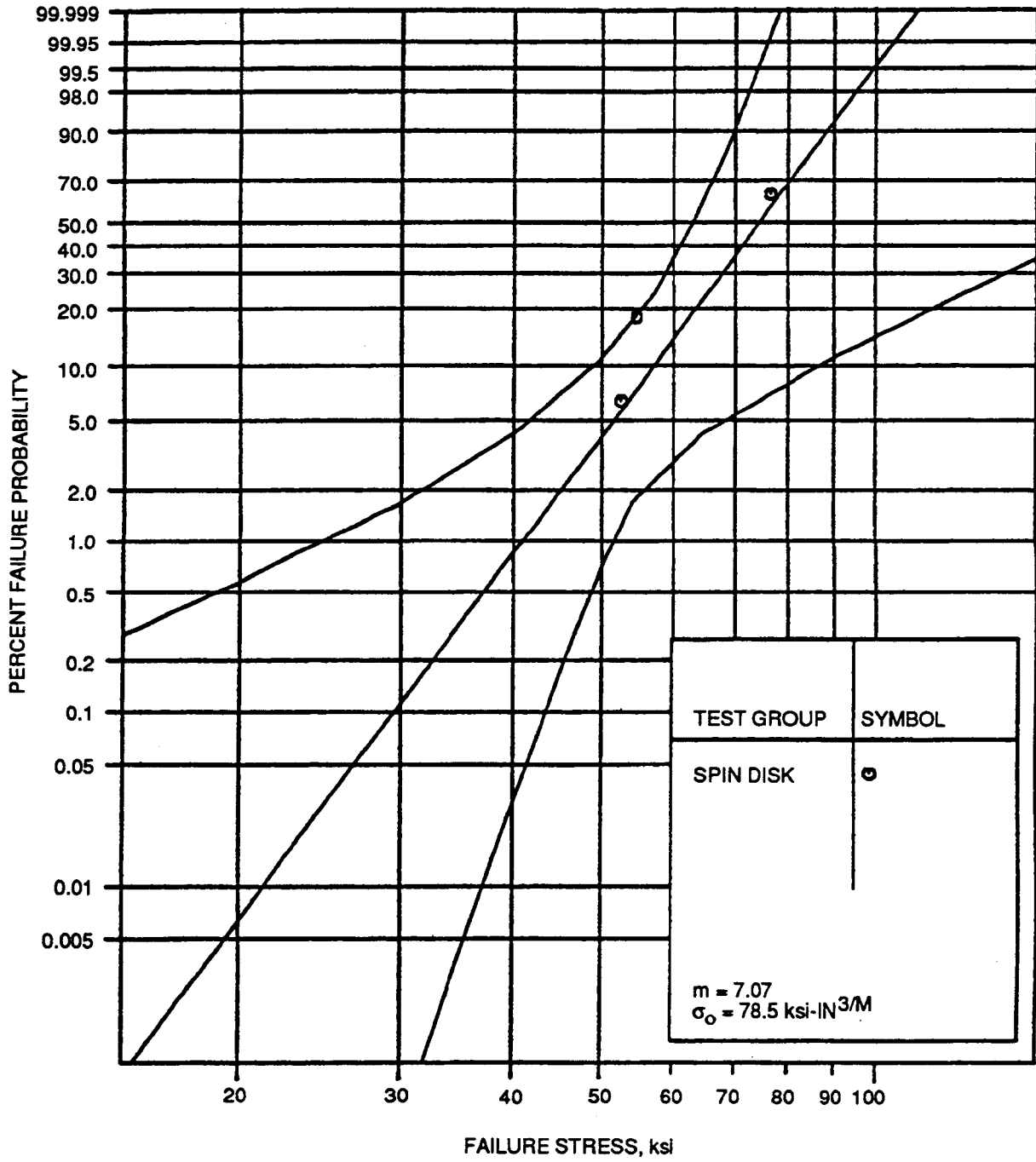
GC11591-588

Figure 5-89. Predicted (Lines) And Observed (Points) Surface Failures In Spin Disks Tested At 2200F.



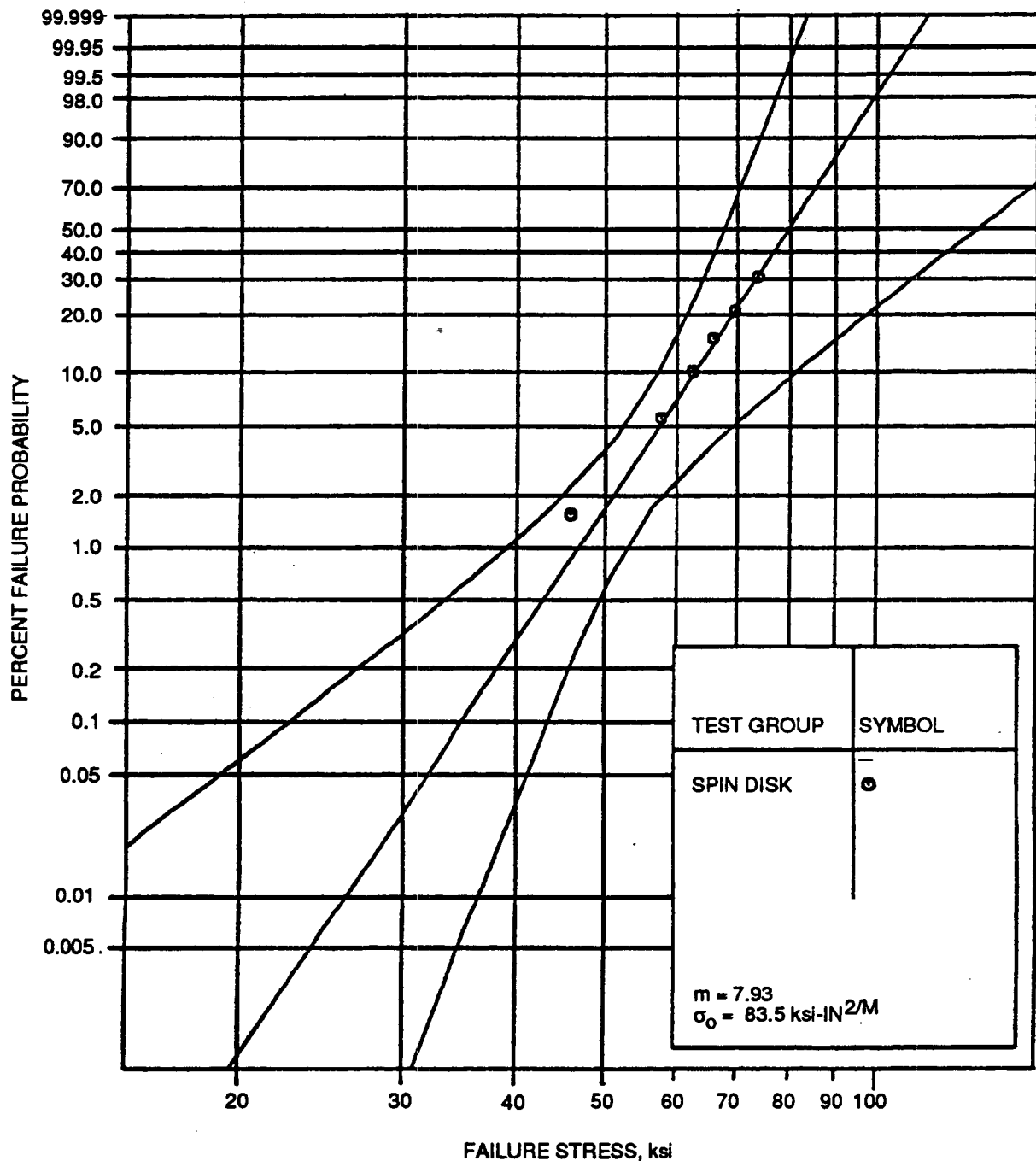
GC11591-589

Figure 5-90. Predicted (Lines) And Observed (Point) Volume Failure(s) In Spin Disks Tested At 2200F.



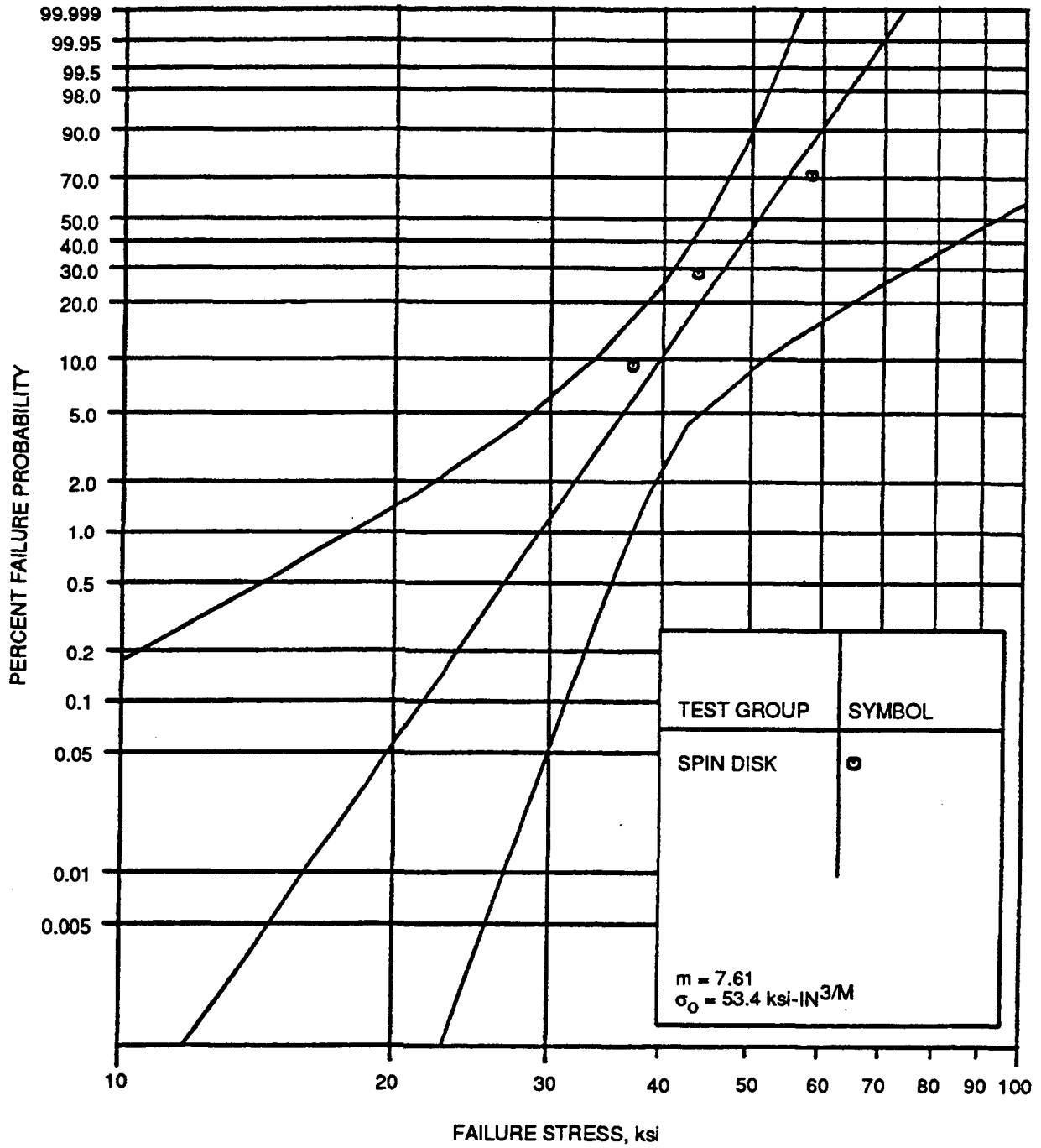
GC11591-590A

Figure 5-91. Raw Data Analysis Of Spin Disk Room-Temperature Volume Failure Mode.



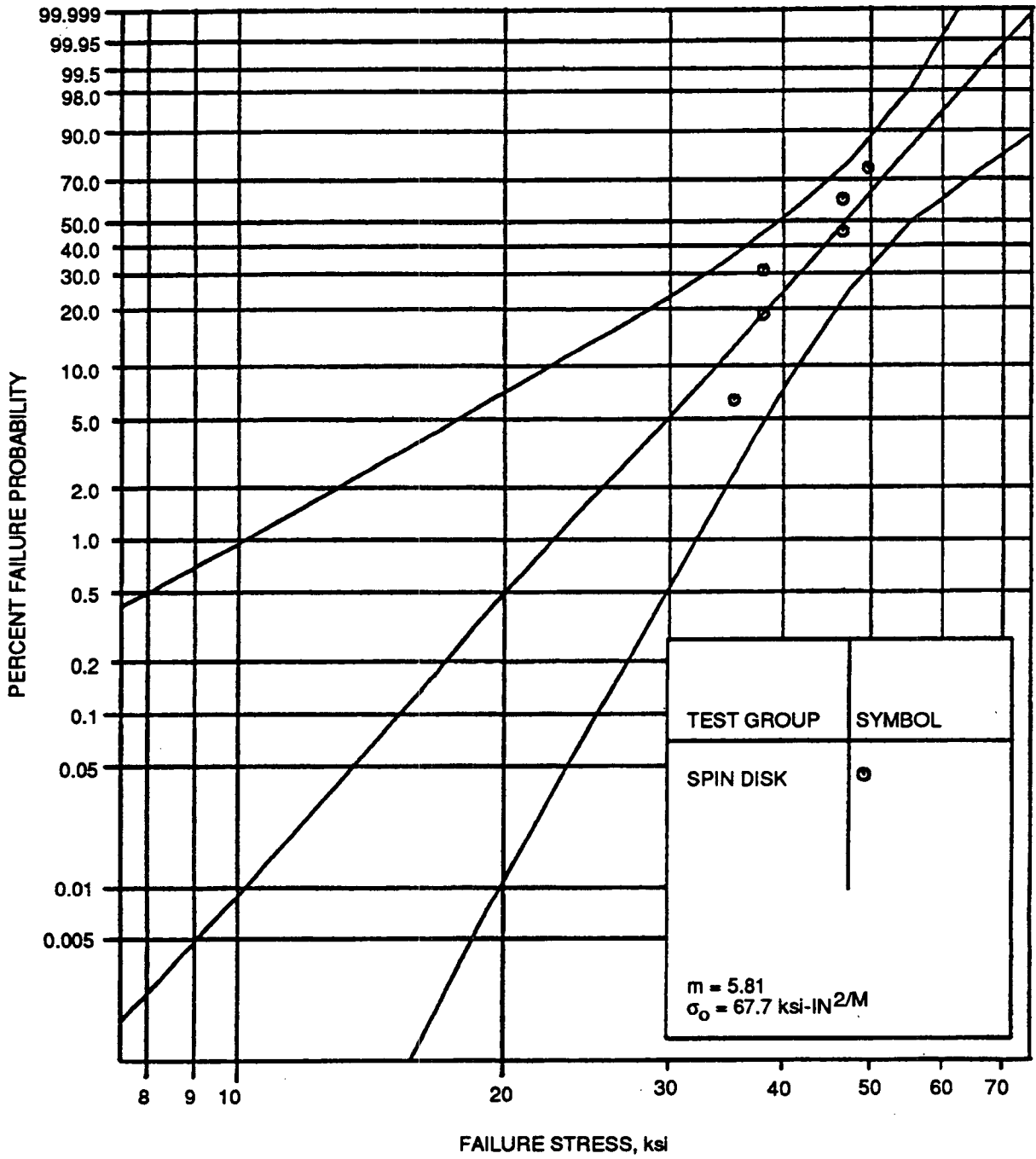
GC11591-591A

Figure 5-92. Raw Data Analysis Of Spin Disk Room-Temperature Surface Failure Mode.



GC11591-592A

Figure 5-93. Raw Data Analysis Of Spin Disk 2200F Volume Failure Mode. (Data Used In SCG Life Prediction.)



GC11591-593A

Figure 5-94. Raw Data Analysis Of Spin Disk 2200F Surface Failure Mode. (Data Used In SCG Life Prediction.)

As can be seen from Table 5-21, the predicted lives from stress-rupture correlations were much longer than the observed lives. Some possible reasons are:

- (1) Surface damage due to improper machining as reported earlier, that led to a higher creep rupture or subcritical crack growth rate
- (2) Lack of size scaling or multiaxial stress model. The predictions at 2200F that included size scaling were reasonable, whereas the 2500F predictions were not. Recall also that the notched tensile creep rupture predictions were reasonable, based on the deterministic stress-life relationship. However, the specimen sizes in that case were comparable. The spin disk, on the other hand, has biaxial stresses and was orders of magnitude larger in size than the baseline smooth stress rupture specimens.

Given that the failure location corresponds to that of the heavy machining damage, an attempt at a worst-case analysis was made. The analysis assumed that failure was caused by subcritical crack growth from the machining damage. The analysis consisted of the following steps:

- (1) Estimate the "effective" initial crack size for the machining damage. This was accomplished by first estimating the fast fracture burst speed at 2500F from the stress rupture tests since no fast fracture burst tests were made. The extrapolated burst speed was 59,300 rpm. The initial flaw size (assuming a semi-elliptical surface flaw) was then calculated from the stress at the failure location and the fracture toughness.
- (2) Assume that the tensile stress rupture failures at 2500F in the core test program were caused by subcritical crack growth. The subcritical crack growth parameters "A" and "n" were then derived: $A = 9.92E-14$, $n = 15.1$ (units in terms of ksi, hours).
- (3) Integrate the subcritical flaw growth life from the initial flaw size to the final flaw size (determined from the stress at speed and fracture toughness).

The results are shown in Table 5-21. These results are encouraging in that they show the importance of taking into account the initial surface condition(s). It should be noted that the predictions shown in Table 5-21 are the median lives. The replicate tensile stress rupture tests conducted at constant stress levels showed between one and two orders of magnitude scatter in life. This should be taken into consideration when comparing the predicted and the observed lives.

In the follow-on Phase II program, more extensive fractography will be conducted. Additional tensile stress rupture tests with transversely-machined surfaces will also be conducted to better define the relationship between the initial surface condition(s) and life.

5.4.4 Prediction Summary

Confirmatory test specimens were designed and tested to verify the underlying brittle failure theory, including multiaxial effects, and the statistical and time-dependent methodologies developed during this program. These specimens were of sizes representative of turbine engine components and tested under similar conditions. Results from these specimens successfully demonstrated the applicability of the brittle failure theory. Encouraging results were obtained for the time-dependent failure modes and the statistical methodologies. Areas were identified where additional understanding of the damage mechanisms are required and further method advancements are needed.

The capabilities of the life prediction methods developed in this program were verified by comparing predicted and measured strengths and lives of the confirmatory test specimens. The results of these comparisons are summarized in Table 5-22.

TABLE 5-22. SUMMARY OF STRENGTH AND LIFE PREDICTION CAPABILITIES FROM COMPARISON OF PREDICTED AND MEASURED CONFIRMATORY SPECIMEN STRENGTHS AND LIVES

	Fast Fracture		Elevated Temperature Fast Fracture		Slow Crack Growth (2200F)		Creep Rupture (2500F)
	Volume	Surface	Volume	Surface	Volume	Surface	Combined
Notched Tensile							
Kt=1.6	N/A	Good	N/A	N/A	Mod	Mod	Mod
Kt=2.1	N/A	Inc	N/A	N/A	Mod	Mod	Mod
Tension-Torsion	Mod	Good	N/A	N/A	N/A	N/A	N/A
Spin Disk	Good	Inc	Mod	Inc	Mod	Mod	Inc
Notes: Inc = Inconclusive Mod = Moderate success N/A = Not applicable, tests were not performed for these conditions.							

Volume fast fracture predictions were generally very successful. Volume strength properties (Weibull parameters) were found to be very consistent in all baseline flexure and tensile specimens. This allowed 405 strength data points to be combined for predictions, and this provided confidence that the same volume strength distribution would exist in the confirmatory specimens. Volume failures were observed in the tension-torsion specimens (15 volume failures) and spin disks (6 volume failures).

More volume failures were expected from the spin disks, because they had higher volume stress than surface stress and a large volume exposed to high stress. However, the surface strength in these disks was apparently much lower than represented by the other specimens, and the majority of the failures initiated from the surface. Volume failures observed in these specimens were in good agreement with the predictions. This demonstrates that the probabilistic method for fast fracture can predict the effects of multiaxial stresses, size scaling, and competing failure modes.

Surface strength prediction had moderate success. Apparently the surface strength/ flaw distributions were not consistent in the different specimen geometries. An additional heat treatment was applied to some specimens to heal severe surface damage with the intent of bringing these different surface strength values closer together. The re-heat treatment did increase transverse surface strength, which helped in sampling volume failure in the spin disks, but it did not produce similar surface strength in different specimens. Therefore it was not possible to predict failures in confirmatory specimens from flexure or tensile specimens with different surface strength properties.

This inconsistency in surface strength was not a result of oversight; considerable effort was made to achieve consistent machined surface properties. The inconsistency is more indicative of the general lack of understanding of the influences of machining practices on ceramic mechanical properties and the need for continued support of machining technology initiatives such as the DOE/ORNL Cost-Effective Ceramic Machining Program (ref. 1-1).

The surface strength predictions did have some success. The tension-torsion specimens have surfaces very similar to the tensile specimens, and predictions for these specimens were generally very successful. The pure torsion tests were first used to confirm the anisotropy model and shear sensitivity value for surface flaws. After these were defined, the torsion and tension-torsion surface failures were all accurately predicted from flexure and tensile specimen data. This demonstrated that surface strength can be predicted under tension-compression multiaxial stresses. However, this was not an adequate test of size-scaling prediction methods for surface failures.

The inconsistent surface properties also made time-dependent failure predictions more difficult. Subcritical crack growth lives are based on predicting the time for flaws, determined from flexure and tensile fast fracture tests, to grow to critical sizes. This is based on the assumption that the distribution of surface flaws in flexure and tensile specimens were the same as the confirmatory specimens, which was apparently not true. However, when confirmatory specimen strength data were used to define the initial flaw size distribution, the subcritical crack growth life predictions were generally successful. The lives of the notched tensile specimens in the 100-hr range were accurately predicted. But the lives of these specimens were more sensitive to stress than predicted, possibly due to the discrepant surface properties, stress relaxation, or effects of the stress gradient on the rate of crack growth. The spin disk stress rupture lives also fell within the predicted range of lives, when 2200F spin disk fast fracture data was used to define the initial surface flaw size. These stress rupture confirmatory tests show the difficulties in obtaining meaningful design data from specimens. However, predictions based on component data generally confirmed prediction capabilities.

At 2500F, creep and environmentally-enhanced crack growth are the controlling failure modes. As described previously, a creep rupture model was developed that correlates a wide range of stress-temperature-life results from tensile specimen tests. This model has not yet been expanded into a component prediction tool to account for multiaxial stress, competing failure modes, and size effects. However, predictions were made for the notched tensile specimens and spin disks tested at 2500F, to assess the significance of modeling component complications. The predicted lives of the notched-tensile specimen were similar to the measured lives; specimen life predictions can be further improved if creep stress relaxation is considered in the life prediction. However, the spin disk life predictions were many orders of magnitude greater than observed in the spin pit tests. Life prediction using a crack growth approach, based on the observed surface damage, was successful in narrowing the discrepancy between observed and predicted lives. This indicates that surface damage, size effects, and/or multiaxial stresses have to be taken into account. In the follow-on Phase II ceramic life prediction program, these variables will be studied in more detail.

Overall, the predictions demonstrated the success of the strength and life prediction methods. The strength (fast fracture) methods are considered to be more advanced than the time-dependent methods and were expected to provide more accurate predictions. The subcritical crack growth methods still require advancements before scatter in lives can be reliably predicted; however, the results were encouraging relative to the prediction of average lives. In the regime where creep is predominant, further work is needed to extend these models to component prediction tools. These life prediction development areas will be addressed in the planned Phase II Ceramic Life Prediction Program efforts.

REFERENCES - SECTION 5.0

- (5-1) K. Palaniswamy and W.G. Knauss, "On the Problem of Crack Extension in Brittle Solids", Mechanics Today, Vol. 4, pp 87-148, 1978.
- (5-2) D. Singh and D.K. Shetty, "Microstructural Effects on Fracture Toughness of Polycrystalline Ceramics in Combined Mode I and Mode II Loading", ASME Paper 88-GT-208, 1988.
- (5-3) D. Singh and D.K. Shetty, "Fracture Toughness of Polycrystalline Ceramics in Combined Mode I and Mode II Loading", J. Am. Ceram. Soc., 72 [1], 78-84 (1989).
- (5-4) M.K. Ferber and M.G. Jenkins, "Evaluation of the Strength and Creep-Fatigue Behavior of Hot Isostatically Pressed Silicon Nitride", J. Am. Ceram. Soc., 75 [9], 2453-2462 (1992).
- (5-5) S.M. Wiederhorn, B.J. Hockey, D.C. Cranmer, and R. Yeckley, "Transient Creep Behavior of Hot Isostatically Pressed Silicon Nitride", J. Mater. Sci., 28 [2], 445-453 (1993).
- (5-7) W. Luecke, S.M. Wiederhorn, B.J. Hockey, and G.G. Long, "Cavity Evolution During Tensile Creep of Si_3N_4 ", pp. 467-472 in Silicon Nitride Ceramics - Scientific and Technological Advances, Proceedings of the Material Research Society Symposium, Boston, MA, Nov-Dec 1992, 287, Edited by I-W Chen et. al., Materials Research Society, Pittsburgh, PA, 1993.
- (5-6) H.J. Frost and M.F. Ashby, p. 13, in Deformation-Mechanism Maps, Pergamon Press, NY, 1982.
- (5-8) F.F. Lange, "Non-Elastic Deformation of Polycrystals with a Liquid Phase", pp. 361-381 in Deformation of Ceramic Materials, Edited by R.C. Bradt and R.E. Tressler, Plenum Press, NY, 361-381, 1975.
- (5-9) I.M. Lifshitz, "On the Theory of Diffusion-Viscous Flow of Polycrystalline Bodies", Soviet Phys., JETP, 17 [4], 909-920 (1963).
- (5-10) M.K. Ferber, M.G. Jenkins, T.A. Nolan and R. Yeckley, "Mechanical Performance of a HIPped Silicon Nitride: I - Creep/Fatigue Behavior", Unpublished data, Oak Ridge National Laboratory, Oak Ridge, TN, 1992 (recently submitted for publication).
- (5-11) R.M. Arons and J.K. Tien, "Creep and Strain Recovery in Hot-Pressed Silicon Nitride", J. Mater. Sci., 15 [8], 2046-2058 (1980).
- (5-12) A. Bouarroudj, P. Goursat, and J.L. Besson, "Oxidation Resistance and Creep Behavior of a Silicon Nitride Ceramic Densified with Y_2O_3 ", J. Mater. Sci., 20 [4], 1150-1159 (1985).
- (5-13) R. Raj and C.K. Chyung, "Solution-Precipitation Creep in Glass Ceramics", Acta Metall., 29 [1], 159-166 (1981).
- (5-14) R. Raj, "Creep in Polycrystalline Aggregates by Matter Transport Through a Liquid Phase", J. Geophys. Res. B, 87 [7], 4731-4739 (1982).
- (5-15) R. Raj and P.E.D. Morgan, "Activation Energies for Densification, Creep, and Grain-Boundary Sliding in Nitrogen Ceramics", J. Am. Ceram. Soc., 64 [10], C143-C145 (1981).
- (5-16) T. Rouxel, J.-L. Besson, C. Gault, P. Goursat, M. Leigh, and D. Hampshire, "Viscosity and Young's Modulus of an Oxynitride Glass", J. Mater. Sci. Lett., 8 [10], 1158-1160 (1989).
- (5-17) D.R. Clarke, "High-Temperature Microstructure of a Hot-Pressed Silicon Nitride", J. Am. Ceram. Soc., 72 [9], (1989), 1604-1609.

- (5-18) J.E. Marion, A.G. Evans, M.D. Drory, and D.R. Clarke, "High Temperature Failure Initiation in Liquid Phase Sintered Materials", *Acta Metall.*, 31 [10], 1445-1457 (1983).
- (5-19) R.L. Tsai and R. Raj, "Creep Fracture in Ceramics Containing Small Amounts of a Liquid Phase", *Acta Metall.*, 30 [6], 1043-1058 (1982).
- (5-20) "ANSYS Engineering Analysis System User's Manual", Swanson Analysis Systems Inc., P. O. Box 65, Houston, PA 15342, 1990.
- (5-21) R.W. Evans, J.D. Parker, and B. Wilshire, "An Extrapolation Procedure for Long-Term Creep Strain and Creep Life Prediction With Special Reference To 0.5Cr-0.5Mo-0.25V Ferritic Steels", pp. 135-175, in Recent Advances in Creep and Fracture of Engineering Materials and Structures, Edited by B. Wilshire and D.R.J. Owen, Pineridge Press, Swans, 1982.
- (5-22) R.W. Evans and B. Wilshire, "The Q Projection Concept", pp. 197-256, in Creep of Metals and Alloys, Chapter 6, The Institute of Metals, London, 1985.
- (5-23) R.W. Evans, T. Murakami, and B. Wilshire, "Rate Controlling Processes During Creep of Silicon Nitride Ceramics", *Br. Ceram. Trans. J.*, 87 [2], 54-57 (1988).
- (5-24) M.N. Menon, "A Model for Primary, Secondary and Tertiary Creep Rates", pp. 163-169 in Creep: Characterization, Damage and Life Assessment, Proceedings of the Fifth International Conference on Creep, ASM International, 1992.
- (5-25) F.F. Lange, B.I. Davis, and D.R. Clarke, "Compressive Creep of $\text{Si}_3\text{N}_4/\text{MgO}$ Alloys", *J. Mater. Sci.*, 15 [3], 601-618 (1980).
- (5-26) D. Cubicciotti and K.H. Lau, "Kinetics of Hot-Pressed Silicon Nitride", *J. Electrochem. Soc., Solid-State Science and Technology*, 126 [10], 1723-1728 (1979).
- (5-27) A. Tsuge, K. Nishida, and M. Komatsu, "Effect of Crystallizing the Grain-Boundary Glass Phase on the High-Temperature Strength of Hot-Pressed Si_3N_4 Containing Y_2O_3 ", *J. Am. Ceram. Soc.*, 58[7-8], 323-326 (1975).
- (5-28) D.C. Drucker, "Engineering and Continuum Aspects of High Strength Materials", pp. 795-833 in High Strength Materials, Edited by V.F. Zackay, Wiley, NY, 1965.
- (5-29) H. Riedel, pp. 172-197 in Fracture at Higher Temperatures, Springer-Verlag, Berlin, 1986.
- (5-30) C.W. Li, C.J. Gasdaska, J. Goldacker, and S.C. Liu, "Damage Resistance of In Situ Reinforced Silicon Nitride", pp. 473-480 in Silicon Nitride Ceramics - Scientific and Technological Advances, Proceedings of the Material Research Society Symposium, Boston, MA, Nov-Dec 1992, 287, Edited by I-W Chen, et. al., Materials Research Society, Pittsburgh, PA, 1993.
- (5-31) Y.R. Xu, T.S. Yen, and X.R. Fu, "Grain Boundary Tailoring of High Performance Nitride Ceramics and Their Creep Property Studies", pp. 739-750, in Proceedings of the Third International Symposium on Ceramic Materials and Components for Engines, Edited by V.J. Tennery, 1988.
- (5-32) J.B. Conway, "Stress-Rupture Parameters: Origin, Calculation and Use", Gordon and Breach, 1969.
- (5-33) D.I.G. Jones, "Stress Rupture of Ceramics: Time-Temperature Relationships", Paper No.87-GT-81, presented at the Gas Turbine Conference and Exhibition, Anaheim, CA, May 31-June 4, 1987, American Society of Mechanical Engineers, New York.

- (5-34) F.C. Monkman and N.J. Grant, "An Empirical Relationship between Rupture Life and Minimum Creep Rate in Creep-Rupture Tests", Proc. Am. Soc. Test. Mater., 56, 593-620 (1956).
- (5-35) R. Castillo, A.K. Koul, and E.H. Toscano, "Life Prediction Under Constant Load Creep Conditions for a Cast Ni-Base Superalloy", J. Eng. for Gas Turbines and Power, 109 [1], 99-106 (1987).
- (5-36) A. Tasooji, "Thermophysical and Mechanical Properties of Single Crystal CMSX-3 Blade Alloy", Report No. 22-3517, April, 1990, AlliedSignal Propulsion Engines, Phoenix, AZ 85010.
- (5-37) A. Tasooji, Private communication, 1992.
- (5-38) C.J. Lin, M.G. Jenkins, and M.K. Ferber, "Tensile Dynamic and Static Fatigue Relations for a HIPped Silicon Nitride at Elevated Temperatures", Oak Ridge National Laboratory, Oak Ridge, TN, (accepted for publication in J. Europ. Ceram. Soc.), 1993.
- (5-39) K.C. Liu, C.O. Stevens, and C.R. Brinkman, "Tensile Cyclic Fatigue of Structural Ceramics", pp. 31-34 in ORNL Report ORNL/CF-92/285, Oak Ridge National Laboratory, Oak Ridge, TN, December 1992.
- (5-40) J.L. Schienle, "Tensile Rupture Testing (ORNL)", pp. 4-6 in Thirty-Second Bi-Monthly Technical Progress Report, Advanced Turbine Technology Applications Project, Contract DEN3-335, November - December 1992, Report No. 31-6990(32), December 23, 1992, AlliedSignal Auxiliary Power, Phoenix, AZ; prepared for NASA-Lewis Research Center, Cleveland, OH, 44135.
- (5-41) B.J. Hockey and S.M. Wiederhorn, "Microstructural Analysis of Structural Ceramics", pp. 271-281 in Ceramic Technology Project Semiannual Progress Report for October 1991 Through March 1992, ORNL-TM-12133, Oak Ridge National Laboratory, Oak Ridge, TN, September 1992.
- (5-42) A.G. Evans and A. Rana, "High Temperature Failure Mechanisms in Ceramics", Acta Metall., 28 [2], 129-141 (1980).
- (5-43) R.J. Charles, "Static Fatigue of Glass. II", J. Appl. Phys., 29[11], 1554-1560 (1958).
- (5-44) C.E. Inglis, "Stresses in a Plate due to the Presence of Cracks and Sharp Corners", Trans. Inst. Naval Architects, 55 [3], 219-241 (1913).
- (5-45) G. Grathwohl, "Regimes of Creep and Slow Crack Growth in High-Temperature Rupture of Hot-Pressed Silicon Nitride", pp. 573-586, in Deformation of Ceramic Materials II, ed. by R.E. Tressler and R.C. Bradt, Plenum Press, 1984.
- (5-46) G.D. Quinn, "Static Fatigue Resistance of Hot Pressed Silicon Nitride", pp. 319-332 in Fracture Mechanics of Ceramics, Vol. 8, ed. by R.C. Bradt, A.G. Evans, D.P.H. Hasselman and F.F. Lange, Plenum Press, 1986.
- (5-47) S.M. Wiederhorn, G.D. Quinn and R. Krause, "Fracture Mechanism Maps: Their Applicability to Silicon Nitride", presented at the ASTM Conference on Life Prediction Methodology and Data for Ceramic Materials, Cocoa Beach, Florida, January, 1993 (to be published also as ASTM-STP 1201, ed. by C.R. Brinkman and S.Q.F. Duffy, American Society for Testing of Materials, Philadelphia).
- (5-48) R.L. Orr, O.D. Sherby and J.E. Dom, "Correlations of Rupture Data for Metals at Elevated Temperatures", Trans. Am. Soc. Met., 46, p.113, 1954.

- (5-49) M.K. Ferber, Private Communication, Oak Ridge National Laboratory, Oak Ridge, TN 37831, 1993.
- (5-50) Weibull, W., "A Statistical Theory of the Strength of Materials," Royal Swedish Academy of Engineering Sciences Proceedings, Volume 151, pp 1-45, 1939
- (5-51) Batdorf, S. B. , and Crose, J. G., "A Statistical Theory for the Fracture of Brittle Structures Subjected to Nonuniform Polyaxial Stresses," *Journal of Applied Mechanics*, 41, pp 459-464, 1974.
- (5-52) Batdorf, S. B. , and, Heinisch, H. L., "Weakest Link Theory Reformulated for Arbitrary Fracture Criterion," *Journal of the American Ceramic Society*, Vol. 61 (No. 7-8), pp 355-358, 1978.
- (5-53) Evans, A. G., "A General Approach for the Statistical Analysis of Multiaxial Fracture," *Journal of the American Ceramic Society*, 61, 7-8, pp 302-308, 1978.
- (5-54) Chao L. and Shetty D. K., "Equivalence of Physically Based Statistical Fracture Theories for Reliability Analysis of Ceramics in Multiaxial Loading," *J. AM. Ceram. Soc.*, 73, 7, 1917-1921, 1990
- (5-55) Tucker, W. T., and Johnson, C. A., "The Multiaxial Equivalence of Stressed Volume", *Life Prediction Methodology and Data for Ceramic Materials*, ASTM STP 1201, C. R. Brinkman, and S. F. Duffy, Eds., American Society for Testing and Materials, Philadelphia, 1993.
- (5-56) Batdorf, S. B., and Heinisch, H. L., "Fracture Statistics of Brittle Materials With Surface Cracks," *Engineering Fracture Mechanics*, Vol. 10, pp 831-841.
- (5-57) Nemeth, N. N., Manderscheid, J. M., and Gyekenyesi, J. P., " Ceramic Analysis and Reliability Evaluation of Structures (CARES): Users and Programmers Manual," NASA Technical Paper 2916, Aug., 1990.
- (5-58) Shetty, D. K., "Mixed Mode Fracture Criteria For Reliability Analysis and Design with Structural Ceramics." *J. Eng. Gas Turbines and Power*, Vol., 109, No. 3, July 1987, pp 282-289.
- (5-59) Rice, R. W., and Mecholsky, J. J., Jr., "The Effect of Grinding Direction on Flaw Character and Strength of Single Crystal and Polycrystalline Ceramics," *J. Mat. Sci.*, 16, 853-862 (1981).
- (5-60) Rice, R. W., and Mecholsky, J. J., Jr., pp. 351 in *The Science of Ceramic Machining and Surface Finishing II*, National Bureau of Standards Special Pub. 562, edited by J. Hockey and R. W. Rice, 1979.
- (5-61) Nelson, W., *Applied Life Data Analysis*, John Wiley & Sons, 1982.
- (5-62) Batdorf, S. B., Sines, G., "Combining Data for Improved Weibull Parameter Estimation," *Journal of the American Ceramic Society*, Vol., 63, No. 3-4, pp. 214-218, 1980.
- (5-63) Johnson, C. A., and Tucker, W. T., "Advanced Statistical Concepts of Fracture in Brittle Materials," *Engineered Materials Handbook Volume 4: Ceramics and Glasses*, ASM, pp 709-715, 1992.
- (5-64) Johnson, C. A., "Fracture Statistics of Multiple Flaw Distributions," *Fracture Mechanics of Ceramics*, Vol. 5, Edited by R. C. Bradt, A. G. Evans, D. P. H. Hasselman, and F. F. Lange, Plenum Publishing Corp., 1983
- (5-65) Chuck, L., Goodrich, S.M., Hecht, N.L., and McCullum, D.E., "High Temperature Tensile Strength and Tensile Stress Rupture Behavior of Norton/TRW NT-154 Silicon Nitride",

Ceramic Engineering and Science, Proceedings of the 13th Annual Conference on Composites and Advanced Ceramic Materials, 1990.

- (5-66) G.G. Trantina and C.A. Johnson, "Probabilistic Defect Size Analysis Using Fatigue and Cyclic Crack Growth Rate Data," *Probabilistic Fracture Mechanics and Fatigue Methods: Applications for Structural Design and Maintenance*, ASTM STP 798, J.M. Bloom and J.C. Ekvall eds., American Society for Testing and Materials, Philadelphia, PA, 1983, pp. 67-78.
- (5-67) CERAMIC Users Manual, AlliedSignal Engines Document No. 32-3968, September 1993.
- (5-68) Johnson, L. G., "The Statistical Treatment of Fatigue Experiments," Research Laboratories, General Motors, pp. 44-50, 1959.
- (5-69) Johnson, C. A., and Tucker, W. T., "Weibull Estimators for Pooled Fracture Data," *Life Prediction Methodology and Data for Ceramic Materials*, ASTM STP 1201, C. R. Brinkman, and S. F. Duffy, Eds., American Society for Testing and Materials, Philadelphia, 1993.
- (5-70) Cox, D. R., and Oakes, D., "Analysis of Survival Data", Chapman and Hall, Chapt. 3.3, 1984.
- (5-71) Efron, B. and Tibshiriami, R., "Bootstrap Methods for Standard Errors, Confidence Intervals, and Other Measures of Statistical Accuracy," Statistical Science, Vol. 1, pp. 54-57, 1986.
- (5-72) ANSYS44A, Swanson Analysis Systems Inc., Houston, PA.
- (5-73) Greenberg, M. D., *Foundation of Applied Mathematics*, Prentice-Hall Inc. Englewood Cliffs, N. J., 1978.
- (5-74) Ritter, J.E., "Engineering Design and Fatigue Failure of Brittle Materials", Fracture Mechanics of Ceramics, Vol. 4, pp. 667-686, Plenum Press, New York, NY, 1978.
- (5-75) SAS Computer Code, SAS Institute, Inc., Box 8000, Cary, NC 27511-8000.
- (5-76) Conover, W.J., Practical Non-Parametric Statistics, 2nd Ed., John Wiley and Sons, NY 1980.
- (5-77) T. Fett and D. Munz, "Methods of Determining Subcritical Crack Growth by Static Lifetime Tests with Natural and Artificial Cracks", Journal of Testing and Evaluation, Vol. 19, No. 6, pp. 461-466, Nov. 1991.

6.0 NDE METHODS DEVELOPMENT AND APPLICATION

6.1 NDE Program Objectives

Nondestructive evaluation (NDE) is an important element in the quality assurance process for gas turbine engine hardware. Historically, a variety of NDE methods have been used for both in-process control and final component inspection. Initially, NDE methods were primarily qualitative in nature, but as design methodologies have changed from traditional design methods based on material property minimums to damage-tolerant and/or probabilistic design methods, the need for quantitative NDE information has grown. NDE is now integrated into both the design and manufacture of turbine engine components.

For ceramic materials targeted for turbine engine applications, the critical flaw size is expected to be at or beyond current production NDE detection limits. However, because the Weibull modulus (m) of ceramic materials is relatively low (m of approximately 7 to 12), the distribution of flaws around the critical flaw size will be relatively wide, as shown in Figure 6-1. If surface and volumetric NDE methods are characterized to identify the minimum detectable flaw sizes, minimum resolution, and the reliability of detection, then NDE can be used as a screening tool to assess and characterize the upper limit of the initial flaw distribution in ceramic materials (Figure 6-1).

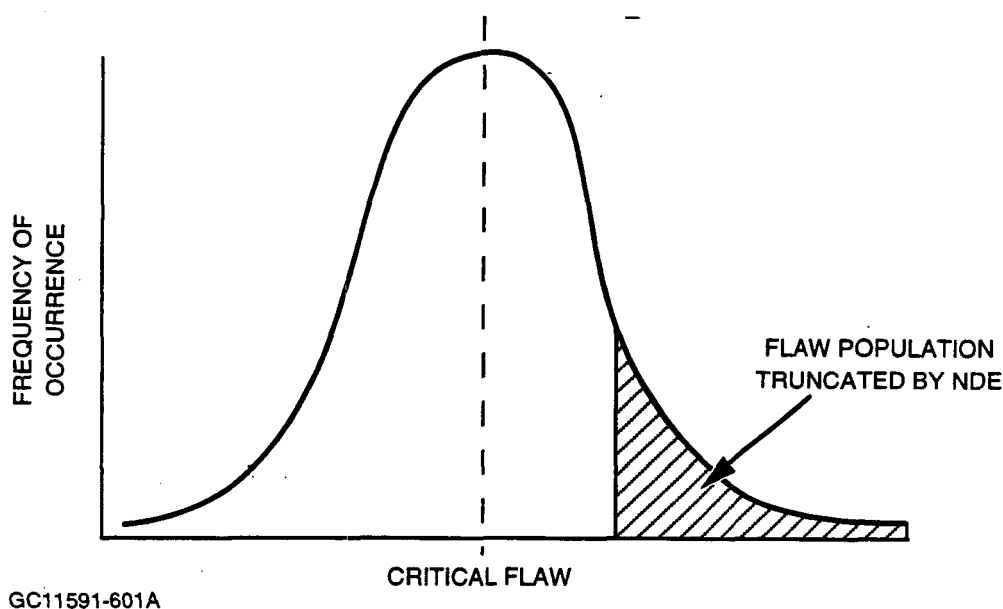


Figure 6-1. NDE Can Be Used As An Effective Screening Tool To Assess The Upper Limit Of The Inherent Flaw Population In Ceramics.

Specifying the NDE detection limits will identify the portion of the flaw distribution that can effectively be truncated from the initial flaw distribution, thereby improving the material used in actual components. The objective of this program was to select, develop, and apply NDE techniques to ceramic specimens and to identify the limits of the NDE techniques under simulated production conditions. The NDE program objective was broken into three specific task areas:

- Develop and fabricate reference standards for evaluation and calibration of NDE methods
- Develop and apply appropriate surface and volumetric NDE methods for inspecting the ceramic specimens in the test matrix
- Correlate NDE results with fractography data to quantify minimum detectable flaw sizes for each NDE technique.

The NDE objectives were successfully addressed through the efforts of a team of individuals at AlliedSignal and the two major subcontractors: General Electric (Dr. R. Gilmore, Mr. M. Keller, and Mr. J. Portaz) contributed to the development of computed tomography and acoustic microscopy methods for this program and provided inspection services in the same areas; and Argonne National Laboratory (Dr. W. Ellingson and Mr. G. Forester) was subcontracted to develop digitization and enhancement techniques to aid in the evaluation of film radiographs.

NDE method selection included both surface and volumetric techniques applicable to the complex geometries typical of turbine engine components. The selected methods were:

- **Surface Methods**

- Visual Inspection
- Fluorescent Penetrant Inspection (FPI)
- Acoustic Microscopy (AM)

- **Volumetric Methods**

- Acoustic microscopy (AM)
- Computed Tomography (CT)
- Projection microfocus radiographic inspection (RT), with and without digital enhancement.

6.2 NDE Reference Standards Development And Fabrication

In order to characterize the capabilities and limitations of each NDE technique under development, appropriate reference standards were required to identify these limits. Four different fabrication approaches were used to generate the following standards in this program:

- Laser-drilled hole standards
- Photolithographically etched and bonded standards
- Surface crack standards
- Volume seeded defect standards.

A total of twenty ceramic NDE standards were designed and fabricated.

6.2.1 Laser Drilled Standards

Laser drilling is capable of generating holes in the 10 to 600 micron (μm) range required for NDE technique development. While holes in the 250 to 600 μm range can be fabricated by other techniques, laser drilling was selected for its ability to maintain close tolerances and to minimize variation in the hole shape. Laser drilling studies performed as part of this program demonstrated the capability to repeatedly fabricate holes in silicon nitride as small as 10 μm in diameter and 5 to 200 μm in depth.

In general, laser drilling can be used to fabricate either blind or through-drilled holes in silicon nitride with aspect ratios ranging from 0.5:1 to 20:1 while maintaining a 2-degree maximum cone angle. For holes 25 μm and larger, a 40:1 aspect ratio was achieved. However, only one source, Resonetics, Inc. in Nashua, NH, had laser drilling capabilities for hole sizes less than 250 μm . The smaller hole capability is a function of the laser used for fabricating the holes. The Excimer laser used by Resonetics functions in a pulsed mode and employs the ultraviolet (UV) spectrum for cutting, rather than the infrared (IR) spectrum of conventional YAG lasers. The UV spectrum laser has a shorter wavelength and is capable of much higher peak power than the IR spectrum laser and is therefore capable of machining finer details.

Laser drilling was used to fabricate standards for surface and volumetric AM detection and calibration, radiographic inspection and computed tomography. Laser-drilled standards for AM were used to measure the inspection sensitivity similar to the conventional American Society for Testing and Materials (ASTM) standard blocks with flat-bottomed holes used at lower ultrasonic inspection frequencies. The design of the AM standards incorporated both the laser drilling parameter limits and the theoretical depth-of-field limits for the

transducers. The maximum depth of field planned for the inspections was 1 mm from a 50 MHz F:8 transducer. Using the limit of a 40:1 aspect ratio from the laser drilling study and the 1 mm minimum separation from the depth-of-field calculation, the smallest hole for volumetric AM at varying depths was 25 μm . A typical volumetric AM detection/sensitivity standard is shown in Figure 6-2 which demonstrates how an ultrasonically machined counterbore was used to place the deeper holes at the desired depth. This figure shows two internal AM standards typical of the standards designed for this program.

The standard ASTM E1025-84 penetrameter design for measuring radiographic image quality was modified to contain smaller hole sizes than for metals as shown in Figure 6-3. The design for the penetrameter contained four laser-drilled holes in each thickness penetrameter with hole diameters varying as a function of thickness. The largest hole fabricated in each standard was twice the penetrameter thickness, and the smallest hole fabricated was 0.1 times the penetrameter thickness. The thinnest penetrameter fabricated was 0.13 mm.

In addition to the ultrasonic and radiographic sensitivity standards, laser drilling was also used to fabricate both sensitivity and resolution standards for evaluating CT capabilities. These standards are shown in Figure 6-4. Sensitivity is important because it establishes the minimum flaw size that can be detected above the background noise for a particular technique while resolution is the ability of a technique to separate two closely-spaced defects. The sensitivity and resolution standards were designed with high-contrast machined defects, so that the effects of X-ray absorption were negligible in this evaluation. Seeded defect standards were used to evaluate typical defect contrast.

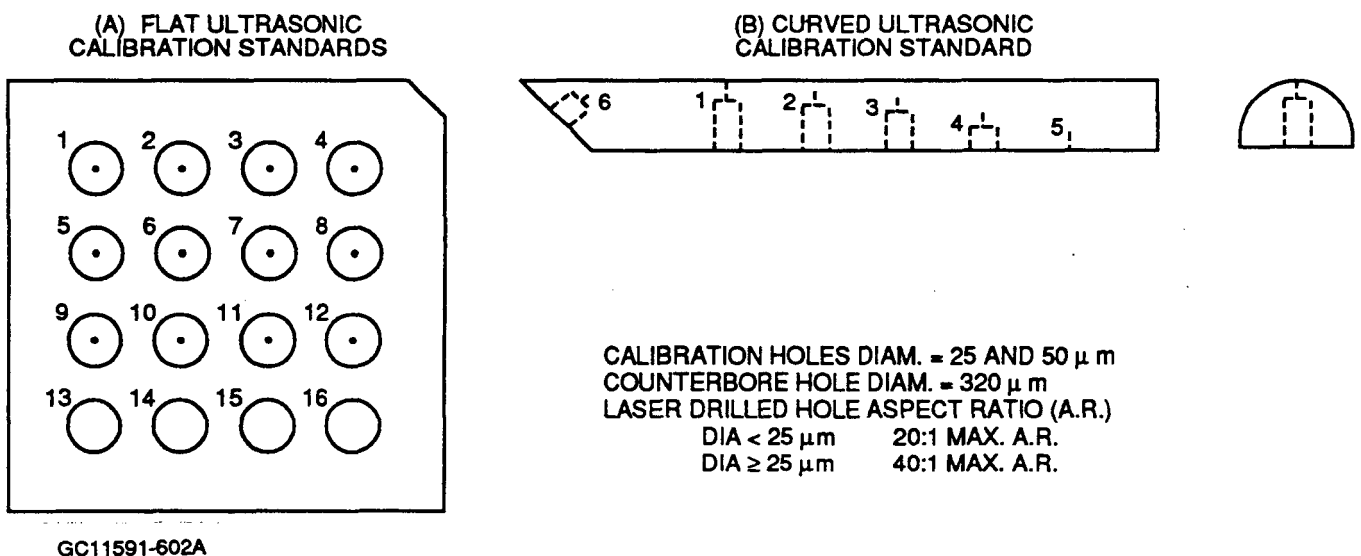
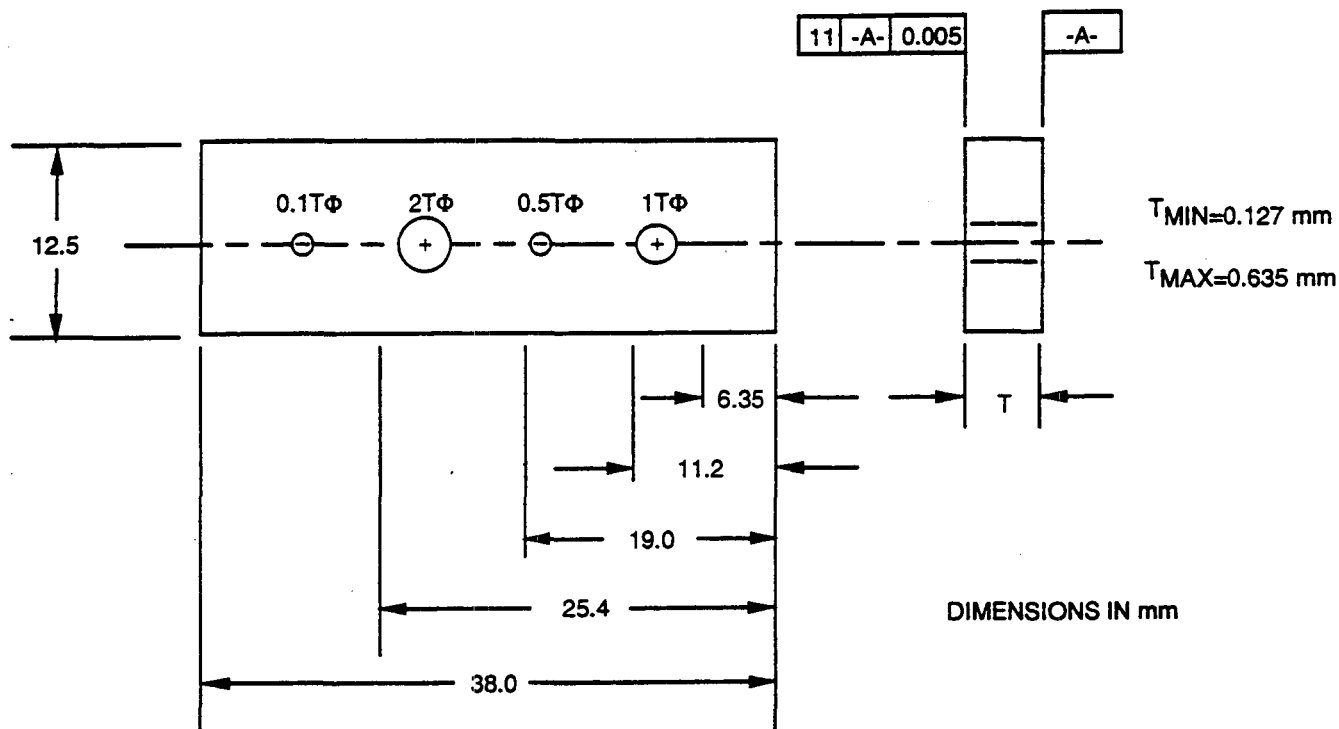
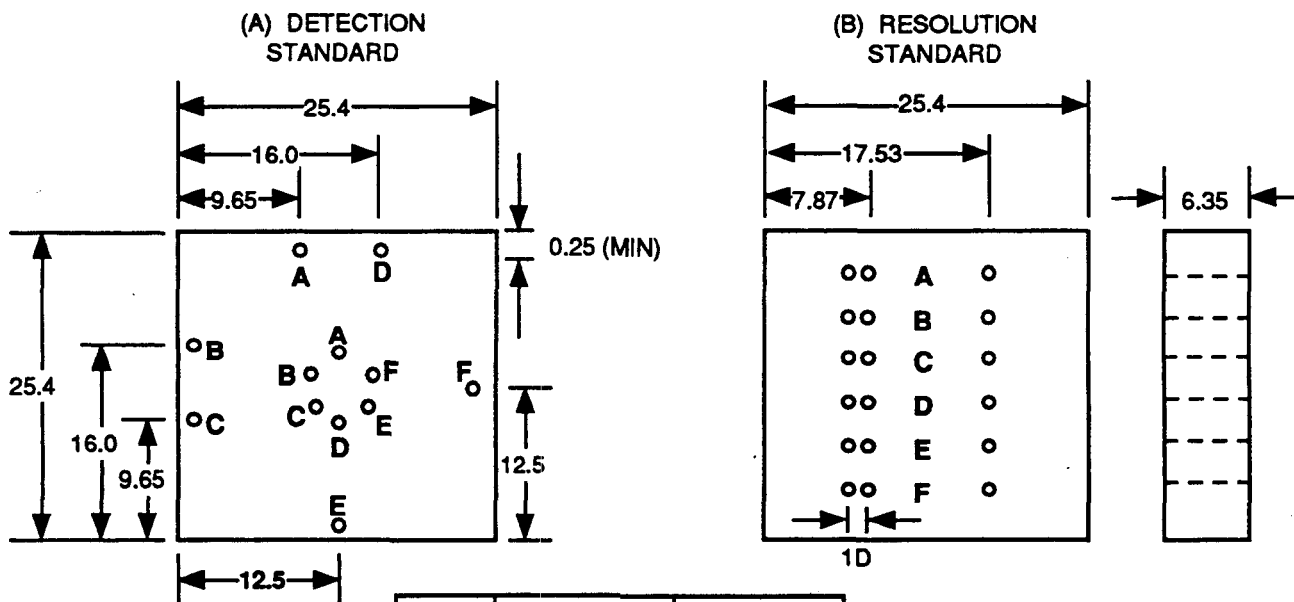


**Figure 6-2. Laser Drilling Was Used To Fabricate NDE Standards.
(Size Table Applies to Both (A) and (B))**



GC11591-603

Figure 6-3. ASTM Penetrant Design Was Modified For Small Flaw Detection.



HOLE	DIAMETER, D	TOLERANCE
A	0.05	±0.01
B	0.10	±0.03
C	0.20	±0.03
D	0.30	±0.03
E	0.41	±0.03
F	0.51	±0.03

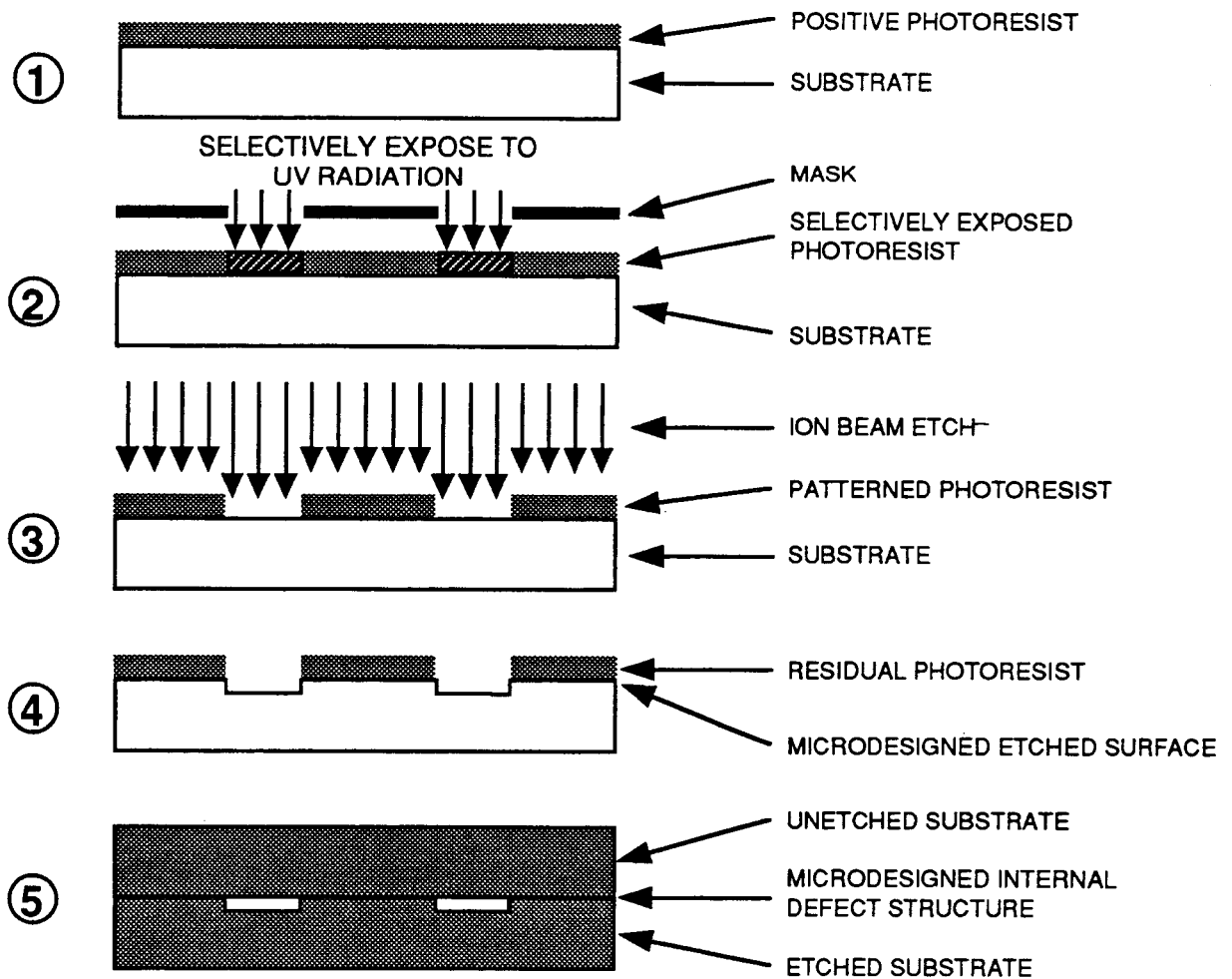
ALL DIMENSIONS IN mm

GC11591-604A

Figure 6-4. Computed Tomography Standards Were Designed To Evaluate Both Detection And Resolution.

6.2.2 Photolithographically Etched And Bonded Standards

A resolution standard design was developed for AM that allowed the determination of volumetric resolution capabilities, using a fabrication technique developed by Drs. A. Glaeser and J. Rodel at the University of California at Berkeley. A pattern was generated and deposited on the surface of a substrate using photolithography. Then the pattern was etched into the surface using an ion beam etching process developed specifically for each material. When the etched surface is bonded to another nonetched surface, the etched pattern remains unbonded, forming internal voids corresponding to the etched pattern. The entire process is illustrated in Figure 6-5 and described in further detail in references (6-1) and (6-2).



GC11591-605

Figure 6-5. Photolithographic Process For Sapphire AM Resolution Standard Developed At UC Berkeley.

Because the mask used to form the void pattern on the surface is computer generated and then etched in a controlled manner on the substrate, small high-resolution voids (as small as 2 μm in diameter and 0.2 μm deep) can be precisely placed on the substrate. Furthermore, there are very few limitations to the artificial void shape that can be produced. The maximum void depth and minimum aspect ratio attainable are a function of the etching rate of the material and the mask thickness. The successful fabrication of the resolution standards indicates that this technique offers a precise way of manufacturing void standards for NDE.

The pattern selected for the resolution standard is defined in MIL-STD-150 and is commonly referred to as the USAF 1951 Resolution Target. The USAF 1951 Resolution Target is a line-pair pattern used originally for measuring photographic lens quality. Use of the line-pair pattern for ultrasonic imaging was first suggested by Gilmore, et. al. (ref 6-3) in 1986, but the feasibility of fabricating an embedded resolution standard had not previously been demonstrated until this program employed the photolithography technique developed by Glaeser and Rodel (ref 6-1 and 6-2). Since the resolution target described in MIL-STD-150 is fabricated in high contrast black lines on a clear substrate, the pattern was ideal for a photolithography mask.

The material selected for the resolution standard was c-axis single crystal sapphire because it is transparent and because sapphire supports longitudinal, shear, and surface wave velocities along the c-axis that are very similar to silicon nitride. The acoustic similarity between silicon nitride and sapphire produced acoustic beam geometries in the sapphire which were almost identical to those of NT154; while the transparency of sapphire allowed optical verification of the line-pair pattern without destructive analysis. In addition, the etching and bonding parameters previously developed for sapphire reduced both the cost and fabrication time of the standard.

A total of three line-pair standards were fabricated:

- Surface (i.e. not bonded to another defect free substrate)
- 2 mm Coverplate and 4 mm thick substrate
- 2 mm Coverplate and 10 mm thick substrate.

6.2.3 Surface Crack And Volumetrically Seeded Standards

Surface crack standards were fabricated using an indentation technique followed by surface grinding to remove the indent and leave only the cracks. The residual cracks varied from 100 to 380 μm in surface length. Although the grinding resulted in a surface finish much better than that encountered on actual components, the cracks were used in screening tests to select the best frequency and scan resolution for surface wave inspection.

Volumetrically seeded samples were designed to relate the response from artificial defects, such as laser drilled holes, to the response from more naturally occurring material defects such as large grains, and high, low, and near density inclusions. Three different defect types were selected based on a review of typical fabrication defects occurring in silicon nitride materials, and the expected reaction of intentionally seeded defects during processing. Four different defect sizes were selected in the 10 to 150 μm range. Titanium nitride was chosen as a near but higher density defect for seeding and was seeded in four different nominal seed sizes. Titanium had been observed in some inclusions in NT154 and the titanium nitride was selected in order to minimize the reaction with the NT154. Aluminum oxide was seeded to cause bulk density variations or grain growth which might be caused when sintering aids are unevenly distributed in the material.

Finally, tungsten carbide was seeded as a high-density inclusion because previous work (ref 6-4) indicated that tungsten carbide does not react with silicon nitride. While tungsten carbide may no longer represent a realistic type of inclusion because the manufacturing process no longer uses tungsten carbide grinding media, it was used as another detection reference for the seeding study. The seed sizes for each defect type are shown in Table 6-1.

TABLE 6-1. SEEDED DEFECT SPECIMEN DIAMETERS

Defect Type	Nominal Size, μm
Aluminum Oxide	98
Aluminum Oxide	138
Titanium Nitride	25
Titanium Nitride	50
Titanium Nitride	100
Titanium Nitride	150
Tungsten Carbide	28
Tungsten Carbide	108
Tungsten Carbide	196

The volumetrically seeded samples were the least predictable type of standards fabricated for this program. The original goals of the volumetric seeding effort were to:

- Achieve spherical defects
- Maintain a seeding density of 15 defects/cm³ regardless of defect size
- Control the seed size within $\pm 5 \mu\text{m}$.

While none of these goals were met completely due to the numerous challenges in obtaining and fabricating the standards, the resultant standards still provided useful information about the NDE techniques. Because of the small number of defects actually needed for fabrication by this technique, the control on the powder (used to seed the defects) was limited to conventional mesh screening techniques. The powder screening technique affected both the size and shape variation of the end defect. For example, 100 μm nominal seed sizes were achieved by screening the powder through two different size meshes: a 140 mesh which allowed particles 106 μm and smaller (in one dimension) to pass, and a 170 mesh which allowed particles 90 μm and smaller to pass. Thus, for a nominal 100 μm particle size, the actual particles could range between 90 to 106 μm (140 to 170 mesh) in the largest dimension. Larger (longer) particles with high aspect ratios could also pass through the screens, provided at least one dimension was smaller than the mesh size.

A particle size distribution analysis was performed using Microtrac analysis to assure that 90 percent of the particles were within the desired $\pm 5 \mu\text{m}$ range. Additional screenings were performed on the powders until the desired 90 percent of the powder was in the $\pm 5 \mu\text{m}$ range. Actual particle sizes varied substantially from the desired spherical shape, depending on the method used to form the powders. Nominal powder size, shape, and density were supplied by the powder manufacturer. The powders ranged from spherical to oval for titanium nitride and were more rectangular flakes or needles for tungsten carbide. The size and shape variations were observed during radiographic inspection of the detectable defects.

The number of defects seeded was based on the calculated weight of a spherical particle. The defects were introduced into the ceramic material by assuming the particles were spheres, calculating the weight of the average size sphere for each seed size and then multiplying by the desired number of defects in the unit volume (15 defects/ cm^3) by the weight of a single particle. The approximate number of defects was seeded in each specimen by weight. Using the weight approach for determining seed quantities, the smallest aluminum oxide, titanium nitride, and tungsten carbide powders could not be accurately weighed for seeding, so the standards were not fabricated. Additionally, a large variation in seeds per unit volume was noted in the different seed sizes and types during NDE. This indicates either a settling problem during fabrication, a large difference in the average volume of the particles so that the weight estimate was incorrect, or that an error was made in calculating or measuring the seed weight. The settling of seeds during fabrication is least suspect, as tabs cut from both ends of the specimens exhibited similar seed/unit volume variations.

6.3 NDE Technique Development And Calibration

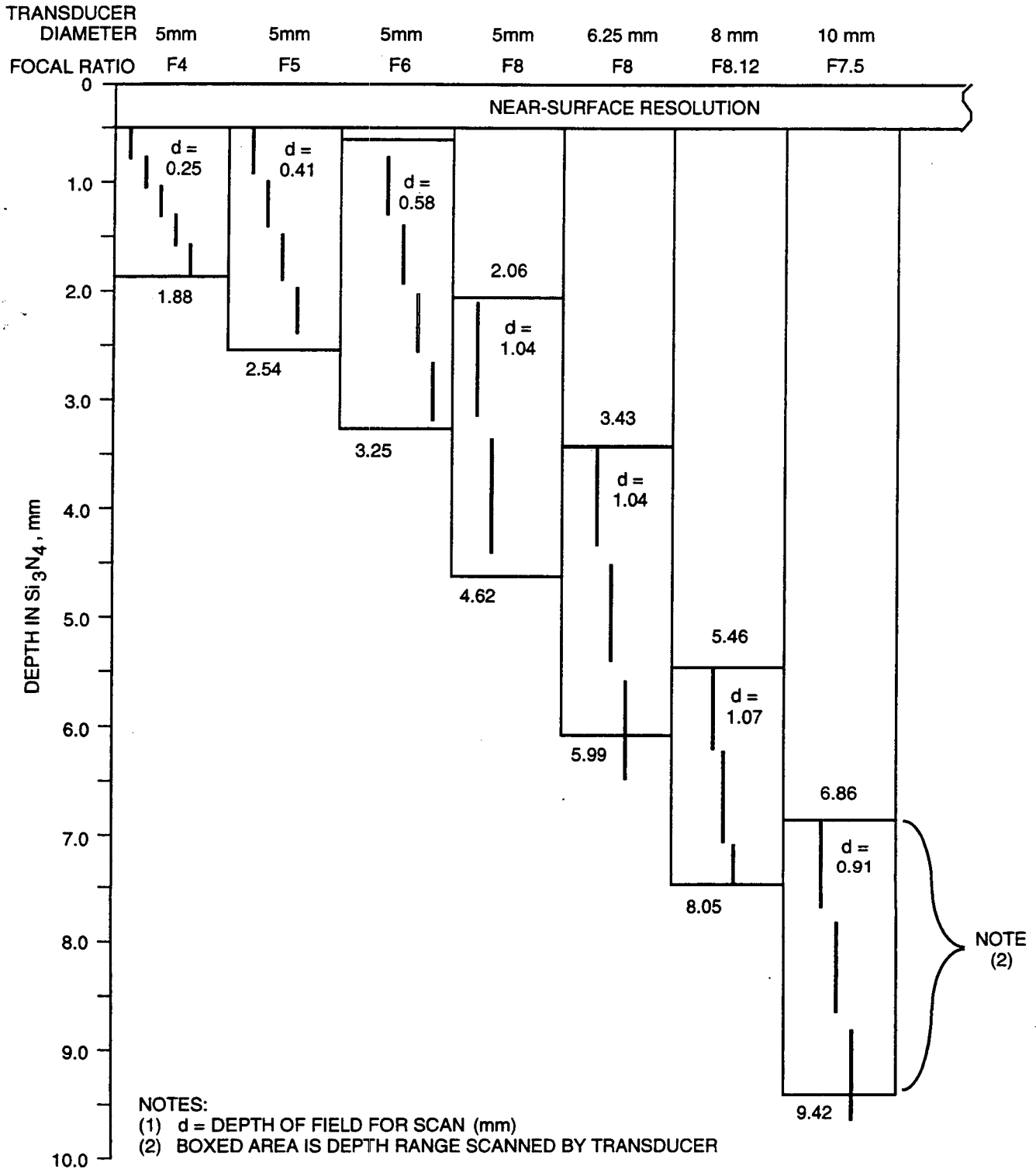
6.3.1 Acoustic Microscopy Development And Calibration

Transducer selection and design for acoustic microscopy (AM) was initially based on estimates of a 25 to 50 μm critical flaw size for Si_3N_4 . Based on this critical flaw size, a desired goal of 25 μm was established as the minimum detectable flaw size. Calculations by Dr. R. Gilmore at the General Electric Corporate Research and Development Center (GE-CRDC) predicted that the 25 μm flaw size could theoretically be detected using 50 MHz focused transducers. Based on these calculations, a series of transducers were selected and ordered. Figure 6-6 identifies the commercial transducers selected and graphically presents the limits of the inspection zones to the -3 dB depth of field for each transducer. In addition to these transducers, a limited number of 75 and 100 MHz transducers was evaluated to compare the increased sensitivity achievable at higher frequencies.

Transducer selection was limited to transducers with a maximum focal number of F:8 [focal length (F)/element diameter (d)] which produces a -3 dB depth of field of 1 mm and a -3 dB focal spot size of 0.25 μm . Water paths were evaluated and limited to between 0.6 and 12 mm to preserve the high-frequency components of the ultrasonic wave and prevent superimposing the material interface signal onto the initial pulse.

Evaluation of the transducers shown in Figure 6-6 for flat entry surfaces produced mixed results. The goal of 25 μm detection was not achieved for all depths required for component inspection, for two reasons: the water path had a much greater effect on inspection sensitivity than originally anticipated; and the inspection sensitivity degraded unexpectedly in the 0.2 to 2.5 mm material thickness range.

Additional inspections were added to improve the near-surface sensitivity. However, for the deep inspections, 50 MHz, F:8 long-focal-length transducers were not available to improve the inspection. For the deep inspections, lower sensitivity inspections were performed by inspecting beyond the focal zone of existing transducers. A nominal 50 mm void detection was achieved for the deep scans. Figure 6-7 shows typical scans of a calibration standard. The figure also shows typical indications detected in some of the specimens with similar amplitude to the 50 mm detection threshold.



GC11591-606A

Figure 6-6. Commercial Transducers Provided Full Inspection Coverage For Flat Specimens.

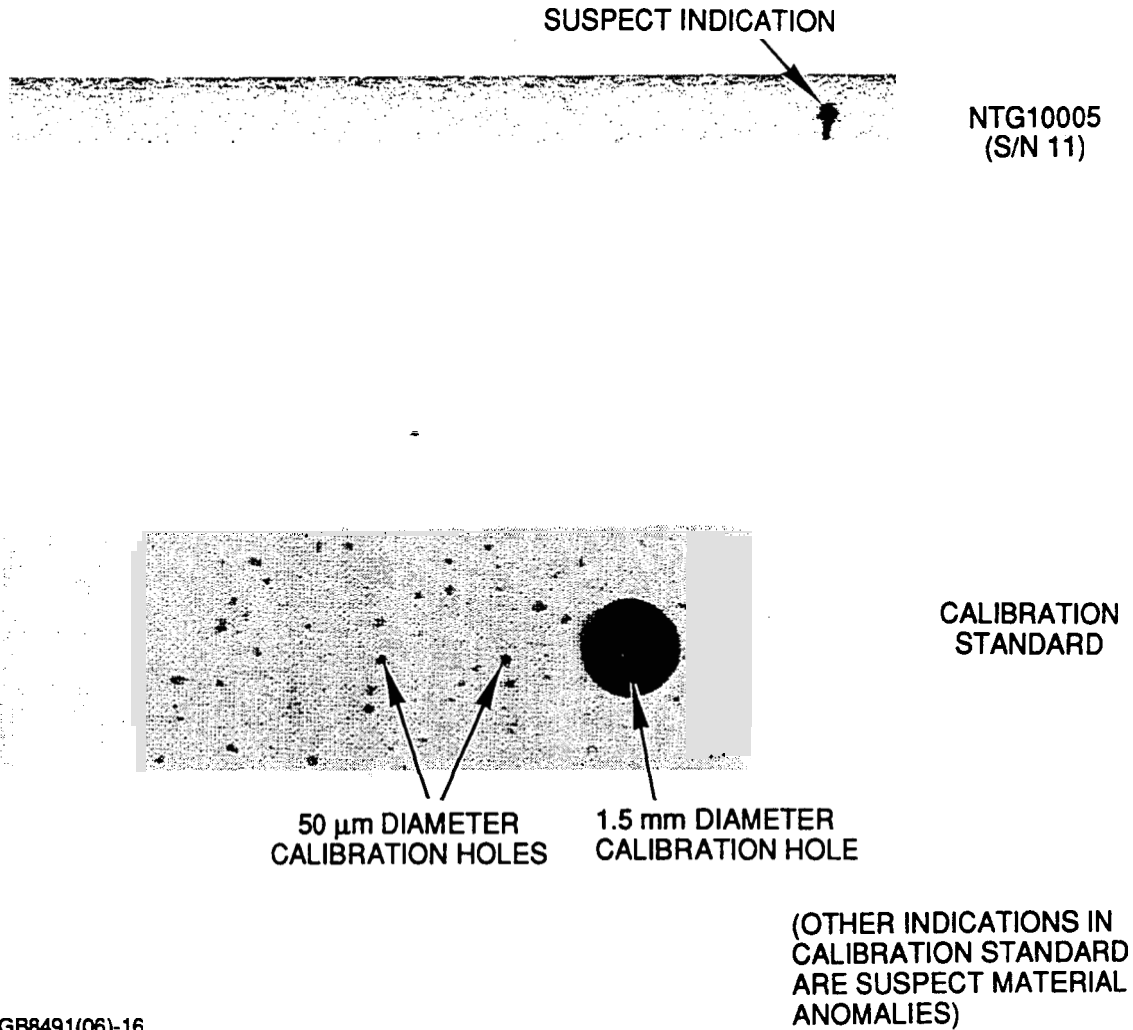


Figure 6-7. Acoustic Microscopy Calibration Verified 50 Micron Detection Capability.

To maintain uniform inspection sensitivity throughout the inspection volume of small-diameter cylindrical geometries (less than 3 mm diameter), a compound curvature lens was designed for subsurface inspection for both polymer and piezoelectric buffer rod transducers. The polymer design did not yield the desired 50 MHz signal in the reference standard and had very low energy output. Discussions with several transducer manufacturers indicated the piezoelectric element/buffer rod designs presented significant fabrication difficulties and were long-lead-time, high-risk efforts. No quotes were received for these designs. As a result, a simple focus transducer was used to inspect the 3-mm-diameter round reference standards.

The ultrasonic beam integrity could not be maintained at the surface, due to the defocusing effects of the entry surface radius of curvature, and sensitivity was degraded to an estimated 200 μm or greater flaw size. Due to these results, AM volumetric inspection of the gage section of tensile specimens was abandoned.

Successful design and fabrication in this program of an embedded USAF 1951 Resolution Target allowed the determination of resolution as a function of depth. The largest element in the target used is Group Zero, starting with a 1 mm line-space pair (each 0.5 mm wide); the line pairs decrease in size in six equal steps until the spacing of Group One is reached. The largest Group One element contains two line-space pairs per mm while the line-pair spacing of the first element in Group n is 2^n .

The -3dB diameter, ϵ_{x1} , produced by a circular lens of diameter d focusing a pulse of wavelength λ at a distance F has been shown to be (ref 6-3):

$$\epsilon_{x1} = 1.03\lambda(F / d) \quad [6-1]$$

Provided that the refracted angle is less than 30 degrees of arc, the corresponding -3dB depth of focus, ϵ_{x2} , is:

$$\epsilon_{x2} = 4.00\lambda(F / d)^2 \quad [6-2]$$

Using these equations, the beam diameters for several transducers were calculated and are given in Table 6-2.

TABLE 6-2. TRANSDUCER BEAM DIAMETERS AND VOID DETECTION CAPABILITY

Transducer Frequency, MHz	F: No., F/d	-3dB Beam Diameter, mm	Void Diameter, mm
100	F:4	0.060	0.015
75	F:4	0.080	0.020
50	F:3	0.100	0.025
50	F:4	0.125	0.030
50	F:6	0.175	0.045
50	F:8	0.200	0.050
25	F:8	0.400	0.125

The ability of an acoustic beam to detect a void and to resolve and/or image the void are different. For low-noise materials in the vicinity of the near-field limit of an unfocused transducer, or when focused in the focal zone, voids can be detected that have a diameter equal to 25 percent of the wavelength or the beam diameter, whichever is smaller. The longitudinal velocity in both sapphire and silicon nitride is 11.2 mm/msec and therefore the wavelength at 50 MHz is 0.22 mm. A 1/4-wavelength void is therefore 56 μ m in size. Table 6-2 shows that the detection capability can be improved significantly below 1/4-wave by focusing the beam.

The resolution inherent in a raster-scanned image is controlled by:

- The diameter of the scanned beam
- The spacing of the scan lines
- The acoustic pulse spacing along the scan line.

The line-pulse spacing determines the pixel size making up the image. Nyquist's theorem states that the minimum spatial resolution of a two-dimensional (2-D) array of points is twice the point spacing. Therefore, the spatial resolution of the beam is twice its -3 dB diameter because the point spacing in the image acquisition is the interrogating beam. In order to support the -3dB diameters listed in Table 6-2, these beams must be scanned at less than half of the beam diameter. The beam, however, cannot resolve objects closer than twice the beam diameter, as demonstrated in the AM resolution target image at a depth of 2 mm shown in Figure 6-8. Table 6-3 lists the minimum resolution (line-pairs) for the transducers selected for specimen inspections in this program.

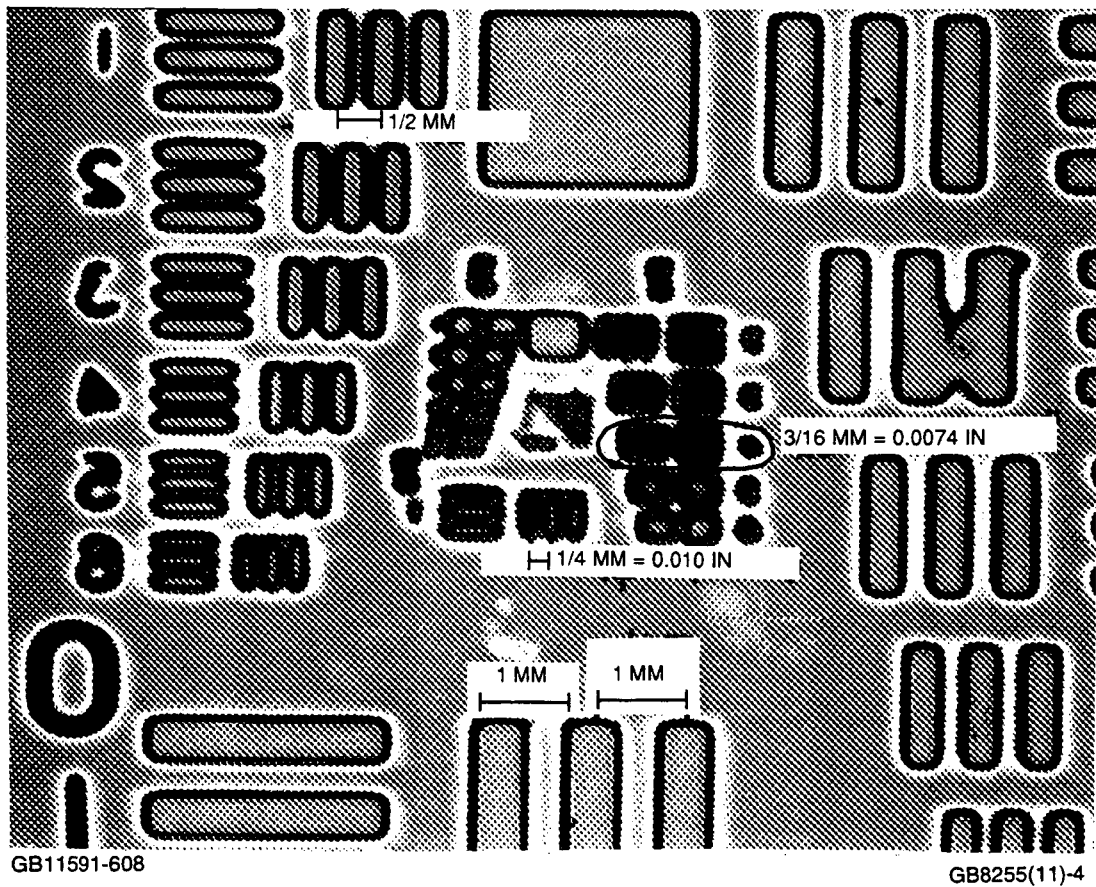


Figure 6-8. Resolution Standard Used To Verify Theoretical Resolution Limits In Acoustic Microscopy.

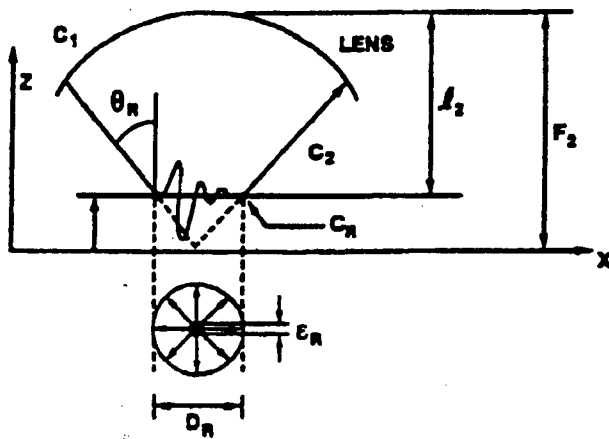
TABLE 6-3. RESOLUTION VARIATION IS A FUNCTION OF FREQUENCY, F: NUMBER, AND SCANNING PARAMETERS. (MATERIAL PATH = 2 mm)

Transducer Frequency, MHz	F: No., F/d	Minimum Resolvable Line Pairs/mm
100	F:2	7.13
100	F:4	6.35
75	F:2	5.66
50	F:2	5.04
50	F:3	5.04
50	F:4	4.00
50	F:8	4.00

Surface wave inspection results exceeded the 25 μm detection goal, once a water jet was added to the transducer to prevent particles and air bubbles from settling on the specimen. Surface-wave AM included the evaluation of both unidirectional and converging surface waves for flat entry surfaces with varying machined finishes. The unidirectional surface wave was achieved using the conventional approach of launching the ultrasonic beam at the critical angle to convert the incident beam into a surface wave.

The unidirectional surface wave has, in general, higher amplitude than the converging surface wave approach. The drawback to this approach is that this inspection is sensitive to the defect orientation. Defects parallel to the direction of the surface wave are difficult to detect, while those perpendicular to the defect are more easily detectable. Therefore, to maintain the same ultrasonic sensitivity, surface wave scans must be performed from multiple directions. After evaluating the effect of machining lines on the surface wave signal, all surface wave inspections were performed parallel to the machining direction, due to the additional noise caused when scanning at any other angle to the machining lines.

Converging surface wave inspection can be achieved for high refractive index materials by using a very short focal length transducer focused slightly below the surface. In this case, the lens on the transducer effectively launches ultrasonic waves into the material at varying angles. The ultrasound from the outer area of the element is at the critical angle for surface wave conversion and the surface wave is launched in all directions, converging at the center for the circular aperture for flat entry surfaces, as shown in Figure 6-9. For a typical machined surface (20 μinch surface finish), 12 μm diameter detection (minimum depth of 5 μm) was achieved using the unidirectional surface wave approach; however, at this inspection sensitivity, some surface features had amplitudes equal to the reference reflector, making interpretation of the images challenging. Comparison of the unidirectional and converging surface wave inspections on typical component surface finishes showed the signal-to-noise ratio was unacceptable for the converging surface wave and degraded the inspection sensitivity for near-surface defects. Unidirectional surface wave scanning was selected for the actual test specimens. For surface wave inspection, the 75 MHz unidirectional surface wave had the best sensitivity and highest signal-to-noise ratio.



D_R	$= 2Z \tan \theta_R$	D_R	= Diameter of entry circle produced by the intersection of the Rayleigh critical angle cone with the entry surface.
	$= 2 [F_2 - l_2] \tan \theta_R$	λ_R	= Wavelength of the Rayleigh wave on the entry surface.
λ_R	= SW WAVELENGTH	C_R	= Velocity of the Rayleigh wave on the entry surface.
C_R	= SW VELOCITY	ϵ_R	= -3 dB diameter of the amplitude maximum caused by the convergence of the Rayleigh wave at the center of the Rayleigh entry circle. Defines 1 shade of gray or resolution produced by the beam convergence.
ϵ_R	$\left \begin{array}{l} = 0.32 \lambda_R \\ -3dB \end{array} \right.$	ϵ_R	= -1dB diameter of the amplitude maximum described above. Used to specify the pixel size/spacing for the image.
ϵ_R	$\left \begin{array}{l} = 0.15 \lambda_R \\ -1dB \end{array} \right.$	ϵ_{RZ}	= -3 dB sensitivity drop of a broadband Rayleigh wave (less than 2 wave pulse length) beneath the surface of propagation.
ϵ_{RZ}	$\left \begin{array}{l} = \lambda_R \\ -3dB \end{array} \right.$		

GC11591-609

Figure 6-9. Surface Wave Propagation Is Achieved At The Outer Diameter When The Ultrasonic Beam Is At The Critical Angle For Surface Wave Mode Conversion. [Figure After Gilmore, et al. (Ref. 6-3)]

6.3.2 Computed Tomography (CT) Development

Computed tomography (CT) parameter selection involved developing standards to allow evaluation of system performance, varying key system parameters, measuring the system response, and selecting the combination of parameters that provided the best results. The following variables were evaluated:

- Tube voltage (420, 320, or 220 kV)
- Views-per-image (1500 or 3000)
- Integrations (4 or 8)
- Detector Pressure (1000, 800, or 600 psi)
- Detector collimator size (0.25 or 0.13 mm)

Table 6-4 summarizes selected CT parameter test data and illustrates the effect of the different parameters on detectability and resolution. The CT parameters which provided the best imaging results were:

- Tube voltage = 320 or 220 kV
- Views-per-image = 3000
- Integrations = 4
- Detector pressure = 900 psi
- Detector collimator = 0.25 mm

TABLE 6-4. CT PARAMETER OPTIMIZATION EVALUATED KEY VARIABLES

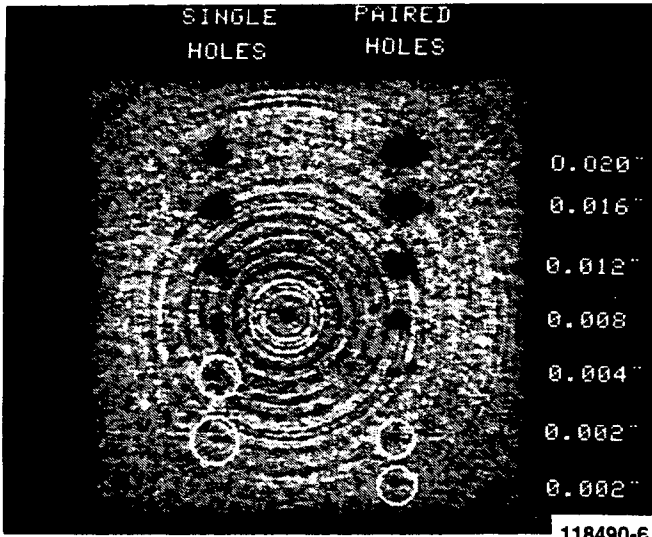
Test	Detector Pressure, psi	Collimator Size, mm	Tube Voltage, kV	No. Views	No. Integrations	Results
A	1000	0.250	420	1500	4	0.20 mm
B	1000	0.250	320	1500	4	0.10F*
C	1000	0.250	220	1500	4	0.10F
D	1000	0.250	320	1500	8	0.10
E	1000	0.250	320	3000	4	0.05F
F	1000	0.125	320	1500	8	0.10F
G	900	0.250	320	3000	4	0.05
H	900	0.125	320	3000	4	0.20
I	800	0.250	320	3000	4	0.05F
J	800	0.125	320	3000	4	0.20
K	600	0.125	320	3000	4	0.10F

*Indicates the hole was seen on the image but was a faint indication.

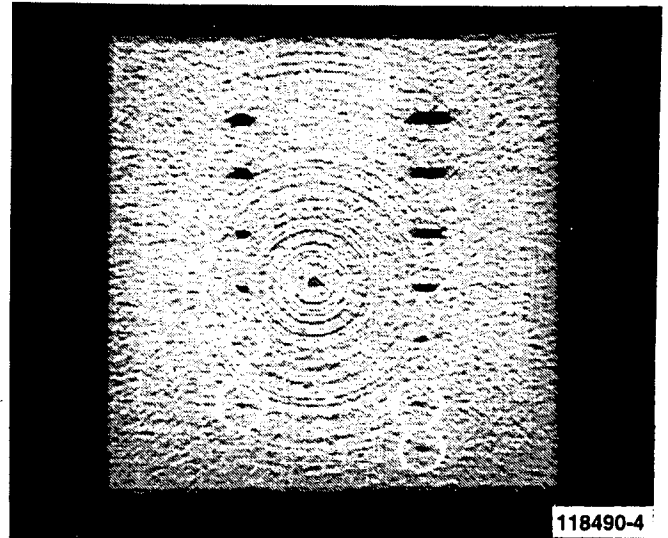
Digital high-pass and low-pass filtering was also performed on those images which displayed good detectability (Figures 6-10(a) through (d)). In some cases, the filtering helped smooth out the image and decrease the system noise. Although image viewing was easier, the system detectability was not increased. The inspections used both filtered and non-filtered images.

Figures 6-10(a) and (c) show how ring artifacts contributed significantly to the image noise. These artifacts made it difficult to pick out the smaller defects. Although these artifacts could be reduced by cleaning the detector array to eliminate uncharacterized variations between detector elements, they were not eliminated entirely. Since most of the samples inspected were small in cross-sectional area, they were fixtured away from the center of rotation of the system to avoid most of the ring artifacts. For the larger samples, the specimens were imaged twice and the specimen was moved between scans to adequately inspect the entire cross section. Additionally, digital filtering was used to reduce the effect of the ring artifacts.

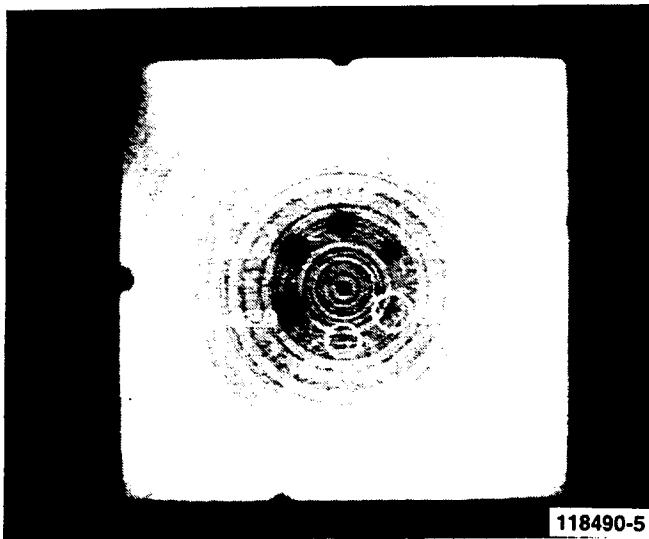
A CT study was conducted to determine whether the resolution varied toward the outside of the reconstruction area. The detection standard was imaged in multiple locations to duplicate the conditions of the center and outside diameter of the largest specimen in the test matrix (spin disk). The smallest hole diameter visible in the center and the outside reconstruction was 0.20 mm; however, the 0.20 mm hole was more difficult to see toward the outside of the reconstruction, because the image noise was higher. This implied defects toward the outside of the reconstruction area were more likely to be masked by the noise.



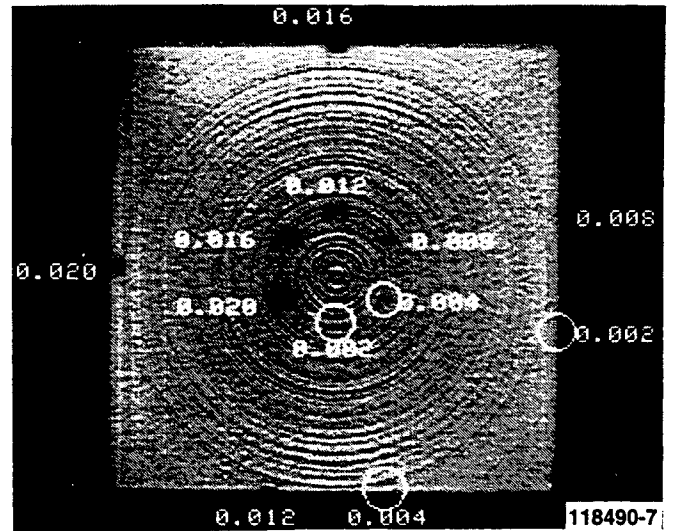
(A)
RAW IMAGE -
CT RESOLUTION
GAGE



(B)
FILTERED IMAGE -
CT RESOLUTION
GAGE



(C)
RAW IMAGE -
CT DETECTION
GAGE



(D)
FILTERED IMAGE -
CT DETECTION
GAGE

GB11591-610

Figure 6-10. Filtering The CT Images Improved Quality.

6.3.3 Radiographic Inspection And Film Enhancement Development

Digital image enhancement of film radiographs acquired using microfocus film radiography can provide additional information about material anomalies not visible during visual evaluation of the radiographic films. Development efforts for radiographic inspection and enhancement centered on three areas:

- Selection of optimum radiographic exposure parameters
- Development of digitization techniques
- Development of digital enhancement/filtering techniques for improved defect detection.

The first area, evaluation of exposure parameters, involved comparing film types, projection techniques, and exposure energies. The second area, development of digitization techniques, centered on evaluation of 8-bit and 14-bit digitization systems. The third area was to identify and assess the effectiveness of various filtering/enhancement routines.

6.3.3.1 Selection Of Optimum Radiographic Exposure Parameters

In an effort to determine optimum radiographic inspection parameters for ceramic component inspection, digital evaluation was used to compare variations in different exposure parameters. Parameters evaluated included film types, comparison of projection techniques, and comparison of X-ray energy levels.

Film type variation was evaluated measuring the average gray scale level (GSL) variation of the film, and noting the change in GSL at the location of an imaged defect. The film types evaluated were Dupont NDT55, NDT45, NDT30, and AGFA D2. These films were chosen because they represented variations in both grain size and film speed and were characteristic of films typically used in industrial radiography of aerospace components. Little average GSL variation was detected between the different film types, even though a change in the grain size was visually apparent on the images. On the basis of the fact that slower films yield better contrast, and that the apparent grain size of the faster films approached the desired defect detection limit, Dupont NDT30 and AGFA D2 fine grain films were selected for specimen inspection.

In order to detect small flaws, low-energy (high-contrast) radiography is required. The drawback of low-energy radiography is that reducing the X-ray exposure energies (lower voltage setting) decreases the penetrating ability of the rays, increasing exposure time and causing an increase in the amount of scattered radiation. In order to determine the optimum voltage setting for the best exposure, films of seeded defect specimens exposed at 60 kV and 110 kV were compared, noting the GSL differences on a 2-percent

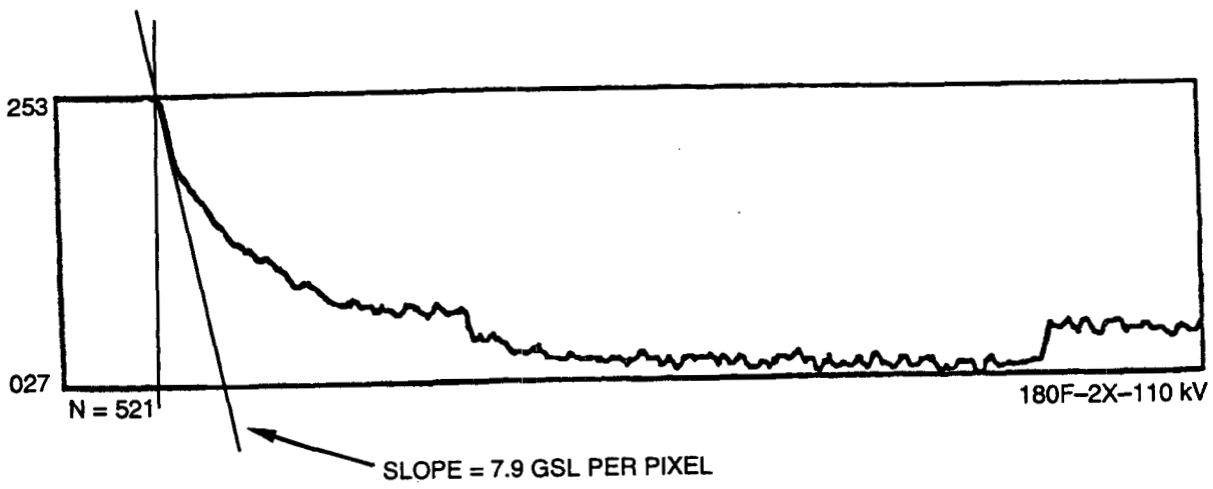
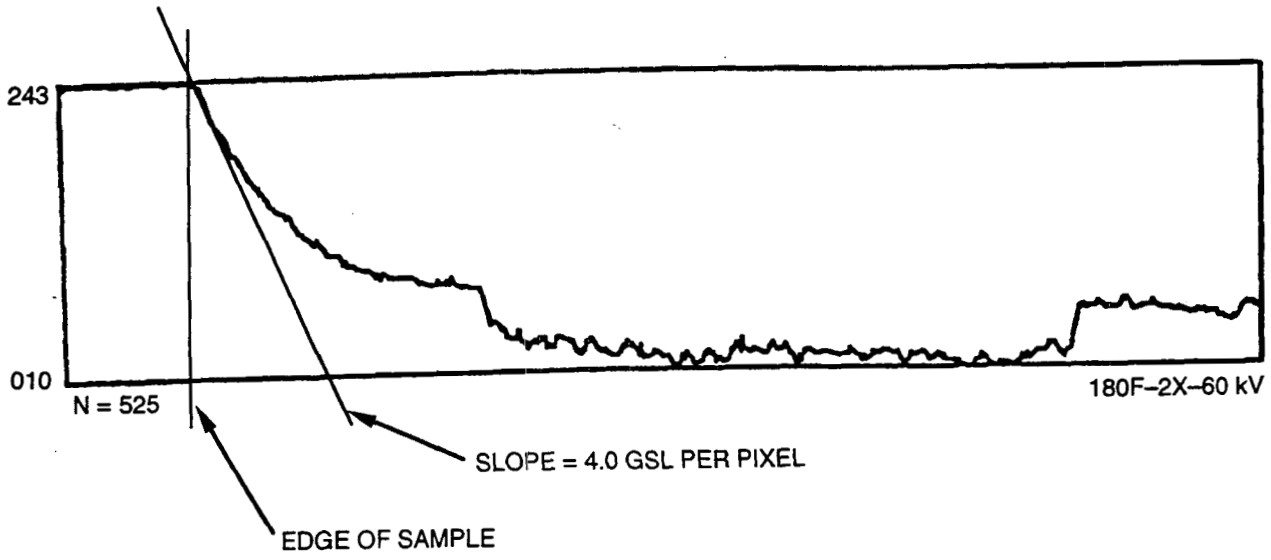
penetrameter step, and also at the location of seeded iron defects. The test results indicated that the average signal-to-noise ratio at the penetrameter step for the 60 kV exposures was nearly twice that observed at 110 kV (3.07 versus 1.75). However, at the locations of the seeded iron defects, the signal-to-noise ratio was nearly identical, 2.00 on average at 60 kV, and 1.96 on average at 110 kV (see Table 6-5).

TABLE 6-5. COMPARISON OF CT EXPOSURES USING PENETRAMETER EDGE VERSUS GRAIN NOISE VALUES IN GRAY SCALE LEVELS

Sample Enlargement	315G 2X	315G 3X	180F 2X	180F 3X	Average
110KV					
Penetrameter step	29.0	34.5	35.0	27.8	31.6
Grain "noise"	18.3	24.2	19.1	10.5	18.0
Ratio step/noise	1.59	1.42	1.83	2.64	1.75
60 KV					
Penetrameter step	42.8	35.7	43.1	53.9	43.9
Grain "noise"	14.0	12.5	11.7	19.1	14.3
Ratio step/noise	3.06	2.86	3.68	2.82	3.07

Gray scale level (GSL) line scans for the two voltage settings, 60 and 110 kV, respectively, were acquired at a sharp edge of the specimen image and the slope of the GSL line scans were compared for the different exposure voltages. The slope of the GSL line was half as great for the 60 kV exposure, indicating reduced image sharpness (see Figure 6-11). This decrease in the image sharpness was probably due to the increased scatter at the lower exposure energy. Visually, both images appeared to be equally sharp. While there is not a clear advantage of one exposure voltage over the other, the lower voltage setting was selected, due to the better contrast of low-density (void-like) defects without visual degradation in the image sharpness.

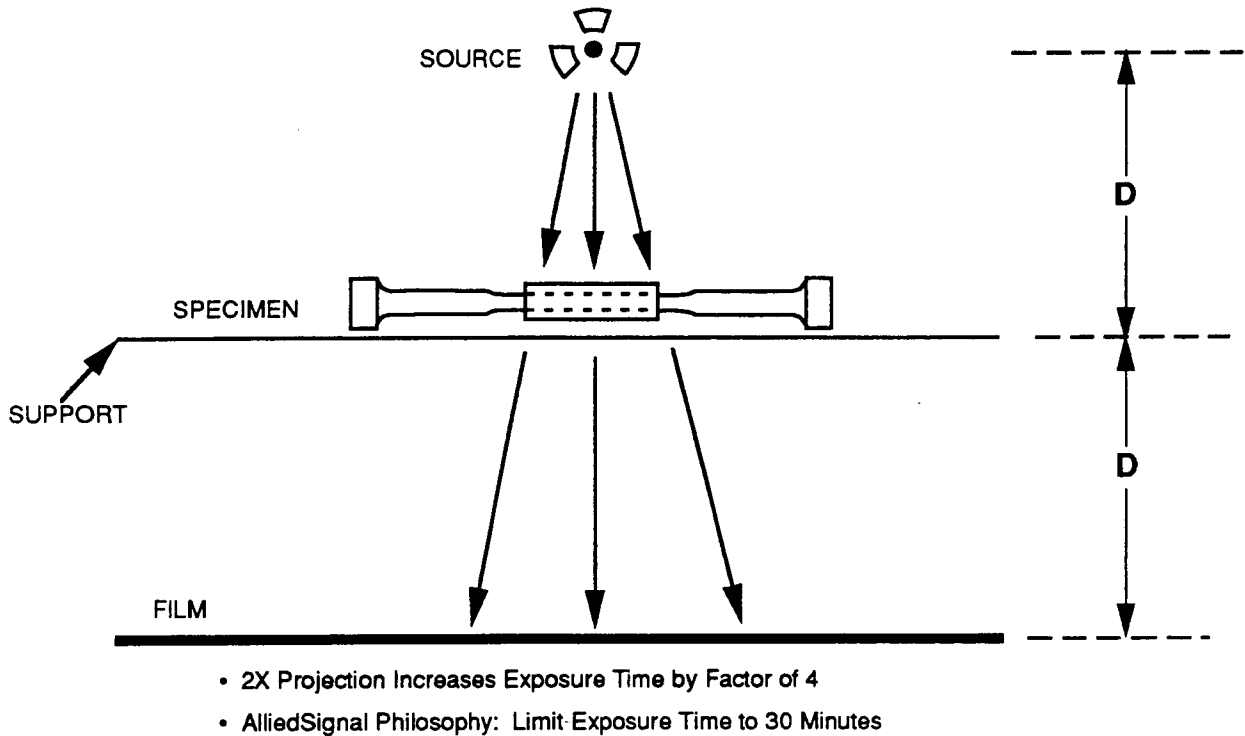
To be imaged using radiography, a defect must cast a shadow on a minimum number of film grains; so for imaging of small flaws, a projection radiography technique (see Figure 6-12) was used. By varying the source-to-object and source-to-film distances, different exposure magnifications were obtained. Projection radiography is limited in its usefulness to relatively low magnifications, as the intensity of radiation impinging on the film is inversely proportional to the square of the distance from the radiation source, consequently quadrupling the exposure time with each doubling of the source-to-film distance. Additionally, the geometric unsharpness of an image increases as the object-to-film distance increases, also limiting the usefulness of this technique.



GC11591-611A

Figure 6-11. Grey Scale Line Scans Show Reduced Noise (Less Variation) For 60 kV Voltage Setting.

Projection Radiography Setup



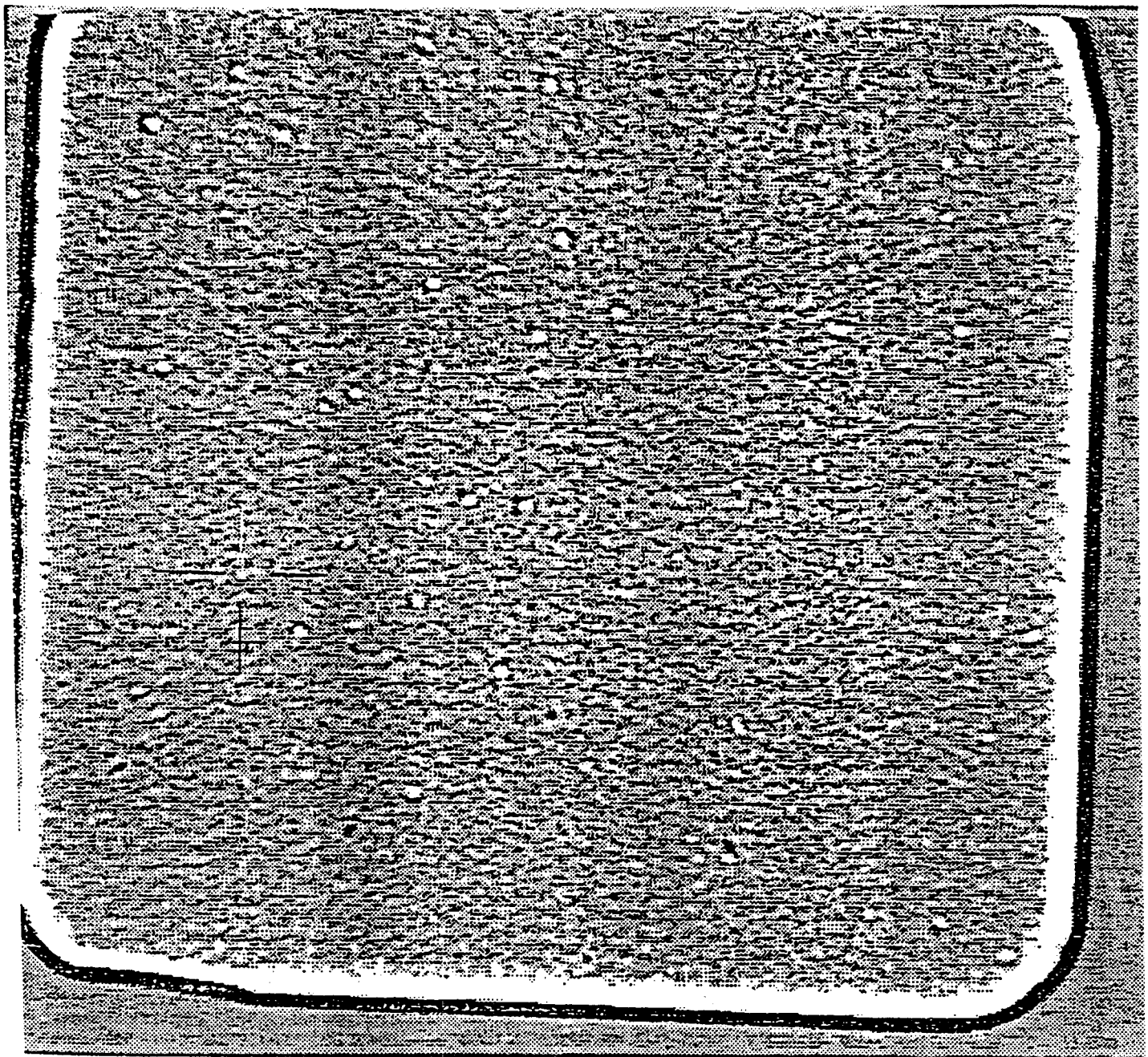
GC11591-612

Figure 6-12. Magnification Attained Through Projection Radiography Is Limited By Exposure Time.

Radiographs were compared with projection image ratios varying from 1X to 3X magnification. This comparison was more subjective than quantitative, as selecting appropriate parameters for measurement was difficult on seeded defect images and penetrameters. An increase in the number of observable defects was noted between 1X and 2X images, as shown in Figures 6-13 and 6-14; however, little improvement in observable defects was noted between 2X and 3X images, yet a significant penalty in exposure time was required. The 2X projection image was selected as the best compromise for specimen inspection.

6.3.3.2 Development Of Digitization Techniques

At the onset of this program, film digitization and enhancement was planned using an IBM PC-based system. However, shortly into the program, a 10-bit (8-bit image resolution) Macintosh-based enhancement system was selected, because the imaging software available for the Macintosh at that time was more powerful than that available for PC (DOS)-based systems. Later in the program, a 14-bit (12-bit image resolution) camera was made available and used in combination with UNIX-based software on a workstation to add further capabilities to the enhancement work. The decision to switch from a 10-bit to the 14-bit system was based on

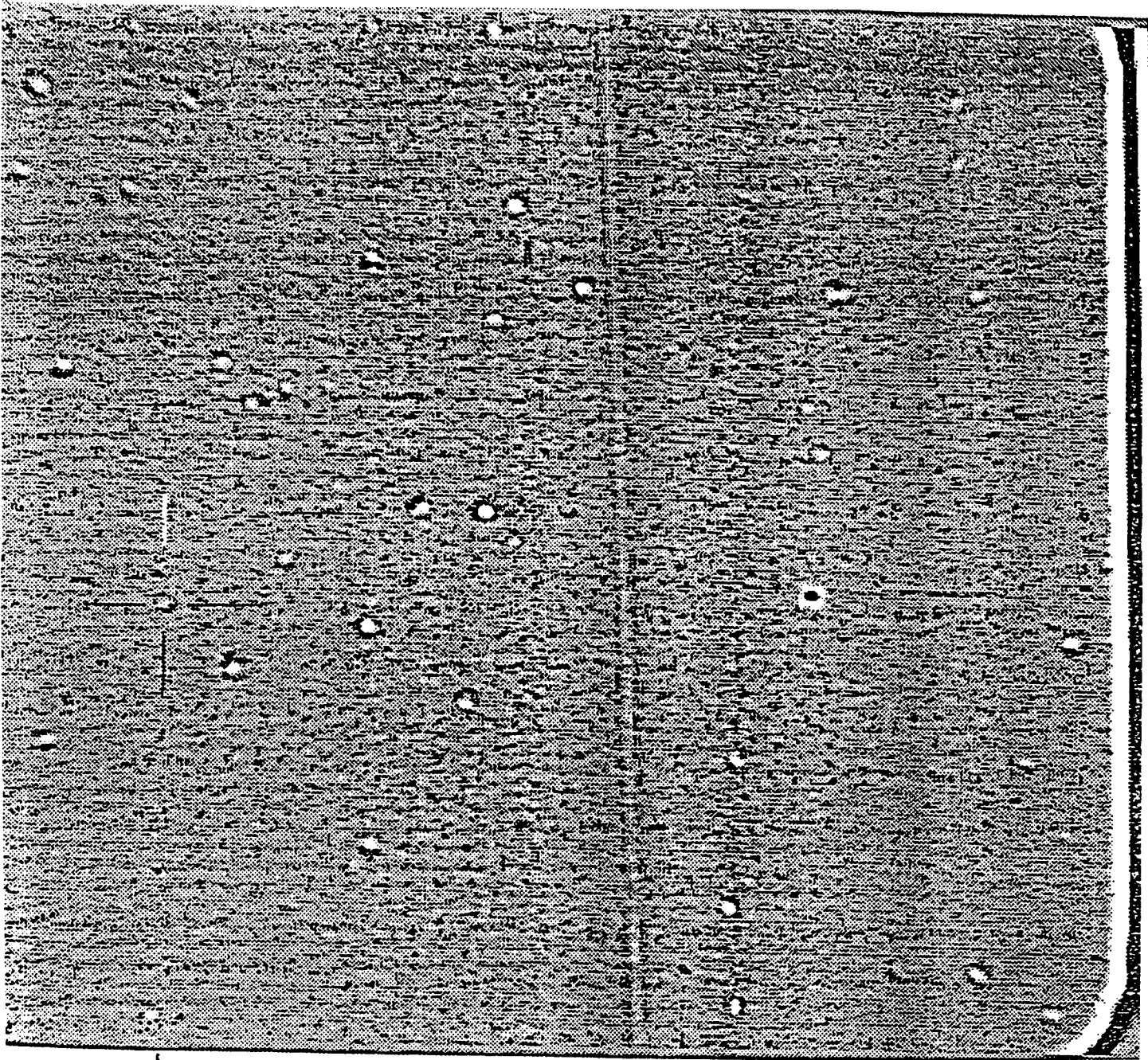


↑
A

Sample: 129180F-M1
Enlargement: 1X
Film: Agfa D2

GB11591-613

Figure 6-13. Projection Radiographic Image At 1X Enlargement Of Seeded Iron Defects.



↑
A

Sample: 129180F-M1
Enlargement: 2X
Film: Agfa D2

GB11591-614

Figure 6-14. Projection Radiographic Image At 2X Enlargement Improves Visual Detection Of Some Iron Defects.

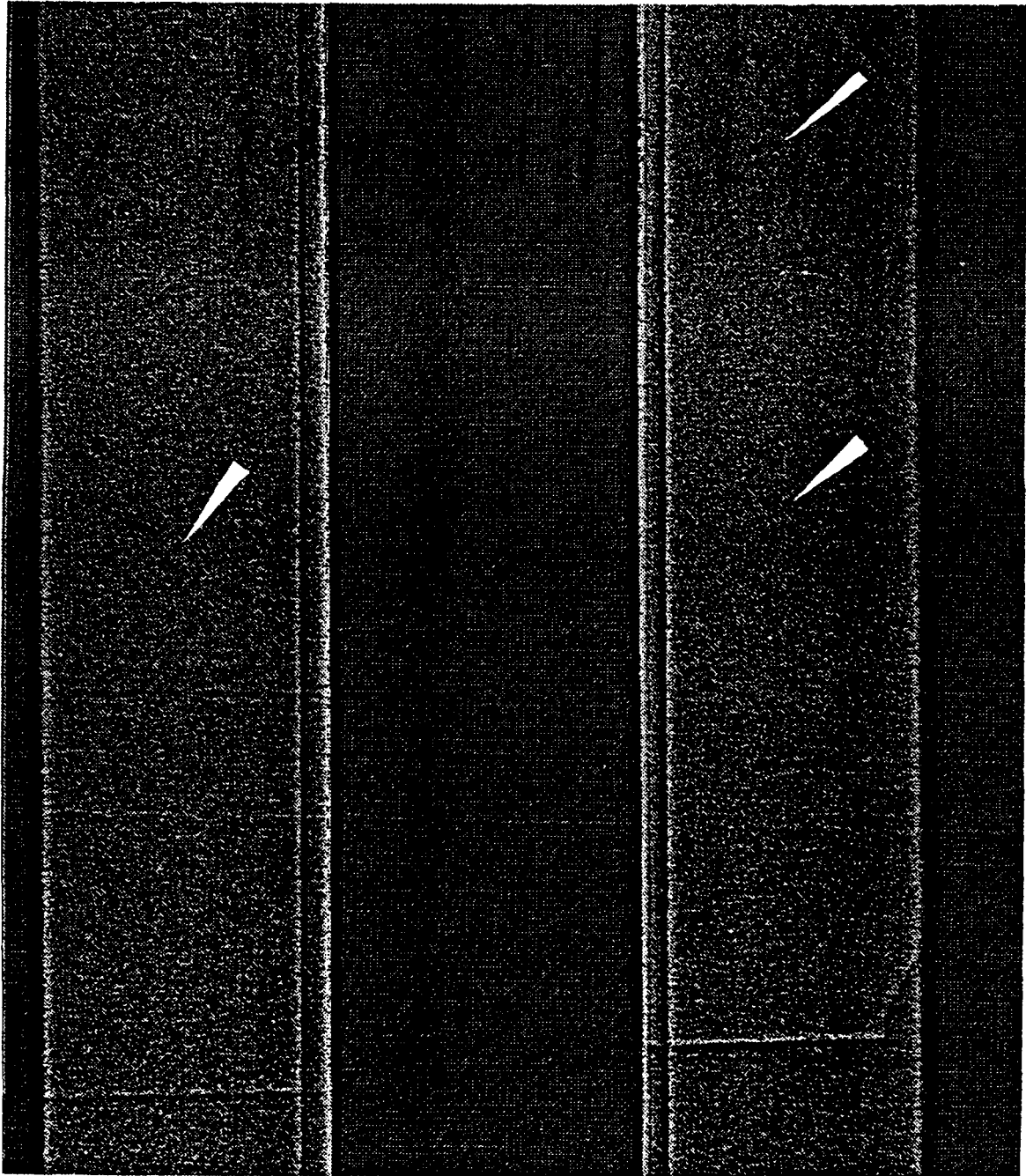
comparisons of the systems along with the recommendations outlined in a report issued by the Nuclear Regulatory Commission in May 1992 regarding the digitization of radiographic films. (ref. 6-5)

The 8-bit digitization system consisted of a 512 x 512 pixel Charge Coupled Device (CCD) camera, an 8-bit frame grabber board and a Macintosh Model II FX computer. The image software was a public domain program, IMAGE, developed by the National Institutes of Health (NIH). The system was evaluated, and digital processing routines were optimized, using radiographic films of seeded defect specimens (available from another program) that contained both high and low material density defects. The defect types included iron to simulate high-density inclusions, polystyrene spheres to simulate pores, and pre-densified Si_3N_4 to simulate agglomerates.

One element of the enhancement effort was to determine the best filtering routine, or combination of routines, that would increase the probability of visually observing the seeded defects in the images. Of the various techniques available with the NIH IMAGE software, low-pass subtraction demonstrated the best results in enhancing the seeded defect images. This technique involved replacing each individual pixel in an image file with an average of the surrounding pixel array (either 3 x 3 or 5 x 5) and subtracting this averaged image pixel-by-pixel from the original. Low-pass subtraction was performed to enhance small details and edges while equalizing the background gray scale.

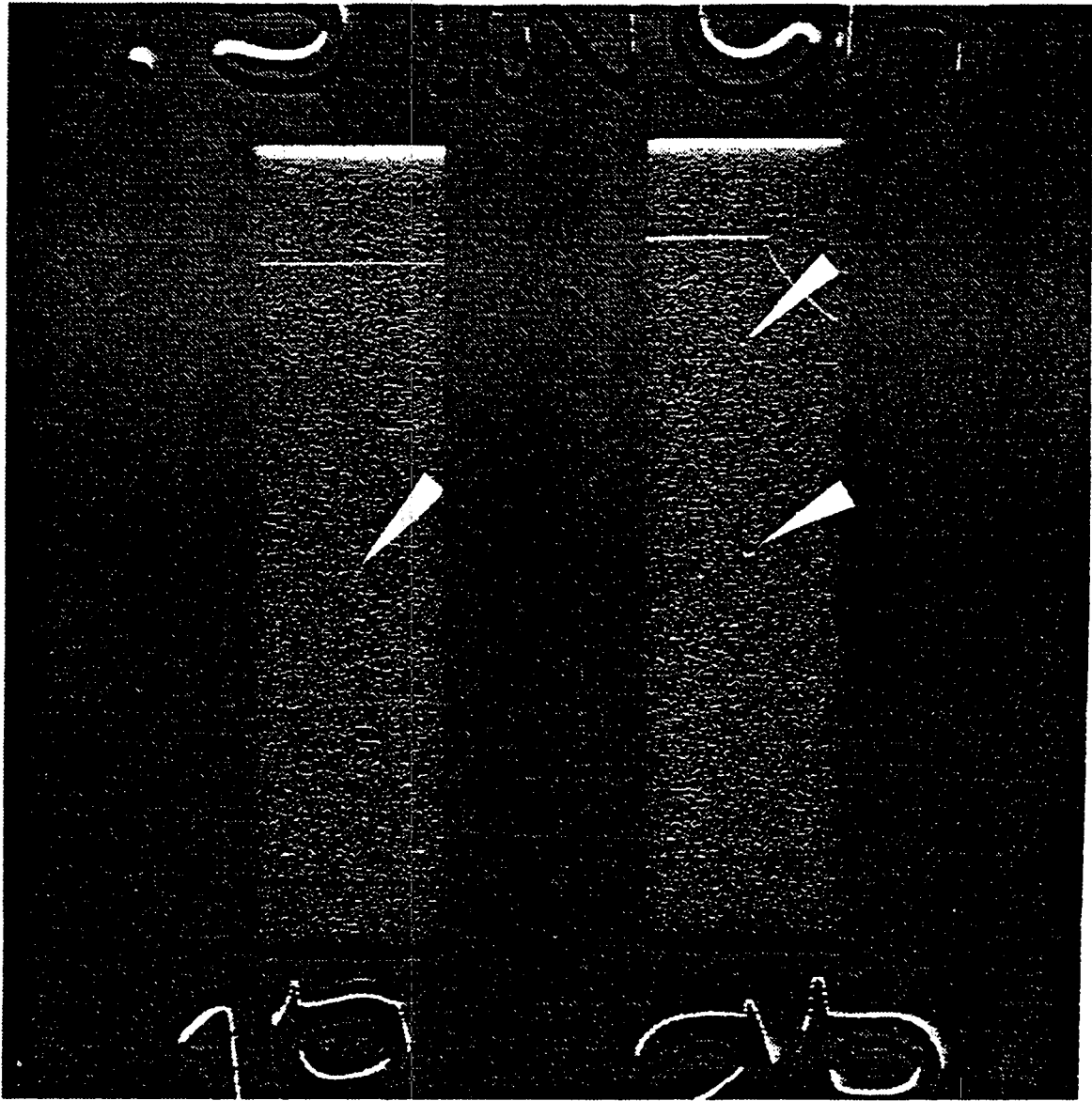
The 14-bit digitizer system included a Photometrics AT200 video camera with a 1024 x 1024 pixel CCD array, a special zoom lens, and a 14-bit digitizer board. The video camera was equipped with PMIS software for setting the camera parameters, as well as capturing and manipulating images. The advantage of the 14-bit digitization was lost if the images were converted to files acceptable by the NIH software, because the NIH software was designed for an 8-bit image. This problem was resolved by switching to the work station-based KHROS image processing software, a public domain program developed by the University of New Mexico. The KHROS software package was capable of handling the full 1024 x 1024 pixel image files from the 14-bit camera and also was capable of performing more powerful filtering routines than the NIH IMAGE program. An additional advantage that the 14-bit system had over the 8-bit predecessor was that the new system provided 16 times more gray scale levels (4096 vs. 256), thus allowing a more faithful reproduction of the original radiograph.

Several image filtering techniques were evaluated using the 14-bit system, including the low-pass subtraction routine found useful on the 8-bit system. Two other filtering techniques, the Laplacian filter and the Sobel filter, were found to provide improved image evaluation compared to the low-pass subtraction routine selected previously. The Laplacian filter reduced the lower spatial frequencies in the image, (generally attributable to noise), while the Sobel filter enhanced density gradients. The Sobel filter resulted in a shadowed or three-dimensional (3-D) appearance of the image (Figures 6-15 through 6-18), which gave the most visual improvement for image evaluation.



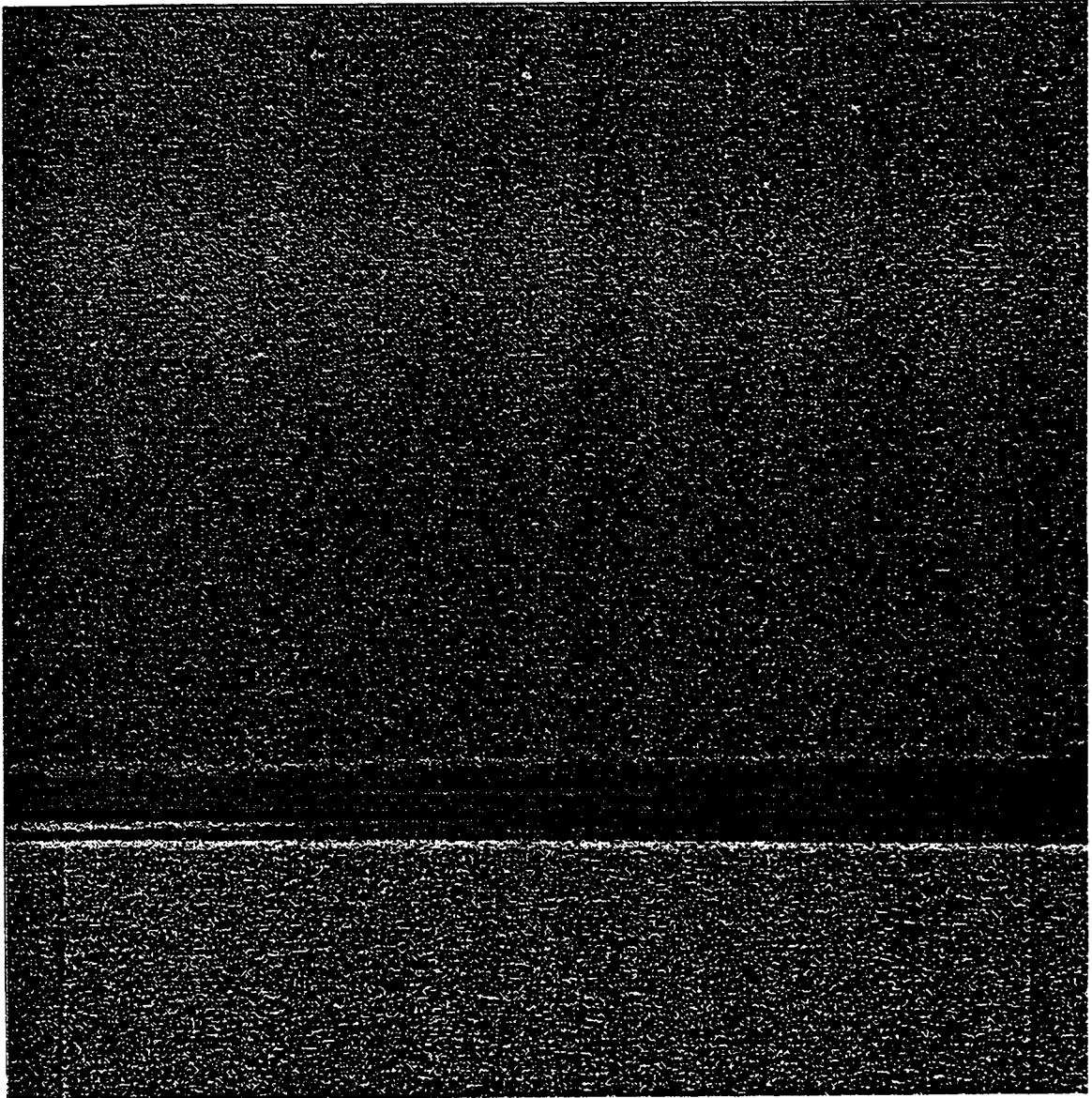
GB11591-615

Figure 6-15. LaPlacian Filtering Improves Visual Detectability Of Holes In Parameters.



GB11591-616

Figure 6-16. Sobel Filtering Improves Visual Detectability Of Holes In Penetrimeters.



GB11591-617

Figure 6-17. LaPlacian Filtered Image Of Seeded Iron Inclusions.



GB11591-618

Figure 6-18. Sobel Filtered Image Of Seeded Iron Inclusions Improves Visual Detection Slightly Over The LaPlacian Filtering.

6.4 Specimen Inspection

Based on the results of the NDE development effort, an inspection matrix for all test specimens was developed. The test matrix concentrated inspection coverage in the areas where specimens were expected to fail, in order to minimize the inspection time required for each specimen. For example, on the A- and B-size flexure specimens, failures are expected to occur primarily from the surfaces, so internal inspections of these specimens were minimized. The inspection matrix is shown in Table 6-6.

TABLE 6-6. INSPECTION MATRIX CONCENTRATED NDE COVERAGE IN THE AREAS WHERE SPECIMENS WERE EXPECTED TO FAIL

Specimen Type	Inspection Parameters		
	High Sensitivity/Resolution	Moderate Sensitivity	High Sensitivity
	Surface	Surface/Internal	Internal
A - Size flexure	Tensile surface only	All	--
B - Size flexure	Tensile surface and edges	All	1/2 volume
E - Size flexure	Tensile surface and edges	All	1/2 volume
Tensile/SR/creep	Gage section surface only	All	Entire gage section
Notched tensile	--	All	Notch only
Square tensile	--	All	--
Rectangular cross-section	Tensile surface only	All	--
Spin disk	Shaft fillet/backface transition	All	Hub area

Written procedures were established for each specimen and inspection method to provide uniform inspections between multiple inspectors. Initial AM inspections revealed surface conditions not observed in the NDE resolution standards. Some of the surface conditions were attributed to a lack of cleanliness, so special cleaning procedures were established immediately prior to the surface inspections to alleviate the problem. Other surface conditions appeared to result from deposits on the surface that could not be removed by rigorous cleaning and were possibly caused by unclean surfaces before the heat treatment cycle. The unusual surface conditions were more prevalent on the tensile specimens and spin disks than on other specimens.

Surface AM inspections revealed variations in the surface and near-surface conditions of the specimens; some variations correlated with visual indications, while others were not identified as atypical for the fabrication process during visual inspection. Figures 6-19 and 6-20 provide examples of the variations observed between a typical tensile specimen and a tensile specimen with transverse indications in the gage section. The transverse indications were prevalent on many tensile specimens.

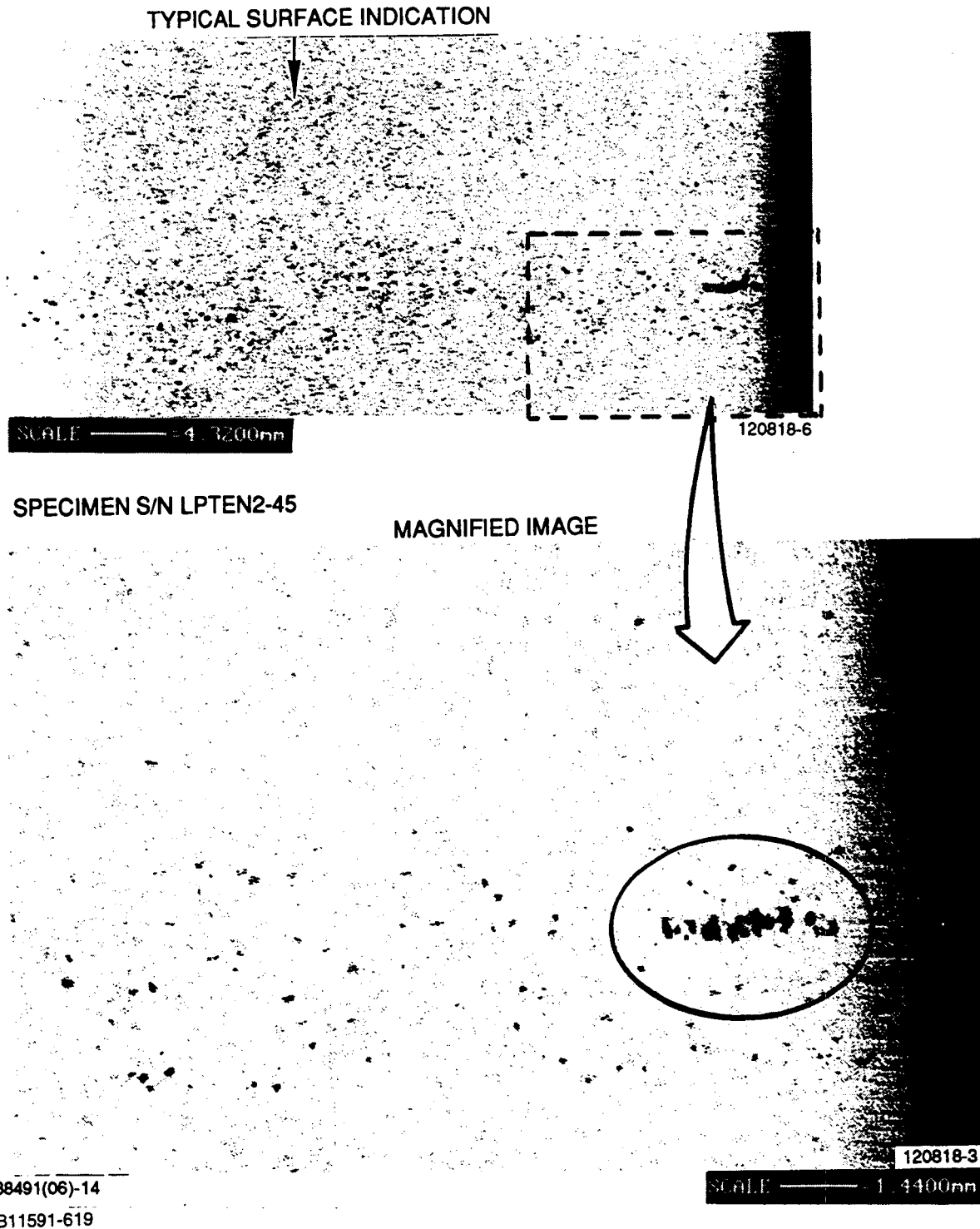
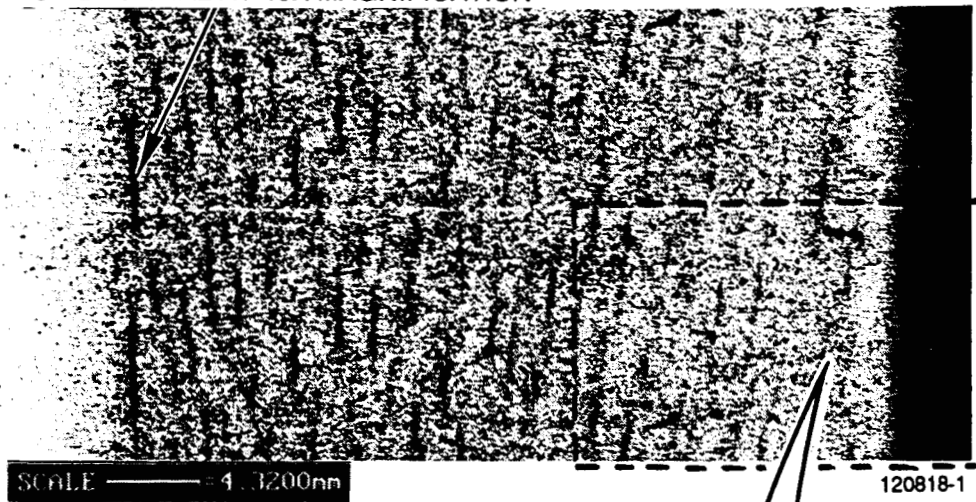


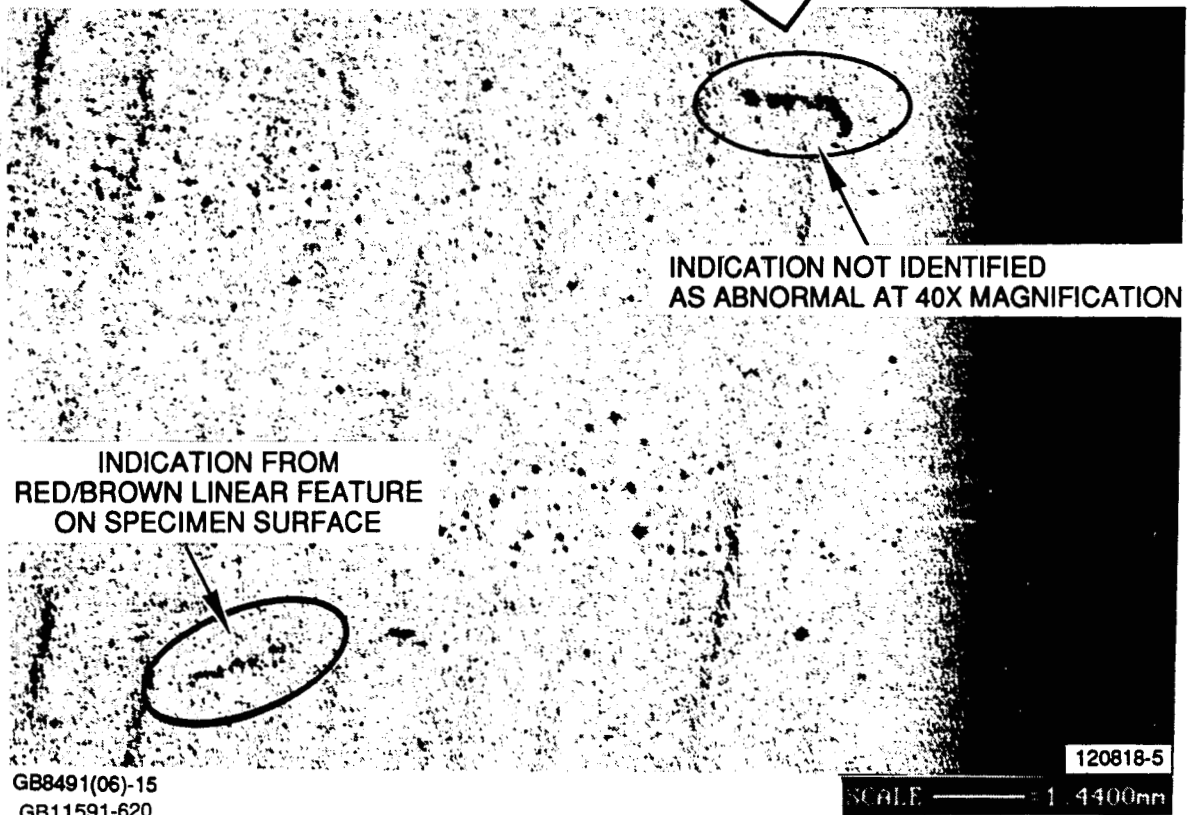
Figure 6-19. Acoustic Microscopy Indications Confirmed By Visual Inspection As Atypical Of The Machining Process Were Removed Prior To Testing.

TRANSVERSE LINES NOT IDENTIFIED
AS ABNORMAL AT 40X MAGNIFICATION



SPECIMEN S/N LPTEN2-69

MAGNIFIED IMAGE



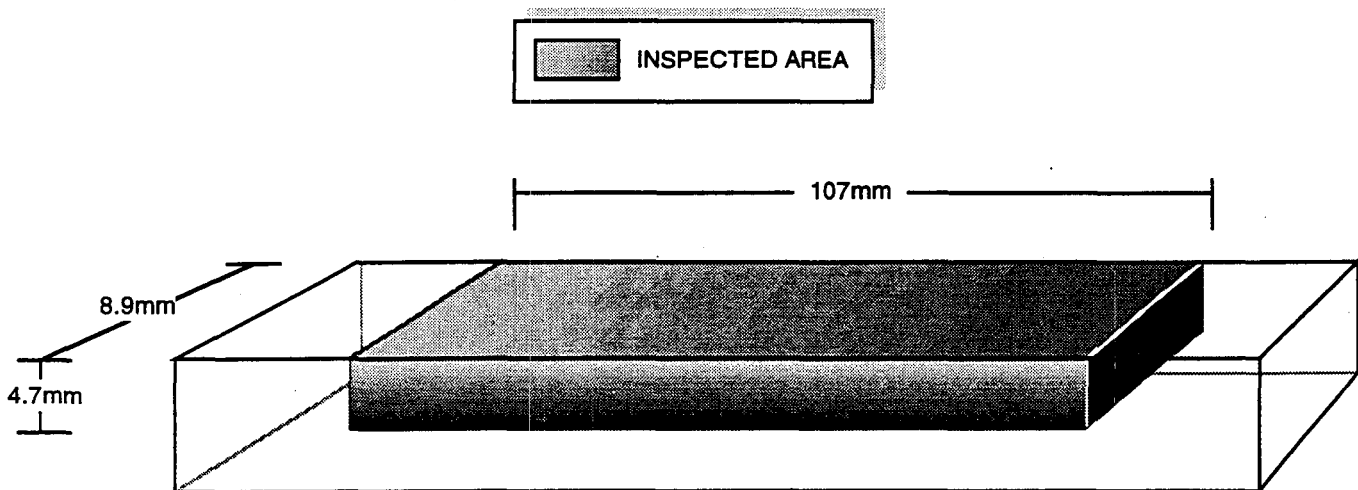
GB8491(06)-15
GB11591-620

Figure 6-20. Acoustic Microscopy Inspections Revealed Variations In Tensile Rods That Were Tested As-Received.

In addition to the transverse marks in Figure 6-19, several tensile specimens were documented during visual inspection that contained atypical machining "chatter" marks and were remachined and reinspected prior to testing (Figure 6-19, expanded view). Several other tensile specimens exhibited similar surface wave indications (Figure 6-20, expanded view), but were not identified during visual inspection as requiring remachining prior to testing. Surface wave inspections of the flexure specimens showed less surface variation than the tensile specimens except near the chamfered edges. On the large (E-size) specimens, some of the chamfer indications appeared to have some subsurface extent because they were also detected in the near-surface scans.

Volumetric AM was performed on selected large flexure specimens, diametral compression disks, and on spin disks. For the flexure specimens, the volumetric inspections were limited to the volume immediately below the tensile surface, as shown in Figure 6-21. The volumetric inspection area of the spin disk was limited by the available transducers and access at the shaft. The inspected area is shown in Figure 6-22.

The volumetric inspections revealed material variations from specimen to specimen. Two distinct material conditions were observed. The first was specimens (flexure, diametral compression, and spin disks) with few or no indications exceeding the amplitude of the reference reflector threshold (25 to 50 mm, depending on the zone) set during calibration. If indications were detected in these materials, they tended to be relatively large in extent and much higher amplitude than the response of the reference reflector. A typical scan of this type specimen is shown in Figure 6-7. In this figure, the amplitude is higher than the amplitude of a 50 mm reference reflector at the same depth. Other specimens had many small, low-amplitude indications throughout the material. The amplitude was similar to the amplitude from the 25 mm reference reflector.



GC11591-621

Figure 6-21. E-Size Flexure Specimens Received Partial Volumetric Inspection With Acoustic Microscopy

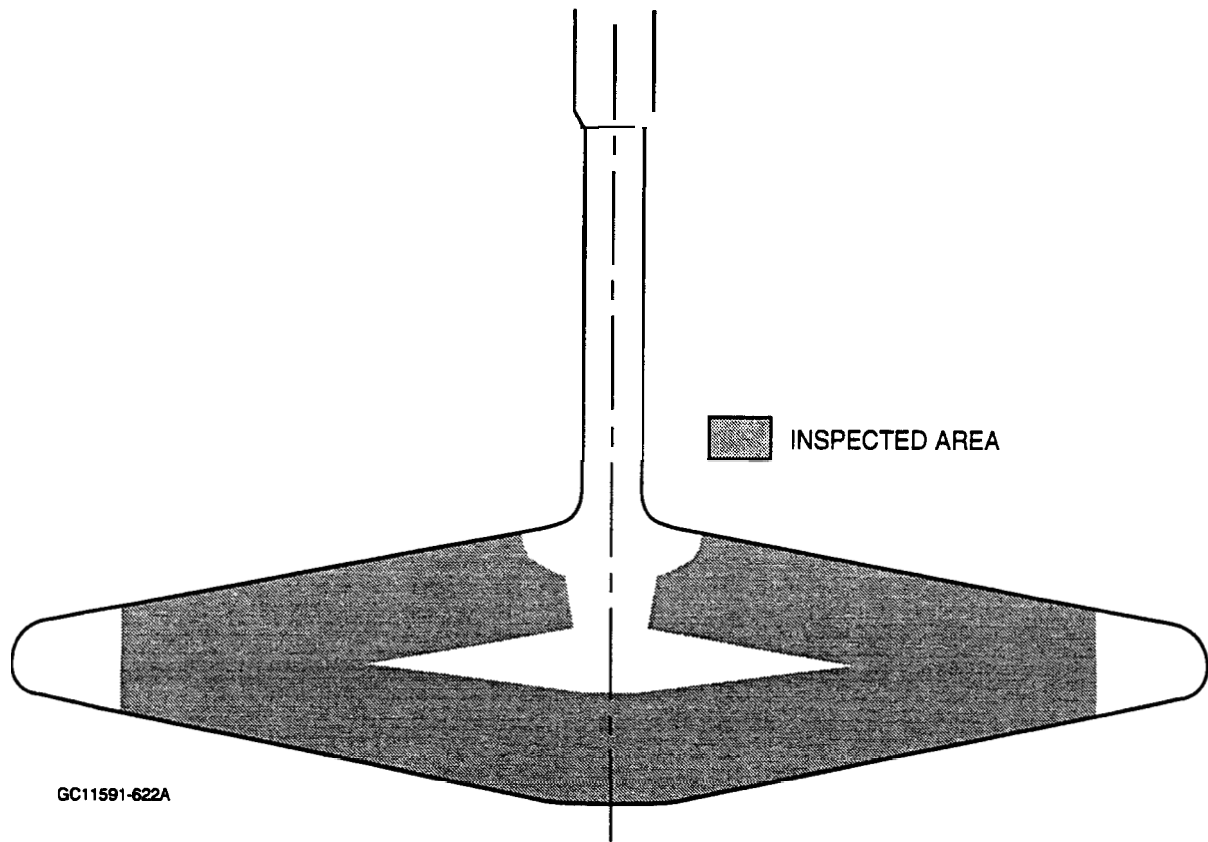
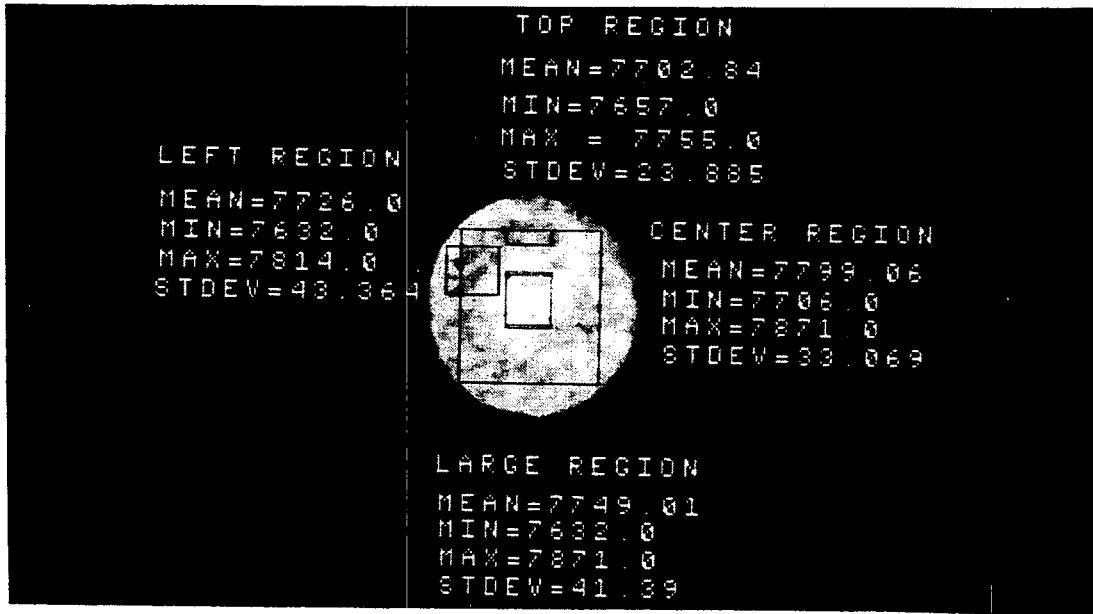


Figure 6-22. Spin Disk Inspection Coverage During Acoustic Microscopy Included Most Of Disk.

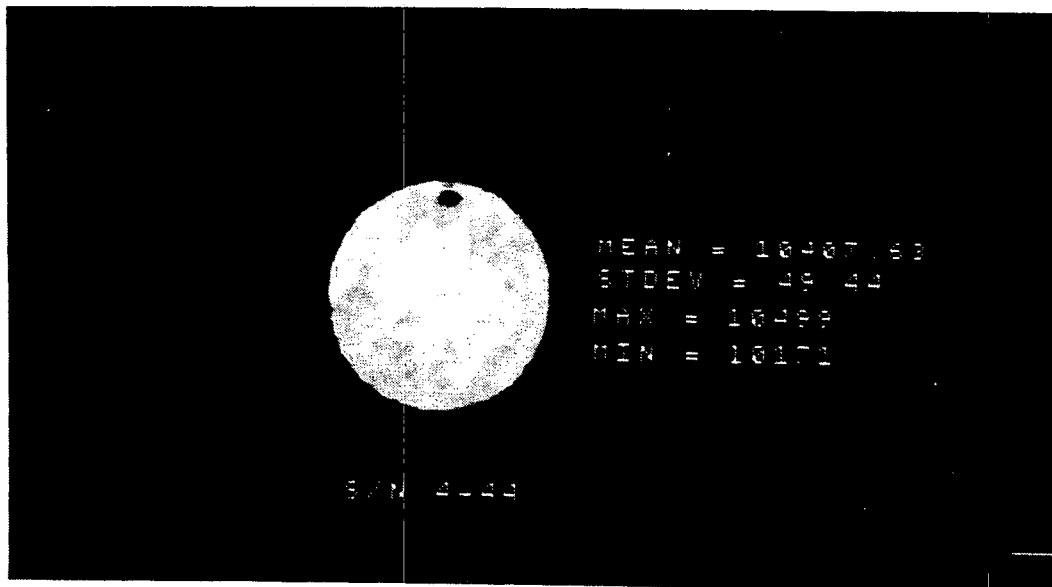
Radiographic (RT) and computed tomographic (CT) inspections revealed a number of specimens having apparent density variations. Based on the radiographic development work, component inspection was limited to two film speeds, and all films were exposed to achieve a nominal 2.0 density. Some specimens exhibited discrete high- or low-density indications in both CT and RT, while others showed more diffuse variations. Figure 6-23 show typical discrete and diffuse indications observed during CT. The indications revealed by the CT inspection were not detected during visual evaluation of the radiographic film of the same specimen. Film radiographic evaluation was compounded by numerous nonrelevant indications from the processing and grain variations, which greatly reduced the confidence in the inspection.

6.5 Data Review And Correlation

The data review and correlation effort was composed of three tasks. The first task was to review and compile the data collected from each method in a usable format. The second task was to compare the data from the various NDE methods and identify possible correlations between the methods; and the third task was to



(a) DIFFUSE INDICATION THROUGHOUT



(b) DISCRETE, LESS DENSE INDICATION

GB8491(06)-17

GB11591-623

Figure 6-23. CT Tensile Rod Inspections Showed Density Variation In Cross Sections.

compare the most suspect indications from the NDE methods with the destructive test data. The volume of data collected made the correlation effort a significant task.

The major portion of the NDE data was acquired on the tensile specimens, large volume flexure specimens, and the spin disks. The correlation effort between the NDE methods and the destructive test data was limited to these specimens. For the tensile specimens, possible NDE method correlation of only one indication was established. Tensile rod S/N 2-98 exhibited a low-density indication 0.08 mm in diameter which correlated with a surface indication from acoustic microscopy (AM). This indication also corresponded to a visually darker, rounded indication on the surface. This particular tensile specimen failed from an internal inclusion at the same location. In a final evaluation of the AM, RT, and destructive (DEST) test data, the RT indications were attributed to the internal indication. Correlation with the internal indication is more likely than with the surface indication, because many other test specimens had indications of similar appearance confirmed visually and by AM, that were not detected by radiography.

The two specimens having the most pronounced radiographic indications, S/Ns 2-62 and 2-73, were not among the specimens selected for computed tomographic (CT) inspection, so no correlation was possible. Three of the fifty specimens receiving CT inspection exhibited apparent more dense indications in the 0.25 mm size range, noted in Table 6-7. None of these indications were confirmed by visual evaluation or digital enhancement of radiographic inspection (RT) films. It is possible that the variations observed during the CT inspection are inherent in the material, which would indicate that the image evaluation threshold should be raised so that these variations are not apparent. None of the CT indications correlated with failure origins.

Review of the large-volume flexure specimens revealed several possible NDE and destructive test data correlation points. In this case, because only a sample of the specimens received volumetric AM inspection, not all internal failures were from specimens that were inspected with all methods. Table 6-8 summarizes the possible data correlation points from all methods.

Some differences were noted between specimen data during AM. Comparison of spin disk and E-size flexure data revealed spin disks exhibited more indications in excess of the reference reflector per unit volume than the E-size flexure specimens. An average of one indication with an amplitude greater than the amplitude of the reference reflector occurred every 1.7 cm^3 in the spin disks, while the flexure specimens exhibited the same type of indication every 4.5 cm^3 . This observation was further investigated by performing inspections of the seeded defect specimens to determine whether the difference in observed indications was due to the difference in the detection between the refracted longitudinal inspection and the normal longitudinal inspection. The large-volume flexure specimens were inspected using refracted longitudinal waves to minimize the edge effects of the specimen.

TABLE 6-7. SUMMARY OF TENSILE SPECIMENS WITH SUSPECT NDE INDICATIONS

Specimen S/N	Inspection Technique	Apparent Indication Size in mm	
		Surface	Internal
1-12	AM	>0.25	--
1-21	AM	>0.25	--
1-22	AM	>0.25	--
2-14	AM	>0.25	--
2-29	AM	>0.25	--
2-40	AM	>0.25	--
2-49	CT	--	0.25, More Dense
2-61	RT	--	>0.25, More Dense
2-69	AM	>0.25	--
2-73	RT	--	>0.25, More Dense
2-88	AM	>0.25	--
2-97	AM	>0.25	--
2-99	AM	>0.25	--
2-141	AM	>0.25	--
2-144	AM	>0.25	--
3-28	AM	>0.25	--
3-33	AM	>0.25	--
3-68	AM	>0.25	--
3-78	AM	>0.25	--
3-80	AM	>0.25	--
3-100	CT	--	0.25, More Dense
3-107	AM	>0.25	--
3-130	AM	>0.25	--
4-17	AM	>0.25	--
4-44	CT	--	0.25, More Dense

AM = Acoustic Microscopy. CT = Computed Tomography. RT = Radiography.

TABLE 6-8. SUMMARY OF E-SIZE FLEXURE SPECIMEN CORRELATION DATA

Specimen S/N	Inspection Methods	Methods Correlating	Location From Left in mm
1-24	RT	RT, DEST	109.2*
2-3	AM, RT	AM, RT	127.0
2-8	AM, RT	AM, DEST	63.5*
2-8	AM, RT	AM, RT	81.3
2-21	RT	RT, DEST	55.9*
2-37	AM, RT	AM, RT	63.5
2-42	AM, RT	AM, RT	76.2
2-55	AM, RT	AM, DEST	68.6*
3-34	RT	RT, DEST	55.9*
* Indicates internal failure at the location where correlation was observed.			
AM = Acoustic Microscopy. RT = Radiography, DEST = Destructive Test.			

The refracted longitudinal inspection was documented to be less sensitive than the straight beam longitudinal inspection. The refracted longitudinal inspections were not originally planned; therefore, no calibration standards were available to determine the sensitivity of the refracted longitudinal inspection relative to a void-like reflector used for establishing sensitivity for other scans. The seeded defect specimens were evaluated to determine whether the lower sensitivity of the refracted longitudinal inspection was effecting detection in the flexure specimens and could therefore explain the observed differences in number of volumetric indications between the spin disks and flexure specimens.

Calculating the number of observed indications per unit volume by seeded inclusion size revealed that for seeded inclusions greater than 100 μm , no difference was noted in detection between the refracted and normal longitudinal inspections. For seeded inclusions in the 25 to 50 μm range, a difference between the refracted and normal longitudinal inspections was noted. The normal longitudinal inspection detected approximately 40 percent more indications per unit volume than the refracted longitudinal inspection. Since the sizes of the indications detected in the spin disks and flexure specimens were not known, it was not possible to determine whether the observed difference in these specimens was due only to the sensitivity variation of the inspection or from a material variation also.

Enhancement and evaluation of images of large flexure specimens was limited to a 30 mm square area in the zone of failure for correlation with AM. The large volume flexure specimens were selected for enhancement, because the rectangular geometry of these bars aided in the ease of enhancement, since no density

before additional enhancement can occur. The large-volume flexure specimens were also the only specimens where correlation with other NDE techniques was observed. The image search area used was 61 mm², which combined with the fact that the images were at 2X projection, resulted in a 30 μm per pixel resolution. On the basis of earlier data, this approach was sufficient for detecting flaws 60 μm and larger, provided that sufficient density variation occurred between the parent material and the defect. The results are shown in Table 6-9. No additional indications were detected when compared to the visual film evaluations; however, the detection of visual indications was improved by the enhancement.

TABLE 6-9. POSSIBLE DEFECTS DETECTED IN ENHANCED IMAGES

Specimen	Possible Defects		Number That Correlate
	Side	Top	
1-13	2	1	1(L)
1-16	0	--	0
1-24	4	4	3(1H)
1-25	2	2	1(L)
2-8	2	1	1(H)
2-21	0	--	0
2-39	2	3	0
2-51	4	**	--
2-52	2	3	0
2-55	0	--	0
3-1	5	3	2
3-5	*	1	1(L)
3-10	7	4	2(H)
3-20	0	--	0
3-33	0	--	0

L Indication of low density inclusion
H Indication of high density inclusion
* Indication in top view out of range on side view
** Image file lost

The seeded defect specimens were evaluated to compare the responses from the seeded defects to the calibration responses for each NDE method and the actual indications from the specimen inspections. The titanium nitride seeded specimens had responses most similar to actual indications noted in the test specimens. For acoustic microscopy, the average amplitudes of the various sizes and types of seeded specimens are compared to calibration and actual indications in Table 6-10. Radiographically, the indications from the 50 and 100 μm titanium nitride inclusions were most similar to the more dense indications observed in the actual specimens.

TABLE 6-10. COMPARISON OF CALIBRATION RESPONSE AMPLITUDES WITH SEEDED DEFECT AMPLITUDES AT 6 mm FOCAL LENGTH

Defect Type	Size μm	Amplitude, mV
Hole	25	113
Hole	50	308
Aluminum Oxide	50	--
Aluminum Oxide	100	187
Titanium Nitride	25	164
Titanium Nitride	50	229
Titanium Nitride	100	Sat*
Tungsten Carbide	25	217
Tungsten Carbide	100	Sat*
*Sat - Saturated		

The seeded defect specimens were evaluated using CT procedures similar to those used for specimen evaluation. Tungsten carbide and titanium nitride seeded defects were detectable through the one-inch cross section when the seed size exceeded the noise threshold. The smallest detectable titanium nitride inclusion was 150 μm , while the smallest detectable tungsten carbide inclusion was 50 μm . The difference in CT number (apparent density measurement for CT) between the parent material and the seeded defect was most similar to the indications observed in the actual specimens for the 150 μm titanium nitride inclusions.

6.6 Conclusions

Several surface and volumetric NDE methods were applied to the inspection of ceramic test specimens and subelements representative of turbine engine components. During the development of these techniques, three methods of fabricating reference standards for calibration and inspection quality control were identified for generating small defects in ceramic materials:

- Laser machining of surface or internal void-like defects
- Photolithographic generation of small void-like defects and bonding them to a defect-free substrate
- Volumetric seeding known inclusions of varying sizes during the actual fabrication process.

Each fabrication method has potential application for future standards development work for ceramic inspection. The first two methods are more appropriate for calibration standards, where precise information about the reference reflector is required. The third method is more appropriate for studies where more accurate simulation of typical material defects is required.

Acoustic microscopy (AM) is a useful technique for both surface and volumetric inspection for small flaw detection. Comparison of AM and radiographic (RT) data indicated that volumetric AM detects some types of flaws better than RT; however, due to the limited amount of data available for correlation, confirmation of this observation requires further investigation.

Computed tomography (CT) data were the most difficult to evaluate, and no correlations were observed between CT data and any other NDE or destructive method. This indicates the defects in the actual specimens were below the detection and imaging threshold of the CT system. Seeded specimen evaluation was promising and indicates that further development of the CT method, possibly through the addition of microfocus CT, may improve the usefulness of CT for small flaw detection.

Digital enhancement of X-ray films for flaw detection will improve detection for interpretation of films by nonspecialists; however, the improvement in defect detection over direct viewing of the film by trained specialists was not demonstrated conclusively during this program. Improved detection through digital enhancement of films is limited by the radiographic technique ability to detect small defects. Since many of the limiting factors are film related, direct digital X-ray imaging offers the most promise for improved detection capabilities; however, to date, no direct digital methods even approach the sensitivity of the films used in this program. High spatial resolution is necessary for detection of small defects (a minimum of 2×2 pixels per defect). This work confirmed the findings of the Nuclear Regulatory Commission (ref 6-5) that at least 12-bit image digitization is required to faithfully reproduce a film radiograph.

Application of the NDE methods for specimen inspection showed that the inherent defects (defects which cause failures) in the mechanical property specimens are at or beyond the limit of detection for the NDE methods applied during this program. Some correlation with defects causing failure was observed, but other defects causing failure were not detected. Some missed defects were expected when the inspection matrices were established, because, effectively, the planned inspections sampled the specimen volume in order to complete the inspections within the schedule of the program. Thus, if a defect was optimally oriented in the sampled volume, the chance for detecting the defect was greater than for a non-ideally located defect in the sample volume, or a defect outside the sample volume. In addition to the missed defects which caused failure, indications were noted in all NDE methods that did not cause failure. The usefulness of NDE methods in

production is dictated by how reliably the NDE technique detects defects at the large end of the normal flaw distribution curve (Figure 6-1). The larger flaws are critical to turbine engine applications in three specific cases: 1) Component design stresses are much lower than specimen failure stresses; therefore, the flaw size that needs to be screened to prevent premature failure is correspondingly larger; 2) Larger components are predicted to have larger flaw sizes, particularly in the tail of the distribution curve; 3) Production components still tend to have larger flaws not normally seen in test specimens. Further work is required to determine the proper inspection sensitivity for each method. Once appropriate inspection sensitivities are established for inspection, NDE technique reliability studies need to be conducted.

REFERENCES - SECTION 6.0

- (6-1) Rodel, J. and Glaeser, A.M., "Production of Controlled Morphology Pore Arrays: Implications and Opportunities," J Amer Ceram Soc 70, 8, pp. 172-176, 1987.
- (6-2) Rodel, J. and Glaeser, A.M., "Photolithography: A New Tool for Ceramic Science," Materials Research Society Symposium Proceedings, 155, pp. 293-306, 1989.
- (6-3) Gilmore, R.S., Tam, K.C., Young, J.D., and Howard, D.R., "Acoustic Microscopy From 10 to 100 MHz for Industrial Applications," Phil Trans Royal Soc, London, A320 pp. 215-235, 1986.
- (6-4) Richerson, D.W. and Johansen, K.M., Ceramic Gas Turbine Engine Demonstration Program Final Report, DARPA Contract No. N00024-76-C-5352, Garrett Turbine Engine Co., Phoenix, AZ, 1982.
- (6-5) Muscara, J., "Review and Evaluation of Technology, Equipment, Codes, and Standards for Digitization of Industrial Radiographic Film," NUREG-1452/GAR, Nuclear Regulatory Commission, Washington, DC, May 1992.

INTERNAL DISTRIBUTION

Central Research Library (2)
Document Reference Section
Laboratory Records Department (2)
Laboratory Records, ORNL RC
ORNL Patent Section
M&C Records Office (3)
C. R. Brinkman
S. A. David

M. K. Ferber
D. R. Johnson (5)
M. A. Karnitz
K. C. Liu
R. W. McClung
V. J. Tennery
S. G. Winslow

EXTERNAL DISTRIBUTION

James H. Adair
University of Florida
Materials Science & Engineering
317 MAE Bldg.
Gainesville, FL 32611-2066

Dennis Assanis
University of Illinois
Dept. of Mechanical Engineering
1206 W. Green Street
Urbana, IL 61801

Mufit Akinc
Iowa State University
322 Spedding Hall
Ames, IA 50011

John M. Bailey
Consultant
Caterpillar, Inc.
P.O. Box 1875
Peoria, IL 61656-1875

Norman C. Anderson
Ceradyne, Inc.
Ceramic-to-Metal Division
3169 Redhill Avenue
Costa Mesa, CA 92626

B. P. Bandyopadhyay
ELID Team
Wako Campus
2-1 Hirosawa Wako-shi
Saitama 351-01
JAPAN

Frank Armatis
3M Company
Building 60-1N-01
St. Paul, MN 55144-1000

David L. Baty
Babcock & Wilcox - LRC
P.O. Box 11165
Lynchburg, VA 24506-1165

Everett B. Arnold
Detroit Diesel Corporation
Mechanical Systems Technology
13400 Outer Drive West
Detroit, MI 48239-4001

M. Brad Beardsley
Caterpillar Inc.
Technical Center Bldg. E
P.O. Box 1875
Peoria, IL 61656-1875

Larry D. Bentsen
BFGoodrich Company
R&D Center
9921 Brecksville Road
Brecksville, OH 44141

Tom Bernecki
Northwestern University
1801 Maple Avenue
Evanston, IL 60201-3135

Bruce Boardman
Deere and Company Technical Ctr.
3300 River Drive
Moline, IL 61265

Steven C. Boyce
Air Force Office of Scientific
Research
AFOSR/NA Bldg. 410
Bolling AFB, DC 20332-6448

P. Brehm (5)
AlliedSignal Engines
2739 E. Washington Street
P.O. Box 52180
Phoenix, AZ 85072-2180

Sherman D. Brown
University of Illinois
Materials Science and
Engineering
105 South Goodwin Avenue
Urbana, IL 61801

Roger Cannon
Rutgers University
P.O. Box 909
Piscataway, NJ 08855-0909

David Carruthers
Kyocera Industrial Ceramics
Company
P.O. Box 2279
Vancouver, WA 98668-2279

James D. Cawley
Case Western Reserve University
Materials Science & Engineering
Cleveland, OH 44106

Nam S. Chang
Chrysler Corporation
12000 Chrysler Drive
Highland Park, MI 48288-0001

Gary M. Crosbie
Ford Motor Company
20000 Rotunda Drive
MD-2313, SRL Building
Dearborn, MI 48121-2053

J. C. Cuccio (5)
AlliedSignal Engines
2739 E. Washington Street
P.O. Box 52180, MS:1302-2Q
Phoenix, AZ 85072-2180

Bill Durako
Sundstrand Aviation Operations
P.O. Box 7002
Rockford, IL 61125-7002

J. J. Eberhardt
U.S. Department of Energy
Office of Transportation Matrl's
CE-34, Forrestal Building
Washington, DC 20585

H. T. Fang (5)
AlliedSignal Engines
2739 E. Washington Street
P.O. Box 52180
Phoenix, AZ 85072-2180

J. P. Gallagher
University of Dayton Research
Institute
300 College Park, JPC-250
Dayton, OH 45469-0120

Stephen T. Gonczy
Allied Signal Research
P.O. Box 5016
Des Plaines, IL 60017

Robert J. Gottschall
U.S. Department of Energy
ER-131, MS:G-236
Washington, DC 20585

Thomas J. Gross
U.S. Department of Energy
Transportation Technologies
CE-30, Forrestal Building
Washington, DC 20585

John P. Gyekenyesi
NASA Lewis Research Center
21000 Brookpark Road, MS:6-1
Cleveland, OH 44135

J. Hartman (5)
AlliedSignal Engines
2739 E. Washington Street
P.O. Box 52180
Phoenix, AZ 85072-2180

Thomas P. Herbell
NASA Lewis Research Center
21000 Brookpark Road, MS:49-3
Cleveland, OH 44135

Osama Jadaan
U. of Wisconsin-Platteville
1 University Plaza
Platteville, WI 53818

Curtis A. Johnson
General Electric Company
P.O. Box 8
Schenectady, NY 12301

Martha R. Kass
U.S. Department of Energy
Oak Ridge Operations
Building 4500N, MS:6269
Oak Ridge, TN 37831-6269

Pramod K. Khandelwal
General Motors Corporation
Allison Gas Turbine Division
P.O. Box 420, MS:W05
Indianapolis, IN 46206

James W. McCauley
Alfred University
Binns-Merrill Hall
Alfred, NY 14802

W. Meade (5)
AlliedSignal Engines
2739 E. Washington Street
P.O. Box 52180
Phoenix, AZ 85072-2180

M. N. Menon (5)
AlliedSignal Engines
2739 E. Washington Street
P.O. Box 52180
Phoenix, AZ 85072-2180

Ken Michaels
Chrysler Motors Corporation
P.O. Box 1118, CIMS:418-17-09
Detroit, MI 48288

A. Peralta (5)
AlliedSignal Engines
2739 E. Washington Street
P.O. Box 52180
Phoenix, AZ 85072-2180

John J. Petrovic
Los Alamos National Laboratory
Group MST-4, MS:G771
Los Alamos, NM 87545

George Quinn
NIST
Ceramics Division, Bldg. 223
Gaithersburg, MD 20899

Maxine L. Savitz
AlliedSignal, Inc.
Ceramic Components
P.O. Box 2960, MS:T21
Torrance, CA 90509-2960

Robert B. Schulz
U.S. Department of Energy
Office of Transportation Matrls.
CE-34, Forrestal Building
Washington, DC 20585

Dinesh K. Shetty
University of Utah
Materials Science and
Engineering
Salt Lake City, UT 84112

Jay R. Smyth
AlliedSignal Engines
111 S. 34th Street, MS:503-412
Phoenix, AZ 85034

J. Z. Song (5)
AlliedSignal Engines
2739 E. Washington Street
P.O. Box 52180
Phoenix, AZ 85072-2180

T. Strangman (5)
AlliedSignal Engines
2739 E. Washington Street
P.O. Box 52180
Phoenix, AZ 85072-2180

Thomas N. Strom
NASA Lewis Research Center
21000 Brookpark Road, MS:86-6
Cleveland, OH 44135

Janet Wade (5)
AlliedSignal Engines
P.O. Box 52180, MS:1303-2
Phoenix, AZ 85072-2180

Thomas J. Whalen
Ford Motor Company
SRL Bldg., Mail Drop 2313
P.O. Box 2053
Dearborn, MI 48121-2053

Sheldon M. Wiederhorn
NIST
Building 223, Room A329
Gaithersburg, MD 20899

J. M. Wimmer (5)
Supervisor
AlliedSignal Engines
2739 E. Washington Street
P.O. Box 52180, MS:1302-2P
Phoenix, AZ 85072-2180

D. C. Wu (5)
AlliedSignal Engines
2739 E. Washington Street
P.O. Box 52180
Phoenix, AZ 85072-2180

Department of Energy
Oak Ridge Operations Office
Asst. Manager for Energy
Research and Development
P.O. Box 2001
Oak Ridge, TN 37831-8600

Department of Energy
Office of Scientific and
Technical Information
Office of Information Services
P.O. Box 62
Oak Ridge, TN 37831